

SECURITY INFORMATION N-22111

AD-B184 362

CONFIDENTIAL  
CLASSIFIED

Copy 325

~~Hartfield today 7-10~~

NATIONAL ADVISORY COMMITTEE  
FOR AERONAUTICS

(1)

NACA CONFERENCE ON AIRCRAFT  
LOADS, FLUTTER, AND STRUCTURES

A COMPILATION OF THE PAPERS PRESENTED

Langley Aeronautical Laboratory  
Langley Field, Va.

DTIC  
SELECTED  
MAY 19 1994  
SF D

MARCH 2-4, 1953

CLASSIFICATION CHANGE

"DTIC USERS ONLY"

UNCLASSIFIED  
By Authority of NASA GEN S-7 DTD 6-29-66  
Classified by K.A. Karpow Date 1/1/81



94 5 17 087

CLASSIFIED DOCUMENT

This material contains information affecting the National Defense of the United States within the meaning of the espionage laws, Title 18, U.S.C., Secs. 793 and 794, the transmission or revelation of which in any manner to an unauthorized person is prohibited by law.

SECURITY INFORMATION

94-14783



UNCLASSIFIED

CONFIDENTIAL

UNCLASSIFIED

NACA CONFERENCE ON  
AIRCRAFT LOADS, FLUTTER, AND STRUCTURES  
A Compilation of the Papers Presented

Langley Aeronautical Laboratory  
Langley Field, Va.

March 2-4, 1953

Accession For	
NTIS	CRA&I
DTIC	FAB
Unannounced	
Justification	
By	
Distribution /	
Availability Codes	
Dist	Avail and/or Special
12	

"DTIC USERS ONLY"

DTIC QUALITY INDEX RATED 3

CONFIDENTIAL

UNCLASSIFIED

~~CONFIDENTIAL~~

TABLE OF CONTENTS

	Page
INTRODUCTION . . . . .	ix
LIST OF CONFEREES . . . . .	xi
TECHNICAL PAPERS PRESENTED	
GENERAL CHAIRMAN: Richard V. Rhode	
SESSION CHAIRMAN: Floyd L. Thompson	
FACTORS INFLUENCING MAXIMUM LOADS . . . . .	1
1. Some Notes on Maximum Lift and Pitch-Up in Relation to Maximum Load Factors . . . by George S. Campbell . . . . .	3
2. Investigation of the Use of Controls During Service Operations of Fighter Airplanes . . . by John P. Mayer, Carl R. Huss, and Harold A. Hamer . . . . .	11
3. Loads Experienced in Flight in Regions of Reduced Stability by Hubert M. Drake, Glenn H. Robinson, and Albert E. Kuhl . . . . .	25
LOAD DISTRIBUTION ON LIFTING SURFACES . . . . .	33
4. Prediction of the Load Distribution on Sweptback Wings . . by Harold J. Walker and William C. Maillard . . . . .	35
5. A Study of Aerodynamic Loads on Sweptback Wings at Transonic Speeds . . . by Claude V. Williams and Richard E. Kuhn . . . . .	49
6. Wing Loads as Affected by Auxiliary Devices . . . by Wilbur H. Gray and Jack F. Runckel . . . . .	63
7. Loadings on Thin Wings at Supersonic Speeds . . . by John E. Hatch, Jr., and Kenneth Margolis . . . . .	71
LOADS ON BODIES, INTERFERENCE EFFECTS, AND EXTERNAL STORES . . . .	83
8. Division of Loads for Various Wing-Fuselage Combinations . by Clarence L. Gillis . . . . .	85

<sup>111</sup>  
~~CONFIDENTIAL~~  
~~UNCLASSIFIED~~

CONFIDENTIAL

UNCLASSIFIED

Page

9. Some Effects of Body Shape and Wing Position on the Loading on Sweptback-Wing—Body Combinations at Transonic Speeds . . . by Donald L. Loving . . . . .	99
10. The Effects of Angle of Attack and Wing Incidence on the Loadings on a Rectangular Wing and Body Combination at Supersonic Speeds . . . by Jack N. Nielsen and William C. Pitts . . . . .	109
11. Aerodynamic Loads Associated With External-Store Installations . . . by H. Norman Silvers and Thomas C. O'Bryan . . . . .	119
<b>LOADS ASSOCIATED WITH CONTROLS . . . . .</b>	<b>133</b>
12. Load Distributions Associated With Controls At Supersonic Speeds . . . by Douglas R. Lord and K. R. Czarnecki .	135
13. Loads Due to Flaps and Spoilers on Sweptback Wings at Subsonic and Transonic Speeds . . . by Alexander D. Hammond and Franklin E. West, Jr. . . . . .	153
<b>TAIL LOADS . . . . .</b>	<b>167</b>
14. Some Measurements of Tail Loads in Flight at High Speeds by John T. Rogers, George E. Cothren, and Richard D. Banner . . . . .	169
15. Analytical Study of Sideslip in Rolls During High g Maneuvers . . . by Ralph W. Stone . . . . .	175
16. Effects of Horizontal-Tail Height, Fuselage Size, and Wing Height on Vertical-Tail Loads . . . by Alex Goodman and Harleth G. Wiley . . . . .	187
<b>TECHNIQUE FOR FLIGHT LOADS MEASUREMENTS . . . . .</b>	<b>199</b>
17. A Strain-Gage Calibration Procedure for Flight Loads Measurements . . . by T. H. Skopinski . . . . .	201

CONFIDENTIAL  
UNCLASSIFIED

## CONFIDENTIAL

Page

SESSION CHAIRMAN: Hartly A. Soule

GUST LOADS . . . . .	209
18. The Variation of Atmospheric Turbulence With Altitude and Its Effect on Airplane Gust Loads . . . by Robert L. McDougal, Thomas L. Coleman, and Philip L. Smith . . .	211
19. Theoretical Lift Developed on Rectangular Wings Entering Gusts at Subsonic and Supersonic Speeds . . . by Harvard Lomax . . . . .	227
20. Some Recent Flight-Test Results Relating to Gust Loads . by Jack Funk, Harry C. Mickleboro, and Richard H. Rhyne . . . . .	239
21. Loads on a Tailless Missile in Rough Air . . . by A. James Vitale . . . . .	245
FLUTTER AND BUFFETING . . . . .	255
22. Some Remarks on the Theoretical Aspects of Unsteady Air- Force Coefficients . . . by Charles E. Watkins, Harry L. Runyan, and Julian H. Berman . . . . .	257
23. Some Effects of Wing Profile on the Two-Dimensional Flutter Derivatives for Wings Oscillating in Pitch at High Subsonic Speeds . . . by John A. Wyss . . . . .	275
24. Discussion of Three-Dimensional Oscillating Air Forces Based on Wind-Tunnel Measurements . . . by Sherman A. Clevenson and Sumner A. Leadbetter . . . . .	287
25. Flutter Investigation of Wing Plan Forms at Transonic Speeds . . . by Hugh C. DuBose and Laurence K. Loftin, Jr. . . . .	295
26. Tunnel Experiments With Dynamic Flutter Models Relating to the Effects of External Stores . . . by Dennis J. Martin and John L. Sewall . . . . .	303
27. Experiments on Panel Flutter . . . by John E. Baker and Maurice A. Sylvester . . . . .	313

## CONFIDENTIAL

	Page
28. Flight Flutter Experiences With Spoilers on Swept Wings and With Triangular Wings . . . by David G. Stone and Richard I. Sears . . . . .	319
29. Some Observations on Stall Flutter and Buffeting . . . by A. Gerald Rainey . . . . .	327
30. Study of Fluctuating Forces and Wakes on Two-Dimensional Airfoils . . . by Charles F. Coe, Perry P. Polentz, and Milton D. Humphreys . . . . .	339
31. Pressure Fluctuations Due to Jets . . . by Leslie W. Lassiter and Harvey H. Hubbard . . . . .	353
<b>LANDING LOADS</b> . . . . .	<b>361</b>
32. An Experimental Investigation of Wheel Spin-Up Drag Loads by Benjamin Milwitzky and Dean C. Lindquist . . . . .	363
33. Some Measurements of Static Deflections and Yawed Rolling Characteristics of Large Tires . . . by Upshur T. Joyner and Walter B. Horne . . . . .	379
34. Some Measurements of Landing Contact Conditions of Transport Aircraft in Routine Operations . . . by Norman S. Silsby and Emanuel Rind . . . . .	389
35. A Study of the Effects of Interaction Between a Nonlinear Landing Gear and a Flexible Airframe During Landing Impact . . . by Francis E. Cook and Benjamin Milwitzky . . . . .	397
36. Estimation of Water Landing Loads on Hydro-Ski Equipped Aircraft . . . by Emanuel Schnitzer . . . . .	407
<b>LOADS IN CRASH LANDINGS</b> . . . . .	<b>421</b>
37. Accelerations and Harness Forces Measured in Full-Scale Crash Studies . . . by Jacob C. Moser . . . . .	423

## CONFIDENTIAL

Page

SESSION CHAIRMAN: Robert R. Gilruth

FATIGUE . . . . .	435
38. Some Recent Research in Fatigue of Aircraft Materials by Herbert F. Hardrath and Walter Illg . . . . .	437
39. Results of Constant-Level Fatigue Tests of C-46 Wing Structures . . . by M. James McGuigan, Jr. . . . .	449
STRUCTURAL HEATING . . . . .	457
40. Recent Research on Aerodynamic Heating at Supersonic Speeds . . . by Leo T. Chauvin and Joseph P. Maloney .	459
41. Supersonic Jet Tests of Simplified Wing Structures . . . by Richard R. Heldenfels and Richard J. Rosecrans . . .	465
42. Transient Temperature Distribution in an Aerodynamically Heated Multiweb Wing . . . by George E. Griffith . . .	475
43. Structural Efficiencies of Various Aluminum, Titanium, and Steel Alloys at Elevated Temperatures . . . By George J. Heimerl and Philip J. Hughes . . . . .	483
44. An Investigation of Strength Characteristics of Structural Elements at Elevated Temperatures . . . by Eldon E. Mathauser and Charles Libove . . . . .	493
STRESSES AND DEFLECTION . . . . .	505
45. Remarks on Stress Analysis of Circular Semimonocoque Cylinders With Rectangular Cutouts . . . by Harvey G. McComb, Jr., and Floyd R. Schlechte . . . . .	507
46. A Simple Method of Analysis of Swept-Wing Deflections . . by William A. Brooks, Jr., and George W. Zender . . . .	517
STRENGTH . . . . .	529
47. Some Recent Data on the Strength Characteristics of Wings With Thick Skins . . . by Roger A. Anderson, Richard A. Pride, and Aldie E. Johnson, Jr. . . . . .	531

## CONFIDENTIAL

	Page
48. A Study of Integrally Stiffened Plates . . . by Norris F. Dow, Charles Libove, and L. Ross Levin . . . . .	543
49. Calculations on Plastically Orthotropic Sheet . . . by Elbridge Z. Stowell and Richard A. Pride . . . . .	555
DYNAMICS . . . . .	563
50. Moment of Inertia and Damping of Fluid in Tanks Undergoing Pitching Oscillations . . . by Edward Widmayer, Jr., and James R. Reese . . . . .	565
51. Correlation of Calculation and Flight-Test Studies of the Effect of Wing Flexibility on Structural Response Due to Gusts . . . by John C. Houbolt . . . . .	573
52. On Traveling Waves in Beams . . . by Robert W. Leonard and Bernard Budiansky . . . . .	583
53. Shear-Lag Effects in Beam Vibrations and the Substitute- Stringer Approach . . . by William W. Davenport and Edwin T. Kruszewski . . . . .	591

CONFIDENTIAL

**INTRODUCTION**

This document contains reproductions of technical papers on some of the most recent research results on aircraft loads, flutter, and structures from the NACA Laboratories. These papers were presented by members of the staff of the NACA Laboratories at the NACA Conference held at the Langley Aeronautical Laboratory March 2-4, 1953. The primary purpose of this conference was to convey to contractors of the military services and others concerned with the design of aircraft these recent research results and to provide those attending an opportunity to discuss the results.

The papers in this document are in the same form in which they were presented at the conference in order to facilitate their prompt distribution. The original presentation and this record are considered as complementary to, rather than as substitutes for, the Committee's more complete and formal reports.

A list of the conferees is included.

CONFIDENTIAL

## CONFIDENTIAL

## LIST OF CONFEREES

The following were registered at the NACA Conference on Aircraft Loads, Flutter, and Structures, Langley Aeronautical Laboratory, Langley Field, Va., March 2-4, 1953:

ABBOTT, Ira H.	NACA Headquarters
ADES, Clifford S.	Bendix Aviation Corp.
ALLEN, Ralph W.	NAMTC - Point Mugu, Calif.
ALLEN, Robert	Civil Aeronautics Administration
AMBROSE, Lt. Col. Elmer E., USAF	NACA Subcommittee on High-Speed Aerodynamics
AMES, Milton B.	NACA Headquarters
ANDERSON, Maj. Philip B., Jr.	Wright Air Development Center
ANDERSON, Roger A.	NACA - Langley Laboratory
ARKUS-DUNTOV, Yura	Curtiss-Wright Corp.
ARNOLD, Jack A.	Stanley Aviation
ATKINSON, R. J.	British Ministry of Supply
BAILEY, F. J., Jr.	NACA - Langley Laboratory
BAIRD, Eugene F.	Grumman Aircraft Engineering Corp.
BAKER, John E.	NACA - Langley Laboratory
BANK, Herman	Jet Propulsion Laboratory - C.I.T.
BECK, Edgar	NACA Headquarters
BECKER, John V.	NACA - Langley Laboratory
BECKETT, Lt. Col. Walter R., USAF	AFDFR - Langley AFB, Va
BERLER, Irving	Sperry Gyroscope Co.
BERMAN, Julian H.	NACA - Langley Laboratory
BIOLETTI, Carlton	NACA - Ames Laboratory
BIRD, John D.	NACA - Langley Laboratory
BISPLINGHOFF, Raymond L.	NACA Subcommittee on Aircraft Structures
BLOM, Trygve	Wright Air Development Center
BLOMQUIST, Richard F.	Forest Products Laboratory
BOSONETTO, Henry A.	General Motors Corp.
BOUTON, Innes	NACA Subcommittee on Aircraft Loads
BOWMAN, Richard	Republic Aviation Corp.
BREUER, Delmar W.	USAF Institute of Technology
BREWER, Jack	NACA Headquarters
BRIGHT, Philip N.	General Motors Corp.
BROOKS, Doyle T., Jr.	TEMCO Aircraft Corp.
BROOKS, William A., Jr.	NACA - Langley Laboratory
BROWN, Harvey H.	NACA Headquarters
BRYAN, Guy Lee	Research & Development Board
BUCKLEY, Edmond C.	NACA - Langley Laboratory
BUDIANSKY, Bernard	NACA - Langley Laboratory
BUTERBAUGH, Floyd F.	NADC - Johnsville, Pa.
BUTLER, Joseph P.	Boeing Airplane Co.

## CONFIDENTIAL

CALHOUN, John T.	Beech Aircraft Corp.
CAMPBELL, George S.	NACA - Langley Laboratory
CANTWELL, Raymond A.	Headquarters - ARDC
CENTER, Kenneth W.	Grumman Aircraft Engineering Corp.
CHAPLIN, Harvey R.	Naval Ordnance Laboratory
CHARAK, Mason T.	NACA Headquarters
CHAUVIN, Leo T.	NACA - Langley Laboratory
CHEILEK, Harold A.	Cornell Aeronautical Laboratory
CHILDERS, Milford G.	Lockheed Aircraft Corp.
CLARKE, Martyn V.	Civil Aeronautics Board
CLEVENSON, Sherman A.	NACA - Langley Laboratory
CLOUSING, Lawrence A.	NACA - Ames Laboratory
COE, Charles F.	NACA - Ames Laboratory
COLEMAN, Donald G.	Forest Products Laboratory
COLEMAN, Thomas L.	NACA - Langley Laboratory
CONLON, Emerson W.	NACA Committee on Aircraft Construction
COOK, Francis E.	NACA - Langley Laboratory
COOPER, George E.	NACA - Ames Laboratory
COX, William E.	Northrop Aircraft, Inc.
CREEL, Ralph L.	NACA Subcommittee on Aircraft Structures
CROSSFIELD, A. S.	NACA High-Speed Flight Research Station
CROSSLAND, Frank J.	Boeing Airplane Co.
CROWLEY, John M.	Office of Naval Research
CUMMINGS, John L.	General Electric Co.
CZARNECKI, K. R.	NACA - Langley Laboratory
DANFORTH, Clarence E.	General Electric Co.
DAUM, Fred L.	Wright Air Development Center
DAVENPORT, William W.	NACA - Langley Laboratory
DAWSON, John R.	NACA - Langley Laboratory
DE LOS SANTOS, Socrates T.	David Taylor Model Basin
DEUTSCHMAN, Jerome N.	Bell Aircraft Corp.
DEVINE, Robert L., Jr.	Project Meteor - M.I.T.
DEYARMOND, Albert B.	Ryan Aeronautical Co.
DIEHL, Capt. W. S., USN (Ret.)	NACA Subcommittee on Stability and Control
DILL, Douglas G.	Douglas Aircraft Co., Inc.
DILWORTH, John A., III	Consolidated Vultee Aircraft Corp.
DOLKAS, Constantine	Fairchild Engine and Airplane Corp.
DONEY, Philip	NACA - Langley Laboratory
DONLAN, Charles J.	NACA - Langley Laboratory
DONOVAN, Allen F.	NACA Subcommittee on Vibration and Flutter
DOTY, Ralph J., Jr.	Boeing Airplane Co.
DOUGHERTY, James E., Jr.	NACA Subcommittee on Aircraft Structural Materials
DOW, Norris F.	NACA - Langley Laboratory
DRAKE, Hubert M.	NACA High-Speed Flight Research Station
DRALEY, Eugene C.	NACA - Langley Laboratory
DRINKWATER, William D.	NOTS - Inyokern

**CONFIDENTIAL**

DRYDEN, Hugh L.	NACA Headquarters
DUBERG, John E.	NACA - Langley Laboratory
DuBOSE, Hugh C.	NACA - Langley Laboratory
DUNN, Maurice B.	Boeing Airplane Co.
ELY, Lt. Col. Lawrence H.	Headquarters - ARDC
EPSTEIN, Albert	Republic Aviation Corp.
ERICKSON, Albert L.	NACA - Ames Laboratory
FANTI, Roy	United Aircraft Corp.
FEARNOW, Dwight	Civil Aeronautics Administration
FEDZIUK, Henry A.	NACA - Langley Laboratory
FERO, Lester K.	Bell Aircraft Corp.
FIEDLER, Henry	Northrop Aircraft, Inc.
FOOTE, Joe R.	Wright Air Development Center
FORMHALS, Edward J.	Bureau of Aeronautics
FREDERICKS, Carl	Wright Air Development Center
FRIEND, Carl	Lockheed Aircraft Corp.
FUNG, Yuan Cheng	California Institute of Technology
FUNK, Jack	NACA - Langley Laboratory
GARRICK, I. E.	NACA - Langley Laboratory
GASKELL, Chester W., Jr.	Douglas Aircraft Co., Inc.
GATEWOOD, Buford E.	USAF Institute of Technology
GEISSLER, Ernst D.	Redstone Arsenal
GILLIS, Clarence L.	NACA - Langley Laboratory
GILRUTH, Robert R.	NACA - Langley Laboratory
GILSON, Robert D.	Fairchild Engine and Airplane Corp.
GILSTAD, Douglas A.	NACA Subcommittee on Aircraft Loads
GOLDIN, Robert	Bell Aircraft Corp.
GOODMAN, Alex	NACA - Langley Laboratory
GORANSON, R. Fabian	NACA Headquarters
GOUGH, Melvin N.	NACA - Langley Laboratory
GRAY, Wilbur H.	NACA - Langley Laboratory
GREEN, G. Garner	NACA Subcommittee on Aircraft Structures
GREENE, Hubert L.	Redstone Arsenal
GREENE, L. P.	NACA Subcommittee on High-Speed Aerodynamics
GRIFFITH, George E.	NACA - Langley Laboratory
HALCIN, Edward J.	Douglas Aircraft Co., Inc.
HALL, Claude H.	TEMCO Aircraft Corp.
HALSEY, Robert M.	Civil Aeronautics Administration
HAMER, Harold A.	NACA - Langley Laboratory
HAMMOND, Alexander D.	NACA - Langley Laboratory
HARDRATH, Herbert F.	NACA - Langley Laboratory
HARRINGTON, J. H.	NACA Subcommittee on Aircraft Loads
HARRIS, Thomas A.	NACA - Langley Laboratory

## CONFIDENTIAL

HARRISON, Marvin	Eastman Kodak Co.
HATCH, John E., Jr.	NACA - Langley Laboratory
HATELEY, James C.	North American Aviation, Inc.
HATHAWAY, Melvin E.	NACA - Langley Laboratory
HAYNES, Emanuel	Headquarters - ARDC
HEDRICK, Ira G.	Grumman Aircraft Engineering Corp.
HEIMERL, George J.	NACA - Langley Laboratory
HELDENFELS, Richard R.	NACA - Langley Laboratory
HERZOG, Albrecht J.	Wright Air Development Center
HIGGINS, Thomas P., Jr.	The RAND Corporation
HILL, Paul R.	NACA - Langley Laboratory
HOBEN, Harold E.	American Airlines, Inc.
HODGES, Beverly W.	Boeing Airplane Co.
HONG, James	Lockheed Aircraft Corp.
HOOD, Manley J.	NACA - Ames Laboratory
HORNE, Walter B.	NACA - Langley Laboratory
HOUBOLT, John C.	NACA - Langley Laboratory
HREBEC, Capt. George M.	Headquarters - SAC
HUBBARD, Harvey H.	NACA - Langley Laboratory
HUDSON, Francis L.	Project Thor - Johns Hopkins Univ.
HUGHES, Philip J.	NACA - Langley Laboratory
HULTZ, Burton E.	Air Technical Intelligence Center - Wright-Patterson AFB, Ohio
HUMPHREYS, Milton D.	NACA - Langley Laboratory
HUNTLEY, Harold W.	North American Aviation, Inc.
HUNTZINGER, Richard S.	NADC - Johnsville, Pa.
HUSIC, William J.	Civil Aeronautics Administration
HUSS, Carl R.	NACA - Langley Laboratory
ILLG, Walter	NACA - Langley Laboratory
JABLECKI, Lt. Col. Leon S.	Headquarters - ARDC
JENKINS, David R., III	Battelle Memorial Institute
JENNEY, William W.	Douglas Aircraft Co., Inc.
JEPPESEN, Gordon L.	Goodyear Aircraft Corp.
JEWETT, Frederic D.	The Glenn L. Martin Co.
JOHNSON, Aldie E., Jr.	NACA - Langley Laboratory
JOHNSON, H. Clay	NACA Subcommittee on Vibration and Flutter
JOHNSON, J. B.	NACA Subcommittee on Aircraft Structural Materials
JOHNSTON, J. Ford	Lockheed Aircraft Corp.
JOYNER, Upshur T.	NACA - Langley Laboratory
KAMM, Robert W.	Arnold Engineering Development Center
KANTOR, Lt. Morton	Bureau of Aeronautics
KAPLAN, Carl	NACA - Langley Laboratory
KEARNS, J. P.	APL - Johns Hopkins Univ.
KELLER, Ernest G.	General Electric Co.

## CONFIDENTIAL

KELLY, Curtis	Wright Air Development Center
KERLEY, James J., Jr.	Vitro Corporation of America
KINTAS, John	Beech Aircraft Corp.
KIRK, Donald R.	NACA Committee on Aircraft Construction
KLEPINGER, Richard H.	Wright Air Development Center
KLINKE, Gordon M.	NACA Subcommittee on Aircraft Structural Materials
KNEMEYER, Franklin H.	NOTS - Inyokern
KOCH, Charles	The Glenn L. Martin Co.
KOEGLER, Richard K.	Cornell Aeronautical Laboratory
KOTCHER, Ezra	Wright Air Development Center
KREBS, Charles V.	Civil Aeronautics Administration
KRUSZEWSKI, Edwin T.	NACA - Langley Laboratory
KUHL, Albert E.	NACA High-Speed Flight Research Station
KUHN, Paul	NACA - Langley Laboratory
KUHN, Richard E.	NACA - Langley Laboratory
KULLAS, Albert J.	The Glenn L. Martin Co.
KUNEN, Alfred	Republic Aviation Corp.
KVILJORD, Arnold	NAMC - Philadelphia, Pa.
LARSEN, Harold C.	USAF Institute of Technology
LASSITER, Leslie W.	NACA - Langley Laboratory
LATHAM, Maj. Donald R.	AFDFR - Moffett Field, Calif.
LAUBER, J. Edward	Douglas Aircraft Co., Inc.
LAVENDER, Robert E.	Redstone Arsenal
LEADBETTER, Sumner A.	NACA - Langley Laboratory
LEONARD, Robert W.	NACA - Langley Laboratory
LEVIN, L. Ross	NACA - Langley Laboratory
LEVY, Samuel	NACA Subcommittee on Aircraft Structures
LINDQUIST, Dean C.	NACA - Langley Laboratory
LIPPMAN, Hugh S.	Wright Air Development Center
LITTLE, Alfred A., II	NAMC - Philadelphia, Pa.
LOFTIN, Laurence K., Jr.	NACA - Langley Laboratory
LOMAX, Harvard	NACA - Ames Laboratory
LORD, Douglas R.	NACA - Langley Laboratory
LOUDEN, F. A.	NACA Committee on Aerodynamics
LOVE, Sol	United Aircraft Corp.
LOVING, Donald L.	NACA - Langley Laboratory
LUECHT, John W.	Chrysler Corp.
LUECK, Capt. David W., USAF	NACA Subcommittee on Aircraft Loads
LUNDQUIST, Eugene E.	NACA - Langley Laboratory
LUNN, Rose E.	North American Aviation, Inc.
LUNNEY, Edward J.	Wright Air Development Center
MADSEN, Alfred P.	Consolidated Vultee Aircraft Corp.
MALONEY, Joseph P.	NACA - Langley Laboratory
MANGURIAN, George N.	Northrop Aircraft, Inc.

## CONFIDENTIAL

MANONI, Lawrence R.	United Aircraft Corp.
MANSON, Samuel	NACA - Lewis Flight Propulsion Laboratory
MARGOLIS, Kenneth	NACA - Langley Laboratory
MARTIN, Dennis J.	NACA - Langley Laboratory
MATHAUSER, Eldon E.	NACA - Langley Laboratory
MATHEWS, Kenneth C.	Cook Research Laboratory
MATHEY, Austin V.	Curtiss-Wright Corp.
MATTHEWS, Clarence B.	Boeing Airplane Co.
MAYER, John P.	NACA - Langley Laboratory
MCBREARTY, Jerome F.	NACA Committee on Aircraft Construction
McCOMB, Harvey G., Jr.	NACA - Langley Laboratory
McDOUGAL, Robert L.	NACA - Langley Laboratory
McGUGAN, M. James, Jr.	NACA - Langley Laboratory
MELLQUIST, Victor G.	Aircraft Industries Association of America, Inc.
MEVAY, Frank	Republic Aviation Corp.
MICKLEBORO, Harry C.	NACA - Langley Laboratory
MICKS, William R.	The RAND Corporation
MILLER, William B.	NACA Subcommittee on Aircraft Structures
MILWITZKY, Benjamin	NACA - Langley Laboratory
MINHINNICK, I. T.	British Ministry of Supply
MIROWITZ, Leo I.	McDonnell Aircraft Corp.
MITCHELL, Nathan I.	Consolidated Vultee Aircraft Corp.
MONROE, Lt. Comdr. Gerald M.	Bureau of Aeronautics
MORTON, Earl E.	Fairchild Engine and Airplane Corp.
MOSELEY, David L.	Douglas Aircraft Co., Inc.
MOSER, Jacob C.	NACA - Lewis Flight Propulsion Laboratory
MYKYTOW, Walter	Wright Air Development Center
NEPPEL, Arthur B.	David Taylor Model Basin
NIELSEN, Jack N.	NACA - Ames Laboratory
O'BRYAN, Thomas C.	NACA - Langley Laboratory
O'MALLEY, James A., Jr.	Bell Aircraft Corp.
OSBORN, Earl P.	NACA Subcommittee on Aircraft Loads
PAHL, John F.	Civil Aeronautics Board
PALMER, Carl	NACA Headquarters
PARKINSON, John B.	NACA - Langley Laboratory
PEARSON, E. O.	NACA Headquarters
PEARSON, Henry A.	NACA - Langley Laboratory
PEPPING, Raymond A.	NACA Subcommittee on Vibration and Flutter
PHILLIPS, F. W.	NACA Headquarters
PIERPONT, William G.	Beech Aircraft Corp.
PINES, Samuel	Republic Aviation Corp.
PLASS, Harold J., Jr.	Defense Research Laboratory - Univ. of Texas

CONFIDENTIAL

POOR, C. L.	NACA Subcommittee on High-Speed Aerodynamics
PORTR, 2d Lt. Edwin H., Jr.	Wright Air Development Center
PRESS, Harry	NACA - Langley Laboratory
PREWITT, Carl H.	Beech Aircraft Corp.
PRIDE, Richard A.	NACA - Langley Laboratory
RABER, William H.	NADC - Johnsville, Pa.
RAFEL, Norman	Naval Ordnance Experimental Unit - NBS
RAINEY, A. Gerald	NACA - Langley Laboratory
RASUMOFF, Abner	Hughes Aircraft Co.
RAY, George D.	NACA Subcommittee on Aircraft Structures
RAYE, Alexander H.	Curtiss-Wright Corp.
REEDER, John P.	NACA - Langley Laboratory
REESE, James R.	NACA - Langley Laboratory
REGIER, Arthur A.	NACA - Langley Laboratory
REID, H. J. E.	NACA - Langley Laboratory
RHOADS, Donald W.	Cornell Aeronautical Laboratory
RHODE, Richard V.	NACA Headquarters
RHYNE, Richard H.	NACA - Langley Laboratory
RIND, Emanuel	NACA - Langley Laboratory
ROBINSON, Glenn H.	NACA High-Speed Flight Research Station
ROCHE, J. A.	AFDFO - Langley AFB, Va.
ROGERS, John T.	NACA High-Speed Flight Research Station
ROSCHÉ, Melvin G.	NACA Headquarters
ROSECRANS, Richard J.	NACA - Langley Laboratory
ROSENBAUM, Robert	NACA Subcommittee on Vibration and Flutter
ROSENFIELD, Maurice S.	NAMC - Philadelphia, Pa.
RUEGG, Col. R. G.	NACA Committee on Aerodynamics
RUNCKEL, Jack F.	NACA - Langley Laboratory
RUNYAN, Harry L.	NACA - Langley Laboratory
RUSSELL, Col. Herbert O., USAF	Arnold Engineering Development Center
SCHLECHTE, Floyd R.	NACA - Langley Laboratory
SCHLEICHER, Richard L.	NACA Committee on Aircraft Construction
SCHNITZER, Emanuel	NACA - Langley Laboratory
SCHUETTE, Evan H.	Dow Chemical Co.
SCOTT, Merit	Vitro Corporation of America
SEARS, Richard I.	NACA - Langley Laboratory
SEMLER, Donald G.	Stanley Aviation
SEWALL, John L.	NACA - Langley Laboratory
SHORR, Melvin	NACA Subcommittee on Stability and Control
SHORTAL, Joseph A.	NACA - Langley Laboratory
SHOTLAND, Edwin	APL - Johns Hopkins Univ.
SIBILA, Alfred I.	NACA Subcommittee on Aircraft Loads
SILSBY, Norman S.	NACA - Langley Laboratory
SILVERS, H. Norman	NACA - Langley Laboratory
SKOPINSKI, T. H.	NACA - Langley Laboratory

CONFIDENTIAL

SMETHERS, Rollo G.	Bureau of Aeronautics
SMITH, Dana W.	NACA Subcommittee on Aircraft
SMITH, Frank C.	Structural Materials
SMITH, Henry G.	National Bureau of Standards
SMITH, Howard W.	Hughes Aircraft Co.
SMITH, John A.	NACA Subcommittee on Aircraft Loads
SMITH, Morgan G.	Westinghouse Electric Corp.
SMITH, Norman Y.	Ballistic Research Laboratory
SMITH, Philip L.	North American Aviation, Inc.
SNODGRASS, Richard B.	NACA - Langley Laboratory
SOULÉ, Hartley A.	Headquarters - SAC
SPAULDING, E. H.	NACA - Langley Laboratory
	NACA Subcommittee on Aircraft
	Structures
SPEAKER, Robert F.	Bureau of Aeronautics
SPERRAZZA, Joseph	Ballistic Research Laboratory
STACK, John	NACA - Langley Laboratory
STEINBACHER, Franz R.	Lockheed Aircraft Corp.
STEVENS, John E.	United Aircraft Corp.
STEVENSON, Clinton H.	Douglas Aircraft Co., Inc.
STICKLE, George W.	Operations Analysis - TAC
STOLLER, Morton J.	NACA - Langley Laboratory
STONE, David G.	NACA - Langley Laboratory
STONE, Ralph W.	NACA - Langley Laboratory
STOWELL, Elbridge Z.	NACA - Langley Laboratory
STRANG, Charles R.	NACA Subcommittee on Aircraft
	Construction
SWEET, Lt. Col. Floyd J., USAF	USAF Research and Development
SYLVESTER, Maurice A.	NACA - Langley Laboratory
TALLEY, James C.	Naval Proving Ground
TARGOFF, Walter P.	Cornell Aeronautical Laboratory
TENNANT, Samuel M.	TEMCO Aircraft Corp.
THOMAS, Edwin L.	TEMCO Aircraft Corp.
THOMPSON, Floyd L.	NACA - Langley Laboratory
THOMPSON, Hugh B.	Northrop Aircraft, Inc.
THORP, Arthur G., II	Westinghouse Electric Corp.
THORSON, Kenneth R.	Boeing Airplane Co.
TOBEY, Harry	NACA Subcommittee on Aircraft Loads
TRAHERN, Arlie R., Jr.	Chrysler Corp.
TURNER, M. J.	NACA Subcommittee on Vibration and
	Flutter
UNDERWOOD, Robert E.	Douglas Aircraft Co., Inc.
UNDERWOOD, Robert H.	Arnold Engineering Development Center
UNDERWOOD, William J.	NACA Liaison Office, Wright-Patterson
	AFB, Ohio
VETERITO, Michael	Fairchild Engine and Airplane Corp.
VITALE, A. James	NACA - Langley Laboratory

CONFIDENTIAL

WALKER, Harold J.	NACA - Ames Laboratory
WALSH, James E., Jr.	NACA Subcommittee on Vibration and Flutter
WATKINS, Charles E.	NACA - Langley Laboratory
WEAVER, Preston R.	National Bureau of Standards
WEBB, Howard M.	Douglas Aircraft Co., Inc.
WEEKS, Lawrence M.	McDonnell Aircraft Corp.
WEHLE, Louis B.	Grumman Aircraft Engineering Corp.
WEISMAN, Yale	Consolidated Vultee Aircraft Corp.
WEST, Franklin E., Jr.	NACA - Langley Laboratory
WESTERBACK, Ivar S.	Sperry Gyroscope Co.
WIDMAYER, Edward, Jr.	NACA - Langley Laboratory
WILLIAMS, Claude V.	NACA - Langley Laboratory
WILLIAMS, W. C.	NACA High-Speed Flight Research Station
WILSON, Leo E.	Southwest Research Institute
WILSON, Robert E.	United Aircraft Corp.
WITHERS, Wayne B.	Wright Air Development Center
WITTE, Norbert F.	NOTS - Inyokern
WOERSCHING, Thomas B.	Goodyear Aircraft Corp.
WOOD, Clotaire	NACA Headquarters
WOODS, Robert J.	NACA Committee on Aerodynamics
WYSS, John A.	NACA - Ames Laboratory
YATES, William	The Glenn L. Martin Co.
ZENDER, George W.	NACA - Langley Laboratory
ZIMMERMAN, Charles H.	NACA - Langley Laboratory
ZIMMOCK, Vincent P.	NAMC - Philadelphia, Pa.
ZUPANICK, Joseph E.	Sperry Gyroscope Co.

**CONFIDENTIAL**

**1**

## **FACTORS INFLUENCING MAXIMUM LOADS**

**CONFIDENTIAL**

SOME NOTES ON MAXIMUM LIFT AND PITCH-UP IN  
RELATION TO MAXIMUM LOAD FACTORS

By George S. Campbell

Langley Aeronautical Laboratory

INTRODUCTION

Two lines of particular interest on an airplane's V-G diagram are the trace of maximum lift against Mach number and the usual arbitrary design limit. About maximum lift, there can be little argument, and the problem is simply one of collecting the necessary aerodynamic data. An arbitrary design limit, however, should always be used with special care, because its use implies, among other things, that the airplane has a sufficient amount of stability so that the pilot has complete control over airplane attitude at all times. However, recent flight experience with high-speed aircraft of both research and production types (refs. 1 to 11) has indicated that pilots are frequently unable to cope with the dynamic overshoot, or pitch-up, caused by apparently moderate pitching-moment nonlinearities. A discussion of the significance of pitch-up in relation to the loads problem is presented in this paper; in addition, the maximum lift situation is reviewed briefly in the light of recent data.

REVIEW OF MAXIMUM-LIFT DATA

The variation of maximum lift coefficient with Mach number shown in figure 1 for straight, swept, and delta wings of 6 percent thickness was presented about two years ago in a paper by Lowry and Cahill (ref. 12), along with the limiting lift at supersonic speeds determined by a condition of zero absolute pressure on the upper surface of a wing. Since that time, a series of thin, highly tapered wings has been tested to maximum lift in the Langley high-speed 7- by 10-foot tunnel by using the transonic-bump technique. Included in the tests were five pointed wings of aspect ratio 4 and 3 percent thickness with the angle of sweepback varying from  $0^\circ$  to  $45^\circ$ , as indicated by the appropriate plan form outlines given in figure 1. Data was also obtained for five aspect-ratio-3 wings obtained by cutting off the tips of the pointed wings.

The values of maximum lift for all wings of the "pointed wing series" fall within the shaded area shown in figure 1, the heavier shading representing results for the wings having the least amount of sweep. The

data show the same pronounced rise in  $C_{L_{max}}$  at transonic Mach numbers as that shown by the earlier tests. Also as in the previous tests, the wings having least sweep had the largest change in maximum lift at transonic speeds. After adding the new data to the old, then, the maximum lift picture remains unchanged in its more important aspects.

#### SIGNIFICANCE OF PITCH-UP IN RELATION TO MAXIMUM LOAD FACTORS

In attempting to account for the effect of pitching-moment nonlinearities on the flight behavior of a proposed airplane, it is not possible, simply by inspection, to tell whether the nonlinearities are of sufficient importance to warrant major revisions in the design. However, the designer may predict the likelihood of exceeding design loads due to pitch-up by calculating time histories from measured wind-tunnel data. In order to illustrate the usefulness of such calculations, the pitching moments shown in figure 2 have been converted to time histories (fig. 3) by using typical mass, inertia, and geometric properties for a fighter airplane. On the plot of airplane pitching-moment coefficient against angle of attack, a severe instability is shown for curve A, curve B has a region of essentially neutral stability, and curve C represents a linear pitching moment having the same initial slope as the nonlinear curves. On the time histories of angle of attack and stabilizer position, the letters A, B, and C refer to the type of pitching-moment variation shown in figure 2. The pilot, in each case, was assumed to pull back on the stick at a constant rate until reaching an angle of attack of about  $14^{\circ}$ , indicated by vertical ticks on the response curves. At this point, the pilot either held the control fixed or applied corrective control at a stabilizer rate of 4 degrees per second.

The most apparent result from the calculations is the greater degree of control which the pilot had over the amount of overshoot for the milder nonlinearity than he had with the severe instability. It should be mentioned that, even with higher rates of corrective control, up to 10 degrees per second, the pilot could do little to reduce dynamic overshoot once he had entered an instability as severe as curve A.

In order that no one will infer that curve B is a desirable or even tolerable pitching-moment, it should be noted that, when the pilot of airplane B held the control fixed, as he might have if he had been distracted for only a second or two, the airplane reached an attitude nearly as high as that for the severe instability.

In order to obtain a more general picture of the significance of pitch-up, a typical variation with Mach number of the normal-force coefficient for the onset of pitch-up is illustrated in figure 4. A cross-hatched band, rather than a definite line, has been used to indicate

onset of pitch-up because it is not possible to look at a pitching-moment curve or a time history and select a particular normal-force coefficient as the one uncontested point at which pitch-up begins. Also shown in figure 4 are the usual parameters appearing on a V-G diagram, airplane maximum normal-force coefficient and a design limit. A design limit of 7.3 g's has the variations shown for altitudes of 25,000 and 50,000 feet with a wing loading of 50 lb/sq ft. Flight-test results for the D-558-II have been used to define the representative pitch-up and  $C_{N_{max}}$  boundaries up to a Mach number of 1.2, wind-tunnel data being used to extend the boundaries to higher Mach numbers.

From figure 4, it is seen that, depending on the altitude, entry into the pitch-up region can result in an overshoot beyond the design limit and on up toward maximum lift. In predicting the likelihood of the airplane pitching up inadvertently, it is important to consider whether the pilot has an advance warning from buffeting. Such a warning allows the pilot to start corrective-control motion early enough to prevent excessive overshoot.

Although it is customary to assume that pitch-up is critical from a loads standpoint at lower altitudes, such an assumption results from the bulk of flight experience being at subsonic Mach numbers. At supersonic Mach numbers, however, pitch-up can be important over a wide range of altitudes. To illustrate, the boundaries in figure 4 show that the design limit could be exceeded inadvertently at 25,000 feet when the pilot enters pitch-up near a Mach number of one after decelerating from supersonic Mach numbers, for example, in a turn or gradual pull-up. At 50,000 feet altitude, pitch-up could lead to excessive loads during a maneuver at nearly constant Mach number, such as a diving turn at a Mach number of 1.4. For such cases in which the significance of pitching-moment nonlinearities cannot easily be obtained from static data at several isolated Mach numbers, dynamic calculations are particularly useful for integrating all the aerodynamic results into a loads history during a realistic maneuver.

#### RÉSUMÉ

Recent maximum-lift data for a series of 3-percent-thick, highly tapered wings show the same pronounced increase in  $CL_{max}$  at transonic Mach numbers as indicated by earlier results for 6-percent-thick wings of varying plan form. Among what might be called new factors influencing maximum loads, pitch-up emerges as an important problem confronting airplane designers. When pitch-up is encountered during a maneuver, the airplane may overshoot its design limit before the pilot can check the motion. By using wind-tunnel data to calculate airplane time histories,

CONFIDENTIAL

the designer can predict in advance the likelihood of exceeding design loads due to pitch-up and then take the necessary action for insuring the integrity of his design. Such action may involve modifying the configuration sufficiently to provide more satisfactory stability characteristics or making structural changes to account for high inadvertent loads.

CONFIDENTIAL

## REFERENCES

1. Williams, W. C., and Crossfield, A. S.: Handling Qualities of High-Speed Airplanes. NACA RM L52A08, 1952.
2. Sjoberg, S. A., Peele, James R., and Griffith, John H.: Flight Measurements With the Douglas D-558-II (BuAero No. 37974) Research Airplane. Static Longitudinal Stability and Control Characteristics at Mach Numbers up to 0.87. NACA RM L50K13, 1951.
3. Fischel, Jack, and Nugent, Jack: Flight Determination of the Longitudinal Stability in Accelerated Maneuvers at Transonic Speeds for the Douglas D-558-II Research Airplane Including the Effects of an Outboard Wing Fence. NACA RM L53A16, 1953.
4. Rathert, George A., Jr., Ziff, Howard L., and Cooper, George E.: Preliminary Flight Investigation of the Maneuvering Accelerations and Buffet Boundary of a 35° Swept-Wing Airplane at High Altitude and Transonic Speeds. NACA RM A50L04, 1951.
5. Anderson, Seth B., and Bray, Richard S.: A Flight Evaluation of the Longitudinal Stability Characteristics Associated With the Pitch-Up of a Swept-Wing Airplane in Maneuvering Flight at Transonic Speeds. NACA RM A51I12, 1951.
6. McFadden, Norman M., Rathert, George A., Jr., and Bray, Richard S.: The Effectiveness of Wing Vortex Generators in Improving the Maneuvering Characteristics of a Swept-Wing Airplane at Transonic Speeds. NACA RM A51J18, 1952.
7. Anderson, Seth B., Matteson, Frederick H., and Van Dyke, Rudolph D., Jr.: A Flight Investigation of the Effect of Leading-Edge Camber on the Aerodynamic Characteristics of a Swept-Wing Airplane. NACA RM A52L16a, 1953.
8. Anon.: Flight Handbook. USAF Series F-86A Aircraft. AN 01-60JLA-1, USAF and BuAero, July 30, 1952.
9. Sadoff, Melvin, and Sisk, Thomas R.: Summary Report of Results Obtained During Demonstration Tests of the Northrop X-4 Airplanes. NACA RM A50I01, 1950.
10. Sadoff, Melvin, Ankenbruck, Herman O., and O'Hare, William: Stability and Control Measurements Obtained During USAF-NACA Cooperative Flight-Test Program on the X-4 Airplane (USAF No. 46-677). NACA RM A51H09, 1951.

**CONFIDENTIAL**

11. Finch, Thomas W., and Walker, Joseph A.: Static Longitudinal Stability of the Bell X-5 Research Airplane With 59° Sweepback. NACA RM L53A09b, 1953.
12. Lowry, John G., and Cahill, Jones F.: Review of the Maximum-Lift Characteristics of Thin and Swept Wings. NACA RM L51E03, 1951.

**CONFIDENTIAL**

## CURRENT STATUS OF MAXIMUM-LIFT DATA

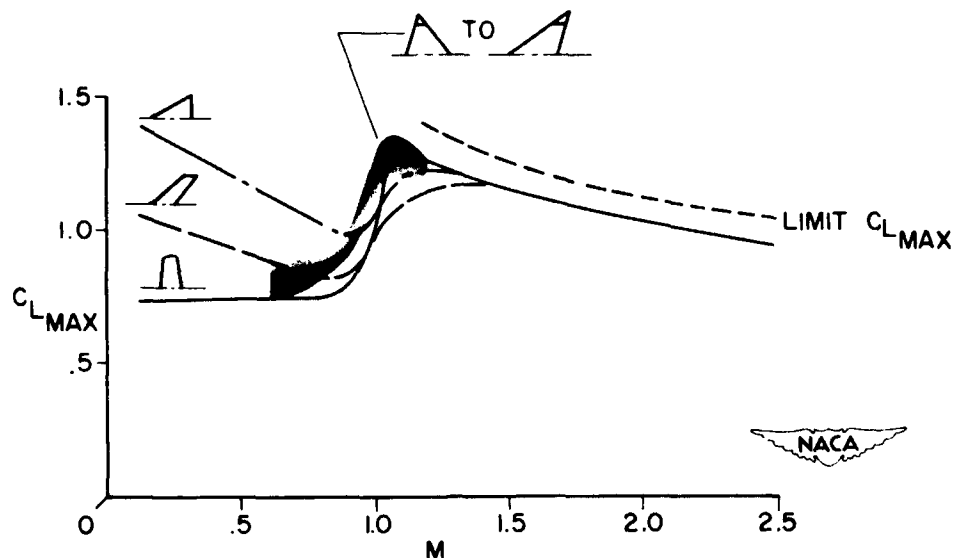


Figure 1.

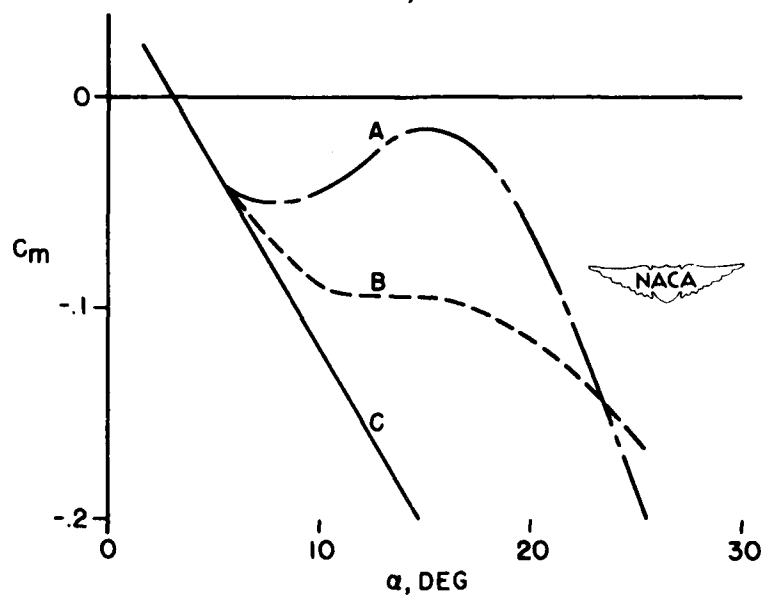
INFLUENCE OF PITCHING-MOMENT SHAPE ON SEVERITY  
OF PITCH-UP; STATIC DATA

Figure 2.

INFLUENCE OF PITCHING-MOMENT SHAPE  
ON SEVERITY OF PITCH-UP; TIME HISTORIES

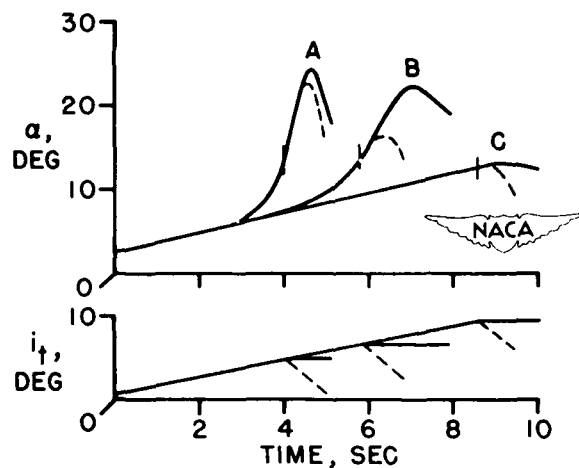


Figure 3.

TYPICAL BOUNDARIES FOR A SWEPT-WING AIRPLANE

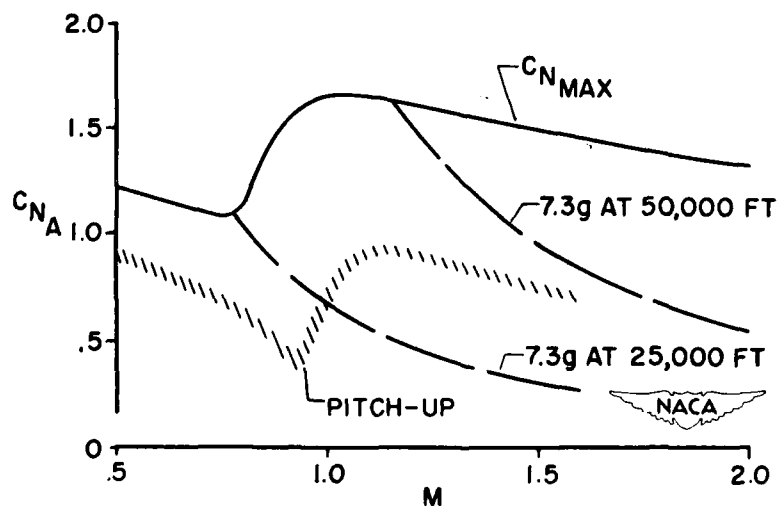


Figure 4.

INVESTIGATION OF THE USE OF CONTROLS DURING  
SERVICE OPERATIONS OF FIGHTER AIRPLANES

By John P. Mayer, Carl R. Huss,  
and Harold A. Hamer

Langley Aeronautical Laboratory

The present methods for determining airplane design loads require, among other things, a knowledge of the motion of the control surfaces. In the usual methods the maximum design loads are obtained by specifying what are believed to be the critical motions of the controls, or by specifying the critical airplane response; however, the actual control motion and airplane response obtained in regular operational flying may differ appreciably from the specified variations.

In order to obtain some preliminary information on the airplane response and the actual amounts and rates of control used by service pilots in the performance of their regular training missions, the NACA with the cooperation of the Air Force and Bureau of Aeronautics, Navy Department, has been conducting a flight program with several jet-propelled fighter airplanes. In addition to the data on airplane-control motions, this information was needed to determine the most important quantities and ranges of measurements to be used in the design of an instrument for statistical loads measurements. No attempt has been made, at this time, to make a statistical analysis of the data obtained in these preliminary studies; however, the data obtained are believed to be of general interest and are presented at this time as envelopes of maximum values.

Four fighter airplanes have been tested: the F-86, F2H, F-84, and F-94 airplanes. (Refs. 1 to 5 present preliminary data on these airplanes.) Two views of the test airplanes with information on the use of boost and tip tanks during the tests are shown in figure 1. The airplanes are flown by regular service pilots and are instrumented and the data evaluated by NACA personnel. Approximately 20 flights were obtained with each airplane and about 10 different pilots flew each airplane. In these flights, about 500 maneuvers were performed with each airplane. These flights were made in conjunction with the normal squadron operational training; however, data were recorded only on those flights which involved mostly acrobatics, ground gunnery, aerial gunnery, and dive bombing. Although only a relatively few hours were obtained on each airplane (about 20 hours), it is believed that the data are representative of many more hours of normal flying since data were not recorded in cross-country flying or other operational uses where few maneuvers were made. At this time, it must be emphasized that the data to be presented are not an indication of what the airplane or pilot can

do but what they do do in the performance of their normal operational missions. In addition, with the exception of the F-86, the airplanes of this investigation were not the type to experience the pitch-up discussed in the previous paper by George Campbell. Pitch-up was experienced on the F-86 airplane in several maneuvers but, in general, the pilots avoided the pitch-up region.

The operational V-n diagram for the F-86 airplane is shown in figure 2. The black symbols are those for the test airplane of this program. The open symbols are from 1150 hours of operational training in many F-86A airplanes in this country (ref. 6). With the exception of the 4 square symbols, the points shown define the envelope of all the points obtained in the tests. The square symbols represent all the points obtained above the structural limit. The service limit for the F-86A airplane is 6g. The structural limit is 7.33g and the ultimate load factor is 11g. It may be seen that the pilots reach the positive service limit almost over the entire speed range; however, the negative load-factor range was rarely entered. In the Air Force data (shown by the open circles) the service limit was exceeded 28 times and the structural limit was exceeded 5 times. The ultimate load factor was exceeded twice, once at a speed of 438 knots and once at an unknown airspeed. For the test airplane, the service limit was reached but not exceeded by any appreciable amount (shown by the black symbols). In the negative load-factor region, there are very few points in both sets of data. In the Air Force data a load factor of -1.0g was reached once; whereas in the present test program on the F-86 the maximum negative load factor was about -0.3g. It is interesting to note that, below the service limit, the two sets of data are very similar.

The V-n diagrams for the other test airplanes were quite similar to that for the F-86. In general, the positive maximum load factor was reached throughout most of the speed range; however, none of the airplanes approached the negative maximum load factor at any speed. The highest negative load factor measured was -1.1 for the F-84G airplane. One contributing factor to the lack of negative load factors may be in the limitations of jet-engine operation at negative accelerations.

Envelopes of the maximum pitching angular accelerations for the test airplanes are shown in figure 3. If the normal load factor and pitching angular acceleration are known, the maneuvering horizontal-tail load may be determined. The maximum maneuvering horizontal-tail load will occur when maximum load factors are combined with maximum pitching accelerations. The curves shown represent the envelope of hundreds of test points for each airplane. The maximum positive and negative pitching accelerations increase with airspeed until a point corresponding approximately to the upper left-hand corner of the V-n diagram is reached and then decrease with further increases in airspeed. The difference between the accelerations reached with all the airplanes is not great. The maximum positive pitching acceleration was about 1.7 and the maximum negative

pitching acceleration reached was about -2.0 radians per second per second. It may also be noted that the maximum positive and negative pitching accelerations are about equal although there was a slight tendency in these tests toward higher negative pitching accelerations. The relatively high pitching accelerations shown at the lowest speeds were obtained in stalls and spins. A comparison of the test data with several design requirements or methods is shown in figure 4. The test boundary represents the boundary of the maximum pitching accelerations reached on all the test airplanes. The boundary indicated as A is based on the airplane reaching its limit load factor with an elevator deflection in which the maximum elevator angle is reached in 0.2 second. The boundary labeled B is a semiempirical method based on a maximum elevator rate of 3.5 radians per second. The line labeled C is the design requirement of 6 radians per second squared at the upper left-hand corner of the V-n diagram. There are several other design requirements or methods not shown here; however, they are somewhat similar and reach about the same value of maximum pitching acceleration.

The design curves shown apply only to the F-86 airplane but the curves for the other airplanes are quite similar. It can be seen that the flight values of pitching acceleration are less than one-half of the calculated or design values. It should be emphasized that these design curves represent the maximum values that could be obtained, and a pitching acceleration of about 5 is within the maximum capabilities of the pilot and the airplane for most of these airplanes; however, the test points represent what the service pilots actually used in the performance of their missions. In other results which are not shown here, it is also indicated that the maximum pitching accelerations may occur at maximum load factor.

The maximum elevator rates associated with these maximum pitching accelerations are shown in figure 5. Also shown are two design curves which are similar to those of figure 4. The elevator rates for the test airplane decrease with speed throughout the speed range, and the positive and negative rates are approximately equal. Of these airplanes only the F-86 was equipped with boost; however, all the airplanes were equipped with power-driven trim tabs. It is not known what use, if any, the pilots made of the trim tab in maneuvering the airplanes. In addition, the F-86A airplanes are equipped with an elevator rate restrictor which restricts the maximum elevator rate to about 0.8 radian per second. The high rates shown at the lowest speeds were obtained in stalls and landing approaches and did not affect the airplane motion. It may be seen that the elevator rates used in these operational tests were below the maximum possible rates. In regard to the other control-surface rates, the maximum rudder rates for unstalled maneuvers were about 1.3 radians per second and decreased rapidly with airspeed. Rudder rates as high as 2.8 radians per second were measured on the F-94 airplane in stalls.

The maximum aileron rates measured were about 1.4 radians per second; however, the maximum aileron rates did not decrease with airspeed.

The envelopes of the maximum sideslip angles reached in these operational tests are shown in figure 6. The maximum sideslip angle decreased rapidly with airspeed for all airplanes. The maximum angles for the F-84 and F-94 airplanes are approximately equal at the higher airspeeds. The angles reached with the F-2H airplane were somewhat less throughout the speed range. No angles are shown for the F-86 airplane since sideslip angle was measured in only 5 percent of the maneuvers. The maximum angles shown here were reached in rolling pull-outs, rolls with normal acceleration, sideslips, and rudder kicks. The boundaries shown are defined by all these maneuvers; no one maneuver was more critical than another. The highest sideslip angle measured was over  $32^{\circ}$  on the F-84 airplane and occurred in a spin. One design criterion states that an angle of  $5^{\circ}$  of sideslip be designed for at the limit diving speed; this is about 5 times the value reached in these tests.

Data on angles of attack are not shown here; however, angles of attack over  $\pm 30^{\circ}$  were measured on the F-84 airplane in spins.

An indication of the vertical-tail loads reached is shown in figure 7 where the sideslip angle  $\beta$  is multiplied by the dynamic pressure  $q$  and plotted against airspeed. This parameter is roughly proportional to the vertical-tail load. The highest vertical-tail loads indicated in these tests were obtained at a speed which corresponds roughly to the upper left-hand corner of the V-n diagram. The two relatively high points shown for the F-94 airplane at higher speeds were obtained in inadvertent airplane lateral oscillations and were not the result of one of the critical maneuvers listed before. It is interesting to note that stability deficiencies, such as uncontrolled lateral oscillations, may produce loads as high as those in controlled maneuvers.

Also shown in figure 7 is the value of  $\beta q$  obtained from the requirement that a full aileron roll be made at 0.8 of the limit load factor. It can be seen that this requirement results in a value of  $\beta q$  greater than obtained in these tests. The criterion of  $5^{\circ}$  of sideslip at limit speed will result in a point off scale at a value of  $\beta q$  of about 5000.

In figure 8 the envelopes of the maximum transverse load factors measured in these tests are shown. In general, they increase with airspeed up to some airspeed between 250 and 300 knots and then decrease at the highest airspeeds. The points shown for the F-86 and F2H airplanes outside the boundaries are isolated points which fell above the mass of data. The maximum transverse load factor measured was about

0.45g on the F-86 airplane. One design requirement states that the airplane shall be designed to withstand 2g side load factor. This value is in considerable excess of any load factors measured in these tests.

One of the critical maneuvers for design of the vertical tail is the rolling pull-out type of maneuver which consists of high normal load factors combined with rolling velocities. The envelopes of the transverse load factors plotted against normal load factor are shown in figure 9. The several points which are located above the curves are isolated values of the transverse load factor obtained in the tests. It may be seen that the data indicate, in general, that the transverse load factor appears to decrease somewhat with normal load factor; however, the points which fall outside these boundaries indicate that relatively high values of transverse acceleration can be obtained at high normal acceleration as well as at low accelerations. All the isolated high points were obtained in rolling pull-out type of maneuvers and at altitudes of less than 8000 feet except for the F-86 point at 0.38g. This value was obtained at 20,000 feet.

The rolling velocities associated with the normal load factors for the four test airplanes are shown in figure 10. The rolling velocity increases with load factor at low load factors, reaches a peak at about 2 to 3g, and then decreases with further increase in normal load factor. The maximum rolling velocity reached was about 3.5 radians per second at 3g with the F-84 airplane.

The envelopes of the aileron angles used are shown in figure 11 as a function of airspeed. The full-throw maximum aileron angles for the test airplanes are about  $20^\circ$  for the F-94 and F2H airplanes,  $18^\circ$  for the F-84 airplane, and  $15^\circ$  for the F-86 airplane. At the lower speeds, almost full aileron is used for the F-84G airplane but, as the speed increases, the maximum aileron angle used decreases rapidly. All these airplanes have aileron boost systems. It is interesting to note that the maximum curves for all airplanes are similar at higher airspeeds.

In regard to the other control-surface angles, the maximum elevator angles ranged from  $30^\circ$  up to  $11^\circ$  down. The maximum rudder angles were about  $10^\circ$  except in stalls and landings where angles up to  $24^\circ$  were used.

Recently, it has been suggested that a more realistic rolling requirement than those presently used would be that the airplane roll to  $90^\circ$  in one second. The envelopes of the minimum times for the test airplanes to roll to  $90^\circ$  are shown in figure 12. It may be seen that the minimum time to roll to  $90^\circ$  for all the test airplanes is about one second except at the lowest and highest speeds.

CONFIDENTIAL

On the basis of the approximately 2000 maneuvers performed in these tests of operational airplanes, no definite conclusions may be made at this time; however, it is indicated that the service pilots do utilize the positive V-G envelope but rarely approach the negative V-G envelope. The maneuvers performed which are critical as far as horizontal-tail loads are concerned appear to be less severe than any present design requirements. The maneuvers critical for the vertical tail also appear to be mild compared to present design requirements. This does not mean that the present design requirements are overly conservative since these airplanes could reach the design limits if the pilots controlled the airplane in the manner specified by the requirements. The data presented do indicate, however, that, in these tests, the service pilots in performing their normal operational missions did not approach the design limits of the airplane.

There may be a question as to whether higher rates and accelerations might be obtained in combat than in training. That question has not been answered as yet; however, in World War II it was found that the airplanes reached higher normal load factors in training than in combat, and at this time there is no reason to believe that the present trend is much different.

CONFIDENTIAL

## REFERENCES

1. Hamer, Harold A., and Henderson, Campbell: Time Histories of Maneuvers Performed With an F-86A Airplane During Squadron Operations. NACA RM L51K30, 1952.
2. Huss, Carl R., Andrews, William H., and Hamer, Harold A.: Time-History Data of Maneuvers Performed by a McDonnell F2H-2 Airplane During Squadron Operational Training. NACA RM L52B29, 1952.
3. Henderson, Campbell, Thornton, James, and Mayo, Alton: Time-History Data of Maneuvers Performed by an F-86A Airplane During Squadron Operational Training. NACA RM L52C19, 1952.
4. Huss, Carl R., Fisher, Raymond A., and Gainer, Patrick A.: Time-History Data of Maneuvers Performed by a Lockheed F-94B Airplane During Squadron Operational Training. NACA RM L53B27, 1953.
5. Hamer, Harold A., and Mayo, Alton P.: Time-History Data of Maneuvers Performed by a Republic F-84G Airplane During Squadron Operational Training. NACA RM L53C27, 1953.
6. Gray, Frank P.: Flight Load Data From Operational F-86A Aircraft. ATI 158813 (Memo. Rep. No. WCNSS3-4515-12-15), WADC, Aero. Div., U. S. Air Force, Jan. 15, 1952.

CONFIDENTIAL

## AIRPLANES INVESTIGATED

AIRPLANE	BOOST		TIP TANKS	
	ELEV.	AIL.	ON	OFF
F-86A	YES	YES	NO	YES
F2H-2	NO	YES	YES	NO
F-84G	NO	YES	YES	YES
F-94B	NO	YES	YES	YES



Figure 1.

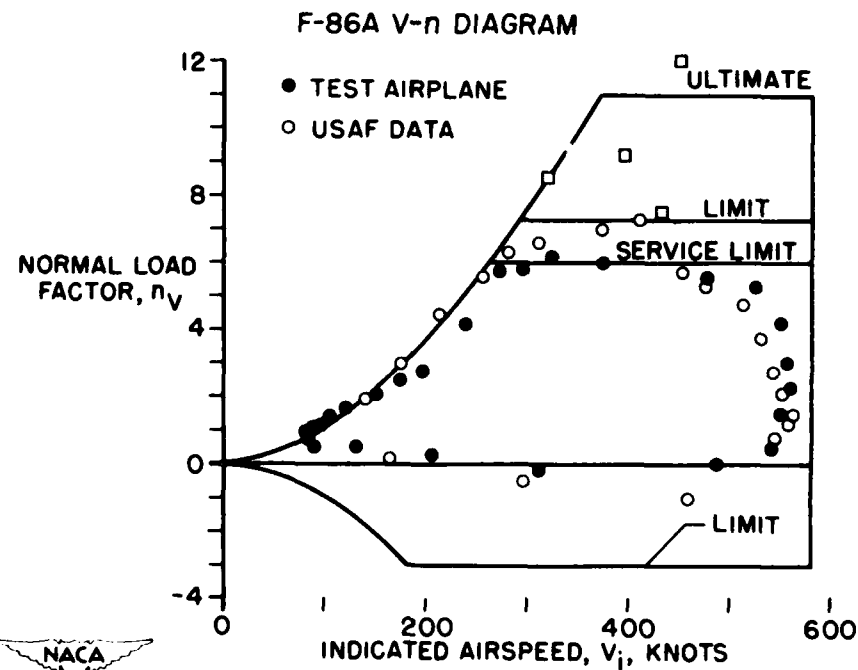


Figure 2.

CONFIDENTIAL

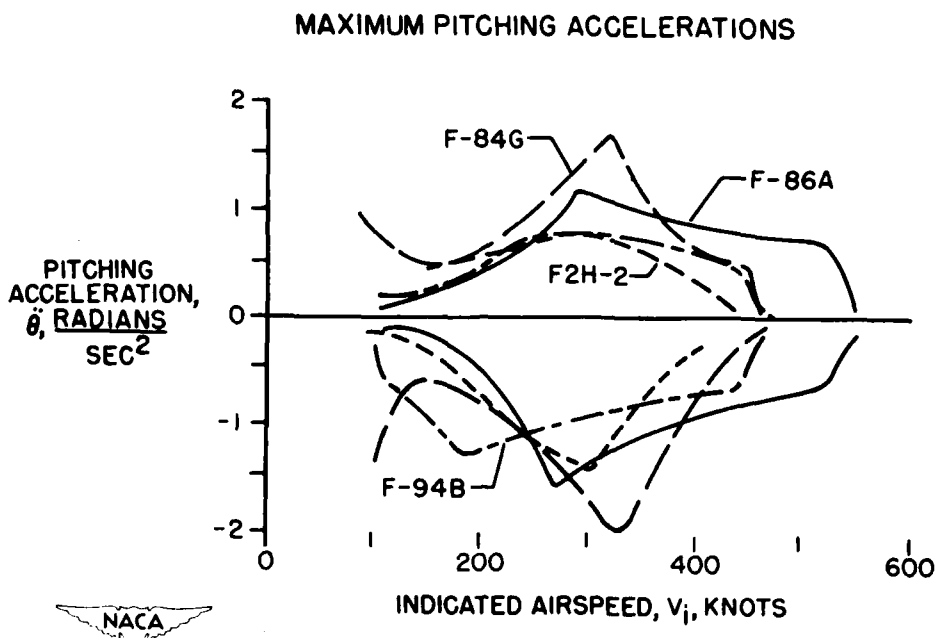


Figure 3.

## COMPARISON OF DESIGN METHODS AND FLIGHT TESTS

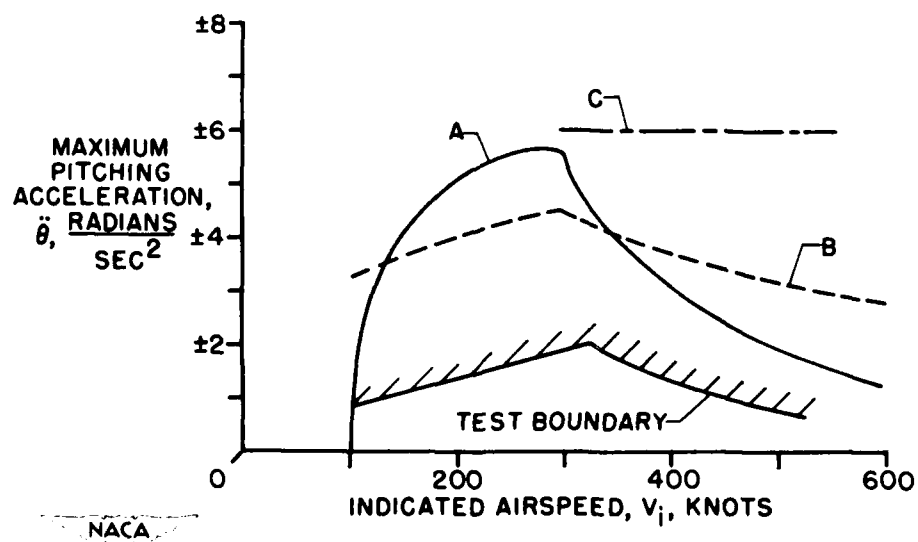


Figure 4.

CONFIDENTIAL

## MAXIMUM ELEVATOR RATES

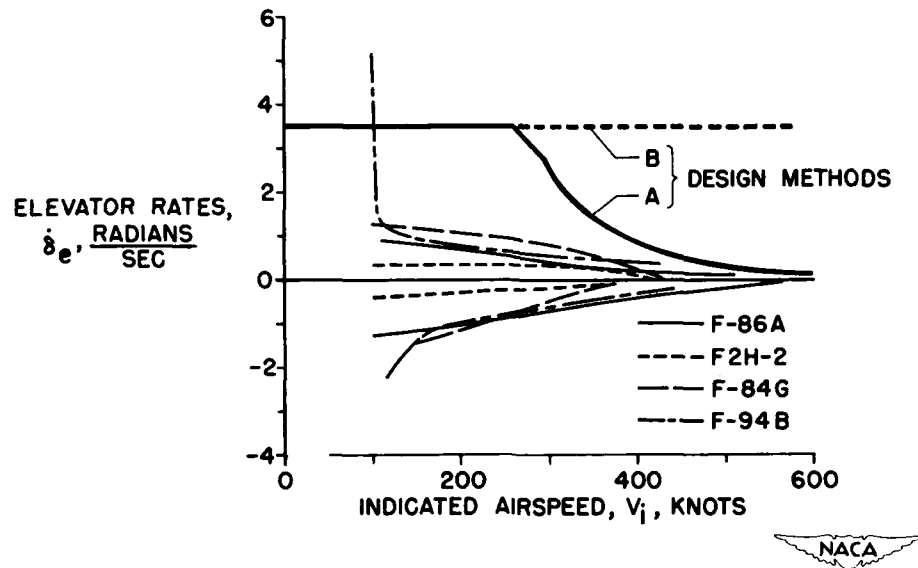


Figure 5.

## MAXIMUM SIDESLIP ANGLES

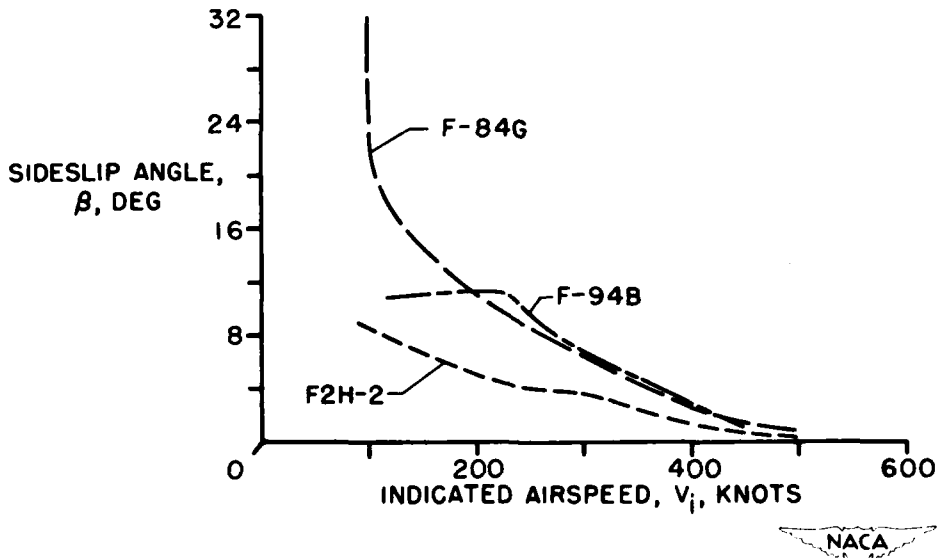


Figure 6.

CONFIDENTIAL

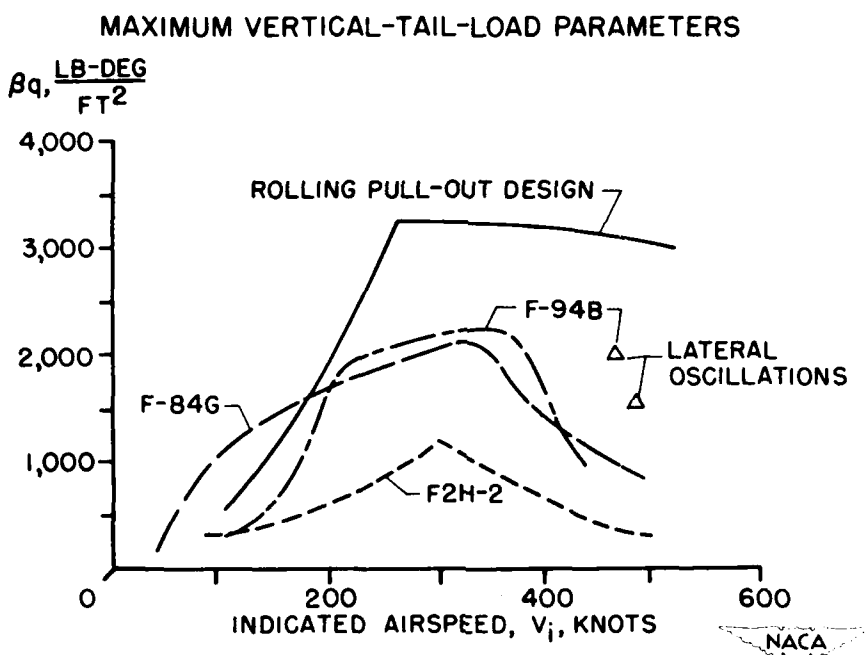


Figure 7.

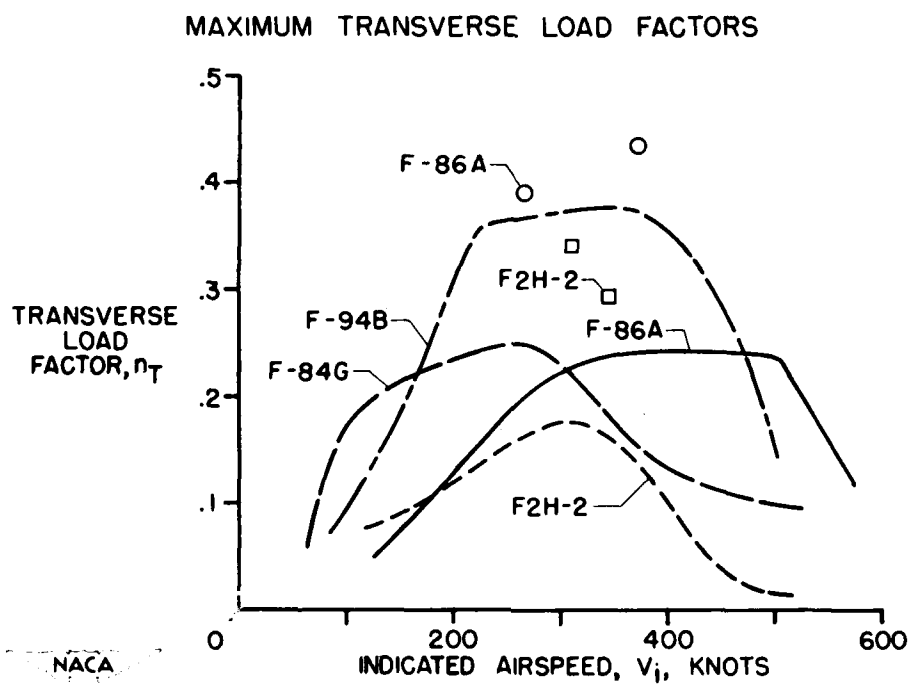


Figure 8.

## MAXIMUM TRANSVERSE AND NORMAL LOAD FACTORS

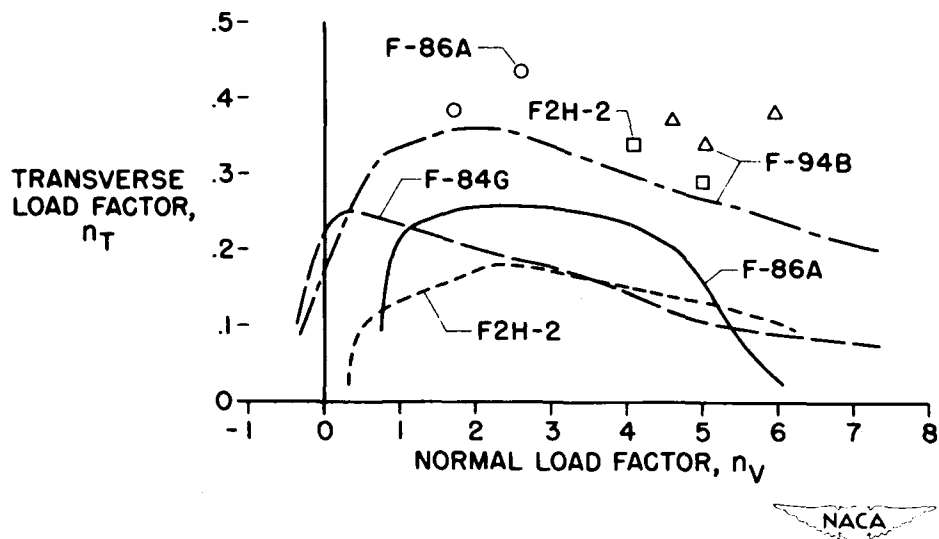


Figure 9.

## MAXIMUM ROLLING VELOCITIES AND NORMAL LOAD FACTORS

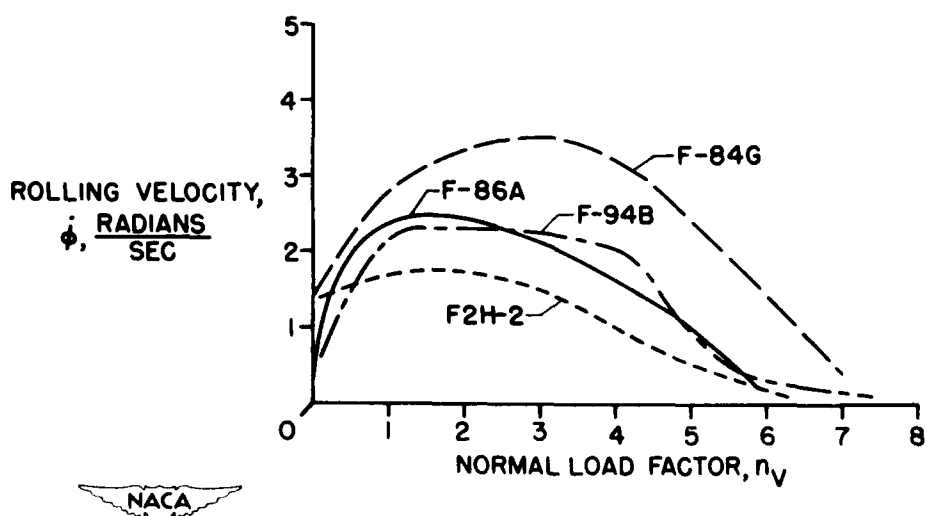


Figure 10.

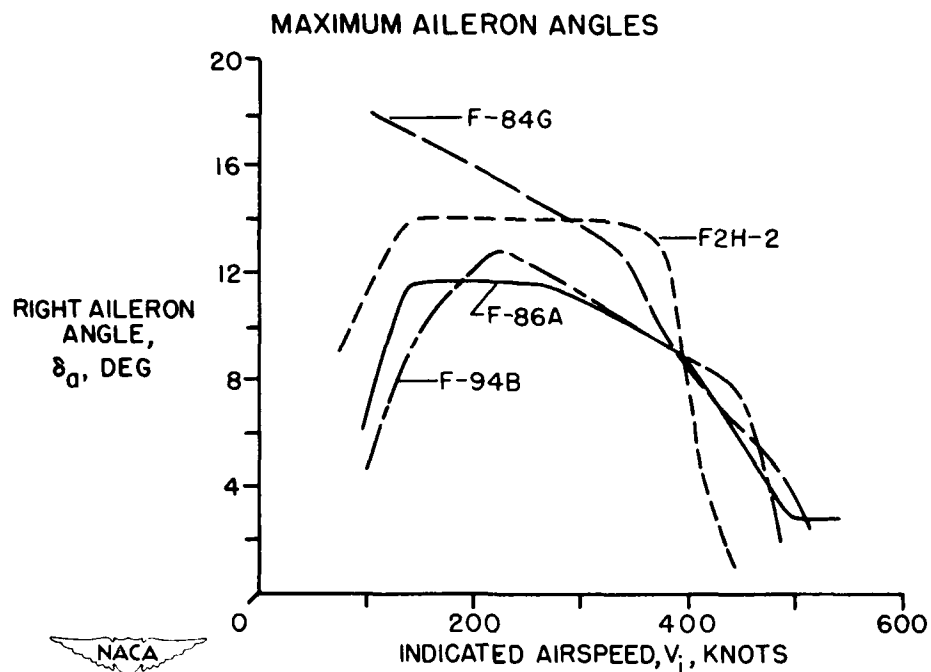


Figure 11.

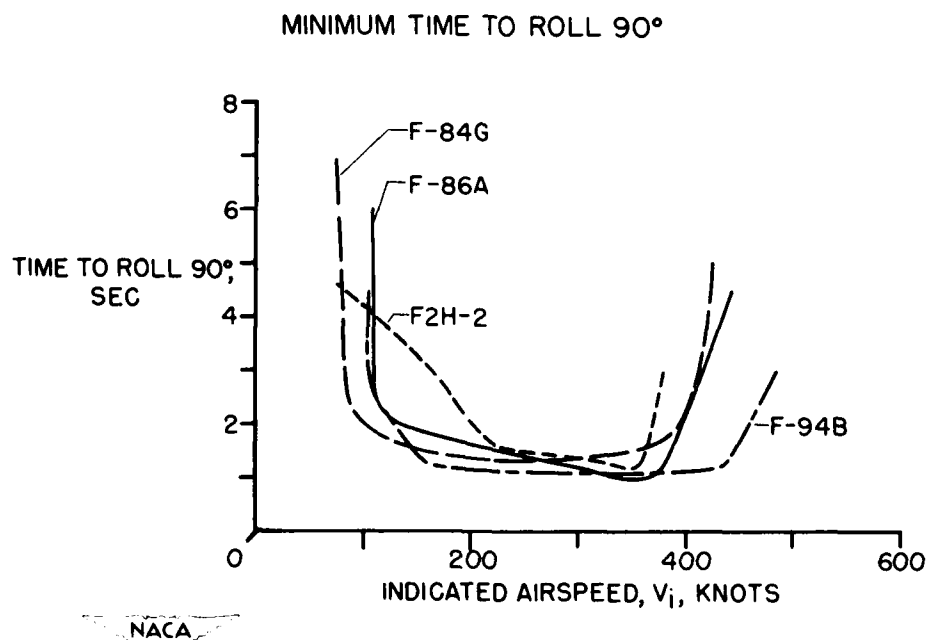


Figure 12.

LOADS EXPERIENCED IN FLIGHT IN REGIONS  
OF REDUCED STABILITY

By Hubert M. Drake, Glenn H. Robinson,  
and Albert E. Kuhl

NACA High-Speed Flight Research Station

In a previous paper, George S. Campbell has outlined some of the problems resulting from the reduction of longitudinal stability which occurs at moderate lift with swept wings. Such regions of reduced stability were traversed during flight tests of the Bell X-5 and Douglas D-558-II research airplanes. Figure 1 shows the general arrangement of these two airplanes. The X-5 has the horizontal tail located almost in line with the wing and for this investigation was flown at  $59^{\circ}$  sweepback. The D-558-II airplane has a  $35^{\circ}$  sweepback wing and a horizontal tail located halfway up the vertical tail. The turns and pull-ups which were performed were intended only to reach the stability boundary but the reductions of stability were such as to cause the airplanes to pitch up to large angles of attack. At these high angles of attack, the D-558-II would occasionally, and the X-5 would usually, encounter a directional divergence which would result in large angles of sideslip and roll. This behavior was not unexpected and the maneuvers were therefore performed, whenever possible, at high altitudes in order to prevent the development of excessive loads. The loads that were experienced are the subject of this paper.

The maximum angles of attack and sideslip measured during these inadvertent maneuvers are shown in figure 2 for each airplane. The line in the upper part of the figure is the stability boundary at which the airplane pitches, and the points indicate the peak values of angle of attack that have been attained as a result of this longitudinal divergence. The extreme angles of attack at low Mach numbers for the X-5 were encountered during a spin which resulted from the longitudinal and directional instabilities. The lower portion of figure 2 shows the angles of sideslip reached as a result of the directional instability at high angles of attack. No directional divergence has been encountered at supersonic Mach numbers with the D-558-II, but oscillations of the amplitude shown have been encountered during the recoveries from pull-ups.

Because the pitching motions result from stability deficiencies, rather than from control motions, it is of interest to see what range of pitching accelerations were encountered in these motions. In figure 3 are presented the accelerations attained both during the pitch-up and during the pitch-down in the recovery from the maneuver. Most of the pitch accelerations were smaller than 2 radians per second per

second although a few were considerably larger. However, the Navy design requirement,  $\pm 6$  radians per second per second, was not exceeded, although it was approached by the D-558-II airplane.

Examples of the variations of horizontal-tail load during the pitch-ups are shown in figure 4. The variations with angle of attack of the airplane and wing normal-force coefficients are shown to indicate the lift conditions existing during the maneuver. The pitch-up, indicated by the ticks, usually occurs just before the break in the normal-force curve and the airplane is pitched to angles of attack near, or even exceeding, maximum lift. Were the pitch-up not present, the usable flight region would extend to higher lifts and be limited by the buffeting occurring at angles of attack near maximum wing lift, and the angles of attack beyond maximum lift normally would not be penetrated.

The horizontal-tail loads are shown in the center portion of figure 4. The curve labeled "structural" indicates the actual tail load measured by the strain gages. Correcting this load for the tail-inertia load produced by the measured tail acceleration gives the curve entitled "aerodynamic." By use of the measured pitching angular accelerations the aerodynamic loads were corrected to a condition of zero pitching acceleration and are termed "balancing." In a subsequent paper on tail loads by John T. Rogers, George E. Cothren, and Richard D. Banner, the tail-load variations in the linear lift range will be discussed. The present discussion will be limited to the angle-of-attack range above the lift break, that is, the range which would normally not be penetrated by a stable, controllable airplane.

The balancing tail loads at high angles of attack decrease to quite low values. The pitching of the airplane, however, produces a large positive increment and results in an aerodynamic load that continually increases with angle of attack. The structural load is relieved somewhat by the tail inertia, but has a variation similar to that of the aerodynamic load.

The envelope of the structural buffet loads encountered by the tail during these maneuvers is shown at the bottom of figure 4. Although not indicated in this figure, the X-5 buffets even at zero lift because its tail is almost directly behind the wing and is immersed in the disturbed wing wake. The magnitude of the buffeting is very low and is barely perceptible to the pilot. As the airplane pitches to high lift there is an increase in the buffet magnitude. The greatest magnitude measured has been about  $\pm 400$  pounds at 40,000 feet.

The buffeting of the D-558-II for the subsonic example shown in figure 4 starts at about  $3^\circ$  angle of attack as compared with about  $16^\circ$  angle of attack for the supersonic maneuver. There is an abrupt

increase in magnitude as the linear lift range is exceeded, with a peak value of about  $\pm 2,000$  pounds being reached at  $24^{\circ}$  angle of attack, after which the buffet loads decrease slightly. The peak buffet loads in the maneuver shown at supersonic speeds are smaller; however, maximum lift was not attained during this maneuver.

The maximum measured total structural tail loads, including buffet loads, were reached near a Mach number of 0.90 for both airplanes and did not exceed 1,500 pounds for the X-5 or 3,500 pounds for the D-558-II at 40,000 feet. A comparison of these values with the tail design loads indicates that in pitch-ups to these high angles of attack the limit load of the horizontal tail would not be exceeded at altitudes above 10,000 feet for either airplane.

The wing loads resulting from the instability are critical only for certain ranges of altitude, as shown in figure 5. The maximum lift determined at high altitude, shown by a solid line, was used to establish the altitude above which the limit load factor,  $7.33g$ , could not be exceeded. The dashed line represents the altitude variation below which the stability boundary cannot be reached without exceeding the limit load factor. The shaded area between the two lines is therefore the altitude range where the limit load factor may be inadvertently exceeded as a result of the instability. The upper boundary has not been defined through the entire Mach number range. Figure 5 shows that, for the present speed range of the X-5, flight testing above 30,000 feet should prevent inadvertently exceeding the limit load factor. The D-558-II, however, because of its large speed range, requires altitudes considerably above 50,000 feet if the region above the stability boundary is to be safely investigated at supersonic speeds. One point that this figure brings out is that the horizontal-tail loads discussed previously do not limit the airplanes anywhere in the flight range, as the over-all design limit load factor can be exceeded at higher altitudes than that at which the horizontal-tail loads become critical.

One change in the loading of the wing that results from the reduction of longitudinal stability is shown in figure 6. Here the measured variation of the lateral center of pressure of the additional air load with Mach number is shown for the stable flight range and for the region above the stability boundary. The lateral center-of-pressure location for the exposed wing area of the X-5 remains constant with Mach number at about 52 percent of the semispan in the stable range, but moves 20 to 25 percent inboard when the stability boundary is passed. The center of pressure for the D-558-II shows a similar, though smaller, shift inboard from the constant location it has in the stable range. These inboard shifts result in a decreased wing bending moment as the stability boundary is passed.

Turning now to loads resulting from lateral-stability deficiencies, figure 7 shows several lateral divergences at high lift for the X-5. In the top portion of the figure are the variations of angles of attack and sideslip existing during the divergences. The variations of unsymmetrical horizontal-tail load and aerodynamic vertical-tail load are shown in the lower plots. The large rolling and pitching motions accompanying these divergences are probably the cause of some of the variations in the measured loads. These vertical-tail-load measurements show that, even though the airplane has become directionally unstable, the vertical tail is still being loaded up as the airplane sideslips to large angles. The vertical-tail load per degree of sideslip measured for the X-5 in divergences over the Mach number range is slightly less than that measured in the normal flight range; this result indicates that only a slight reduction in the vertical-tail effectiveness occurs at these large angles of attack. The vertical-tail loads measured would not be critical above about 15,000 feet if the same divergences were encountered at low altitude.

The unsymmetric horizontal-tail loads measured during these maneuvers are nonlinear and, although probably affected by the rolling motions, generally indicate positive effective dihedral through about  $10^{\circ}$  sideslip. The variations of these unsymmetric loads are about half the magnitude of the tail structural loads which were discussed previously.

Mention might be made of one occurrence of unexpectedly high loads resulting from stability deficiencies on the X-5 airplane. A spin resulted from the longitudinal and directional instabilities at a Mach number of 0.7 and an altitude of 43,000 feet. As a result of the high rate of rotation in the spin, centrifugal forces tending to unsweep the wing were developed. This subjected the sweep mechanism to a compressive load three times greater than the maximum expected in normal flight at  $59^{\circ}$  sweep. Fortunately, the mechanism was designed for compression loads equal to the expected tension load, which was approximately the value obtained in the spin.

Briefly summarizing: The pitch accelerations and horizontal-tail loads developed during pitch divergences to high angles of attack with the X-5 and D-558-II airplanes were not excessive. The over-all airplane limit load could be inadvertently exceeded over a range of altitudes which varied widely with Mach number and was determined by the stability boundary and the maximum-lift boundary. At angles of attack above the stability boundary, there is an inward shift of the lateral center of pressure which results in reduced wing bending moments. The vertical tail of the X-5 was nearly as effective during lateral divergences at high angles of attack as it was at normal altitudes. Unexpectedly large internal wing structural loads were obtained during a spin resulting from a pitch-up.

## GENERAL ARRANGEMENT OF X-5 AND D-558-II AIRPLANES

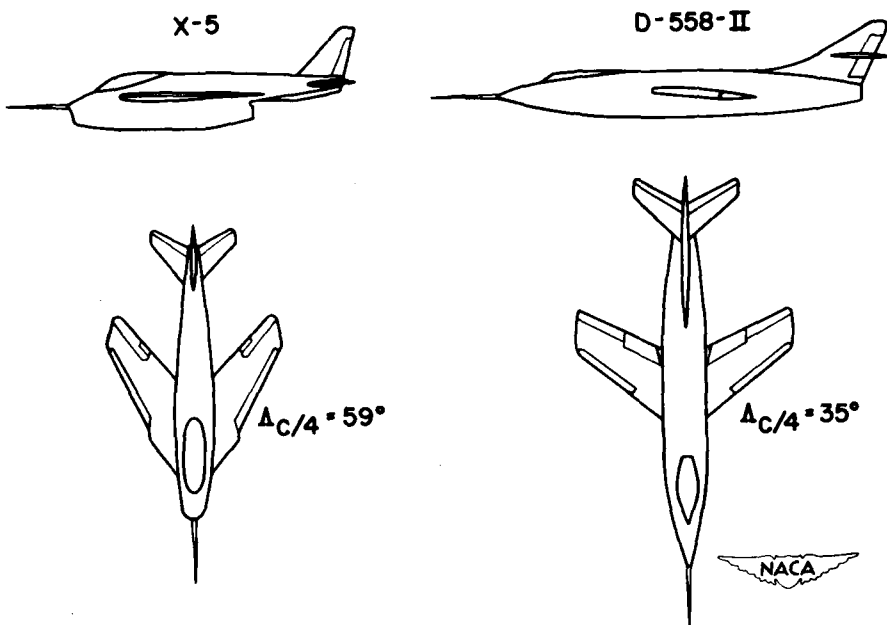


Figure 1.

## MAXIMUM MEASURED ANGLE OF ATTACK AND SIDESLIP

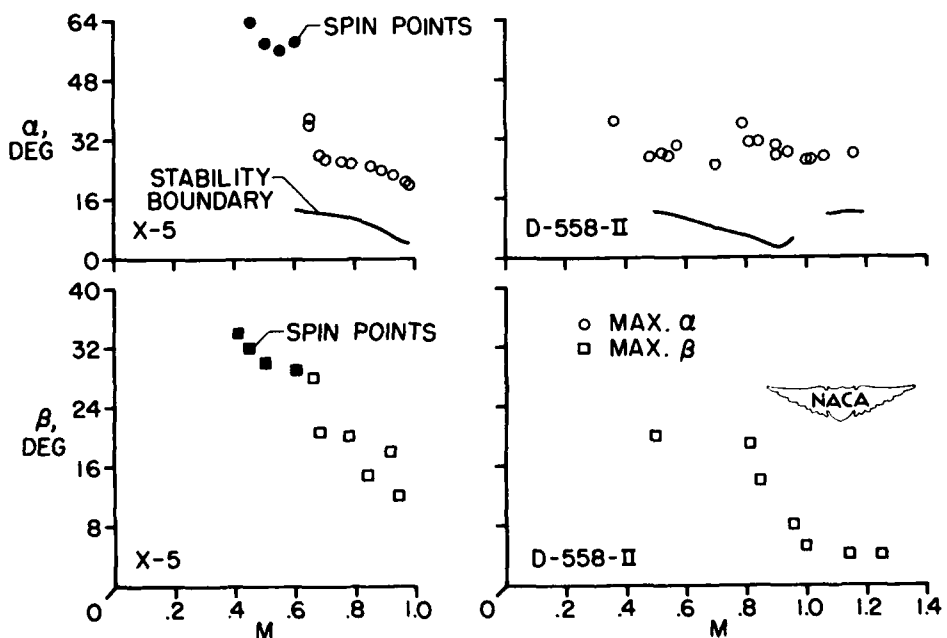


Figure 2.

CONFIDENTIAL

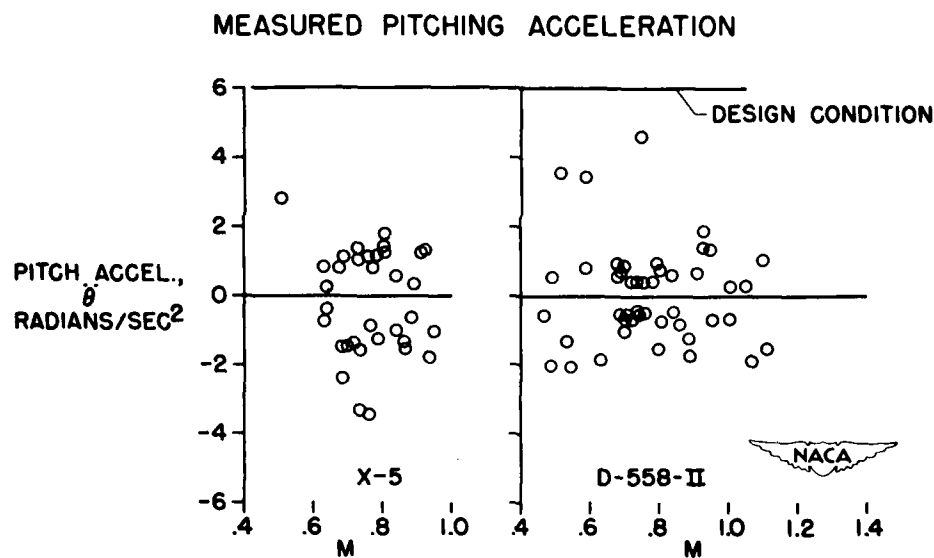


Figure 3.

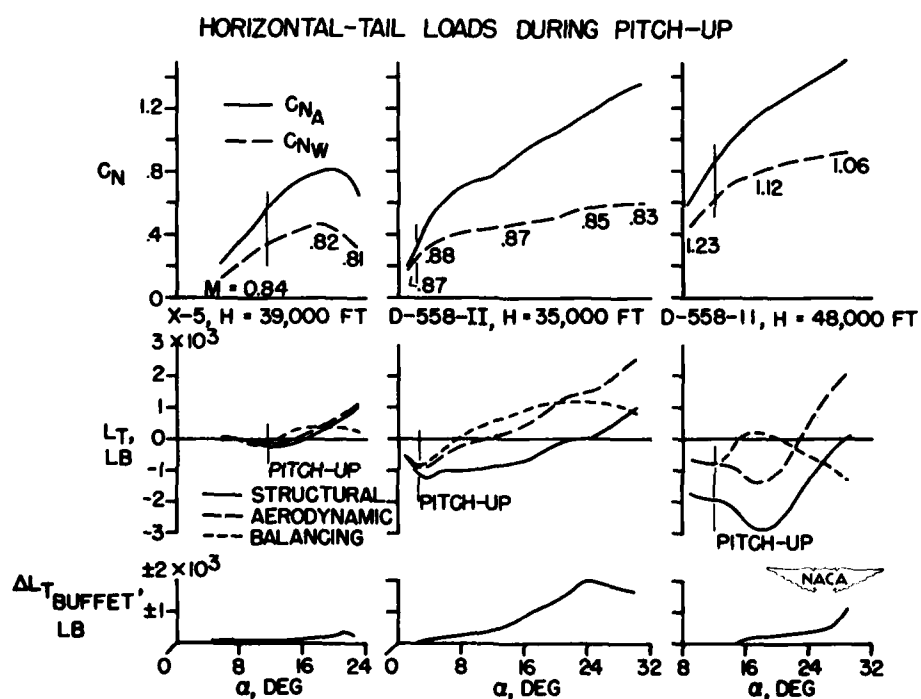


Figure 4.

CONFIDENTIAL

## ALTITUDES WHERE LIMIT LOAD CAN BE INADVERTENTLY EXCEEDED

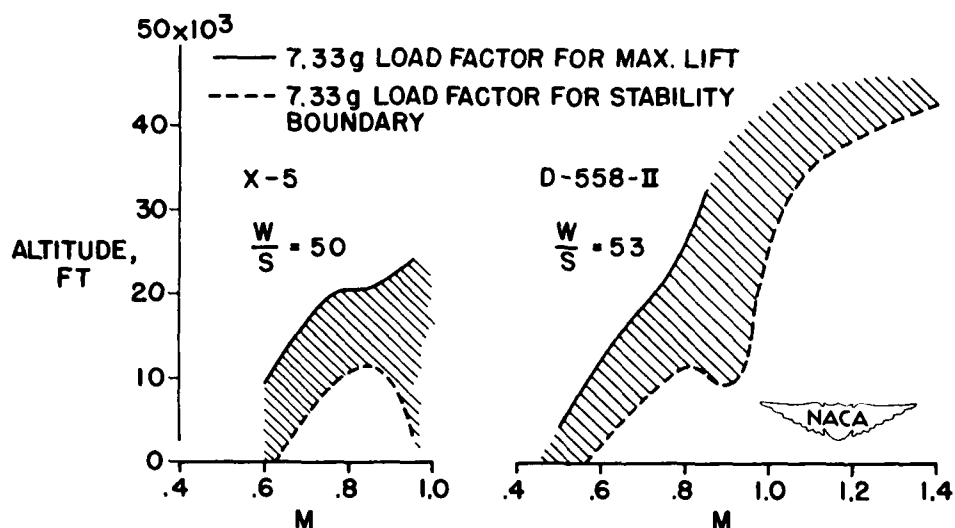


Figure 5.

## LOCATION OF LATERAL CENTER OF PRESSURE

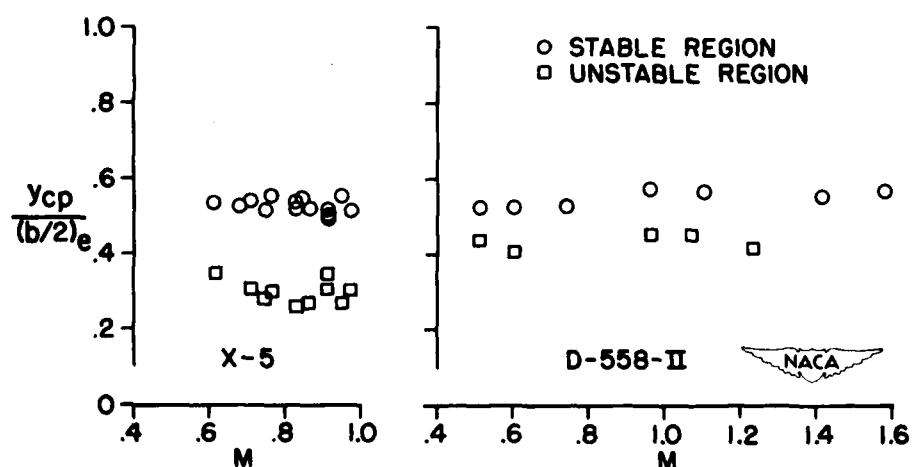


Figure 6.

## X-5 TAIL LOADS DURING DIRECTIONAL DIVERGENCE

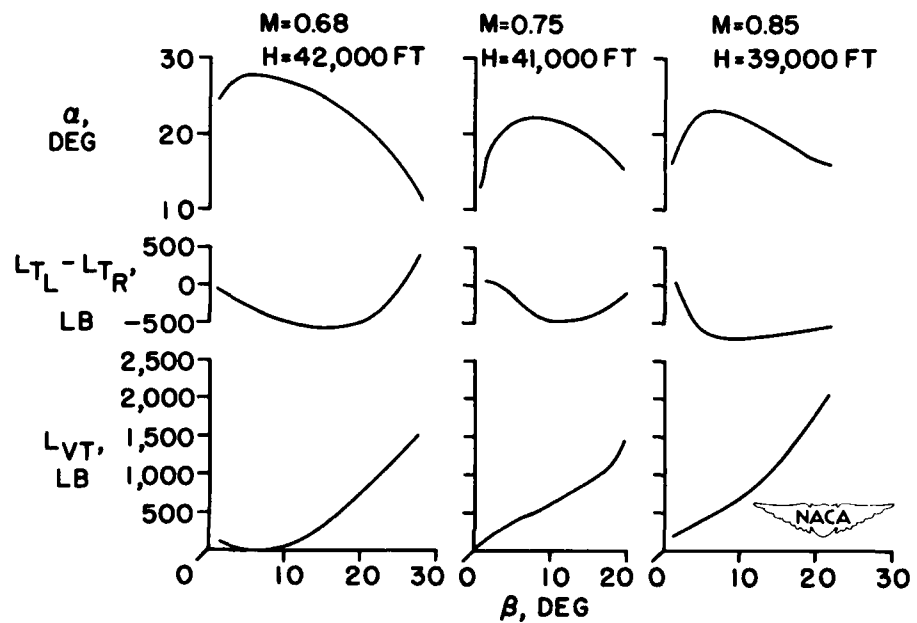


Figure 7.

**CONFIDENTIAL**

**33**

## **LOAD DISTRIBUTION ON LIFTING SURFACES**

**CONFIDENTIAL**

## PREDICTION OF THE LOAD DISTRIBUTION ON SWEPTBACK WINGS

By Harold J. Walker and William C. Maillard

Ames Aeronautical Laboratory

Many experimental studies of the load distribution on sweptback wings have been made and various methods for calculating the loading have been developed, but rather limited attention has been given to defining the limiting conditions beyond which experiment and theory are no longer compatible. Since it is of interest to the designer to know approximately what these limiting conditions are and, in general, what changes in loading may be expected to occur when these conditions are exceeded, an experimental study was recently made in which the loading characteristics of a typical  $45^{\circ}$  sweptback wing at subsonic and supersonic Mach numbers are compared with predicted loadings. The purpose of this paper is to present a brief discussion of the principal findings of this study (as yet unpublished). The results presented for the representative model are compared with those for wings of other shape and scale, with a view toward defining a common limit above which good load predictions can no longer be made. It is pointed out that the results pertain to wings without high-lift or stall-control devices.

The principal features of the model under consideration are shown in figure 1. The wing has  $45^{\circ}$  of sweepback, an aspect ratio of 5.5, a taper ratio of 0.5, and is mounted on a slender body of revolution. Six rows of pressure orifices, indicated by the dotted lines, were employed to measure the loads on the model. The tests were made at Mach numbers from 0.50 to 0.95 at a Reynolds number of about  $2.5 \times 10^6$  in the Ames 16-foot high-speed tunnel, and at Mach numbers from 1.2 to 1.7 at a Reynolds number of  $1.8 \times 10^6$  in the Ames 6- by 6-foot supersonic tunnel.

As is customary in analyzing the loads on wings, the distributions of loading along the span and the chord are treated separately, the span loadings being considered first. In figure 2, measured span loadings for three representative normal-force coefficients at a Mach number of 0.70 are compared with the theoretical loading predicted by the Weissinger method (ref. 1) corrected for the interference of the body and the elastic deformation of the wing. Experiment and theory are seen to agree closely until the loading at the outer sections begins to diminish. The lateral centers of loading in relation to the wing semispan are also shown in figure 2. The loss in loading at the outer sections is seen to be accompanied by an inboard shift of the center of loading. This condition would result in a conservative prediction of wing-root bending moment, but an unconservative prediction of inboard section loads at the higher normal-force coefficients. The normal-force

coefficient at which the center of loading begins to shift inboard has been chosen as the limit below which the spanwise loading can be satisfactorily predicted by existing methods. The trends shown in figure 2 are typical of those for subsonic Mach numbers.

Similar comparisons of the experimental and theoretical spanwise load distributions are shown in figure 3 for a Mach number of 1.23. The theoretical loading was determined by conical flow theory (ref. 2) corrected, as before, for the interference of the fuselage and the elastic deformation of the wing. The deviation of the experimental from the theoretical loads observed over the outer sections was found to be about the same for all normal-force coefficients investigated, and is possibly due to the fact that wing-thickness effects are not taken into account in conical flow theory. The experimental and theoretical lateral centers of loading, shown in figure 3, differ by a nearly constant amount. In view of this deviation, which, in general, is representative of those obtained throughout the supersonic Mach number range, the loadings can be estimated with only fair accuracy to the highest normal-force coefficients so far investigated.

The limiting normal-force coefficients for good prediction of spanwise loading are shown for the entire Mach number range in figure 4. The tests at the supersonic Mach numbers have not yet been carried to normal-force coefficients high enough to determine the limits for good prediction, and the line shown for these Mach numbers represents only the limit of the test data. It is interesting to observe that the limit rises somewhat at the higher subsonic Mach numbers. This rise is believed to be due to extensive supersonic flow over the upper wing surface which causes a delay in flow separation.

In this paper the chordwise loadings on swept wings will, for the most part, be predicted from two-dimensional airfoil data (as yet unpublished) in the manner employed in reference 3 for low Mach numbers. The concept employed is illustrated in figure 5, which depicts the chordwise pressure distributions at a midsemispan station of a  $35^{\circ}$  swept wing of aspect ratio 5 for a Mach number of 0.80 and a normal-force coefficient of 0.65 (ref. 4). In the diagram on the left (see fig. 5), the solid line represents the pressure distribution measured on the three-dimensional wing in a plane normal to the quarter-chord line of the wing. The short dashed line represents the pressure distribution for the two-dimensional airfoil section in this plane at the appropriate component of the free-stream Mach number, namely, 0.65 for this degree of sweep. The pressure distributions are compared at equal normal-force coefficients and are seen to be in fairly close agreement. A similar comparison of the pressure distributions for a streamwise section is illustrated in the diagram on the right. The pressure distribution, represented by the dashed line, was obtained for a two-dimensional airfoil with the streamwise section at the free-stream Mach number of 0.80. The two pressure distributions

in this case are seen to be markedly different. It is apparent from these comparisons that, to obtain satisfactory predictions of the chordwise loadings, the sweep of the wing must be taken into account by considering the effective wing section and Mach number component to be normal to the quarter-chord line. All subsequent comparisons, therefore, will be based on sections taken in this direction.

Typical comparisons at equal normal-force coefficients of the chordwise loading predicted from two-dimensional data with experimental loadings in the vicinities of the wing root, midsemispan, and tip of the  $45^{\circ}$  sweptback wing at a Mach number of 0.70 are shown in figure 6. It is important to note that, although the wing pressure distributions were measured in the directions indicated, the two-dimensional distributions shown for comparison still pertain to the section and component of Mach number normal to the quarter-chord line. The agreement, indicated for the midsemispan station, is representative of that obtained over the shaded region of the wing shown in figure 6. The root and tip loadings deviate from the predicted loadings to the extent indicated by the displacement of the load centroids; however, the loadings are still considered to be in fairly good agreement. The influence of the ends becomes negligible at approximately 1 local chord length from each end. (See ref. 5.)

No simple criterion exists for distinguishing good predictions from poor predictions in the case of the chordwise loadings; hence, the boundary between the two is largely a matter of judgment. In figure 7 are shown typical load distributions at the midsemispan station for a Mach number of 0.70. The measured loadings are indicated by the solid lines; the predicted loadings, by the short dashed lines. At a section normal-force coefficient  $c_n$  of 0.37, the loadings are in close agreement and the prediction is considered to be good. At  $c_n = 0.45$ , the flow has begun to separate near the leading edge, and the measured loading deviates noticeably from the two-dimensional loading. The limiting normal-force coefficient for good prediction was chosen as that corresponding to a load distribution approximately midway between the two loadings shown. For sweptback wings with leading-edge flow separation, such as the present one, the loading changes markedly and unpredictably in the vicinity of the quarter-chord point as the normal-force coefficient is increased further. Because of the nature of the change in loading for this section, very little shift in the center of pressure occurs until much higher normal-force coefficients than those shown in figure 7 are reached.

The limiting normal-force coefficients for good prediction of chordwise loading are shown in figure 8 as a function of Mach number  $M$  for those regions of the wing not significantly affected by the root and tips. At the supersonic Mach numbers, sufficient data to determine the prediction limit has not yet been obtained and the solid line shown represents merely the limit of the test data. Below this line the

predictions, although not as good as those obtained at subsonic Mach numbers, were considered to be fair. At subsonic Mach numbers above 0.90, little resemblance was found between the measured and predicted loadings, principally because of the presence of strong shocks extending outboard from the wing-body juncture; hence, the boundary drops rapidly to zero at  $M = 0.90$ .

Between Mach numbers of 0.50 and 0.85, it is noted that the limiting normal-force coefficients for good prediction of chordwise loading may be closely approximated by the maximum lift coefficient for the corresponding infinite yawed wing, represented by the broken line. This relationship suggests that, by the use of a parameter equal to the ratio of limiting normal-force coefficient to the maximum lift coefficient of the infinite yawed wing, the prediction limits of chordwise loading for wings of various shape, profile, and scale can be correlated. In figure 9, experimentally determined limits for good prediction are shown in terms of this parameter as a function of Mach number for the midsemispan stations of plane and cambered  $45^\circ$  sweptback wings of aspect ratios 3 and 6 (refs. 3, 6, and 7), and of plane wings of  $35^\circ$  (ref. 4) and  $45^\circ$  sweepback. It is noted that the respective limits do tend to group together in the vicinity of the limit for the infinite yawed wing, except at the higher Mach numbers. At the lower Mach numbers, limits greater than those for the infinite yawed wing occur, because, in most cases, it was possible to predict the chord loads by using theoretical rather than experimental two-dimensional loadings after the maximum lift coefficient for the infinite yawed wing had been exceeded. At the higher Mach numbers, the limits fall to zero, primarily a result of the spread over the wing of strong shocks from the wing root. Good predictions for the  $35^\circ$  swept wing were obtained at somewhat higher Mach numbers than for the  $45^\circ$  swept wing of aspect ratio 5.5 even though the critical Mach number for the  $35^\circ$  swept wing is lower because of the difference in sweep angle. Predictions of the loading near the midsemispan of the  $35^\circ$  swept wing were possible beyond the point where shocks first appeared on the wing, because these shocks were mainly a result of local flow conditions and were essentially two-dimensional. On the other hand, the shocks on the  $45^\circ$  swept wing, because of the increased sweep and the presence of a fuselage, originated at the wing-body juncture and, being three-dimensional, could not be predicted from two-dimensional airfoil characteristics. The limits for the wings of aspect ratio 3 break before those for the wing of aspect ratio 5.5, because relatively larger regions of the low-aspect-ratio wings are influenced by the shocks extending from the root. The limit for the cambered wing drops slightly before that for the symmetrical wing because of the formation of shocks at a lower Mach number on the cambered wing.

The prediction limits for the spanwise load distributions on the various wings are shown in figure 10 in terms of the same parameter used for the chordwise loads. Again the limits, with the exception of those

for the plane wing of aspect ratio 3, tend to group together at Mach numbers below 0.80; however, the general level of the grouping is above that for the infinite yawed wing by roughly 15 percent. Thus, the spanwise loadings can be predicted to higher normal-force coefficients than the chordwise loadings. This result can be explained by examining further the local section-lift characteristics of the  $45^\circ$  swept wing of aspect ratio 5.5.

The variations of the section normal-force coefficients with angle of attack at five semispan stations for the  $45^\circ$  swept-wing model are shown in figure 11 for a Mach number of 0.50. The solid lines refer to the measured variations; the dashed lines, to those predicted using span loading theory and section data for an infinite yawed wing. The measured maximum-force coefficients approximate the predicted maximum values at the outer sections, but become increasingly greater than the predicted values for stations approaching the wing root. This increase in maximum normal-force coefficient is due principally to the tendency for boundary-layer air to flow laterally across the wing when flow separation is imminent. (See ref. 8.) This secondary flow relieves the buildup of low-energy air in the boundary layer in much the same manner as do suction slots or other boundary-layer control devices, thereby increasing the lifting capacity of the wing sections. Since the lateral flow is most effective near the root, the loads at high angles of attack at the inboard sections of the wing are very much greater than those at the tip. Whereas the normal-force coefficient for the tip station reaches a maximum at an angle of attack of  $9^\circ$ , that for the root station is still increasing at an angle of attack of  $20^\circ$ . From the spanwise loading curves for this wing it was determined that the first section to reach a maximum normal-force coefficient is located at approximately 85 percent of the semispan. This section has a maximum normal-force coefficient higher than the predicted value but slightly lower than the corresponding wing normal-force coefficient. It is for this reason that the limits for good span load prediction, shown in figure 10, lie above those for the infinite yawed wing. At present, no method exists for calculating the maximum normal-force coefficients of the inboard sections.

The limits for good chordwise load prediction at the three intermediate stations, on the other hand, generally lie close to those for the infinite yawed wing, as shown in figure 11 by the circled points. The limit for the root section is above that for the infinite yawed wing, principally because of the relieving effect of lateral flow previously mentioned. The limit for the tip section is below that for the infinite yawed wing, since this section is affected by spanwise boundary-layer flow from the inboard sections which have already reached the maximum lift coefficient for the infinite yawed wing.

The subject of load prediction for sweptback wings may be brought to a close at this point by briefly recalling several of the more significant results.

First, the spanwise load distributions, and, hence, the root bending moments, may be satisfactorily predicted at subsonic speeds up to a normal-force coefficient somewhat higher than that for the infinite yawed wing. Above the limit for good prediction, the loading generally shifts inboard with the result that the root bending moments are generally overestimated.

Second, the limiting wing normal-force coefficient below which good prediction of chordwise load distributions can be made at subsonic speeds is approximately equal to the maximum lift coefficient for the corresponding infinite yawed wing, except when strong shock waves from the root section are present.

Third, the maximum normal-force coefficients of the inboard wing sections, because of the lateral drainage of separated boundary-layer air, are much greater than those predicted from two-dimensional wings in yawed flow; hence, the loading at these sections may be seriously underpredicted.

Fourth, the chordwise and spanwise load distributions at supersonic speeds may be predicted by conical flow theory with only fair accuracy.

## REFERENCES

1. DeYoung, John, and Harper, Charles W.: Theoretical Symmetric Span Loading at Subsonic Speeds for Wings Having Arbitrary Plan Form. NACA Rep. 921, 1948.
2. Cohen, Doris: Formulas for the Supersonic Loading, Lift and Drag of Flat Swept-Back Wings With Leading Edges Behind the Mach Lines. NACA Rep. 1050, 1951.
3. Hunton, Lynn W.: Effects of Finite Span on the Section Characteristics of Two  $45^{\circ}$  Swept-Back Wings of Aspect Ratio 6. NACA RM A52A10, 1952.
4. Tinling, Bruce E., and Lopez, Armando E.: The Effects of Reynolds Number at Mach Numbers up to 0.94 on the Loading on a  $35^{\circ}$  Swept-Back Wing Having NACA 65<sub>1</sub>A012 Streamwise Sections. NACA RM A52B20, 1952.
5. Kuchemann, D.: A Simple Method for Calculating the Span and Chordwise Loadings on Thin Swept Wings. Rep. No. Aero. 2392, British R.A.E., Aug. 1950.
6. Kolbe, Carl D., and Boltz, Frederick W.: The Forces and Pressure Distribution at Subsonic Speeds on a Plane Wing Having  $45^{\circ}$  of Sweepback, an Aspect Ratio of 3, and a Taper Ratio of 0.5. NACA RM A51G31, 1951.
7. Boltz, Frederick W., and Kolbe, Carl D.: The Forces and Pressure Distribution at Subsonic Speeds on a Cambered and Twisted Wing Having  $45^{\circ}$  of Sweepback, an Aspect Ratio of 3, and a Taper Ratio of 0.5. NACA RM A52D22, 1952.
8. Furlong, G. Chester, and McHugh, James G.: A Summary and Analysis of the Low-Speed Longitudinal Characteristics of Swept Wings at High Reynolds Number. NACA RM L52D16, 1952.

CONFIDENTIAL

## PRESSURE - DISTRIBUTION MODEL

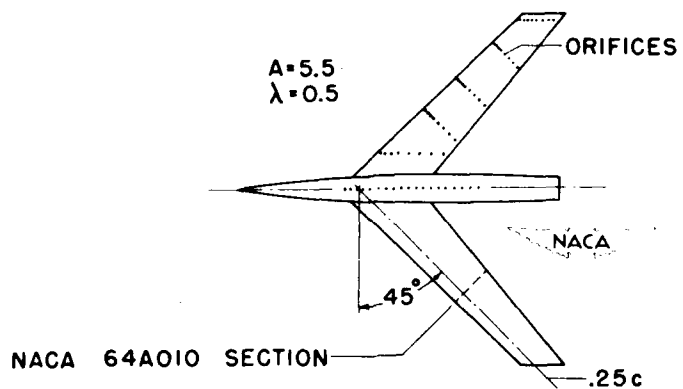


Figure 1.

## MEASURED AND THEORETICAL SPAN LOADINGS, M = 0.70

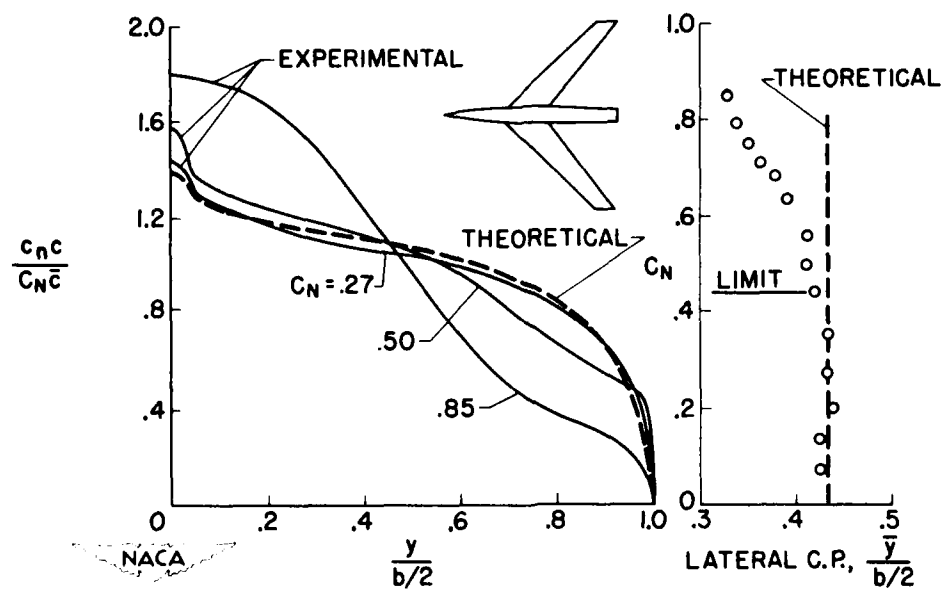


Figure 2.

CONFIDENTIAL

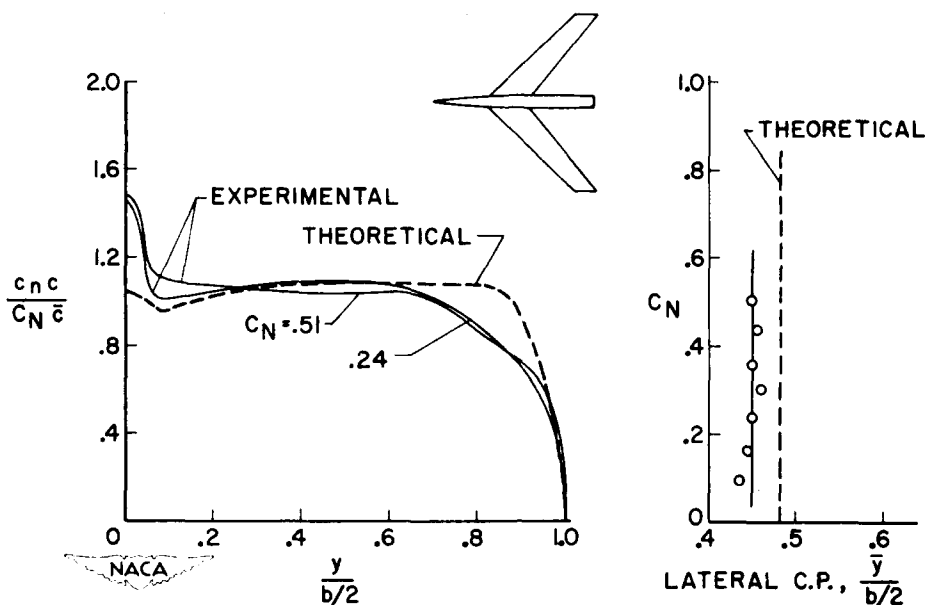
MEASURED & THEORETICAL SPAN LOADINGS,  $M = 1.23$ 

Figure 3.

## LIMIT FOR PREDICTION OF SPANWISE LOADING

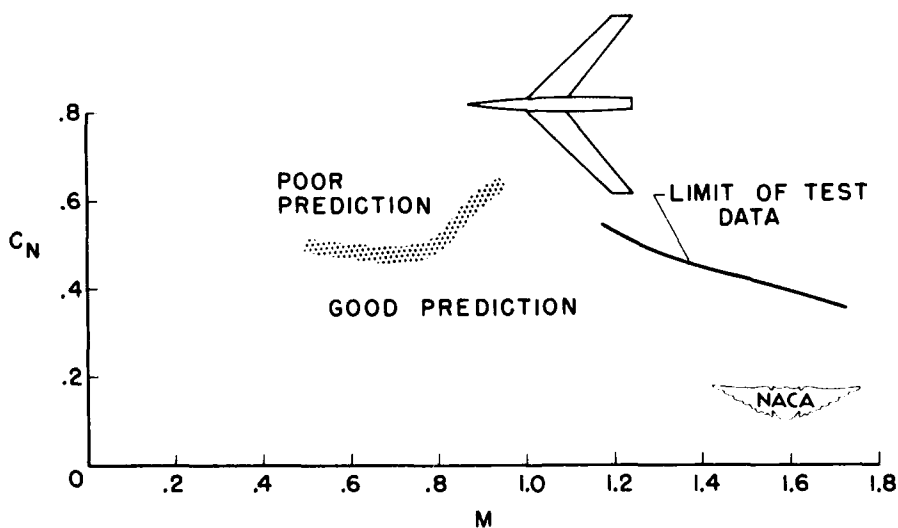


Figure 4.

CONFIDENTIAL

## COMPARISON OF CHORDWISE PRESSURE DISTRIBUTIONS

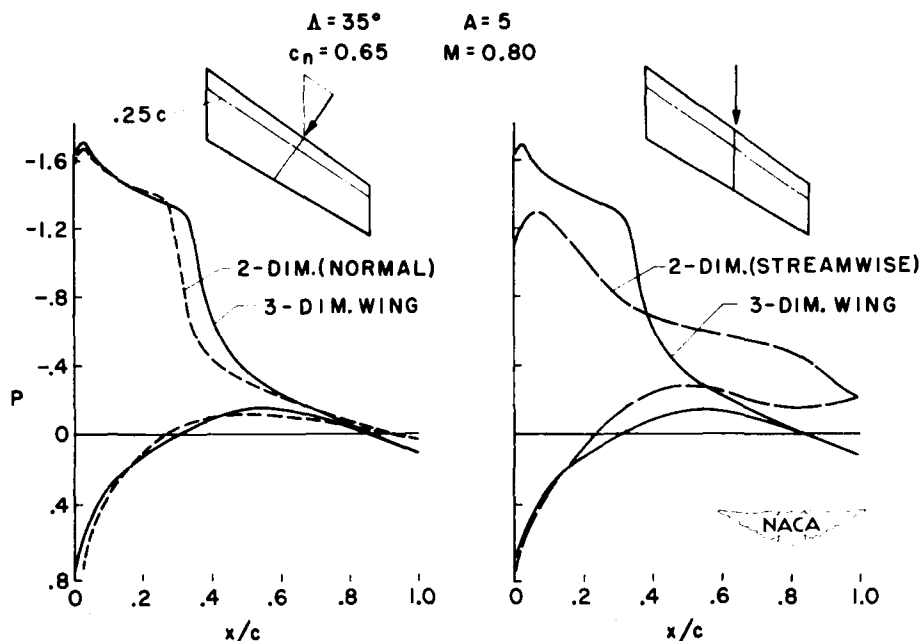


Figure 5.

## EXPERIMENTAL LOAD DISTRIBUTION

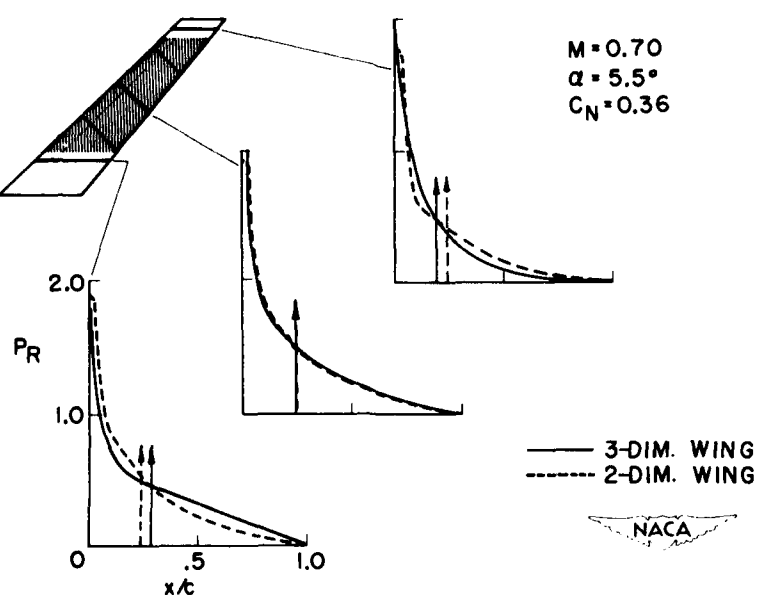


Figure 6.

CONFIDENTIAL

## EXPERIMENTAL LOAD DISTRIBUTION AT MIDSEMISPAN

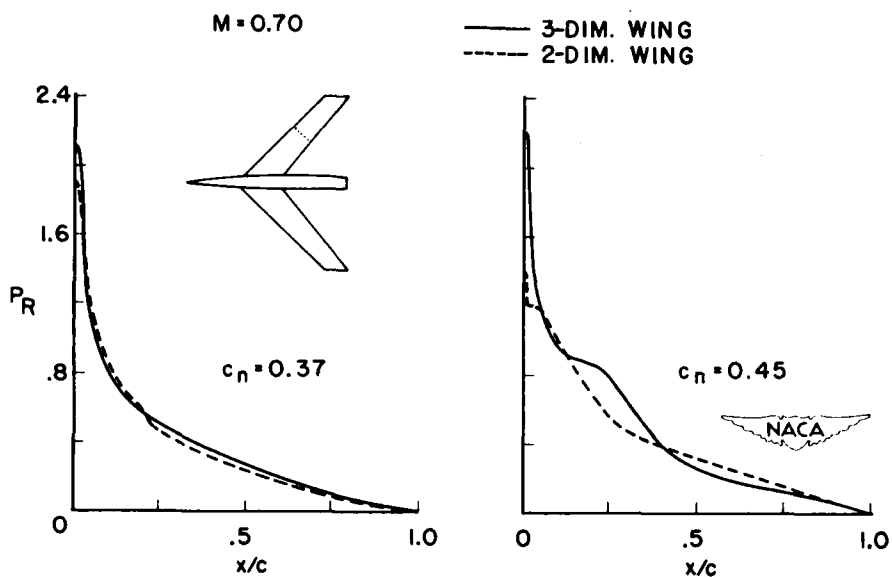


Figure 7.

## LIMIT FOR PREDICTION OF CHORD LOAD DISTRIBUTION

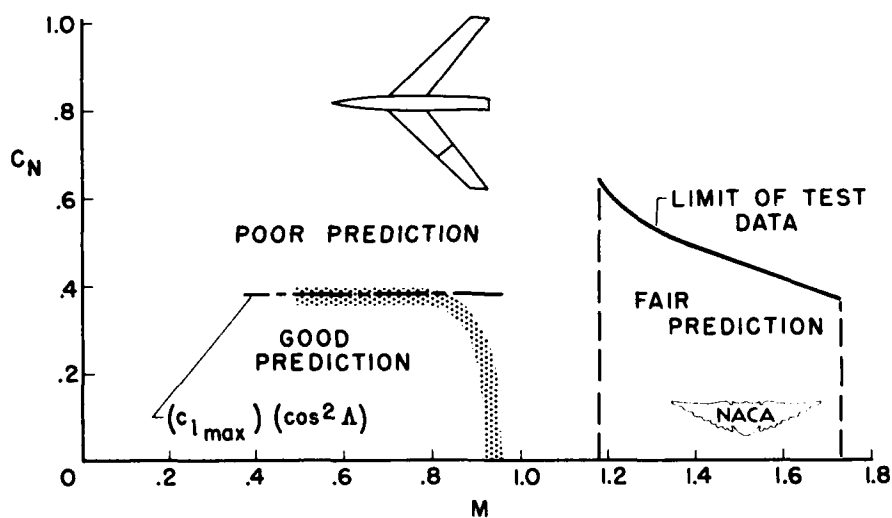


Figure 8.

## CHORD LOAD PREDICTION LIMIT

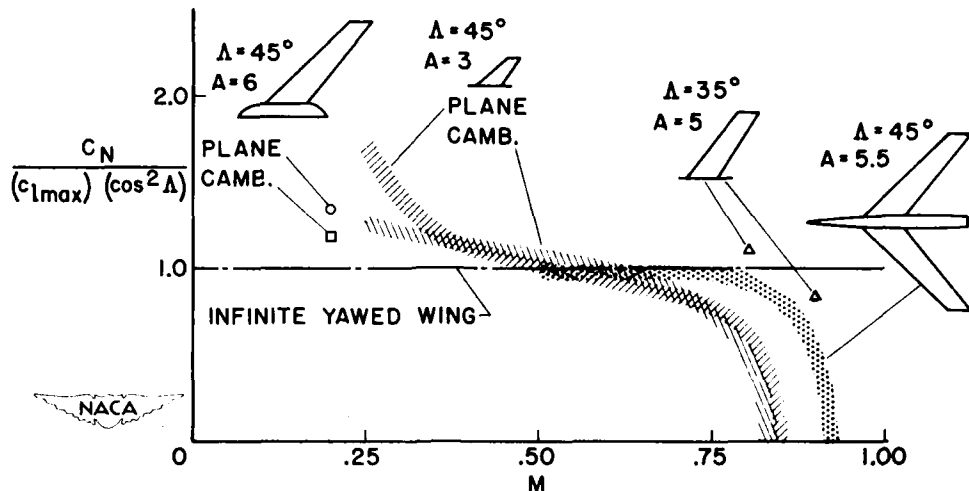


Figure 9.

## SPAN LOAD PREDICTION LIMIT

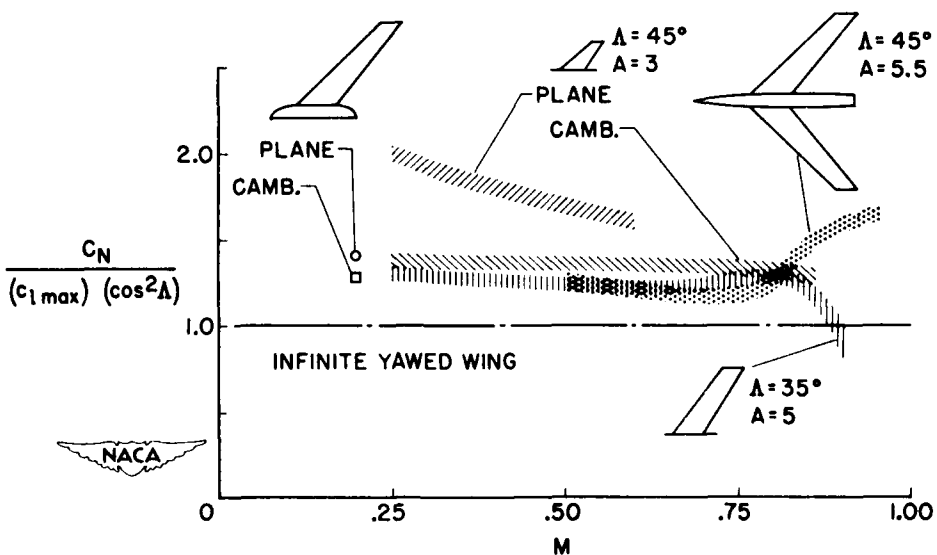


Figure 10.

## SECTION NORMAL-FORCE CURVES

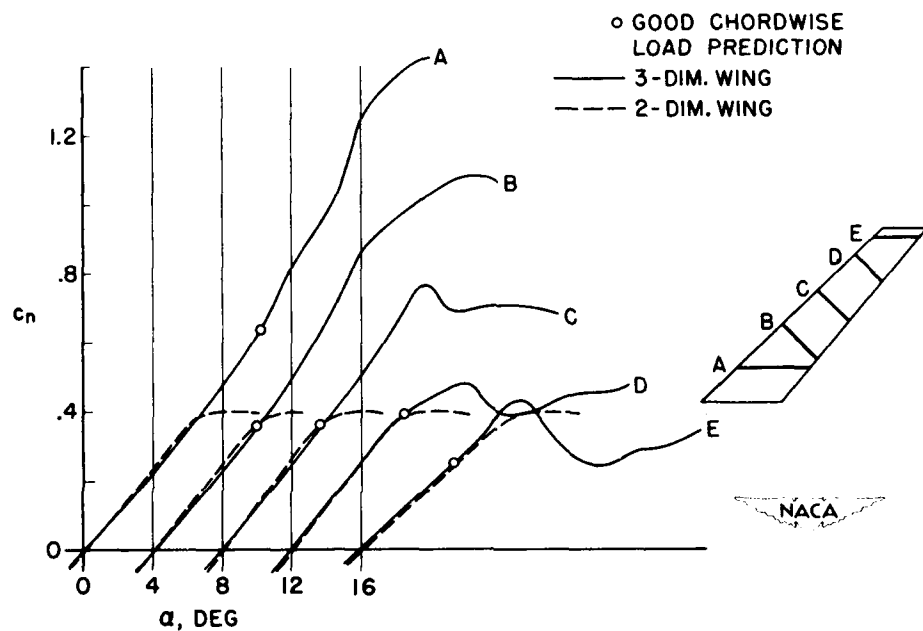
 $M=0.50$ 

Figure 11.

A STUDY OF AERODYNAMIC LOADS ON SWEPTBACK  
WINGS AT TRANSONIC SPEEDS

By Claude V. Williams and Richard E. Kuhn

Langley Aeronautical Laboratory

At the present time, the regions of separated and mixed flows which exist about configurations operating at transonic speeds seriously hinder accurate theoretical calculations of the various loading parameters used in the structural design of aircraft wings, and, therefore, these parameters must continue to be evaluated by experimental means. The purpose of this paper is to present some experimental information obtained from recent transonic-speed investigations of the loads on sweptback wings.

At transonic speeds, wing-section-thickness ratio appears to be one of the most important geometrical parameters. For example, a recent high-subsonic-speed wind-tunnel investigation has indicated that variation of Reynolds number from 2,000,000 to approximately 4,500,000 caused rather large changes in the spanwise load distribution of a representative thick swept wing (ref. 1). However, a comparison of the data obtained from transonic-speed investigations of a typical thin swept wing has shown that variation of Reynolds number from 2,000,000 to approximately 6,000,000 produced little or no effect on the spanwise load distribution on the wing (refs. 2 and 3).

The effects of thickness ratio on the spanwise or lateral center-of-pressure variations with Mach number  $M$  are shown in figure 1. Spanwise center-of-pressure data are of interest in that, for a given design load, the spanwise location of the center of pressure directly determines the values of the wing root bending moments. In figure 1, as in the following figures, the spanwise center-of-pressure location  $y_{cp}$  is expressed in terms of the semispan of the wing outside the body  $(b/2)_e$ .

The dashed-line curve in figure 1 shows the typical inward movement of the spanwise center of pressure with increase in Mach number that has been observed for thick swept wings. These particular data were obtained from flight measurements on a current fighter-type airplane having a wing sweep angle  $\Lambda$  of  $35^\circ$  and approximately 9-percent-thick streamwise airfoil sections (ref. 4). The solid-line curve indicates the typical outward shift of the spanwise center of pressure with increase in Mach number that has been noted for thin swept wings. These data were interpolated from transonic wind-tunnel measurements of a 6-percent-thick,  $45^\circ$  swept-back wing (ref. 2). The curves are presented for a normal-force coefficient of 0.4 which is within the moderate normal-force-coefficient

range where the wing tips are relatively free from stall effects, and, therefore, the variations shown are indicative of the conditions when the spanwise center of pressure is at, or near, its most outboard position. A rather limited analysis of the available transonic-speed, sweptback-wing data has been made, and this analysis indicated that the transition from thick-wing to thin-wing characteristics takes place at thickness ratios on the order of 6 or 7 percent.

Because of certain aerodynamic advantages, primarily the reduction of the wing drag at transonic and supersonic speeds, most future airplanes will have thin wings. In view of the opposing trends shown by the curves in figure 1, it is apparent that care should be used when extrapolating center-of-pressure data obtained from current thick-wing configurations for use in the structural design of future thin-wing airplanes to avoid a serious underestimation of the values of the root bending moments of the thin wing.

Since thin wings will be utilized in future aircraft designs, a more detailed discussion of the center-of-pressure characteristics of the typical thin swept wing should be of interest. This analysis will be based on the data of figure 2 which shows the spanwise center-of-pressure variation with Mach number at several angles of attack  $\alpha$  for the thin-wing—curved-body configuration shown in the figure. The data presented were obtained from reference 2 except for the variation at an angle of attack of  $10^\circ$  which was obtained from unpublished data. The wing had  $45^\circ$  sweepback of the quarter-chord line, aspect ratio of 4, taper ratio of 0.6, and NACA 65A006 streamwise airfoil sections. Data obtained from this model were presented at the NACA Conference on Aircraft Loads, March 5-6, 1951, and since that time, further information on modifications of this basic configuration has been obtained, and is presented in this and a subsequent paper by Donald L. Loving.

From the curves of figure 2, it may be seen that in the transonic speed range, the spanwise center of pressure was relatively outboard at angles of attack of  $4^\circ$  to  $10^\circ$  which at a Mach number of 1.0 corresponds to normal-force coefficients on the order of 0.35 to 0.75. However, the most outboard location occurred at an angle of attack of  $8^\circ$  and a Mach number of 1.0. This most outboard location of the spanwise center of pressure generally represents the critical conditions for maximum root bending moments.

Pitch-up occurs at angles of attack somewhat higher than  $8^\circ$  for this configuration and in a previous paper by George S. Campbell it was shown that, if pitch-up occurs, the maximum design loads can be exceeded by a considerable amount. For the pitch-up case, the maximum loads would occur at some angle of attack higher than  $8^\circ$  for this configuration; this angle of attack depends upon the particular dynamic characteristics of the specific airplane in question.

Further, in the design of a wing, the combination of bending and twisting loads at the critical loading condition would be considered. However, since these twisting effects are usually small in relation to the effects of the bending loads, defining the critical root bending conditions by considering only the bending loads gives a good approximation of the critical loading conditions.

Another factor to consider when determining the critical loading condition is the effect of various wing auxiliary devices such as a fence. At subsonic speeds, fences on a swept wing delay the onset of tip stall, which would result in a more outboard location of the spanwise centers of pressure for the higher angles of attack. However, in the transonic-speed range, wing fences generally become ineffective and, therefore, the critical loading conditions would be unaffected by a wing fence. A discussion of various wing auxiliary devices is presented in the subsequent paper by Wilbur H. Gray and Jack F. Runckel.

The data shown in figure 3 indicate some of the effects on the variations of the spanwise center-of-pressure location with Mach number that result from increases in the angle of sweep of a thin wing. These data were obtained from an investigation in the Langley high-speed 7- by 10-foot tunnel and as yet have not been published. All of the wings shown in the figure had an aspect ratio of 3, taper ratio of 0.14, and NACA 65A003 streamwise airfoil sections. These data are in the unstalled lift-coefficient range where the most outboard centers of pressure occur and show that the location of the spanwise center of pressure is relatively constant at subsonic speeds, moves outboard in the transonic-speed range, and then moves inboard again at supersonic Mach numbers. Also, in the transonic-speed range, increase in sweep angle progressively moved the spanwise center-of-pressure locations outboard and raised the Mach number at which the maximum outboard locations of the center of pressure occurred. Although the center-of-pressure movements shown may appear to be small, it should be pointed out that at the 40-percent-semispan station, for example, a center-of-pressure shift of 3 percent of the semispan changes the value of the root bending moment by some  $7\frac{1}{2}$  percent of its value. Also in figure 3, it may be noted that the  $37^{\circ}$  sweptback wing had a plan form similar to a delta wing, and, therefore, the center-of-pressure characteristics shown give some idea of the characteristics of delta wings at transonic speeds. A detailed discussion of delta wings at supersonic speeds is given in a subsequent paper by John E. Hatch, Jr. and Kenneth Margolis.

Recently, a geometrically-twisted, sweptback wing has been investigated in the Langley 8-foot transonic tunnel. This wing had a plan form that was identical to the plan form of the wing for which the critical bending moment conditions were determined from the data of figure 2. A

comparison of these two wings gives some idea of the changes in loading that result from aeroelastic twisting due to the deflection of a swept-back wing under load.

A plan-form view of the model is shown in figure 4. Also, in figure 4 is shown the spanwise variation of the local section angles of attack when the body center line was at an angle of attack of  $0^\circ$ . As seen from the plot, the wing was twisted about the quarter-chord line

such that the tip was washed out approximately  $\frac{1}{2}^\circ$ . The twist of this

wing is considered to be a typical variation, and does not represent the twist of any particular type of wing structural system. In the following figures, the twisted wing will be compared with the similar untwisted wing shown in figure 2. In the future discussion, this untwisted wing will be referred to as the plane wing. Both the plane and twisted wings were investigated on the body shown in figure 4 instead of the curved body shown in figure 2. The effect of this change in body shape is discussed in a subsequent paper by Donald L. Loving. These wings are to be compared at the critical bending conditions of Mach number of 1.0 and angle of attack of  $8^\circ$  determined for the plane wing. Also, to provide an idea of the twist effects at subsonic speeds, a parallel comparison at a typical subsonic Mach number of 0.80 is presented.

Figure 5 presents the comparison of the spanwise distributions of the section normal-loading coefficient for the subsonic and critical transonic-speed conditions. The section normal-loading coefficient is defined as the section normal-force coefficient  $c_n$  multiplied by the ratio of the local section chord  $c$  to the average wing chord  $\bar{c}$ . These data are compared at wing normal-force coefficients  $C_{N_W}$  equivalent to an angle of attack of  $8^\circ$  for the plane wing; that is, 0.46 for the subsonic case and 0.53 for the transonic-speed case. For the twisted wing these normal-force coefficients correspond to angles of attack of approximately  $10\frac{3}{4}^\circ$  and  $10^\circ$ , respectively. It may be seen from the figure that, although the general shapes of the distributions at the two Mach numbers are dissimilar, the general effects of twist in both cases is, as would be expected, a reduction in the load over the outboard regions of the span and an increase in load over the inboard sections of the wing.

Figure 6 presents a comparison of the distributions of the pressure coefficient  $P$  for the plane and twisted wings at the subsonic Mach number of 0.80, and wing normal-force coefficient of 0.46. One of the first things to be noted in this figure is that the pressure-coefficient distributions over the lower surfaces of the wings are essentially the same. By referring to figure 5, the changes in loading may be correlated with the variations of the upper-surface pressure-coefficient distributions.

The pressure-coefficient distributions shown in figure 6 indicate that the increase in load for the twisted wing was located over the forward portion of the chord for the most inboard station. At the center sections of the span, the load over most of the chord was reduced, and at the tip, the distributions were virtually unchanged.

For the transonic-speed, critical-bending case, the pressure-coefficient distributions shown in figure 7 indicate, as for the subsonic speed case, that the major differences in loading between the plane and twisted wings were concentrated on the upper surfaces of the wings. Over the inboard regions, the difference in loading extended over much of the chord length, but at the outboard sections, the distributions show that the main reductions in loading were restricted to the trailing edges of the wing tip region. From practical considerations, this change in loading would have considerable effects on any control surfaces located in this region of the span.

Figures 8 and 9 present a summary of the center-of-pressure characteristics of the plane and twisted wings at Mach numbers of 0.80 and 1.00, respectively. The plan-view sketch in figure 8 shows the convention used to define the locations of the spanwise and chordwise centers of pressure. The chordwise center of pressure  $x_{cp}$  is expressed in terms of the average wing chord  $\bar{c}$ .

In figure 8, it may be seen that the location of the spanwise center of pressure of the twisted wing was inboard of that for the plane wing throughout the wing-normal-force-coefficient range of this investigation. The data presented correspond to angles of attack from  $4^\circ$  to  $20^\circ$ . At the higher normal-force coefficients, the tips of the twisted wing have not stalled to as great a degree as the tips of the plane wing, and therefore the curves tend to converge.

The chordwise center-of-pressure curves in figure 8 indicate that at subsonic speeds twisting the wing had little or no effect on the location of the chordwise center of pressure.

Figure 9 shows that at a Mach number of 1.00 in the low and moderate wing-normal-force-coefficient range, the spanwise center of pressure of the twisted wing, as at subsonic speeds, was relatively inboard of that for the plane wing. Also, it may be seen that the tip stall trend at the higher normal-force coefficients pointed out for the subsonic case has progressed to a degree where the curves are the same.

At this point, it will be of interest to point out the relationship of the chordwise center of pressure to the characteristics of the spanwise center of pressure. It has been shown that twisting the wing moved the spanwise center of pressure inboard. However, for a conventional

wing which usually has the elastic axis located in the 35- to 40-percent-chord region, the forward location of the chordwise center of pressure ahead of the elastic axis, such as is shown in figure 9, would tend to increase the local section angles of attack, and therefore move the spanwise center of pressure outboard. In general, however, these effects are small and, for any specific case, would depend upon the structural rigidity of the particular wing in question. The chordwise center-of-pressure curves in figure 9 show that at a Mach number of 1.00 for moderate wing normal-force coefficients, the chordwise center of pressure of the twisted wing lies somewhat ahead of that for the plane wing. Therefore, the twisted wing would tend to increase the local angles of attack of its airfoil sections to a greater extent than would the plane wing. As the normal-force coefficient is further increased, the twisting effect for both wings diminishes as the chordwise center of pressure approaches the elastic axis. This effect is also seen in figure 8 for a Mach number of 0.80.

All of the preceding discussion has been concerned with flight conditions that produce symmetrical loading over the wings. However, in flight, an airplane frequently experiences sideslip motions either through actions of the pilot or owing to the dynamic response of the airplane. An extensive investigation at high subsonic speeds of this unsymmetrical loading condition has recently been made in the Langley high-speed 7- by 10-foot tunnel, and a few representative curves selected from these tests are presented in figures 10 and 11. These loads were measured on the  $45^{\circ}$  swept-wing—curved-body configuration shown in figure 2.

The data in figure 10 show for Mach numbers of 0.70 and 0.93 at an angle of attack of  $4^{\circ}$  that increase in sideslip angle  $\beta$  from  $0^{\circ}$  to  $8^{\circ}$  caused the load over the forward wing to increase, while the load over the rearward wing decreased by about the same amount. However, at an angle of attack of  $8^{\circ}$ , the load on the forward wing increased somewhat over the reduction in load shown for the rearward wing especially at a Mach number of 0.93.

Figure 11 shows the variation of the spanwise center of pressure with sideslip angle at Mach numbers of 0.70 and 0.93. These data show that variation of sideslip angle from  $0^{\circ}$  to  $12^{\circ}$  had no effect on the spanwise center of pressure for either the forward or the rearward wing. At the top of the figure is plotted the variations of the root bending-moment coefficient  $C_B$  with sideslip angle and from these curves it may be seen that although the spanwise center of pressure of the wings remained the same with increase in sideslip angle, the increase in load over the forward wing shown in figure 10 produced the increase in bending-moment coefficient shown in figure 11 for the forward wing.

In conclusion, the main points in the preceding discussion are as follows: First, it was noted that for thick wings the spanwise center

of pressure moves inward, whereas for thin wings, the spanwise center of pressure moves outboard with increase in Mach number. Also, increasing the sweep angle of a thin wing causes the spanwise center of pressure to move progressively outward. Then, washing out a thin swept wing shifted the spanwise center of pressure inboard and at a Mach number of 1.0, this inboard shift was primarily due to the loss in load over the trailing edges of the outboard portions of the span. Finally, an investigation of the effects of sideslip on the loads over a swept-wing—curved-body combination has shown that increase in sideslip angle increased the relative load over the forward wing such that even though the spanwise center of pressure of the wings remained constant, the root bending-moment coefficients were increased.

## REFERENCES

1. Tinling, Bruce E., and Lopez, Armando E.: The Effects of Reynolds Number at Mach Numbers up to 0.94 on the Loading on a  $35^{\circ}$  Swept-Back Wing Having NACA 65<sub>1</sub>A012 Streamwise Sections. NACA RM A52B20, 1952.
2. Loving, Donald L., and Williams, Claude V.: Aerodynamic Loading Characteristics of a Wing-Fuselage Combination Having a Wing of  $45^{\circ}$  Sweepback Measured in the Langley 8-Foot Transonic Tunnel. NACA RM L52B27, 1952.
3. Solomon, William, and Schmeer, James W.: Effect of Longitudinal Wing Position on the Pressure Characteristics at Transonic Speeds of a  $45^{\circ}$  Sweptback Wing-Fuselage Model. NACA RM L52K05a, 1953.
4. Rolls, L. Stewart, and Matteson, Frederick H.: Wing Load Distribution on a Swept-Wing Airplane in Flight at Mach Numbers up to 1.11, and Comparison With Theory. NACA RM A52A31, 1952.

CONFIDENTIAL

## EFFECTS OF THICKNESS ON CENTER-OF-PRESSURE LOCATION

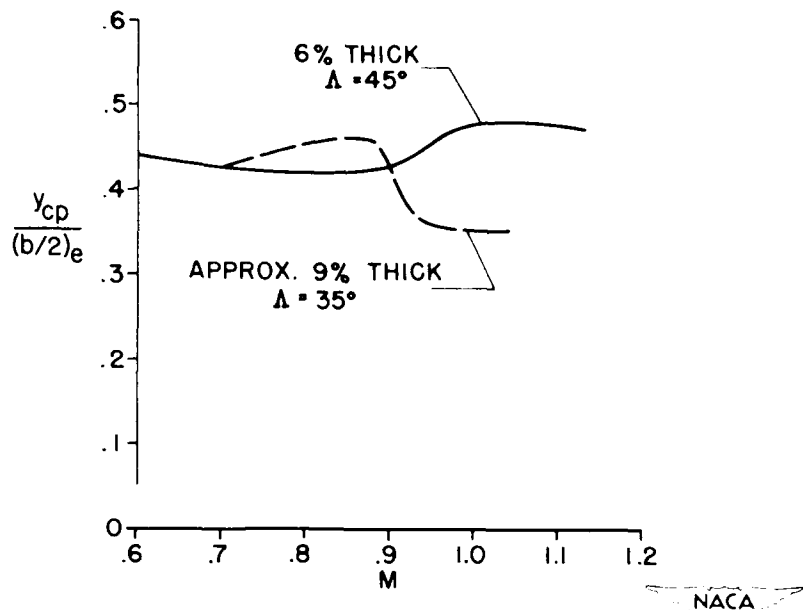


Figure 1.

## VARIATION OF SPANWISE CENTER OF PRESSURE

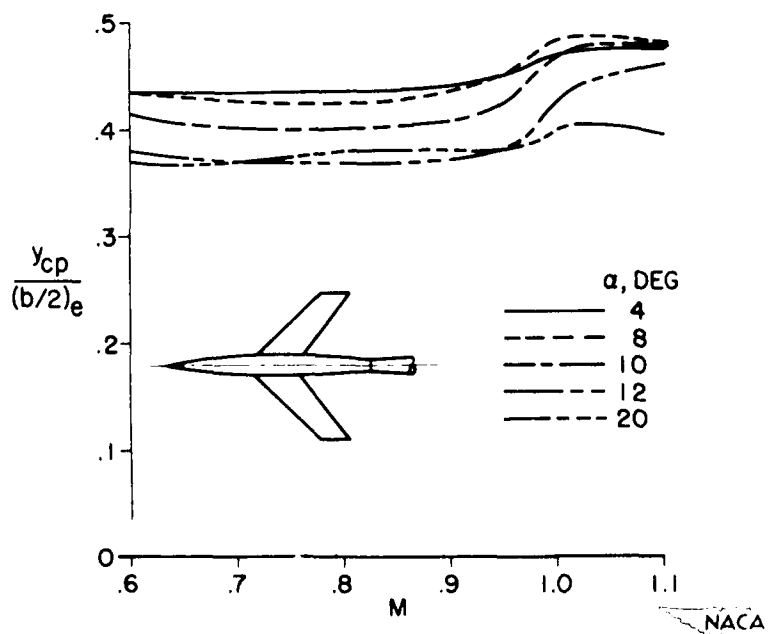


Figure 2.

CONFIDENTIAL

SWEET EFFECTS ON SPANWISE CENTER OF PRESSURE  
 $A = 3; \lambda = 0.14; t/c = 0.03$

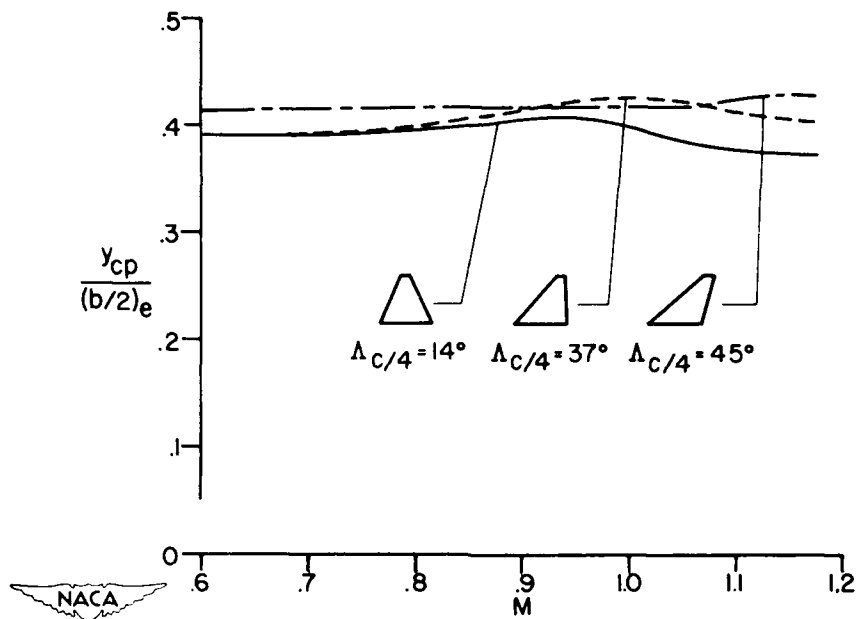


Figure 3.

## DETAILS OF WING-BODY CONFIGURATION

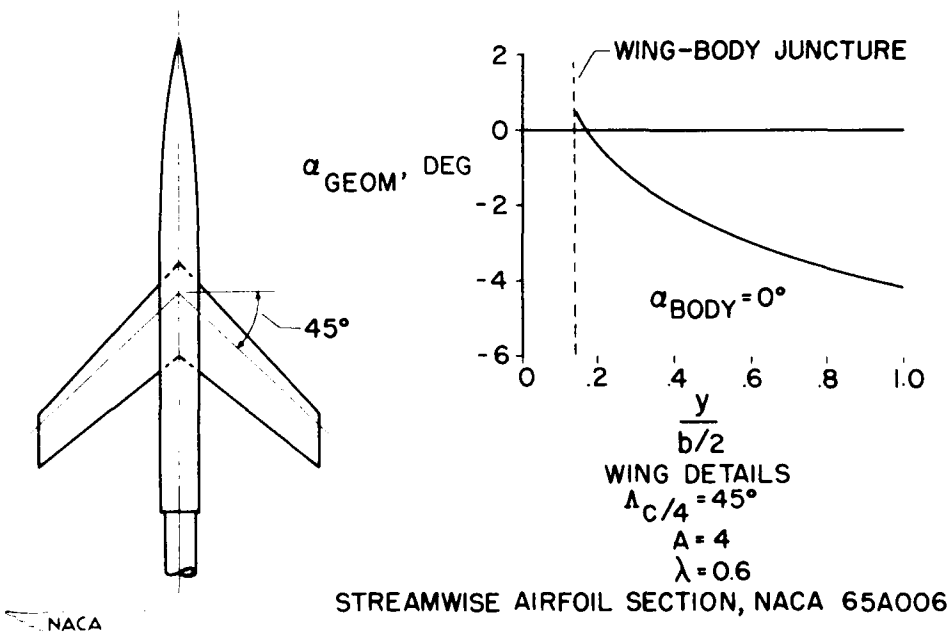


Figure 4.

CONFIDENTIAL

## WING SPANWISE LOAD DISTRIBUTION

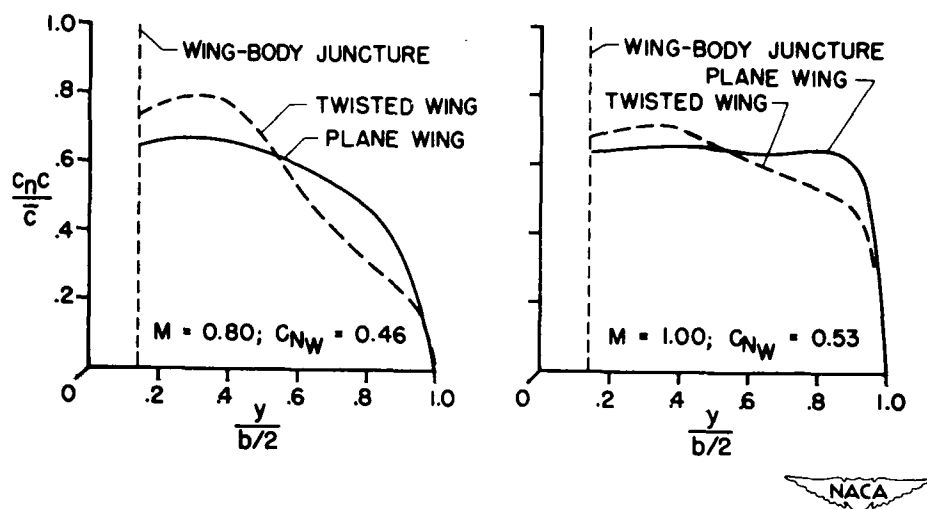


Figure 5.

## COMPARISON OF PRESSURE-COEFFICIENT DISTRIBUTIONS

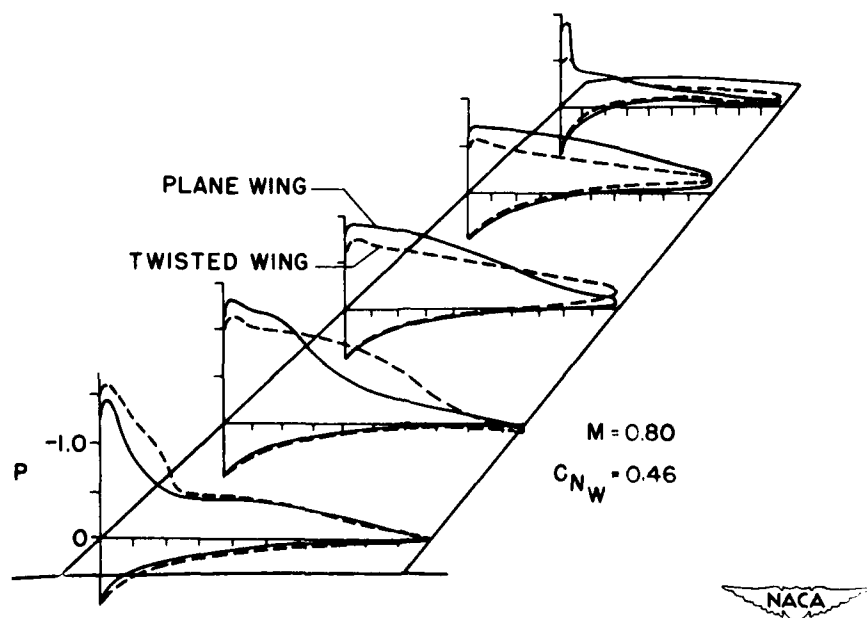


Figure 6.

CONFIDENTIAL

## COMPARISON OF PRESSURE-COEFFICIENT DISTRIBUTIONS

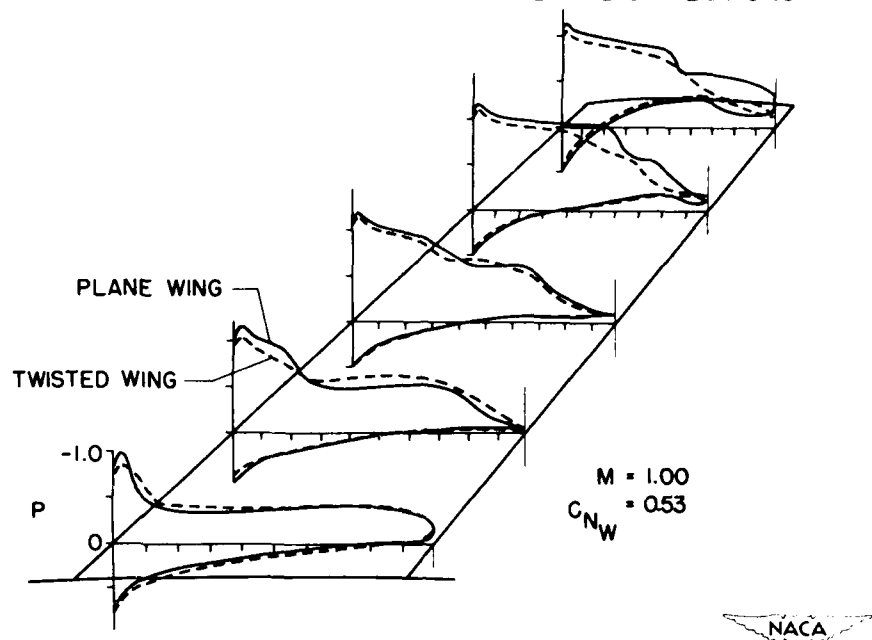


Figure 7.

## CENTER-OF-PRESSURE COMPARISON

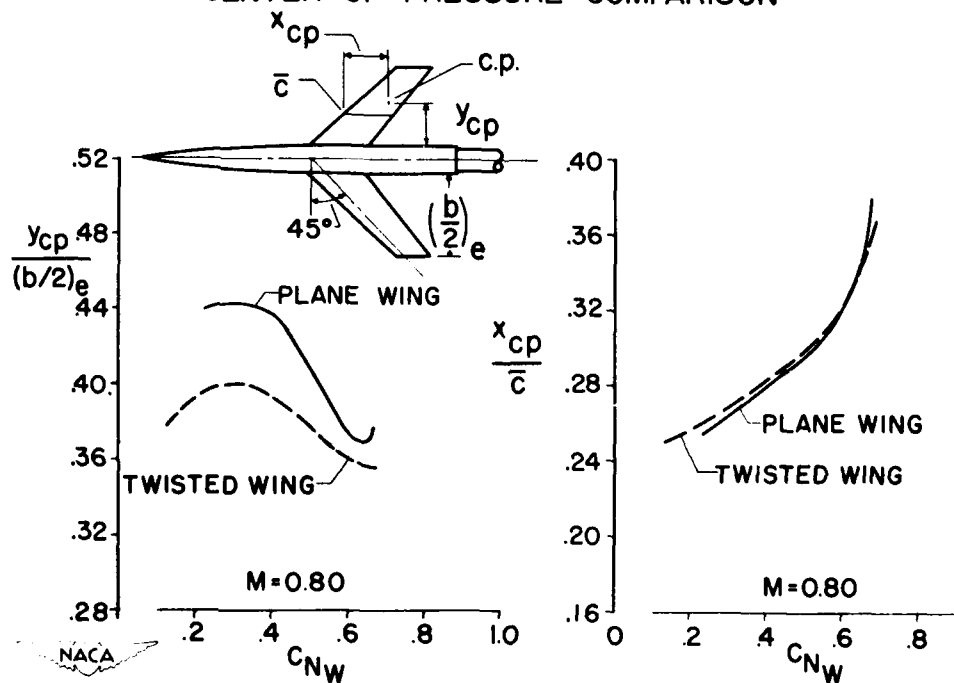


Figure 8.

## CENTER - OF - PRESSURE COMPARISON

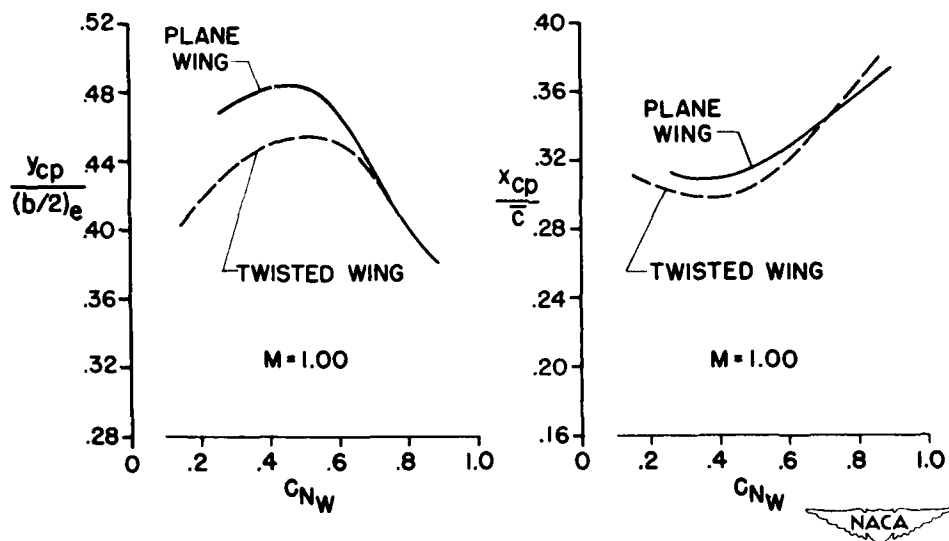


Figure 9.

## EFFECTS OF SIDESLIP

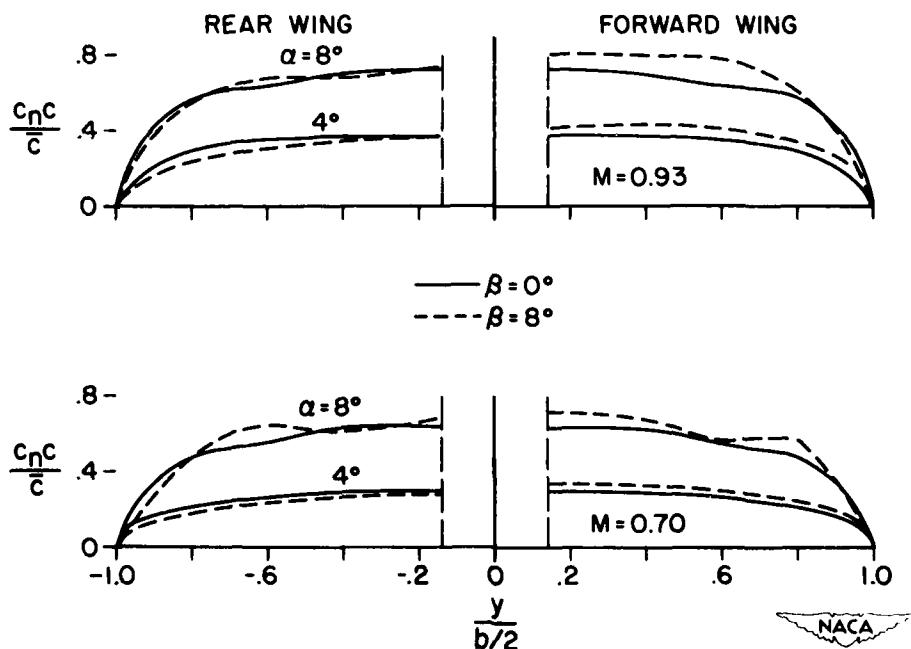


Figure 10.

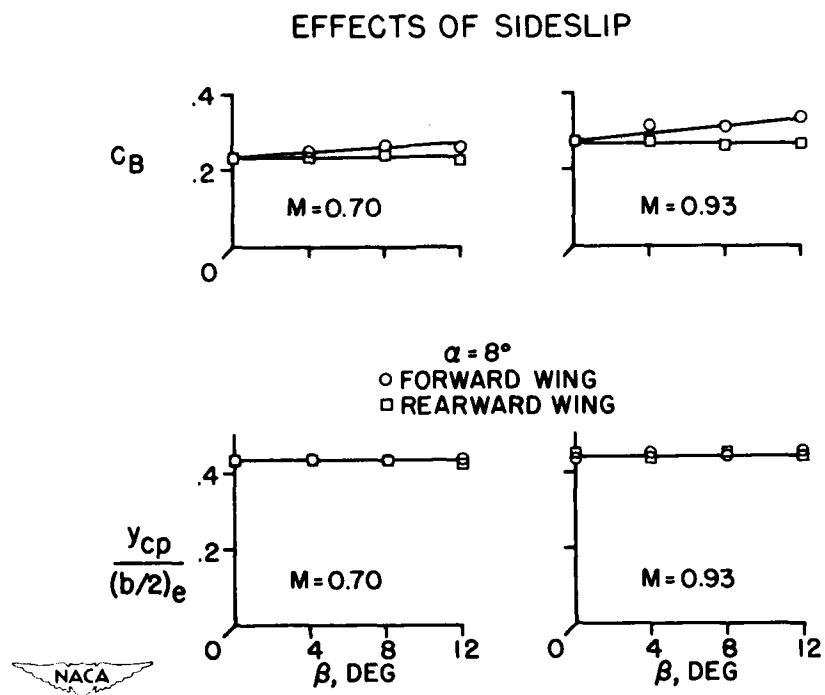


Figure 11.

## WING LOADS AS AFFECTED BY AUXILIARY DEVICES

By Wilbur H. Gray and Jack F. Runckel

Langley Aeronautical Laboratory

The pitch-up problem for the swept wing discussed by George S. Campbell in a previous paper has led to numerous efforts to reduce the tendency to pitch-up. The problem and its solution is fundamentally aerodynamic and the aerodynamics are reviewed briefly before the load changes are discussed. Where the wing has been considered to be primarily at fault, various devices have frequently been employed which have been more or less effective in reducing or delaying the pitch-up. As shown in figure 1, typical devices which will be discussed in this paper are fences, leading-edge chord-extensions, and slats. On wings with swept leading edges where these devices have proved to be especially effective, the pitch-up arises from flow breakdown or readjustment over the outer wing panel. The spanwise loading illustrated on the swept wing (fig. 1) without an auxiliary device agrees very well with theory at low normal-force coefficients. At higher normal-force coefficients, however, the spanwise loading deviates more and more from the theoretical loading as a progressive loss in lift starts near the tips and works inboard. The auxiliary devices partially regain the lost tip load and readjust the load distribution as nearly as possible to the theoretical loading. Figure 2 illustrates the main causes of the separated-flow regions on thin sweptback wings which persist through the subsonic Mach number range. The leading-edge separation vortex or bubble exists for speeds up to a Mach number of about 0.85. This vortex grows as it moves spanwise along the leading edge until it can no longer be supported on the wing panel near the tip and is swept chordwise, causing the tip sections to develop relatively low lifts.

At high subsonic Mach numbers there is a transition from the vortex type of flow to flows in which shocks and shock-boundary-layer interaction play a predominant role; however, the results are similar to those obtained at lower Mach numbers. These shocks cause the reduction in effectiveness of auxiliary devices for improving the wing pitch-up characteristics in a Mach number range approximately from 0.90 to 1.00. At low supersonic speeds the pitch-up tendencies of the swept wing have diminished and it is expected that auxiliary devices would have little effect on the wing loading distribution.

The object of this paper is to illustrate a few of the typical wing-loading changes experienced when auxiliary devices are added and to discuss briefly what may be expected of the loads on the devices themselves.

The most commonly used device on swept wings is the boundary-layer fence which provides a physical barrier against spanwise flow. Some

recent unpublished data from the Langley high-speed 7- x 10-foot tunnel for a  $45^\circ$  swept wing on which a fence was installed at 65 percent of the semispan are presented in figure 3. The static pitching-moment curves for the basic wing (the solid line) and for the wing with the fence added (the dashed line) at two Mach numbers, 0.70 and 0.91, are shown in the upper part of the figure. The lower part of the figure shows the span load distributions for a few typical cases. The small difference in spanwise loading distribution indicated at the low angles of attack at each Mach number is typical of the agreement which would be expected when there is little change in the pitching moment. The differences in the loading distribution at  $12^\circ$  angle of attack are typical of the changes to be expected over the region of angle of attack where the pitching-moment curves diverge. The important thing to notice is the increase in tip loads and the reduction in wing-root-section loads with the fence, indicating an approach to the theoretical distribution. In order to show the detailed chordwise distribution of loading over the wing with a fence, resultant pressure coefficients, obtained from the difference in pressure on the top and bottom surfaces of the wing, are plotted at several spanwise stations in figure 4. The greatest difference in loading is seen to occur near the leading edge at the 80-percent-semispan station. Such a concentration of load with the fence on the wing may form a critical local design condition.

The addition of chord-extensions to the wing results in loading changes very similar to those illustrated in figures 3 and 4 for the fence. The chord-extension was generally a more effective device for reducing the pitch-up tendencies and, therefore, larger changes in load were experienced. The concentrations of load near the leading edge and the changes in load on other portions of the wing chord which exist on the wing with a fence are somewhat increased in magnitude although distributed over a longer chord when the chord-extension is added.

Similar data have been obtained with a slat added to the  $45^\circ$  swept wing discussed previously. Figure 5 shows the pitching-moment curves obtained with these slatted wings and the chordwise distribution of the loads at Mach numbers of 0.60 and 0.94. The loads over the slats were not measured and have been approximated by utilizing unpublished data. The principal observation to be made at the lower Mach number is that the concentration of load near the 80-percent-semispan station when the fence was added is not present when the slat is added. Although the load is still concentrated near the leading edge, it is more evenly distributed spanwise. At the higher Mach number, 0.94, large increases in loading over the outer wing panel behind the slats, as well as on the slats, are found. Slats were found to produce the largest improvement in pitch-up characteristics of any of the auxiliary devices discussed in the Mach number region from 0.90 to 0.95 and, consequently, illustrate the greatest changes in loading at these speeds.

Figure 6 shows typical bending-moment diagrams expressed in coefficient form for the basic wing and for the wing with the auxiliary devices. At a Mach number of 0.9 the addition of the fence and the addition of the chord-extension have restored the tip load to the extent that the bending moments have been greatly increased and exceed those for the basic wing for a wide range of normal-force coefficients. If the airplane is designed for a Mach number of 0.9, the addition of the auxiliary devices will therefore produce a critical wing-loading condition. If, however, the airplane design condition is at a Mach number of 1.0, the pitch-up for the basic wing is less severe, the center of load is farther outboard, and the need for the device has begun to diminish. The increase in the bending moments caused by the addition of the chord-extension is smaller than at a Mach number of 0.9, as indicated by the top curve compared with the bottom curve. However, if an approximation is made to evaluate the amount of the increased bending moment caused only by the increased wing area at the outer panel, it can be seen, as indicated by the middle curve, that this will account for about half of the increased bending moments. The remainder reflects the increase in load due to the aerodynamic benefits of the chord-extension. As the Mach number is increased above 1.0, the available data indicate little effect of auxiliary devices on the pitching moments. Presumably, therefore, there would be little effect on the wing loading distribution and the basic-wing loads would be approached at supersonic speeds even though auxiliary devices are added.

Some mention should be made of the loads carried by the auxiliary devices themselves. Chord-extensions and slats, as contrasted to fences, are integral parts of a wing structure and failure of these parts cannot be tolerated. In the discussion of the effect of these devices on restoring the load to the wing tip, it has been seen that an appreciable increment of the load has been carried by the chord-extensions or slats themselves. Information on slat loads is available in references 1 and 2. Among the most recently obtained data has been an extensive study of the forces and moments of a 20-percent-chord slat deflected  $10^\circ$  on a  $45^\circ$  swept wing which differed in aspect ratio and taper ratio from the one previously discussed. A portion of these data is illustrated in figure 7 where the slat normal-force coefficients and the slat chord-force coefficients are plotted against airplane angle of attack. The shift in the curves which occurs between those for the slats open and closed is due, in part, to the downward rotation of the slat when open. The shape of the curves illustrates the development of leading-edge suction and its ultimate decay. The effects of Mach number are generally small and the differences that do exist are caused by a decrease in leading-edge suction with increased Mach number as was found in the investigation by Cahill and Nuber (ref. 3).

In summary, it may be stated that the auxiliary wing devices are effective in restoring the load normally lost at the tips of thin swept

wings at subsonic speeds. At supersonic speeds, the indications are that, because of the reduction in effectiveness of auxiliary devices, the basic-wing loads are approached even though these devices are added.

## REFERENCES

1. Kemp, William B., Jr., and Few, Albert G., Jr.: Pressure Distribution at Low Speed on a  $\frac{1}{4}$ -Scale Bell X-5 Airplane Model. NACA RM L51I25, 1951.
2. Kelly, John A., and Hayter, Nora-Lee F.: Aerodynamic Characteristics of a Leading-Edge Slat on a  $35^{\circ}$  Swept-Back Wing for Mach Numbers From 0.30 to 0.88. NACA RM A51H23, 1951.
3. Cahill, Jones F., and Nuber, Robert J.: Aerodynamic Load Measurements Over a Leading-Edge Slat on a  $40^{\circ}$  Sweptback Wing at Mach Numbers From 0.10 to 0.91. NACA RM L52G18a, 1952.

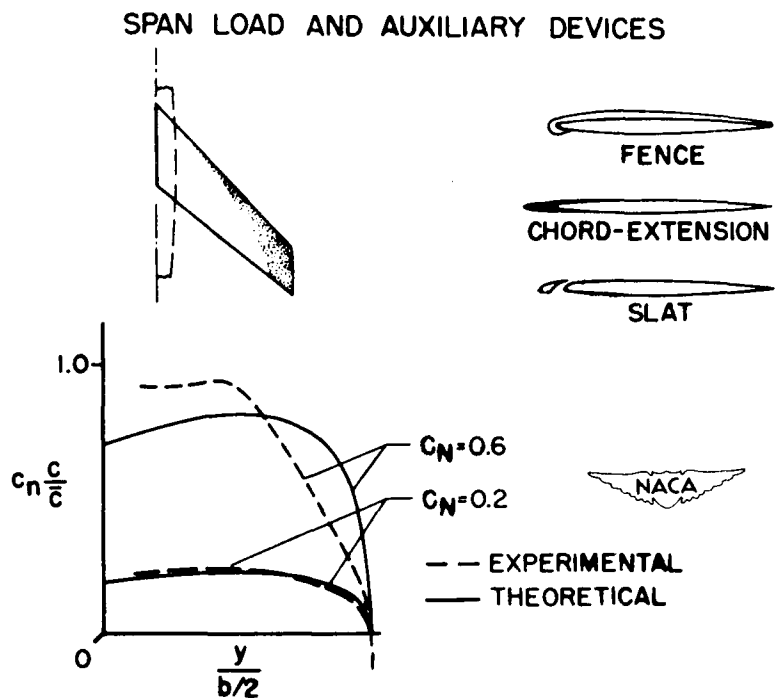


Figure 1.

## FLOW AND SHOCK PATTERNS

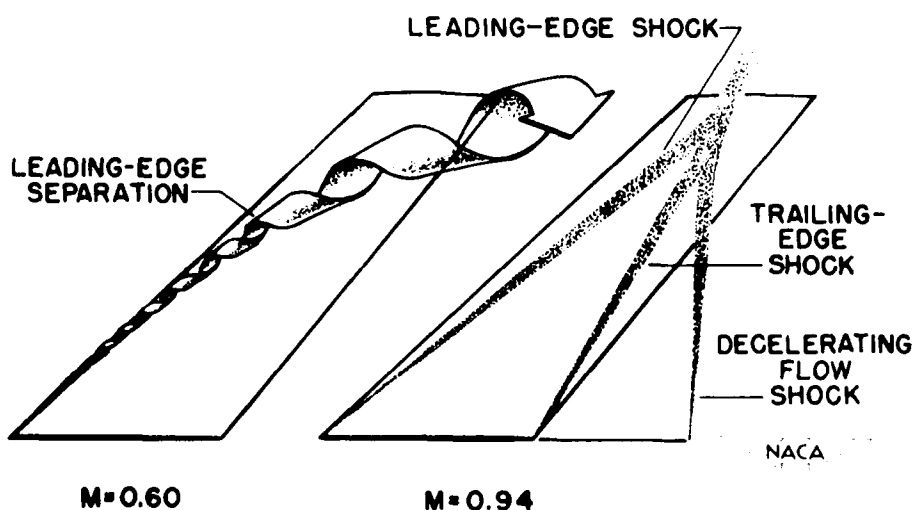


Figure 2.

CONFIDENTIAL

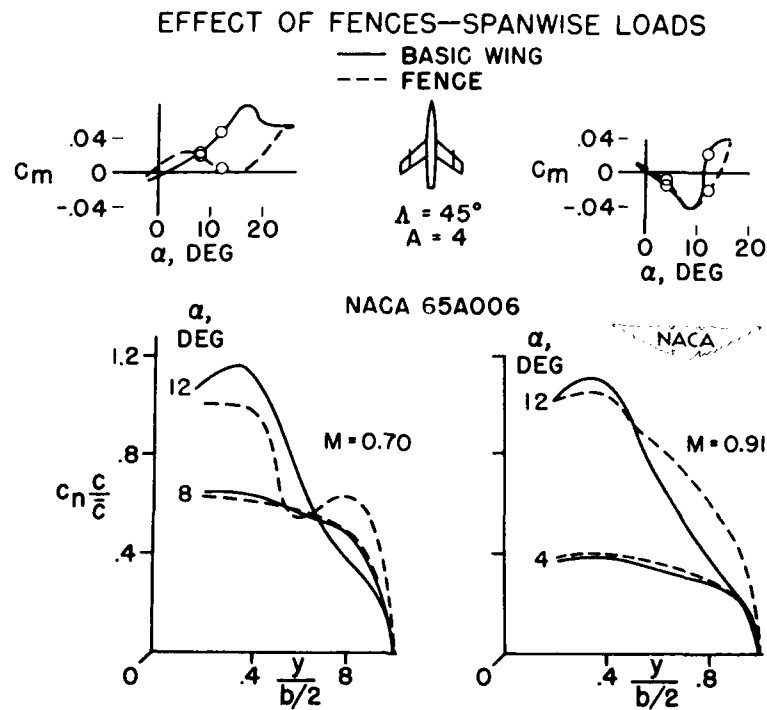


Figure 3.

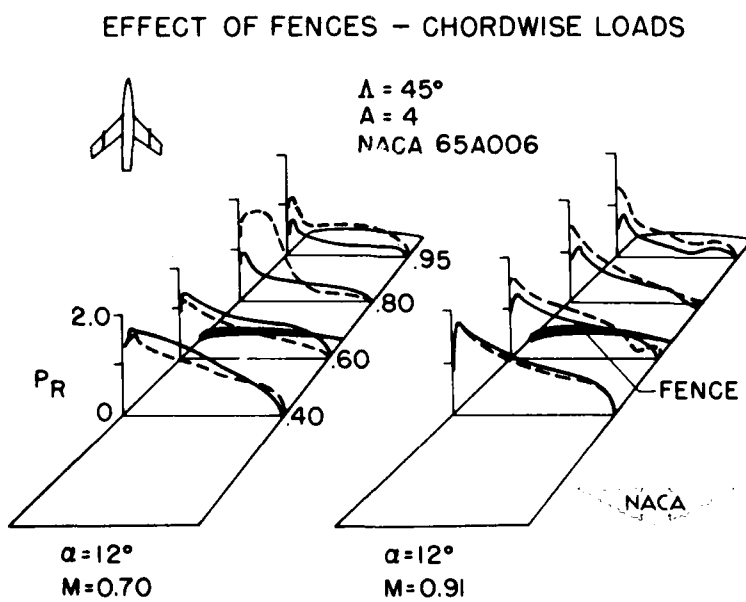


Figure 4.

CONFIDENTIAL

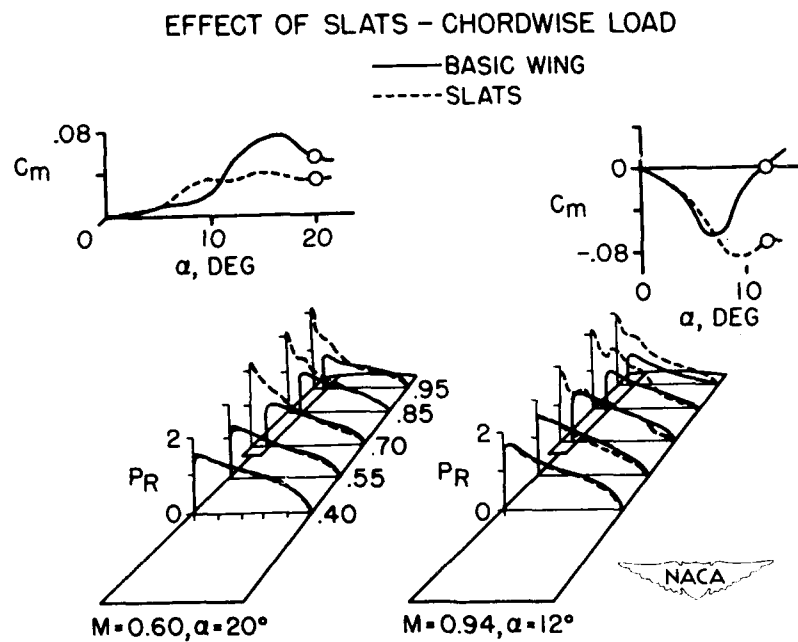


Figure 5.

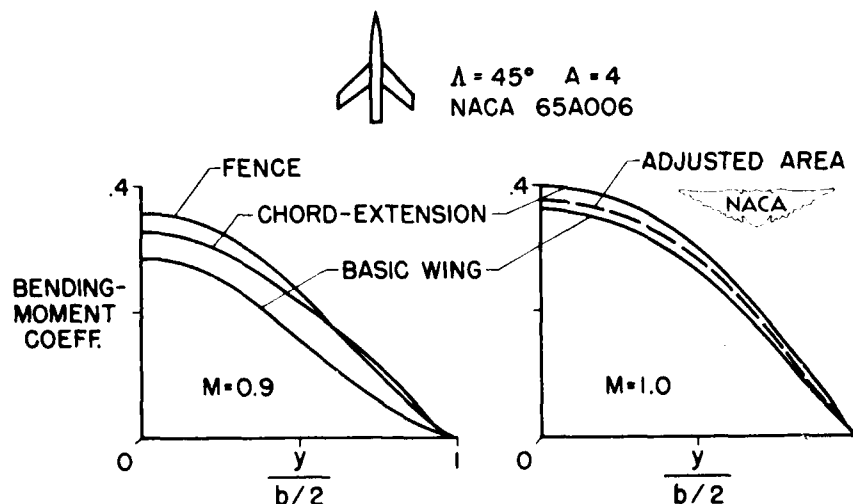
DISTRIBUTION OF BENDING MOMENT AT  $C_{NA} = 0.75$ 

Figure 6.

CONFIDENTIAL

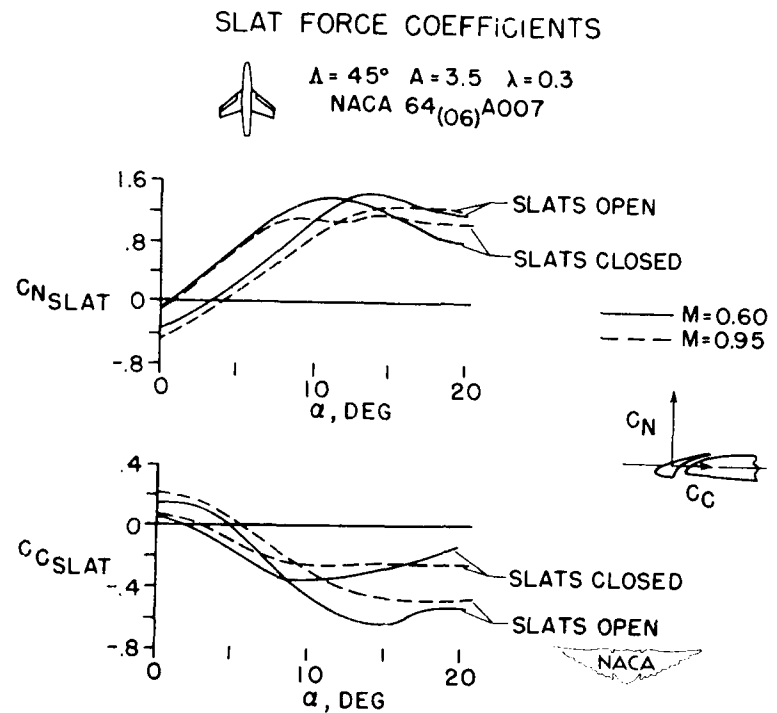


Figure 7.

CONFIDENTIAL

## LOADINGS ON THIN WINGS AT SUPERSONIC SPEEDS

By John E. Hatch, Jr., and Kenneth Margolis

Langley Aeronautical Laboratory

## INTRODUCTION

Since the NACA Conference on Aircraft Loads, March 5-6, 1951, theoretical methods for calculating loads have been extended and utilized to calculate wing loadings due to various motions covering a wide range of Mach numbers and plan forms. Further experimental data have also been obtained which give additional information on the change in wing loading as Reynolds number, Mach number, and wing plan form are varied.

The present paper shows some comparisons between experimental loadings obtained at the Langley Laboratory and the corresponding loadings calculated by the linear theory for several wings at angles of attack. In addition, some incremental loadings resulting from motions other than constant angle of attack are presented for each of the wings considered.

## SYMBOLS

$P_R$	lifting-surface pressure coefficient, $\frac{p_L - p_U}{q}$
$p_L$	wing-lower-surface pressure
$p_U$	wing-upper-surface pressure
$q$	free-stream dynamic pressure
$C_L$	wing lift coefficient
$\frac{c_{nc}}{\bar{c}}$	span-loading coefficient
$\frac{\Delta c_{nc}}{\bar{c}}$	change in span-loading coefficient

$c_n$	section normal-force coefficient
$c$	local chord
$\bar{c}$	average chord
$\alpha$	angle of attack, deg
R	Reynolds number, based on wing mean aerodynamic chord
M	Mach number

### RESULTS AND DISCUSSION

The effect of Reynolds number on the loading over a  $68^\circ$  delta wing at Mach number 2.4 has been reported in reference 1. The wing was composed of NACA 00-series sections with the maximum thickness (located at the 30-percent-chord position) varying from 4 percent at the root to about 6 percent near the tip. Additional information for this same wing is now available at Mach numbers 1.6 and 1.9.

Figure 1 presents some typical chordwise loadings for the wing at  $M = 1.9$  and an angle of attack of  $6^\circ$  for Reynolds numbers of  $2.2 \times 10^6$  and  $18.4 \times 10^6$  based on the mean aerodynamic chord. The loadings are shown for the 33.3-percent-semispan and the 77.7-percent-semispan stations. At the inboard station the low Reynolds number data show an abrupt change in pressure at about the 30-percent-chord point, whereas the data obtained at a Reynolds number of  $18.4 \times 10^6$  show no such sharp pressure change. The abrupt pressure change indicates the existence of a standing shock wave which was found to lie along a ray through the wing apex. At Mach numbers of 1.6, 1.9, and 2.4 an increase in Reynolds number delayed the formation of the shock wave and its resulting effect on the loading to a higher angle of attack. The effect of Reynolds number on the loading at this station was to change the distribution and magnitude of loading coefficients, especially over the forward 30 percent of the chord. Theory and experiment agree fairly well at this inboard station.

At the 77.7-percent-semispan station the higher Reynolds number tests result in loading coefficients about 15 to 20 percent higher than those obtained at a Reynolds number of  $2.2 \times 10^6$ . Over this outboard region theory and experiment are not in good agreement. This difference is due primarily to flow separation over the wing upper surface near the tip region.

It should be emphasized that the changes in loading which occurred with Reynolds number as shown in figure 1 are representative of those obtained for the wing at each of the test Mach numbers, with the greatest changes in loading coefficient occurring as the Reynolds number was increased from  $2.2 \times 10^6$  to  $7.4 \times 10^6$ . As the Reynolds number was further increased to  $18.4 \times 10^6$  the loading continued to vary but the changes in loading over that obtained at a Reynolds number of  $7.4 \times 10^6$  were small. Figure 1 illustrates that Reynolds number has a significant effect on the distribution and magnitude of chordwise loading coefficients. It is of importance, then, to examine the effects of Reynolds number on the spanwise loadings which are obtained from the integrated pressure distributions at each chordwise station.

Figure 2 shows the variation in experimental loading across the span for the wing at an angle of attack of  $6^\circ$  at  $M = 1.9$ . It may be seen at once that when the integrated loadings are plotted across the span the effects of Reynolds number are small. At an angle of attack of  $6^\circ$  the data obtained at a Reynolds number of  $18.4 \times 10^6$  result in a lift coefficient approximately 4 percent higher than the lift coefficient obtained at a Reynolds number of  $2.2 \times 10^6$ . The high Reynolds number data and theory show good agreement across the span.

At an angle of attack of  $6^\circ$  and  $M = 1.9$  the high Reynolds number tests result in a lift coefficient of 0.19. For the wing at this lift coefficient it will be of interest to examine the spanwise load distributions over the wing as the Mach number is varied from 1.6 to 2.4.

At  $M = 1.6$  (see fig. 3) experiment and theory agree very well across the span. Figure 4 shows that as the Mach number is increased to 1.9 for the same lift coefficient the differences between theory and experiment become more noticeable, with the experimental loading indicating an inboard movement of the lateral center of pressure. As the Mach number is further increased to 2.4 for the same lift coefficient of 0.19, the trend of inboard movement of the lateral center of pressure is continued. It may be noticed that when comparisons of spanwise loadings are based on equal lift coefficients there is less agreement between theory and experiment as the Mach number is increased. As the Mach number increases, however, the wing angle of attack also increases from about  $5.5^\circ$  at  $M = 1.6$  to  $8^\circ$  at  $M = 2.4$  in order to maintain the same lift coefficient. The agreement between the linear theory and experiment, of course, decreases as the angle of attack increases.

Up to this point the loadings presented for the  $68^\circ$  delta wing have been for a moderate lift coefficient of 0.19. The loading over the wing at higher lift coefficients is also of interest. Figure 5 shows some

experimental spanwise loadings over the wing at  $M = 2.4$  as the lift coefficient varies from 0.15 to 0.48. It may be seen that as the lift coefficient increases up to 0.48 ( $\alpha = 20^\circ$ ) the shape of the loading across the span changes from nearly elliptical to triangular. Spanwise loadings at  $M = 1.9$  and 1.6 also show the same trend, becoming triangular in shape at the higher lift coefficients.

Spanwise loadings have thus far been shown only for a delta wing. In order to gain some knowledge as to the variation of loading with plan form, it will be of interest to examine the loading for two other wings suitable for supersonic flight. Figure 6 shows the loading over a wing of trapezoidal plan form at  $M = 1.6$  and a lift coefficient of 0.21. The wing has an aspect ratio of 3.1, a taper ratio of 0.389, and a leading-edge sweepback of  $23^\circ$ . The wing sections are composed of sharp-leading-edge,  $\frac{1}{2}$ -percent-thick symmetrical hexagons. The agreement between theory and experiment is very good across the span except for slight deviations near the tip where theory falls below the experimental point. For this wing the experimental and theoretical locations of the lateral center of pressure are practically the same. It might be observed that the loading for this wing is not elliptical as was the loading over the delta wing at  $M = 1.6$  and approximately the same lift coefficient.

Figure 7 shows the loading over a  $40^\circ$  sweptback wing at the same Mach number and lift coefficient as the trapezoidal wing (i.e.,  $M = 1.6$  and  $C_L = 0.21$ ). The wing has an aspect ratio of 4 and a taper ratio of 0.5 and is composed of symmetrical circular-arc sections 8 percent thick. (See ref. 2.) The wing was tested in the presence of a body, and as a result there will be some influence of the body on the pressures over the wing. It is believed, however, that except for the inboard station the influence of the body on the loading across the span was small. Over the outboard 50 percent of the wing the experimental loading was somewhat less than that predicted by the linear theory; this fact indicates that the lateral center-of-pressure location lies inboard of the location as predicted by the linear theory. The disagreement between theory and experiment over the tip region was partly due to flow separation on the wing upper surface and the presence of a detached bow wave. At lower lift coefficients, however, reference 2 indicates that theory and experiment are in very good agreement for this wing.

The loadings so far considered have been due to constant angle of attack. In addition to the angle-of-attack loadings the designer is confronted with other loads, some of which are due to steady roll, steady pitch, and constant vertical acceleration. Few, if any, experimental data are available on wing loadings resulting from these motions at supersonic speeds. Theory must therefore be used to estimate the relative magnitudes and load distributions resulting from these additional motions.

Figure 8 shows some incremental loadings due to steady roll, steady pitch, and constant vertical acceleration calculated by use of the linear theory for the  $40^{\circ}$  sweptback wing and the trapezoidal wing at  $M = 1.6$ . These calculations are based in part on the material presented in reference 3. The assumed values for rate of rolling, pitching, and constant vertical acceleration used in calculating these incremental loads are believed to be near maximum values. The incremental loadings due to steady roll, for example, were calculated for a wing with a span of about 40 feet rolling at the rate of approximately  $225^{\circ}$  per second at  $M = 1.6$  at an altitude of 25,000 feet. The calculations of the incremental loadings due to steady pitch were based on the assumption that the wing was pitching at a steady rate of about  $75^{\circ}$  per second about the 50-percent-root-chord point, and the calculations of the loadings due to constant vertical acceleration were based on the assumption that the wing was undergoing a constant angle-of-attack change of about  $75^{\circ}$  per second. It should be mentioned that these incremental loads due to steady roll, steady pitch, and constant vertical acceleration do not necessarily occur simultaneously.

To obtain the total loading over the wing, any incremental loads which occur must be added to the basic angle-of-attack loading. In order to give some idea of the magnitudes of the incremental loadings considered relative to the angle-of-attack loading, the basic loading over each wing is shown for a lift coefficient of 0.21. This lift coefficient was chosen as being representative of an aircraft with a wing loading of 50 making a 6g pullout at an altitude of 25,000 feet at  $M = 1.6$ .

The loading due to steady roll is positive on the semispan considered, whereas on the opposite semispan the loading is negative. The other loadings shown are symmetrical about the wing center line. It may be seen that the incremental loadings due to steady pitch and constant vertical acceleration are small for these wings, whereas the incremental loading due to steady roll is of considerable magnitude when compared with the angle-of-attack loading. As a further illustration of the way these incremental loadings vary with plan form, figure 9 shows calculated loadings for the  $68^{\circ}$  delta wing at  $M = 1.6$  and a lift coefficient of 0.21. These incremental loadings were calculated from reference 4 for the same rates of pitch, roll, and vertical acceleration as were used for the previous wings. The loading due to steady roll is again seen to be the most important of the incremental loads shown.

The incremental loadings presented, however, can vary significantly with aspect ratio, taper ratio, sweepback, axis of pitch, and Mach number, and for other wings the loadings due to steady pitch and constant vertical acceleration could assume more importance. Detailed calculations for these as well as other load distributions that are applicable to a wide variety of wings at supersonic speeds are presented in references 3 to 5 and in some papers still in preparation.

## CONCLUSIONS

Experimental and theoretical loadings have been presented for several wings at supersonic speeds from which the following conclusions may be drawn:

1. A large change in Reynolds number was shown to have a definite effect on the magnitude and distribution of chordwise loading on a delta wing but had little effect on the resultant spanwise loading.
2. The effect of increasing the experimental lift coefficient from moderate to high values for the delta wing indicated that the spanwise loading varied from an elliptical- to a triangular-shaped distribution.
3. Comparisons between experimental and theoretical spanwise load distributions for wings of various plan form at angles of attack in general showed good agreement.
4. Some incremental loadings resulting from steady roll, steady pitch, and constant vertical acceleration were calculated. The loading due to steady roll was the most important of the incremental loadings considered, but it was pointed out that the loadings due to steady pitch and constant vertical acceleration could assume more importance with different combinations of plan-form parameters and Mach numbers.

## REFERENCES

1. Hatch, John E., Jr., and Hargrave, L. Keith: Effects of Reynolds Number on the Aerodynamic Characteristics of a Delta Wing at a Mach Number of 2.41. NACA RM L51H06, 1951.
2. Cooper, Morton, and Spearman, M. Leroy: An Investigation of a Supersonic Aircraft Configuration Having a Tapered Wing With Circular-Arc Sections and 40° Sweepback. A Pressure-Distribution Study of the Aerodynamic Characteristics of the Wing at Mach Number 1.59. NACA RM L50C24, 1950.
3. Martin, John C., and Jeffreys, Isabella: Span Load Distributions Resulting From Angle of Attack, Rolling, and Pitching for Tapered Sweptback Wings With Streamwise Tips. Supersonic Leading and Trailing Edges. NACA TN 2643, 1952.
4. Hannah, Margery E., and Margolis, Kenneth: Span Load Distributions Resulting From Constant Angle of Attack, Steady Rolling Velocity, Steady Pitching Velocity, and Constant Vertical Acceleration for Tapered Sweptback Wings With Streamwise Tips - Subsonic Leading Edges and Supersonic Trailing Edges. NACA TN 2831, 1952.
5. Margolis, Kenneth, Sherman, Windsor L., and Hannah, Margery E.: Theoretical Calculation of the Pressure Distribution, Span Loading, and Rolling Moment Due to Sideslip at Supersonic Speeds for Thin Sweptback Tapered Wings With Supersonic Trailing Edges and Wing Tips Parallel to the Axis of Wing Symmetry. NACA TN 2898, 1953.

CONFIDENTIAL

EFFECT OF REYNOLDS NUMBER ON CHORDWISE LOADING  
 $M = 1.9; \alpha = 6^\circ$

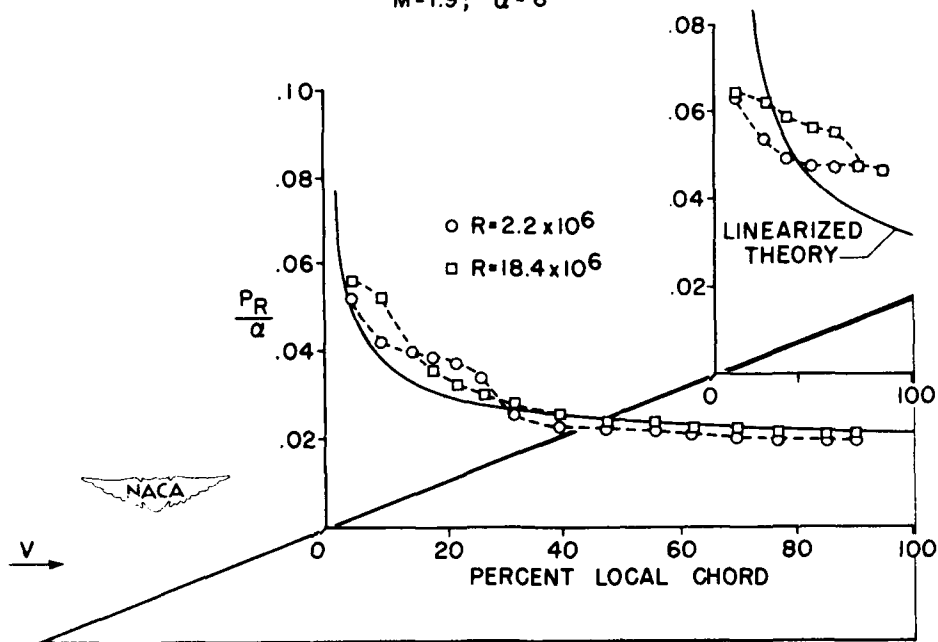


Figure 1.

EFFECT OF REYNOLDS NUMBER ON SPANWISE LOADING

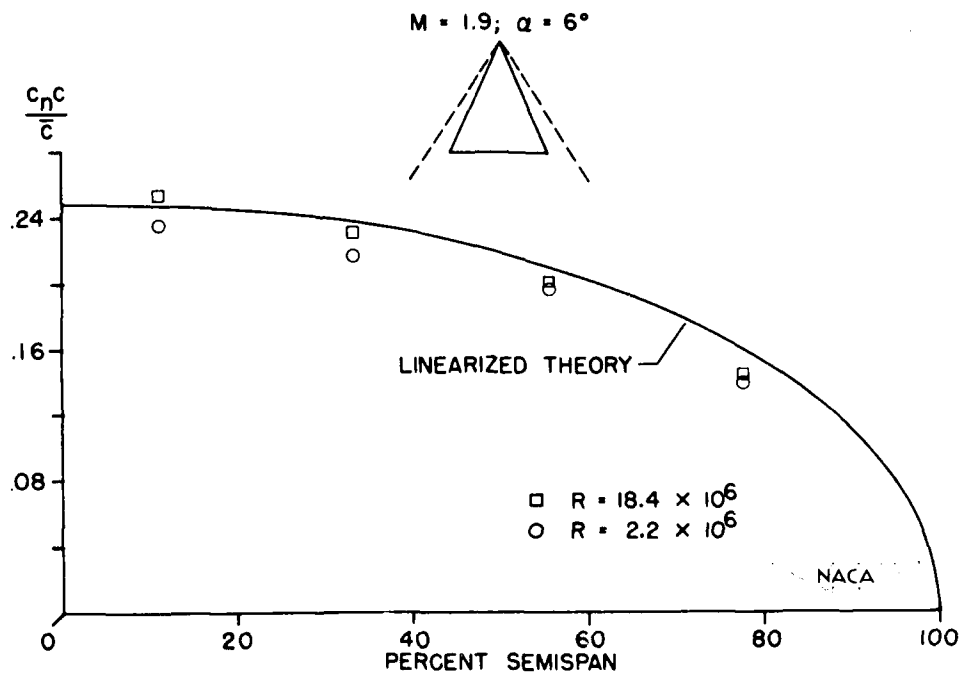


Figure 2.

CONFIDENTIAL

## SPANWISE LOADING

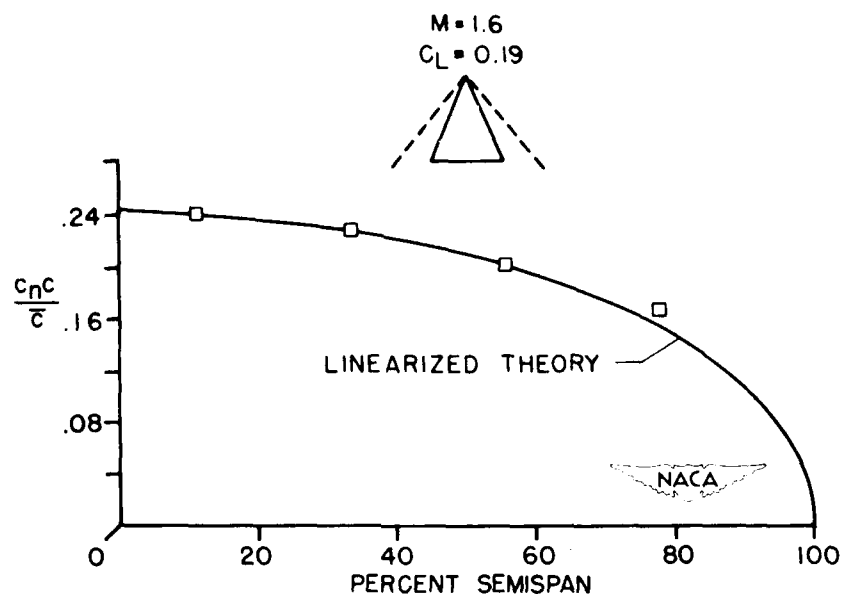


Figure 3.

## SPANWISE LOADINGS

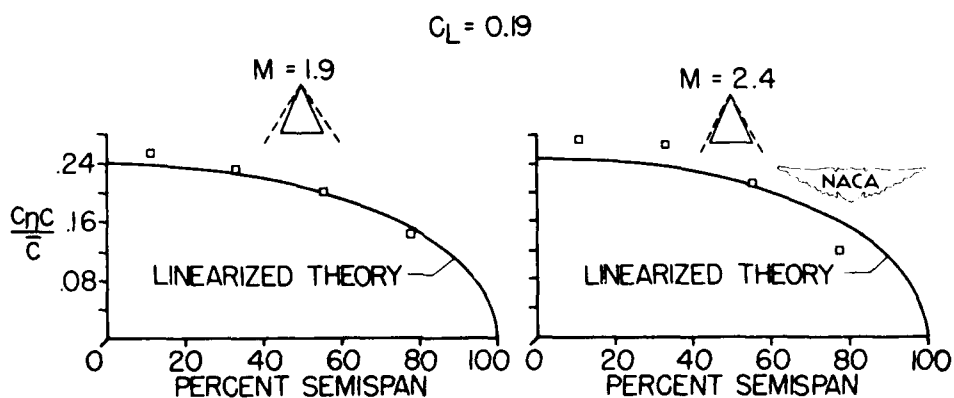


Figure 4.

CONFIDENTIAL

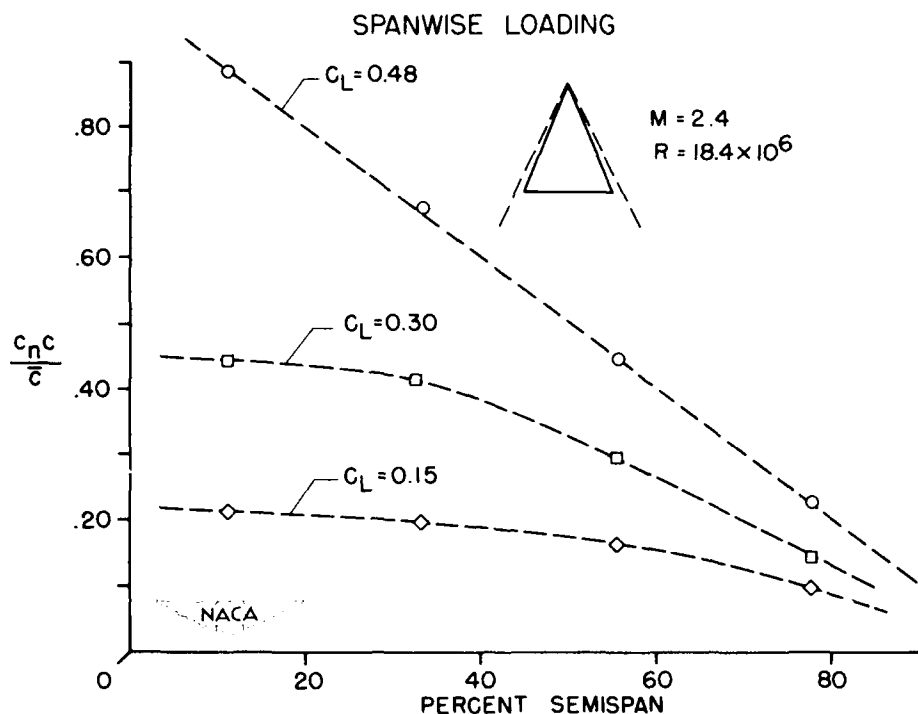


Figure 5.

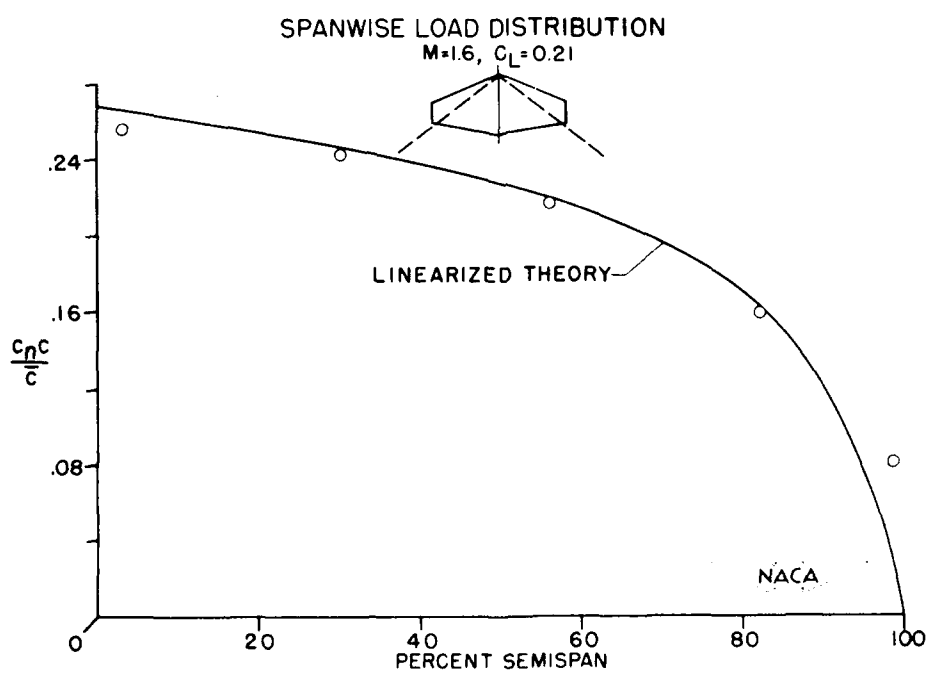


Figure 6.

CONFIDENTIAL

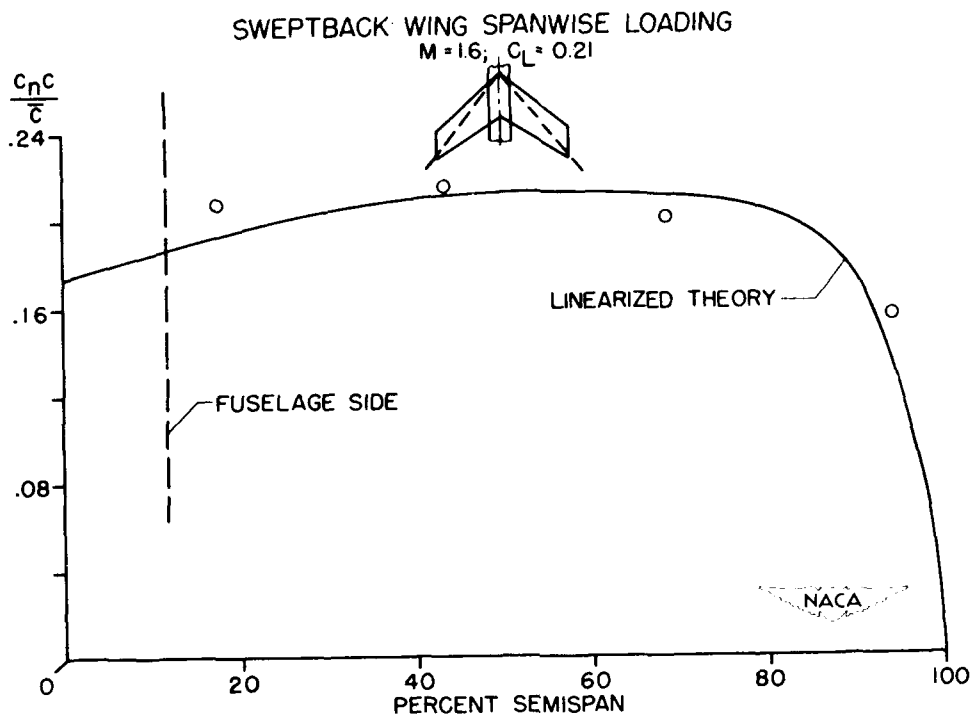


Figure 7.

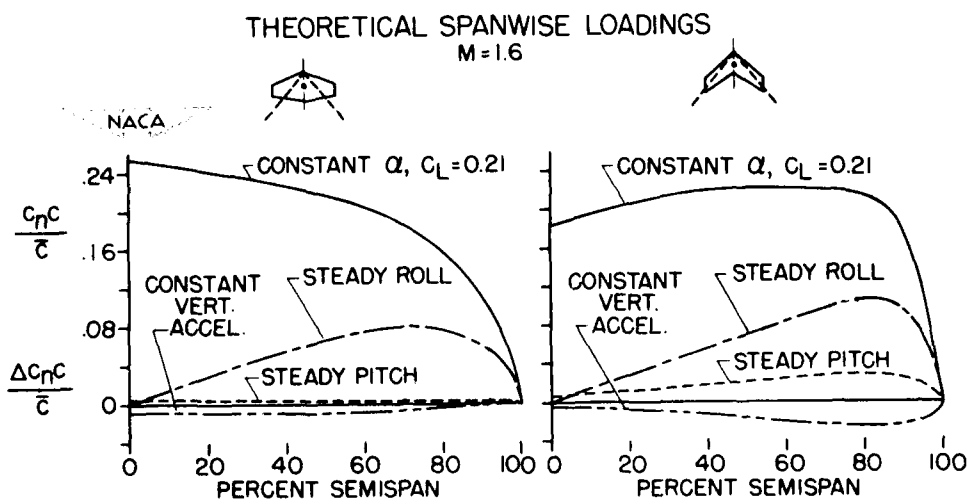


Figure 8.

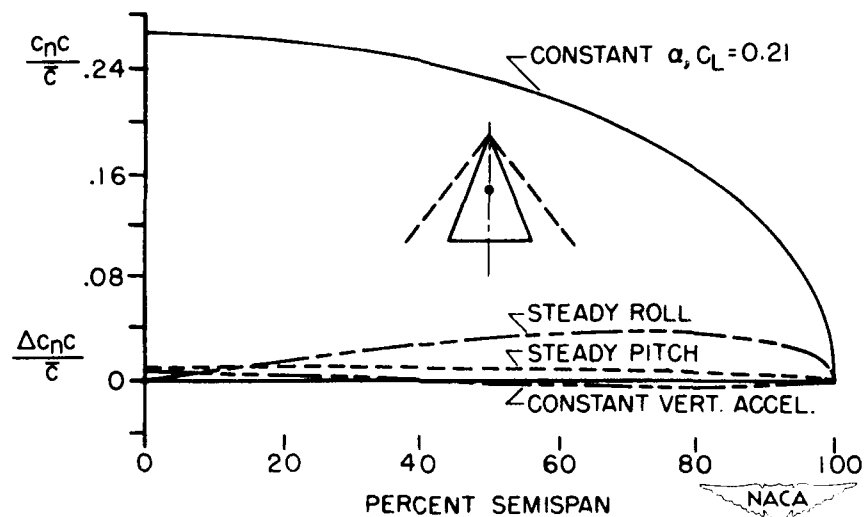
THEORETICAL SPANWISE LOADINGS  
M=1.6

Figure 9.

**LOADS ON BODIES,  
INTERFERENCE EFFECTS,  
AND EXTERNAL STORES**

DIVISION OF LOADS FOR VARIOUS  
WIND-FUSELAGE COMBINATIONS

By Clarence L. Gillis

Langley Aeronautical Laboratory

INTRODUCTION

The purpose of this paper is to summarize the presently available experimental data on division of normal-force loads between the wing and fuselage of aircraft configurations and to make comparisons with theoretical results. The experimental information presented herein was obtained by means of four different test methods: wind tunnels, free-fall models, rocket-propelled models, and airplane flight tests. The data were measured by various combinations of pressure distributions, strain gages, internal balances, and accelerometers. Further details on the methods of measurement can be found in the reference reports.

RESULTS

Several means have commonly been used to estimate the division of lift or normal-force loads between the wing and fuselage, as illustrated in figure 1. The simplest scheme for estimating the proportion of lift carried by the wing is to take the ratio of the exposed wing area to the total wing area assuming that there is no spanwise variation in the section lift coefficients of the wing and that the span loading is not affected by the addition of a fuselage. A somewhat more refined method is to obtain the span loading for the wing without a fuselage and to form the ratio of the load on the exposed wing to the load on the entire wing as if it were unaffected by the presence of the fuselage. This method accounts for spanwise variations of section lift coefficient and thus might be expected to account for the major effects of taper and sweepback.

In actuality, the load buildup on the wing-fuselage combination is more complex than indicated by either of these simple concepts. In addition to the loads that would occur on the isolated wing and fuselage, as indicated by the symbols  $F$  and  $W$  in figure 1, increments of load exist on the fuselage caused by the presence of the wing  $F(W)$  and on the wing caused by the fuselage  $W(F)$ . Both the experimental and theoretical results presented herein include these interference effects.

The theoretical results at subsonic speeds follow a method outlined in reference 1 in which a combination of theoretical results from Multhopp, Weissinger, DeYoung, and Lennertz is used. For supersonic speeds theoretical methods have been presented in references 2 and 3 by Nielsen and his associates and in reference 4 by Tucker. All these results apply to supersonic speeds and wings with trailing edges that are not swept back. Recently, Nielsen has shown that his theory is valid at subsonic and transonic speeds also and is, in fact, equivalent to the subsonic theory outlined in reference 1. Tucker has extended his theoretical analysis (unpublished) to cover wings with sweptback trailing edges at supersonic speeds. Although the simpler methods of estimating the division of load between the wing and fuselage may give very good results for some cases, there is little reason to use these methods in any case because of the relative ease of applying the theoretical methods which include all the interference effects. Convenient charts have been set up by both Nielsen and Tucker; thus, the computation of the wing and fuselage loads by either method is only a matter of minutes.

Figure 2 shows data that have been obtained on low-aspect-ratio unswept wings to show the effect of relative wing-fuselage size. The abscissa in this case is the ratio of fuselage diameter to wing span. The ordinate  $dC_{N_W}/dC_{N_{WF}}$  is the rate of change of wing normal-force coefficient with wing-fuselage normal-force coefficient and represents the proportion of the total wing-fuselage load that is being carried by the wing over that part of the lift range where linearity exists. The distance above the curve to the ordinate 1.0 is, of course, the proportion being carried by the fuselage.

The data on the left side of figure 2 are from reference 1 and were obtained in the Ames 7- by 10-foot tunnel at a Mach number of 0.25 on a wing of aspect ratio 3 with three sizes of body. The tests included both changes in angle of attack of the entire configuration (indicated by squares) and changes in wing incidence (indicated by circles). It can be seen that the theoretical calculations agree very well with the experimental results for both variable incidence and variable angle of attack. An area-ratio and a load-ratio estimate give fairly good results for the variable angle-of-attack case.

On the right side of the figure are shown data, from reference 5, at three supersonic speeds from the Langley 9-inch supersonic tunnel. Variations in the ratio of diameter to span were obtained by altering the wing span so that the aspect ratio also varied. Theoretical calculations from both Tucker and Nielsen are shown. Both sets of calculations indicate the correct variation with the diameter-to-span ratio but Tucker's results appear to predict the variation with Mach number somewhat better.

Figure 3 shows a summary of the effects of Mach number on unswept wings of aspect ratio 3. The points represented by symbols were taken from figure 2. The short solid curve at transonic speeds was obtained at the Ames Laboratory from a free-fall model. The fuselage lift on the free-fall model was obtained from pressure measurements in the vicinity of the wing; thus, any lift on the nose of the fuselage is not included in the data and has also been omitted from the comparable theoretical results. The Nielsen theory is independent of Mach number and agrees very well with the experimental data but the Tucker theory gives somewhat higher values. The longer solid curve is experimental data obtained at the Langley Laboratory (ref. 6) from a rocket-propelled model. Values of both theoretical calculations are higher than the experimental values, but the Nielsen theory, again independent of Mach number, gives somewhat better agreement, particularly with the subsonic experimental data. Both the experimental data and the Tucker theory indicate some decrease in the proportion of load carried by the wing as the Mach number increases at low supersonic speeds.

Turning now to swept wings, figure 4 presents data measured on the full-scale Douglas D-558-II airplane at Mach numbers from 0.4 to 1.5. The curve indicates that the proportion of load carried by the wing decreases above a Mach number of 0.8 and then increases again as supersonic speed is attained. The theoretical values are again somewhat higher than the experimental values.

Figure 5 presents a summary of available data on wings with  $45^{\circ}$  of sweepback. Information on aspect-ratio-4 wings has been obtained in the Langley 8-foot and 16-foot transonic tunnels (refs. 7 and 8). The results from the two tunnels agreed very well, and the single line shown represents both sets of data. Data at the higher Mach numbers were obtained from two rocket-propelled models (ref. 9) which were geometrically identical but had different wing stiffnesses. The wings differed in stiffness by a factor of 3 since the wing labeled rigid was solid steel and the flexible wing was solid aluminum. Over most of the Mach number range where data were obtained, the flexible wing carries a slightly smaller proportion of the wing-fuselage load than does the rigid wing. This does not mean that the effect of wing flexibility on lift-curve slope is small. The reduction in lift-curve slopes due to flexibility was about 5 to 7 percent for the relatively rigid wing and about 15 to 20 percent for the flexible wing but, when the ratio of the wing to the wing-fuselage slope is taken, the difference due to flexibility is only a few percent as shown here. In this case, the agreement between theory and experiment is very good. All the experimental data indicate a slight increase in the proportion of load carried by the wing in the Mach number region near 1.0.

Data on aspect-ratio-6 wings have been obtained on two free-fall models, one having a plane wing and one a cambered and twisted wing, and

on one rocket-propelled model. These data also indicate a general increase in the proportion of load carried by the wing in the transonic region. The theoretical results indicate the same trends with Mach number as the experimental data but give smaller absolute values. Although the Nielsen theory is not strictly applicable to swept wings, the error involved in its use is small and a calculation made for the free-fall models gave a value of 0.81 which agrees very well with the measurements.

Figure 6 presents data that have been obtained on  $60^{\circ}$  swept wings from the full-scale Bell X-5 airplane and a rocket model having the X-5 wing (ref. 10). The model wing differed from that on the airplane in that it did not have the radius at the trailing-edge tip and the leading edge at the root did not simulate the nonmoving portion of the full-scale variable-sweep wing. Reference to the two area ratios indicates that the data for the X-5 airplane should be higher than for the model. The reason for the different variations with Mach number for the two sets of experimental data is not known but it may be associated with the differences in fuselage shape and wing-root fairing. The theoretical and experimental results are in very good agreement.

The experimental information available on triangular-wing configurations is not so extensive as that on unswept and swept wings. Figure 7 presents data obtained in the Ames 7- by 10-foot tunnel on the effects of fuselage size with aspect-ratio-2 triangular wings at a Mach number of 0.25. The ratio of the body diameter to wing span was varied by using two bodies and three wings. The results obtained when the wing incidence was varied were fairly linear and agreed well with theory. When the angle of attack of the entire configuration was varied, the data were not linear and two values of slope are shown here, one being the slope at an angle of attack of  $0^{\circ}$  and the other being the slope of a line drawn through  $\alpha = 0^{\circ}$  and  $\alpha = 10^{\circ}$ . The theoretical calculations agree better with the slopes measured between  $0^{\circ}$  and  $10^{\circ}$ . It can be seen that a simple area ratio fails by a wide margin to predict the relative proportions of load carried by the wing and fuselage. The load-ratio estimation gives much better agreement but is still not so good as the theoretical calculations.

Figure 8 presents information that has been obtained on two triangular-wing configurations at transonic and low supersonic speeds. The aspect-ratio-4 wing was flown on a free-fall model and the aspect-ratio-2.31 wing was flown on a rocket-propelled model (ref. 11). Again, the simple area ratio fails by a wide margin to predict the experimental results. Both the Nielsen and Tucker theoretical methods give fairly good agreement with the measured data.

Up to this point only data at low angles of attack over what is usually a linear range have been considered. Critical load conditions may also occur at high angles of attack where flow separation exists and

theoretical calculations no longer apply. Although data at high angles of attack are not as plentiful as for the low angle-of-attack range, some information on a number of configurations has been obtained and is summarized in figures 9 and 10.

The information in figure 9 is presented as wing normal-force coefficient against total airplane normal-force coefficient and, in all cases, extends to angles of attack above the pitch-up boundary. Data have been obtained at supersonic speeds for the D-558-II airplane and the first plot in figure 9 shows these data. The Mach number for the maneuver from which these data were obtained started at about 1.45 and decreased to 1.04 as the higher angles of attack were attained. The data indicate that the linear range extends to a wing normal-force coefficient of about 0.7 above which the proportion of the load carried by the wing decreases considerably as the angle of attack increases, similar to the behavior at lower speeds reported previously (ref. 12). The dashed line is an extension of the linear range to present a comparison with the measured curve.

Similar data have been obtained on three rocket-model configurations as shown in the other plots in figure 9 and indicate the same effect of a decrease in the proportion of load carried by the wing at the higher angles of attack. Two models having  $45^\circ$  swept wings of aspect ratio 4, one with a rigid wing and one with a flexible wing, as discussed previously, entered the pitch-up region at slightly different Mach numbers but gave similar curves, the linear region extending to a  $C_{N_W}$  of about 0.6. Similar results at a Mach number of 0.90 are shown for a rocket model with a  $60^\circ$  triangular wing with the linear range extending to a  $C_{N_W}$  of 0.6. Another rocket model having a  $45^\circ$  swept wing of aspect

ratio 6 exceeded the linear range three times between Mach numbers of 0.69 and 0.82, and the data all plot on the single curve shown. Although this model attained lift coefficients above the pitch-up boundary for the wing, it did not experience any violent pitch-up maneuvers, probably because of the location of the horizontal tail below the wing. In general, the departure of the curves of  $C_{N_W}$  against  $C_{N_A}$  from linearity occurred at about the same angles of attack as the departure from linearity of the basic lift curves for these configurations. The measured angles of attack at the breaks in the curves were about  $13^\circ$  for the D-558-II airplane,  $9^\circ$  for the aspect-ratio-4 models,  $14^\circ$  for the delta-wing model, and  $8^\circ$  for the aspect-ratio-6 model.

The data on the configurations in figure 9 were obtained at only a few Mach numbers. A more extensive coverage of the Mach number range is available on the two configurations shown in figure 10. The test results shown at the top of the figure for a  $45^\circ$  swept wing of aspect ratio 4 were run in the Langley 8-foot transonic tunnel (ref. 7). Only a few

angles of attack were tested so it is not possible to plot continuous curves as in figure 9; however, the ratio of the wing normal-force coefficient to the wing-fuselage normal-force coefficient is shown in figure 10 to indicate the effects of high angles of attack. Only very small differences in this ratio occurred for the small angles of attack, indicating the linearity, and only one curve is shown here for 4° and 8° angles of attack. For 20° angle of attack, however, a consistently smaller proportion of the load was carried by the wing over the Mach number range from 0.60 to 1.13.

On the full-scale X-5 airplane, the Mach number range from 0.70 to 1.00 has been covered fairly completely. The curves shown here represent less than half the data that have been obtained. Again, the decrease in the wing load above the linear range at all Mach numbers is noted. Of particular interest in this case, also, is the small range of linearity, the break in the curves occurring at a wing normal-force coefficient of about 0.35 at a Mach number of 0.70 and decreasing to 0.30 at a Mach number of 1.00. On this configuration the break in the curves of  $C_{N_W}$  against  $C_{N_A}$  occurred fairly consistently at an angle of attack about 1° to 3° lower than the break in the lift curve for the complete airplane. A brief effort at correlating the data for the configurations shown in figures 9 and 10 indicates that the ratio of the lift-curve slope  $dC_N/d\alpha$  above the break in the curves to the slope below the break is roughly 30 percent less for the exposed wing than for the complete airplane.

#### CONCLUDING REMARKS

To summarize, it appears that the division of normal-force loads at low angles of attack between the wing and fuselage of aircraft can be fairly well calculated by theoretical methods except possibly at Mach numbers just above 1.0. The theoretical methods have been reduced to simple procedures so that only a matter of minutes is necessary for the calculations for one configuration. Although the simple area ratio and load ratio used for approximate estimations may give fairly good results for wings that do not have much taper, there is little reason for using these simple methods in any case because of the simplicity of the theoretical calculations which account for all interference effects. Based on the data shown herein, the theory of Nielsen appears to give a closer prediction of experimental results at the low supersonic Mach numbers; whereas, the theory of Tucker may give a somewhat better prediction of the results at higher Mach numbers, although insufficient data are available to establish firmly this conclusion.

The linear range, to which the preceding statements apply, extended to wing normal-force coefficients varying from 0.7 to 0.3 depending on

aspect ratio and sweepback. At higher angles of attack, above the range of linearity, the proportion of the normal force carried by the wing becomes progressively less as the angle of attack increases, as shown by a variety of wings including a  $60^{\circ}$  delta wing and swept wings ranging from  $35^{\circ}$  to  $60^{\circ}$  sweepback. As indicated by two swept-wing configurations, this decrease in proportionate wing load at high angles of attack occurs generally throughout the subsonic- and transonic-speed regions.

## REFERENCES

1. Hopkins, Edward J., and Carel, Hubert C.: Experimental and Theoretical Study of the Effects of Body Size on the Aerodynamic Characteristics of an Aspect Ratio 3.0 Wing-Body Combination. NACA RM A51G24, 1951.
2. Nielsen, Jack N., Katzen, Elliott D., and Tang, Kenneth K.: Lift and Pitching-Moment Interference Between a Pointed Cylindrical Body and Triangular Wings of Various Aspect Ratios at Mach Numbers of 1.50 and 2.02. NACA RM A50F06, 1950.
3. Nielsen, Jack N., and Kaattari, George E.: Method for Estimating Lift Interference of Wing-Body Combinations at Supersonic Speeds. NACA RM A51J04, 1951.
4. Tucker, Warren A.: A Method for Estimating the Components of Lift of Wing-Body Combinations at Supersonic Speeds. NACA RM L52D22, 1952.
5. Coletti, Donald E.: Investigation of Interference Lift, Drag, and Pitching Moment of a Series of Rectangular Wing and Body Combinations at Mach Numbers of 1.62, 1.93, and 2.41. NACA RM L52E26, 1952.
6. McFall, John C., Jr., and Hollinger, James A.: Longitudinal Stability, Control Effectiveness, and Drag Characteristics at Transonic Speeds of a Rocket-Propelled Model of an Airplane Configuration Having an Unswept Tapered Wing of Aspect Ratio 3.0 and NACA 65A004.5 Airfoil Sections. NACA RM L52L04, 1953.
7. Loving, Donald L., and Williams, Claude V.: Aerodynamic Loading Characteristics of a Wing-Fuselage Combination Having a Wing of 45° Sweepback Measured in the Langley 8-Foot Transonic Tunnel. NACA RM L52B27, 1952.
8. Hallissy, Joseph M., and Bowman, Donald R.: Transonic Characteristics of a 45° Sweptback Wing-Fuselage Combination. Effect of Longitudinal Wing Position and Division of Wing and Fuselage Forces and Moments. NACA RM L52K04, 1952.
9. Vitale, A. James: Effects of Wing Elasticity on the Aerodynamic Characteristics of an Airplane Configuration Having 45° Sweptback Wings As Obtained From Free-Flight Rocket-Model Tests at Transonic Speeds. NACA RM L52L30, 1953.

10. Vitale, A. James, McFall, John C., Jr., and Morrow, John D.: Longitudinal Stability and Drag Characteristics at Mach Numbers From 0.75 to 1.5 of an Airplane Configuration Having a 60° Swept Wing of Aspect Ratio 2.2 $\frac{1}{4}$  As Obtained From Rocket-Propelled Models. NACA RM L51K06, 1952.
11. Peck, Robert F., and Mitchell, Jesse L.: Rocket-Model Investigation of Longitudinal Stability and Drag Characteristics of an Airplane Configuration Having a 60° Delta Wing and a High Unswept Horizontal Tail. NACA RM L52K04a, 1953.
12. Mayer, John P., and Gillis, Clarence L.: Division of Load Among the Wing, Fuselage, and Tail of Aircraft. NACA RM L51E14a, 1951.

## METHODS OF ESTIMATION

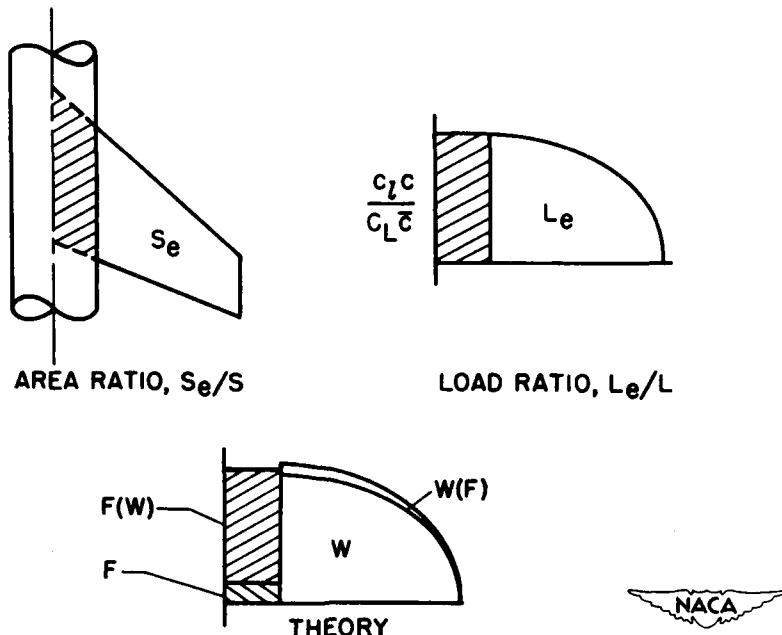


Figure 1.

## EFFECT OF BODY DIAMETER, UNSWEPT WINGS

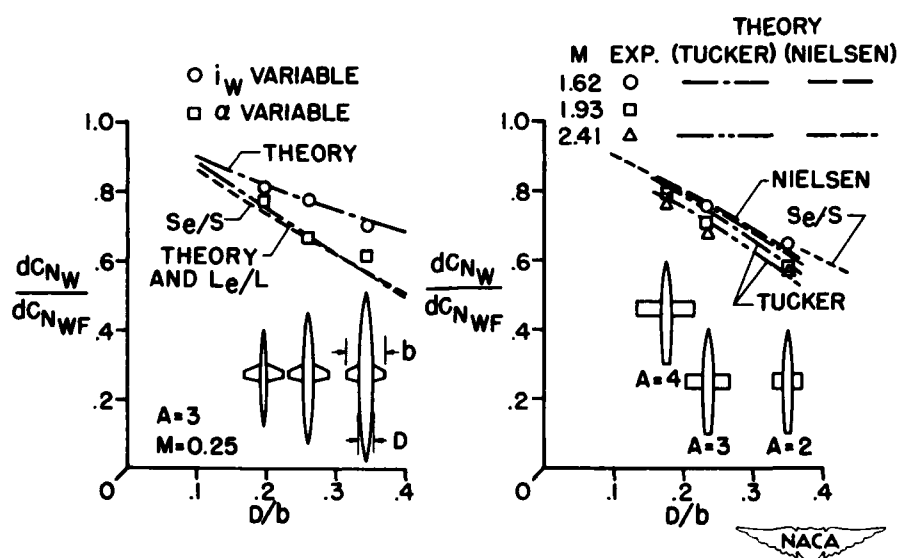


Figure 2.

EFFECT OF MACH NUMBER  
UNSWEPT WINGS OF ASPECT RATIO 3

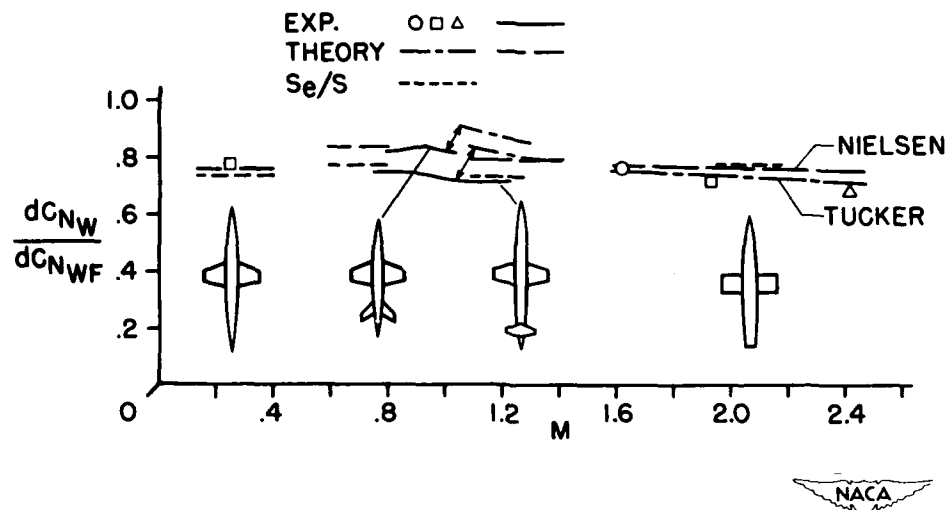


Figure 3.

## EFFECT OF MACH NUMBER, 35° SWEPT WING

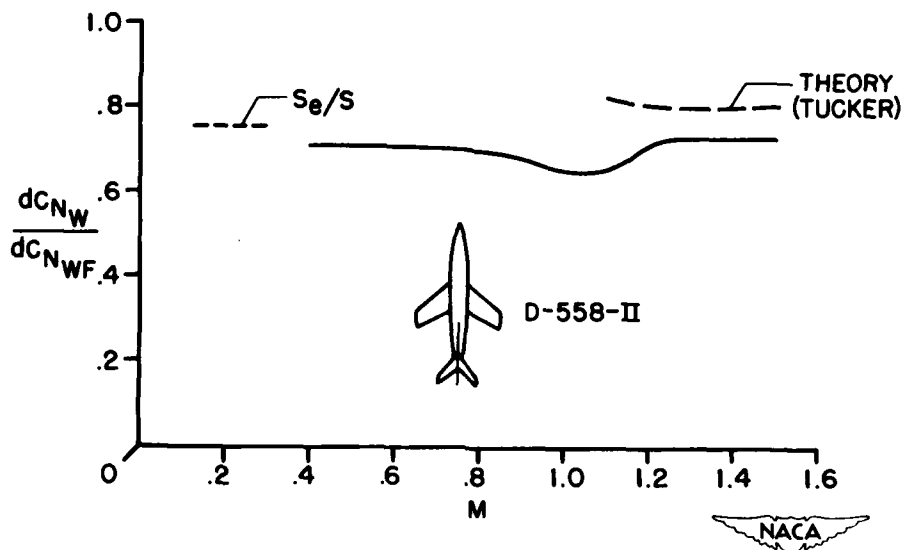


Figure 4.

CONFIDENTIAL

## EFFECT OF MACH NUMBER, 45° SWEPT WINGS

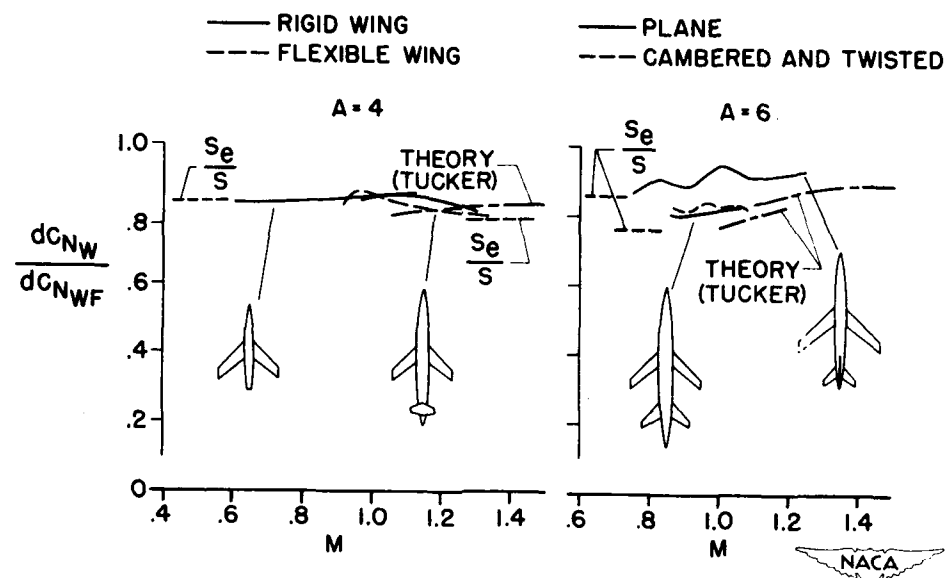


Figure 5.

## EFFECT OF MACH NUMBER, 60° SWEPT WINGS

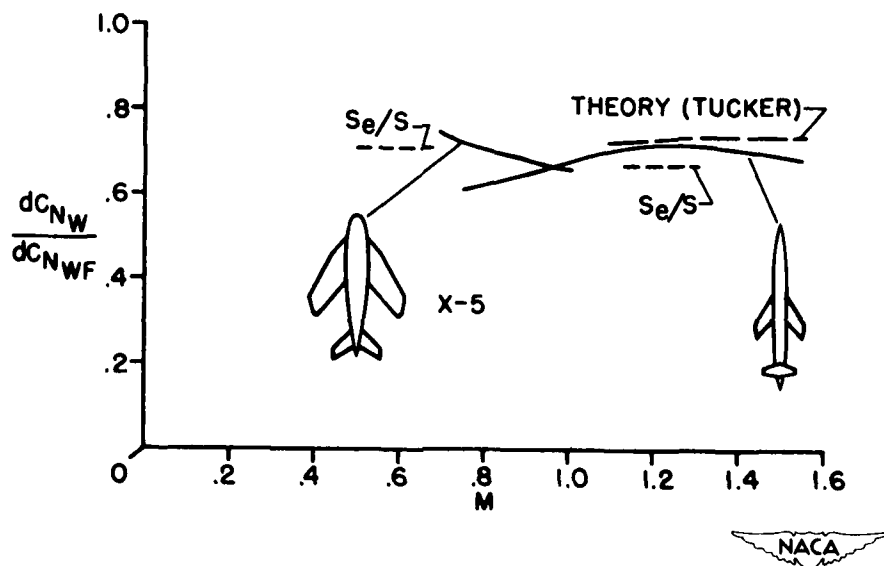


Figure 6.

CONFIDENTIAL

## EFFECT OF BODY DIAMETER, TRIANGULAR WINGS

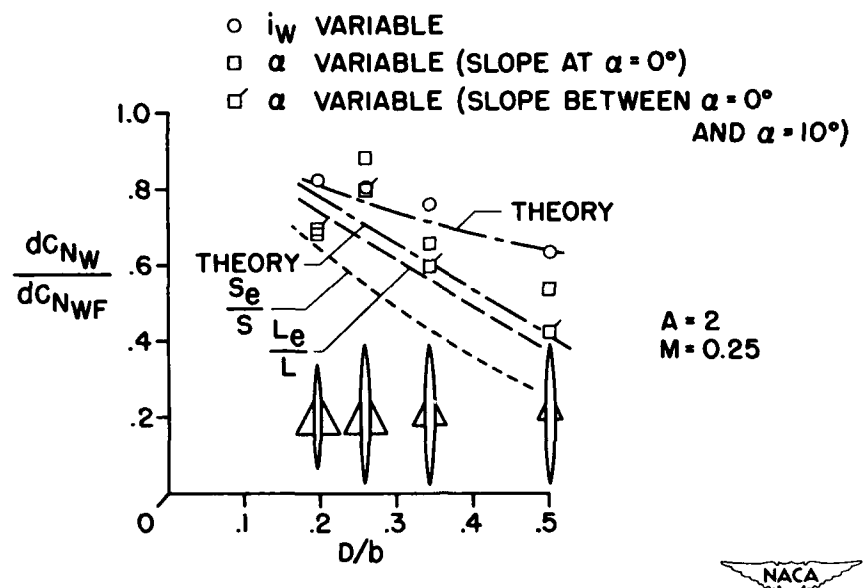


Figure 7.

## EFFECT OF MACH NUMBER

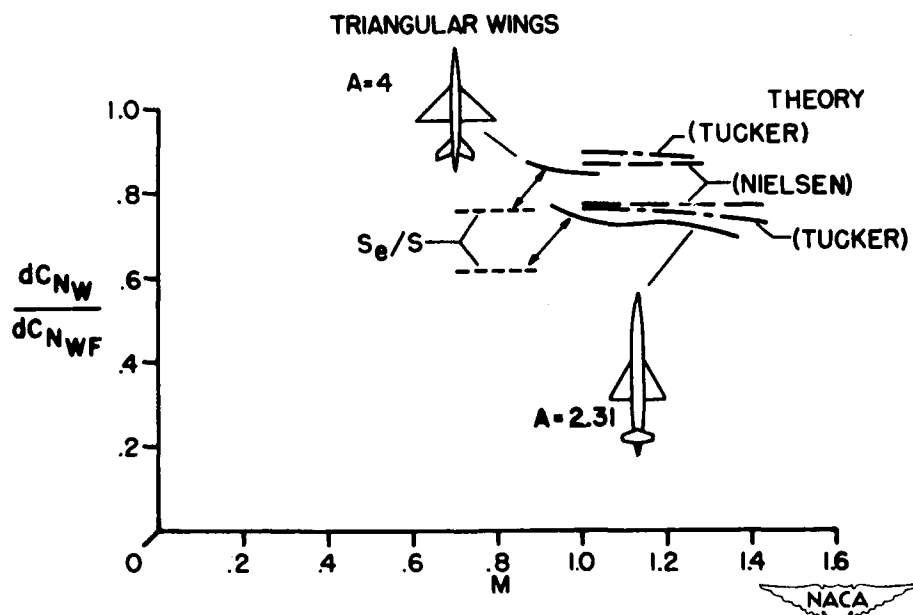


Figure 8.

CONFIDENTIAL

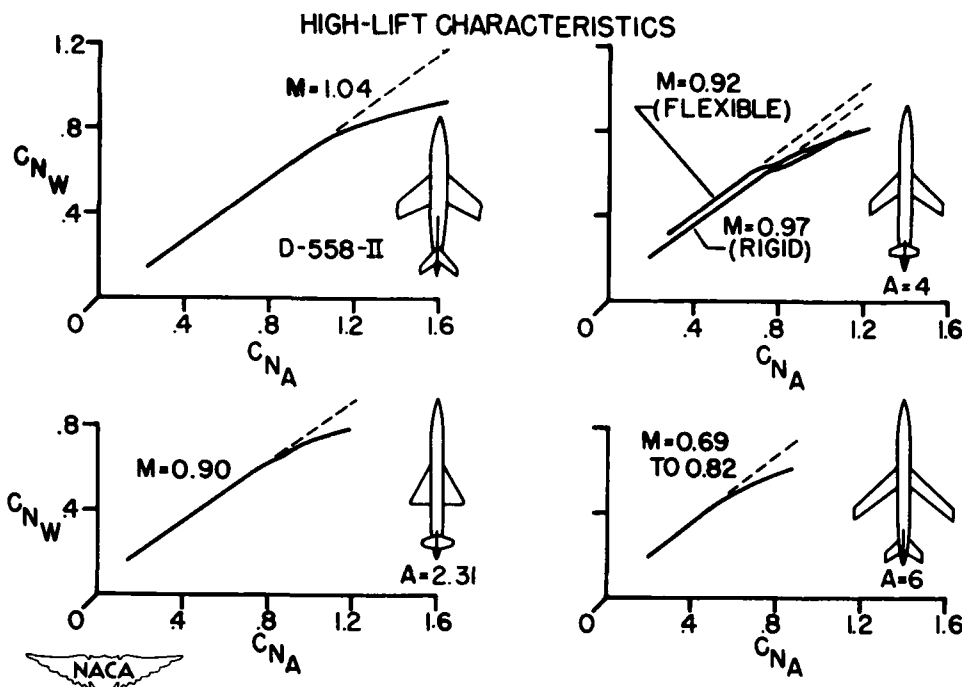


Figure 9.

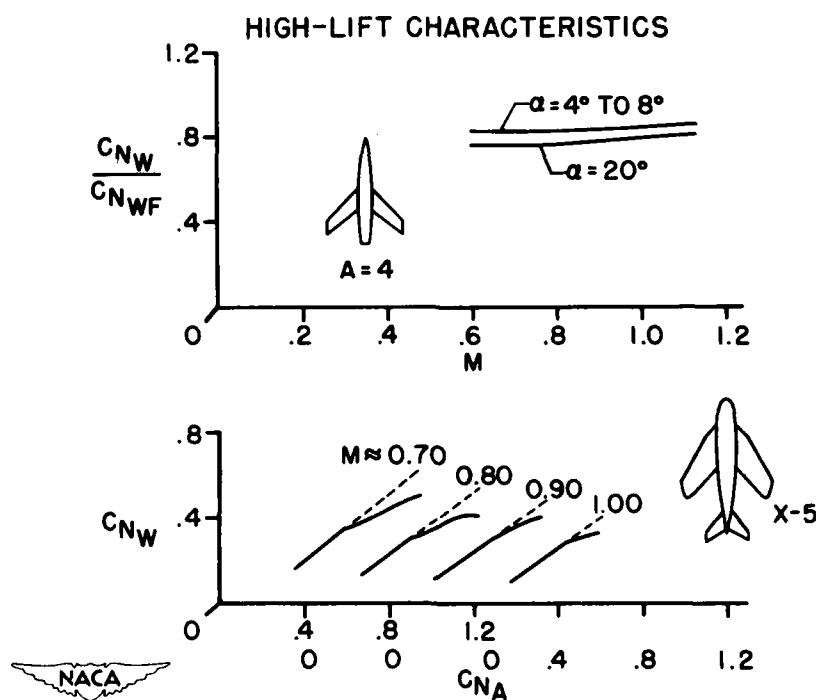


Figure 10.

CONFIDENTIAL

SOME EFFECTS OF BODY SHAPE AND WING POSITION ON THE  
LOADING ON SWEPTBACK-WING—BODY COMBINATIONS  
AT TRANSONIC SPEEDS

By Donald L. Loving

Langley Aeronautical Laboratory

The question of body-shape and wing-position effect on the loading on  $45^{\circ}$  sweptback wing—body combinations arose as the result of observations of the pronounced influence that a precise body shape has on the flow and shockwave pattern at a Mach number of 1.00. In figure 1 is shown a diagram of the shock-wave system which causes the change in flow and consequently the loading at a Mach number of 1.00. A difference in the flow field extending a considerable distance away from the body in the neighborhood of the speed of sound as affected by an afterbody shape which was curved toward the rear was previously reported (ref. 1). Force tests have indicated that a change in the body shape and a change in wing position on this body produced sizeable changes in drag and pitching moment (refs. 2, 3, and 4). The shock system shown in figure 1 is qualitatively representative of the situation for a cylindrical body, although the intensity of the shocks would be different. The shock along the trailing edge should have the most predominant effect on the loads of the wing. Now the question has arisen as to whether or not this flow problem at a Mach number of 1.00 is of significance to the study of aircraft loads. It is recognized, of course, that every fuselage incorporated in airplane design will be different; consequently, the strength of the induced velocities and the shock system will vary, but it is hoped that enough will be shown to give some idea of the nature and order of magnitude of the problem.

A previous paper by Claude V. Williams and Richard E. Kuhn showed in some detail that, for a  $45^{\circ}$  sweptback wing of airplanes which will maneuver at the speed of sound, the critical bending load will probably occur at an angle of attack of  $8^{\circ}$ , which corresponds to a wing normal-force coefficient of 0.5. Therefore, comparisons in this discussion have been chosen for an angle of attack of  $8^{\circ}$  and a Mach number of 1.00. Data for a Mach number of 0.8 are included to present the subsonic case. An analysis of the results for the supersonic conditions has indicated that the results are no more serious than those for the transonic case and, therefore, are not presented.

The effect of body shape on the loading of the wing and body as measured in the Langley 8-foot transonic tunnel will now be considered. The wing of this investigation is the same wing used to show the effects

of twist and yaw in the paper by Williams and Kuhn. This wing had 45° of sweepback, an aspect ratio of 4, and was 6 percent thick. As shown in figure 2, the curved body had a curved profile from the nose to the base. The cylindrical body was developed by extending the curved forebody forward a distance equal to twice the maximum diameter and then making the body cylindrical from the leading edge of the wing to a plane behind the trailing edge of the wing tip. The wing remained in the same position relative to the base of the body for both investigations.

In figures 2 and 3 are presented the pressure distributions for the wing in combination with the curved body, shown as a solid line, and in combination with the cylindrical body, shown as a dashed line, for an angle of attack of 8° and Mach numbers of 0.80 and 1.00. The angle of attack of 8° is at the upper limit of the linear portion of the wing lift curve. This angle of attack is also slightly lower than that at which pitch-up occurs.

At subsonic speeds ( $M = 0.80$ ), figure 2, the difference in pressures for the two configurations is very small and is indicative only of a small change in the induced flow system. At a Mach number of 1.00, figure 3, the changes due to body shape also are small, but of particular interest is the observation that the changes which do exist are mainly at the tip region of the wing. A shock occurs across the span near the trailing edge and causes separation, as shown by the flat pressure distributions, toward the tips in the region of the usual control surfaces. Primarily because of afterbody shape, the shock system of the cylindrical body is reduced in strength and the separation effects are less extensive on the outboard stations. The smaller differences between the upper and lower surface pressures for the wing on the cylindrical body indicate reduced loadings along the trailing edge, especially at the outer region. As may be noticed, repeated reference is made to the outboard regions of the wing. Up to the present time, mention of wing-body interference has immediately focused attention on the wing-body juncture. Data at transonic speeds have now been obtained which indicate that wing-body-interference effects are mainly at the tip regions of the sweptback wing. A small reduction in the loading on that portion of the body influenced by the wing is indicated by the slightly more positive pressures on the top of the cylindrical body.

In order to show the effects of these pressure changes on the loads, the spanwise distributions of section loading and moment are presented in figures 4 and 5. In figure 4 are shown the spanwise distributions of section load  $\frac{c_{nc}}{c}$  on the wing in the presence of the bodies and the average of the section loads on the bodies in the presence of the wing. The effect on spanwise distribution of loading due to a change in body shape at a Mach number of 0.8 is small. This agrees with the usual assumption that the effect would be small for subsonic conditions.

While there is a difference in size as well as shape between the curved and cylindrical bodies, the greater load on the cylindrical body is associated mostly with afterbody shape. At a Mach number of 1.00, the change in body shape from curved to cylindrical resulted in a moderate reduction in loading over the entire wing. The reductions on the outboard sections were larger than inboard. These changes are associated with losses in load at the trailing edge but especially at the outboard tip sections as pointed out on the pressure diagrams and are manifest in a small inboard shift in the center of loading. Again, because of increased loads near the body base, the over-all load on the cylindrical body is larger than for the curved body.

In figure 5 are presented the spanwise variations of the twisting moments  $\frac{c_m c^2}{c^2}$  about the section quarter chord. At subsonic speeds, a change in body shape produces a forward shift in center of pressure on the most inboard and outboard portions of the wing, as shown by the more positive moments for the cylindrical-body case. This shift in center of pressure is associated with the reduction of induced velocities on the cylindrical body. At a Mach number of 1.00, the more positive twisting moments across the exposed semispan are indicative of the reduction of load at the wing trailing edge associated with the shock-wave system of the cylindrical afterbody.

In figure 6, the shifts in loading on the wing are summarized. On the left of this figure is shown the variation with wing normal-force coefficient  $C_{N_W}$  of the lateral position of the center of pressure  $y_{cp}$  in terms of the exposed semispan. At subsonic speeds, for all practical purposes, the change in body shape did not affect the lateral position of the center of pressure. At the critical loading condition for this wing, at a normal-force coefficient of approximately 0.5 and a Mach number of 1.00, a small inboard shift in center of pressure is indicated for the wing on the cylindrical body compared to the curved body. This shift represents a 1.5-percent change in root bending moment. The data at the higher values of normal force are beyond the usual design limit of the V-g diagram for maneuvering aircraft; however, these data are available. On the right of this figure is presented the variation with wing normal-force coefficient  $C_{N_W}$  of the chordwise position of the center of pressure on the wing  $x_{cp}$  with relation to the quarter-chord line in terms of the average chord of the wing. The twisting axis of sweptback wings, which usually ranges between 35 and 40 percent of the chord on present-day airplanes, also is shown relative to the quarter-chord line. The center of pressure shifts forward when the shape of the body is changed to cylindrical for Mach numbers of both 0.80 and 1.00. This effect appears to become more pronounced when the normal-force coefficient is increased. At a normal-force coefficient of 0.5, the

CONFIDENTIAL

shift in center of pressure is in a direction forward of the twisting-axis range. Normally, this shift would not be critical with regard to the design of the wing structure, but it is of interest to the extent that it imparts a twist to the wing and thereby affects the stability. Actually, the principal loading problem is associated with the lateral position of the center of pressure.

In going from a curved to a cylindrical body, the effects just pointed out are obtained. If the shape were changed from cylindrical to a reversed curve, such as an indented body, it is quite possible that the effects would be greater. Force data have shown that when an indented body is substituted for the curved body (ref. 5), the change in pitching moments to more positive values is three times greater than when going from a curved to a cylindrical body (ref. 2). It might be expected that the inboard shift in load associated with this greater moment shift would be similar in magnitude.

Now the effect of wing position on the loading of the wing and body as measured in the Langley 16-foot transonic tunnel (ref. 6) will be considered. The wing and body of this investigation, as shown in figure 6, are similar to the curved body with wing used to show the effects of a change in body shape. The quarter chord of the mean aerodynamic chord of the wing in the forward position was located at the 60-percent fuselage station compared to the 82-percent fuselage station for the wing rearward.

The pressure distributions are presented in the same manner as for the body-shape discussion. Little change in the pressures due to wing location was noted for the subsonic case; therefore, the data are not presented. At a Mach number of 1.00, the effect of changing the wing position appears to be confined mainly to the wing trailing edge and again especially at the outboard sections. When the wing is moved rearward, the shock system simply is located farther forward on the wing with the result that the upper and lower surface pressures change by about the same amount. Hence, little change occurs in the actual loading on the wing and no change occurs in either the lateral or chordwise centers of pressure. It is of interest to note, however, that although the bending and twisting characteristics are not affected, changing of the surface pressures will create a difference in skin loading, especially at the tip.

In conclusion: The critical loading on a sweptback wing is affected by body shape. Contrary to the usual assumption that wing-body-interference effects would be near the wing-body juncture, the effects of body shape and wing position are confined mainly to the outboard tip region of the wing.

CONFIDENTIAL

The change in body shape from curved to cylindrical resulted in a moderate reduction in loading on the wing with an inboard and forward shift in the center of pressure.

Changing the wing position on the curved body had little effect on the total loading or center-of-pressure location. The predominant effect here would be a change in skin loading due to a change in the flow over the wing.

## REFERENCES

1. Whitcomb, Richard T., and Kelly, Thomas C.: A Study of the Flow Over a 45° Sweptback Wing-Fuselage Combination at Transonic Mach Numbers. NACA RM L52D01, 1952.
2. Loving, Donald L., and Wornom, Dewey E.: Transonic Wind-Tunnel Investigation of the Interference Between a 45° Sweptback Wing and a Systematic Series of Four Bodies. NACA RM L52J01, 1952.
3. Loving, Donald L.: A Transonic Wind-Tunnel Investigation of the Effects of Longitudinal Wing Location and Varying Body Size on the Interference Characteristics of a 45° Sweptback Wing. NACA RM L52L16, 1953.
4. Hallissy, Joseph M., and Bowman, Donald R.: Transonic Characteristics of a 45° Sweptback Wing-Fuselage Combination. Effect of Longitudinal Wing Position and Division of Wing and Fuselage Forces and Moments. NACA RM L52K04, 1952.
5. Robinson, Harold L.: A Transonic Wind-Tunnel Investigation of the Effects of Body Indentation, as Specified by the Transonic Drag-Rise Rule, on the Aerodynamic Characteristics and Flow Phenomena of a 45° Sweptback-Wing—Body Combination. NACA RM L52L12, 1953.
6. Solomon, William, and Schmeer, James W.: Effect of Longitudinal Wing Position on the Pressure Characteristics at Transonic Speeds of a 45° Sweptback Wing-Fuselage Model. NACA RM L52K05a, 1953.

## SHOCK SYSTEM ABOUT CURVED-BODY CONFIGURATION

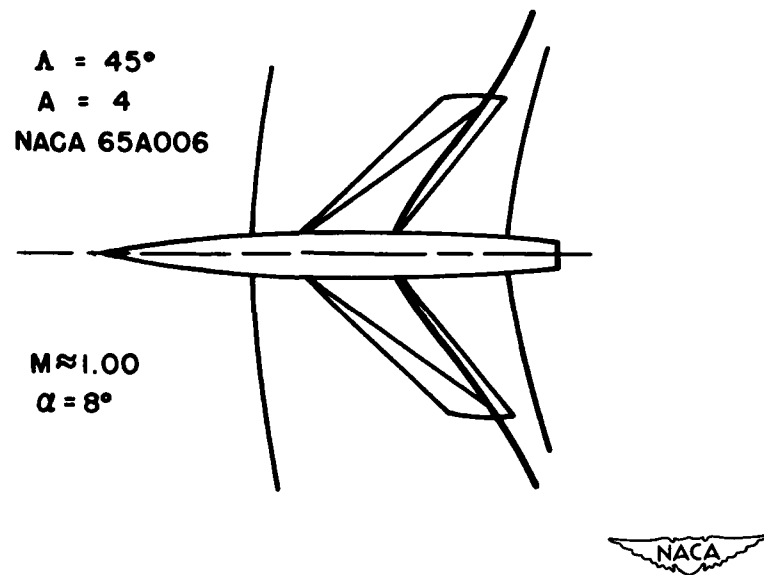


Figure 1.

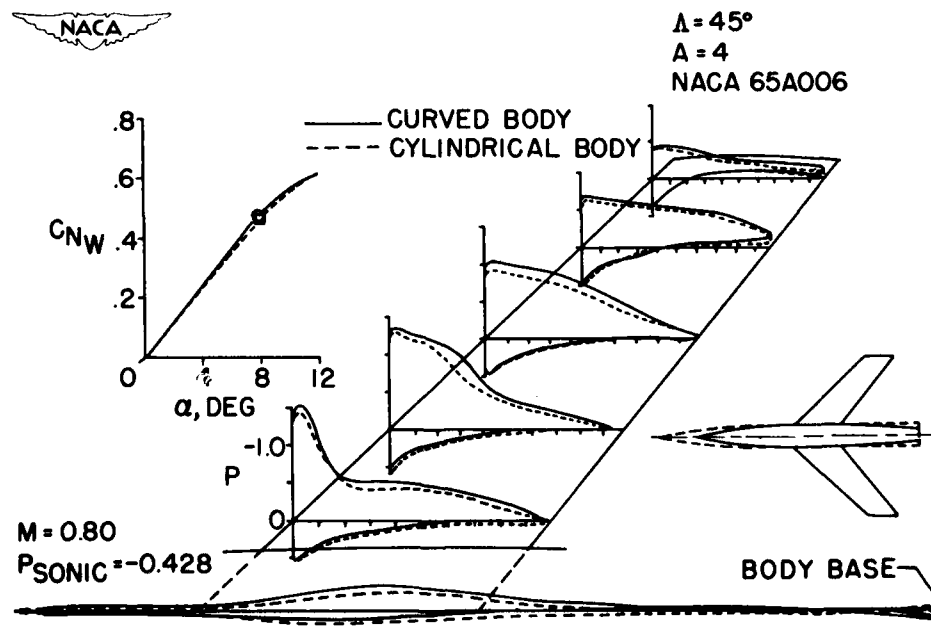
PRESSURE DISTRIBUTIONS MEASURED ON WING AND BODIES,  $\alpha=8^\circ$ 

Figure 2.

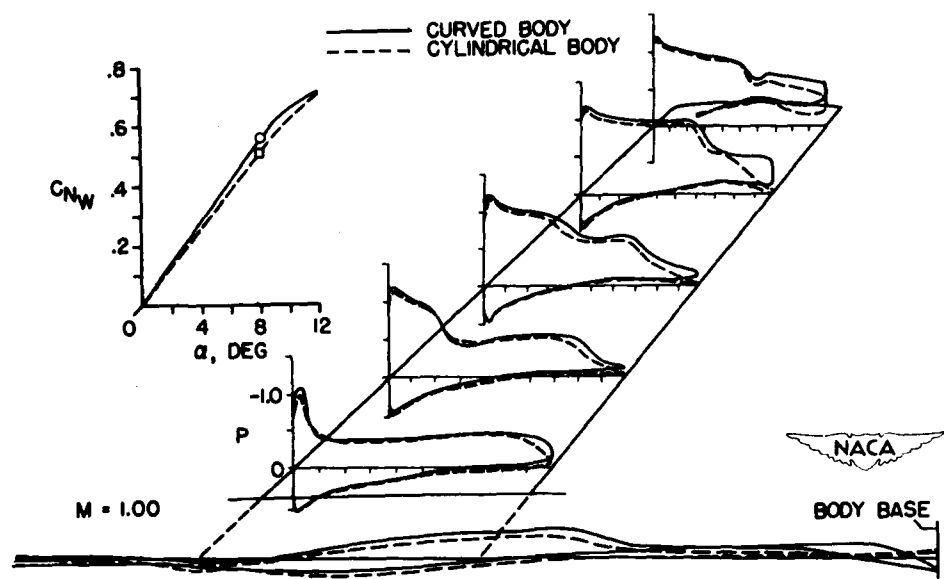
PRESSURE DISTRIBUTIONS MEASURED ON WING AND BODIES,  $\alpha = 8^\circ$ 

Figure 3.

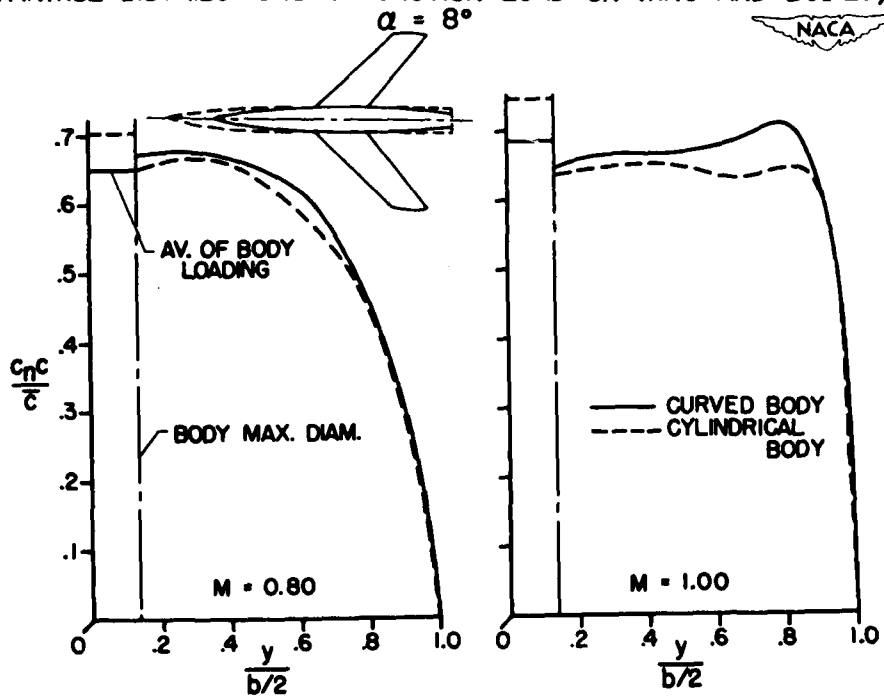
SPANWISE DISTRIBUTIONS OF SECTION LOAD ON WING AND BODIES,  
 $\alpha = 8^\circ$ 

Figure 4.

SPANWISE DISTRIBUTION OF SECTION MOMENT ON WING,  
 $\alpha = 8^\circ$

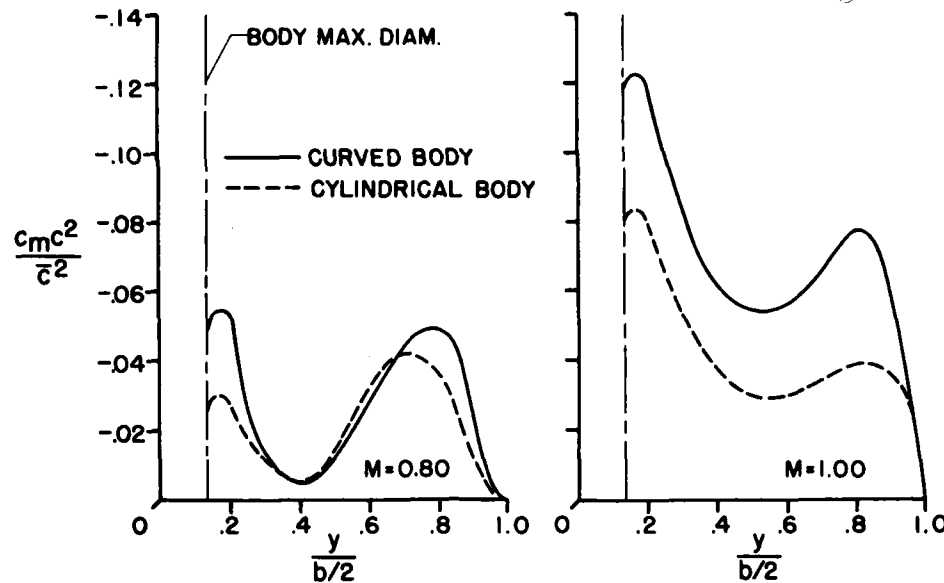


Figure 5.

LATERAL AND CHORDWISE POSITIONS  
 OF CENTER OF PRESSURE ON EXPOSED WING

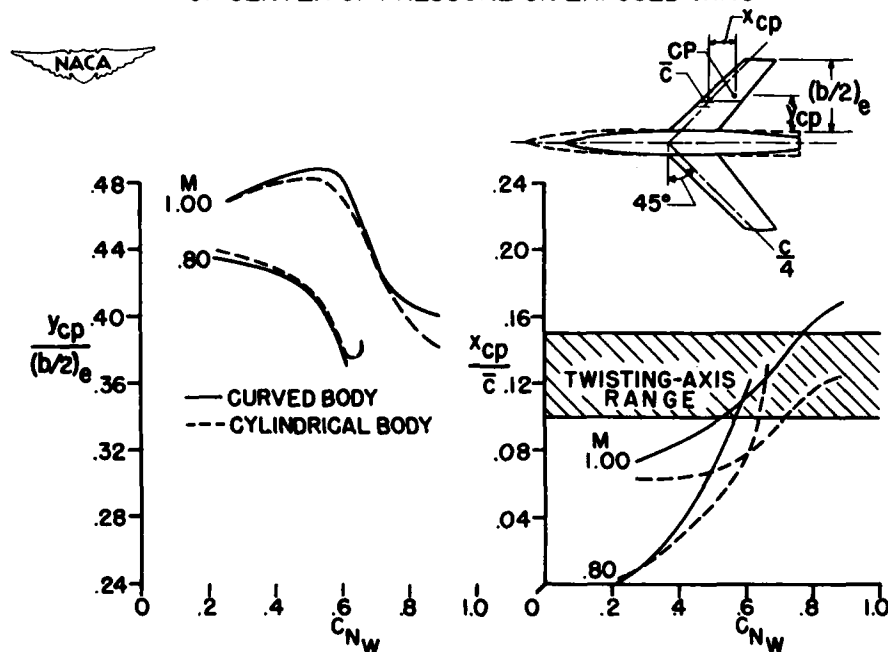


Figure 6.

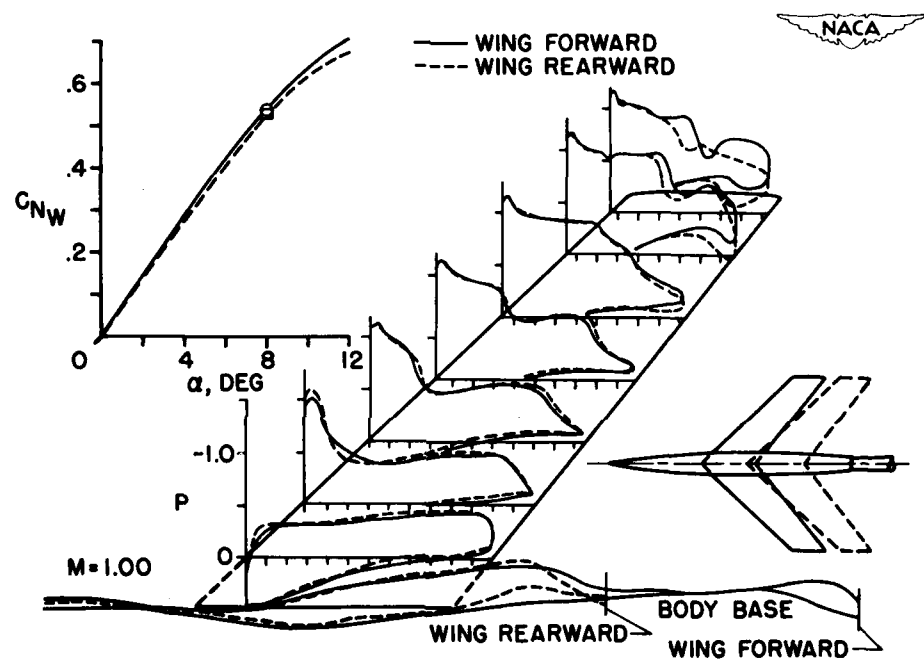
PRESSURE DISTRIBUTIONS MEASURED ON WINGS AND BODY,  $\alpha = 8^\circ$ 

Figure 7.

THE EFFECTS OF ANGLE OF ATTACK AND WING INCIDENCE  
ON THE LOADINGS ON A RECTANGULAR WING AND BODY  
COMBINATION AT SUPERSONIC SPEEDS

By Jack N. Nielsen and William C. Pitts

Ames Aeronautical Laboratory

#### INTRODUCTION

The primary purpose of this paper is to present a comparison between the measured pressure distributions of a rectangular wing and body combination and the theoretical distributions calculated by the method of NACA TN 2677 (ref. 1). By this method, the flow is treated as illustrated in figure 1. The body, if at angle of attack, produces an upwash field in the vicinity of the wing. The flow field of the wing without regard for the presence of the body is then calculated by the use of linear-wing theory and includes the effects of upwash. In the method, the wing leading edges are assumed to be supersonic so that the upper and lower parts of the combination are independent in the region of the wing. As shown, the wing induces velocities normal to the position to be occupied by the body. The presence of the body reduces these normal velocities to zero and sets up the interference pressure field that acts on both body and wing. The mathematical details of the pressure-distribution calculation are presented in NACA TN 2677. Phinney (ref. 2) has recently applied the method to the calculation of the pressures on a circular cylinder due to an oblique shock wave. That work suggests the application of the method to problems of external stores such as the forces on tip tanks. Furthermore, the method can be applied to the determination of the pressure field due to protuberances, such as canopies, on round fuselages. An experimental investigation has been undertaken for the specific purpose of determining the accuracy of the method.

#### EXPERIMENTAL CONSIDERATIONS

The wing-body pressure-distribution model used in the investigation is shown in figure 2. The model, which was sting-supported, was tested in the Ames 1- by 3-foot supersonic tunnel No. 1. The upper surface of the wing containing the orifices was flat so that flat-plate data would be obtained. The wing incidence is taken to be the angle between the flat surface of the wing and the body axis. The wing was rotated about its leading edge in order to vary the angle of wing incidence between  $0^\circ$  and  $-6^\circ$ . The angle of attack varied between  $-6^\circ$  and  $6^\circ$ . The data

presented herein are for a Reynolds number of  $1.5 \times 10^6$  based on the wing chord and for Mach numbers of 1.5 and 2.0. The body diameter is 1.5 inches, the wing chord is 3 inches, and the span of the wing-body combination is 9 inches.

#### RESULTS AND DISCUSSION

Before the discussion of the pressure distributions, it should be noted that the pressure orifices are considered to be mounted on the upper surface of the model on the right side facing forward. The basic data are for a Mach number of 1.5. Two cases are considered: the case of variable angle of attack at zero wing incidence, and the case of variable wing incidence at zero angle of attack.

The pressure distributions for variable angle of attack are shown in figure 3 for the wing-body juncture. The pressure distribution was measured at the location of the dark line in the upper sketch, which also shows the Mach lines. In this figure, the abscissa represents distance downstream from the wing leading edge in multiples of the body radius. The distance has been divided by  $\beta$ ,  $\sqrt{M^2 - 1}$ , to obtain a generalized distance independent of Mach number. The ordinate represents the local pressure coefficient  $P$  divided by angle of attack and multiplied by  $\beta$  to obtain pressure-distribution curves independent of angle of attack and Mach number. The experimental data points for negative angles of attack are shown by solid symbols, and those for positive angles are shown by open symbols. The linear theory of NACA TN 2677 is indicated in the figure together with the two-dimensional theory. At the leading edge, linear theory indicates a value of  $\beta P/\alpha$  of -4, twice the two-dimensional value because of body upwash. For angles of attack of  $\pm 2^\circ$ , the experimental pressure coefficients are in close accord with the coefficients predicted by linear theory except at the station farthest downstream.

Although the experimental pressure distributions as plotted should all fall on the same curve if the predictions of linear theory are correct, they do not. Thus, nonlinear effects of angle of attack cause a spread of the data. This spread has been calculated on the basis of shock-expansion theory with and without body upwash, and the theoretical results are shown by the vertical lines (fig. 3). Although the spread as calculated applies only to the leading edge, it can be applied to the first few orifice locations. The pressure coefficients for negative angles of attack are of greater magnitude than those for positive angles. It is apparent that the spread as measured is in closer accord with that predicted by neglecting upwash than with that including it. This result means that, although the upwash influences the linear effects of angle

of attack, it has no apparent influence on the nonlinear effects. The explanation for this paradox is not clear.

A phenomenon not accounted for by theory is exhibited by the data for large values of  $x/\beta r$ . On the basis of linear theory the pressures should increase in magnitude behind the Mach wave from the left wing panel for values of  $\frac{x}{\beta r} > \pi$ . For negative angles of attack the experimental data exhibit the influence of the left wing panel in front of the theoretical position of the Mach wave. This phenomenon is explained by the facts that, for negative angles of attack, the Mach number above the wing is less than the free-stream Mach number, and that the influence of the left wing moves forward through the body boundary layer. For positive angles of attack, the effect moves behind the theoretical position of the Mach wave.

In figure 4 the wing-incidence pressure distributions for  $i_w = -2^\circ$  and  $-6^\circ$  are shown. As shown by the comparison between the data points and the lower curve, the agreement between experiment and theory is good. The upper curve is the theoretical curve taken from the preceding figure. A comparison of the two theoretical curves shows the large effects of upwash.

In figure 5 a comparison is made between experiment and theory for the angle-of-attack pressure distributions on top of the body. The data points for negative angles of attack are again shown by solid symbols. The theory indicates that no pressure should be felt in front of the point on top of the body where the Mach lines from the wing-body juncture meet, but a rapid rise in pressure should occur shortly thereafter. The data show that the pressure increases in magnitude before this point is reached, a fact explainable mainly by the presence of a boundary layer. For positive angles of attack, the total rise in pressure is approximately that predicted by theory. At these angles of attack, the body boundary layer encounters an expansion wave due to the wing so that the effects of boundary-layer shock-wave interaction are small. For negative angles of attack, however, the boundary layer must traverse a shock wave and large deviations between theory and experiment are obtained as shown by the solid symbols of the figure for  $\alpha = -6^\circ$ .

The wing-incidence pressure distributions on the top of the body for  $i_w = -2^\circ$  and  $-6^\circ$  exhibit the same behavior as the pressure distributions for negative angles of attack. The only difference is that the magnitudes of the pressure coefficients for the wing-incidence case are less than those for the angle-of-attack case.

In figure 6 are shown the angle-of-attack pressure distributions for a position on the wing near the midspan. The theory is shown for

positions in front of the Mach wave from the wing-body juncture. Although the method of NACA TN 2677 is applicable to determining the pressures behind the wave from the wing-body juncture, the calculation was not carried out pending the determination of wing influence functions which simplify the problem. The Mach wave systems for  $\alpha = 0^\circ$  and  $-6^\circ$  are shown in the sketch in the figure, and the points at which the waves intersect the row of the orifices under consideration are shown by the circled numbers on the scale of the abscissa.

For angles of attack of  $\pm 2^\circ$ , the measured pressure coefficients lie slightly above the linear-theory pressure coefficients. For the higher angles of attack, the nonlinear effects found at the juncture are again manifest. For small values of  $x/\beta r$  the data for negative angles of attack have higher values than those for positive angles of attack in accordance with nonlinear theory as for the wing-body juncture. For the largest values of  $x/\beta r$  this trend is reversed. This result is explained by the fact that the influence of the wing-tip Mach cone occurs at lower values of  $x/\beta r$  for  $\alpha = -6^\circ$  than for  $\alpha = 0^\circ$ , as indicated by conditions 3 and 4 on the abscissa scale.

The wing-incidence pressure distributions exhibit the same general behavior as those for negative angles of attack. However, the effect of upwash at this station on the wing is not so great as at the wing-body juncture.

In figure 7 the span-load distributions for variable  $\alpha$  and variable  $i_w$  are shown. The abscissa is the spanwise distance in body radii, and the ordinate is the nondimensional span loading obtained by integrating pressure distributions of the type shown previously. Also shown in the figure is the Mach wave pattern for  $\alpha = 0^\circ$  or  $i_w = 0^\circ$ . The trailing-edge intersections of the Mach waves are indicated on the scale of the abscissa. The theoretical span loading for wing incidence as determined by the method of NACA TN 2677 is shown in the figure. For variable angle of attack, the span loading on the wing is not shown since, as mentioned earlier, the wing pressure distributions were not calculated for this case and are awaiting the calculation of the wing influence functions. For the wing-incidence case, three regions can be distinguished in the theory. Between the origin and point 1, the problem is one of wing-body interference. Outboard of point 2, the problem is solely a wing problem. Between points 1 and 2, both types of problem are present.

When experiment and theory for angle of attack are compared, the loading on the body is seen to be predicted with reasonable accuracy at  $\alpha = 2^\circ$ . At  $\alpha = 6^\circ$ , there is a small effect of angle of attack on top of the body ( $\frac{y}{r} = 0$ ) because of boundary-layer effects. Generally

speaking, however, there are no nonlinear effects of angle of attack on span loading similar to those on pressure distribution inasmuch as the loading gained on the pressure surface of the wing is lost on the suction surface.

For the wing-incidence case the experimental and theoretical span loadings are in good accord. The effect of body upwash is clearly shown by comparing the span loadings for the angle-of-attack and wing-incidence cases. As previously mentioned, outboard of the point 2 (fig. 7) the span loading for wing incidence is solely a wing problem. Thus, the present results can be extended to any aspect ratio by moving the tip solution outboard. For the angle-of-attack case, a similar procedure could be followed if the linear-theory wing-tip solution including body upwash were available. For distances of 4 to 5 radii and greater from the body center line, the effects of upwash can be ignored, and no distinction between the two cases need be made.

In order to convey an idea of the importance of interference for the present wing-body combination, the total wing-lift forces for three conditions were determined by integrating the span-load distributions. The first condition was for variable angle of attack and the second was for variable wing incidence, as shown in figure 7. The third condition was for the wing alone, which was considered to have the same span as the combination, and includes no effects of wing-body interference. The comparison shows that the wing lift for the wing-incidence condition was 10 percent less than that for the wing-alone condition. This difference means that wing-body interference with no body upwash causes a loss of lift. The comparison also shows that the wing lift for the angle-of-attack condition was 20 percent greater than that for the wing-alone condition. This difference means that wing-body interference including body upwash had a favorable effect on wing lift. For larger diameter-span ratios, the differences will usually increase.

Consider now the effects of Mach number on span loading. In figure 8 it can be seen that Mach number has no effect on the agreement between theory and experiment between  $M = 1.5$  and  $M = 2.0$ .

#### CONCLUDING REMARKS

For a rectangular wing and body combination, the method of NACA TN 2677 predicts within an accuracy of about  $\pm 10$  percent the pressure distributions and span loadings due to angle of attack and wing incidence except where nonlinear angle-of-attack effects and viscous effects are important. Furthermore, the method has application to problems of external stores and fuselage protuberances.

**CONFIDENTIAL**

**REFERENCES**

1. Nielsen, Jack N., and Pitts, William C.: Wing-Body Interference at Supersonic Speeds With an Application to Combinations With Rectangular Wings. NACA TN 2677, 1952.
2. Phinney, R. E.: Wing-Body Interference. Progress Rep. No. 4, Univ. of Michigan, Eng. Res. Ins., 1952.

**CONFIDENTIAL**

## INTERFERENCE VELOCITIES OF WING-BODY COMBINATION

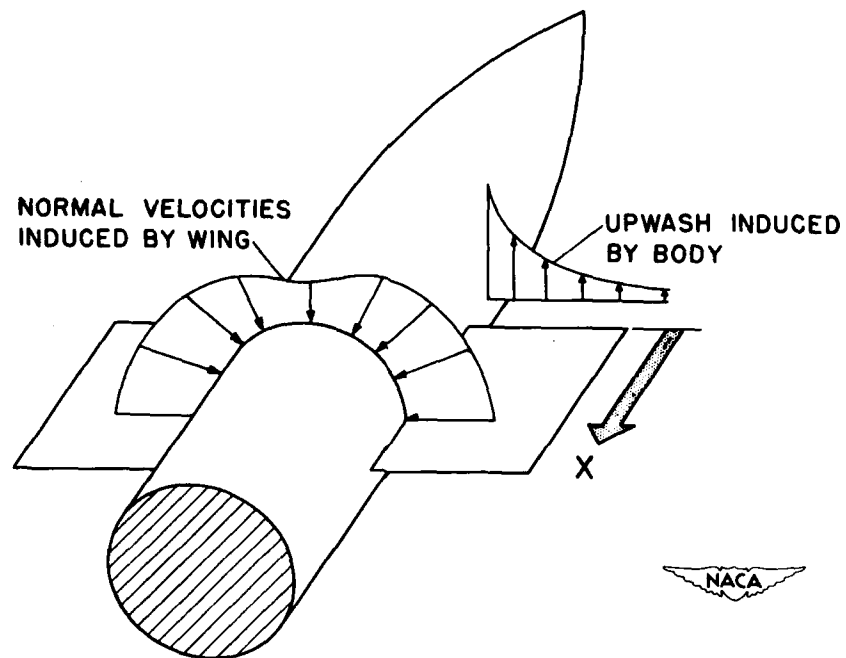


Figure 1.

## PRESSURE DISTRIBUTION MODEL

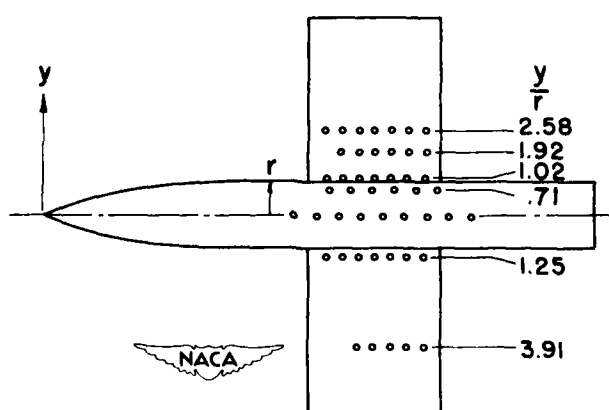


Figure 2.

## PRESSURES AT JUNCTURE DUE TO ANGLE OF ATTACK

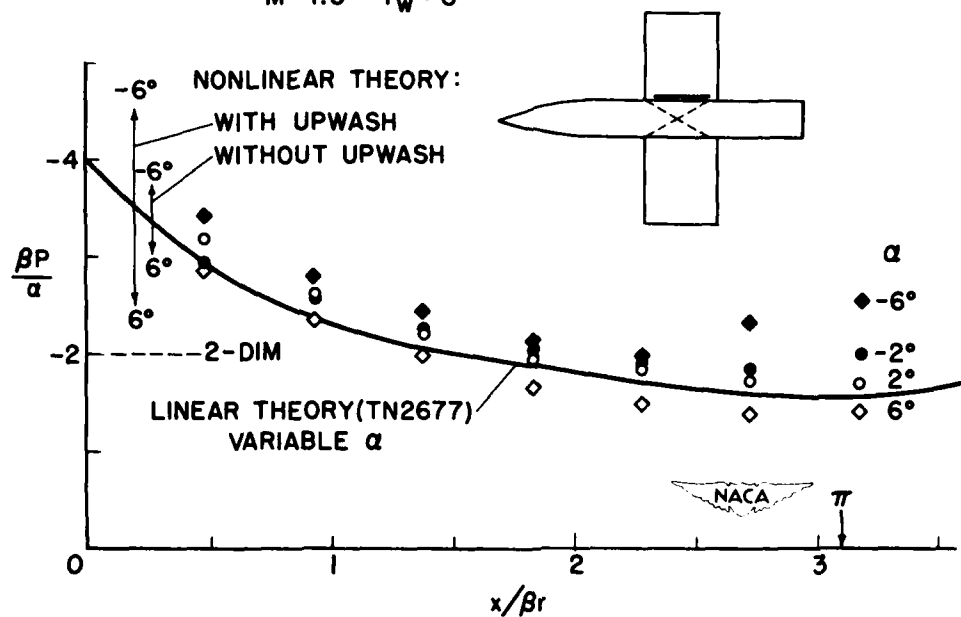
 $M = 1.5 \quad i_w = 0$ 

Figure 3.

## PRESSURES AT JUNCTURE DUE TO WING INCIDENCE

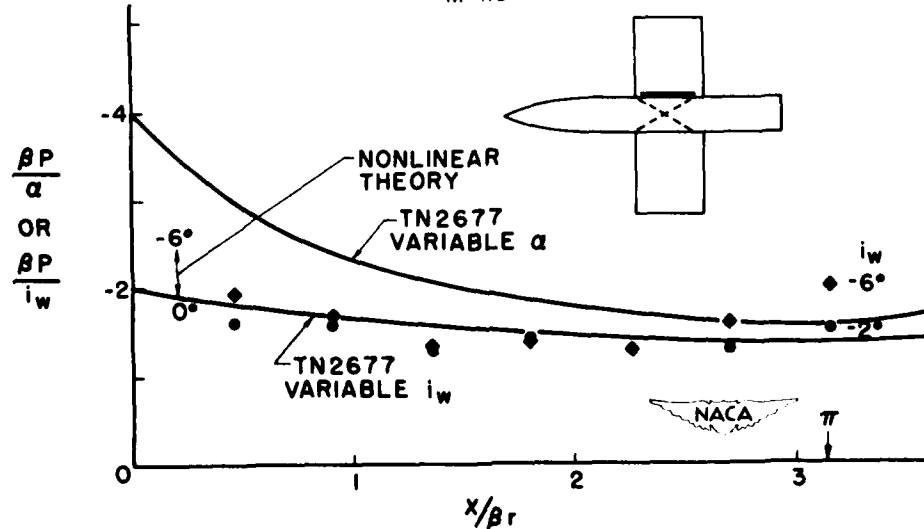
 $M = 1.5$ 

Figure 4.

## PRESSURES AT TOP OF BODY DUE TO ANGLE OF ATTACK

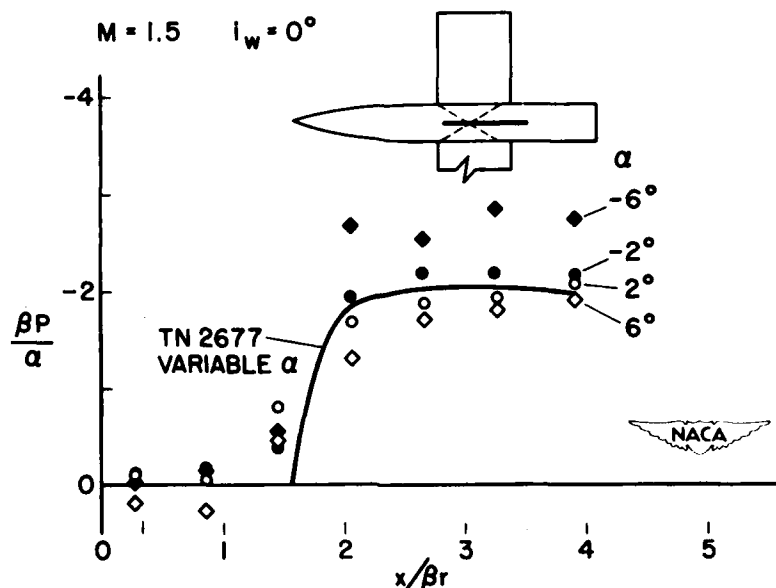


Figure 5.

## PRESSURES ON WING DUE TO ANGLE OF ATTACK

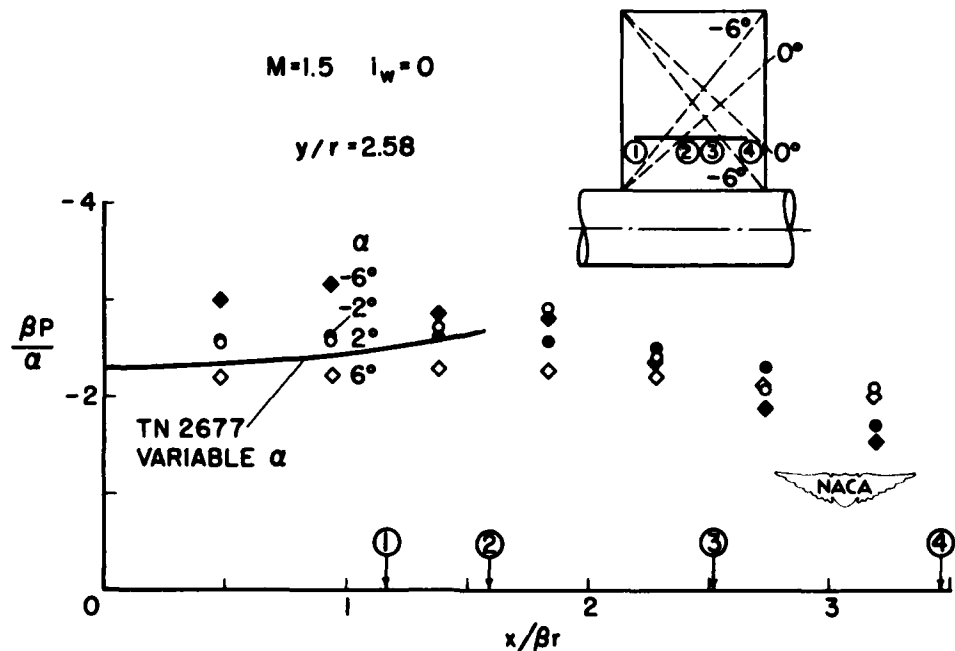


Figure 6.

CONFIDENTIAL

## SPAN LOADINGS AT M=1.5

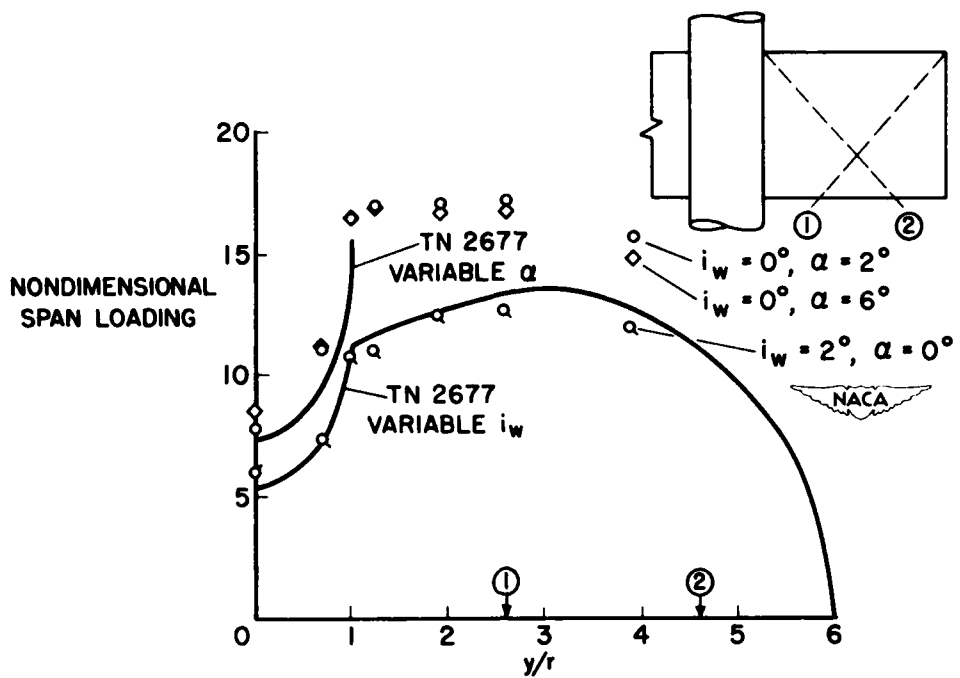


Figure 7.

## EFFECT OF MACH NUMBER ON SPAN LOADING

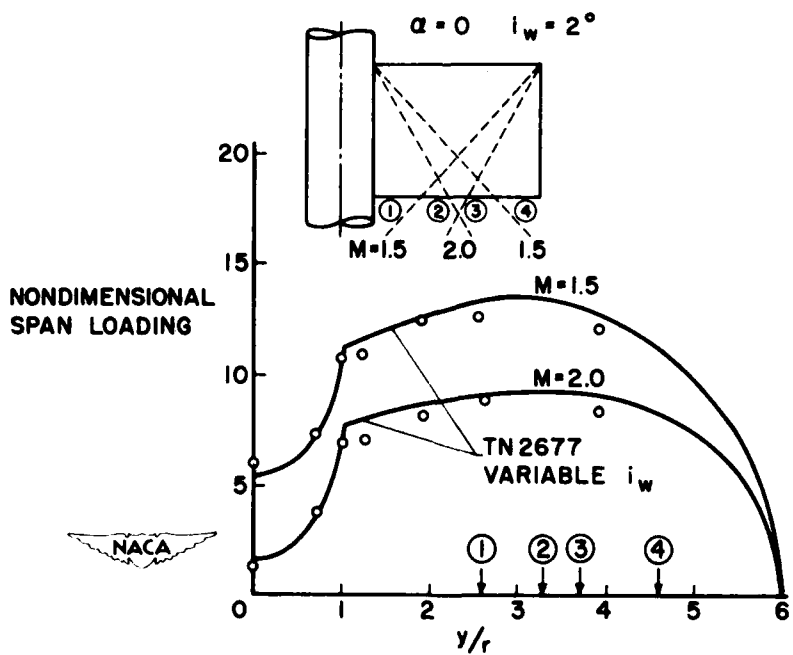


Figure 8.

CONFIDENTIAL

CONFIDENTIAL

119

AERODYNAMIC LOADS ASSOCIATED WITH  
EXTERNAL-STORE INSTALLATIONS

By H. Norman Silvers and Thomas C. O'Bryan

Langley Aeronautical Laboratory

INTRODUCTION

The continued use of external stores on airplanes has intensified the interest in general loads information in this field. Until recently, the only results available had been obtained to answer a certain specific problem and were of little use in relation to the general requirements of designers. Several external-store load programs intended to provide general design information are currently being performed by the National Advisory Committee for Aeronautics. It is the purpose of this paper to review the available results of some of these investigations conducted, for the most part, at subsonic speeds to indicate some observations that may prove helpful in the design of future external-store installations.

STORE-INDUCED WING LOADS

The loads associated with external-store installations can be considered in two parts. One part is concerned with the effects of the store installation on the loading of wings, and the other is concerned with the direct loads on the stores. The first part of this paper deals with store-induced wing loads.

In order to determine the store-induced wing loads, tests have been made of a  $45^{\circ}$  sweptback wing of aspect ratio 4.0 in combination with a fuselage. As shown in figure 1, the wing was equipped with pressure orifices at five stations across the span. In the analysis of the results, all five pressure stations were considered as being on the same wing panel at semispan locations of 20, 40, 60, 80, and 95 percent. Two arrangements of the external stores were investigated - an inboard arrangement and a wing-tip arrangement. In both arrangements, the stores were attached directly to the wing surface.

In this investigation the distributions of section normal forces over the wing semispan have been obtained at subsonic and low transonic speeds. Considering first the inboard external-store installation, figure 2 shows the effect of this installation on the spanwise distribution of section normal-force coefficient and on the static aerodynamic pitching-moment coefficient at a subsonic Mach number of 0.70.

CONFIDENTIAL

The variation in the static aerodynamic pitching moment has proven to be a useful guide to changes in span loading over a sweptback wing. One of the most significant changes in span loading indicated is the loss in wing-tip load that is related to airplane pitch-up - pitch-up is characterized by a rapid positive increase in static aerodynamic pitching moment. At an angle of attack of  $12^\circ$ , which is well beyond the onset of pitch-up for this wing, the loss in experimental wing-tip load is apparent in the distribution of section normal forces by comparison with the span loading calculated by potential-flow methods. Before the onset of wing pitch-up (as represented by the results at  $\alpha = 4^\circ$ ), the load distribution calculated by potential-flow methods is in good agreement with experiment.

The static aerodynamic pitching moment also illustrates the principal effect of inboard stores on the loading of the plain wing. That effect is to delay pitch-up to higher angles of attack. In this respect an inboard external store behaves in much the same way as certain auxiliary devices designed to delay wing pitch-up. Some of these devices are discussed in a previous paper by Wilbur H. Gray and Jack F. Runckel. The distribution of section normal-force coefficient over the wing panel at an angle of attack of  $12^\circ$  with the store on the wing shows increased loading at the wing tip that is represented fairly well by the calculated loading of the plain wing. At a lower angle of attack ( $\alpha = 4^\circ$ ), the calculated loading of the plain wing is almost identical to the experimental loading of the wing-store combination.

To illustrate chordwise loading, the chordwise distribution of pressure at an angle of attack of  $12^\circ$  and a Mach number of 0.70 is presented in figure 3. The results show that, on the inboard side of the store, the store reduces the loads of the plain wing by promoting thickened boundary-layer conditions. The additional tip loading due to the store is seen to come from a small region of loadings similar to those that can be predicted by potential-flow methods just outboard of this store and increased normal-force loads coming from reduced separation losses outboard of this region.

The points of design interest shown by these results are that at subsonic speeds in place of more detailed loading information the static aerodynamic pitching moment can be used as a guide to indicate the limit of the angle-of-attack range over which the span load distribution of a plain wing, calculated by potential-flow methods, may be used to represent the span load distribution of a swept-wing-fuselage combination having inboard external stores. Furthermore, an inboard external store extends the range in which calculated span loadings can be used in the same way as auxiliary devices designed to delay wing pitch-up. The amount of extension, however, is likely to depend upon the store arrangement. It follows that, if the design limit of a swept-wing airplane is not attained prior to pitch-up, recourse must be taken to experimental span loadings for design purposes.

Although the information available on the effect of inboard external stores at transonic speeds is limited, results obtained on the installation just discussed at a Mach number of 0.91 (fig. 4) provide some insight into the loading conditions that may be expected in this speed range. The delay in wing pitch-up caused by the inboard external store at subsonic speeds has vanished at a Mach number of 0.91. The similarity between auxiliary devices designed to delay wing pitch-up and inboard stores is again apparent, since both lose effectiveness in delaying wing pitch-up with entry into the transonic speed range. At an angle of attack of  $12^\circ$ , the plain wing and the wing-store combination are experiencing wing-tip separation, as evidenced by pitch-up, and the loading characteristics are similar. The calculated distribution does not provide a reliable indication of the experimental loadings in this angle-of-attack range. However, where there is negligible wing separation prior to pitch-up, illustrated by the results at an angle of attack of  $4^\circ$ , the inboard store again has no major effect on the wing span loading.

The discrepancy between the calculated loading and the experimental loadings of the plain wing and the wing-store combination can be attributed to the fact that theory does not adequately estimate the lift-curve slope of the model at this Mach number.

The diminution of the span loading of the wing tip with increase in Mach number (figs. 2 and 4) is represented in the chordwise loading (figs. 3 and 5) by the reduced suction pressures on the outboard side of the store and beyond this region in the reduced section loads associated with the stalled type of pressure distributions of the chordwise loadings. Theory cannot be expected to predict stalled-type loadings such as these. The attainment of supercritical flow conditions terminated by compression shock on the wing and the wing-store combination at the wing-fuselage juncture as evidenced by the second peak in the pressure distributions is one of the reasons the lift-curve slope of the model is not adequately estimated by theory in this speed range.

Turning now to tip stores, it is well-known that this store arrangement has some significant aerodynamic advantages on straight-wing airplanes that appear also to exist but to a somewhat lesser degree on wings with sweepback. The advantages come from an additional loading of the wing tip induced by the tip store that can be interpreted as an effective increase in wing aspect ratio. In figure 6 this additional tip loading is shown at a Mach number of 0.70 in the distribution of section normal force at an angle of attack of  $4^\circ$ . The calculated span load distributions for the plain wing and for the wing-store combination are included. Span loading was calculated by the method of reference 1. The calculated and experimental increments in span load due to the tip store are in good agreement. The loading over the tip store also calculated by this method is in good agreement with the measured store load. The experimental distribution over the store was obtained by distributing a measured store total normal force according to the theoretical distribution.

It is of interest to note that, of the total additional loading over the wing and the tip store, about 40 percent is carried directly on the store.

Inasmuch as the additional tip loading due to the store is proportional to angle of attack, it is evidenced in the aerodynamic pitching moment by a change in stability. Beyond the effect on stability at the lower angles of attack, the tip store has no major effect on the variations in static aerodynamic pitching moment. Therefore, the distribution of section load at the higher angles of attack would be expected to be similar as they are shown to be at an angle of attack of 12°.

At supersonic speeds, information is available on the effect of stores on the lateral center of pressure. The results were obtained on a small-size semispan model with a 45° sweptback wing at Mach numbers of 1.4, 1.6, and 2.0. The results are shown in figure 7 in terms of the incremental change in location of the lateral center of pressure due to the store. The nose sections shown in this figure represent the locations of the stores in both the chordwise and spanwise directions. The lateral centers of pressure were obtained over the angle-of-attack range ( $\alpha = 0^\circ$  to  $8^\circ$ ) where the wing-root bending moment varied linearly with lift coefficient and can be considered to represent conditions discussed previously at subsonic speeds for the low angle of attack.

The tip-mounted store results in a measurable outboard movement in the lateral center of pressure that is equivalent to an additional tip load; however, there is little change in the lateral center of pressure for inboard stores. The dashed fairing approaching the wing tip indicates a region of uncertainty as to the change in lateral center of pressure due to stores in these locations. The cross-hatched region represents the entire change in the incremental lateral center of pressure due both to Mach number and store chordwise position. Thus, in a qualitative sense external stores show characteristics at supersonic speeds similar to those at subsonic speeds. Unpublished results also indicate that the same type of changes in lateral center of pressure due to stores was obtained on an unswept wing at supersonic speeds.

#### STORE LOADS

Several investigations have been made to evaluate the second part of the loading of external-store installations, that is, direct store loading. One such investigation was made on a North American F-86A-1 airplane with 245-gallon auxiliary fuel tanks equipped with small horizontal fins. The installation on the airplane is shown in figure 8. Normal and side forces on one of the tanks were obtained by pressure measurement. The pressure orifices were located in meridian planes along the tank length.

The variations of normal and side forces on the tank with airplane lift coefficient are shown in figure 9. Keeping in mind that a full 245-gallon tank has a fuel load of about 1,500 pounds, it is apparent that the maximum normal forces attained, designated by  $N_S$ , are small in comparison to the fuel load and are in a direction to compensate for it. Higher normal forces would of course be shown at altitudes below the 30,000-foot level of these tests, but even at sea level where the forces may be as much as three times as large, they would still be considerably less than the fuel load.

Side forces, designated by  $Y_S$ , however, reach levels at the higher Mach numbers that are considerably above the normal-force loads. Such characteristics are indeed interesting since it would not be expected that loads as large as these would be encountered in flight where there was no intentional sideslip. The side forces are important because they indicate that the largest loads may occur in the plane of least structural strength of the installation. For this reason, another factor arising from performance requirements may introduce design problems in the lateral plane of pylons. For performance reasons at high speeds, it is recommended that the pylons supporting external tanks be kept thin, perhaps as much as several percent thinner than wings, and free of external bracing. Such a criterion may become difficult to follow with lateral loads of the size suggested by these and other results to be presented subsequently.

Systematic wind-tunnel investigations of direct store loads are also being made. Models on which some results have been obtained are shown in figure 10. The wing-fuselage models employed a straight and a swept-back wing. On each model inboard and wing-tip store arrangements were investigated. One store in each arrangement was equipped with an internal strain-gage balance that measured the store forces and moments. Results of the tunnel investigations at zero yaw are shown at a subsonic Mach number of 0.50. The store force coefficients are based on the store maximum frontal area, whereas moment coefficients are based upon store maximum frontal area and length. Some of the results presented herein have been taken from results presented in reference 2.

Store yawing-moment coefficient, designated by  $C_{YS}$ , and store side-force coefficient, designated  $C_{NS}$ , are presented in figure 11. The directions of all store load coefficients are the same as those employed in aerodynamic practice. These results indicate that the large lateral loading of the inboard store is primarily a result of wing sweep since both the store yawing-moment coefficients and side-force coefficients are considerably less for the inboard stores on the straight-wing model than for the swept-wing model. The side-force coefficient at an angle of attack of  $10^\circ$  would be equivalent on a fighter airplane at sea level in unyawed flight to a load of about 1,000 pounds. Although the data are extremely limited, there is evidence that the lateral loading of tip stores may also become large enough to be considered.

The store normal-force coefficients are presented in figure 12 and they indicate that the level of loading for inboard arrangements including the effect of sweeping a wing from  $3.6^\circ$  to  $46.7^\circ$  is low. The order of magnitude of the tunnel result is, in fact, about the same as that predicted by viscous theory for an isolated external store.

Somewhat higher normal-force coefficients are shown for the tip arrangements probably because of the pressure field around the wing tip. The rapid increase in up load with angle of attack of the tip store may not result in loads large enough to produce structural overload since the coefficients shown here suggest normal loads of the same order of magnitude as those produced by fuel loads for such a store used as a tank. The moment loads due to these normal forces may on the other hand become critical. Before continuing with the pitching-moment coefficients, it is noted, however, that the method of reference 1 estimates well the slope of the normal-force coefficients of the tip store.

The pitching-moment coefficients of the wing-tip store are shown in figure 13 in the plot on the right. The pitching-moment coefficients are presented about an axis on the tank that coincides with the approximate location of the torsional axis of airplane wings. The pitching-moment coefficients of the tip store increase rapidly with angle of attack as did the normal-force coefficients. In effect these results show that, if an airplane equipped with tip stores executes a pull-up to high angles of attack at low altitude, the store pitching load that must be absorbed by the wing panel is proportional to angle of attack and may result in significant wing torsional loads. Experience has demonstrated that, on several straight-wing airplanes in which wing failure occurred during such a maneuver, wing torsional effects coming from tip-store loadings such as these are large enough to contribute to the wing failure. Since the aerodynamic store loading is upward, these conditions are of course more critical for stores without internal load. The method of reference 1 again estimates, at least for this installation, the slope of the pitching-moment curve. It is not yet clear whether as good prediction of the pitching loads by this method of calculation can be expected with other geometrically different tip-store arrangements.

The pitching-moment coefficients of inboard stores shown in the plot on the left are seen to be as correspondingly low as the normal-force coefficients of this arrangement. They are less even than predicted by viscous theory for an isolated external store.

Since fins are commonly used on external stores, it is of interest to examine some results (fig. 14) that show the effects of one arrangement of fins on store moment coefficients. The fins were located at  $45^\circ$  from the horizontal and the vertical and were of a size and shape similar to those under consideration for use on one type of external store. The fins were large enough to more than neutralize the pitching-moment

coefficients of the store alone. The results show that the fins reduced the pitching-moment load but increased the yawing-moment load on the tip store, but they increased the pitching-moment load and decreased the yawing-moment load on the inboard store. The arrangement of fins tested is the type found on bombs and is not intended to represent fins selected to neutralize any particular component of store loads. Fins such as these, however, if employed on either arrangement of external stores, may be expected to increase at least one component of store load.

#### RESUME

In summary, results have been presented that indicate that the effects of stores on wing load distributions may be predicted by available methods at the lower angles of attack where wing flow separation is negligible. A store located inboard on a swept wing may act as an auxiliary device designed to delay wing pitch-up and results in corresponding changes in span load distribution. The chordwise loading for the angle-of-attack range where the store delays wing pitch-up is still largely unpredictable. The normal force and pitching moment of a wing-tip store can be handled quite well by available methods. Severe external-store lateral loads may be encountered on an inboard arrangement of stores on swept wings in unyawed flight. No theoretical treatment of these loads is presently available.

#### REFERENCES

1. Robinson, Samuel W., Jr., and Zlotnick, Martin: A Method for Calculating the Aerodynamic Loading on Wing—Tip-Tank Combinations in Subsonic Flow. NACA RM L53B18, 1953. (Prospective NACA paper)
2. Silvers, H. Norman, and King, Thomas J., Jr.: Investigation at High Subsonic Speeds of Bodies Mounted From the Wing of an Unswept-Wing—Fuselage Model, Including Measurements of Body Loads. NACA RM L52J08, 1952.

## WING-FUSELAGE MODEL WITH STORES

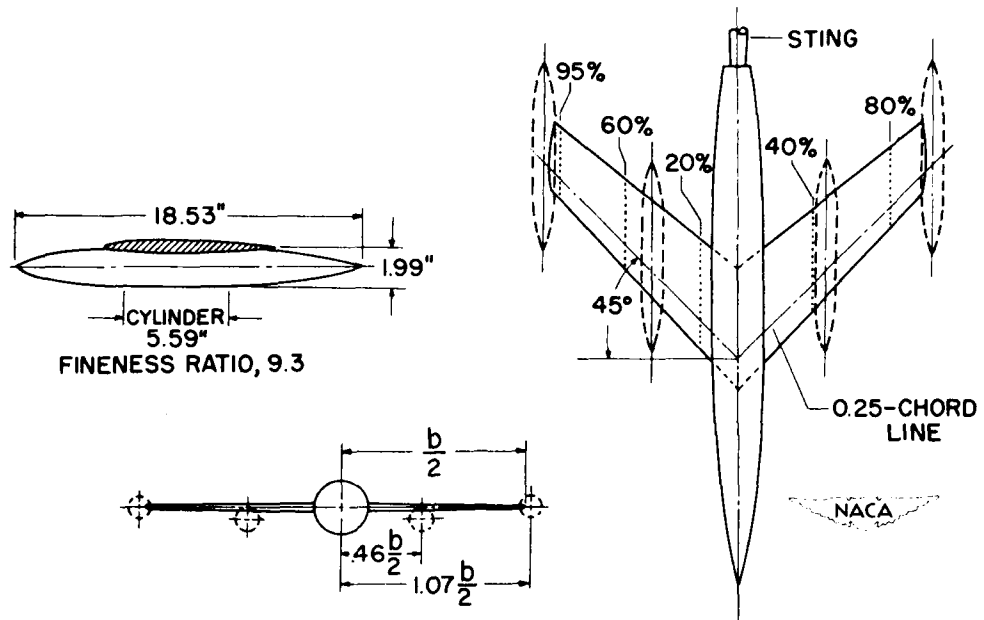


Figure 1.

## SPAN LOADING-INBOARD EXTERNAL STORES

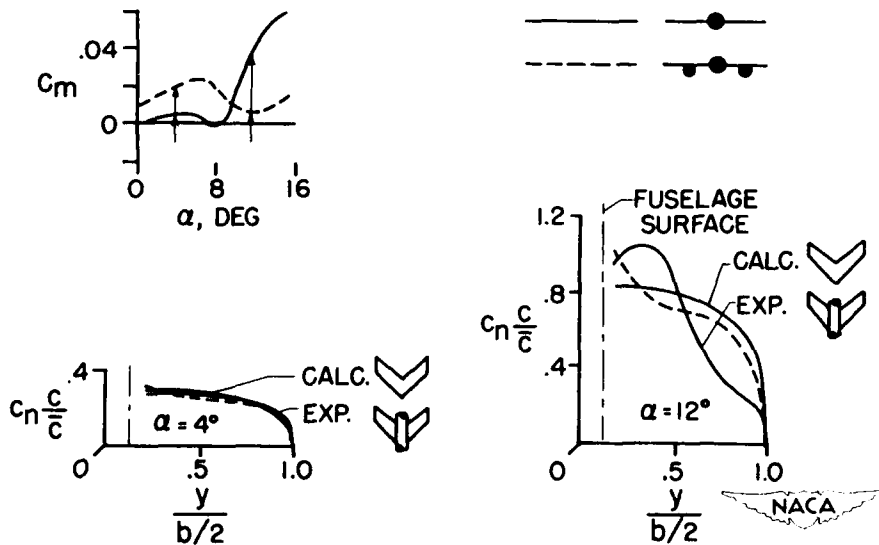
 $M = 0.70$ 

Figure 2.

## PRESSURE DISTRIBUTION - INBOARD STORES

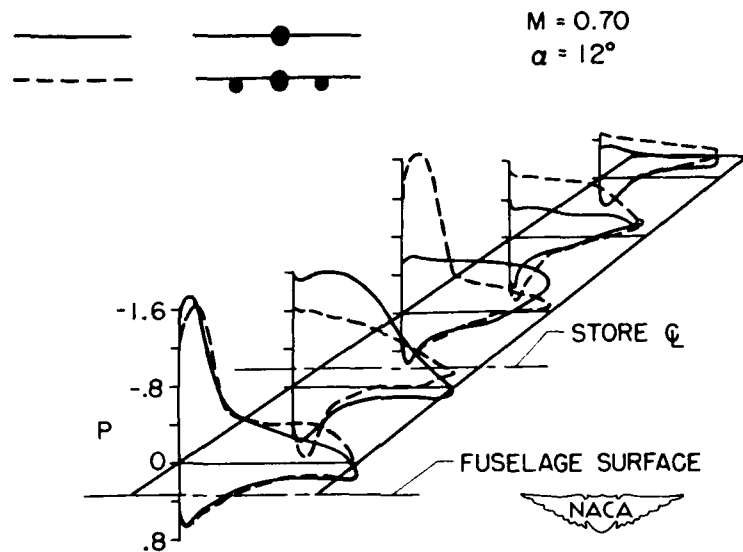


Figure 3.

## SPAN LOAD - INBOARD EXTERNAL STORES

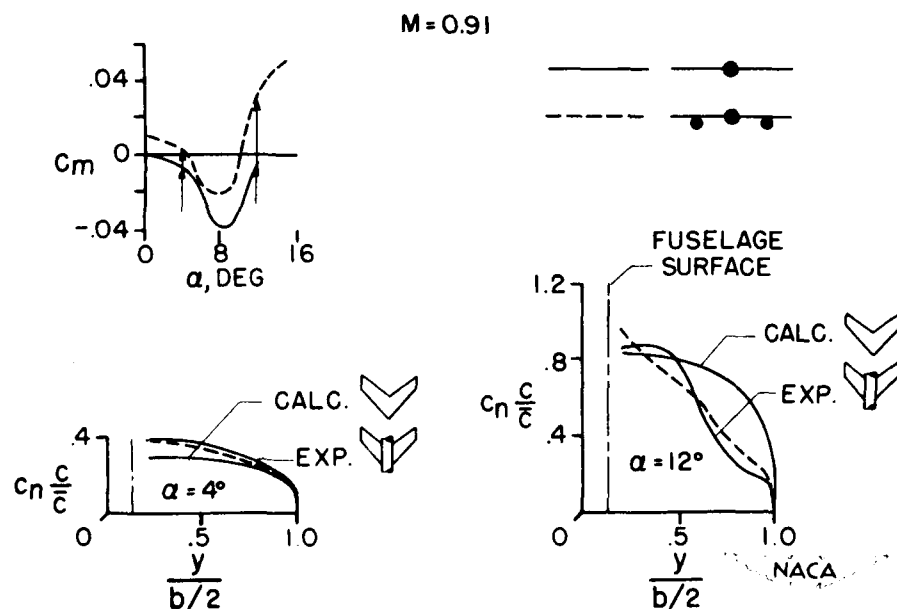


Figure 4.

## PRESSURE DISTRIBUTION - INBOARD STORES

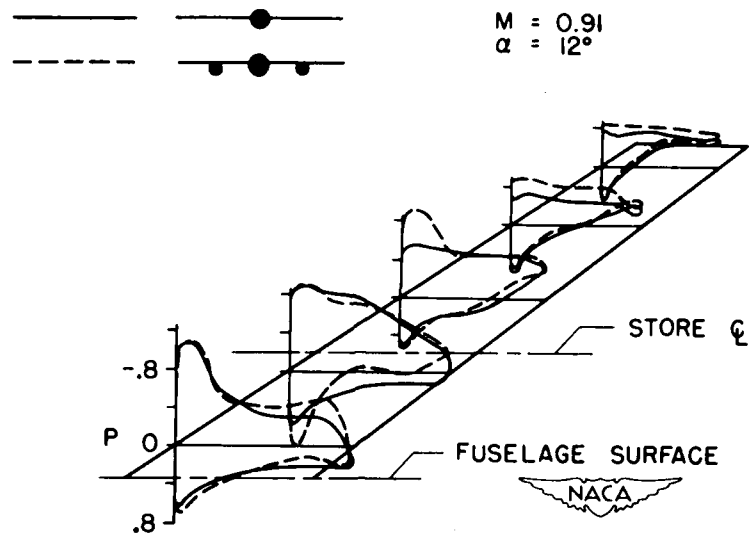


Figure 5.

## SPAN LOADING-TIP EXTERNAL STORES

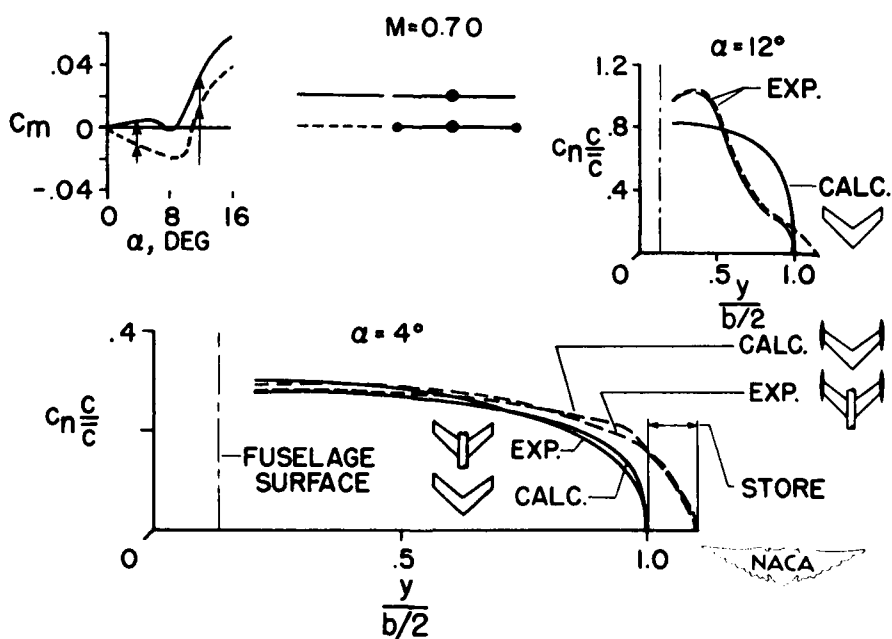
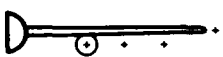


Figure 6.

## WING LATERAL CENTER OF LOAD

NACA 65A006  
 $\Lambda = 45^\circ$   
 $A = 4$



$M = 1.4, 1.6, 2.0$   
 $\alpha = 0^\circ \text{ TO } 8^\circ$

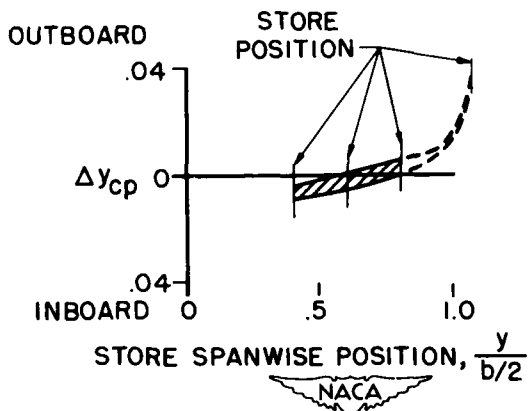
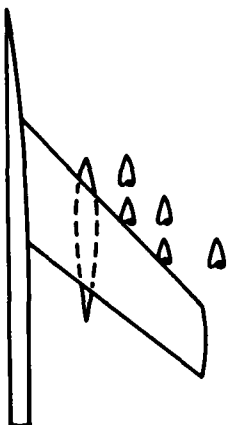


Figure 7.

## F-86A-1 AIRPLANE WITH 245-GALLON TANKS

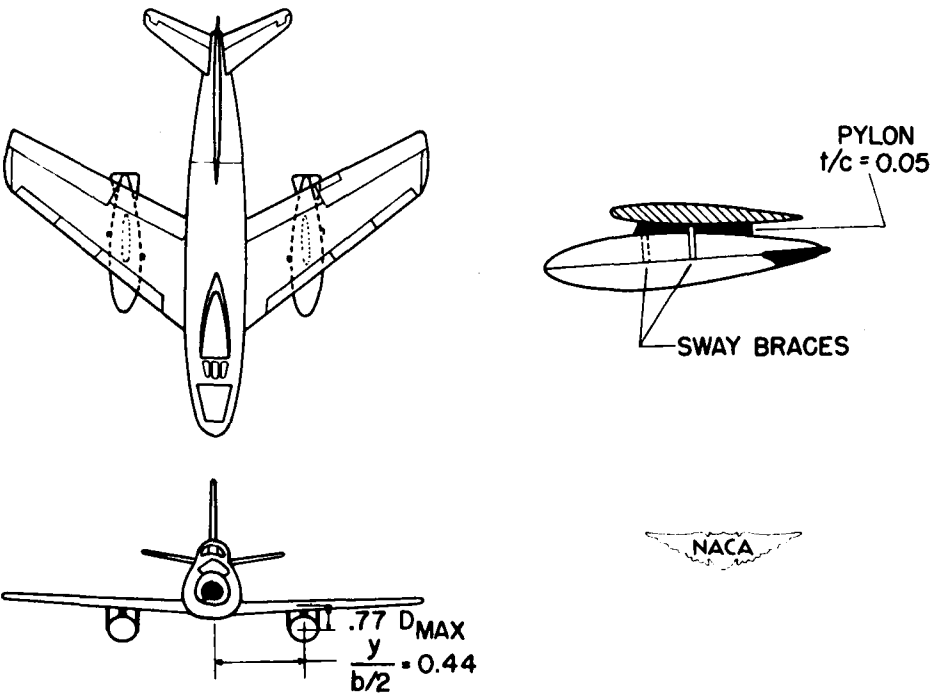


Figure 8.

## FORCES ON 245-GALLON TANK

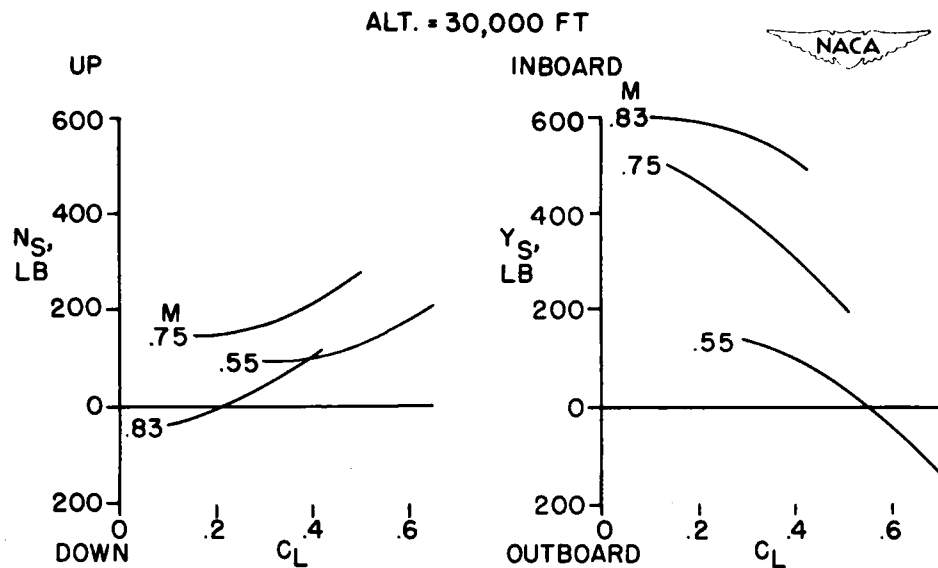


Figure 9.

## WING-FUSELAGE MODELS WITH STORES

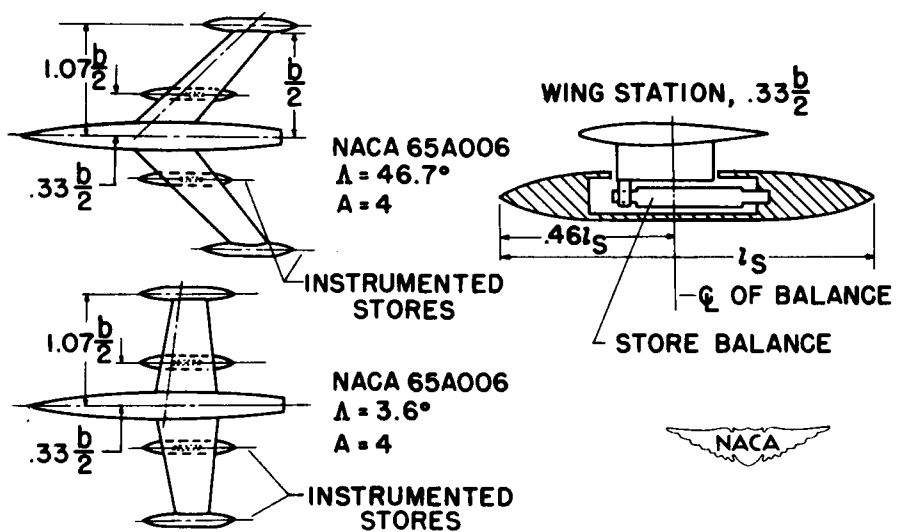


Figure 10.

## LATERAL LOADS ON STORES

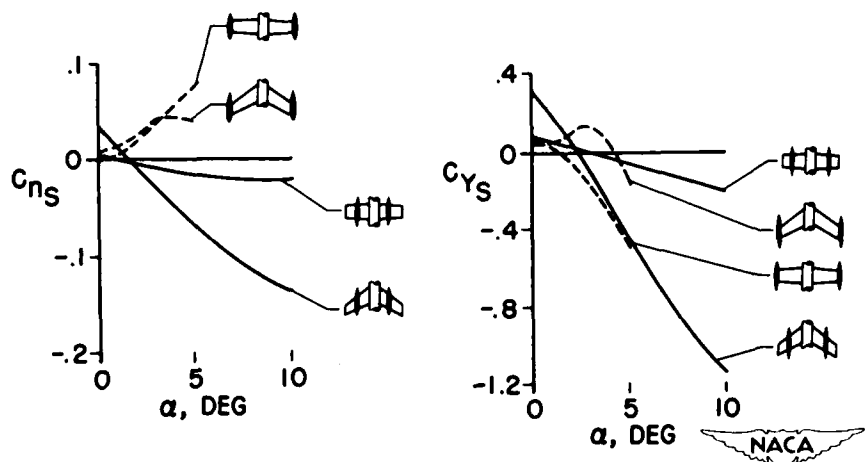
 $M = 0.50$ 

Figure 11.

## NORMAL-FORCE LOADS ON STORES

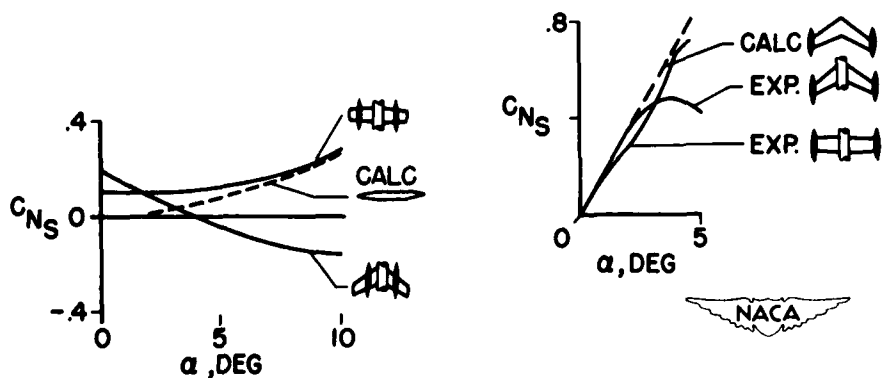
 $M = 0.50$ 

Figure 12.

## PITCHING-MOMENT LOADS ON STORES

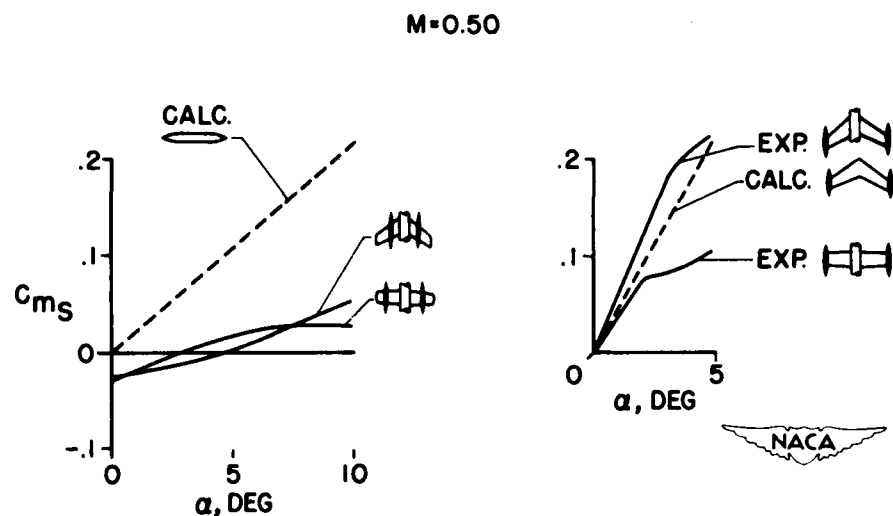


Figure 13.

## MOMENT LOADS ON STORES

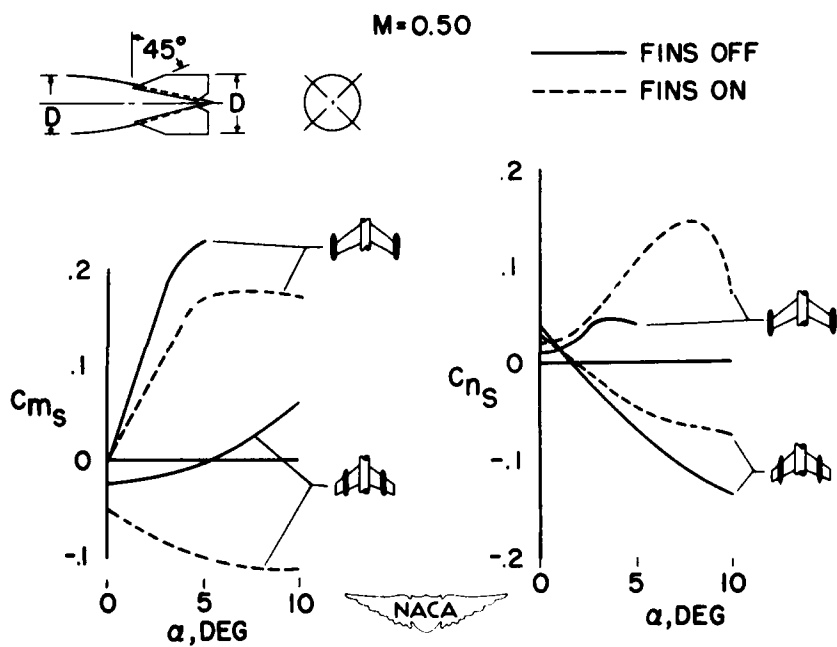


Figure 14.

**20G**

**CONFIDENTIAL**

**133**

**LOADS ASSOCIATED  
WITH CONTROLS**

**CONFIDENTIAL**

LOAD DISTRIBUTIONS ASSOCIATED WITH CONTROLS AT  
SUPersonic SPEEDS

12

By Douglas R. Lord and K. R. Czarnecki

Langley Aeronautical Laboratory

Until recently there was available only a limited amount of data at supersonic speeds on the loads associated with various control surfaces. As a result, the discussions of supersonic control loads had to be of a qualitative nature limited to chordwise loadings for the conventional flap-type control on unswept and swept wings. In the past few years much work has been done at the Langley Aeronautical Laboratory on chordwise and spanwise control loadings, wherein the loadings were obtained by means of pressure studies.

The first two figures (figs. 1 and 2) show a brief résumé of the scope of the loads investigations being made. On the left side of figure 1 is shown the trapezoidal wing which has been tested in the Langley 4- by 4-foot supersonic pressure tunnel at Mach numbers of 1.6 and 2.0 for a Reynolds number range from  $1.6 \times 10^6$  to  $6.5 \times 10^6$ . This wing has a modified hexagonal section of 4.5-percent thickness with sharp leading and trailing edges and a flat midsection. Six flap-type control configurations have been tested on the wing in order to determine the effect of control plan form, position, and trailing-edge thickness on the control loadings. Tests were made for angles of attack from  $0^\circ$  to  $15^\circ$  for control deflections from  $-30^\circ$  to  $30^\circ$ . A typical group of orifice stations is shown.

On the right side of the same figure, the two-dimensional balanced trailing-edge controls (ref. 1) which have been tested in the Langley 9-inch supersonic tunnel are shown. The wing was 6 percent thick and the investigation was made at a Mach number of 2.4 and a Reynolds number of  $0.8 \times 10^6$ , with and without fixed transition. Tests were made for angles of attack from  $0^\circ$  to  $10^\circ$  for control deflections from  $-20^\circ$  to  $20^\circ$ . The variables considered were: gap between the wing and control, amount of balance of the control, control profile, and wing trailing-edge bevel.

In figure 2 is shown the delta wing which has been tested in the Langley 4- by 4-foot supersonic pressure tunnel for approximately the same range of conditions as has the trapezoidal wing. This wing was 3 percent thick at the root with a round leading edge, flat midsection, and tapered trailing edge. Eleven control configurations were tested with this wing, seven of the tip-type and four of the more conventional flap-type. Variations in the flap controls amounted to changing the trailing-edge thickness and testing the inboard and outboard sections of the full-span control, together and independently.

In addition to the controls shown in these two figures, detailed two-dimensional studies have been made of the flow over a spoiler at  $M = 1.93$  in the Langley 9-inch supersonic tunnel (ref. 2), and an extensive investigation of the effect of attaching a spoiler to three-dimensional wings has been made in the Langley 4- by 4-foot supersonic pressure tunnel at  $M = 1.6$  and 2.0.

Before the control loadings determined in these investigations are discussed, note that it has been established previously that, at supersonic speeds, the chordwise loadings on flap-type controls were essentially rectangular in nature and that the spanwise loadings were fairly uniform for regions not strongly influenced by end effects. Further, investigations in the Langley 9-inch supersonic tunnel (refs. 3 and 4) and in the Langley 9- by 9-inch Mach number 4 blowdown jet (ref. 5) indicated that for controls in essentially two-dimensional flow, shock-expansion theory was in excellent agreement with experimental results when the boundary layer was turbulent. For the purposes of this paper, these findings are presumed to apply to the appropriate regions and the main part of the paper illustrates and discusses conditions where these findings do not apply. More specifically, the main discussion is limited to illustrations of the loadings associated with one of the flap and one of the tip controls on the delta wing, the full-span flap control on the trapezoidal wing, a few of the two-dimensional overhang-balanced controls, and some two- and three-dimensional applications of spoilers.

In figure 3 is shown a typical spanwise variation of the chordwise loadings on the delta wing equipped with the full-span trailing-edge control for a moderate angle of attack,  $6^\circ$ , and a large control deflection,  $30^\circ$ . The Mach number is 1.6. The figure illustrates two important effects which will be discussed in more detail in connection with subsequent figures. One of these effects is the large amount of load carryover ahead of the hinge line due to separation of the turbulent boundary layer ahead of the lower or high-pressure surface of the control as a result of shock-boundary-layer interaction. The other effect is the increase in loading experienced by the control along the span toward the wing tip. This increased tip loading occurs as a consequence of the conical flow over a delta wing at angle of attack which induces the highest wing loadings along the wing leading edge when the leading edge is subsonic. The high experimental loadings shown along the wing leading edge in this figure are evidences of this conical flow.

Typical experimental and theoretical loadings due to control deflection alone are shown in figure 4 for three stations on the control configuration shown in figure 3. The pressure loading is plotted against percent root chord; therefore, the leading-edge locations for the local chords are shown by ticks. Inasmuch as the wing is at zero angle of attack, the linear theory predicts that the entire load will be carried

on the control and that the distribution will be rectangular except when the Mach line from the intersection of the wing leading edge and the control hinge line crosses the orifice station. At this control deflection of  $20^\circ$ , the experimental load is beginning to build up ahead of the control because of the turbulent boundary separation. It was found that, for the Mach numbers of these tests, the turning angle of the control lower surface which causes the initial separation was always near  $13^\circ$ , except when the local Mach number was less than 1.4.

The experimental loading on the control is essentially rectangular; however, the linear theory generally overestimates the loading by a significant amount. By neglecting the thickness effect, assuming linear theory for the lifting pressures to be adequate ahead of the hinge line, and using two-dimensional shock-expansion theory to predict the control loading, the agreement between theory and experiment is improved. Flow studies also show that, at these large deflections, the trailing-edge shock causes separation from the control upper surface, and here again the separation angle is approximately  $13^\circ$ . If this separation from the control upper surface is considered, good agreement between theory and experiment is obtained. At station 6, the agreement is poorer than at the inboard stations because of the tip effect. Beyond the point where separation occurs on the lower wing surface ahead of the hinge line, or beyond  $20^\circ$  deflection for this particular control, the exact procedure for applying the combined linear-theory—shock-expansion—separation technique for estimating loads has as yet not been established because of the complicated way in which the separated flow reattaches to the control ahead of the trailing edge.

The experimental and theoretical combined loadings due to an angle of attack of  $12^\circ$  and a control deflection of  $20^\circ$  are shown in figure 5. Leading-edge flow separation on the upper surface is known to exist for this condition. The separation limit line shown on the sketch of the wing plan form was determined from the upper-surface pressure distributions and indicates the extent of the separated region from the leading edge.

The carryover of load ahead of the hinge line has increased slightly because of the addition of angle of attack to the condition shown on the previous figure (fig. 4). At station 6, the flow is completely separated and the experimental loading bears little resemblance to the linear-theory prediction. The linear-theory predictions of control loadings are again much too large; however, by using the shock-expansion technique previously described and considering the separation from the control upper surface, it is possible to get a much closer approximation to the experimental loadings. Hence, it may be concluded that by the judicious use of the combined linear-theory—shock-expansion—separation theory, control loadings can be estimated with good accuracy for this type of control except when the flow begins to separate ahead of the hinge line and except in regions affected by tip effects or leading-edge separation.

In figure 6 are shown spanwise loadings and center-of-pressure locations for the full-span trailing-edge control on the delta wing for conditions which cannot be handled by the advanced theoretical technique. Curves are shown for the load on the control alone and for the complete wing. The angle of attack is only  $6^{\circ}$ , but the control deflection is  $30^{\circ}$ . The results indicate that linear theory badly overestimates the control loading at all stations across the span and that it underestimates the effect of angle of attack on the span load distribution. The shape of the predicted and experimental spanwise loadings for the complete wing are in good agreement, and, although the linear theory overestimates the loads, the discrepancy between theory and experiment is much less than for the control alone. Since it would be expected that the deficiency in control loading would also be evident on the complete wing loading, the improvement in agreement must be due to the increased load on the wing from the carryover.

The linear-theory prediction of the spanwise variation of the chordwise center of pressure of the load on the control, shown on the right of the figure, is in good agreement with the experimental results. The linear theory predicts a somewhat more rearward location of the center of pressure for the complete wing than is obtained experimentally because of the aforementioned forward carryover of the control load.

A typical spanwise variation of the chordwise loadings on the delta wing having a tip control is shown in figure 7. The wing is at an angle of attack of  $6^{\circ}$  and the control deflection is  $30^{\circ}$ , although, for purposes of clarity, the control is shown undeflected. Along the wing leading edge, the rounded distribution characteristic of leading-edge separation is again evident. Farther back along the wing stations, violent loading changes occur because of the unporting effect between the wing and control at the parting line which allows an interchange of pressure from the high-pressure side of the control to the low-pressure side of the wing and from the high-pressure side of the wing to the low-pressure side of the control. These abrupt loading variations occur on both the wing and control and are more pronounced at the stations immediately adjacent to the parting line and tend to fade out with distance from this line.

In figure 8 are shown typical experimental and linear-theory loadings on the tip-control configuration due to control deflection only. Loadings are shown for three typical stations at  $20^{\circ}$  deflection. In the present case, the linear theory predicts that some load will be carried on the wing behind the Mach line from the control apex. At the inboard wing station, linear theory and experiment are in fair agreement, the load being carried on only the last 20 percent of the chord. Near the parting line, the experimental variation of loading is erratic, and neither the shape nor magnitude of the loading is predicted by linear theory. As previously noted, this effect might be expected since the

linear theory does not take into account any unporting of the control. On the control itself, the upper-surface flow tends to separate from the leading edge, with the extent of the separation increasing from the control apex outboard as shown by the separation limit line on the planform view. At station 6, therefore, the flow is separated over much of the upper surface and the experimental loading does not agree with the theoretical loading. The sudden loss in loading at this station behind the 90-percent root-chord station is due to the separation of the flow from the control upper surface previously noted which precludes the expansion around the corner present on the upper surface at that station. It should be mentioned at this point that at the present time no improved theoretical methods of estimating detailed loadings comparable to that of the trailing-edge control are available for the tip-control configuration.

In figure 9 are shown the experimental and theoretical combined loadings due to an angle of attack of  $12^{\circ}$  and a control deflection of  $20^{\circ}$  for the same delta wing and tip control. For this condition, the leading-edge separation starts from the wing apex and covers a large share of the wing and most of the control. At the inboard station, the experimental and theoretical loadings due to angle of attack agree fairly well, but the experimental results indicate little effect due to control deflection. Near the parting line, the agreement over part of the chord is good; however, this agreement is fortuitous in view of the erratic behavior of the loads in this region which cause changes such as that near the trailing edge at this station. At station 6 on the control, the upper-surface flow is completely separated and the linear theory completely overestimates the loading. This overestimation of load is to be expected, inasmuch as at these high angles of inclination of the surface to the air flow, the pressures on the lower surface approach a positive limit (stagnation pressure) and the pressures on the upper surface approach absolute vacuum; therefore, the linear theory which permits the addition of the pressures due to angle of attack and the pressures due to control deflection is no longer valid. Obviously, for this type of control, considerably more analysis is required before satisfactory methods of estimating detailed loadings can be developed.

In figure 10 are shown the experimental and theoretical spanwise loadings and center-of-pressure locations for the tip control on the delta wing. The curves are presented for an angle of attack of  $6^{\circ}$  with control deflections of  $0^{\circ}$  and  $30^{\circ}$ . With the control undeflected, the linear-theory prediction of the loading is in excellent agreement with the experiment, except near the tip where there is a small loss in experimental lift. When the control is deflected, the experimental control loading is considerably less than the theoretical control loading and the spanwise variation of the loading is considerably more linear. In addition, there is little or no carryover load on the wing. This lack of experimental load carryover occurs for nearly all angles of attack and control deflection.

The linear-theory prediction of the center of pressure of the loads on the wing and control are in good agreement, both for the undeflected and the deflected control, despite the differences in loadings shown. On the basis of these experimental results and similar spanwise loadings and center-of-pressure locations at other angular conditions and for other tip-control configurations, it is possible to make fairly reasonable estimates of over-all control bending and hinge moments for tip-type controls despite the inadequacy of the linear theory.

Returning to figure 2, an examination of the various control configurations tested shows that the general conclusions concerning the loads associated with the tip control and flap control already discussed will apply to the other related controls. Ahead of the trailing-edge controls the turbulent boundary layer separates when the deflected control causes a sufficiently large pressure rise. At high control deflections, the separation of the flow from the low-pressure surface and the limiting pressures must be taken into account in any attempt to predict the loadings. Near chordwise parting lines, loadings will be erratic and carryovers negligible. The effect of trailing-edge bevel is to change the angles of control deflection at which separation at the hinge line and on the suction surface will appear. The  $13^{\circ}$  criterion will still hold.

A comparison of the spanwise loadings of trailing-edge controls on a delta and a trapezoidal wing is presented in figure 11. The angle of attack is  $6^{\circ}$ ; the control deflection is  $30^{\circ}$ . The test Mach number is 1.6. In general, the loadings on the controls on both wings are similar if allowance is made for the taper on the trapezoidal-wing control. On the delta-wing control, however, an increase in angle of attack tends to increase the loading on the outboard hinges. No such change in load distribution occurs on the control on the trapezoidal wing with increasing angle of attack except for a very small region close to the wing tip where the tip vortex begins to form. Obviously, the method previously presented for estimating detailed loadings on the delta-wing control will apply even more readily to estimations of loads on the trapezoidal wing for control deflections below the critical value. For control deflection above the critical value the only available theory (linear theory) is, of course, inadequate as indicated by figure 11.

Some of the more important loading characteristics found in tests of two-dimensional flap-type controls with overhang balance are shown in the next three figures. In figure 12 is shown a comparison of the pressure distributions and schematic diagrams of the flow over a typical control configuration with and without bevel of the wing ahead of the control. The angle of attack is  $8^{\circ}$ , the control deflection is  $8^{\circ}$ , and the test Reynolds number is  $0.8 \times 10^6$  for a Mach number of 2.41. Transition was fixed in order to assure a turbulent layer.

On the blunt trailing-edge wing, the flow follows the airfoil contours to the wing trailing edge as indicated in the upper left sketch in figure 12. Behind the trailing edge the wake is very wide and the balance or forward part of the control is immersed largely in a dead-air region. Behind the hinge line the flow generally follows the contour of the control. The experimental pressure distribution corresponding to this flow is shown as a solid line in the plot at the lower left. The theoretical pressure distribution, obtained by means of shock-expansion theory, is shown as dashed lines. Because of the complicated nature of the flow, no theoretical pressures were computed over the control ahead of the hinge line; behind the hinge line, the pressures were computed as if this part of the control were attached directly to the main wing, without forward balance, without any dead-air region, and without any surface discontinuity. A comparison of the theoretical and experimental results shows remarkably good agreement for those parts of the wing and control for which theoretical calculations were made, despite the neglect of the balancing portion of the control. The experimental load on the control balance is negligible, as is to be expected, except where the flow from the lower wing surface impinges slightly ahead of the hinge line.

On the beveled trailing-edge wing the flow does not follow the airfoil contour completely but separates from the upper wing surface ahead of the trailing edge as indicated in the upper right diagram in figure 12. This separation of the turbulent boundary layer occurs as a result of the unporting of the control leading edge. In this respect, the projecting nose of the control acts in the same manner as a spoiler. On the lower surface of the wing the flow impinges much closer to the control leading edge than for the case of the blunt wing. The corresponding theoretical and experimental pressure distributions are indicated in the plot at the lower right. On the upper wing surface behind the fifty-percent-chord station, the separated flow causes an increase in pressure, hence, a decrease in wing loading. On the balance, the pressures on the lower surface are higher and cover a wider area. Except for the separated region, theoretical and experimental pressures are again in good agreement.

In figure 13 is shown the effect of fixing transition on the chordwise loading for a typical control configuration on the blunt trailing-edge wing. The shock-expansion theory predicts the loading very well in the turbulent case, both on the wing and on the control behind the hinge line. In the laminar flow case, the loading over the rear of the wing and over the control behind the hinge line does not agree as well with the shock-expansion theory because of the separation of the laminar boundary layer from the upper surface of the wing and control. Laminar boundary layers are very susceptible to separation at supersonic speeds. In the simpler cases, laminar separation can be treated in a manner similar to that proposed earlier for the turbulent boundary layer, except

that the flow separation angles are on the order of  $1^\circ$  to  $3^\circ$  rather than approximately  $13^\circ$ .

The effect of control unporting on the blunt wing is illustrated in figure 14. The results are shown for the control with 82-percent balance with laminar boundary layer. At  $8^\circ$  control deflection the control is unported and has no effect on the loading over the wing. The control leading edge operates in a dead-air region; therefore, the balance loading is negligible. The experimental results are in good agreement with theory except behind the hinge line where laminar separation occurs on the upper control surface.

When the control is deflected to  $20^\circ$ , the leading edge unports and the flow on the upper wing surface is separated. Because the boundary layer is laminar, separation occurs as far forward as the corner at the 30-percent station. If it is assumed that the lower surface of the control balance is in a dead-air region and that the upper-surface flow attaches to the control at the leading edge and, hence, follows the control contours, then the theoretical loadings indicated herein are obtained. The experimental and theoretical loadings on the balance are in fair agreement, but the loadings on the control behind the hinge line are not. This discrepancy occurs because a small amount of flow from the upper surface through the gap tends to deflect the lower-surface flow downward so that it impinges on the control near the trailing edge.

In considering the remaining variables of the tests, mentioned in the discussion of figure 1, it may be stated that the effect of increasing the gap between the wing and control was to make the control behave more like an isolated airfoil. The effect of increasing the balance was to reduce and spread out the peak load ahead of the hinge line because of the reduction in leading-edge angle of the control. Making the control nose elliptical made the unporting effects appear at lower control deflections. Blunting the trailing edge simply changed the control angles for trailing-edge separation as discussed previously for the flap control on the delta wing.

In order to gain a little insight into some of the characteristics of spoiler loadings at supersonic speeds a two-dimensional schlieren photograph, a schematic flow diagram, and a pressure distribution are shown in figure 15. These tests were made at a Mach number of 1.93 for a Reynolds number of  $1.87 \times 10^6$ , and the condition presented is for an angle of attack of  $0^\circ$  with a 5-percent-chord height spoiler at the 70-percent-chord station. The flow over the surface may be traced by the arrows through the leading-edge shock, past the transition fix, then through the expansion around the corner. Some distance ahead of the spoiler the flow separates, causing a shock at the separation point and a dead-air region ahead of the spoiler. The flow then expands around

the spoiler and tends to follow the rear surface of the spoiler. Because of the presence of the wing, however, the flow separates and reattaches to the wing some distance behind the spoiler. In this reattachment process the flow is usually turned through two angles as indicated by the double shock.

Without the spoiler, the shock-expansion theory (dashed line) adequately estimates the pressure variation along the wing. When the spoiler is attached, the method of Donaldson and Lange (ref. 6) may be used to predict the separation point and pressure rise ahead of the spoiler as shown by the dotted line. The remaining part of the flow was calculated by a rather lengthy iteration procedure based on the flow diagram just discussed. Indications are, nevertheless, that the calculations may be reduced to a simpler flow model involving an initial separation angle of about  $13^\circ$  and an empirically determined ratio of spoiler expansion angle to initial separation angle.

In order to illustrate what might be a limiting case of the applicability of two-dimensional spoiler results to a three-dimensional wing, the results of tests of an unswept spoiler mounted on a delta wing are shown in figure 16. The spoiler height was 5 percent of the wing mean aerodynamic chord and the tests were made at a Mach number of 1.6 for a Reynolds number of  $4.2 \times 10^6$ . Pressure distributions for two stations on the wing are shown in figure 16 for an angle of attack of  $12^\circ$  with the spoilers mounted on the upper or lower surface and with no spoiler on the wing. The calculated separation pressures are based on linear-theory lifting pressures for the wing, neglect of thickness effects, and the assumption of a separation angle of  $13^\circ$ . At the inboard station the effect of the spoiler on the pressure distributions was very similar to that previously shown for the two-dimensional tests. There is a sharp pressure rise ahead of the spoiler, an essentially constant pressure to the spoiler, and then a large expansion and subsequent compression to the trailing edge. At the outboard station, the lower-surface-spoiler effect is still the same; however, the pressure rise ahead of the upper-surface spoiler is almost eliminated. It appears that, since the flow towards the tip of a delta wing tends to separate fairly easily at high angles of attack, in this case the spoiler has caused upper-surface separation from the leading edge with the resultant change in characteristics.

The spanwise variation of the pressure differential across the spoiler, or spoiler chord force, is shown in the lower right of figure 16. The variation is generally constant except at an angle of attack of  $12^\circ$  with a spoiler on the upper surface when there is a decided decrease in chord force at the outer portion of the spoiler span due to the leading-edge separation just described.

In summary, it may be said that there is available a large amount of loads data at supersonic speeds to aid in the estimation of control loads on all types of controls. Also, rapid progress is being made in improving theoretical and empirical techniques of estimating detailed or over-all loadings. As was pointed out in the discussions, nevertheless, much work yet remains to be done before the over-all problem can be considered solved.

## REFERENCES

1. Mueller, James N., and Czarnecki, K. R.: Preliminary Data at a Mach Number of 2.40 of the Characteristics of Flap-Type Controls Equipped With Plain Overhang Balances. NACA RM L52F10, 1952.
2. Mueller, James N.: Investigation of Spoilers at a Mach Number of 1.93 To Determine the Effects of Height and Chordwise Location on the Section Aerodynamic Characteristics of a Two-Dimensional Wing. NACA RM L52L31, 1953.
3. Czarnecki, K. R., and Mueller, James N.: Investigation at Mach Number 1.62 of the Pressure Distribution Over a Rectangular Wing With Symmetrical Circular-Arc Section and 30-Percent-Chord Trailing-Edge Flap. NACA RM L9J05, 1950.
4. Czarnecki, K. R., and Mueller, James N.: Investigation at Supersonic Speeds of Some of the Factors Affecting the Flow Over a Rectangular Wing With Symmetrical Circular-Arc Section and 30-Percent-Chord Trailing-Edge Flap. NACA RM L50J18, 1951.
5. Ullmann, Edward F., and Lord, Douglas R.: An Investigation of Flow Characteristics at Mach Number 4.04 Over 6- and 9-Percent-Thick Symmetrical Circular-Arc Airfoils Having 30-Percent-Chord Trailing-Edge Flaps. NACA RM L51D30, 1951.
6. Donaldson, Coleman duP., and Lange, Roy H.: Study of the Pressure Rise Across Shock Waves Required To Separate Laminar and Turbulent Boundary Layers. NACA TN 2770, 1952.

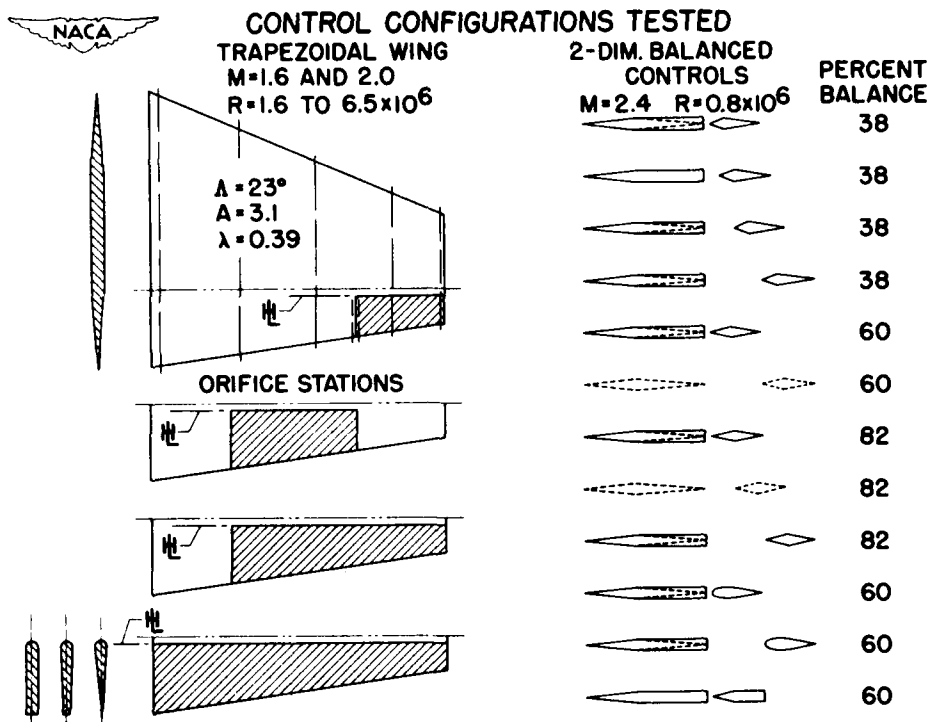


Figure 1.

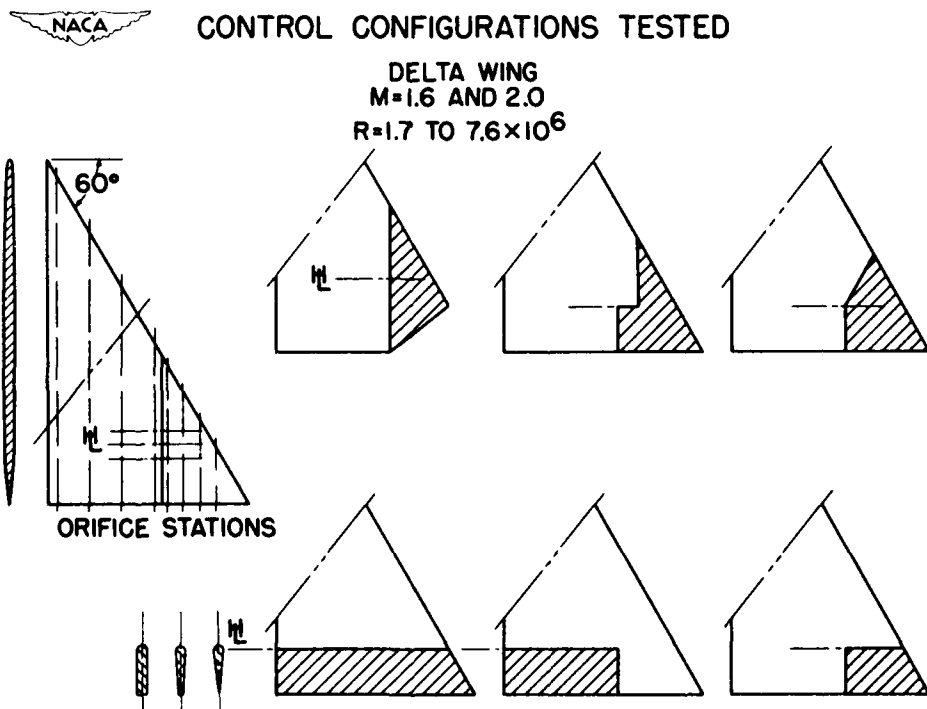


Figure 2.

CONFIDENTIAL

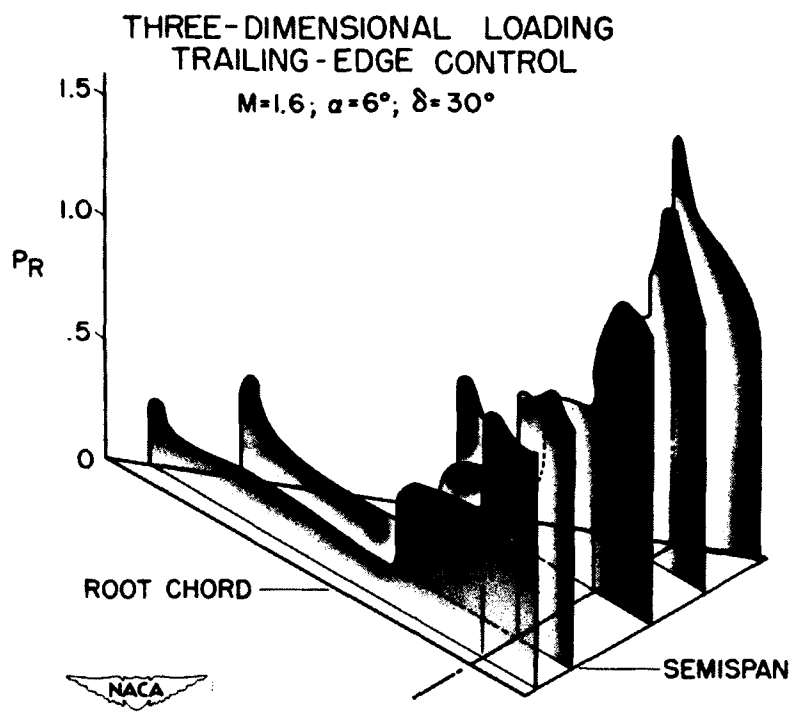


Figure 3.

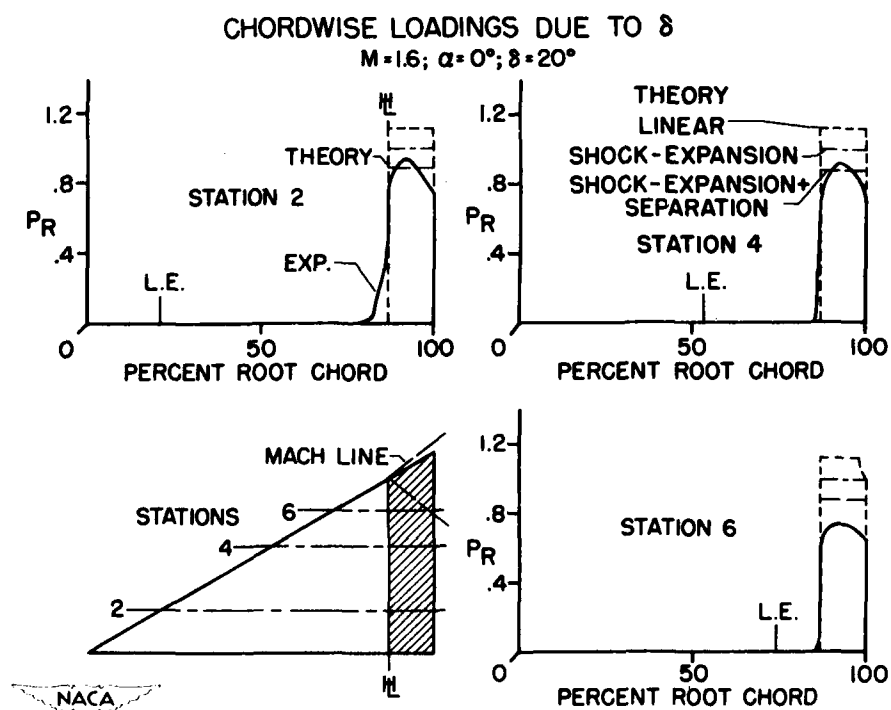


Figure 4.

CONFIDENTIAL

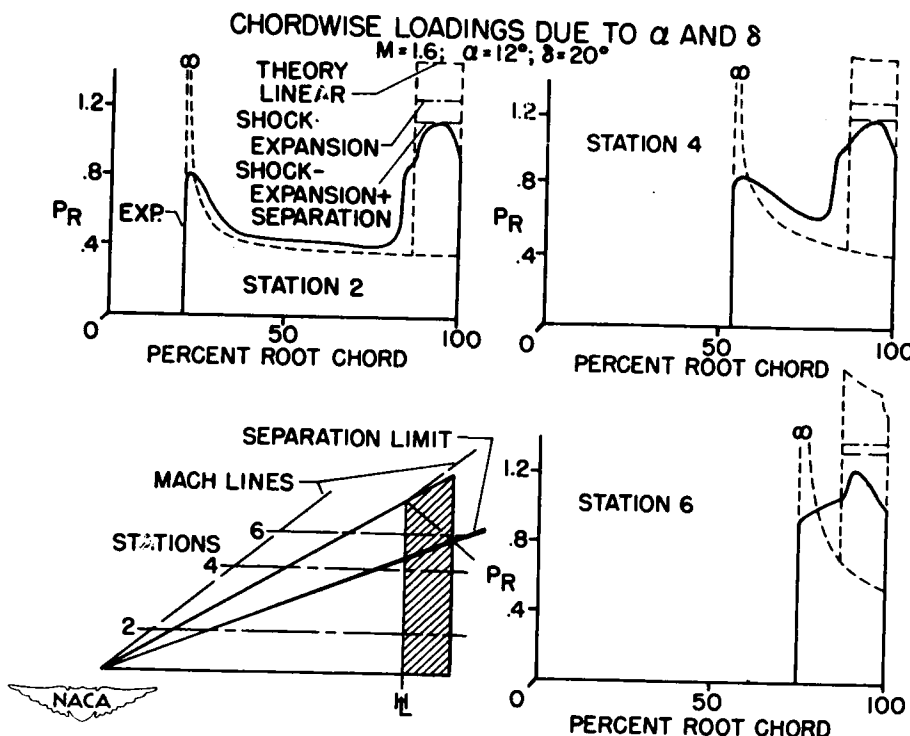


Figure 5.

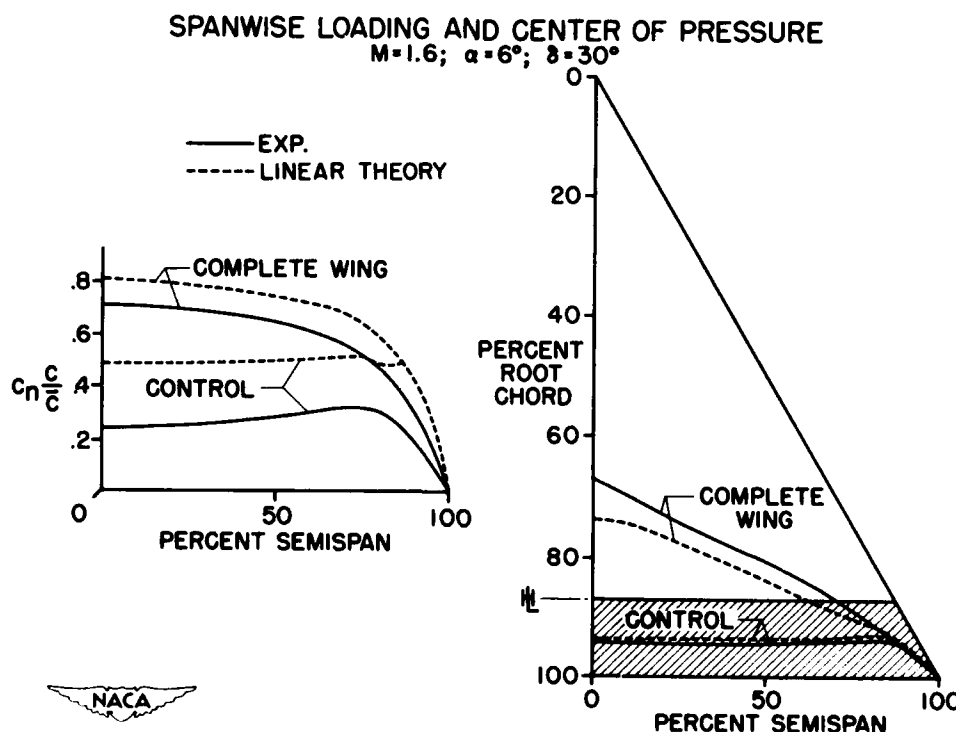


Figure 6.

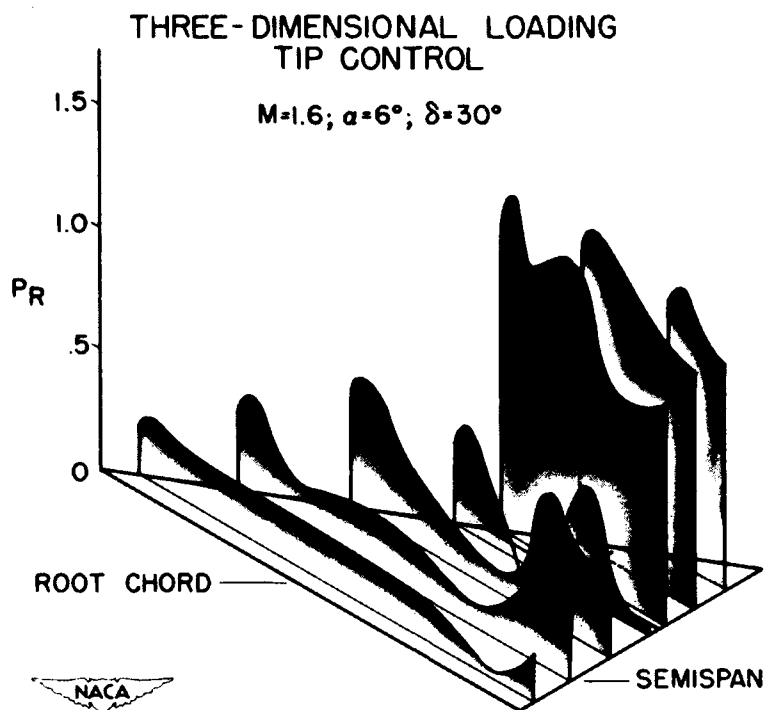


Figure 7.

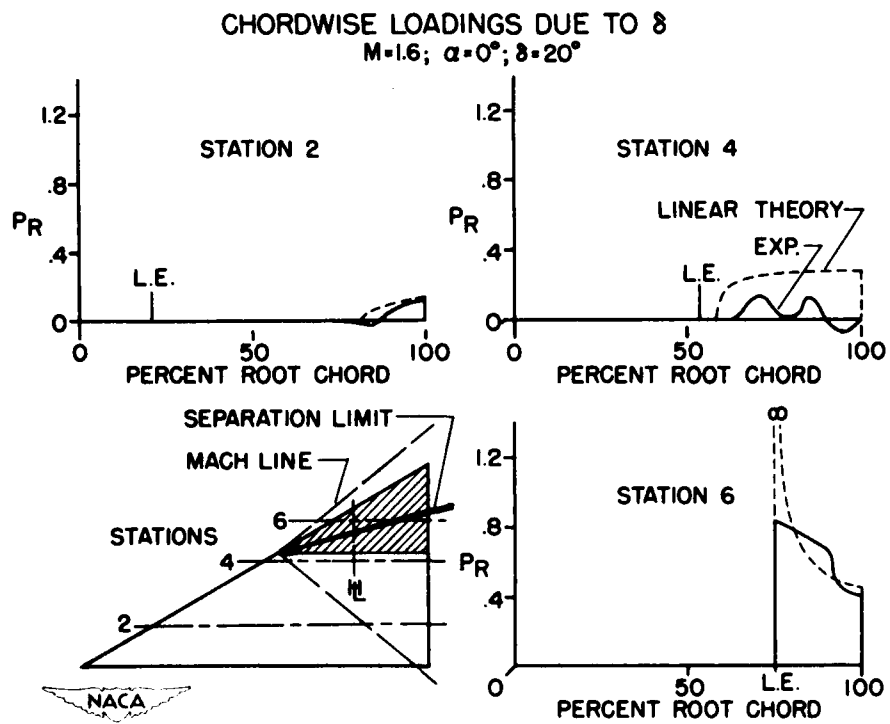


Figure 8.

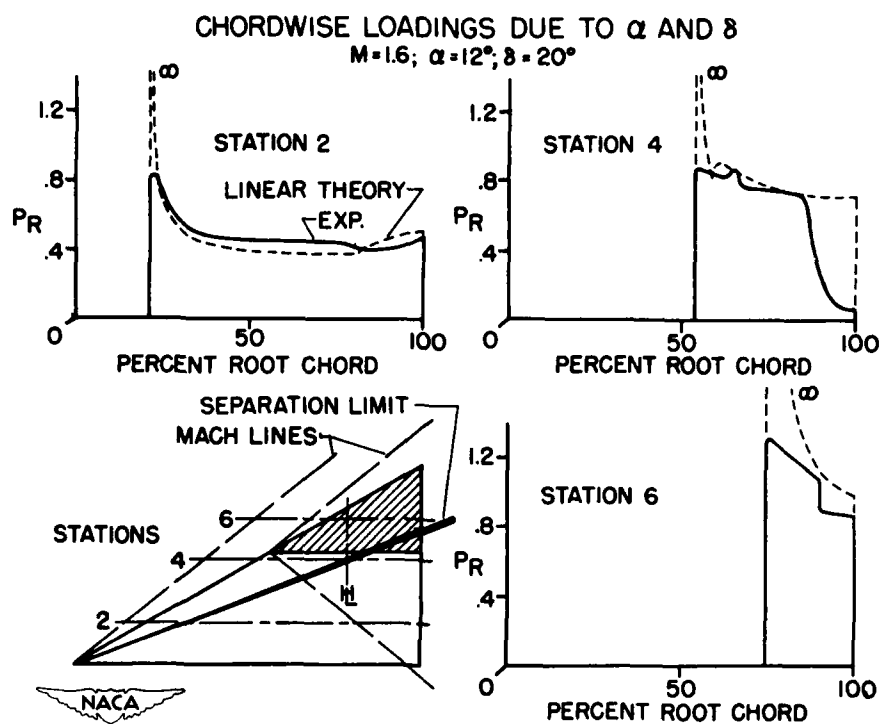


Figure 9.

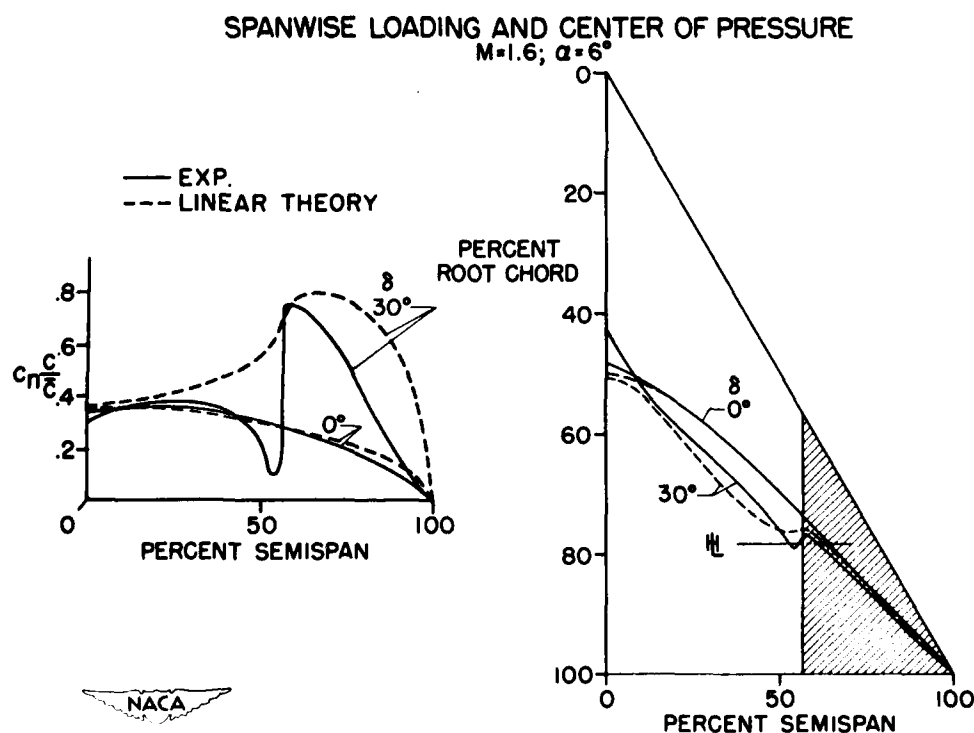


Figure 10.

NACA TRAILING-EDGE CONTROL LOADINGS

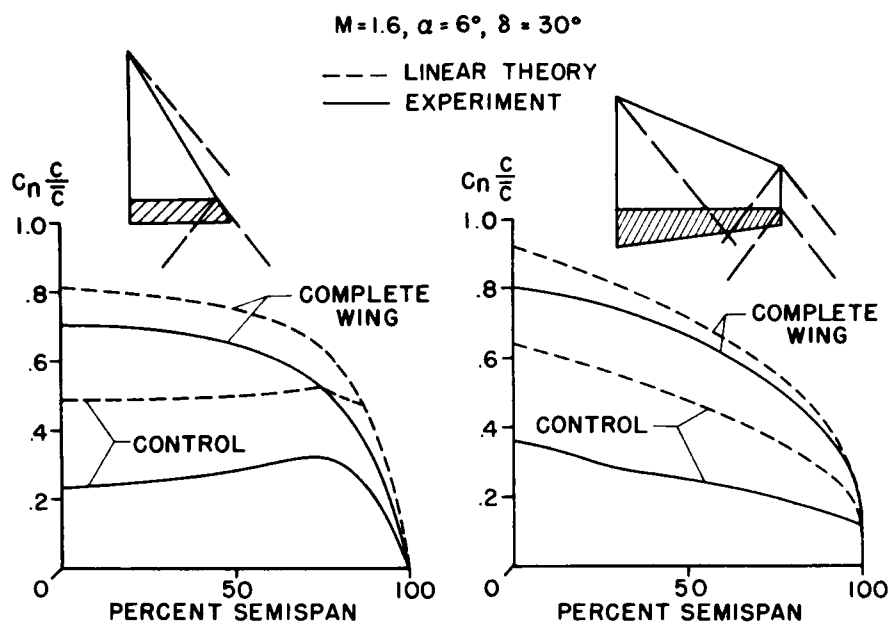


Figure 11.

FLOW CHARACTERISTICS—TWO-DIM. BALANCED CONTROL  
 $M=2.41; R=0.8 \times 10^6; \alpha=8^\circ; \delta=8^\circ$   
 38 PERCENT BALANCE; FIXED TRANSITION

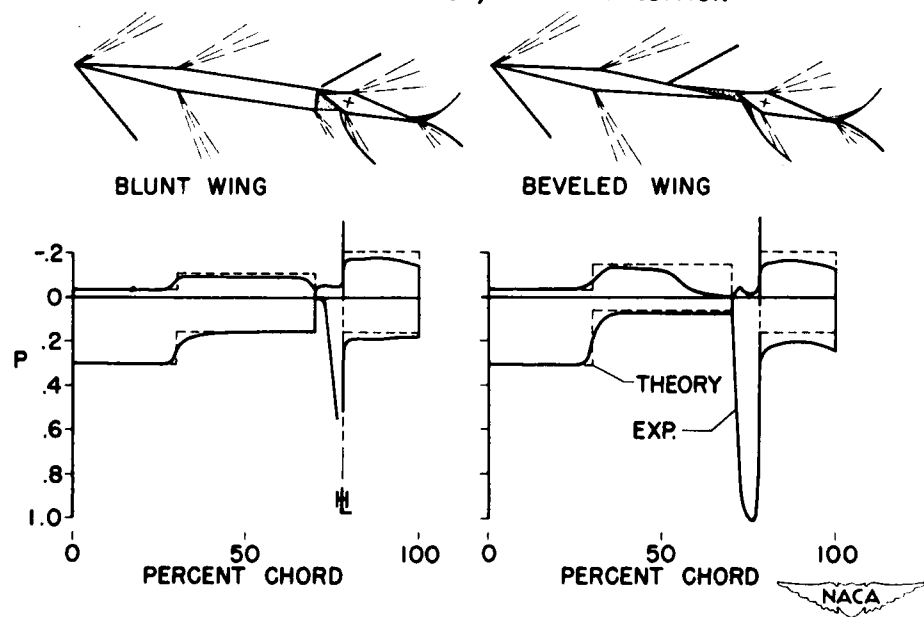


Figure 12.

## EFFECT OF FIXING TRANSITION

$M=2.41; R=0.8 \times 10^6; \alpha=8^\circ; \delta=8^\circ$   
38% BALANCE

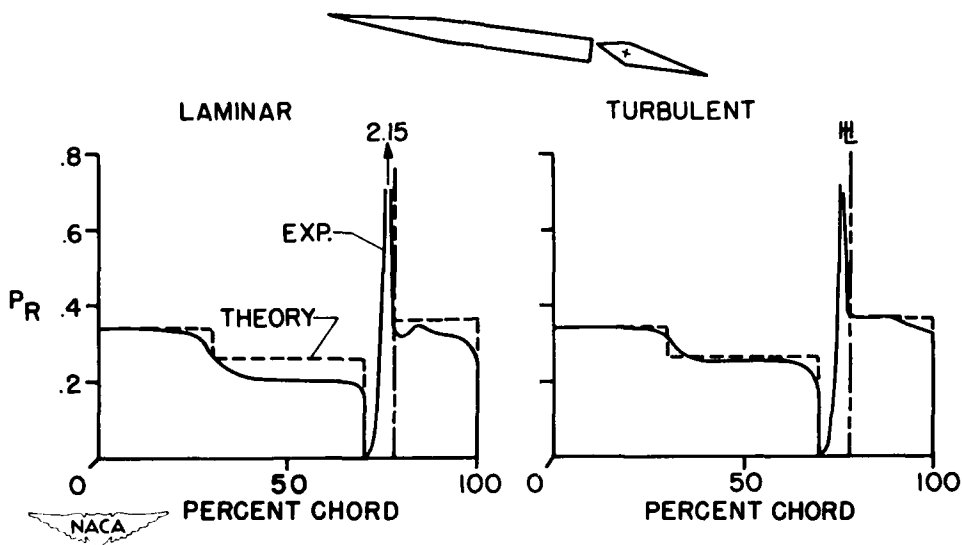


Figure 13.



## EFFECT OF UNPORTING

$M=2.41; R=0.8 \times 10^6; \alpha=2^\circ$

82% BALANCE; LAMINAR BOUNDARY LAYER

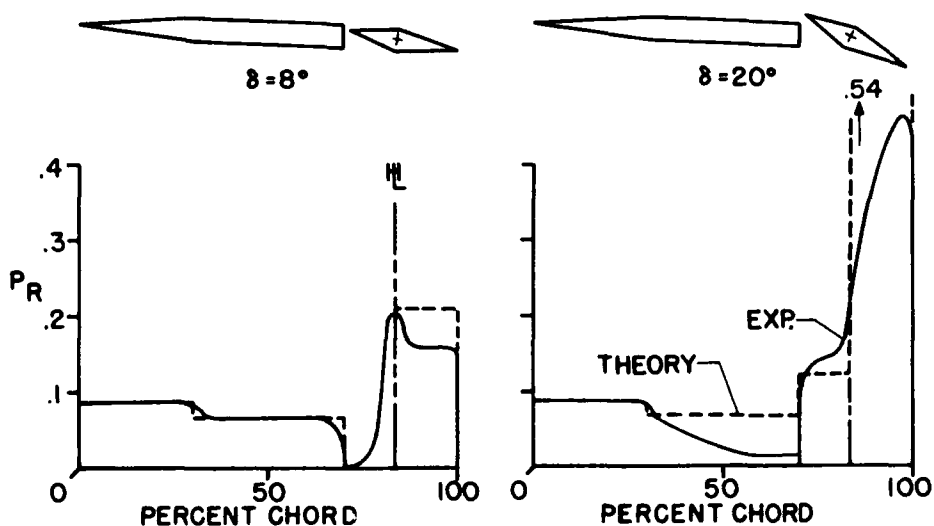


Figure 14.

CONFIDENTIAL

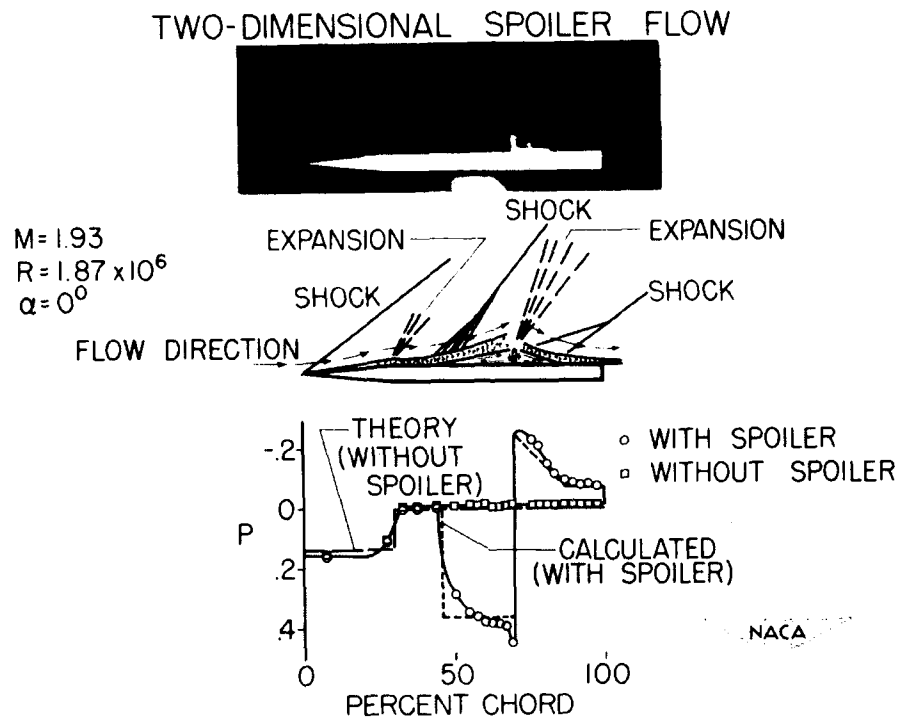


Figure 15.

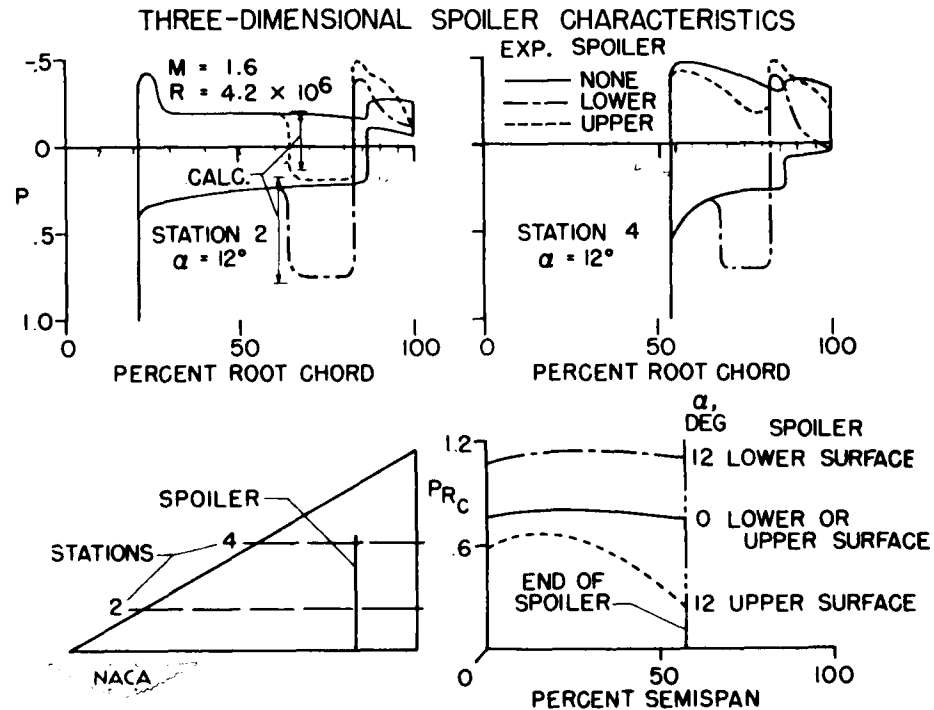


Figure 16.

CONFIDENTIAL

LOADS DUE TO FLAPS AND SPOILERS ON SWEPTBACK WINGS  
AT SUBSONIC AND TRANSONIC SPEEDS

By Alexander D. Hammond and Franklin E. West, Jr.

Langley Aeronautical Laboratory

In the past, most of the data available for showing the effect of flaps (refs. 1 to 5) and spoilers (refs. 6 and 7) on wing loads at high subsonic and transonic speeds have been obtained on moderately thick or very thick wings. This paper presents results of more recent data to show the loads, and their point of application, on thin sweptback wings which result from deflection of flaps and spoilers at high subsonic and transonic speeds. Also shown are the loads on a spoiler on a typical sweptback-wing configuration.

Figure 1 shows some chordwise pressure-distribution measurements obtained in the Langley high-speed 7- by 10-foot tunnel at the midsemispan station of a semispan model (refs. 8 and 9). The wing had  $35^{\circ}$  sweepback of the quarter-chord line, an aspect ratio of 4.0, a taper ratio of 0.6, and an NACA 65A006 airfoil section parallel to the plane of symmetry. The pressure distributions show how the resultant pressure  $\Delta P_R$  caused by the projection of a plug-type spoiler (that is, a spoiler with a slot through the wing behind the spoiler when the spoiler is deflected) and the deflection of a 20-percent-chord flap is distributed across the wing chord. The results are for a spoiler projection of  $0.04c$  and a flap deflection  $\delta$  of  $15^{\circ}$ . These distributions are shown for angles of attack  $\alpha$  of  $0^{\circ}$  and  $16^{\circ}$  at Mach numbers of 0.60 and 0.90. It is evident from the pressure distributions at a Mach number of 0.60 that the center of pressure is farther forward for the spoiler than for the flap, since the loading on the flap is large, whereas the loading on the wing behind the spoiler is small. As the Mach number is increased from 0.60 to 0.90, the center of pressure of the flap moves rearward as does the center of pressure for the spoiler. At the large angles of attack at either Mach number, the gap behind this deflected spoiler is not sufficient to produce much control effectiveness and there is little change in center-of-pressure location. The center of pressure moves rearward, however, with increase in angle of attack for either positive or negative flap deflection at both Mach numbers.

This relationship between the longitudinal center of pressure of the additional load resulting from spoiler and flap deflection has also been obtained, for the symmetrical-loading case, from force-data results on semispan wings equipped with these controls. Figure 2 shows the span and spanwise locations of flap and spoiler configurations that were investigated at transonic speeds on a small-scale semispan model in the Langley

high-speed 7- by 10-foot tunnel. The model had the quarter chord swept-back  $45^\circ$ , an aspect ratio of 4.0, a taper ratio of 0.6, and an NAC. 65A006 airfoil section parallel to the plane of symmetry. In the upper half of the figure are shown several span outboard flaps (flaps starting at the wing tip and extending inboard) and one inboard flap (a flap starting at the inboard end of the wing and extending outboard). The flap configurations were tested utilizing the transonic-bump method (ref. 10). In the lower half of the figure are shown several span inboard spoilers that were tested on a small reflection plane (results are as yet unpublished).

Figure 3 shows a typical example at a Mach number of 0.60 of the results that can be obtained from semispan tests and shows the loci of the centers of additional load resulting from deflection of the spoilers and flaps at near  $0^\circ$  angle of attack. The symbols shown below the configurations of figure 2 were plotted on the  $45^\circ$  sweptback-wing plan form at the location of the centers of additional load for the corresponding configurations. These locations of the centers of additional load hold for deflections of the 30-percent-chord flaps through a range of  $\pm 20^\circ$ . The spoilers located along the 70-percent-chord line were projected 10 percent of the local chord. Although appreciable differences exist in the lateral positions of the centers of additional load resulting from deflection of the various span spoilers and flaps, there is very little effect of control span on the chordwise position of the centers of additional load. The centers of additional load resulting from projection of the various span spoilers fall approximately along the 34-percent-chord line and are farther forward than the centers of additional load resulting from deflection of the various span flaps which fall approximately along the 48-percent-chord line.

Figure 4 shows that the variation at low angles of attack of these common chord lines  $\frac{\Delta x_{cp}}{c}$  with Mach number for a series of model configurations which differ only in wing sweep from the flap configurations shown in figure 2. Data for the flap configurations having sweep angles of  $0^\circ$ ,  $35^\circ$ , and  $60^\circ$  were obtained from the results published in references 11, 12, and 13, respectively. The results shown for the  $45^\circ$  swept wing were obtained from the same investigations as the data presented in figure 3 (ref. 10 and unpublished data). The results show that, as the Mach number is increased, the centers of additional load resulting from deflection of the flaps move rearward and, at the highest Mach number, lie along the 80- to 90-percent-chord lines. There seems to be only a small effect of wing sweep on this movement, except that the rearward movement is delayed to a higher Mach number for the swept wings. The curve for inboard spoilers on the  $45^\circ$  swept wing shows that there is considerably less movement of the longitudinal center of additional load with increase in Mach number than there is for the flaps; in fact, there is a slight forward movement at Mach numbers above 0.90.

Figure 5 shows the variation of the lateral center of additional load  $\frac{\Delta y_{cp}}{b/2}$  (which is measured from the plane of symmetry and expressed as a fraction of the wing semispan) with control span for the outboard flaps (that is, flaps starting at the wing tip and extending inboard) on the wings referred to in the discussion of figure 4. The results are shown for Mach numbers of 0.60 and 1.10. At a Mach number of 0.60 the lateral center of additional load resulting from flap deflection moves inboard with increase in flap span. This variation is greater for the swept wings than for the unswept wing. Also, the center of additional load resulting from flap deflection is farther outboard for the small span controls on the swept wings than on the unswept wing; however, as the Mach number is increased to 1.10, the center of additional load resulting from flap deflection moves inboard with increase in flap span at about the same rate for all the wings. There is, in general, a

nearly linear variation of the lateral center of additional load  $\frac{\Delta y_{cp}}{b/2}$

resulting from flap deflection with increase in Mach number between 0.60 and 1.10 for all flap configurations investigated. This variation is illustrated in figure 6 for 43-percent-semispan flap-type controls on the  $45^\circ$  sweptback wing; however, the outward shift of the lateral center of additional load with increase in Mach number may not be as shown for other span controls on other swept wings, although the variation is nearly linear for the other configurations. The curve for the inboard 43-percent-semispan spoilers also shows a nearly linear variation of the lateral center of additional load with increase in Mach number and, in general, shows the same trend as the inboard flap-type controls on the  $45^\circ$  swept wing.

In figure 7 is shown the theoretical and experimental variation of the lateral center of additional load  $\frac{\Delta y_{cp}}{b/2}$  resulting from control deflection with control span at a Mach number of 0.60 on the  $45^\circ$  swept-wing configurations of figure 2. The theoretical variation of the lateral center of additional load is shown for symmetrically deflected outboard and inboard flaps. This variation was obtained from theoretical control loadings by the method outlined in reference 14 and by assuming an increase in angle of attack of 1 radian over the flapped portion of the semispan. The symbols represent the experimental points for the control configurations of figure 2. There is good agreement between the experimental and theoretical values for the flap-type controls. Similar agreement can be obtained for flap-type controls on wings of other sweeps and, hence, in the low angle-of-attack range, the variation of the lateral center of load resulting from flap deflection with control span can be estimated for Mach numbers up to at least 0.60.

As the span of the inboard spoilers is increased, the lateral center of load moves outboard and, in general, is slightly outboard of the theoretical curve for the flap for most spoiler spans. This fact indicates that, although the magnitude of the lateral center of additional load may not be predicted from the flap theory, the trend of the variation of the center of additional load with span for inboard spoilers is similar to the trend shown for inboard flaps.

Thus far, the centers of additional load at small angles of attack have been discussed. Figure 8 shows the variation of the longitudinal

$\frac{\Delta x_{cp}}{c}$  and lateral  $\frac{\Delta y_{cp}}{b/2}$  locations of the centers of additional load

resulting from spoiler projection on a  $45^\circ$  swept wing with angle of attack. The longitudinal positions of the center of additional load

$\frac{\Delta x_{cp}}{c}$  were measured from the wing leading edge and are expressed as a fraction of the local wing chord  $c$  at the lateral positions of the

center of additional load  $\frac{\Delta y_{cp}}{b/2}$ . The values of  $\frac{\Delta y_{cp}}{b/2}$  were measured from

the fuselage center line and expressed as fractions of the wing semispan  $b/2$ . These data were recently obtained from integrated pressure distributions at seven spanwise stations on a sting-supported model in the Langley 16-foot transonic tunnel.

The  $45^\circ$  swept wing is similar to that shown in figure 2; however, the Reynolds number based on the wing mean aerodynamic chord was about  $6 \times 10^6$  at a Mach number of 1.0 for this model and only about  $0.75 \times 10^6$  at this Mach number for the model of figure 2. The spoiler was of the plug type and was projected to a height of 4 percent of the local wing chord. It was located along the 70-percent-chord line and extended from the wing-fuselage junction ( $0.14b/2$ ) to the 87-percent-semispan station.

The variation of the longitudinal centers of additional load  $\frac{\Delta x_{cp}}{c}$  shows a rather irregular behavior with angle of attack at Mach numbers of 0.60 and 0.98. The lateral centers of additional load show an inboard movement above angles of attack of approximately  $10^\circ$  for both Mach numbers which indicates that the largest additional bending moments will occur in the low angle-of-attack range. The irregular trends of the longitudinal centers of additional load and the inboard movement of the lateral centers of additional load are caused by flow separation over the outboard wing sections at the higher angles of attack.

The weighted spanwise loading parameters at a Mach number of 0.98 associated with the centers of additional load in figure 8 are shown in figure 9. The variations of the weighted section normal force  $\Delta c_{nc}/c$

and the weighted section pitching moment  $\Delta c_{m_c}/4(c/c)^2$  across the semispan are shown for several angles of attack. The vertical dashed line shown in figure 9 represents the spanwise location of the fuselage maximum diameter. Irregular trends of the section pitching-moment parameter with angle of attack are shown here with increase in angle of attack. Also shown is a loss in effectiveness of the control on the outboard sections of the wing at  $16^\circ$  angle of attack which results from flow separation over the outboard wing sections. This loss of effectiveness causes the inboard shift in the lateral center of additional load and results in small section pitching moments over the outboard wing sections. The results shown are for one spoiler configuration on a  $45^\circ$  swept wing and may not be typical of the variation of the load distributions on other plan forms. For example, had leading-edge devices designed to improve the flow over the wing been employed in conjunction with the spoiler on this wing, or had the spoiler configuration been improved so as to increase the effectiveness of the control over the separated-flow region of the wing, the trends of the variation of the centers of additional load and of the span loadings with angle of attack would not be expected to be as shown. The load distributions and centers of additional load vary considerably depending on both the spoiler effectiveness and on the flow-separation phenomenon associated with the wing plan form.

Loadings for the plug-type spoiler, which is described in the discussion of figures 8 and 9, are presented in figures 10 and 11. Figure 10 shows how the pressure coefficients  $P$  are distributed over the front and rear faces of the plug-type spoiler (shown by the dashed curve) at three spanwise stations for a Mach number of 0.98 and angles of attack of  $0^\circ$  and  $16^\circ$ . The solid curve shows the distributions over the front and rear faces of the same spoiler without a gap through the wing. These pressure distributions were measured over the front and rear faces of the spoiler by using pressure orifices distributed from the wing surface to the top of the spoiler at several spanwise stations. The pressure distributions shown are typical of those obtained at other angles of attack and Mach numbers and show that both with and without a gap through the wing behind the spoiler the loading is generally rectangular and the pressure coefficients are generally more positive over the front face of the spoiler than the rear face. The results also show that the loading is generally less for the plug-type spoiler than for the spoiler without a gap. Figure 11 shows how the resultant spoiler normal-force coefficient  $C_{N_s}$  varies with angle of attack at Mach numbers of 0.60 and 0.98 and how the lateral center of pressure  $\frac{y_{cp}}{b/2}$  varies with angle of attack at a Mach number of 0.98. The solid curves of figure 11 were obtained by integrating pressure distributions similar to those shown in figure 10. Also shown as a dashed line connecting the circle symbols are the estimated values of the spoiler normal force and lateral

center of pressure obtained by assuming a rectangular load over the spoilers equal to the difference between the wing pressures measured immediately ahead of and behind the spoiler. These curves show fair agreement with the measured values and show that the spoiler loads may be estimated if the wing pressures ahead of and behind the spoiler are known.

The results show that there is a decrease in spoiler normal-force coefficient and an inboard movement of the lateral center of pressure with increase in angle of attack as is indicated by the pressure distributions of figure 10 for the outboard stations at  $16^{\circ}$  angle of attack.

In conclusion, the results show that the centers of pressure of the additional loads resulting from spoiler-type controls are, in general, farther forward than the centers of pressure of the flap-type controls. The centers of additional load, resulting from deflection of flap-type controls, may be estimated at subsonic speeds in the low angle-of-attack range by existing theory. The variation of the centers of additional loads resulting from control deflections with angle of attack and Mach number through the transonic speed range may be obtained either from pressure distributions or force-data results from semispan investigations of the controls. Spoiler loads may be estimated if the wing pressures immediately ahead of and behind the spoiler controls are known.

## REFERENCES

1. Luoma, Arvo A.: An Investigation of a High-Aspect-Ratio Wing Having 0.20-Chord Plain Ailerons in the Langley 8-Foot High-Speed Tunnel. NACA RM L6H28d, 1946.
2. Luoma, Arvo A., Bielat, Ralph P., and Whitcomb, Richard T.: High-Speed Wing-Tunnel Investigation of the Lateral-Control Characteristics of Plain Ailerons on a Wing With Various Amounts of Sweep. NACA RM L7I15, 1947.
3. Whitcomb, Richard T.: A Compilation of the Pressures Measured on a Wing and Aileron With Various Amounts of Sweep in the Langley 8-Foot High-Speed Tunnel. NACA RM L8A30a, 1948.
4. Krumm, Walter J.: Pressure Coefficients at Mach Numbers From 0.60 to 0.85 for a Semispan Wing With NACA 0012-64 Section, 20-Percent-Chord Plain Aileron, and 0° and 45° Sweepback. NACA RM A50B13, 1950.
5. Krumm, Walter J., and Cleary, Joseph W.: High-Speed Aerodynamic Characteristics of a Lateral-Control Model. III-Section Characteristics, Fence Studies, and Tabulated Pressure Coefficients With Modified NACA 0012-64 Section, 26.6-Percent-Chord, Plain Aileron, 0° and 45° Sweepback. NACA RM A50H17, 1950.
6. Laitone, Edmund V.: An Investigation of the High-Speed Lateral-Control Characteristics of a Spoiler. NACA ACR 4C23, 1944.
7. Luoma, Arvo A.: An Investigation of the Lateral-Control Characteristics of Spoilers on a High-Aspect-Ratio Wing of NACA 65-210 Section in the Langley 8-Foot High-Speed Tunnel. NACA RM L7D21, 1947.
8. Hammond, Alexander D., and McMullan, Barbara M.: Chordwise Pressure Distribution at High Subsonic Speeds Near Midsemispan of a Tapered 35° Sweptback Wing of Aspect Ratio 4 Having NACA 65A006 Airfoil Sections and Equipped With Various Spoiler Ailerons. NACA RM L52C28, 1952.
9. Hammond, Alexander D., and Keffer, Barbara M.: The Effect at High Subsonic Speeds of a Flap-Type Aileron on the Chordwise Pressure Distribution Near Midsemispan of a Tapered 35° Sweptback Wing of Aspect Ratio 4 Having NACA 65A006 Airfoil Section. NACA RM L53C23, 1953.

10. Vogler, Raymond D.: Lateral-Control Investigation of Flap-Type Controls on a Wing With Quarter-Chord Line Swept Back  $45^\circ$ , Aspect Ratio 4, Taper Ratio 0.6, and NACA 65A006 Airfoil Section. Transonic-Bump Method. NACA RM L9F29a, 1949.
11. Hammond, Alexander D.: Lateral-Control Investigation of Flap-Type Controls on a Wing With Unswept Quarter-Chord Line, Aspect Ratio 4, Taper Ratio 0.6, and NACA 65A006 Airfoil Section. Transonic-Bump Method. NACA RM L50A03, 1950.
12. Thompson, Robert F.: Lateral-Control Investigation of Flap-Type Controls on a Wing With Quarter-Chord Line Swept Back  $35^\circ$ , Aspect Ratio 4, Taper Ratio 0.6, and NACA 65A006 Airfoil Section. Transonic-Bump Method. NACA RM L9L12a, 1950.
13. Vogler, Raymond D.: Lateral-Control Investigation of Flap-Type Controls on a Wing With Quarter-Chord Line Swept Back  $60^\circ$ , Aspect Ratio 4, Taper Ratio 0.6, and NACA 65A006 Airfoil Section. Transonic-Bump Method. NACA RM L50A17, 1950.
14. Campbell, George S.: A Finite-Step Method for the Calculation of Span Loadings of Unusual Plan Forms. NACA RM L50L13, 1951.

## CHORDWISE PRESSURE DISTRIBUTION

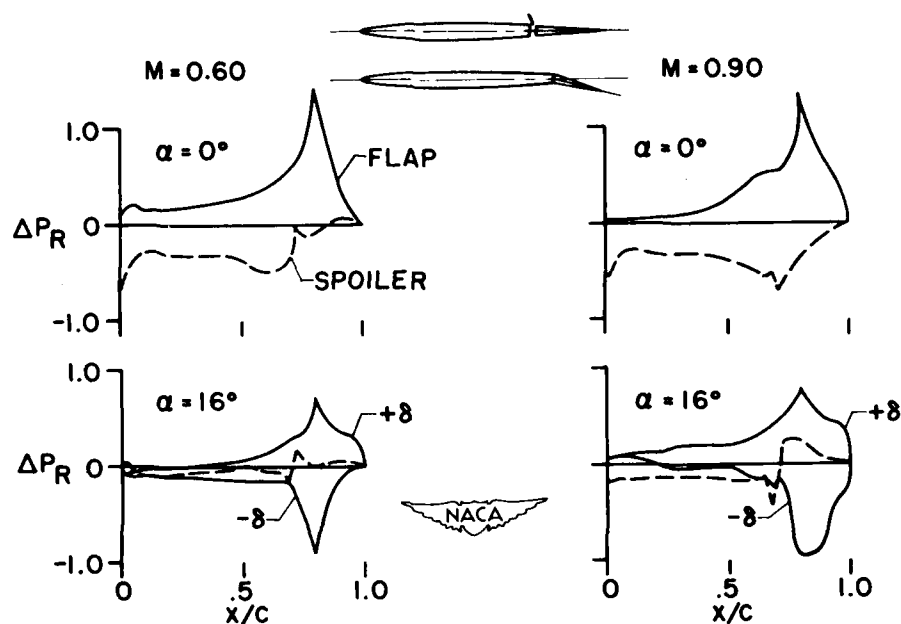


Figure 1.

## CONTROL CONFIGURATIONS

45° SWEPT WING

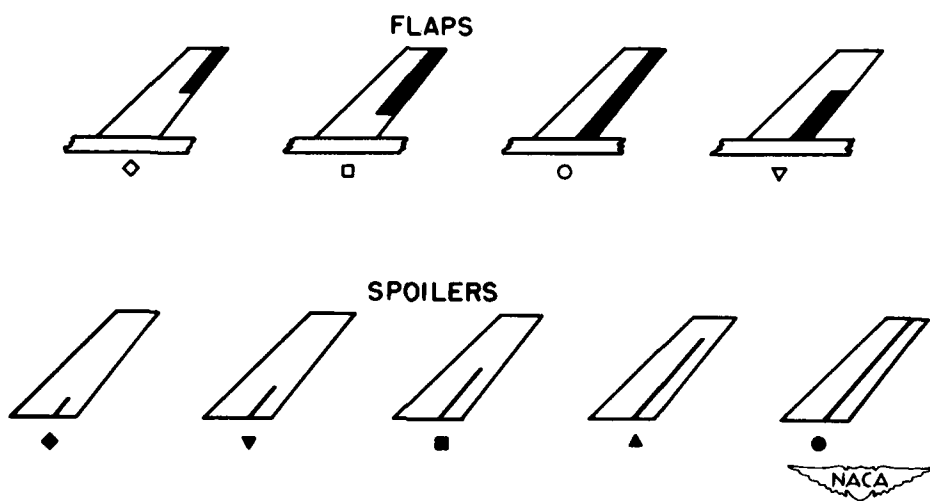


Figure 2.

CONFIDENTIAL

TYPICAL LOCI OF CENTERS OF ADDITIONAL LOAD  
DUE TO SPOILERS AND FLAPS

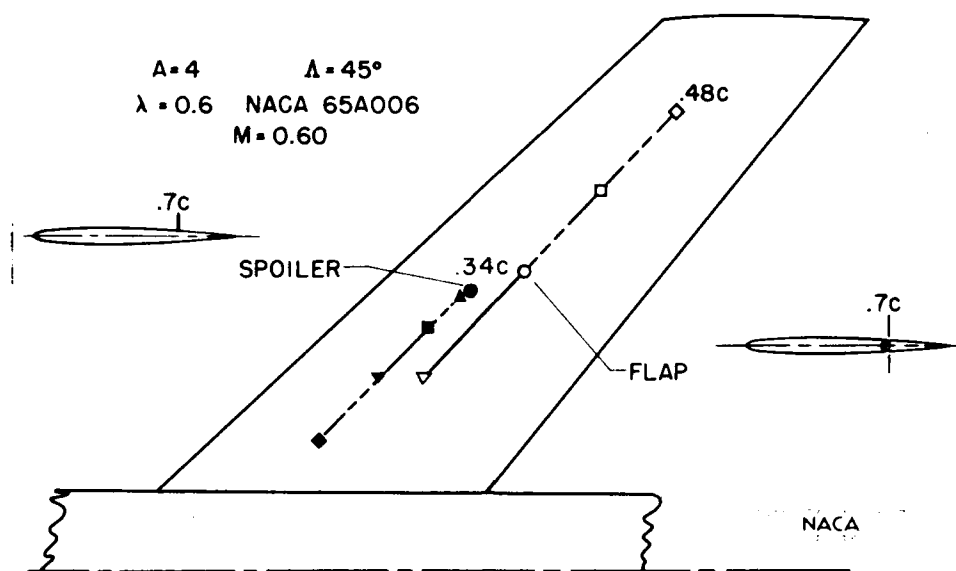


Figure 3.

CHORDWISE CENTERS OF ADDITIONAL LOAD DUE TO  
SPOILERS AND FLAPS

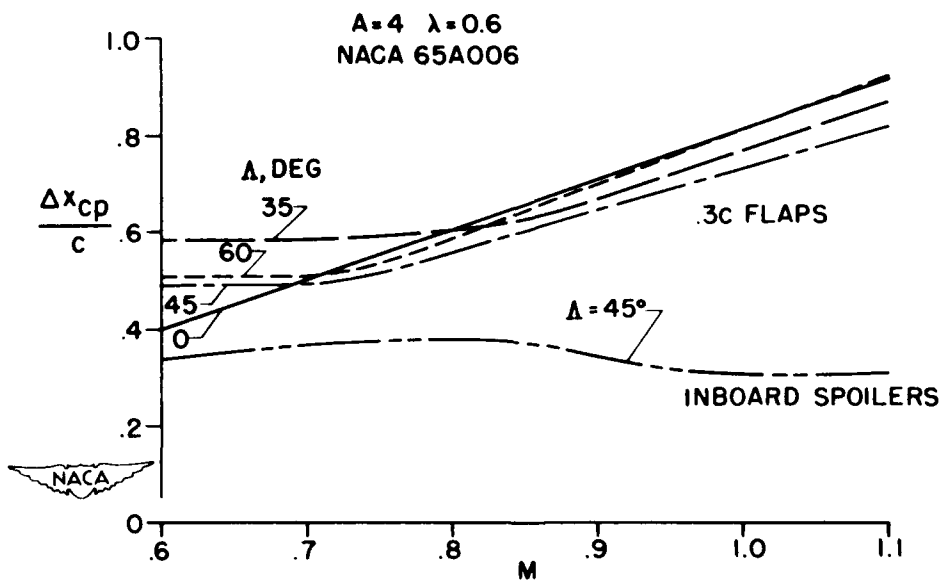


Figure 4.

CONFIDENTIAL

LATERAL CENTERS OF ADDITIONAL LOAD  
DUE TO OUTBOARD FLAPS

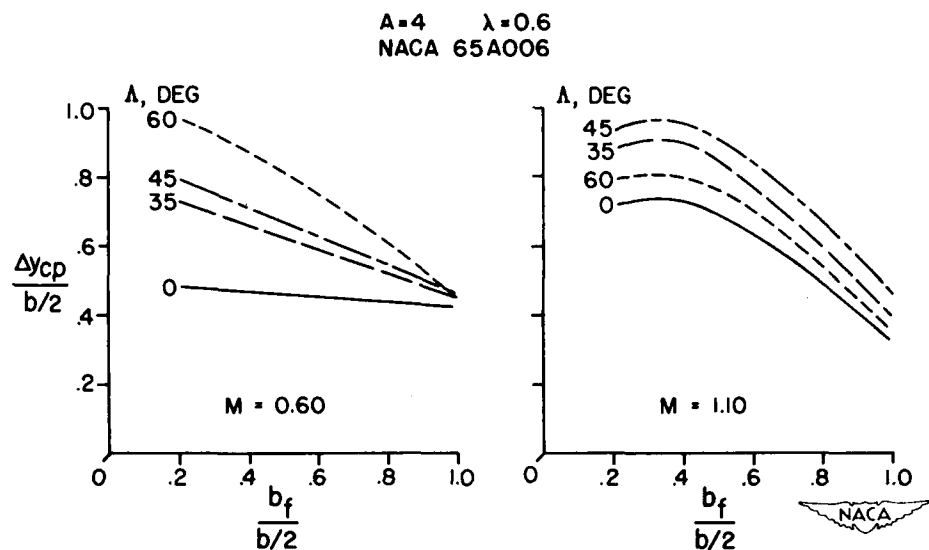


Figure 5.

LATERAL CENTER OF ADDITIONAL LOAD  
EFFECT OF MACH NUMBER

$A = 4$ ;  $A = 45^\circ$ ; CONTROL SPAN,  $0.43 b/2$

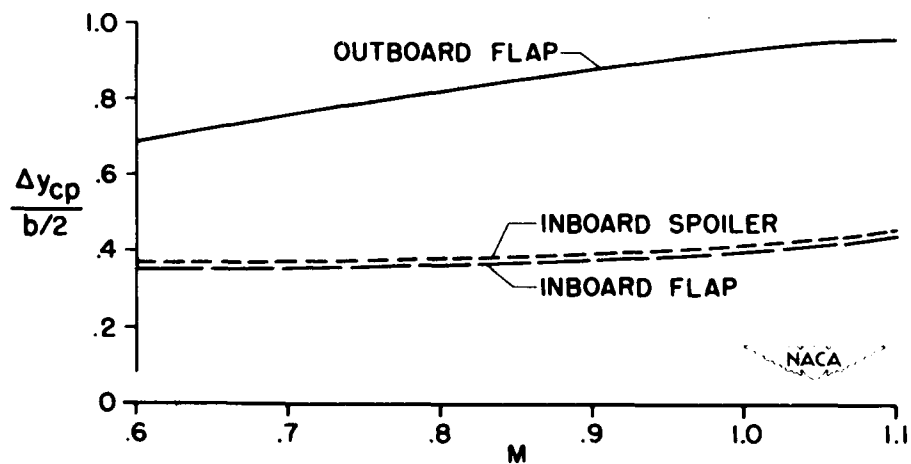


Figure 6.

CONFIDENTIAL

LATERAL CENTER OF ADDITIONAL LOAD  
EFFECT OF CONTROL SPAN

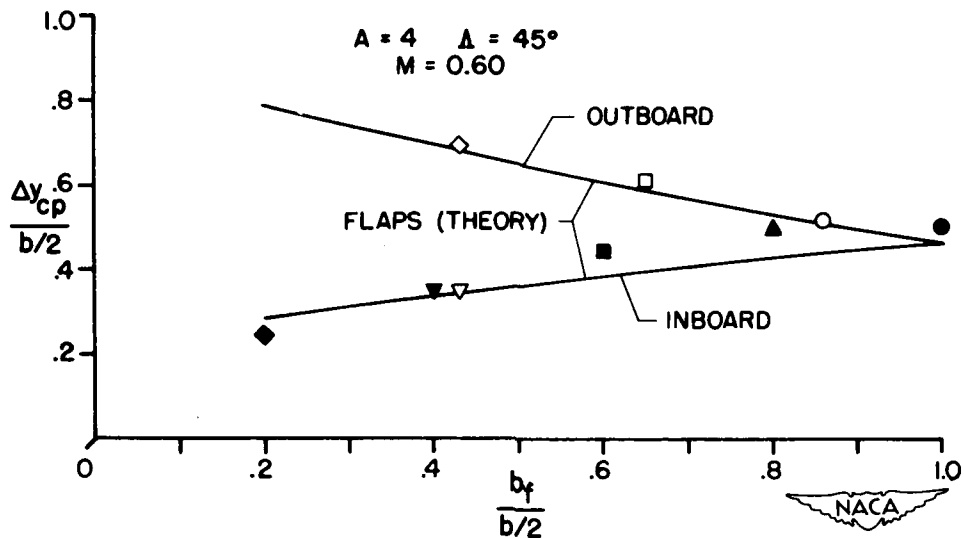


Figure 7.

CENTER OF ADDITIONAL LOAD  
DUE TO SPOILER

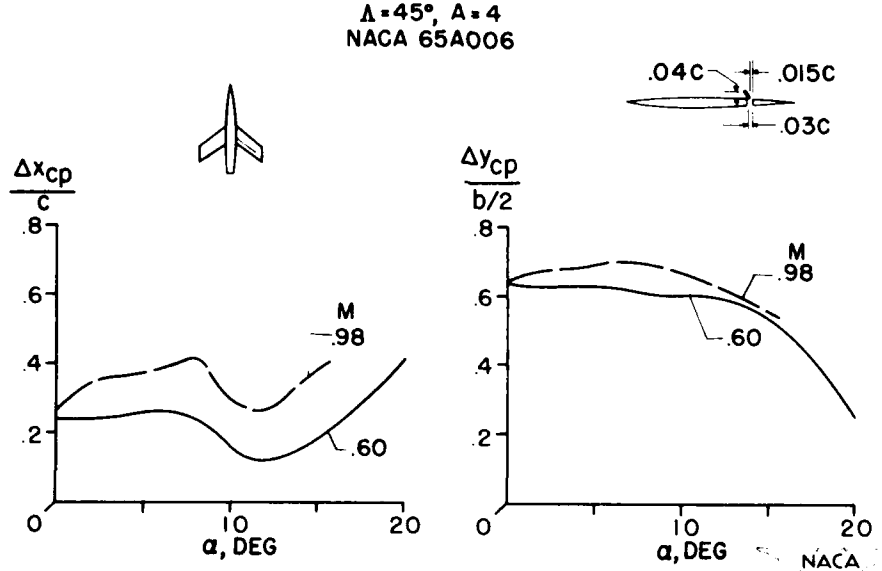


Figure 8.

CONFIDENTIAL

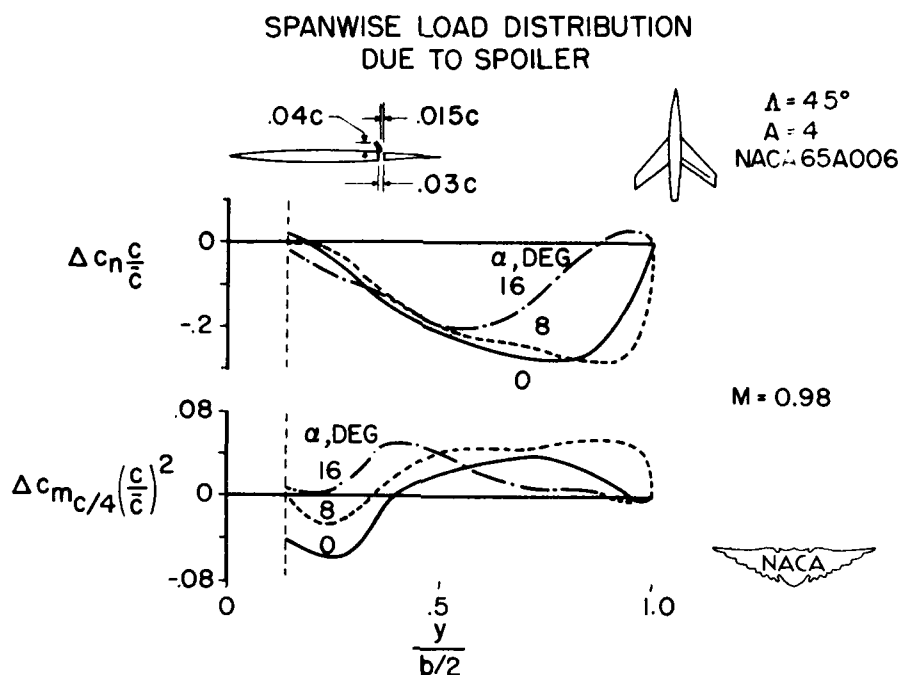


Figure 9.

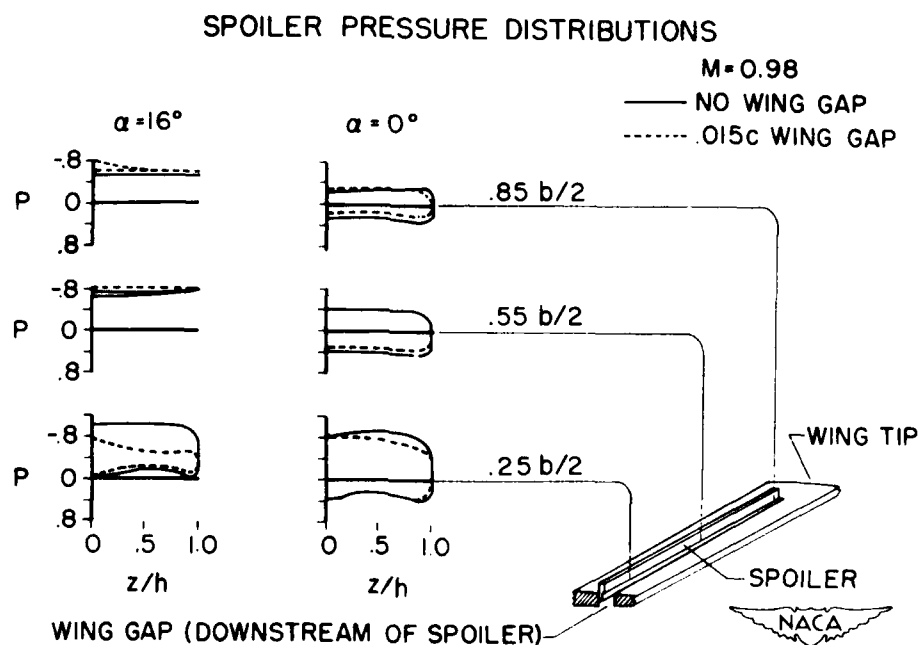


Figure 10.

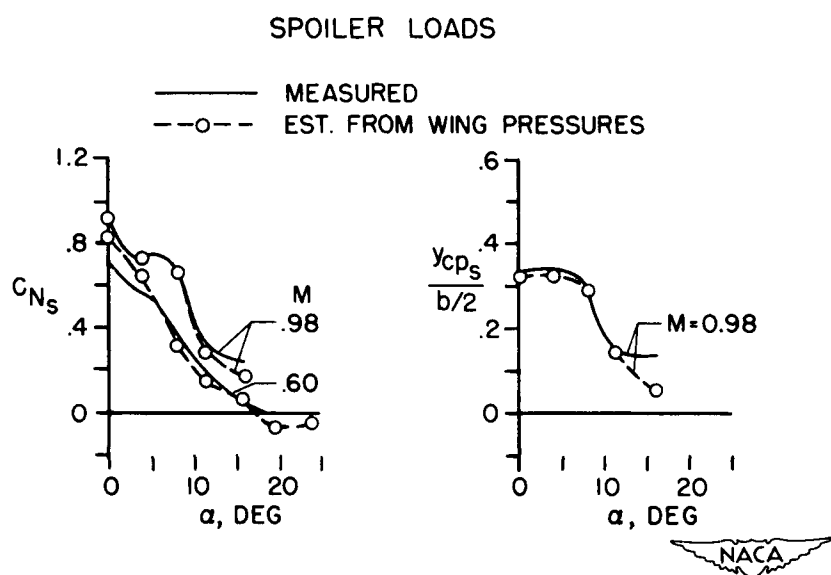


Figure 11.

CONFIDENTIAL

167

## TAIL LOADS

CONFIDENTIAL

## SOME MEASUREMENTS OF TAIL LOADS IN FLIGHT AT HIGH SPEEDS

By John T. Rogers, George E. Cothren, and Richard D. Banner

NACA High-Speed Flight Research Station

As a part of the research airplanes program, flight investigations are under way to determine the horizontal-tail loads for the Bell X-5 and the Douglas D-558-II airplanes for the lift and speed ranges of which the airplanes are capable. It is the purpose of this paper to present some of the results of the measurements thus far obtained from these airplanes. The plan form and side views of the test airplanes are shown in figure 1. The Bell X-1 airplane is also shown since loads information previously obtained from that airplane will be presented where pertinent. It may be noted that the X-1 airplane has a wing sweep angle near  $0^\circ$  and a horizontal tail that, in relation to the wing, is relatively high. The D-558-II airplane having a  $35^\circ$  swept wing and a high horizontal tail is shown in the center of the figure. The X-5 airplane, with the horizontal tail approximately in line with the wing, is shown with the wings positioned at  $45^\circ$  and  $59^\circ$  sweep, the sweep angles for which the loads data were measured. It may be pointed out that the wing translates forward for an increasing sweep angle. All the airplanes are shown to the same scale. The wing thickness ratios are in the thickness range of 8 to 10 percent and the tail thickness ratios are in the range of 6 to 10 percent.

The horizontal-tail loads to be presented were measured by means of strain gages installed at the tail root stations. The measured loads have been corrected for the structural inertia of the tail and the measured angular pitching accelerations and are, therefore, the balancing aerodynamic loads.

Measured tail loads are presented in figure 2 for selected Mach numbers as a variation with airplane normal-force coefficient. The tail loads are presented in coefficient form based on tail area. Data obtained at a Mach number of 0.75 for the D-558-II airplane, for the two configurations of the X-5 airplane, and for the X-1 airplane are shown in the upper left-hand corner of this figure. Similar data are shown for the D-558-II, the X-5 at  $59^\circ$  sweep, and the X-1 for a Mach number of 0.95 in the upper right-hand corner of this figure. The  $45^\circ$  sweep X-5 data have as yet been obtained only to a Mach number of 0.9. Additional data obtained at supersonic speeds on the D-558-II airplane are shown in the lower portion of figure 2 at Mach numbers of 1.3 and 1.6. In the maneuvers shown, the Mach number variation was small except for the maneuver at Mach number of 1.3 in which the Mach number varied from about 1.4 to 1.2. For the X-5 and D-558-II airplanes, a reduction in stability was experienced for each of the maneuvers shown

except the maneuver at a Mach number of 1.6. As pointed out in a previous paper by Hubert M. Drake, Glenn H. Robinson, and Albert E. Kuhl, this abrupt reduction in stability generally occurs before the lift break for these airplanes. The data shown here cover the region prior to this lift break, whereas the paper just mentioned discussed the data obtained in the higher lift region up to the extreme angles of attack which were reached. For the X-5 and D-558-II airplanes, the reduction in stability occurred just prior to the positive increase in tail loads shown in figure 2. The trends of the tail-load variations illustrated at Mach numbers of 0.75 and 0.95 are typical for all the subject airplanes at all subsonic and transonic Mach numbers. The trends illustrated for the D-558-II at a Mach number of 1.3 are typical of the D-558-II at supersonic speeds to this Mach number. For the maneuver at a Mach number of 1.6 the maximum normal-force coefficient reached was about 0.90 even though the pilot used all the elevator and stabilizer control available. It is seen from these data that nonlinear variations exist throughout the lift and Mach number range for all the airplanes except the X-1. Model tests of the X-1 showed nonlinearities near zero lift; however, flight data are not available for this lift range. For linear variations in tail loads as shown for the X-1 airplane a parameter which has been useful for describing the tail-load variation with airplane lift is the parameter tail load per g. However, this term loses its significance for nonlinear variations such as shown here for the X-5 and D-558-II airplanes.

Comparison of existing wind-tunnel results with the measured flight values for the test airplanes indicates that the loads can be predicted early in the design stages from wind-tunnel results if they are available. The nonlinear variations existing for the X-5 and D-558-II airplanes emphasize the need of wind-tunnel tests early in the design stage in order that a reasonable estimate of the tail loads can be made. The calculations based on the wind-tunnel results should then consider the condition of dynamic overshoot discussed previously in a paper by George S. Campbell and in the paper by Hubert M. Drake, Glenn H. Robinson, and Albert E. Kuhl.

Turning now to the unsymmetrical maneuver, sideslips were made with the X-5 and D-558-II airplanes in level flight and the asymmetric horizontal-tail loads were measured. Examples of the variation of these asymmetric loads with sideslip angle at a Mach number of 0.87 are shown in figure 3. The asymmetric load expressed as the load on the left tail minus the load on the right tail is shown as the ordinate and sideslip angle is shown as the abscissa. It may be noted that sideslips in the same direction produce opposite slopes for the X-5 and D-558-II airplanes. Calculations of the mutual interference effects between vertical and horizontal tail surfaces to be presented in a subsequent paper by Alex Goodman and Harleth G. Wiley indicate a reason for this difference.

Details of these calculations will be covered in the paper by Goodman and Wiley. However, diagrams illustrating the load distributions resulting from the mutual interference effects between the vertical and horizontal tail for the two tail configurations are shown in the lower portion of figure 3. The X-5 tail combination with the horizontal tail mounted on the fuselage below the vertical tail is shown in the lower left-hand side of figure 3. The load distribution shown on the vertical tail is the load distribution which might be expected as the airplane sideslips. The vertical-tail load produces the load distribution indicated for the horizontal tail. A right sideslip as shown in the diagram produces an up load on the left horizontal tail and a down load on the right tail. The D-558-II tail combination with the horizontal tail mounted near the vertical-tail midspan is shown in the lower right-hand side of figure 3. For this case, the vertical-tail load produces a down tail load on the left horizontal tail and an up load on the right tail.

Figure 4 shows the variation of the asymmetric load per degree sideslip angle with Mach number. It is shown in this figure that the positive slope shown in the previous figure for the X-5 airplane increases markedly with increasing Mach number. The negative slope for the D-558-II airplane increases very little in the Mach number range from 0.7 to 0.9, but data obtained from a sideslip maneuver at a Mach number of 1.35 indicate that there may be a considerable increase in the negative slope at low supersonic speeds.

#### CONCLUDING REMARKS

1. It has been shown that the horizontal-tail loads of the X-5 and D-558-II airplanes have nonlinear variations throughout the lift and Mach number range. These nonlinear variations emphasize the need for wind-tunnel tests to guide the designer in the determination of the imposed tail loads.
2. It appears that asymmetric horizontal-tail loads developed during sideslip are a function of horizontal-tail position as well as sideslip angle.
3. The asymmetric tail load per degree sideslip angle increases with increasing Mach number for the X-5 and D-558-II airplanes.

## GENERAL ARRANGEMENT OF X-1, D-558-II, AND X-5 AIRPLANE

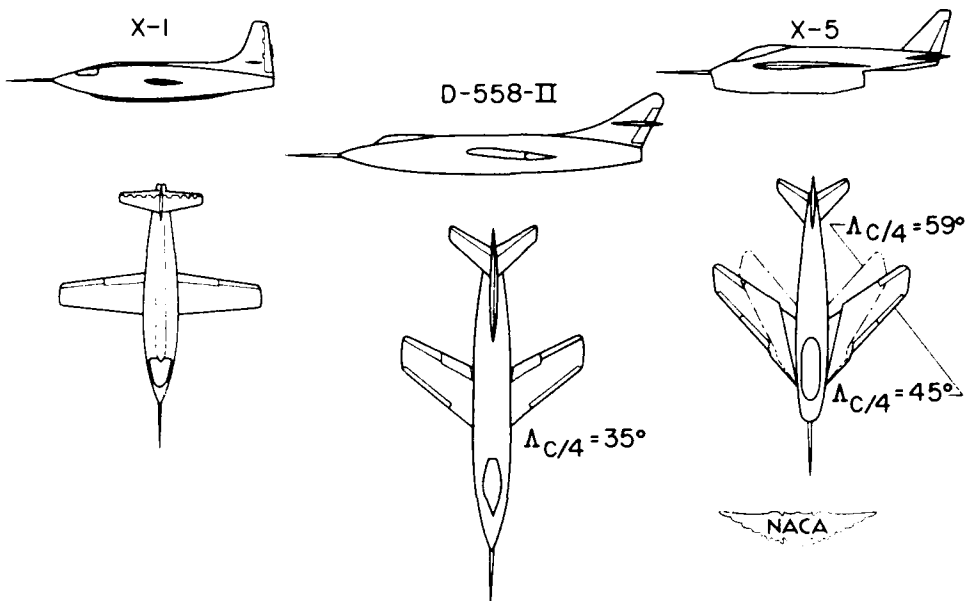


Figure 1.

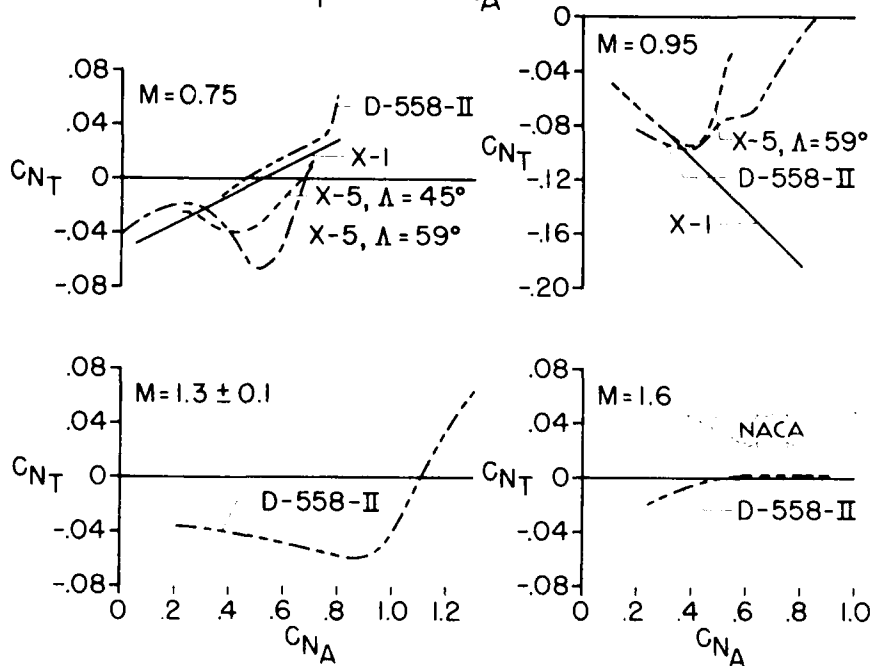
VARIATION OF  $C_{N_T}$  WITH  $C_{N_A}$  FOR TEST AIRPLANES

Figure 2.

**ASYMMETRIC TAIL LOADS DURING SIDESLIP FOR X-5  
AND D-558-II**

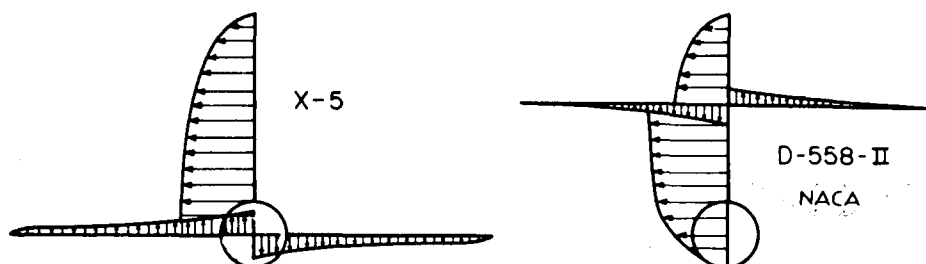
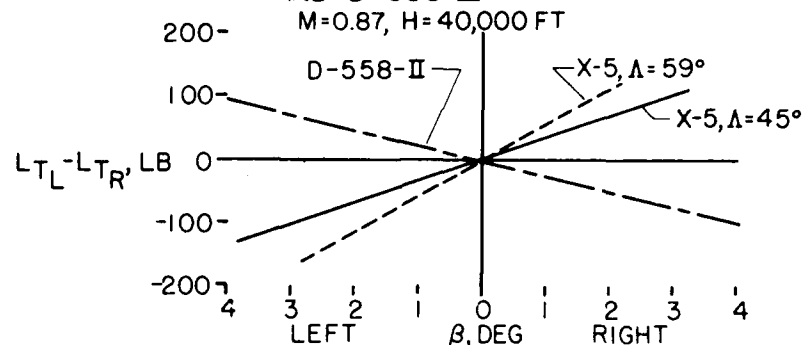


Figure 3.

**VARIATION OF ASYMMETRIC TAIL LOADS PER DEGREE SIDESLIP**

$H = 40,000 \text{ FT}$

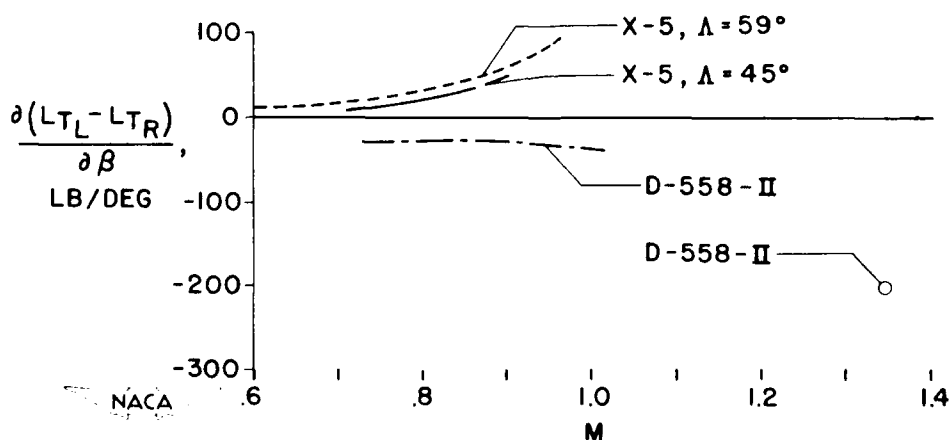


Figure 4.

ANALYTICAL STUDY OF SIDESLIP IN ROLLS  
DURING HIGH  $g$  MANEUVERS

By Ralph W. Stone

Langley Aeronautical Laboratory

Vertical-tail loads which occur primarily in unsymmetrical flight maneuvers are somewhat more complicated to estimate than loads which occur in longitudinal or symmetrical flight where the V-n diagram and control-movement requirements are given. In unsymmetrical flight the design conditions are not for specific loads but for specific control manipulations or airplane motions such as rudder kicks or rolling pull-outs.

The rolling pull-out appears to be one of the most complicated unsymmetrical maneuvers and is a maneuver that should be investigated for vertical-tail-load design, particularly for modern airplanes. The term "rolling pull-out" is used to apply to any rolling maneuver performed during high  $g$  flight, such as rolling out of a tight turn. In the past, researchers have presented simplified expressions for calculating the maximum sideslip angle in a rolling pull-out (see refs. 1 and 2). More recent investigations have indicated that the existing simplified expressions generally may not be applicable for airplanes of current and projected design (ref. 3). This condition is a result not only of large changes in airplane geometric configuration but also of changes in wing loading and mass distribution. For instance, World War II airplanes had weight distributed more or less evenly along the wing and fuselage. Thus, from consideration of mass distribution, the airplane tended to roll about the axis of the imposed moment. In some current or projected airplanes, however, the weight is distributed mostly along the fuselage, thus making the airplane much more apt to roll about the X-axis than to yaw. When a moment is imposed, the airplane tends to roll about the X-axis, the axis of least inertia, and the rolling tends to cause a sideslip angle of the order of magnitude of the initial angle of attack.

Another factor of some importance to the motion, that has been neglected in the past, is cross coupling of inertia moments (see ref. 3), a sort of gyroscopic moments, where, if pitching and rolling angular velocities exist together, a yawing moment is created.

The results of calculations by different methods of the variation of sideslip angle with time for a high-speed modern airplane are shown in figure 1. These calculations, taken from reference 3, are for a rudder-fixed roll in a  $6g$  pull-up where the elevator is also held fixed. For this airplane the ratio of moments of inertia  $I_x/I_y$  is

12, whereas the value for World War II types of airplanes was of the order of 2 to 3. This airplane also has large directional stability ( $C_{n\beta} = 0.0065$ ), about an order of magnitude larger than the World War II types of airplanes had. A previously used simplified expression (ref. 2), which adequately estimated the maximum angle of sideslip in rolling maneuvers for World War II airplanes, far underestimates the maximum angle of sideslip for this airplane. This expression gives about 50 percent of the maximum value obtained by more complete methods because of the aerodynamic and inertia limitations used in the development of this simplified expression. The effects of cross coupling of inertia moments are shown by the comparison of the values of  $\beta$  obtained from solutions of the three linearized lateral equations with those obtained with the effects of inertia cross coupling included, the four nonlinear equations. The effect for this case is about 20 percent.

A point of interest is the increasing value of sideslip angle at the end of the time shown in figure 1. The motion shown is for  $90^\circ$  of roll. It is reasonable to assume that a pilot might roll farther than  $90^\circ$ ; therefore, because of the increasing value of  $\beta$ , the calculations were extended beyond  $90^\circ$  to determine if subsequent peaks in  $\beta$  might be larger than the first. Also, because it might be expected that the airplane would slow down because of the high drag associated with high g flight, a change in velocity was also considered. The results are shown in figure 2 where the variation of  $\beta$  with time as well as a possible variation of velocity and a factor  $\beta q$  which is proportional to the tail load ( $q$  is the dynamic pressure) are plotted. The variation in velocity was estimated on the basis that a deceleration existed proportional to the increment in drag between  $1g$  and  $6g$  flight, for which the calculations were made. The results indicate that the vertical-tail load is larger at the second peak. A 20 percent increase in sideslip angle accompanied by a 10 percent decrease in dynamic pressure result in about a 10 percent increase in load. This case, as previously mentioned, was calculated by holding the elevator fixed. If the pilot attempted to maintain a constant angle of attack or normal acceleration, forward stick would be required at the time of the second peak in  $\beta$  which would tend to reduce the magnitude of the second peak. No simple method exists by which this effect can be evaluated, and whether the first or subsequent peaks in  $\beta$  are critical to the vertical-tail load depends on the individual case.

Since the mass distribution for modern airplanes has an important influence on the sideslip angle in rolling maneuvers, it was thought that an understanding of the variation in  $\beta$  with time in a roll would be desirable. A general concept of the variation of the sideslip angle

in a rolling maneuver considering the effects of mass distribution, previously discussed, is presented in figure 3. The curve  $\eta \sin \phi$  would be the variation in  $\beta$ , if the only aerodynamic moment existing is a rolling moment about the principal body axis or if the moments of inertia are very large except the rolling moment of inertia  $I_X$ . The symbol  $\eta$  is the angle between the principal X-axis and wind axis and is about equal to the angle of attack for high-angle-of-attack flight conditions. The symbol  $\phi$  is the angle of roll. If the airplane has no directional stability ( $C_{n\beta} = 0$ ) but has other adverse yawing moments such as those that exist from aileron deflections ( $C_{n\delta_a} \delta_a$ ), rolling ( $C_{n_p} \frac{p}{2V}$ ), and cross coupling of inertia moments ( $I_X - I_Y$ ) $\dot{\theta}_p$ , the top curve might be obtained. The aileron deflection is  $\delta_a$ ; the rolling velocity,  $p$  and the pitching velocity,  $\dot{\theta}$ . Directional stability  $C_{n\beta}$  will tend to reduce the sideslip angle from that given by the upper curve. Increasing the amount of directional stability reduces the amount of sideslip at the first peak as shown in figure 3. A point of importance is that the first peak in  $\beta$  occurs at a time equal to about one-half the period of the natural oscillation of the airplane. Increasing the value of  $C_{n\beta}$  reduces this time, makes the first peak in  $\beta$  occur at a time when less possible ultimate  $\beta$  exists, and provides more yawing acceleration to reduce  $\beta$  prior to this time.

In order to evaluate accurately the vertical-tail load in rolling pull-outs, it has been shown that accurate calculations of the motion are essential. The calculated motions, however, depend on the stability and control derivatives used. Such derivatives must either be estimated or measured by model tests, in early stages of design, in order to evaluate the loads for which to build the airplanes. A study has been initiated to determine the effects of large variations in the derivatives on the maximum sideslip angle (at the first peak) in order to give an indication of the accuracy needed in the derivatives to get a reasonably accurate value of  $\beta$  and the vertical-tail load.

The results obtained to date are for the three yawing-moment derivatives that have been considered important to the sideslip angle in rolling maneuvers in the past (ref. 2):  $C_{n_p}$ , the yawing-moment coefficient due to rolling;  $C_{n\delta_a} \delta_a$ , the yawing-moment coefficient due to aileron deflection; and  $C_{n\beta}$ , the directional-stability derivative. A brief study has also been made of the effect of the damping derivative  $C_{n_r}$ . The calculations were made for a 6g rolling pull-out for three different mass distributions: when the mass is primarily distributed along the fuselage, where  $I_Z/I_X = 12$ , and for distributions where  $I_Z/I_X = 6$  and 3. A

simplified method of calculation was used, treating the three linear lateral equations of motion, in lieu of the more time-consuming calculations for the motions shown in the first two figures. The effects of cross coupling of inertia moments, however, were included assuming a constant pitching velocity. The actual magnitudes of the maximum sideslip angles probably underestimate those that would be obtained by the longer calculations (used in ref. 3) but the incremental effects of the changes in the derivatives should be reasonably accurate.

Figure 4 shows the effects of varying the yawing-moment coefficient  $C_{n_p}$ , which is the yawing moment due to rolling. Values of  $C_{n_p}$  from 0 to -0.26 were studied. The effects shown for these cases are not large even for extreme variations in  $C_{n_p}$ . However, for some airplanes, variations of  $C_{n_p}$  have had large effects and, therefore, a simple expression has been developed to estimate the effect of  $C_{n_p}$  for the general case. This expression is

$$\Delta\beta = \frac{-qSb^2}{2IZV} \Delta C_{n_p} \phi_{\beta_{max}} \frac{t_{\beta_{max}}}{3}$$

where  $\phi_{\beta_{max}}$  is the angle of roll and  $t_{\beta_{max}}$  is the time at which maximum  $\beta$  occurs. Thus, having estimated a variation of  $\beta$  in a rolling maneuver and knowing  $\phi_{\beta_{max}}$  and  $t_{\beta_{max}}$ , the effect of possible errors in  $C_{n_p}$  can be evaluated by this expression. An application of the expression to the cases shown in figure 4 gives curves which are nearly coincident with those shown. This expression is also applicable to cases where positive values of  $C_{n_p}$  exist.

The most noticeable effect shown in figure 4 is that of mass distribution. Redistributing the weight from a value of the ratio  $I_Z/I_X = 3$  to a value of 12 nearly doubles the maximum sideslip angle and, thus, the vertical-tail load.

Figure 5 shows the effect of varying the yawing-moment derivative  $C_{n_{\delta_a}} \delta_a$ , the adverse yawing moment due to aileron deflection. Values of  $C_{n_{\delta_a}} \delta_a$  from 0 to -0.0070 were studied. The effect of this parameter varies with mass distribution, being least critical for the mass distribution with the mass distributed mainly along the fuselage. The effects shown are not as large as effects of  $C_{n_p} \delta_a$  which have been

noted in the past. A simple expression has been developed, therefore, to estimate the effect of  $C_{n\delta_a} \delta_a$  for the general case. This expression is

$$\Delta\beta = \frac{-qS_b}{I_Z} \Delta C_{n\delta_a} \delta_a \frac{(t_{\beta_{max}})^2}{2}$$

where  $t_{\beta_{max}}$  is the time at which  $\beta_{max}$  is reached. Thus, having estimated a variation of  $\beta$  in a rolling maneuver by more complete methods, the effect of possible errors in  $C_{n\delta_a} \delta_a$  can be evaluated by this expression. An application of the expression to the cases shown in figure 5 gives a conservative estimate of the possible error.

In the past, the damping derivative  $C_{n_r}$  has been shown not to be an important factor affecting the first peak in  $\beta$ , and brief calculations for these mass distribution conditions substantiate this point. This study was not sufficiently extensive, however, to cover the possible case of large damping obtained by artificial means which might be used for some airplanes. The effects of  $C_{n_r}$  may not be small for such cases.

The last derivative which has been studied to date is the directional-stability derivative  $C_{n\beta}$ . Effects on the first peak in  $\beta$  of variations in this derivative are shown in figure 6. Rather large directional stability ( $C_{n\beta} = 0.0065$ ) has been used for all previous calculations and a study of the effects of reducing this value to one-fourth the original value was made. The effect of  $C_{n\beta}$  is very pronounced as has been shown in the past; it is most critical for the mass distribution where  $I_Z/I_X = 3$ . For this mass distribution, reducing  $C_{n\beta}$  to one-fourth its value increased the maximum sideslip angle by  $\frac{21}{2}$  times. For the mass distribution where  $I_Z/I_X = 12$ , the maximum sideslip angle was increased by 65 percent. The maximum sideslip angle, however, is not inversely proportional to  $C_{n\beta}$  as previous simplified expressions (ref. 2) might indicate. The proximity to inverse proportionality becomes less as the mass is distributed more along the fuselage. Thus, larger values of directional stability, although leading to smaller sideslip angles, do not necessarily lead to smaller vertical-tail loads in rolling maneuvers.

Existing methods for estimating the derivatives for subsonic cases have been summarized in reference 4 and use of these procedures should adequately evaluate the derivatives. Efforts are currently underway for

evaluations of derivatives for supersonic cases. Methods for calculating the contributions of different parts of the airplane are given in references 5 to 9. In yet unpublished work by Kenneth Margolis and Percy J. Bobbitt a cumulative effort to evaluate the derivatives for one entire airplane has been made.

Some experimental work with particular regard to the directional-stability derivative  $C_{n\beta}$  is available in the supersonic- and transonic-speed ranges (refs. 10 to 14) and more is planned. Measurements on models of specific configurations show a deficiency in  $C_{n\beta}$  at Mach numbers of the order of  $1\frac{1}{2}$  to 2 and show, in some cases, large nonlinearities and instability (ref. 12, for example). There have also been indications of a loss of directional stability at high angles of attack both at subsonic and supersonic speeds (refs. 15 and 16, and 12, respectively, for examples). Relatively high angles of attack generally exist in rolling pull-outs. Such deficiencies may be the result of sidewash effects which might imply low tail loads for such conditions. However, the airplane could sideslip to large values so as to emerge from the effects of sidewash with the possibility of large vertical-tail loads. From previous discussions,  $C_{n\beta}$  has been shown to be a critical derivative from the standpoint of vertical-tail loads, and consideration of these possible deficiencies in directional stability should be made for each individual case.

To summarize, the following points of interest are noted:

1. Existing simplified expressions for determining vertical-tail loads in rolling maneuvers generally are not applicable for modern high-speed airplanes.
2. In rolling pull-outs an oscillation in sideslip angle is set up and peaks in  $\beta$  subsequent to the first peak may cause larger vertical-tail loads than the first.
3. The directional-stability derivative  $C_{n\beta}$  is the most critical of the yawing-stability derivatives with regard to an adequate estimation of the vertical-tail load.
4. Simple expressions for estimating the effects of possible errors in  $C_{n_p}$  and  $C_{n\delta_a} \delta_a$  on the vertical-tail load, once a motion has been calculated, are available.

## REFERENCES

1. Gilruth, Robert R.: Analysis of Vertical-Tail Loads in Rolling Pull-Out Maneuvers. NACA WR L-181, 1944. (Formerly NACA CB L4H14.)
2. White, Maurice D., Lomax, Harvard, and Turner, Howard L.: Sideslip Angles and Vertical-Tail Loads in Rolling Pull-Out Maneuvers. NACA TN 1122, 1947.
3. Stone, Ralph W., Jr.: Estimation of the Maximum Angle of Sideslip for Determination of Vertical-Tail Loads in Rolling Maneuvers. NACA TN 2633, 1952.
4. Campbell, John P., and McKinney, Marion O.: Summary of Methods for Calculating Dynamic Lateral Stability and Response and for Estimating Lateral Stability Derivatives. NACA Rep. 1098, 1952. (Supersedes NACA TN 2409.)
5. Martin, John C., and Malvestuto, Frank S., Jr.: Theoretical Force and Moments Due to Sideslip of a Number of Vertical Tail Configurations at Supersonic Speeds. NACA TN 2412, 1951.
6. Ribner, Herbert S., and Malvestuto, Frank S., Jr.: Stability Derivatives of Triangular Wings at Supersonic Speeds. NACA Rep. 908, 1948. (Supersedes NACA TN 1572.)
7. Malvestuto, Frank S., Jr., and Margolis, Kenneth: Theoretical Stability Derivatives of Thin Sweptback Wings Tapered to a Point With Sweptback or Sweptforward Trailing Edges for a Limited Range of Supersonic Speeds. NACA Rep. 971, 1950. (Supersedes NACA TN 1761.)
8. Harmon, Sidney M.: Stability Derivatives at Supersonic Speeds of Thin Rectangular Wings With Diagonals Ahead of Tip Mach Lines. NACA Rep. 925, 1949. (Supersedes NACA TN 1706.)
9. Bobbitt, Percy J., and Malvestuto, Frank S., Jr.: Estimation of Forces and Moments Due to Rolling for Several Slender-Tail Configurations at Supersonic Speeds. (Prospective NACA paper)
10. Spearman, M. Leroy: An Investigation of a Supersonic Aircraft Configuration Having a Tapered Wing With Circular-Arc Sections and 40° Sweepback. Static Lateral Stability Characteristics at Mach Numbers of 1.40 and 1.59. NACA RM L50C17, 1950.

11. Spearman, M. Leroy, and Robinson, Ross B.: The Aerodynamic Characteristics of a Supersonic Aircraft Configuration With a 40° Sweptback Wing Through a Mach Number Range From 0 to 2.4 As Obtained From Various Sources. NACA RM L52A21, 1952.
12. Hilton, John H., Jr., Hamilton, Clyde V., and Lankford, John L.: Preliminary Wind-Tunnel Investigation of a 1/20-Scale Model of the Convair MX-1554 at Mach Numbers of 1.61 and 2.01. NACA RM SL52L11a, U. S. Air Force, 1952.
13. Spearman, M. Leroy, and Hilton, John H., Jr.: Aerodynamic Characteristics at Supersonic Speeds of a Series of Wing-Body Combinations Having Cambered Wings With an Aspect Ratio of 3.5 and a Taper Ratio of 0.2. Effects of Sweep Angle and Thickness Ratio on the Static Lateral Stability Characteristics at  $M = 1.60$ . NACA RM L51K15a, 1952.
14. Purser, Paul E., and Mitchell, Jesse L.: Miscellaneous Directional-Stability Data for Several Airplane-Like Configurations From Rocket-Model Tests at Transonic Speeds. NACA RM L52E06b, 1952.
15. Kemp, William B., Jr., and Becht, Robert E.: Stability and Control Characteristics at Low Speed of a 1/4-Scale Bell X-5 Airplane Model. Lateral and Directional Stability and Control. NACA RM L50C17a, 1950.
16. Queijo, M. J., and Wolhart, Walter D.: Experimental Investigation of the Effect of Vertical-Tail Size and Length and of Fuselage Shape and Length on the Static Lateral Stability Characteristics of a Model With 45° Sweptback Wing and Tail Surfaces. NACA Rep. 1049, 1951. (Supersedes NACA TN 2168.)

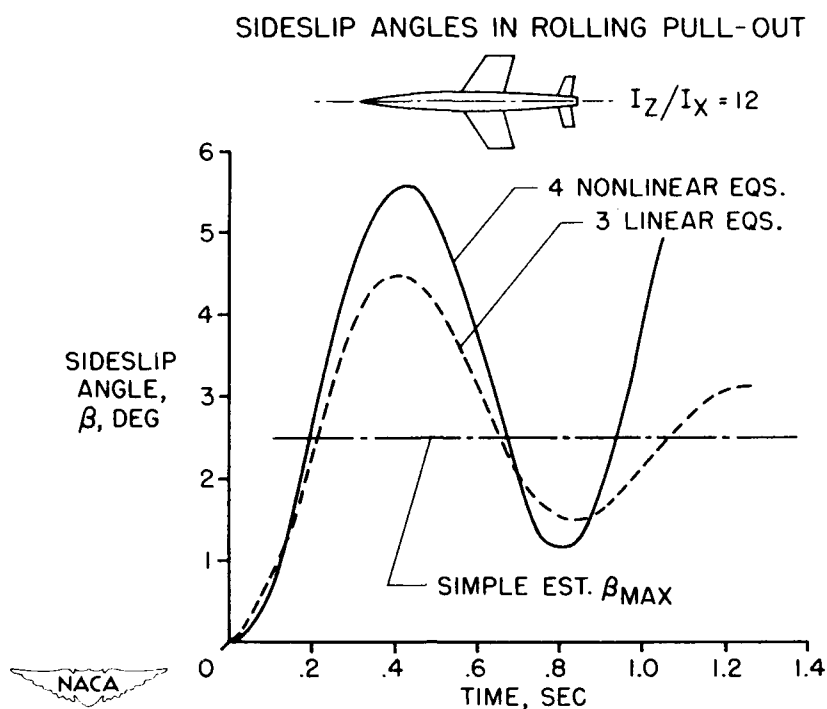


Figure 1.

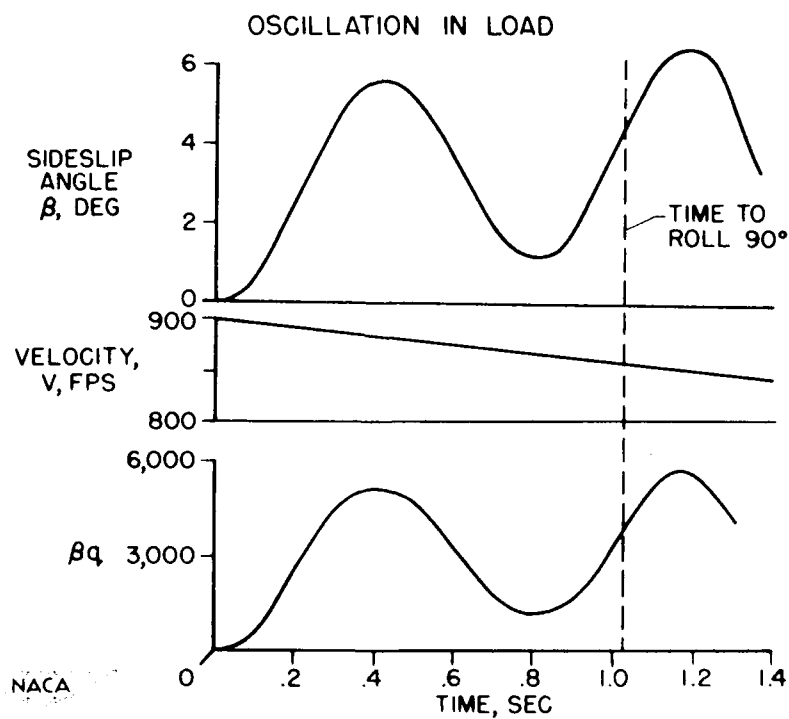


Figure 2.

## GENERAL CONCEPT OF SIDESLIP IN ROLL

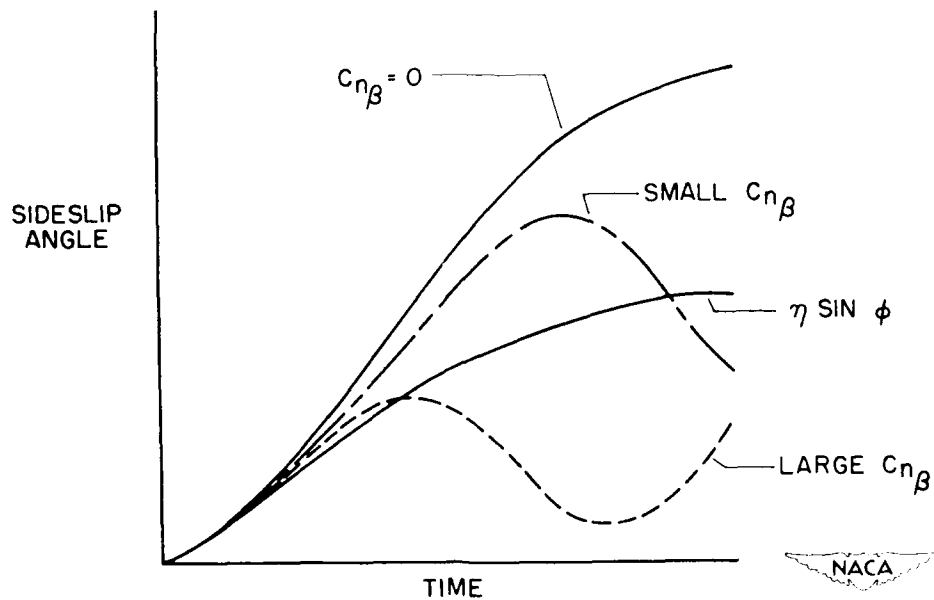


Figure 3.

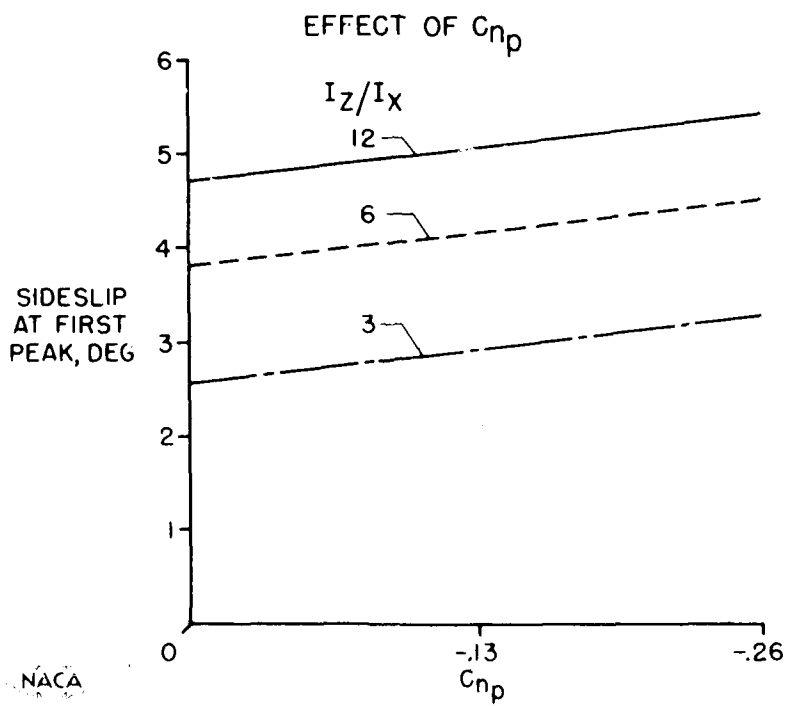


Figure 4.

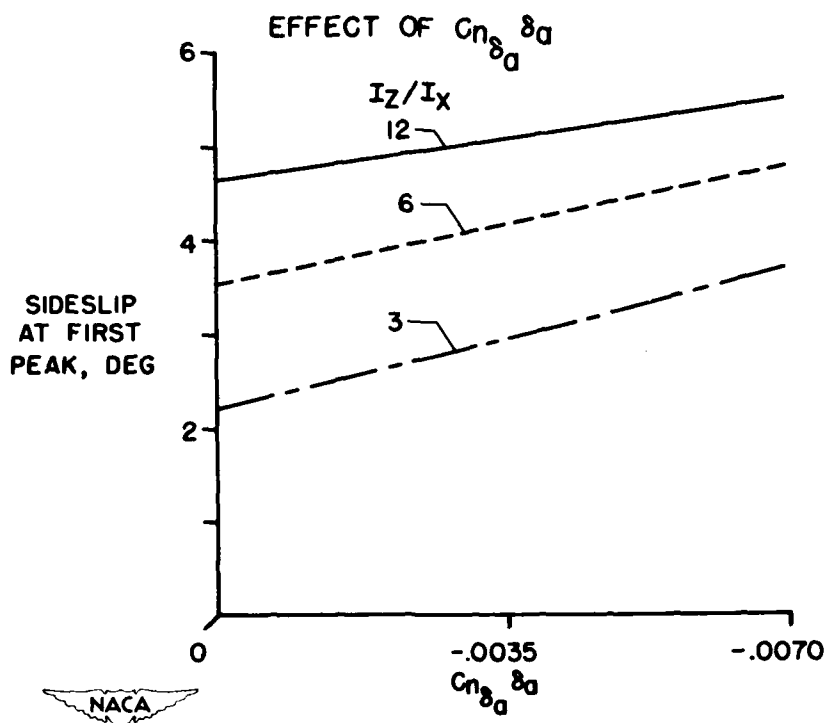


Figure 5.

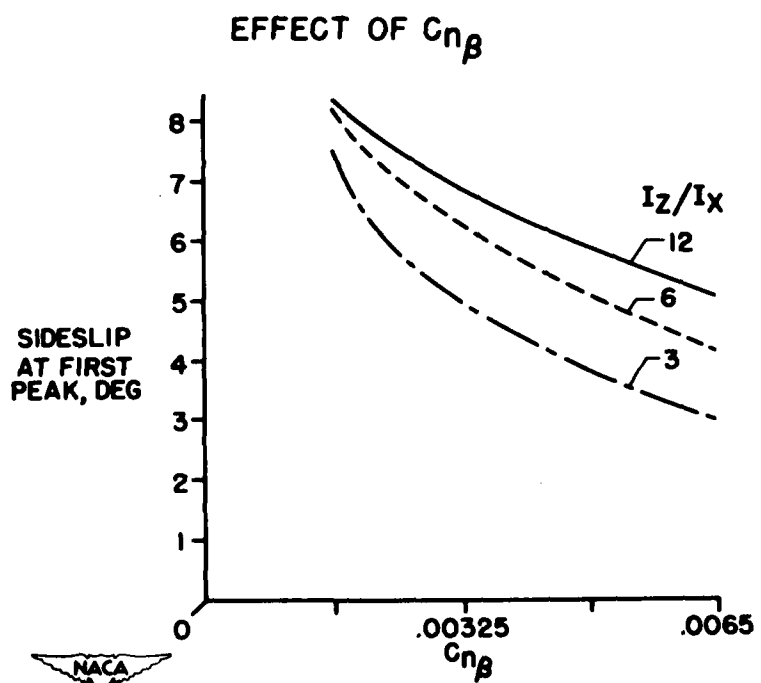


Figure 6.

EFFECTS OF HORIZONTAL-TAIL HEIGHT, FUSELAGE SIZE,  
AND WING HEIGHT ON VERTICAL-TAIL LOADS

By Alex Goodman and Harleth G. Wiley

Langley Aeronautical Laboratory

### INTRODUCTION

In order to predict the vertical-tail design loads, it is necessary not only to know the motions of the airplane as discussed in the previous paper by Ralph W. Stone but also the effects of the airplane geometry on the load distribution. The present paper will deal with the tail-loads problem from the standpoint of the effects of airplane geometry, and effects of Mach number, for some cases, on the vertical-tail loads which occur in a prescribed maneuver. Methods for calculating the vertical-tail-load distribution will be presented which account for several of these effects.

### EFFECTS OF HORIZONTAL-TAIL HEIGHT

One of the more important effects of airplane geometry on the vertical-tail normal force and moment is concerned with the end-plate effect of a horizontal tail. Experimental values of the normal force for the vertical tail and the moment about the fuselage center line of the combination (fuselage torsion), as affected by horizontal-tail height, have been obtained at zero angle of attack, for a range of side-slip angles and Mach numbers in the Langley high-speed 7- by 10-foot tunnel. The configurations shown in figure 1 were used for these tests.

The model shown in the upper portion of the figure consisted of an unswept, untapered vertical tail of aspect ratio of about 2 in combination with a stub fuselage and a horizontal tail of aspect ratio of about 4.5. The vertical tail and the horizontal tail both had NACA 64A010 airfoil sections. The loadings shown in the lower portion of figure 1 for the low-, mid-, and high-tail positions were calculated for  $M = 0.6$  by using a finite-step method described in reference 1. Effects of Mach number were accounted for by a Prandtl-Glauert correction. These load distributions will be referred to when the loads data are discussed.

The effects of horizontal-tail height on the vertical-tail normal force through the sideslip-angle range are shown for Mach numbers of 0.50, 0.80, 0.86, and 0.94 in figure 2. As can be seen, the normal-force coefficient is linear up to  $8^\circ$  of sideslip for all the configurations with the exception of the mid-tail configuration. For the mid-tail

configuration, the normal-force-coefficient curves are nonlinear at low values of sideslip, at Mach numbers of 0.80 and 0.86. This nonlinearity is probably due to the flow breakdown that occurs at these Mach numbers because of the type of intersection of the lifting surfaces. Note, however, that the magnitude of the load at higher values of sideslip angle is still nearly as large as that obtained for the other configurations. The break in the curves that occurs at sideslip angles of  $8^{\circ}$  is probably due to the type of airfoil section used for the tails or because of the low Reynolds number of the tests,  $1.5 \times 10^6$  to  $2 \times 10^6$ . As can be seen there is very little change in the normal-force coefficients between tail-off, low-tail, and mid-tail configurations. In general, loads for the high-tail configuration were the largest of all the configurations tested.

The effects of horizontal-tail height on the torsional moment of the combination, measured about the fuselage center line, are shown for the same Mach numbers in figure 3 as were presented in figure 2. The moment curves are also linear up to about  $8^{\circ}$  of sideslip for most of the configurations. The nonlinearity shown in the previous figure for the mid-tail configuration at  $M = 0.80$  and  $0.86$  is also indicated in this figure. Of interest is the large change in the moment coefficient in going from the low-tail to the high-tail configuration throughout the sideslip-angle range for all Mach numbers. The calculated load distributions shown in figure 1 indicate the reason for this change. For the low-tail configuration, it can be seen that the induced loading on the horizontal tail is such as to reduce the total moment of the combination. For the high-tail configuration the reverse is true; that is, the moment due to the induced loading on the horizontal tail increases the total moment about the fuselage center line. It is interesting to note that the ratio of the moment to the normal force at high sideslip angles is, in general, the same as the ratio of these parameters at low sideslip angles. This would imply that the loadings on the vertical tail as affected by the horizontal-tail location at high sideslip angles is of the same general nature as that calculated for the low sideslip-angle range.

The slopes of the normal-force- and moment-coefficient curves taken through zero sideslip for a range of Mach numbers are compared in figure 4 with values of these parameters obtained from the integration of calculated loadings such as shown in figure 1. The change in normal-force coefficient per unit sideslip angle and the change in the moment coefficient per unit sideslip angle are shown plotted against Mach number. The agreement is fair for the normal-force case and good for the moment case up to the critical Mach number. The nonlinearity that was mentioned before for the mid-tail configuration is indicated by the large reduction in slope shown. However, as mentioned previously, this is not indicative of the load at higher angles of sideslip. Above the critical

Mach number the agreement improves. The agreement between the measured and calculated load parameters indicates that the calculated load distributions are fairly representative of the tail loads up to the critical Mach number.

#### EFFECTS OF FUSELAGE SIZE

Another factor affecting the vertical-tail load is the fuselage size. An investigation has been conducted in the Langley stability tunnel at a Mach number of 0.2 for the purpose of determining the effects of variation in fuselage size on the vertical-tail load and root moment in sideslip.

The type of configurations tested and also some calculated span loadings are shown in figure 5. Unswept tails of aspect ratio 1, 2, and 4 were tested in combination with fuselages which were bodies of revolution having circular-arc profiles. A 45° sweptback tail and a triangular tail, both of aspect ratio 2, were tested in combination with fuselages which were bodies of revolution having parabolic-arc profiles.

The normal force on the tail, and the root moment, in some cases, were measured at zero angle of attack, for sideslip angles of  $\pm 10^\circ$  by means of strain gages.

The calculated span loadings on the unswept, the 45° sweptback, and the triangular tails of aspect ratio 2 are also shown in figure 5. These loadings are for various values of the diameter-span ratio  $D/b_y$  where  $D$  is the diameter of the fuselage measured in the plane of the quarter-chord point of the tail mean aerodynamic chord and  $b_y$  is the exposed tail span measured in the same plane. These loadings were calculated by using a finite-step method described in reference 2.

The measured normal-force and root-moment coefficients are compared with calculated values obtained by integration of the span loadings for the unswept tails in figure 6. The change in normal-force coefficient per unit sideslip angle and the change in root-moment coefficient per unit sideslip angle are shown plotted against the diameter-span ratio. As expected there is a large increase in the magnitude of the normal-force and moment parameters with an increase in aspect ratio.

An increase in fuselage size results in an increase in the normal-force and root-moment parameters; however, these increases are small relative to the increases caused by aspect ratio. A comparison of the ratio of root moment to normal force indicates that there is a very small change in the center of load with aspect ratio. The center of load is at about 50 percent of the tail span.

The results for the swept tails are presented in figure 7. The same parameters - change in normal force and root moment per unit sideslip angle - are presented for the swept tails of aspect ratio 2. The unswept tail of aspect ratio 2 has been included for comparison. The main effect of an increase in sweep from  $0^\circ$  to  $45^\circ$  is to reduce the magnitude of both the normal force and the root moment. Incidentally, no experimental moment data were obtained for the  $45^\circ$  sweptback tail. Again comparing the ratio of the moment coefficient to the normal-force coefficient, an outboard shift in the center of load is indicated for the swept tail and an inboard shift for the triangular tail relative to the mid-tail results. This effect can be seen by comparing the span loadings shown in figure 5.

In general the agreement obtained is good and indicates that the calculated span loadings are fairly representative of the actual tail-load distribution.

#### EFFECTS OF WING HEIGHT

Another factor that should be considered is the effect of wing-fuselage interference on the vertical-tail load. An investigation has been conducted in the Langley stability tunnel at a Mach number of 0.2 in order to evaluate this effect for both the sideslip and rolling case.

The configurations that were tested are shown in figure 8. Three fuselages having fineness ratios of 6, 9, and 12 were tested in combination with a  $60^\circ$  delta wing and a triangular tail of aspect ratio 2. The  $60^\circ$  delta wing was tested in three locations - high, mid, and low on each fuselage. The normal force on the tail was measured by means of a strain gage, through the angle-of-attack range, for sideslip angles of  $0^\circ$  and  $\pm 5^\circ$ , and also for a range of wing-tip helix angles  $p_b/2V$ .

The results obtained with the fuselage having a fineness ratio of 9 are presented in figure 9. In this figure the change in normal-force coefficient per unit sideslip angle is plotted against angle of attack and the change in normal-force coefficient per unit wing-tip helix angle is plotted against angle of attack for the high, mid, and low configurations.

For the sideslip case, the addition of the wing in the mid location essentially had no effect on the tail load. However, for the low wing the tail load is increased and for the high wing the tail load is decreased relative to the mid-wing results. This is mainly due to the change in sidewash at the vertical tail that is caused by the wing-fuselage interference.

In the rolling case, a change in wing height causes a vertical shift in the sidewash pattern due to roll as indicated in reference 3. In the case of the low wing, this produces an increase in normal force, and for the high wing, a decrease in the normal force on the tail relative to the mid-wing results.

In order to arrive at an idea of the importance of these effects, the configurations have been assumed to have performed a maneuver similar to that considered in the previous paper by Ralph W. Stone. It is indicated that the rate of roll that existed at the peak sideslip angle resulted in a reduction of the tail load equivalent to a reduction in sideslip angle of about one-third of a degree. However, later in the maneuver, the effect of the rate of roll on the tail load is equivalent to about a  $1.5^\circ$  reduction in the angle of sideslip.

A summary is presented in figure 10 of the effects of wing height and fuselage size on the vertical-tail loads in sideslip and roll. The change in normal-force coefficient per unit sideslip angle and the change in normal-force coefficient per unit wing-tip helix angle are shown plotted against the ratio  $D_{MAX}/l$  - inverse of fineness ratio - for the high, mid, and low configurations.

For the sideslip case the values of the normal-force parameter at an angle of attack of  $10^\circ$  are presented. As can be seen there is essentially no change in normal force, for the mid-wing case, as the fuselage size increases. However, there is a small increase in the magnitude of the normal-force parameter for the low wing and an equivalent decrease in this parameter for the high wing as the fuselage size is increased. This effect is mainly caused by the increase in sidewash at the vertical tail with an increase in fuselage size. By using a finite-step method such as presented in reference 2 the induced asymmetrical load on the wing can be calculated and the resulting sidewash at the vertical tail can be determined. The tail-load distribution can then be calculated. The calculated values shown in figure 10 were obtained by integration of the calculated tail-load distribution and are in good agreement with the measured values.

For the roll case, data are presented for angles of attack of  $0^\circ$  and  $10^\circ$ . The results indicate small changes in the normal-force parameter with an increase in fuselage size.

#### CONCLUDING REMARKS

The purpose of this paper has been primarily to illustrate a few of the more important effects of airplane geometry on the load carried by a vertical tail in sideslip and roll, and to illustrate that mutual

interference may have a considerable effect on the vertical-tail load. In general, the effects of airplane geometry can be accounted for by various available methods up to the critical Mach number. Also, the methods used yield span load distributions which are fairly representative of the vertical-tail loading.

## REFERENCES

1. Riley, Donald R.: Effect of Horizontal-Tail Span and Vertical Location on the Aerodynamic Characteristics of an Unswept Tail Assembly in Sideslip. NACA TN 2907, 1953.
2. Zlotnick, Martin, and Robinson, Samuel W., Jr.: A Simplified Mathematical Model for Calculating Aerodynamic Loading and Downwash for Midwing Wing-Fuselage Combinations With Wings of Arbitrary Plan Form. NACA RM L52J27a, 1953.
3. Michael, William H., Jr.: Analysis of the Effects of Wing Interference on the Tail Contributions to the Rolling Derivatives. NACA Rep. 1086, 1952. (Supersedes NACA TN 2332.)

## CALCULATED LOAD DISTRIBUTION

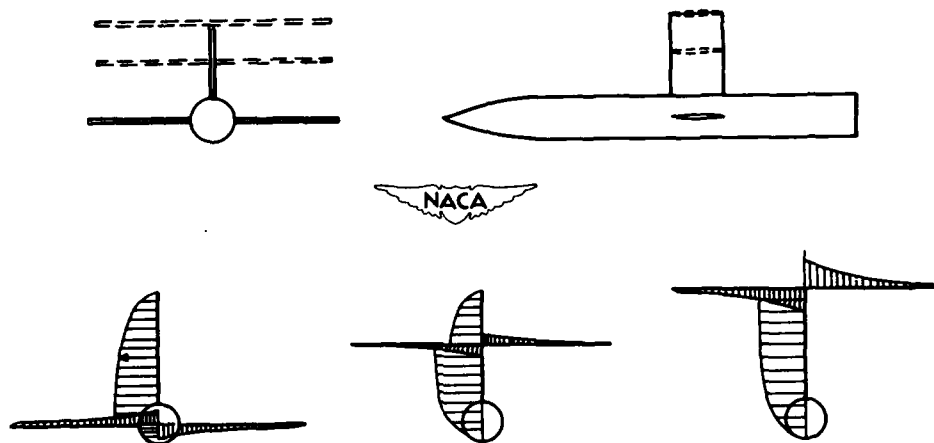


Figure 1.

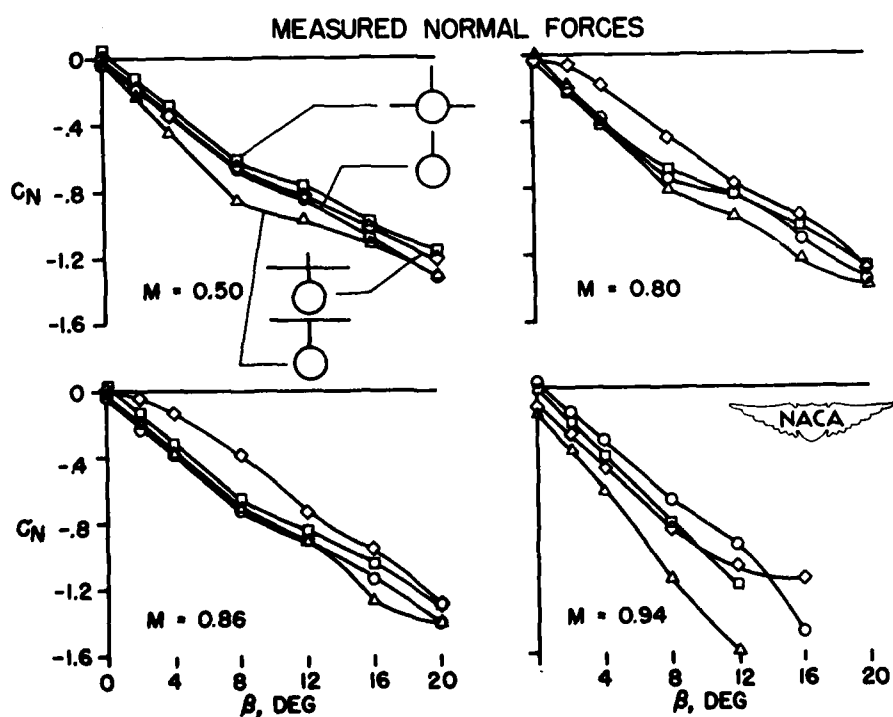


Figure 2.

CONFIDENTIAL

## MEASURED FUSELAGE TORSION

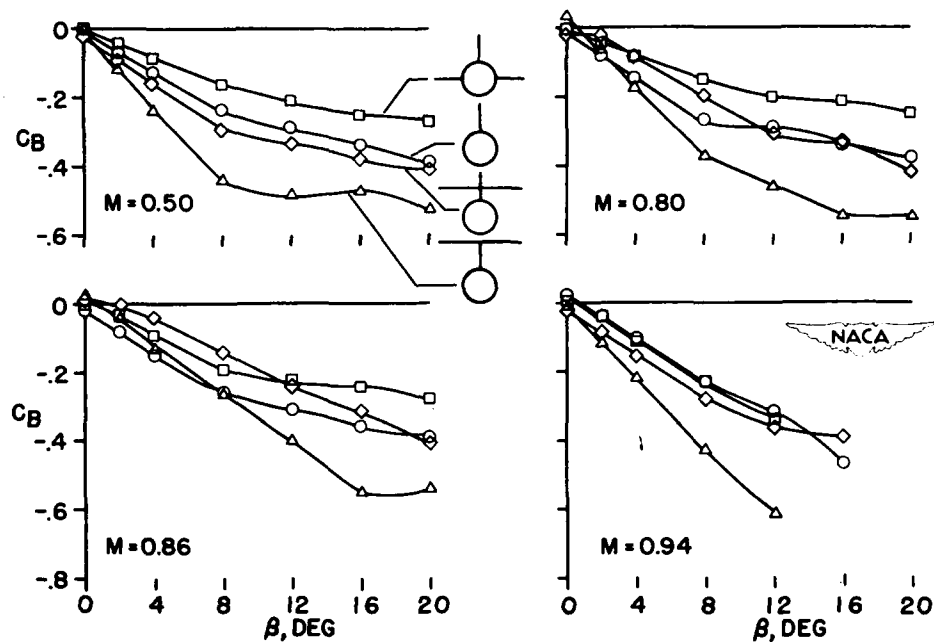


Figure 3.

## MEASURED AND CALCULATED LOADS

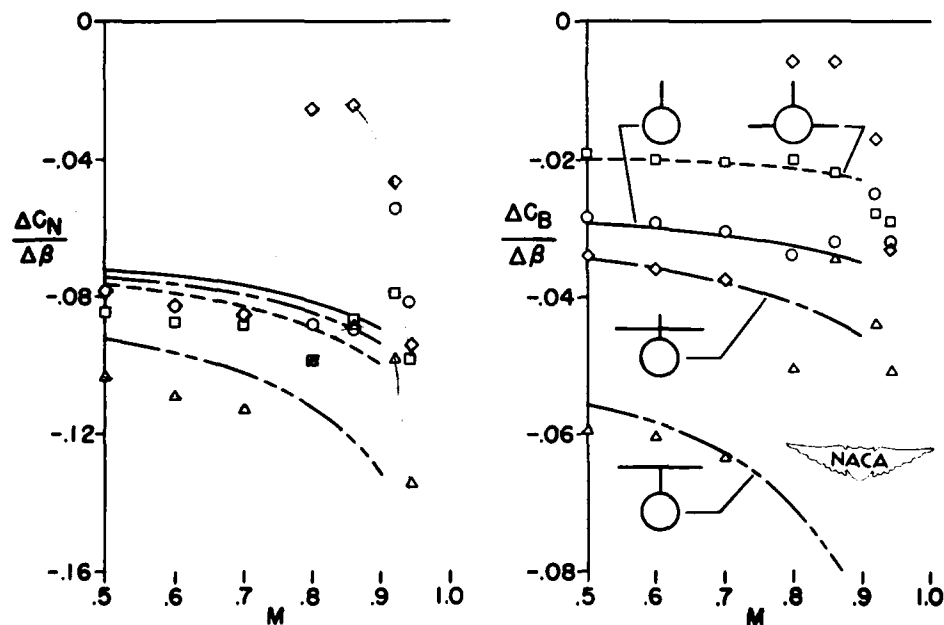


Figure 4.

CONFIDENTIAL

## CALCULATED LOAD DISTRIBUTIONS

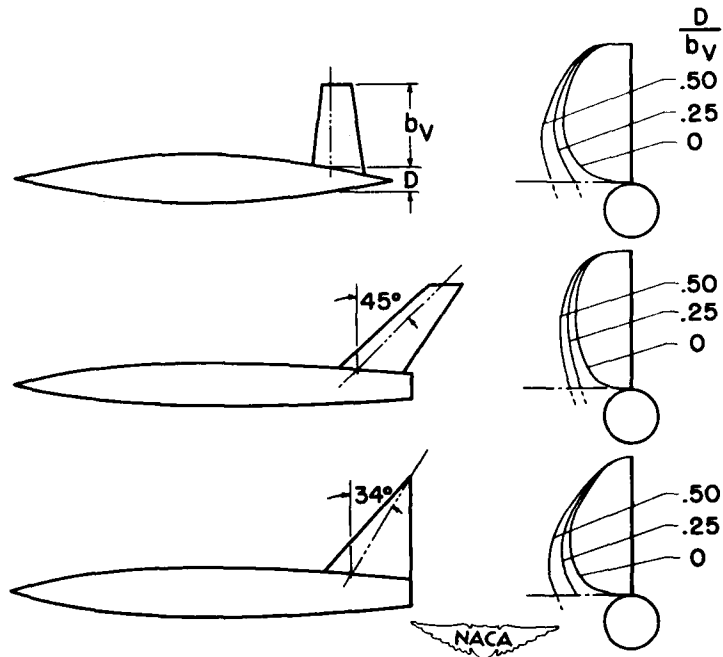


Figure 5.

## MEASURED AND CALCULATED LOAD, UNSWEPT

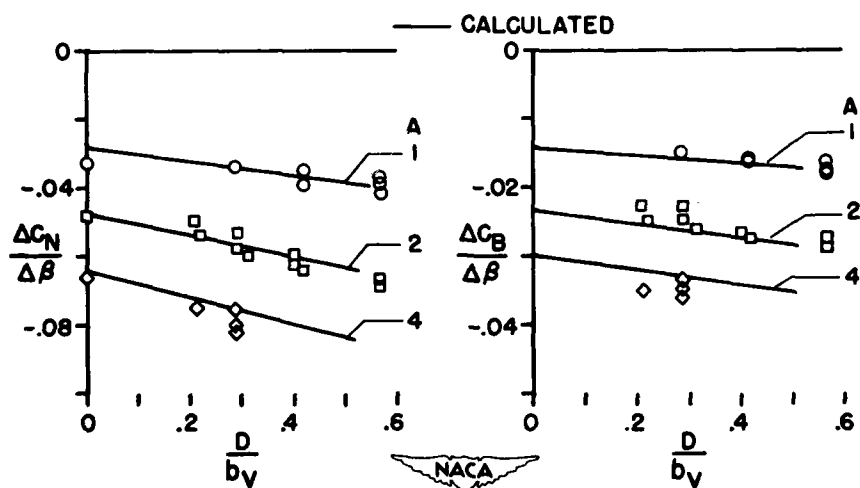


Figure 6.

## MEASURED AND CALCULATED LOAD, SWEPT

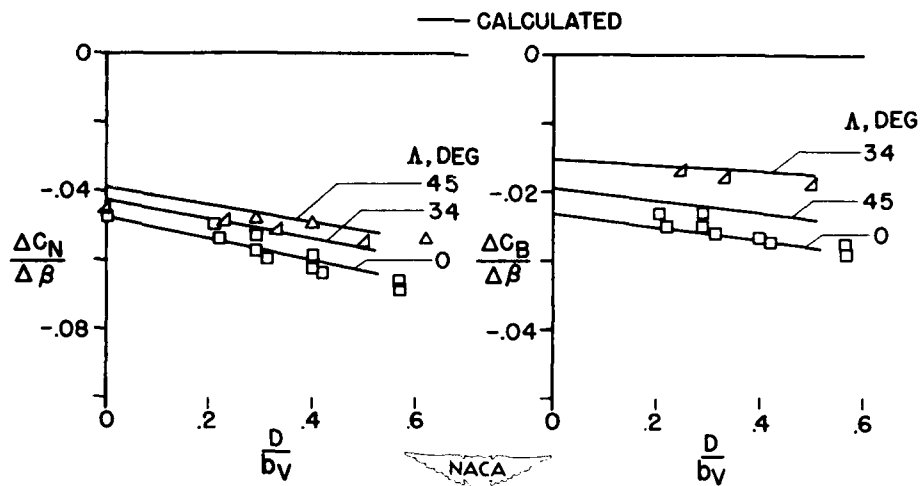


Figure 7.

## WING-HEIGHT CONFIGURATIONS TESTED

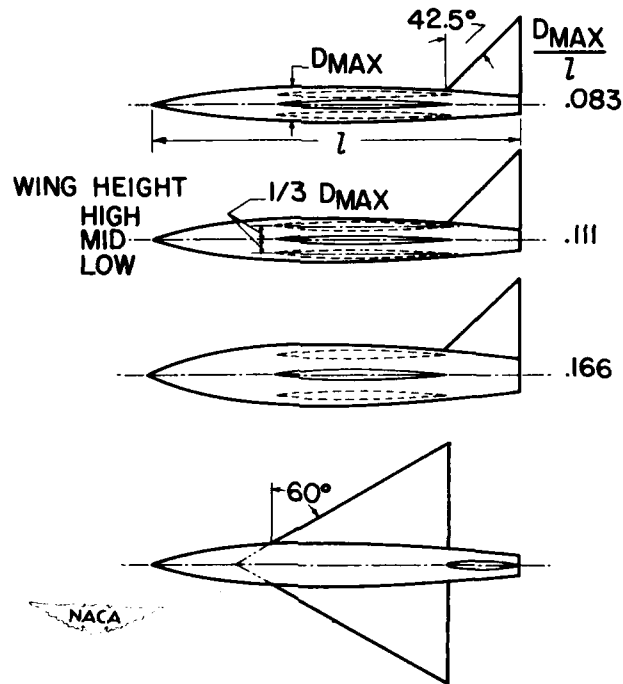


Figure 8.

## EFFECT OF WING HEIGHT ON TAIL LOAD

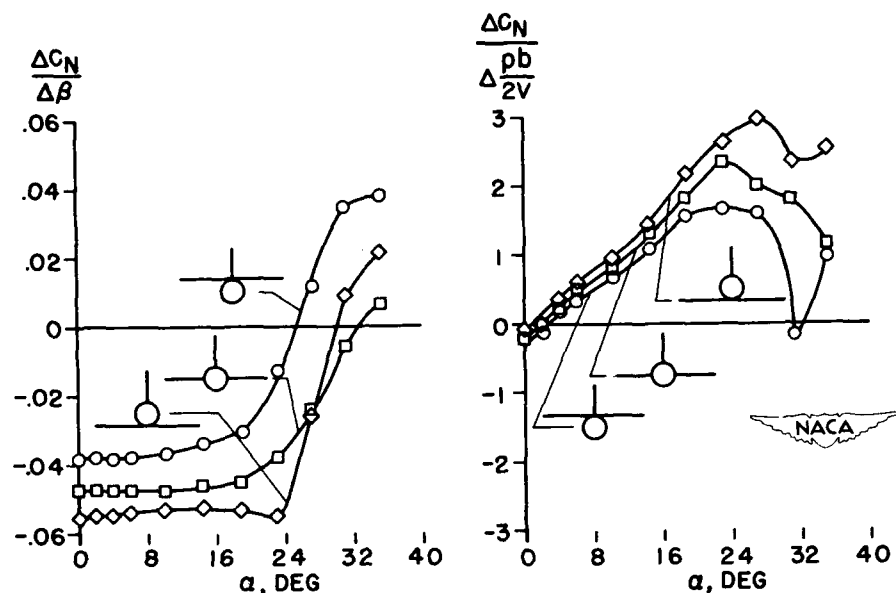


Figure 9.

## EFFECT OF WING AND FUSELAGE

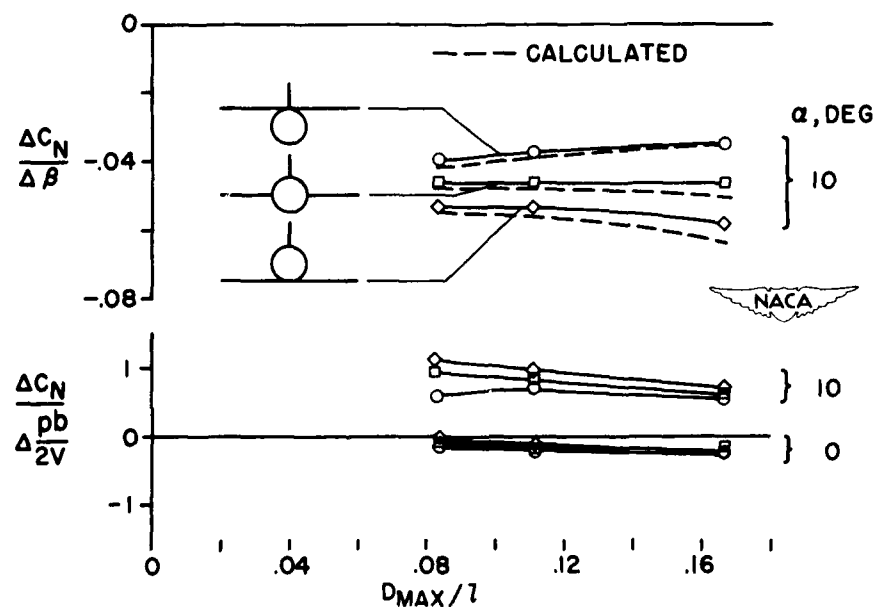


Figure 10.

**TECHNIQUE FOR  
FLIGHT LOADS  
MEASUREMENTS**

## A STRAIN-GAGE CALIBRATION PROCEDURE FOR FLIGHT LOADS MEASUREMENTS

By T. H. Skopinski

Langley Aeronautical Laboratory

Increasing use is being made of the wire-resistance strain gage in research flight testing as well as in structural investigations. Those who have used the strain gage to measure only stresses have probably experienced fewer difficulties than those who have made use of the strain gage to measure loads. The confidence established by the National Advisory Committee for Aeronautics with regard to the use of wire-resistance strain gages for flight loads measurements is based on the agreement of these loads measurements with integrated pressure distributions and with wind-tunnel results. The strain-gage experiences accumulated with research airplanes and many other structures have been detailed in reference 1, which discusses various calibration methods for relating strain-gage responses to applied loads, and also outlines the steps for the installation of the strain-gage bridges, the choice and application of the calibration loads, the evaluation of the calibration data, and the instrumentation techniques used to minimize the effects of drift and sensitivity changes.

Reference 1, however, includes only examples where loads are to be measured at the root stations and where the various gages of the combined bridges do not occur in different bays, as they might if loads were to be measured on a swept surface at an outboard station parallel to the airplane center line instead of perpendicular to the spar. These limitations of reference 1, together with the fact that several inquiries have recently been received with regard to loads calibration methods, make it appear that some further ideas and results obtained in instrumenting the B-47 airplane for loads measurement along the span might well be used to extend some of the principles involved. A B-47 airplane has been instrumented with strain gages at a number of spanwise stations parallel to the airplane center line in order to measure the span loading. However, the discussion and examples presented herein will be confined to briefly describing the laboratory phase of the calibration procedure for measuring the shear, bending moment, and torque at only two stations, one at the root and the other  $4\frac{1}{4}$  inches from the airplane center line (fig. 1). The problems encountered at these two stations are indicative of those normally encountered in measurement of wing or tail loads.

At each span station it is the practice to instrument the webs and flanges of each spar with several four-active-arm bridges, the number depending upon the duration of the tests and the expected bridge combinations. For loads applied outboard of a gage station, the bridges on the spar webs are expected to respond more to shear than to moment while those on or near the flanges are expected to respond more to bending

CONFIDENTIAL

moment than to shear, although each bridge can be expected to respond to the three primary loads at a given station, namely, shear, bending moment, and torque.

A relatively easy and flexible loads calibration procedure which makes use of this result is one in which point loadings are applied along the span at several chordwise positions. Such loadings give rise to influence coefficients which furnish the information about the response characteristics of each bridge as the load is moved along the surface and also provide the data for calculating the calibration constants of the bridge responses used in the load equations. Figure 2(a) shows typical influence coefficients obtained for 3 of the 10 individual bridges which were mounted at the root station and which were necessary to obtain a measure of the shear at this station. The responses of the front-spar shear bridge, the rear-spar shear bridge, and the rear-spar moment bridge to, say a 1,000-pound load, as it is moved to the 17.0-, 37.5-, and 58.0-percent-chord positions at various spanwise stations is indicated by the ordinate scale. It is to be noted that the responses of these particular bridges vary with the point of load application. The varying responses as the load is moved chordwise indicate a torque sensitivity, whereas variation in the spanwise direction indicates a moment sensitivity. Shear sensitivity is indicated by the intercept value at the gage station. It is obvious that none of the bridge responses shown gives a pure result, so the problem (in the case of shear) is to add or combine the available bridge responses in such a fashion as to obtain the same response no matter where the load is placed on the span. The results presented in figure 2(b) show that when the response of the front-spar shear bridge is added to the response of the rear-spar shear bridge the chordwise variation is reduced. In the general case, however, the shear-bridge responses are not usually added directly. When about 17.5 percent of the response from the rear-spar moment bridge shown in figure 2(a) is added to the results shown in figure 2(b), the spanwise and remaining chordwise variations of the shear bridges are eliminated. Figure 2(c) shows the desirable shear-bridge response obtained by these simple additions of various proportions of the individual bridge responses.

This simple picture of addition of individual bridge responses indicates that, in principle, at least, the shear at the root can be obtained by separately recording the responses of these three bridges and then multiplying by calibration constants. Likewise, the bridges can be combined electrically by properly attenuating the outputs of the three bridges to obtain a single record of the shear. Also, only two of the shear bridges, for example, could be electrically combined to reduce the torque sensitivity of these bridges, but the attenuating factors would be based on a shear equation which included an applied-moment term instead of the response of a moment bridge. Influence coefficient plots, of which the one shown in figure 2 is but a sample, have been employed to arrive at

CONFIDENTIAL

electrically combined bridges by means of which the shear, bending moment, and torque at a number of stations along the wing span of the B-47 may be determined. After the bridges were electrically combined on the basis of the foregoing principles, the structure was recalibrated.

Figure 3 shows the responses of the combined bridges for the root station. The horizontal line at the top of figure 3 shows that the electrical combination of three bridge responses to obtain a single record of shear produced the same results as were obtained in figure 2(c) by the simple addition of various proportions of the individual responses. The line sloping upward and passing through zero at the gage station, shown at the bottom of figure 3, indicates that the combined moment bridge responds linearly to the spanwise position of the load but is independent of the chordwise position. The straight line sloping downward at the top of figure 3 and going through zero at the gage station shows that the response of the combined torque bridge depends on the chordwise position of the resultant shear and not on the spanwise position (which is represented by the different symbols). All these desirable combined bridge responses were obtained by the proper attenuation of a multiple set of the three bridges whose characteristics are shown in figure 2(a). Combined bridges having these characteristics will enable an accurate determination to be made of the lateral and chordwise center of pressure.

The bridges at a station slightly outboard of the wing midsemispan were electrically combined and the structure was recalibrated. Figure 4 shows the combined bridge responses that are applicable to this station 414 inches from the airplane center line. The bridge-combination procedure used for this station was different from the one used for the root station in that, because of instrumentation limitations, only one of the secondary sensitivities was reduced or eliminated in the combined bridge responses. The shear-bridge response shown in the top of figure 4 includes a slight torque sensitivity, indicated by the different symbols, and the resultant moment sensitivity of this combined bridge is indicated by the varying response with spanwise position of load. The results for the combined moment bridge given in the bottom of figure 4 indicate that the torque sensitivity was eliminated, and the shear sensitivity present in the resultant response is given by the intercept at the gage station. The results for the combined torque bridge in the upper right portion of figure 4 show no spanwise variation, as indicated by the different symbols, and the response varies linearly with chordwise position of the load. The shear sensitivity of the resultant torque bridge response is represented by the intercept value at the gage station. The results for all three bridges indicate no effect from loads applied inboard of this gage station. The final load equations for measuring the shear, moment, and torque at wing station 414 would include the combined responses necessary to account for the secondary sensitivities noted in these three bridges.

The laboratory calibration of the structure is only one portion of the over-all procedure which must be considered in order to obtain adequate flight data from the strain-gage bridges. Provision must be made for obtaining adequate references, obtaining in-flight changes in sensitivity, accounting for drift, minimizing possible temperature effects, and providing adequate supporting instrumentation so that the structural loads, which the strain gage measures, can be properly analyzed.

The load on the airplane on the ground is a more easily determined reference than an in-flight reference which requires special maneuvers. In-flight changes in sensitivity are obtained by shunting a known resistance across one arm of the bridge and recording the deflection just before a given run. Drift is accounted for by recording the deflection of a galvanometer with the voltage removed from the circuit. The last two procedures, together with trace identification, are usually accomplished through a control box containing the appropriate sequencing switches and shunting resistances.

Some concern has been expressed about possible errors in structural load measurement with strain gages due to temperature effects. Uniform temperature changes throughout the structure cause difficulties only when materials have dissimilar thermal coefficients of expansion or when bridges are poorly matched. A method of correction when such conditions exist, based on measured structural temperatures, is given in reference 2. Temperature gradients associated with transient flight conditions and aerodynamic heating can have a direct effect on strain-gage bridges, and may also result in large additional stresses which would appear as fictitious loads. Some transient wing temperature distributions for dives with a high-speed airplane are given in reference 3. Although appreciable chordwise temperature gradients existed, and large temperature differences were encountered between the skin and adjacent spar caps, the temperatures were symmetrical or very nearly symmetrical about the chord plane or moment-of-inertia axis. For such symmetrical temperature distributions the induced stresses, though large, would also be symmetrical, and would have little effect on the measured structural loads, since the strain gages are also located symmetrically. The chordwise temperature gradients may introduce chord loadings, but, on structures tested so far, chord loads have not affected the usual bending moment or shear-bridge installations. For such cases it would appear, therefore, that flight loads measurements in dives are feasible. Unsymmetrical temperature and stress distributions can contribute fictitious structural loads which are not allowed for in the present loads-measuring methods. When rational design procedures for calculating temperature-induced stresses are developed, however, it should be possible, with the assistance of temperature measurements, to correct measured structural loads for these effects.

The supporting instrumentation used to reduce structural loads to aerodynamic loads can become quite large and, in fact, could comprise a

paper in itself. For instance, to obtain the aerodynamic loading at the root of the B-47 airplane, which has large underslung nacelles, requires measurements of accelerations along the span, a knowledge of the wing weight distribution, measurements of all three linear accelerations at the nacelles, and other measurements which are needed to correct for the gyroscopic moments imposed on the wings by the engine rotation.

In conclusion, it is believed that the present calibration technique, when combined with adequate supporting instrumentation and careful analysis of the results, can give reliable information on structural and aerodynamic loads under a wide range of operating conditions.

#### REFERENCES

1. Skopinski, T. H., Aiken, William S., Jr., and Huston, Wilber B.: Calibration of Strain-Gage Installations in Aircraft Structures for the Measurement of Flight Loads. NACA RM L52G31, 1952.
2. Harper, Paul W.: Wing and Fuselage Loads Measured in Flight on the North American B-45 and F-82 Airplanes. NACA RM L52L09, 1953.
3. Tendeland, Thorval, and Schlaff, Bernard A.: Temperature Gradients in the Wing of a High-Speed Airplane During Dives From High Altitudes. NACA TN 1675, 1948.

## B-47 WING STRAIN-GAGE INSTALLATION

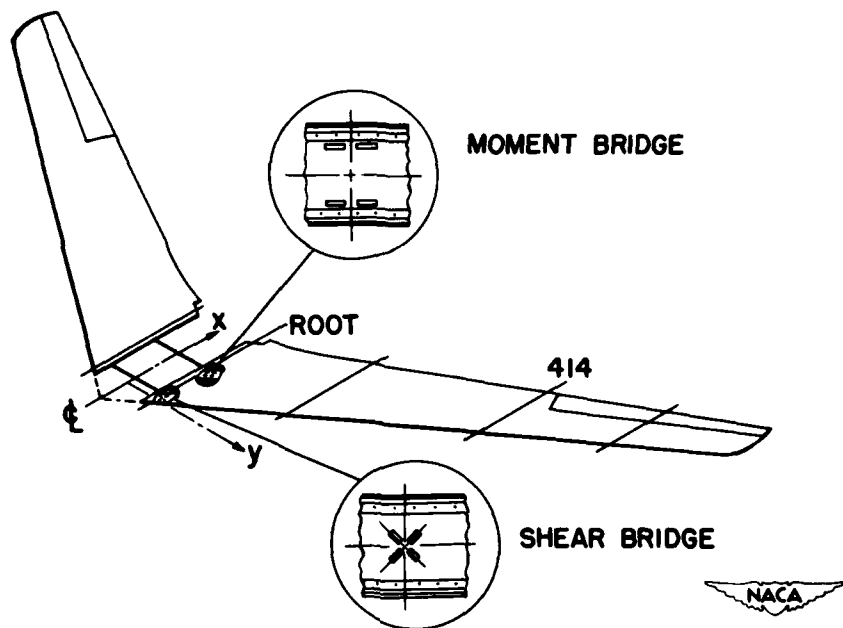


Figure 1.

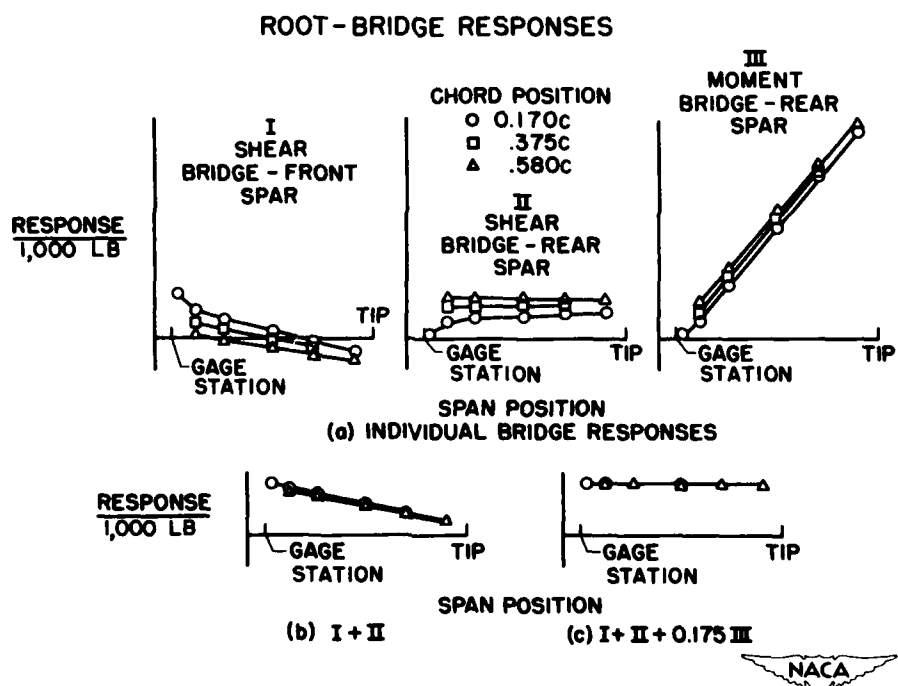


Figure 2.

## COMBINED BRIDGE RESPONSE FOR ROOT STATION

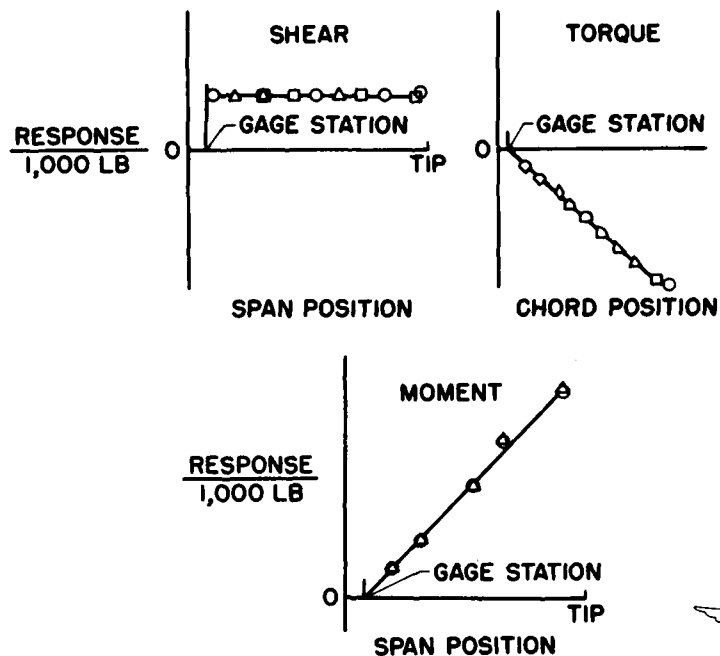


Figure 3.

## COMBINED BRIDGE RESPONSE FOR STATION 414

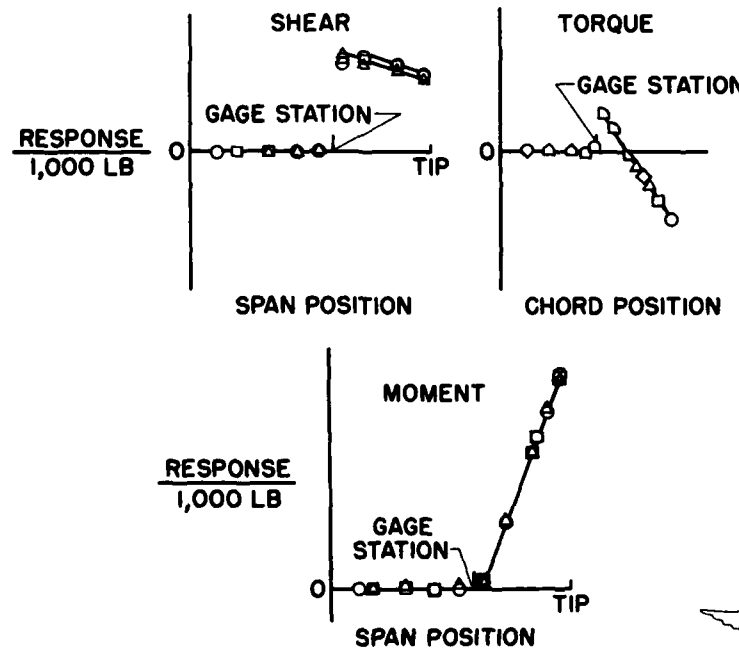


Figure 4.

**CONFIDENTIAL**

**209**

## **GUST LOADS**

**CONFIDENTIAL**

THE VARIATION OF ATMOSPHERIC TURBULENCE WITH ALTITUDE  
AND ITS EFFECT ON AIRPLANE GUST LOADS

By Robert L. McDougal, Thomas L. Coleman,  
and Philip L. Smith

Langley Aeronautical Laboratory

The purpose of this paper is to describe some of the characteristics of high-altitude turbulence pertinent to the gust-load problem and, in addition, to illustrate, by example, some possible trends in gust and load experience for given flight operations at high altitudes.

SOURCES AND SCOPE OF DATA

Investigations of clear-air turbulence at high altitude by the National Advisory Committee for Aeronautics have been in progress for the past several years with the cooperation of the Air Force, the Weather Bureau, and Consolidated Vultee Aircraft Corporation. Figure 1 shows the sources and scope of the data available at this time. The sources are illustrated by the sketches of the parachute and the airplane at the top of figure 1. The numbers in the columns show the scope of the data available from each source.

Telemeter.- The first source of data, the NACA turbulence telemeter, is represented by the sketch of the parachute. The telemeter is transported aloft by a balloon and measurements of the vertical gusts are obtained during the descent of the parachute following balloon burst. The numbers in the column below the parachute indicate that 650 to 800 soundings have been obtained within each 10,000-foot altitude interval up to 60,000 feet over a period of a year. These data were collected from installations at four stations in this country: Caribou, Maine; Grand Junction, Colorado; Greensboro, North Carolina; and Miami, Florida.

Airplane.- The second source of information is time-history records of airspeed, altitude, and nodal acceleration from flights of B-36 airplanes. Records representing 21,000 to 66,000 miles of flight have been collected within each 10,000-foot altitude interval. These flights were conducted mostly over the continental United States and include flight up to altitudes of about 47,000 feet. When these airplane records are used to obtain gust velocities, the vertical arrows indicate that the acceleration data were utilized to evaluate the vertical gusts, whereas the horizontal arrows indicate that the rapid fluctuations in airspeed were utilized to evaluate the horizontal gusts.

## EVALUATIONS OF DATA

In evaluating the airplane acceleration data, a revised gust equation and alleviation curve, as shown in figure 2, have been used. The NACA is now evaluating statistical airplane-acceleration data obtained in turbulent air on this basis, and the work of converting previously reported data to this basis is in progress. The new alleviation or gust factor is based on airplane mass ratio  $(\mu_g = \frac{2W/S}{\rho cmg})$  and the gust shape as shown. Acceleration data reduced by this method yield gust velocities which are directly comparable in magnitude to those required by Air Force - Navy design standards.

The records from both the telemeter and the airplane also have been used to evaluate the length and thickness of the turbulent areas encountered, and the percentage of rough air that might be expected at the different altitudes. Also, an attempt has been made to determine from the telemeter data the effect of geographical location and of season on the variation of the amount of turbulence with altitude.

Certain differences in the types of gust measurements which have been made will affect the results. For example, the telemeter traverses the atmosphere vertically whereas the airplane traverses horizontally. This difference raises a question concerning the equivalence of horizontal and vertical sampling distances. Also, the telemeter and air-speed fluctuation measurements can be considered to be substantially point-source measurements when compared with the normal-acceleration measurements on the airplane which give the integrated effect of the gust over a large flexible wing. For these reasons, differences are found in the gust-intensity data from the three sources. Although these differences have not been completely resolved, the three sets of data show the same trends with increasing altitude.

## RESULTS

The principal results deal with the trends with altitude of the intensity of the turbulence and in the amount of rough air encountered. On the basis of the work to date, it is felt that the trends to be shown are well-established and will not change appreciably with further analysis.

Intensity of turbulence. - Figure 3 shows the variation in the gust intensity or velocity with altitude. The ordinate is altitude and the abscissa is a ratio of indicated gust velocities; that is, the indicated gust velocity expected for operation at a given altitude level to that expected in an equal distance in rough air at the lowest level. The

CONFIDENTIAL

different symbols represent results from the three sources of data. The curve represents an estimated mean variation based on all three sources and indicates that the gust velocity may be expected to decrease by approximately 10 percent for each 10,000-foot increase in altitude. For example, the point at 35,000 feet indicates that the expected maximum indicated gust velocity in the 30,000- to 40,000-foot interval is 0.7 of the maximum indicated gust velocity expected in an equal operating distance in rough air within the 0 to 10,000-foot interval.

Amount of turbulence.- The variation in the amount of turbulent air with altitude is shown in figure 4. The ordinate is altitude and the abscissa is the percent of total-flight distance which was spent in rough air. The curve which shows the variation with altitude is a composite obtained from the telemeter and airplane data. A considerable reduction in the amount of rough air is indicated for increasing altitudes.

Separate studies of the telemeter data from the four stations showed that there was no significant variation from the curve shown in figure 4 with geographic location of the station. In regard to seasonal effects, investigations showed that the percentages of rough air by altitude during the winter months were slightly higher than for the other three seasons.

Size of turbulent areas.- Studies of the data have indicated that the clear-air turbulence occurs in small areas or patches. Figure 5 shows the expected distribution by length for an assumed 1,000 areas of turbulence based on B-36 data for operations above 20,000 feet. The ordinate of the figure is the number of areas and the abscissa is the length of the areas. The bars represent the number of areas out of 1,000 which are expected to fall in the given 10-mile class interval. (For example, 320 of the areas would be expected to be between 10 and 20 miles in length.) The figure shows that the expected number of areas decreases rapidly as the length increases and indicates that areas greater than about 50 miles in length can be considered unusual.

Figure 6 shows the expected distribution by thickness for an assumed 1,000 areas of turbulence based on turbulence-telemeter data taken above 20,000 feet. The figure is similar to figure 5 and indicates that the expected number of turbulent areas decreases rapidly as the thickness increases. As indicated in figure 6 turbulent areas greater than 2,000 feet thick may be expected to occur infrequently.

The distributions of turbulent areas by length and thickness shown in figures 5 and 6 showed no variation with altitude for levels above 20,000 feet. Below this altitude, however, the distribution of the dimensions of the turbulent areas tend to change slightly, more extensive areas becoming more frequent.

It should be specifically pointed out that the atmospheric turbulence discussed in reference to figures 3 to 6 and referred to as clear-air type of turbulence is considered to result from wind shear or mechanical action as distinct from that due to convective activity, such as thunderstorms.

#### APPLICATION TO AIRPLANE OPERATIONS

In actual operation, aircraft encounter not only the more frequent and lower intensity clear-air turbulence which has been discussed in the preceding section but they also encounter convective turbulence. In addition, gust histories to some extent and gust load histories to a greater extent depend upon the airplane and operating characteristics. In order to obtain an estimate of the total gust history for any operation all the gusts which occur in the different conditions must be combined in the proper proportions. A complete discussion of the manner in which this may be done is too detailed to be presented herein. The basic principals involved, however, are outlined.

General considerations.- Operation of an airplane with respect to turbulence can be divided into three phases: operation in smooth air, operation in a clear-air type of turbulence, and operation in convective type of turbulence. For airline operations which are considered in this paper, most of the flight distance is in smooth air. The balance of the flight is spent in either convective or in a clear-air type of turbulence. The shaded areas of figure 7 show the ranges within which the gust distributions for these two types of turbulence are likely to fall. The data used in determining the convective-turbulence region were taken from references 1 to 3 and cover an altitude range from 5,000 to 35,000 feet. The region for the clear-air turbulence was determined from data reported in references 3 to 5 and covers an altitude range from 0 to 10,000 feet.

In order to obtain specific distributions of gusts in rough air for the two types of turbulence, the solid lines were drawn in the respective areas such that the shapes of the gust-frequency distributions obtained from actual airline data were approximated. This was done on the basis that, for the complete distribution of gusts for an airline operation, the shape of the curve at low gust velocities results from clear-air turbulence whereas the shape of the distribution for the large gusts results from flight through convective turbulence (ref. 6). On the basis of these considerations, distribution curves were obtained which were at the upper limit of the clear-air region and close to a mean line for the convective-type turbulence.

In regard to the intensities and number of gusts of the clear-air type encountered, the distribution shown in figure 7 was assumed to represent airline experience in rough air up to 10,000 feet. For the higher altitude intervals, similar curves for clear-air-type turbulence were obtained by multiplying the abscissa of the curve by the gust velocity ratio given in figure 3. In this manner, a family of distributions were obtained that represent the appropriate distribution within each 10,000-foot-altitude interval. The contribution of the clear-air turbulence to the total expected distribution within an altitude interval was then found by multiplying the number of gusts per mile of rough air taken from the distributions by the appropriate percent of flight distance (fig. 8) in rough air for the altitude. The values shown for clear-air turbulence in figure 8 were taken directly from figure 4 which gives the percent distance in clear-air turbulence by altitude.

When the number and intensity of the gusts of the convective-type turbulence are considered, reference 2 has indicated that the turbulence per mile within convective clouds does not vary with altitude; therefore, the curve shown in figure 7 can be assumed representative for operation in turbulence of this type at all altitudes. No straightforward curve (such as given in fig. 4 for clear-air turbulence) has been determined to show the variation in the amount of convective-type turbulence with altitude. The percentages shown in figure 8 for this type turbulence were therefore determined in the following manner:

The amount of turbulence for the lowest level, 0.1 percent, was found as a by-product of selecting typical curves for the two types of turbulence as described previously. Actually, this amount of convective turbulence was assumed to depend on two factors: Whether turbulence exists along the flight path and the chance of avoiding the turbulence by visual means. The variation with altitude of the existence factor was taken to be crudely proportional to the height to which convective-type thunderstorm clouds develop as reported in reference 7. As to the variation with altitude of the avoidance factor, the value from 10,000 to 20,000 feet was assumed to be the same as for the lowest level. From 20,000 to 40,000 feet the chance of avoiding this type of turbulence was assumed to vary linearly at a rate again roughly proportional to cloud heights (ref. 7). Above 40,000 feet this chance was assumed to increase rapidly to 100 percent in the highest interval considered, 50,000 to 60,000 feet; that is, it was assumed that all convective turbulence above 50,000 feet could be avoided. The product of the number of gusts per mile of rough air from the distribution in figure 7 and the percent of flight distance for convective turbulence shown in figure 8 gives the contribution of this type of turbulence to the total distribution in any altitude interval.

The contributions from each of the two types of turbulence for each altitude interval can be added to give a family of gust distributions

representing the number of gusts per mile of flight for each interval as shown in figure 9.

Operational considerations.- The estimated total gust history for a particular operation can now be found by multiplying each of the distributions shown in figure 9 by the appropriate flight distance within that altitude, which can be determined from the expected altitude profile of the particular operation.

The history of acceleration increments or loads can be estimated by use of the gust-load equation shown in figure 2. Two factors, which are not simple airplane characteristics, must be given special consideration depending upon the operating conditions: the operating airspeeds and the operating weights. When the variation with time of airspeed and weight is known, the conversion of the distributions can be performed by using average airspeeds and weights for various flight conditions and altitudes and then combining the separate contributions to the load history in each of the conditions used.

#### EXAMPLE OF AIRLINE OPERATION

In order to illustrate the type of gust-history estimates that can be made and to indicate possible trends in gust loads with altitude, the procedure outlined in the preceding section has been performed for two types of airline operations. Figure 10 shows the altitude and airspeed profiles used in making estimates for a representative present-day airline operation (shown by the dashed lines) and a possible future jet airline operation (shown by the solid line). The future operations represented by the solid line are conducted within the 30,000- to 40,000-foot level whereas the present-day operations represented by the dashed line are conducted at a lower level.

Gust history.- The estimated gust histories for these two operations are shown in figure 11. The ordinate is the number of gusts and the abscissa is gust velocity. The curves show for the two operations the number of gusts of a given intensity which are expected in  $10 \times 10^6$  miles of flight. It is evident from the positions of the curves that the number of gusts estimated for this future operation is substantially less than that for the present-day type of operation. For example, the curves indicate that a gust velocity of 32 feet per second would be equaled or exceeded 100 times during present-day type of operations whereas only ten gusts of this intensity, or one tenth the number, would be expected for the future operations. This reduction is a direct reflection of the increased operating altitude for the future operations, as indicated at the top of figure 10.

Load history.- From these gust histories by taking into account the airspeeds (shown in fig. 11) and the airplane characteristics, the distribution of gust loads for each operation can be calculated and are shown in figure 12. This figure shows the distribution of acceleration increments, or loads, for the two operations. The curves represent the expected number of acceleration increments of a given value which will be equaled or exceeded in  $10 \times 10^6$  miles of flight. In order to show only the effects of the operational differences, no attempt has been made to account for structural and aerodynamic design differences which would undoubtedly exist in airplanes designed to perform these two operations.

The locations of the curves indicate that loads greater than  $1g$ , which are of interest when considering ultimate loadings, occur more frequently for the future operations. For example, accelerations equal to  $1g$  may be expected to occur five times more often for the type of future operations considered here than for present-day operations. This increase in the number of loads is the direct result of the higher operating airspeeds through the lower altitudes (during climb and descent) as were shown in the flight plan in figure 10. The location of the curves for the smaller and more frequent acceleration increments, which are of interest from a structural fatigue standpoint, indicate the same number of loads for both operations; consequently, no change from present conditions is anticipated if future flight operations will be of the type assumed herein. It is, therefore, apparent that the reductions in the number and intensity of the gusts encountered at the higher altitudes may not be reflected in a similar reduction in loads for future operations.

#### EXAMPLE OF MISSILE OPERATION

A similar procedure, such as was used for making estimates for airplane operations, can be used in estimating the gusts expected for missile operations. Considerable judgment, however, is necessary in applying this type of gust data to missiles. Since the configuration, speed, and stability of missiles may differ greatly from those of airplanes, it is doubtful whether the gust data derived from the airplane acceleration data are directly applicable to missiles. Consequently, more reliance has been put on the turbulence-telemeter data and airspeed-fluctuation measurements, which are probably not influenced significantly by airplane characteristics, than on gust data derived from airplane acceleration data. In addition, since the operational plan of the missile may be quite different from the airplane, the percentage of time spent in rough air may be different for the missile than for the airplane.

A comparison of the estimated gust history for a missile operated in clear air with operations assuming a reasonable amount of thunderstorm flight is given in figure 13 as an illustration of the type of results that

can be obtained. The inset in figure 13 shows the flight plan that was assumed for the calculations. The flight covers 200 miles; the climb and descent are made at an angle of  $45^{\circ}$ ; and level flight at 60,000 feet. The ordinate of the figure is the number of gusts and the abscissa, the gust velocity. Two curves are shown representing the distribution of gusts for 1,000 flights of the missile for each of the two operations. The lower curve pertains to flights in which no thunderstorms are encountered. The upper curve pertains to flights in which thunderstorms are encountered to an extent based on the average prevalence of thunderstorms over the United States and for which the assumption is made that there is no chance of avoiding the thunderstorms if they exist. It is obvious that the presence of thunderstorms along the flight path greatly influences the number and intensity of the gusts expected.

#### SUMMARY

In summary, data are available on the number and intensity of atmospheric gusts to altitudes of about 60,000 feet. The trends with altitude of these data, which are not expected to change appreciably, indicate substantial reductions in the amount and severity of turbulence at the higher flight altitudes. By using available information some estimates of gust distributions for particular operations have been made in order to predict possible trends. On the basis of the specific example considered, it was shown that the reduction in the number and intensity of gusts due to higher operating altitudes may not be reflected in a reduction of loads in future high-altitude transport operations.

## REFERENCES

1. Press, H., and Binckley, E. T.: A Preliminary Evaluation of the Use of Ground Radar for the Avoidance of Turbulent Clouds. NACA TN 1684, 1948.
2. Tolefson, H. B.: An Analysis of the Variation With Altitude of Effective Gust Velocity in Convective-Type Clouds. NACA TN 1628, 1948.
3. Steiner, Roy: An Evaluation of Air-Borne Radar as a Means of Avoiding Atmospheric Turbulence. NACA RM L8I01, 1948.
4. Binckley, E. T., and Funk, Jack: A Flight Investigation of the Effects of Compressibility on Applied Gust Loads. NACA TN 1937, 1949.
5. Funk, Jack: Measurements of Atmospheric Turbulence on Seattle-Alaska Airways. NACA RM L7I25, Bur. Ships, 1947.
6. Press, Harry: The Application of the Statistical Theory of Extreme Values to Gust-Load Problems. NACA Rep. 991, 1950. (Supersedes NACA TN 1926.)
7. Anon.: The Thunderstorm. U. S. Dept. of Commerce, June, 1949.

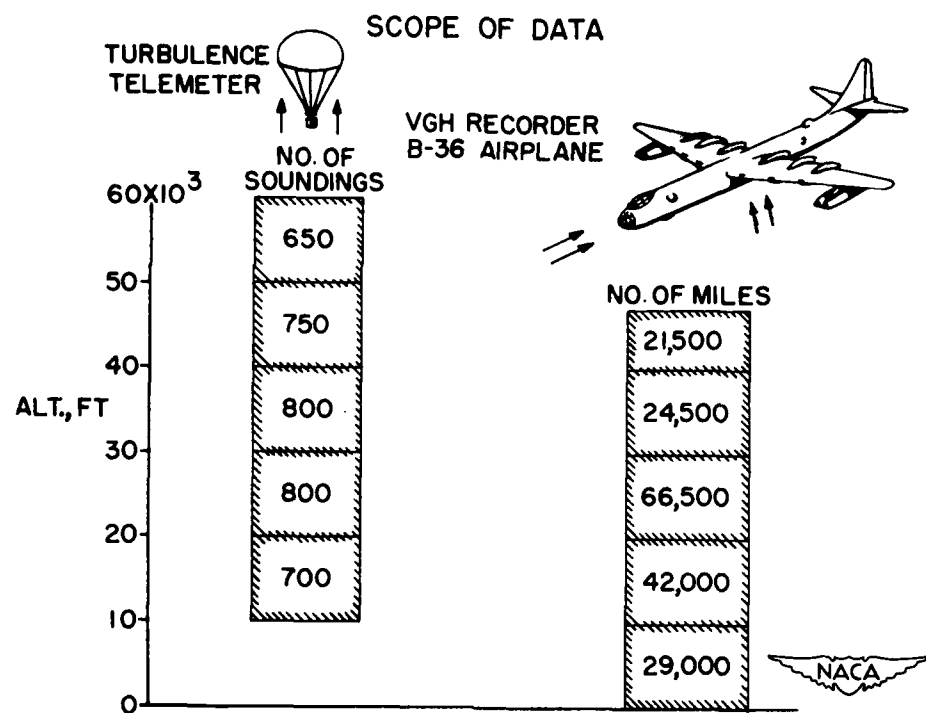


Figure 1.

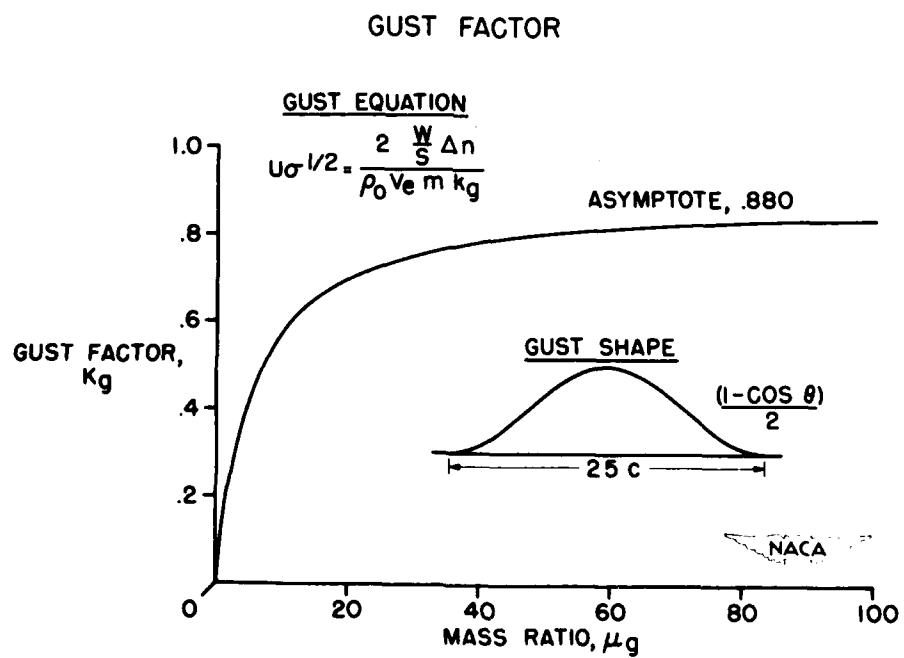


Figure 2.

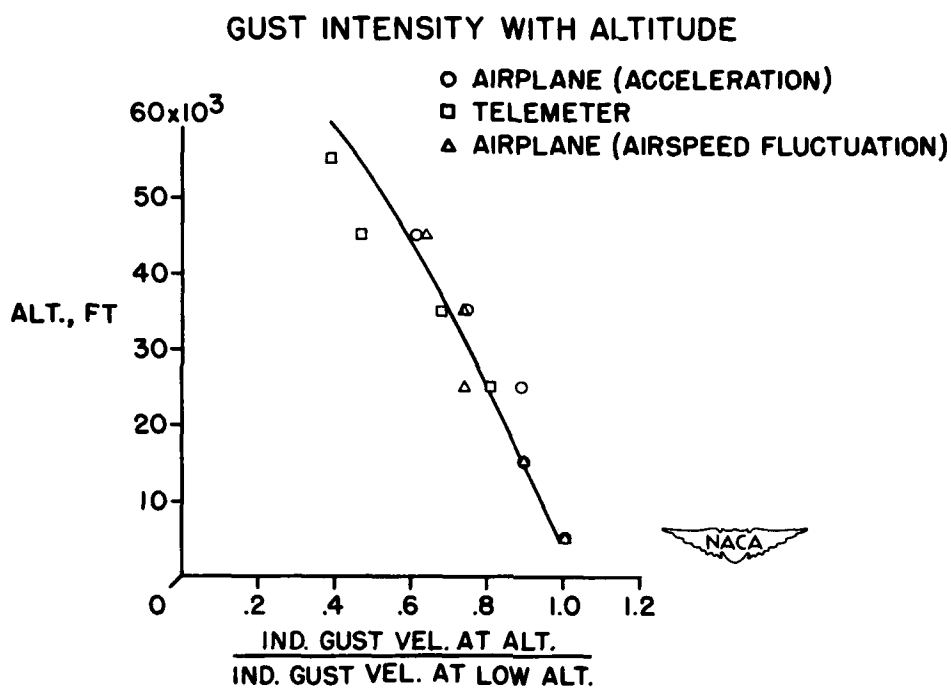


Figure 3.

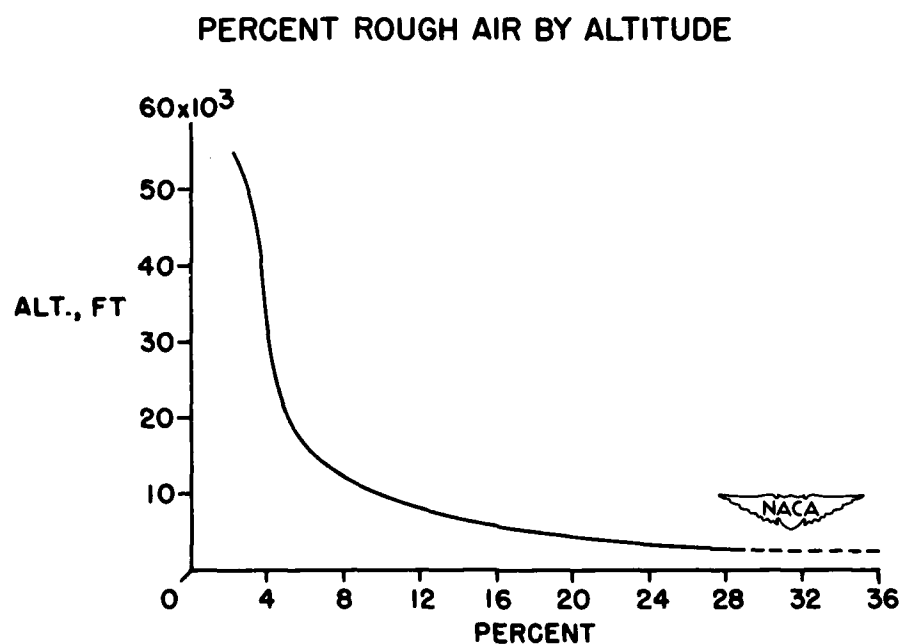


Figure 4.

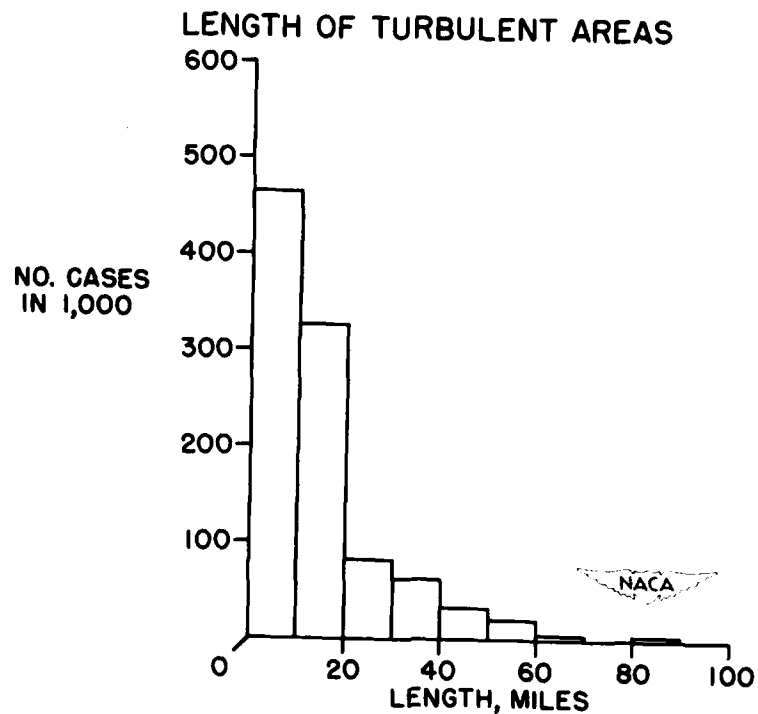


Figure 5.

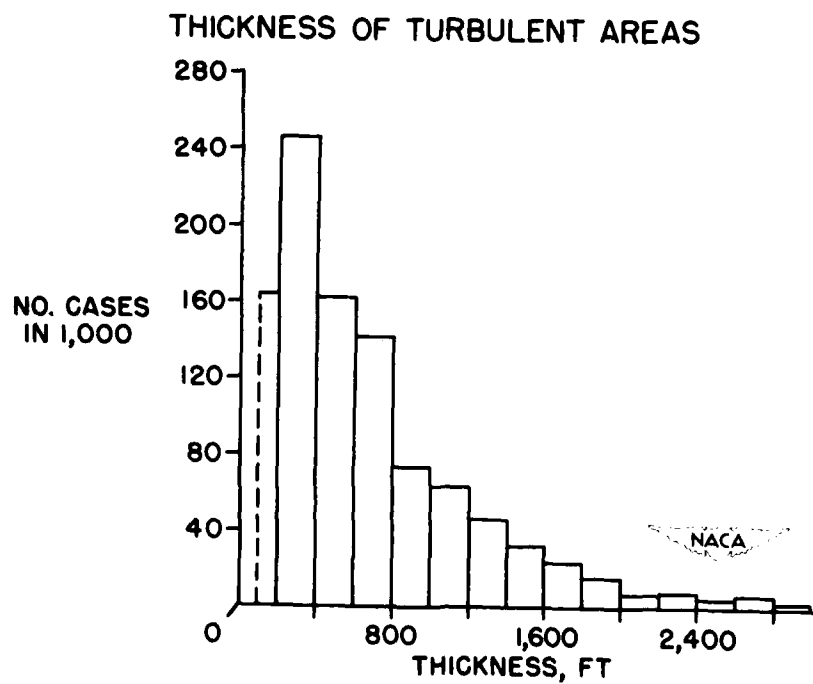


Figure 6.

## DISTRIBUTIONS OF GUST VELOCITIES

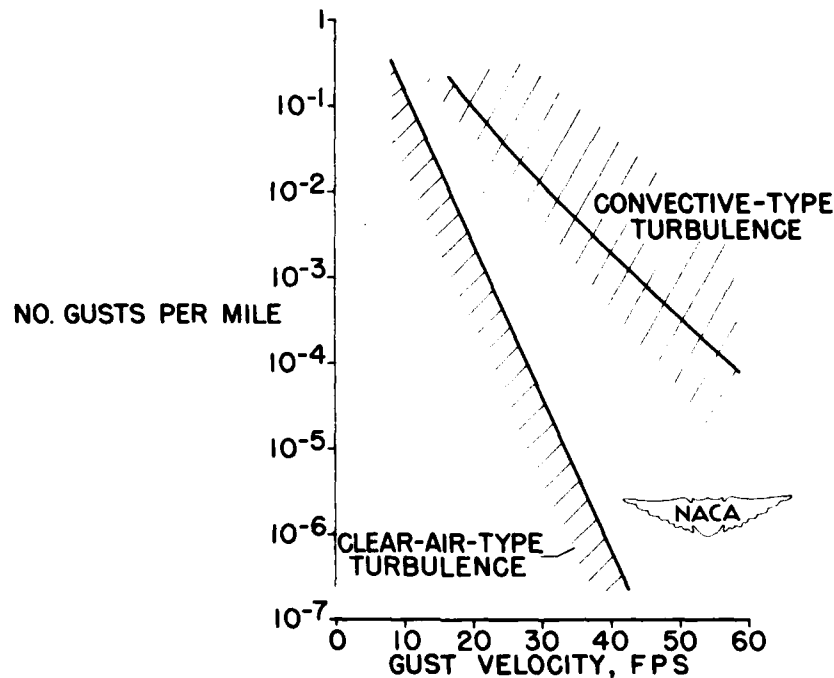


Figure 7.

## TURBULENCE ENCOUNTERED BY ALTITUDE

ALTITUDE, FT	PERCENT DISTANCE IN TURBULENCE	
	CONVECTIVE TYPE	CLEAR-AIR TYPE
50,000 TO 60,000	0	2.2
40,000 TO 50,000	.0017	3.4
30,000 TO 40,000	.0067	3.9
20,000 TO 30,000	.062	4.5
10,000 TO 20,000	.11	6.4
0 TO 10,000	.10	18.0

NACA

Figure 8.

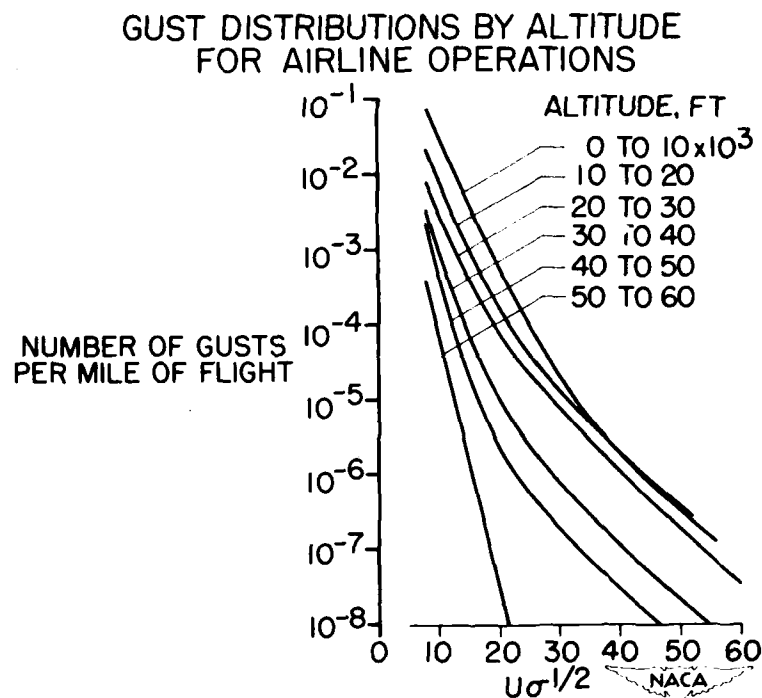


Figure 9

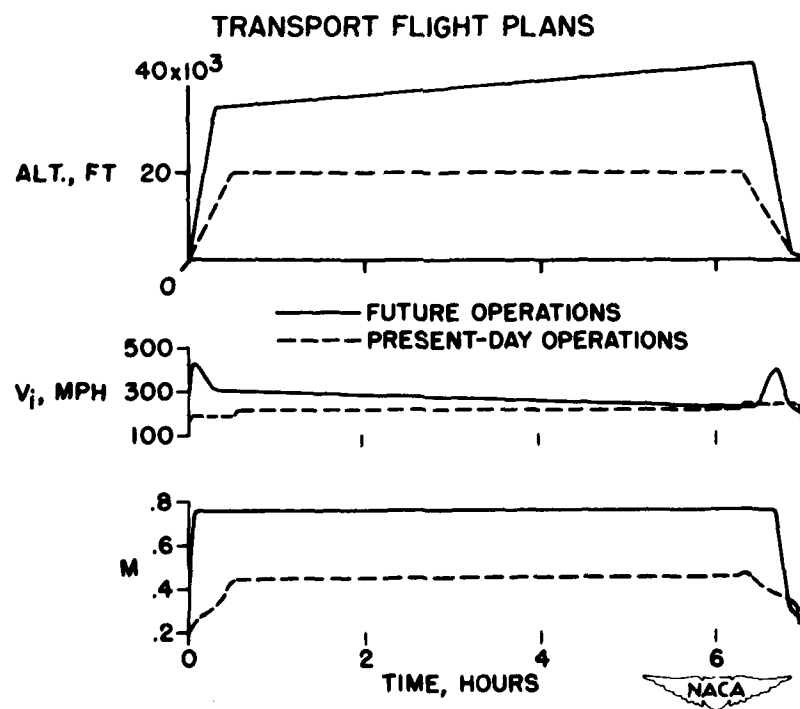


Figure 10.

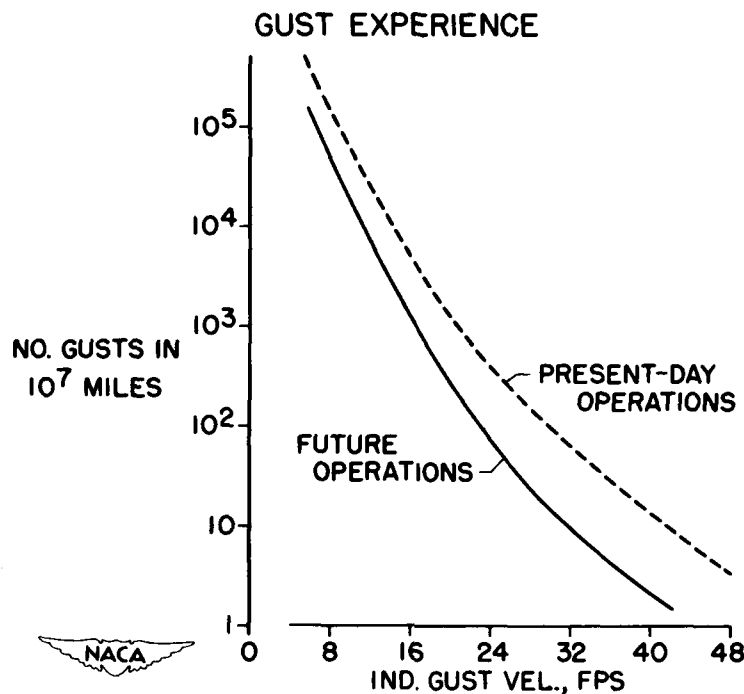


Figure 11.

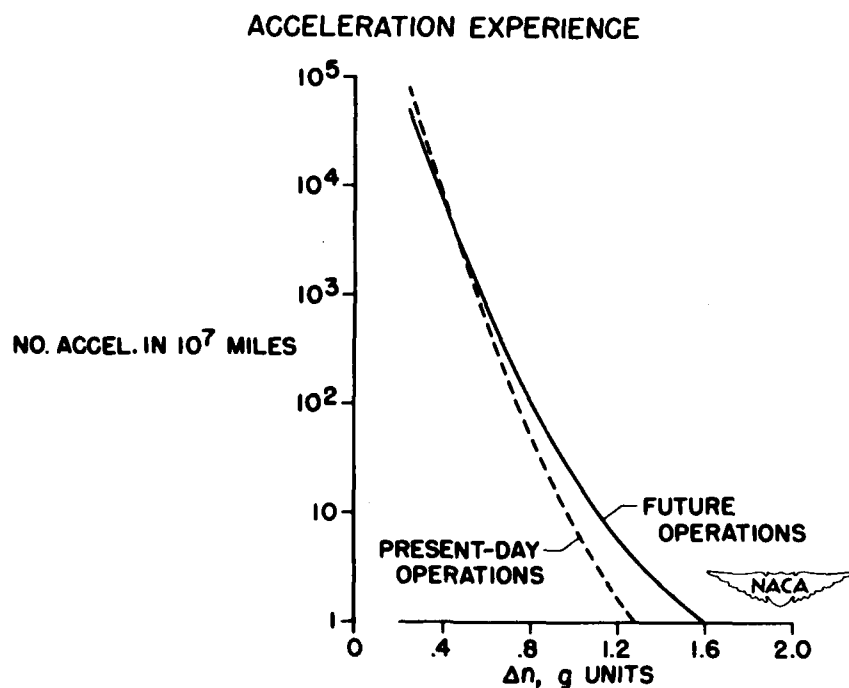


Figure 12.

CONFIDENTIAL

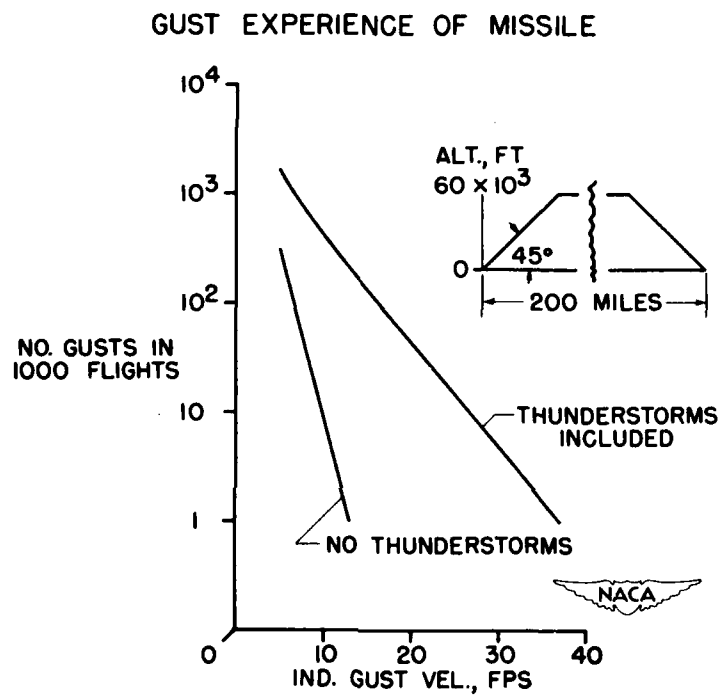


Figure 13.

CONFIDENTIAL

THEORETICAL LIFT DEVELOPED ON RECTANGULAR WINGS ENTERING  
GUSTS AT SUBSONIC AND SUPERSONIC SPEEDS

By Harvard Lomax

Ames Aeronautical Laboratory

INTRODUCTION

Theoretical studies of wings traveling in an incompressible medium and penetrating vertical gusts are well-advanced. These studies are based on the classical solutions of two-dimensional wings in unsteady flow by Wagner, Küssner, and Von Kármán and Sears (refs. 1 to 3) and the extension of these solutions to include wings of finite aspect ratio by Robert T. Jones (ref. 4). Such basic results have been used by several authors to estimate the effects of gust shape, airplane pitching, and wing bending on the airplane response to gust penetration.

Results analogous to the Wagner and Küssner solutions but applicable to wings flying at supersonic speeds have also been obtained (refs. 5 to 8); and Miles and Goodman (refs. 9 and 10) have extended these solutions to include finite-aspect-ratio wings having rectangular plan forms.

The analysis upon which the results of this paper have been derived are based on linearized, compressible-flow, thin-airfoil theory. The methods used to obtain the basic lift responses - analogous to the Wagner and Küssner solutions - for a two-dimensional wing traveling at subsonic speeds are given in reference 11 and the method used to calculate the dynamic response of the unrestrained airplane is given in reference 8. A more detailed presentation of the following material is given in reference 12 (prospective NACA paper).

TWO-DIMENSIONAL WING PENETRATING SHARP-EDGED GUST

Consider the lift response of a two-dimensional wing to a unit sharp-edged vertical gust. If the section is restrained so that it cannot move up or down (represented physically by a high-aspect-ratio, rigid wing mounted on an airplane that is extremely dense relative to the surrounding air), the corresponding increment in lift caused by the gust penetration is shown in figure 1. The wing section represented in figure 1 is moving from right to left and is shown 0.3, 3.3, and 6.3 chord lengths after its leading edge met the gust front. The increment in load distribution is presented at each of these positions for Mach numbers equal to 0, 0.8,

CONFIDENTIAL

1.0, and 1.2. The integrated values of the load distribution, represented by the section lift coefficient, are shown at corresponding positions for the Mach number range 0 to 1.2. (The significance of the results presented in figure 1 can be more readily assessed when it is pointed out that unrestrained airplanes with moderate density ratios - for example, an airplane flying at 12,000 feet and having a wing loading of 80 lb/ft<sup>2</sup> and a mean chord of 15 feet - reach their maximum accelerations after moving from 6 to 10 chord lengths into a sharp-edged gust.)

Note that initially the load distributions on the wings moving at  $M = 0.8$  and  $1.0$  are lower than that on the wing moving at  $M = 0$ . After about 3 chord lengths have been traveled, the loadings are all nearly the same and, at 6.3 chord lengths, the loading shown for  $M = 1$  is considerably above the other two especially in the vicinity of the trailing edge. The variation of section lift coefficient, shown in the upper part of figure 1, is seen initially to decrease with increasing Mach number. After 3.3 chord lengths have been traveled, however, the curves show a slight rise at  $M = 1$  and, at 6.3 chord lengths, a pronounced peak has developed at that Mach number.

It is apparent from these curves that the Prandtl-Glauert rule is not appropriate as a compressibility correction in the range of gust response presented. In fact, the data in figure 1 show that, after a restrained two-dimensional wing flying at  $M = 1$  has moved 6.3 chord lengths into a sharp-edged gust, its section lift is only about 70 percent more than it is at  $M = 0$ .

Figure 2 gives a more comprehensive picture of the Mach number effect on the lift induced by a sharp-edged gust. The values of the lift coefficient shown in figure 1 are cross plots taken from figure 2 at the appropriate chord length of penetration. The results shown apply to a two-dimensional wing: The solid lines represent a wing traveling at supersonic speeds; the dashed lines, one traveling at subsonic speeds; and the broken line, one traveling at the speed of sound. In effect, these curves show the variation of Küssner's solution, the one labeled  $M = 0$ , with Mach number. Note that the variation is complicated because the shapes of the curves differ with time; therefore, a simple compressibility correction to Küssner's curve, applicable throughout the Mach number range shown, is not feasible.

The results just discussed were derived for a restrained wing. When the wing is unrestrained, it begins to move upward as soon as the leading edge strikes the gust front. As indicated in figure 3, the load distribution previously shown for the restrained wing forms then only a component of the total loading. The second component, which is induced by the vertical motion of the wing, acts as a relieving force and eventually reduces the gust-induced lift increment on the unrestrained wing to zero.

CONFIDENTIAL

Physically, the second component corresponds to the lift increment caused by a step change in angle of attack and is referred to as an indicial response. At first this indicial loading is completely different from that induced by the gust on a restrained wing although eventually the two load distributions are identical except for sign.

Figure 4 shows the variation of the indicial lift coefficient with chord lengths of travel for the Mach number range 0 to 2. In effect, figure 4 shows the variation of Wagner's curve, the one labeled  $M = 0$ , with Mach number and, again, it is apparent that no simple compressibility correction can be applied to extend the  $M = 0$  solution throughout the Mach number range shown. The final lift induced by a sharp-edged gust on an unrestrained, rigid, nonpitching wing is determined by superimposing the two components of loading illustrated in figure 3, the proportion of each being governed by an integral equation presented, for example, in reference 8.

The actual difference in lift response between a restrained and an unrestrained wing is shown in figure 5. The upper curves (solid lines) show the variation of section lift on a restrained wing and the lower curves (dashed lines) show the variation on an unrestrained wing. The value of 100 for  $\mu$ , the wing-air density ratio, is probably a lower limit of practical interest for high-performance aircraft; it represents, for example, an airplane flying at sea level with a wing loading of 46 lb/ft<sup>2</sup> and a 10-foot wing chord. The actual expression for  $\mu$  is shown in figure 5 where  $m$  is the airplane mass;  $\rho$ , the air density;  $S$ , the wing area; and  $c$ , the wing chord.

Maximum values taken from these and similar gust-lift response curves are shown in figure 6 as a function of Mach number and for various wing-air density ratios. The compressibility effect inherent in these results is separated out in figure 7 where the ratio of the maximum lift increment at a given Mach number to its value at  $M = 0$  is shown as a function of Mach number for three density ratios. Note that, at Mach numbers where the Prandtl-Glauert compressibility correction, represented by the curve for  $\mu = \infty$ , shows a 100-percent increase in the lift response, the increase due to compressibility for airplanes with density ratios from 100 to 300 is about 50 percent. Note further that at high supersonic speeds there is little difference in  $(\Delta c_l)_{max}$  between wings for which  $\mu = \infty$  and  $\mu = 100$ .

#### THE EFFECT OF ASPECT RATIO

Consider the effect of aspect ratio on the sharp-edged gust response. Typical results applicable to wings flying at supersonic speeds are shown

in figure 8. The increment in lift induced by the gust penetration is shown for  $M = 1.2$  as a function of chord lengths of travel. The dashed curves represent the two-dimensional results previously discussed and the solid curves represent results for a rectangular wing of aspect ratio 5. The effect of aspect ratio is to reduce the lift throughout the time interval shown.

The effect of aspect ratio on the maximum lift increment induced on a rectangular wing penetrating a sharp-edged gust is presented in figure 9. The curves for  $\mu = \infty$  represent the steady-state lift-curve slopes taken from various published sources. The solid lines for values of  $\mu$  equal to 100 and 300 were calculated from the aforementioned solutions given by Jones and Miles (refs. 4 and 9). The dashed lines extending through the subsonic speed range are interpolated values having the  $\mu = \infty$  curve as their guide. It should be mentioned that the solid lines for the  $A = 5$  case are extended down from the supersonic side to the  $M = 1$  line. This extension is possible because the solutions presented by Miles are valid over a wing of aspect ratio 5 for the first 13 chord lengths of travel at  $M = 1$  and this time interval is sufficient to establish the maximum point on the gust-response curves for  $\mu \leq 300$ .

#### THE EFFECT OF GUST SHAPE

Consider the effect of gust structure on the results previously presented. For this purpose, the sharp-edged gust was replaced by a triangular gust having its apex 12 chord lengths from the front. The maximum increment in lift induced on a two-dimensional wing penetrating such a gust is shown in figure 10 for a range of Mach numbers and for several wing-air density ratios. Note that the lift increment at  $M = 1$  is now finite even for a restrained two-dimensional wing, being, in fact, less than twice the  $M = 0$  value. The effect of aspect ratio on an unrestrained wing ( $\mu = 300$ ) entering a triangular gust is shown in figure 11. The curve for  $A = \infty$  was taken from figure 10, and the dashed lines for the wings of finite aspect ratio again represented interpolated values between the incompressible- and supersonic-flow solutions. Figure 11 shows that the reduction in the lift increment caused by decreasing the aspect ratio from 5 to 2 is about the same as that which was caused by decreasing  $A$  from  $\infty$  to 5.

#### SUMMARY OF EFFECTS

Figure 12 presents a summary of the effects of Mach number, wing-air density ratio and aspect ratio on the lift increment developed by rigid,

nonpitching, rectangular wings penetrating sharp-edged and triangular gusts. The extension of these results to gusts of arbitrary structure can be obtained by routine calculations using the same methods. In general, similar methods could be used to find the effect of the wing plan form but these would require special consideration.

## REFERENCES

1. Wagner, Herbert: Über die Entstehung des dynamischen Auftriebes von Tragflügeln. Z.a.M.M., Bd. 5, Heft 1, Feb. 1925, pp. 17-35.
2. Küssner, Hans Georg: Stresses Produced in Airplane Wings by Gusts. NACA TM 645, 1932.
3. Von Karman, Th., and Sears, W. R.: Airfoil Theory for Non-Uniform Motion. Jour. Aero. Sci., vol. 5, no. 10, Aug. 1938, pp. 379-390.
4. Jones, Robert T.: The Unsteady Lift of a Wing of Finite Aspect Ratio. NACA Rep. 681, 1940.
5. Miles, John W.: Transient Loading of Airfoils at Supersonic Speeds. Jour. Aero. Sci., vol. 15, no. 10, Oct. 1948, pp. 592-598.
6. Strang, W. J.: A Physical Theory of Supersonic Aerofoils in Unsteady Flow. Proc. Roy. Soc. (London), vol. 195, series A, no. 1041, Dec. 7, 1948, pp. 245-264.
7. Biot, M. A.: Loads on a Supersonic Wing Striking a Sharp-Edged Gust. Jour. Aero. Sci., vol. 16, no. 5, May 1949, pp. 296-300, 310.
8. Heaslet, Max. A., and Lomax, Harvard: Two-Dimensional Unsteady Lift Problems in Supersonic Flight. NACA Rep. 945, 1949. (Supersedes NACA TN 1621.)
9. Miles, John W.: Transient Loading of Supersonic Rectangular Airfoils. Jour. Aero. Sci., vol. 17, no. 10, Oct. 1950, pp. 647-652.
10. Goodman, Theodore R.: Aerodynamics of a Supersonic Rectangular Wing Striking a Sharp-Edged Gust. Rep. No. AF-723-A-1, Cornell Aeronautical Lab., Inc., Sept. 1950.
11. Lomax, Harvard, Heaslet, Max. A., Fuller, Franklyn B., and Sluder, Loma: Two- and Three-Dimensional Unsteady Lift Problems in High Speed Flight. NACA Rep. 1077, 1952.
12. Lomax, Harvard: Lift Developed on Unrestrained Rectangular Wings Entering Gusts at Sub- and Supersonic Speeds. (Prospective NACA paper)

## RESTRAINED AIRFOIL ENTERING UNIT SHARP-EDGED GUST

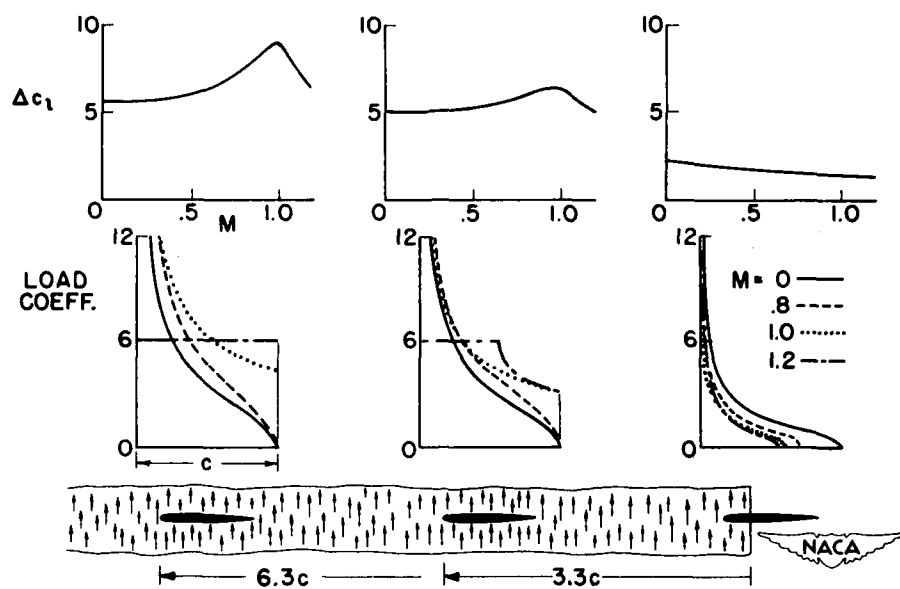


Figure 1.

## LIFT ON RESTRAINED AIRFOIL, UNIT SHARP-EDGED GUST

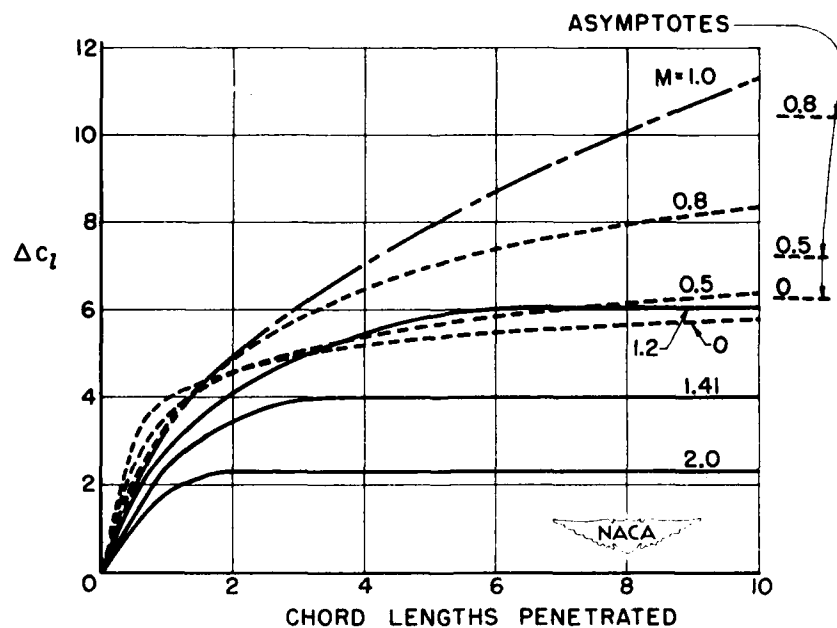
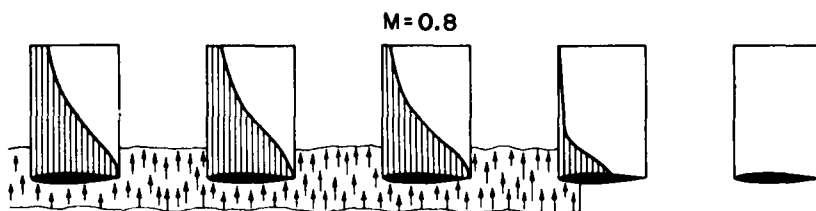


Figure 2.

CONFIDENTIAL

## COMPONENTS OF LOADING ON UNRESTRAINED AIRFOIL



GUST LOAD RESPONSE ON RESTRAINED WING

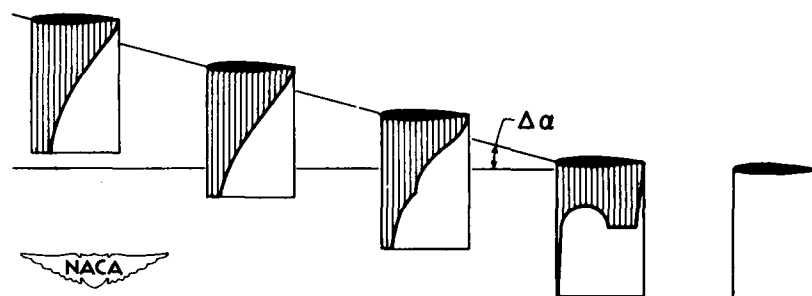
INDICIAL LOAD RESPONSE FOR  $\Delta\alpha$ 

Figure 3.

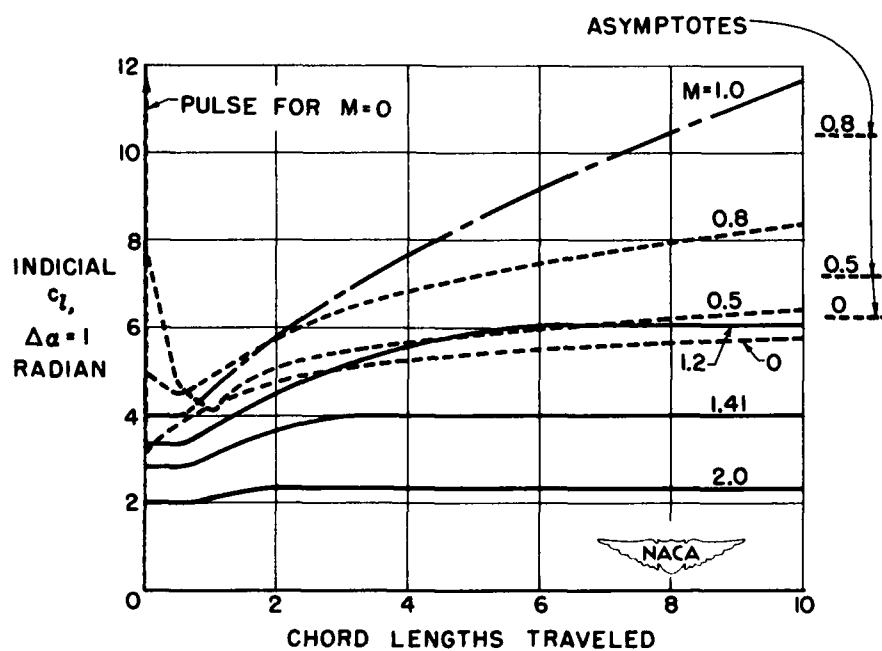
EFFECT ON SECTION LIFT OF UNIT STEP CHANGE IN  $\alpha$ 

Figure 4.

CONFIDENTIAL

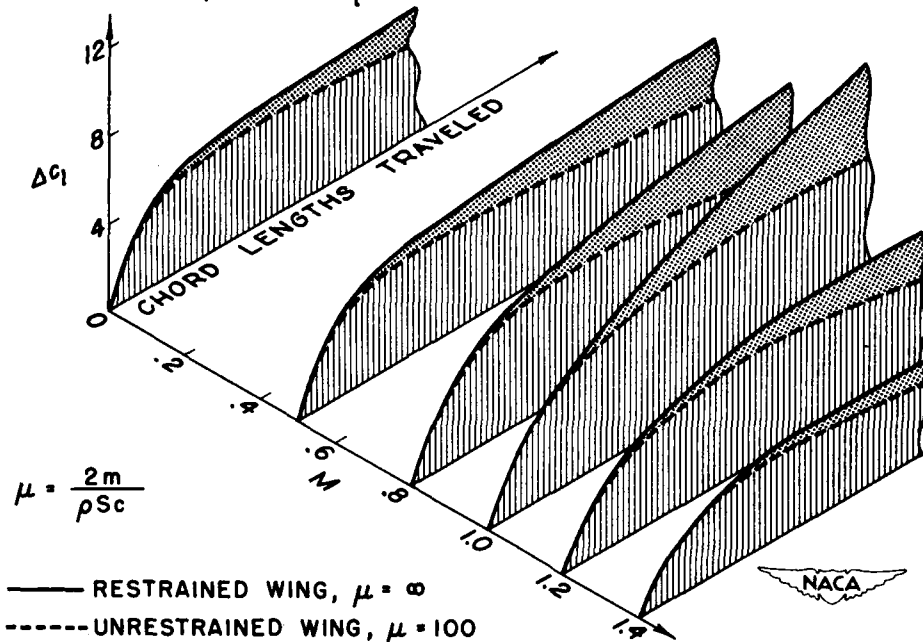
EFFECT OF  $\mu$  ON  $\Delta c_l$  UNIT SHARP-EDGED GUST

Figure 5.

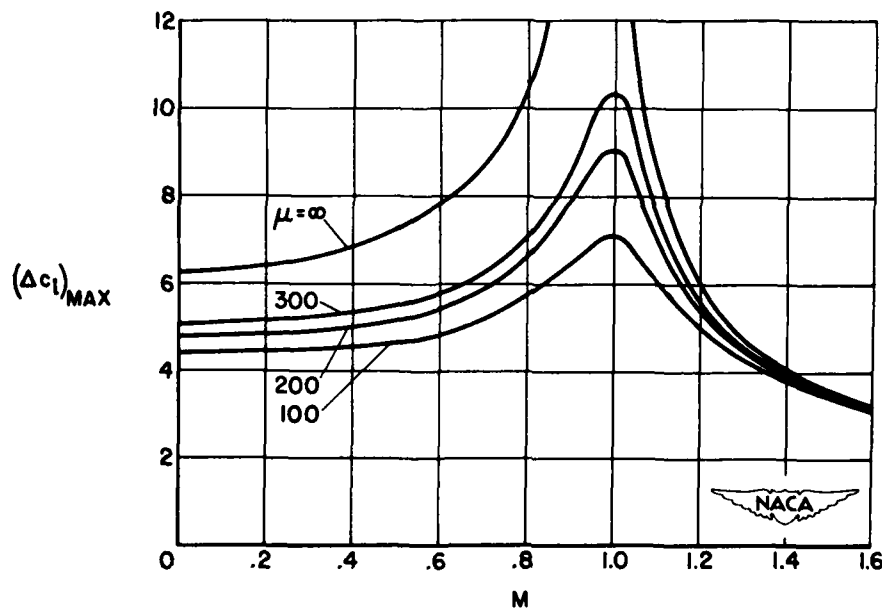
EFFECT OF  $\mu$  ON MAXIMUM  $\Delta c_l$ , UNIT SHARP-EDGED GUST

Figure 6.

CONFIDENTIAL

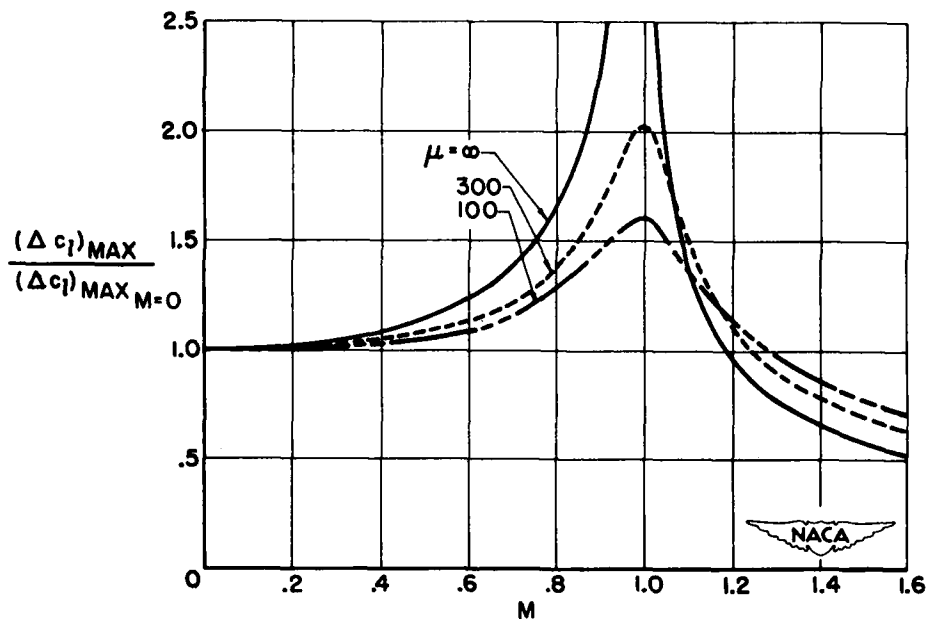
EFFECT OF M ON MAXIMUM  $\Delta c_l$ , SHARP-EDGED GUST

Figure 7.

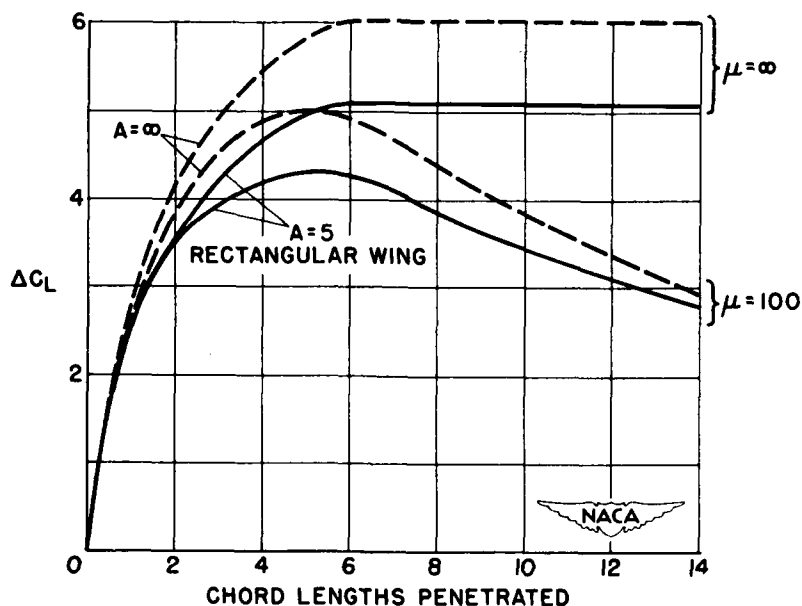
EFFECT OF ASPECT RATIO ON  $\Delta c_L$ , UNIT SHARP-EDGED GUST  
 $M=1.2$ 

Figure 8.

CONFIDENTIAL

$(\Delta C_L)_{MAX}$  ON RECTANGULAR WING, UNIT SHARP-EDGED GUST

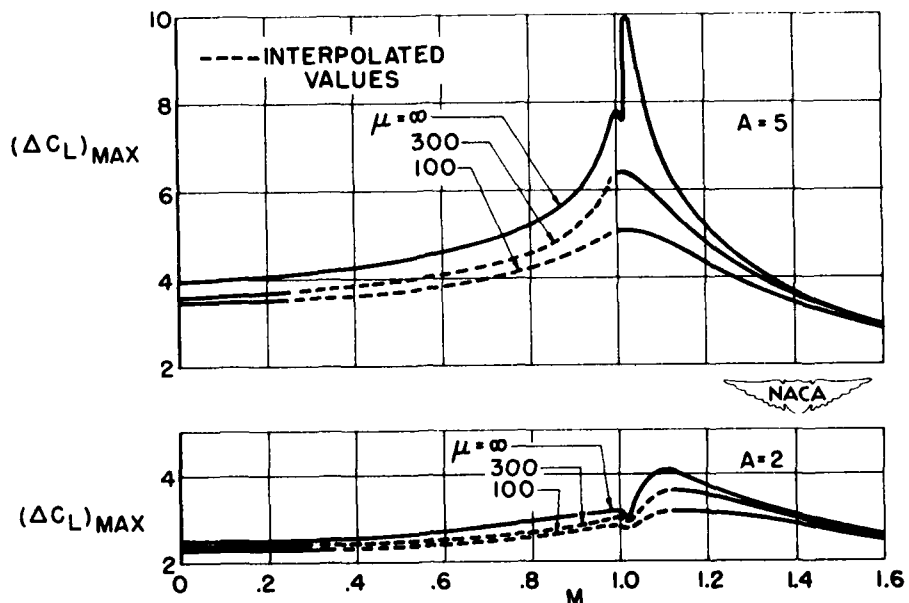


Figure 9.

EFFECT OF TRIANGULAR GUST ON MAXIMUM  $\Delta c_l$

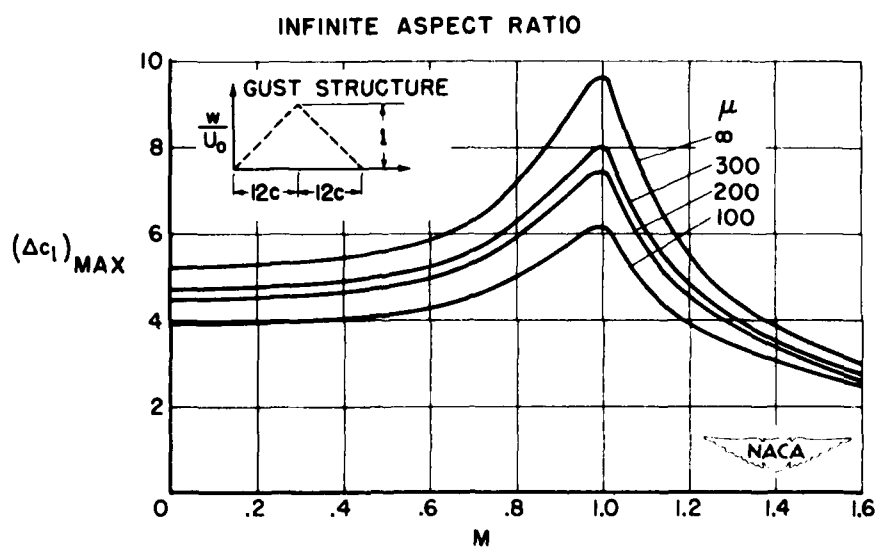


Figure 10.

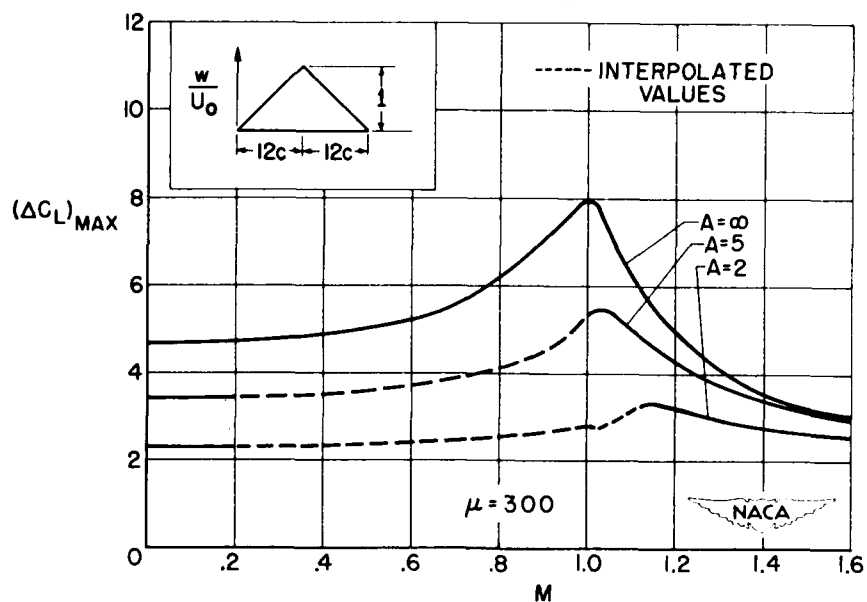
$(\Delta C_L)_{MAX}$  ON RECTANGULAR WING, TRIANGULAR GUST

Figure 11.

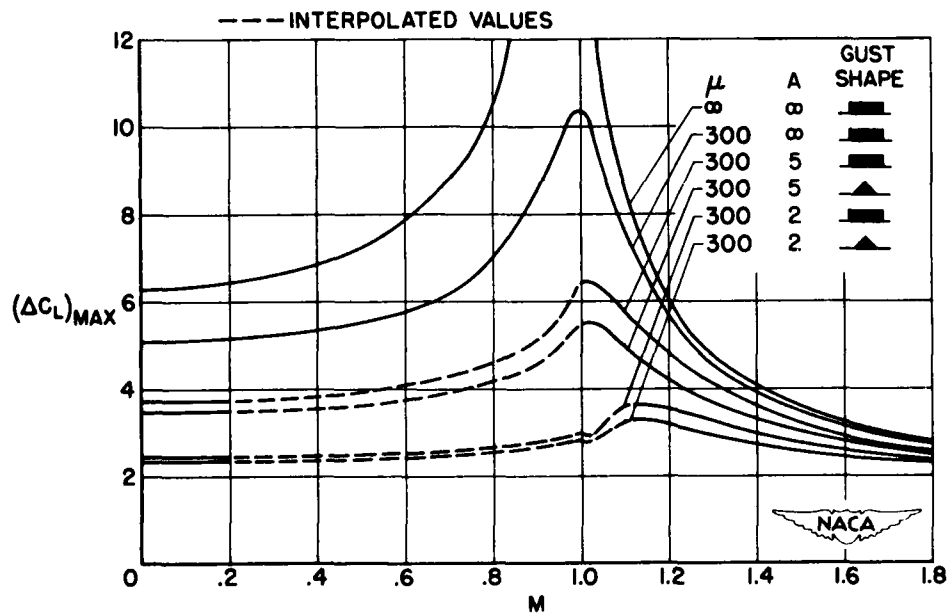
SUMMARY OF RESULTS FOR  $(\Delta C_L)_{MAX}$ , RECTANGULAR WING

Figure 12.

## SOME RECENT FLIGHT-TEST RESULTS RELATING TO GUST LOADS

By Jack Funk, Harry C. Mickleboro,  
and Richard H. Rhyme

Langley Aeronautical Laboratory

Within the last two years, new flight-test results have been obtained concerning some of the problems that relate to the loads on an airplane in rough air. The results of some gust-load measurements on a horizontal tail surface and of some normal-acceleration measurements made in an effort to determine some of the effects of sweep and Mach number on gust loads are discussed herein.

## EFFECT OF SWEEP ON GUST LOADS

Previous information available from the gust-tunnel tests of swept and unswept wings (ref. 1) has indicated a large reduction in gust loads for swept-wing airplanes. The reduction shown by these tests was nearly proportional to the calculated reduction in lift-curve slope due to sweep. In order to verify the gust-tunnel results, flight tests were made in clear-air turbulence with airplanes having sweep angles of  $35^\circ$  and  $59^\circ$ . In order to obtain the data for  $35^\circ$  of sweep, a North American F-86 and a Lockheed F-80 airplane were flown side by side, and limited data from one flight of the Bell X-5 variable-sweep airplane were used to obtain the results for  $59^\circ$  of sweep.

The results from these tests are shown in figure 1. The ordinate in this figure is the acceleration increment for the swept-wing airplane. The abscissa is the acceleration increment for the unswept-wing airplane. The circles are the experimental data and constitute the acceleration increments which occurred an equal number of times in a given flight distance for both the swept and unswept airplanes.

The solid lines in figure 1 represent a calculated relation between the loads on the swept and unswept wings based on the ratio of lift-curve slopes. The lift-curve slopes were calculated by using the formula shown in figure 1 which includes both sweep and aspect-ratio effects. For zero sweep the calculated loads would be in a ratio of 1 to 1 as shown by the upper straight line. For increasing sweep angles, the loads for the swept wings would decrease as shown by the two lower lines.

The results shown in figure 1 indicate large reductions in gust loads for the swept wings. The data for  $35^\circ$  of sweep show a reduction of about 20 percent and, for  $59^\circ$  of sweep, the reduction is about 40 percent. The good agreement of the experimental data for  $35^\circ$  and  $59^\circ$  of

sweep with the computed lines tends to support the previous finding that the reduction in lift-curve slope appears to be the major factor which accounts for the reduction in gust loads due to sweep.

In addition to the lift-curve slope, the apparent size or wave length of the gusts to which the airplane reacted may have been affected by sweep. The acceleration records from the F-80 and F-86 airplanes were accordingly studied to determine the gust selectivity of the two airplanes. The results are shown in figure 2.

In this figure, the distances from 1 g to peak acceleration were taken as a measure of the gust size. The percentages of the gusts which fell within five-chord-length intervals were then plotted against the assumed gust size for each airplane. Comparison of these results indicates that apparently the swept- and unswept-wing airplanes respond to approximately the same sizes of gusts.

#### EFFECT OF MACH NUMBER ON GUST LOADS

In addition to the sweep tests described in the preceding section, other flights were made with the F-86 airplane in an attempt to show the effects of Mach number on gust loads. The results for the basic airplane indicate an increase in loads over the linear variation of loads with speed of about 5 percent at a Mach number of 0.8. When external fuel tanks were added to the airplane, however, the effect of Mach number was to increase the gust loads by nearly 15 percent both with and without fuel in the tanks. Since the changes to the mass distribution of the wing represented by the weight of the fuel in the tanks did not appear to affect the results, the effect of the tanks is probably caused by aerodynamic rather than structural phenomena. The 5- and 15-percent increase in loads caused by compressibility effects at a Mach number of 0.8 for the F-86 is in contrast with the published data for the F-80 airplane (ref. 2), which show no Mach number effects up to a Mach number of 0.68. These results indicate that Mach number effects on gust loads vary for different airplane configurations.

#### GUST LOADS ON A HORIZONTAL TAIL SURFACE

Data on the gust loads on a horizontal tail surface were obtained with a North American B-45 airplane. These data were obtained for two center-of-gravity positions at an indicated air speed of 450 miles per hour at a low altitude.

Some data typical of those which were obtained in these tests is shown in figure 3, in which the incremental gust load on the horizontal tail is plotted against the wing load which occurred at the same time. It is noted from figure 3 that, even though there is considerable scatter about the mean line, a definite correlation appears to exist between the tail and wing loads. The scatter in the data is possibly due to such factors as gust size, phase differences between tail and wing load, effects of airplane motions, and fuselage flexibility.

From the data of which figure 3 is a sample, frequency distributions of wing- and tail-load increments were calculated. From these distributions cross plots were made of the tail load and wing load that occurred an equal number of times. These data are shown in figure 4 along with some calculated relations between wing and tail loads. The squares and circles show the test data for the two center-of-gravity positions. The agreement between the experimental data for the two center-of-gravity positions indicates that the influence of pitching velocity on the tail load is small for this airplane.

The general assumption of the past design requirements is that the gust velocity for the wing is multiplied by the downwash factor in computing the tail-load increment. In order to show the effect of downwash, the dashed-dot line of figure 4 was calculated without the downwash factor and the dashed line was calculated with a downwash factor of 0.525 included. This downwash factor was obtained from the manufacturer's design report for the condition of the high-speed pitching maneuver. From the dashed line, it can be seen that the procedure of simply correcting for the downwash factor overestimates the tail loads for this airplane by about 30 percent.

It was found that the 30-percent difference could be accounted for by the fuselage flexibility. The contribution of fuselage flexibility to the loads on the horizontal tail could be calculated from flight measurements of the angular deflection of the fuselage in rough air. The solid line shows the results of calculations which included fuselage flexibility; these results are in good agreement with the experimental data. It appears from these results that estimating gust loads on the horizontal tail by simply correcting for downwash may not be satisfactory and that the effects of flexibility may have to be taken into account; it also appears from these results that the effect of airplane pitching motion on the ratio of tail-to-wing loads is small.

#### CONCLUSIONS

In conclusion, flight tests have shown that the effect of sweep on gust loads for certain airplanes of current interest can be largely

CONFIDENTIAL

accounted for by the change in the slope of the lift curve due to sweep. The over-all effects of Mach number on gust loads have not been completely resolved, and it is indicated that the effects can be influenced by detailed airplane configuration. Measurements of loads on the horizontal tail of the B-45 airplane indicate that the center-of-gravity position did not affect the ratio of tail-to-wing loads; fuselage flexibility, on the other hand, resulted in as much as 30-percent reduction in gust loads on the horizontal tail.

## REFERENCES

1. Pierce, Harold B.: Gust-Tunnel Investigation of a Wing Model With Semichord Line Swept Back  $60^{\circ}$ . NACA TN 2204, 1950.
2. Binckley, E. T., and Funk, Jack: A Flight Investigation of the Effects of Compressibility on Applied Gust Loads. NACA TN 1937, 1949.

CONFIDENTIAL

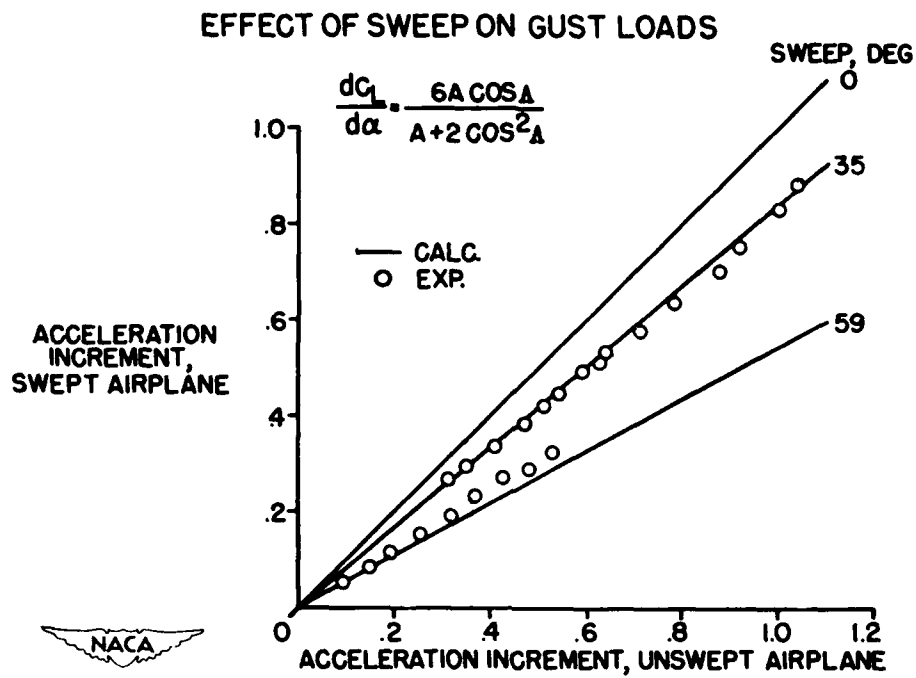


Figure 1.

## EFFECT OF SWEET ON AIRPLANE GUST SELECTIVITY

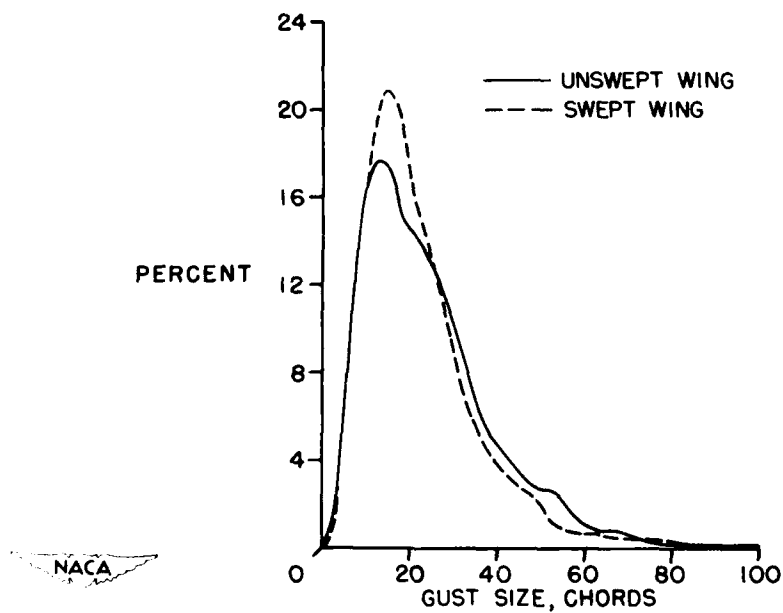


Figure 2.

CONFIDENTIAL

## GUST LOADS ON HORIZONTAL TAIL SURFACES

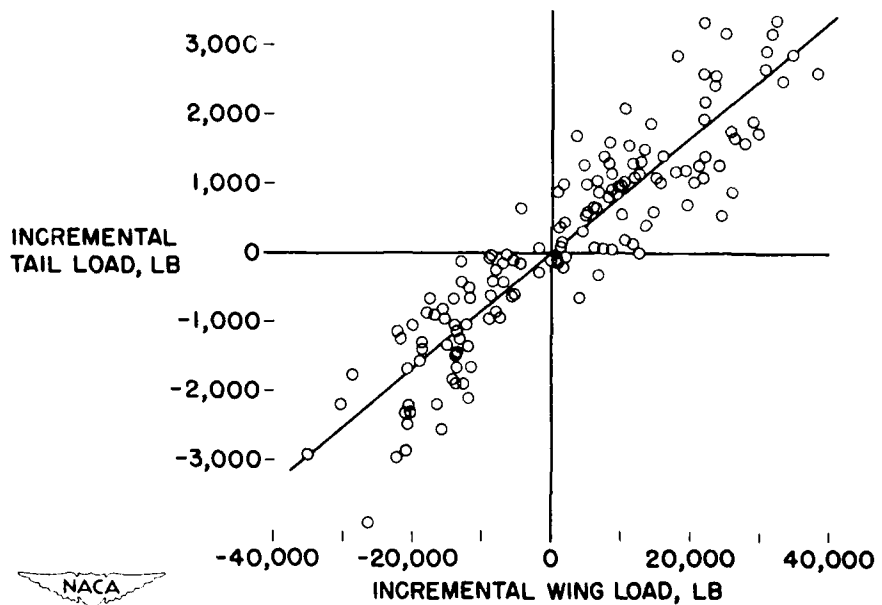


Figure 3.

## MEASURED AND CALCULATED GUST TAIL LOADS

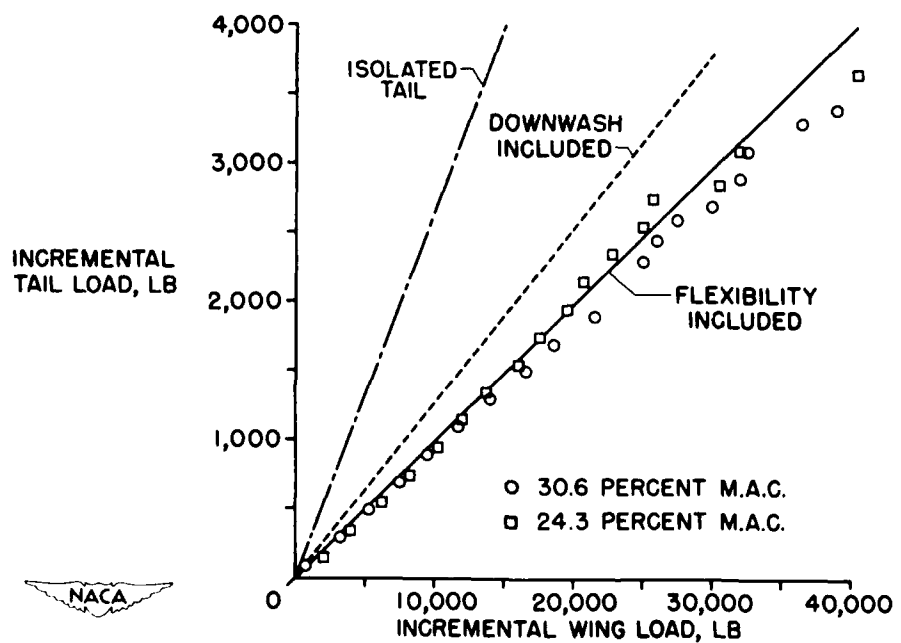


Figure 4.

CONFIDENTIAL

4H

CONFIDENTIAL

245

## LOADS ON A TAILLESS MISSILE IN ROUGH AIR

A. James Vitale

Langley Aeronautical Laboratory

In general, the approach that has been used in the study of gust loads has been to determine the characteristics of discrete gusts from airplane load measurements in rough air and then use these discrete gusts to calculate loads on other airplanes (ref. 1). Most of the conventional airplanes that have been used in these studies have probably all had about the same stability characteristics. Since most of these airplanes met the requirement of damping to one-tenth amplitude in one cycle, they had flat-frequency-response characteristics. The history of loads then showed a tendency to follow the history of gusts, and the discrete-gust method of calculation could be used.

Trends toward high-speed airplanes and the development of missiles have introduced widely different configurations having different stability characteristics. The physical characteristics and some of the stability characteristics of the tailless missile discussed in this paper are shown in figure 1. The missile was flown in continuous rough air at the Langley Pilotless Aircraft Research Station at Wallops Island, Va. The missile instrumentation included a 4-channel telemeter capable of transmitting measurements of angle of attack, normal acceleration at the center of gravity, normal acceleration at the nose, and total pressure for obtaining Mach number. The wing used was swept back  $45^{\circ}$  at the quarter-chord line and had an aspect ratio of 6. The variation of period with Mach number which is given in the lower part of figure 1 shows that the missile short-period frequency is about 10 cycles per second over the Mach number range of 0.80 to 1.0. The damping characteristics in terms of cycles to damp to one-tenth amplitude show an increase in  $c_{1/10}$  from 4 to 8 over the Mach number range of 0.80 to 1.0. In order to illustrate the magnitude of the poor damping of this configuration, the criterion of damping to one-tenth amplitude in one cycle is also shown in figure 1. Because of the poor damping the frequency response of this missile has a sharp peak at the missile short-period frequency, and the history of loads no longer tends to follow the history of gusts.

A comparison of portions of the telemeter record obtained from one flight in which the missile flew through both smooth and rough air is shown in figure 2. The upper part of figure 2 shows smooth-air flight at a Mach number of 0.90 and 5,700 feet altitude where the record shows a smooth trace of normal acceleration and angle of attack. The lower part of figure 2 shows rough-air flight at the same Mach number and 2,700 feet altitude, and the record shows sizable variations in angle of attack and center-of-gravity normal acceleration. The presence of

CONFIDENTIAL

CONFIDENTIAL

smooth air above 5,000 feet altitude was also indicated by survey flights of an F-51 airplane before the missile was launched. A comparison of the record for smooth-air and rough-air flight shows that the normal-acceleration increments experienced by the missile resulted from flight through rough air and were not caused by some aerodynamic phenomena such as buffeting.

With stability derivatives obtained from a smooth-air rocket-model test of an identical configuration, a step-by-step calculation was made to obtain a time history of normal-acceleration response to a typical random variation in gust velocity. The calculated results for a Mach number of 0.99 and the variation in gust velocity are shown in figure 3. The variation in gust velocity shown in figure 3 was not obtained during the missile test, and the level of turbulence indicated is higher than that experienced by the missile. The normal-acceleration response measured in flight is shown in figure 4 for a Mach number of 0.99. The results of the step-by-step calculation using a random variation in gust velocity agree qualitatively with the measured response since they both show an almost undamped oscillation at a frequency of about 10 cycles per second or the missile short period.

Previous wind-tunnel and flight tests have also indicated that the response of some aircraft to turbulent air is a sustained oscillation at the aircraft short-period frequency. Since the discrete-gust method of analysis could not be used for these configurations, an investigation was made in reference 2 of the application of power-spectral methods of generalized harmonic analysis to gust loads on airplanes. A brief outline of the concept of power-spectral analysis as related to the load response of an aircraft to a random input disturbance, such as continuous rough air, is shown in figure 5. Power-spectral methods have been used to determine the response of a linear system to a random input in fields such as communications engineering (ref. 3), but their application to the gust response of an airplane is relatively new. The power of a random disturbance is analogous to electrical power or the time average of the square of the disturbance, and power-spectral density is the term given to the portion of power arising from components having harmonic frequencies between  $\omega$  and  $\omega + d\omega$ . As illustrated in figure 5, the power-spectral density function of the vertical-gust velocity times the square of the airframe normal-acceleration transfer function gives the power-spectral density function of the output or normal acceleration. The mean-square value of normal acceleration which is useful as a measure of load intensity is the area under the normal-acceleration power-spectral density curve.

The power-spectral density function may also be obtained by means of a harmonic analysis of the measured normal-acceleration response. Shown in figure 6 is the power spectrum of normal acceleration obtained

CONFIDENTIAL

from the measured normal accelerations at a Mach number of 0.81. Because of the poor damping characteristics of this missile, the spectrum has a sharp peak at the missile short-period frequency. The small peak at about 35 cycles per second corresponds to the wing first-bending frequency.

By using a power spectrum of the random gust velocity shown in figure 3 and transfer functions computed from the missile characteristics for Mach numbers of 0.81, 0.88, and 0.99, the power spectrums of normal acceleration were calculated by means of the method outlined in figure 5. The root-mean-square values of normal acceleration obtained from the area under the calculated power-spectral curves are compared in figure 6 with experimental values obtained from the normal-acceleration data at Mach numbers of 0.81, 0.88, and 0.99. The line of expected agreement shown in figure 6 is based on the fact that the input gust velocity of figure 3 used in the calculations was of higher level than the missile experienced in flight. Because of the patchy nature of atmospheric turbulence the day that the missile was tested and other factors, the confidence limits of the calculated values are also shown in figure 6. However, the calculated values of root-mean-square normal acceleration show similar variations with Mach number and  $c_1/10$  as obtained experimentally.

Since the power spectrum itself provides a measure of the average power arising from components at various frequencies, it does not give the actual load intensities. The actual load at a given time represents the combined output at various frequencies. If the distribution of load increments in continuous rough air is normal with zero mean value, it is possible to relate the power spectrum of load to specific quantities of concern in load studies by means of the root-mean-square value of normal acceleration.

In figure 7 the frequency distribution of load obtained from a 2-second section of normal-acceleration time history tabulated every 0.01 second is shown for a Mach number of 0.81. Also shown is the fitted normal-distribution curve. The results show that the normal-distribution curve is an adequate representation of the measured load increments.

Quantities that may be of interest for structural analysis are the probability distribution of load intensity and the number and intensity of peak loads. For a normal distribution of load the probability distribution of load is completely described by the root-mean-square value. In figure 8 the data of figure 7 are presented in the form of a relative cumulative frequency distribution and are compared with the fitted probability distribution. The curves for both the probability of exceeding given values and being less than given values of load are given, and the data shows good agreement with the fitted curves.

CONFIDENTIAL

The number and intensity of peak loads per mile of flight obtained from the measured normal-acceleration data are shown in figure 9 for a Mach number of 0.81. These observed data were obtained from counts of peak-load values measured in flight. The power spectrum of normal acceleration can also be used to calculate the number and intensity of peak loads as shown in reference 3. The power spectrum of normal acceleration that was obtained from a harmonic analysis of the measured data at a Mach number of 0.81 and shown previously in figure 6 was used to calculate the number and intensity of peak loads per mile of flight shown in figure 9 by the dotted line. There is good agreement between the observed data and the values calculated from the power spectrum.

From the data and discussion presented previously, the following conclusions may be made. For this tailless configuration having low damping in pitch the history of normal-acceleration response does not follow the history of gust velocity, and the discrete-gust method of analysis cannot be used. Since the load increments from flight through continuous rough air can adequately be represented by a normal distribution curve, the power-spectral method of generalized harmonic analysis can be used to predict the probability distribution of load and the number and intensity of peak-load values.

The power spectrum of normal acceleration for this configuration shows the largest concentration of power at the missile short-period frequency. The power spectrum can be calculated from a power spectrum of atmospheric turbulence and the missile transfer function. Since the transfer function involves the missile aerodynamic characteristics, the power-spectral method offers a means of investigating the effects of changes in stability characteristics on the missile gust response. Further tests are being made with a canard configuration and a conventional tail configuration to investigate the effects of changes in aerodynamic characteristics on the load response in continuous rough air.

CONFIDENTIAL

## REFERENCES

1. Donely, Phillip: Summary of Information Relating to Gust Loads on Airplanes. NACA Rep. 997, 1950. (Supersedes NACA TN 1976.)
2. Press, Harry, and Mazelsky, Bernard: A Study of the Application of Power-Spectral Methods of Generalized Harmonic Analysis to Gust Loads on Airplanes. NACA TN 2853, 1953.
3. Rice, S. O.: Mathematical Analysis of Random Noise. Pts. I and II. Bell Syst. Tech. Jour., vol. XXIII, no. 3, July 1944, pp. 282-332; Pts. III and IV, vol. XXIV, no. 1, Jan. 1945, pp. 46-156.

CONFIDENTIAL

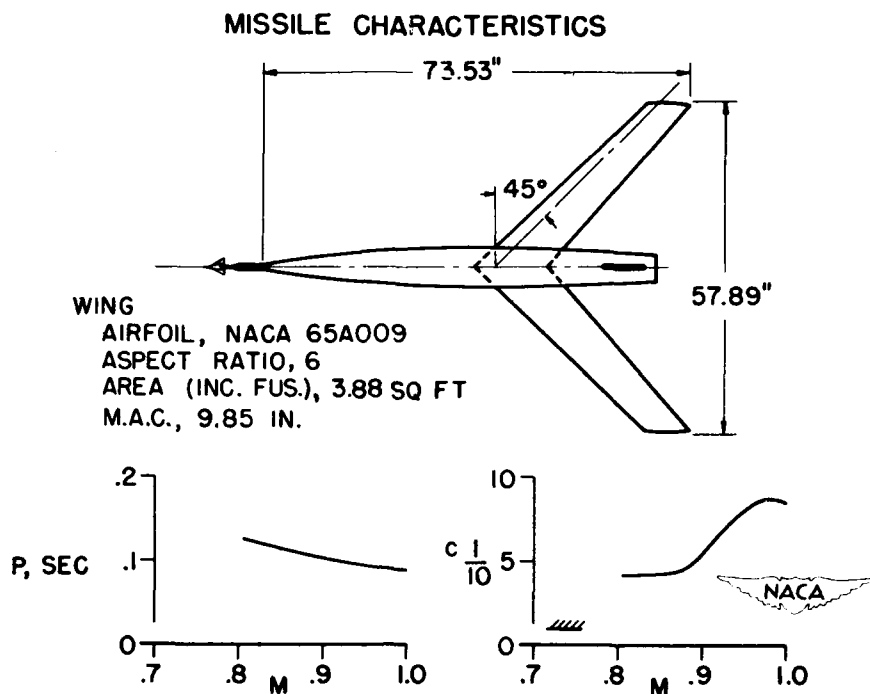


Figure 1.

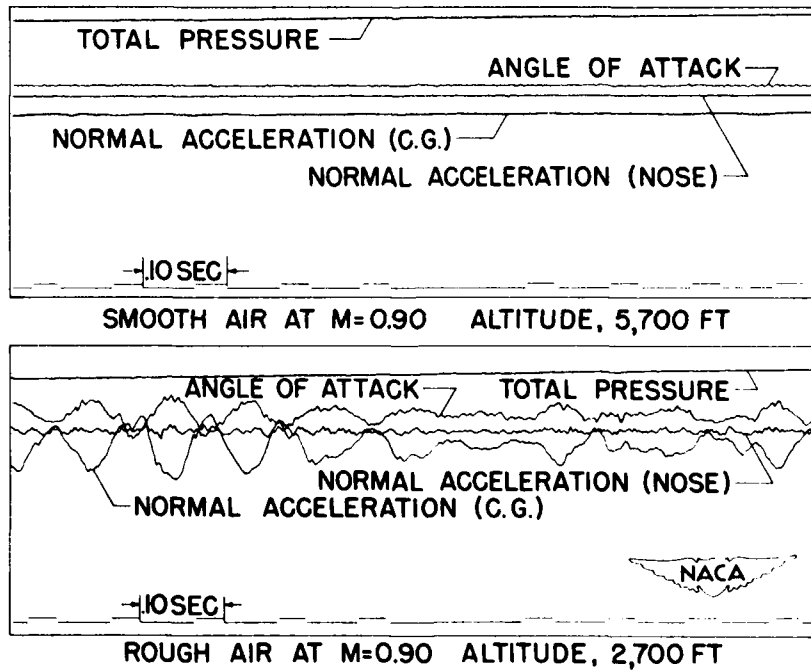
**COMPARISON OF SMOOTH AND ROUGH-AIR PORTIONS OF FLIGHT**

Figure 2.

CONFIDENTIAL

## CALCULATED NORMAL-ACCELERATION RESPONSE, M=0.99

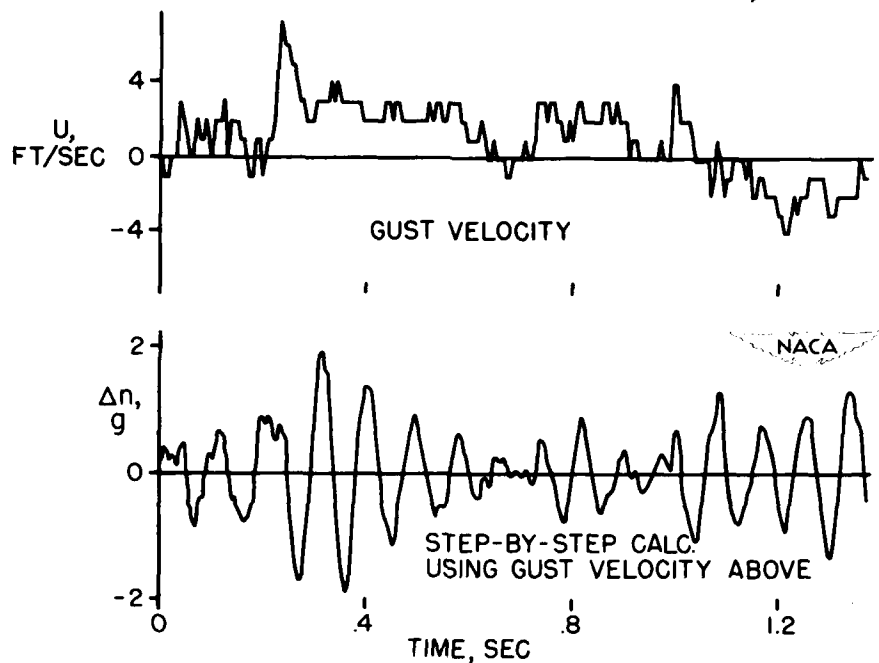


Figure 3.

## NORMAL-ACCELERATION RESPONSE, M = 0.99

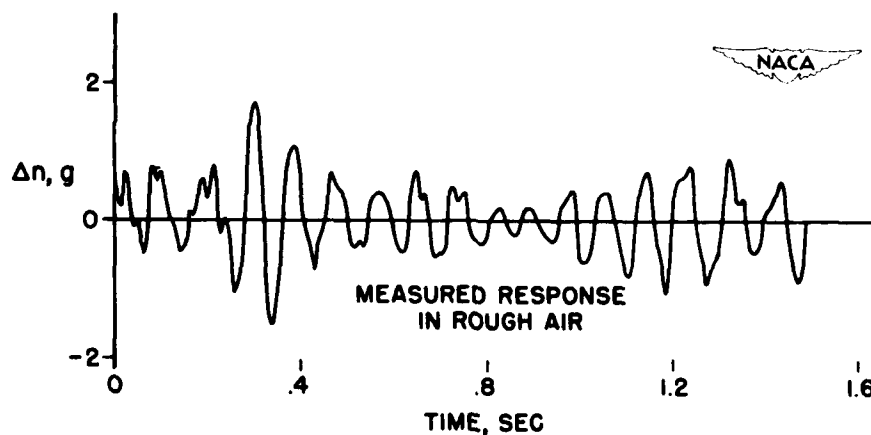


Figure 4.

CONFIDENTIAL

## POWER-SPECTRUM CALCULATIONS

- Φ POWER-SPECTRAL-DENSITY FUNCTION
- i INPUT (VERTICAL GUST VELOCITY)
- o OUTPUT (AIRFRAME NORMAL ACCELERATION)
- T AIRFRAME NORMAL-ACCELERATION TRANSFER FUNCTION FOR A SINUSOIDAL GUST-VELOCITY INPUT
- σ ROOT-MEAN-SQUARE NORMAL ACCELERATION

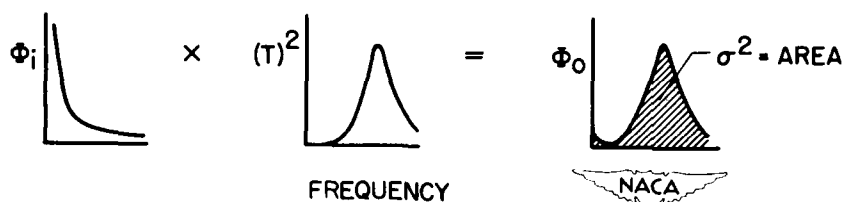
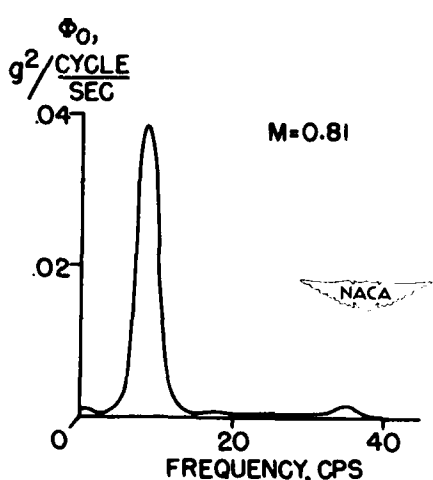


Figure 5.

## POWER SPECTRUM OF NORMAL ACCELERATION



## COMPARISON OF CALCULATION AND EXPERIMENT

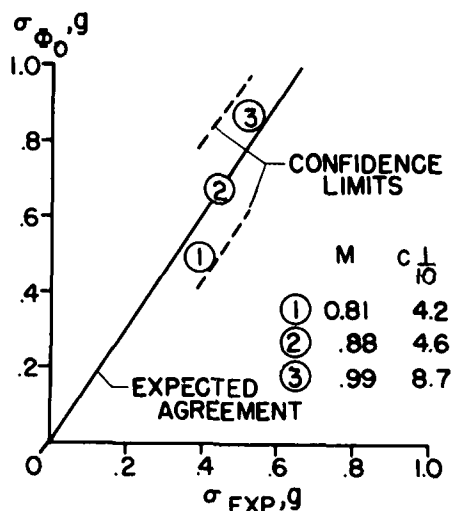


Figure 6.

CONFIDENTIAL

## FREQUENCY DISTRIBUTION OF LOAD INCREMENTS

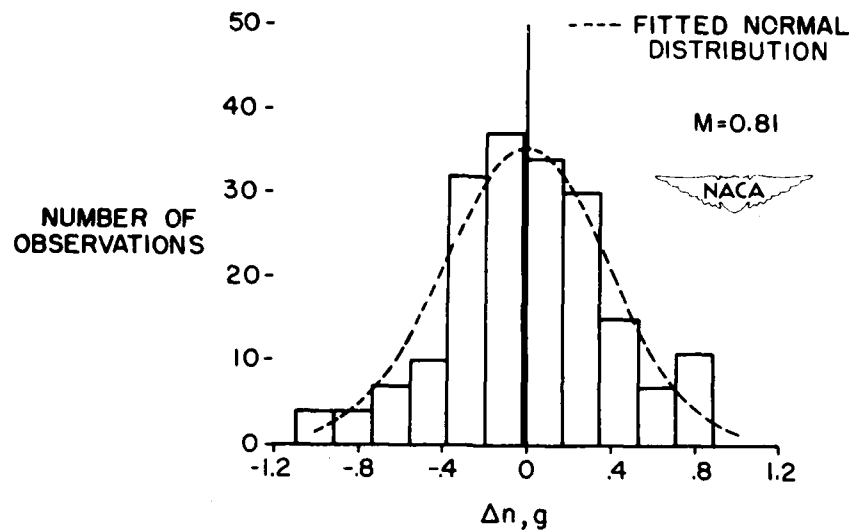


Figure 7.

## RELATIVE CUMULATIVE FREQUENCY DISTRIBUTION

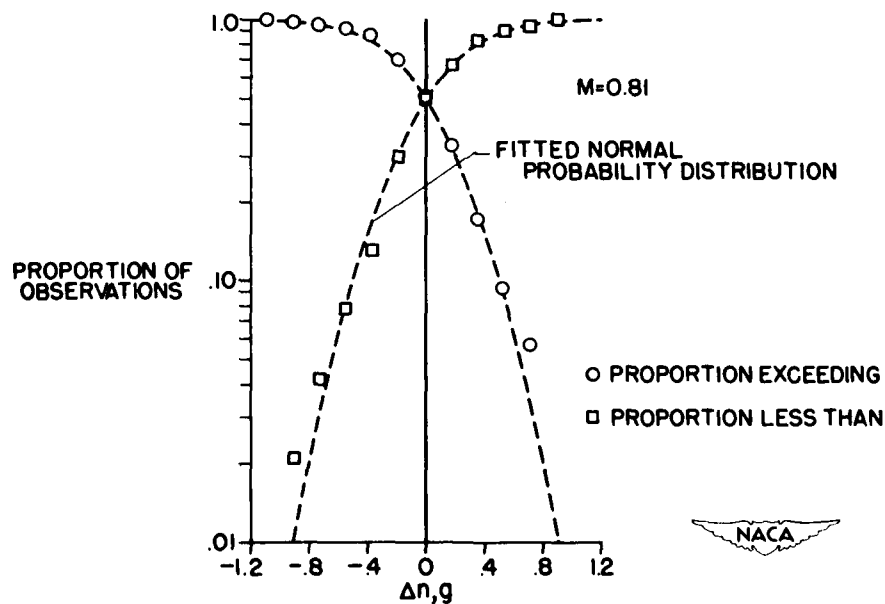


Figure 8.

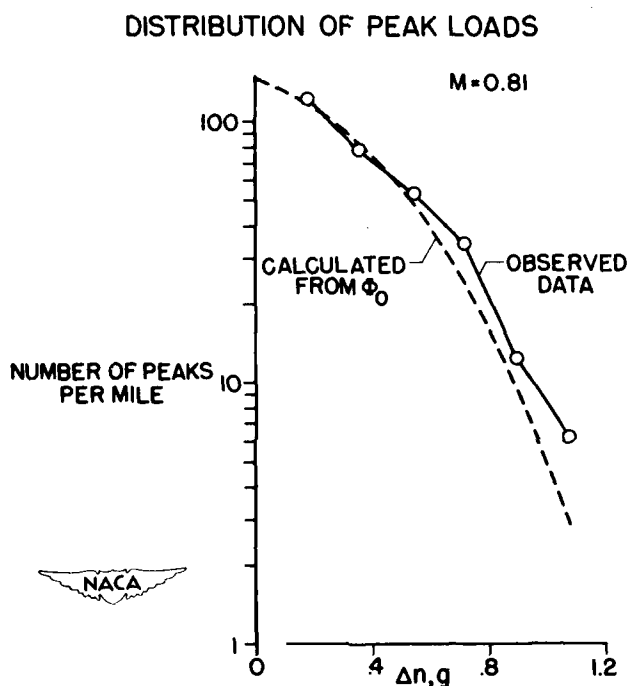


Figure 9.

## **FLUTTER AND BUFFETING**

SOME REMARKS ON THE THEORETICAL ASPECTS  
OF UNSTEADY AIR-FORCE COEFFICIENTS

By Charles E. Watkins, Harry L. Runyan,  
and Julian H. Berman

Langley Aeronautical Laboratory

INTRODUCTION

At the NACA Conference on High-Speed Airplane Aerodynamics, December 4-5, 1951, a rather illuminating schematic diagram was used to discuss the status of theoretical work on unsteady air forces. This diagram is presented herein as figure 1 to serve as a guide in the present discussion. In this figure the abscissa is Mach number and the ordinate is the reduced-frequency parameter defined as

$$k = \omega c / 2V \quad (1)$$

where  $\omega$  is frequency of oscillation,  $c$  is wing chord, and  $V$  is velocity. The airfoil diagrams indicate the plan forms under discussion. Thus the top sketch pertains to air-force coefficients for two-dimensional wings undergoing harmonic translation, pitching, and aileron rotation, and the three lower sketches pertain to coefficients for rectangular, triangular, and swept wings undergoing harmonic translation and pitching. The heavily shaded areas in these sketches indicated ranges of Mach number and reduced frequency where sufficient information, for engineering purposes, regarding theoretically derived air-force coefficients associated with wings undergoing the motions indicated was available. The lightly shaded and unshaded regions indicated ranges in which there was scant knowledge or no knowledge at all of oscillating air-force coefficients.

It is to be noted that unshaded regions in this figure pertain mainly to wings of finite aspect ratio and especially to these wings in the high subsonic Mach number range. This situation leaves designers of aircraft without information regarding time-dependent wing loads that would otherwise enable them to calculate aeroelastic properties of a given airplane in this Mach number range. Such properties are of growing importance in design and construction of most modern aircraft; consequently, the problem of obtaining coefficients to fill in these unshaded regions of figure 1 appears to be of primary importance.

Results of recent investigations give encouraging indications that these coefficients can eventually be obtained and that the gaps indicated by unshaded regions in this figure will gradually be filled in. The main

CONFIDENTIAL

purpose of this paper is therefore to discuss these results and to indicate how they might affect the status, as indicated in figure 1, of analytically derived air forces. Other purposes are to present some remarks on pertinent differences between air forces, based on supersonic flow, for finite wings and those for two-dimensional wings and to present a brief discussion on some related topics.

## DISCUSSION

## Wings in Supersonic Flow

Coefficients for rectangular and triangular wings undergoing harmonic pitching and translation. - Most of the results indicated by heavy shading in figure 1 for finite wings in supersonic flow were obtained by expanding the kernel function of associated integral equations in terms of the frequency of oscillation and deriving the first few terms of a power-series expansion of the velocity potential. (See, for example, refs. 1 to 4.) The results indicated for rectangular and triangular wings (for  $M > 1$ ) were obtained by considering the potentials for these wings expanded to only the third power of the frequency. Although such results may be useful for flutter calculations for Mach numbers beyond about 1.2, they are not very useful for Mach numbers near 1. To obtain more complete results, the expansions of the potentials for rectangular wings and for triangular wings with subsonic leading edges have recently been extended to the fifth power of the frequency. (See ref. 2 for the extensions for triangular wings; extensions for rectangular wings are as yet unpublished.)

To show how these extensions affect the status, as indicated in figure 1, of air forces for these wings, a comparison is made of some results for a two-dimensional wing pitching about its leading edge. Results for a two-dimensional wing are chosen for comparison because in this case approximate results can be compared with exact results so that the extent to which the approximate results converge can be seen. Convergence for three-dimensional wings is at least as good as that for two-dimensional wings. The results to be compared are shown in figure 2, where amplitudes of pitching-moment coefficients and associated phase angles are plotted as functions of a frequency parameter  $\bar{\omega}$  for  $M = 10/9$ . The solid curves represent calculations based on the exact theory and tables of reference 5; the squares denote results of calculations based on the expansion of the velocity potential for a two-dimensional wing to the third power of the frequency (ref. 1); and the circles denote results of calculations based on expansions of the potential to the fifth power of the frequency. The parameter  $\bar{\omega}$ , which is defined as

$$\bar{\omega} = \frac{2M^2 k}{M^2 - 1} \quad (2)$$

CONFIDENTIAL

is chosen as abscissa because it is found that agreement between the approximate and exact theory is the same at a given value of this parameter for all Mach numbers greater than 1. The phase angles considered here are simply the angles whose tangent is the ratio of the imaginary part to the real part of the moment coefficient.

It may be noted in figure 2 that the moments and phase angles based on expansions to the third power of the frequency agree with exact theory for  $\bar{\omega}$  less than about 0.8. For  $M = 10/9$  this value of  $\bar{\omega}$  corresponds to values of  $k$  less than about 0.08, values too low for general flutter analyses. This range is useful, however, for studies of dynamic stability and single-degree-of-freedom types of flutter. The moments and phase angles based on expansions to the fifth power of the frequency agree with exact theory for  $\bar{\omega}$  less than about 1.5. For  $M = 10/9$  this value of  $\bar{\omega}$  corresponds to values of  $k$  less than about 0.14, which is high enough to handle a large class of flutter cases of general experience. It is recognized, however, that this range of  $k$  is insufficient to handle all flutter cases that have been experienced. Nevertheless, extensions of the expansions from the third power of the frequency to the fifth power of the frequency will permit considerably more shading near  $M = 1$  in the charts of figure 1 that pertain to rectangular and triangular wings.

Some illustrative comparisons of coefficients for finite and two-dimensional wings. - Before discussing other results that are to be presented, it may be of interest to consider briefly some pertinent differences in the nature of air forces based on theory for finite wings in supersonic flow as compared with that of air forces based on theory for infinite or two-dimensional wings in supersonic flow. Such a consideration should provide indications of the way results of flutter calculations based on coefficients derived for a finite wing should be expected to differ from results of similar calculations based on coefficients derived for a two-dimensional wing.

For illustrative comparisons some calculations have been made of amplitudes of pitching-moment coefficients and associated phase angles for a two-dimensional wing and for a rectangular and triangular wing, each of aspect ratio 4. The first results to be discussed are based on total forces acting on the wings. These are shown in figures 3 and 4, where amplitudes and phase angles of pitching-moment coefficients for the wings under consideration pitching about their leading edges are plotted as functions of  $\bar{\omega}$  for three Mach numbers,  $M = 1.1, 1.2$ , and  $1.4$ . It should be pointed out that for the moment coefficients plotted in this manner the component of the coefficient that is in phase with wing displacement is given by the product of the amplitude of the coefficient and the cosine of the phase angle  $\phi_m$ . The out-of-phase component is given by the product of the amplitude and the sine of the phase angle. Furthermore, positive values of the in-phase component

correspond to statically stable conditions which prevail when  $\phi_m$  is in the range  $-\pi/2 < \phi_m < \pi/2$ ; statically unstable conditions prevail when  $\pi/2 < \phi_m < 3\pi/2$ . Dynamically stable conditions prevail when  $0 < \phi_m < \pi$  and dynamically unstable conditions when  $-\pi < \phi_m < 0$ .

Hence, the main feature to note in these figures is the change in phase angle with frequency in figure 4 that occurs for a given Mach number in going from the results for a two-dimensional wing to those for wings of aspect ratio 4. Note that for the cases considered the negative out-of-phase components of pitching moment for a two-dimensional wing for Mach numbers less than 1.4 are appreciably larger in numerical value than corresponding components for the rectangular wing and that the pitching moment for a triangular wing has practically no negative components.

As to effects on calculated flutter speeds, the total out-of-phase component of pitching moment is of particular significance with regard to the type of flutter known as single-degree-of-freedom-in-pitch flutter. This type of flutter is affected by such parameters as Mach number, ratio of wing density to air density, structural damping, aerodynamic damping, and so forth. In order for it to occur, the aerodynamic damping, which is the out-of-phase pitching moment, must be negative. The curves in figure 3 thus indicate that coefficients based on a two-dimensional wing would lead to a much lower theoretical single-degree-of-freedom flutter speed than would coefficients based on a finite wing.

With more complicated types of flutter, consideration of the spanwise variation of some coefficients may provide a better perspective as to what differences in flutter speeds might be expected between calculations based on coefficients for finite wings as compared with calculations based on coefficients for two-dimensional wings. The curves in figure 5 serve as illustrations. In this figure are shown the spanwise variations of amplitudes of pitching-moment coefficients and phase angles for a rectangular and a triangular wing, each of aspect ratio 4, pitching about an axis 0.4 chord from the wing leading edge for  $M = 1.3$  and reduced frequency  $k = 1/10$ . Values of moment amplitude and phase angle for a two-dimensional wing for this Mach number, frequency, and pitch-axis location are the same as those shown for the rectangular wing in the region between the root and the point where the tip Mach cone cuts the wing trailing edge. Note that in this region the phase angle is negative and corresponds to dynamically undamped conditions, but in the outer region of the wing, where displacements, and consequently forces, usually are greater, the phase angle is positive and indicates damped conditions. With the triangular wing, just the opposite may be noted; that is, the phase angle is positive in the region near the root and negative in the outer region. If the moments are

integrated over the wings and reduced to coefficient form, the results are as indicated by the arrowheads in the figure; the phase angle for the rectangular wing is negative but smaller than that for the two-dimensional wing, and the phase angle for the triangular wing is positive but very small. (These integrated results are of the same form as the results shown in figs. 3 and 4 and referred to as total coefficients for finite wings.)

The illustrative results shown in figure 5 then seem to imply that, in applications such as flutter calculations, more realistic phase relations between components of aerodynamic coefficients might be taken into account by using coefficients based on local, rather than integrated or total, forces acting on the region of the wing under consideration. They also seem to imply, at least for the Mach number, frequency, and pitch-axis location under consideration, that use of total coefficients for finite wings would lead to higher theoretical flutter speeds than would the use of coefficients based on two-dimensional wings and that use of section coefficients, that is, those based on local forces, for finite wings would in general lead to even higher theoretical flutter speeds than would use of total coefficients for finite wings.

It may be of interest to point out that the material for the rectangular wing presented in figure 5 is taken from some calculations of theoretical flutter speeds based on both section coefficients for finite wings and on coefficients for two-dimensional wings which were compared with the experimental flutter speeds for a series of rectangular wings of aspect ratio of about 4 and various profile shapes and thickness ratios as reported in reference 6. Results of these calculations and experiments are shown in figure 6. In this figure the abscissa is the air-to-wing density-ratio parameter  $\kappa$  and the ordinate is the reduced flutter-speed parameter  $\frac{V}{c\omega_a/2}$ . The circles represent experimental

values; the squares represent calculations based on section coefficients for finite wings; and the triangles represent calculations based on coefficients for two-dimensional wings. It may be noted that the flutter-speed calculations based on coefficients for finite wings are in each case higher than those calculated with the use of coefficients for two-dimensional wings and that the calculations based on coefficients for finite wings are, except for one case ( $\kappa = 0.019$ ), in considerably better agreement with experiment. Results of calculations, not shown in the figure, based on total three-dimensional coefficients gave flutter speeds that were between those based on two-dimensional coefficients and those based on section coefficients.

Coefficients for rectangular and triangular wings undergoing harmonic distortions in supersonic flow. - It is to be recalled that the coefficients discussed in the preceding sections of this paper have been those pertaining to downwash conditions for, or motions of, rigid

wings. In applications they should not necessarily be expected to be useful for treating highly flexible wings. For these wings what may be needed are coefficients based on more realistic downwash conditions. A first step toward obtaining such coefficients for rectangular and triangular wings has recently been undertaken. Rectangular wings of various aspect ratios are being considered at the Ames Laboratory by a procedure that makes use of indicial functions for these wings. Triangular wings with subsonic leading edges have been treated at the Langley Laboratory by the method of expanding the velocity potential. (These investigations are as yet unpublished.) Sketches of the plan forms considered are shown in figure 7. (The sketches under the triangle in fig. 7 indicate other plan forms for which the potential for a triangular wing in supersonic flow can be used to calculate forces thereon.) The downwash conditions considered are, for the rectangular wing,

$$w(x,y) = e^{i\omega t} \left( \sum_{i=0}^n a_i y^i + x \sum_{i=0}^n b_i y^i \right) \quad (3)$$

and, for the triangular wing,

$$w(x,y) = e^{i\omega t} (Ax^2 + By^2 + Cxy + Dy + Ex + F) \quad (4)$$

It is to be noted from these equations that a large variety of downwash distributions can be obtained by simply changing the different coefficients  $a_i$  and  $b_i$  in equation (3) and  $A, B, C$ , and so forth in equation (4).

In order to give some indication of the way coefficients based on such downwash conditions compare with those based on rigid wings, the spanwise variations of lift and phase angle associated with parabolic bending of both rectangular and triangular wings are compared with the results of multiplying the lift associated with these wings undergoing translation by the ordinates of the assumed parabolic mode shape in figure 8. The main features to note in these comparisons are the differences in magnitudes of lift at the root and at the points of maximum lift. These differences are of course associated with induced effects due to bending. It is of interest to note that the maximum values of the two types of lift occur at about the same span position and that the phase angles, calculated by the two methods, are not too different.

## Wings in Subsonic Flow

In regard to the important case of finite wings in subsonic compressible flow, the only results of analytically derived air forces that can be reported at this time are some that have been derived on the basis of incompressible flow. They include, for example, those by Lawrence and Gerber (ref. 7), Dengler and his associates (ref. 8), Woodcock (ref. 9), and Lehrian (ref. 10). These coefficients would be useful for low Mach number cases and would permit additional shading near  $M = 0$  in figure 1 for all finite wings indicated. The coefficients of Lawrence and Gerber might be especially useful for analyzing low-aspect-ratio wings and for evaluating the vanishing-aspect-ratio theory given by Garrick in reference 11 and by Ashley in reference 12.

With regard to the high subsonic Mach number range, there are as yet no analytically derived coefficients to report. However, results of a recent investigation pertaining to the integral equation for this case give promising indications that numerical procedures analogous to some of those used to obtain coefficients for two-dimensional wings in subsonic flow can be employed to obtain coefficients for finite wings in subsonic flow. The results of this investigation may be briefly described as follows.

The integral equation relating a known downwash to an unknown lift distribution for a given wing is

$$w(x,y) = \frac{\omega}{\rho V^2} \int_A \int L(\xi,\eta) K(x_0, y_0) d\xi d\eta \quad (5)$$

where

$w(x,y)$  prescribed downwash

$\omega$  circular frequency

$\rho$  fluid density

$V$  fluid velocity

$A$  region over which integration is performed (wing surface)

$x_0 = x - \xi$

$y_0 = y - \eta$

$L(\xi,\eta)$  unknown lift distribution

The kernel function  $K(x_0, y_0)$  shown in this equation represents the contribution to downwash at any field point  $(x, y)$  due to a pulsating doublet located at any other point  $(\xi, \eta)$  on the wing. It is mathematically defined by the following improper integral:

$$K(x_0, y_0) = \lim_{z \rightarrow 0} \frac{\partial^2}{\partial z^2} e^{-\frac{i\omega}{V} x_0} \int_{-\infty}^{x_0} \frac{e^{iv} [\lambda + M\sqrt{\lambda^2 + \beta^2 y_0^2 + \beta^2 z^2}]}{\sqrt{\lambda^2 + \beta^2 y_0^2 + \beta^2 z^2}} d\lambda$$

where

$$\beta = \sqrt{1 - M^2}$$

$$v = \frac{\omega}{V\beta^2}$$

Evaluation and handling of this integral has been one of the main bottlenecks in obtaining coefficients for finite wings in subsonic flow for a long time. A main result of the investigation under discussion is that this integral has been reduced to a form that can be numerically evaluated and tabulated. This reduced form is

$$K(x_0, y_0) = -\beta^2 e^{-i\beta^2 v x_0} \left\{ \frac{\beta}{r} K_1(\beta v r) + \frac{i\beta v \pi}{2r} [I_1(\beta v r) - L_1(\beta v r)] - \right.$$

$$\frac{1}{Mr^2} (1 + iv Mr) e^{-iv Mr} + \beta^2 v^2 \int_0^{M/\beta} \sqrt{1 + \lambda^2} e^{-i\beta v r \lambda} d\lambda +$$

$$\frac{1}{Mr^2 \sqrt{x_0^2 + r^2}} \left( Mx_0 + \sqrt{x_0^2 + r^2} \right) e^{iv \left[ x_0 - M\sqrt{x_0^2 + r^2} \right]} -$$

$$\left. \frac{i\beta^2}{Mr^2} \int_0^{x_0} e^{iv \left[ \lambda - M\sqrt{\lambda^2 + r^2} \right]} d\lambda \right\}$$

In this expression  $I_1$  and  $K_1$  represent modified Bessel functions of the first and second kinds, respectively, and  $L_1$  is the modified Struve function. These are all tabulated functions. Two integrals remain to be integrated, but it will be noted that these are finite and proper and can be readily handled by numerical procedures. Thus the evaluation of the kernel function is reduced to simple operations. With regard to the important singularities possessed by the kernel function, these can be readily isolated and put into forms appropriate for treatment in applications. Tabulated values of this kernel function should make the problem of analytically obtaining coefficients for finite wings in subsonic flow much less formidable.

#### Related Topics

Effect of airfoil thickness. - An important factor that is not ordinarily taken into account in an analytical derivation of unsteady air forces is the possible effect of airfoil thickness. This effect may be significant, especially for low-frequency oscillations, and has recently attracted the attention of several analysts or investigators; see, for example, references 13, 14, and 15. There are as yet some unresolved discrepancies in the results of these investigations. Moreover, the investigations have been rather incompletely reported. However, it is expected that sufficient interest in this thickness problem has been aroused to prompt more complete investigation and that conclusive results will be forthcoming in the not too distant future.

Wind-tunnel-wall effects on measured coefficients. - Another theoretical investigation that is directly related to the determination of unsteady air forces and that has proceeded for some time concerns wind-tunnel-wall effects on unsteady air forces measured in wind tunnels. Since measured coefficients are to be dealt with in the next two papers by John A. Wyss and by Sherman A. Clevenson and Sumner A. Leadbetter, it may be of interest to consider at this point what has been accomplished with regard to tunnel-wall effects.

A theoretical investigation of these effects for two-dimensional wings was reported in reference 16. This investigation indicated that, under certain conditions of Mach number, tunnel height, and frequency, an oscillating two-dimensional wing could form a resonant condition in a tunnel which would produce very large velocities normal to the airfoil. It is readily apparent that, if such conditions prevail, measured air forces might be highly distorted by tunnel-wall effects. In order to check this theory for two-dimensional wings, some measurements and calculations for a specific wing and tunnel setup have been recently made for Mach number 0.7 (ref. 17). Some results of this work are shown in figures 9 and 10. In figure 9 calculated values of amplitudes of

lift due to pitching (about midchord) with and without tunnel walls are compared with measured values of these amplitudes. The abscissa is the ratio of frequency of oscillation to resonant or critical frequency. The ordinate is the ratio of amplitude of lift, measured and calculated, with tunnel-wall effect, to the amplitude of lift without tunnel walls. Thus, if there were no tunnel-wall effects, the results, when plotted in this manner, should fall along the ordinate 1. The experimental values are indicated by circles with the dashed curve faired through them, and the calculated values are represented by the solid curve. It may be noted that in general both the calculated and experimental values fall well above the ordinate 1, or that there is considerable tunnel-wall effect even when the frequencies are only a small fraction of the critical frequency. It will also be noted that good agreement between theory and experiment is obtained over a good portion of the frequency range and that the calculated critical frequency agrees well with the experimentally determined critical frequency. In figure 10 the ordinate is phase angle in degrees and the abscissa is again the ratio of frequency of oscillation to resonant frequency. The measured phase angles are indicated by circles with the short-dash curve faired through them; calculated phase angles including tunnel-wall effects are indicated by the solid curve and calculated phase angles not including tunnel-wall effects are indicated by the long- and short-dash curve. The agreement between results of calculations including tunnel-wall effects and experiment is, in this instance, remarkably good, but there are very large differences between these results and those of calculations based on no tunnel walls.

The agreement between theory, including tunnel walls, and experiment shown in these figures seems to verify the fact that tunnel-wall interference is something to be reckoned with, when unsteady air-force coefficients are measured in wind tunnels. It must be recalled, however, that what has been discussed pertains only to two-dimensional wings and to two-dimensional closed tunnels with smooth solid walls. It should be emphasized that the data presented represent the results of first efforts at actually calculating this type of tunnel-wall interference. It is to be noted that the ratio of tunnel height to wing chord for this particular case is relatively small. For larger values of this ratio the tunnel-wall effects should be much less pronounced, provided measurements are confined to ranges of frequency away from the resonant frequency. The resonant frequency itself is independent of chord length.

With regard to wings of finite span, there certainly must be similar effects. However, in order to determine what the effects are for this case, it seems necessary first to know what the forces are without tunnel walls. There are reasons to believe that magnitudes of tunnel interference are attenuated by decreasing aspect ratio. Also, since the underlying theory of an oscillating wing in compressible flow is

one of acoustics, it seems reasonable to conjecture that some application of classic principles of sound absorption or energy dissipation may greatly reduce or even eliminate this type of tunnel-wall interference.

#### SUMMARY OF RESULTS

The results of several investigations attempting to furnish some information concerning oscillatory air forces on wings of finite span at high subsonic and low supersonic speeds have been discussed. One of these investigations furnished useful coefficients for rigid rectangular and triangular wings in supersonic flow by extending the expanded potentials for these wings from the third to the fifth power of the frequency. Similarly, another investigation has provided the coefficients for rectangular and triangular wings for downwash conditions associated with wing deformations and distortions. Other investigations furnish useful coefficients for rectangular, triangular, and swept wings at low subsonic speeds. Also, a possible means for obtaining results in the higher subsonic Mach number range for all these wings has been discussed. Finally, an investigation of wind-tunnel-wall effects for two-dimensional flow indicates that wind-tunnel-wall interference must be considered if unsteady air-force coefficients are to be measured in wind tunnels at high subsonic speeds.

## REFERENCES

1. Watkins, Charles E.: Effect of Aspect Ratio on the Air Forces and Moments of Harmonically Oscillating Thin Rectangular Wings in Supersonic Potential Flow. NACA Rep. 1028, 1951.
2. Watkins, Charles E., and Berman, Julian H.: Air Forces and Moments on Triangular and Related Wings With Subsonic Leading Edges Oscillating in Supersonic Potential Flow. NACA Rep. 1099, 1952.
3. Nelson, Herbert C.: Lift and Moment on Oscillating Triangular and Related Wings With Supersonic Edges. NACA TN 2494, 1951.
4. Chang, Chieh-Chien: The Aerodynamic Behavior of a Harmonically Oscillating Finite Swept-Back Wing in Supersonic Flow. NACA TN 2467, 1951.
5. Garrick, I. E., and Rubinow, S. I.: Flutter and Oscillating Air-Force Calculations for an Airfoil in a Two-Dimensional Supersonic Flow. NACA Rep. 846, 1946. (Supersedes NACA TN 1158.)
6. Tuovila, W. J., Baker, John E., and Regier, Arthur A.: Initial Experiments on Flutter of Unswept Cantilever Wings at Mach Number 1.3. NACA RM L8J11, 1949.
7. Lawrence, H. R., and Gerber, E. H.: The Aerodynamic Forces on Low Aspect Ratio Wings Oscillating in an Incompressible Flow. Jour. Aero. Sci., vol. 19, no. 11, Nov. 1952, pp. 769-781.
8. Dengler, M. A., et al.: Theoretical Studies of the Effects of Aspect Ratio on Flutter.
  - (a) Progress Rep. No. 1, Contract No. AF 18(600)-129, Midwest Res. Inst. (Kansas City, Mo.), Apr. 11, 1952.
  - (b) Progress Rep. No. 2, Contract No. AF 18(600)-129, Midwest Res. Inst. (Kansas City, Mo.), June 20, 1952.
  - (c) Progress Rep. No. 3, Contract No. AF 18(600)-129, Midwest Res. Inst. (Kansas City, Mo.), June 30, 1952.
  - (d) Progress Rep. No. 4, Contract No. AF 18(600)-129, Midwest Res. Inst. (Kansas City, Mo.), July 18, 1952.
9. Woodcock, D. L.: Aerodynamic Derivatives for a Delta Wing Oscillating in Elastic Modes. Rep. No. Structures 132, British R.A.E., July 1952.

10. Lehrian, Doris E.: Aerodynamic Coefficients for an Oscillating Delta Wing. Rep. No. 14,156, British A.R.C., July 14, 1951.
11. Garrick, I. E.: Some Research on High-Speed Flutter. Royal Aero. Soc., 1952, pp. 419-446. (Presented at Third International Joint Conference of the R.A.S. - I.A.S., Brighton, England, Sept. 3-14, 1951.)
12. Ashley, Holt: Some Unsteady Aerodynamic Problems Affecting the Dynamic Stability of Aircraft. M.I.T. Thesis, 1951.
13. Jones, W. Pritchard: The Influence of Thickness/Chord Ratio on Supersonic Derivatives for Oscillating Aerofoils. Rep. No. 10,871, British A.R.C., Sept. 10, 1947.
14. Wyllie, Alexander: A Second-Order Solution for an Oscillating Two-Dimensional Supersonic Airfoil. Jour. Aero. Sci., vol. 19, no. 10, Oct. 1952, pp. 685-696, 704.
15. Van Dyke, Milton D.: On Second-Order Supersonic Flow Past a Slowly Oscillating Airfoil. Jour. Aero. Sci. (Readers' Forum), vol. 20, no. 1, Jan. 1953, p. 61.
16. Runyan, Harry L., and Watkins, Charles E.: Considerations on the Effect of Wind-Tunnel Walls on Oscillating Air Forces for Two-Dimensional Subsonic Compressible Flow. NACA TN 2552, 1951.
17. Runyan, Harry L., Woolston, Donald S., and Rainey, A. Gerald: A Theoretical and Experimental Study of Wind-Tunnel-Wall Effects on Oscillating Air Forces for Two-Dimensional Subsonic Compressible Flow. NACA RM L52I17a, 1953.

CONFIDENTIAL

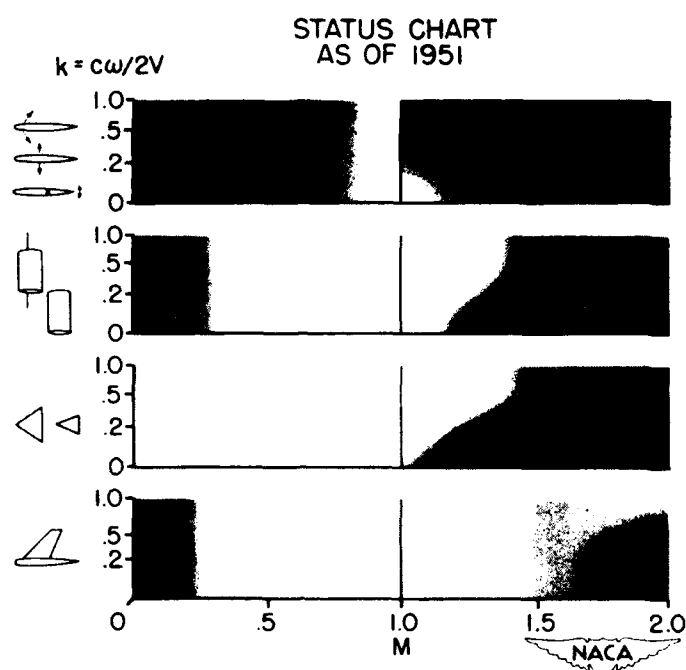


Figure 1.

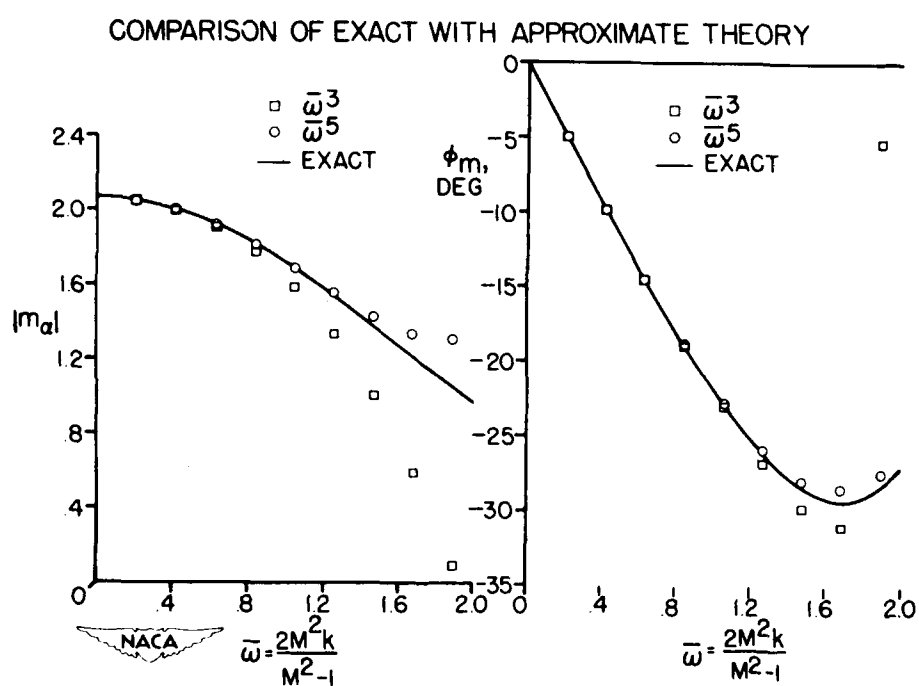


Figure 2.

CONFIDENTIAL

## PITCHING-MOMENT COEFF. FOR 2-DIM. RECT. AND TRI. WINGS

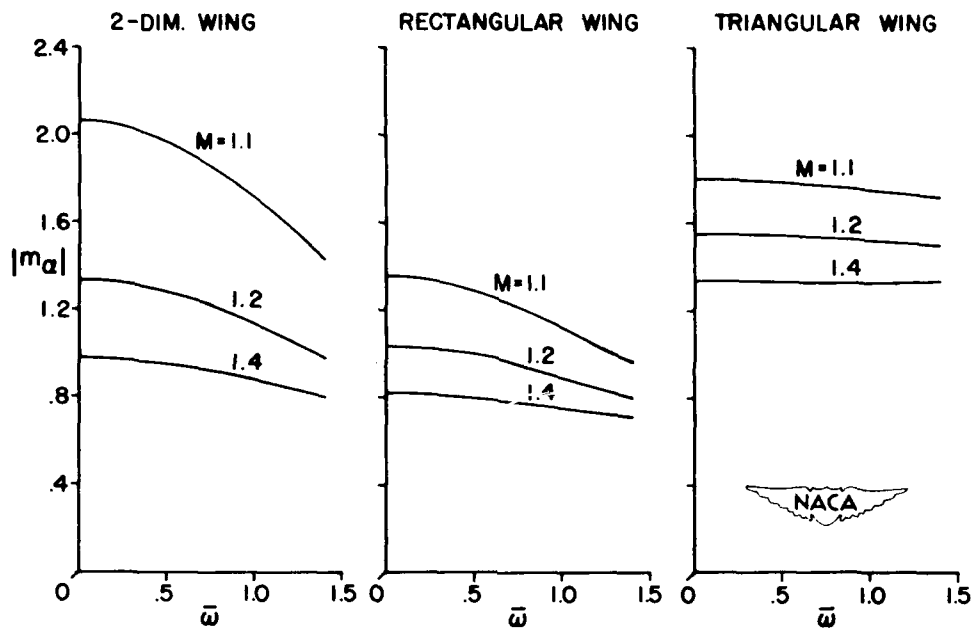


Figure 3.

## PHASE ANGLES FOR 2-DIM. RECT. AND TRI. WINGS

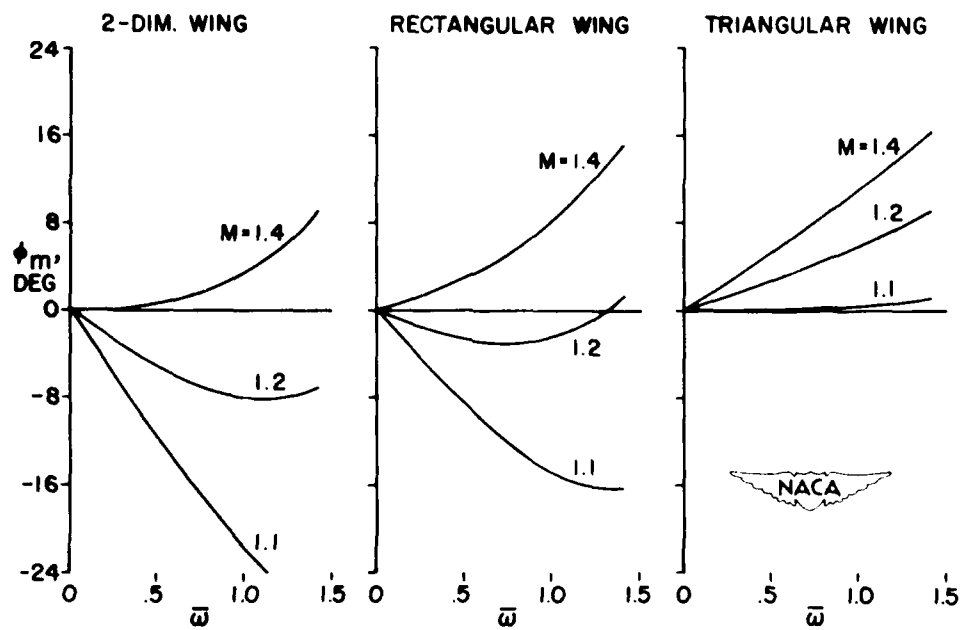


Figure 4.

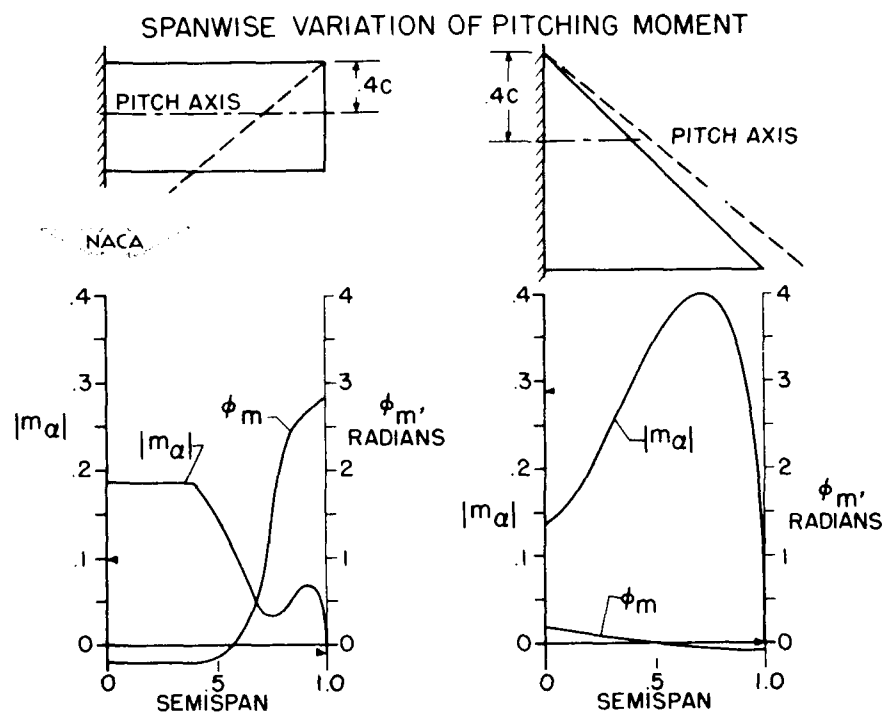


Figure 5.

## COMPARISON OF THEO. AND EXP. FLUTTER SPEEDS

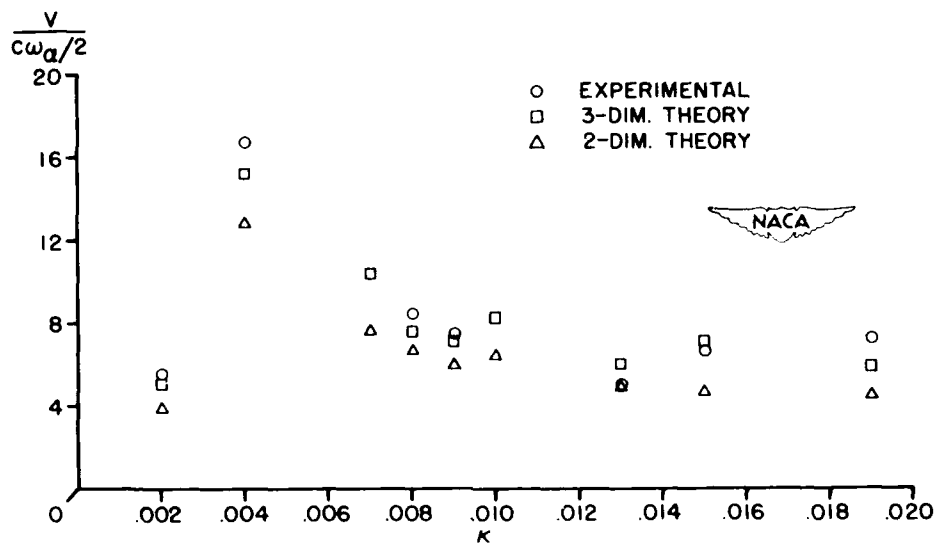


Figure 6.

## PLAN FORMS UNDER CONSIDERATION

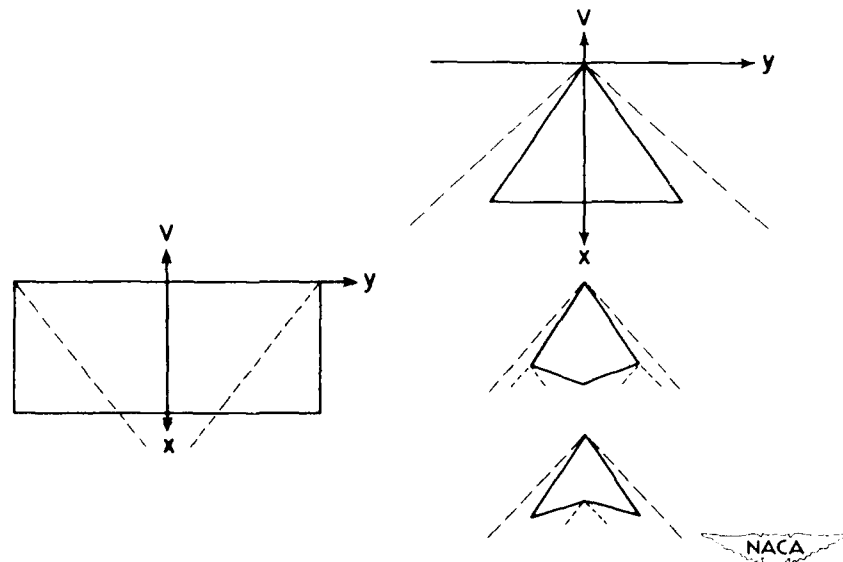


Figure 7.

## SPAN DIST. OF LIFT AND PHASE ANGLES DUE TO PARABOLIC BENDING

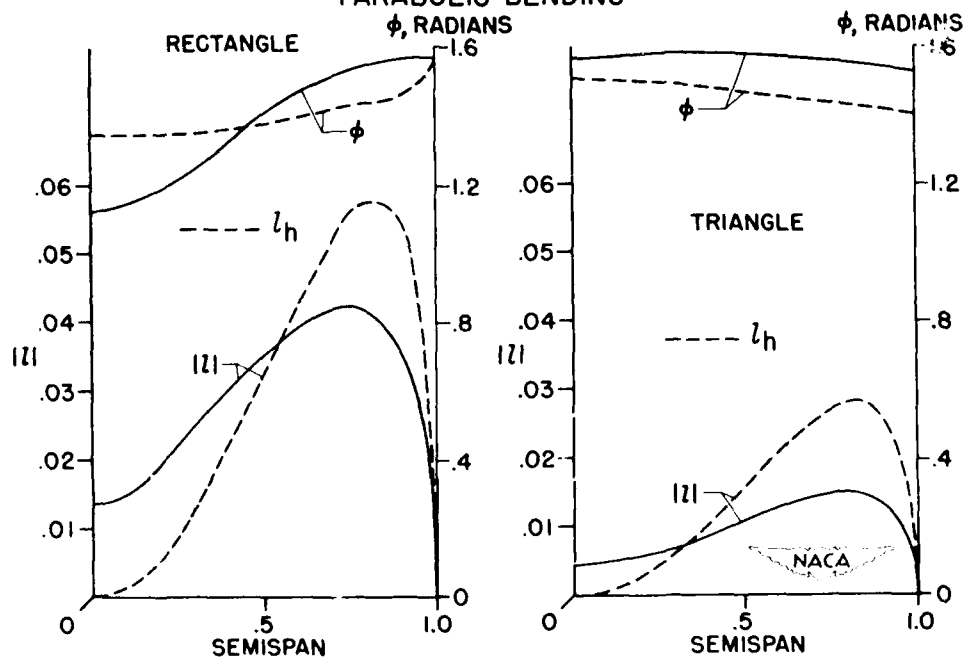


Figure 8.

CONFIDENTIAL

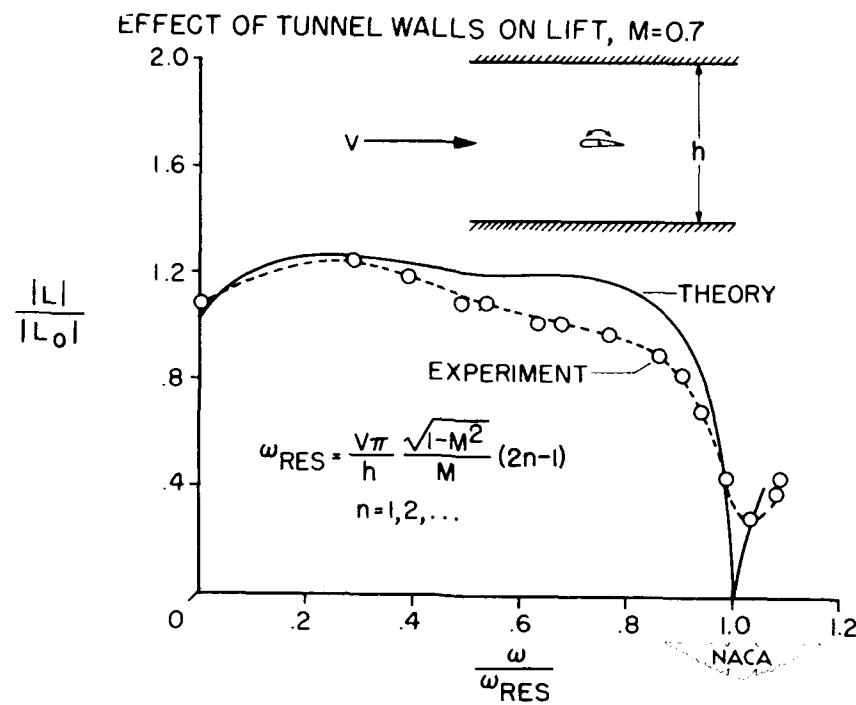


Figure 9.

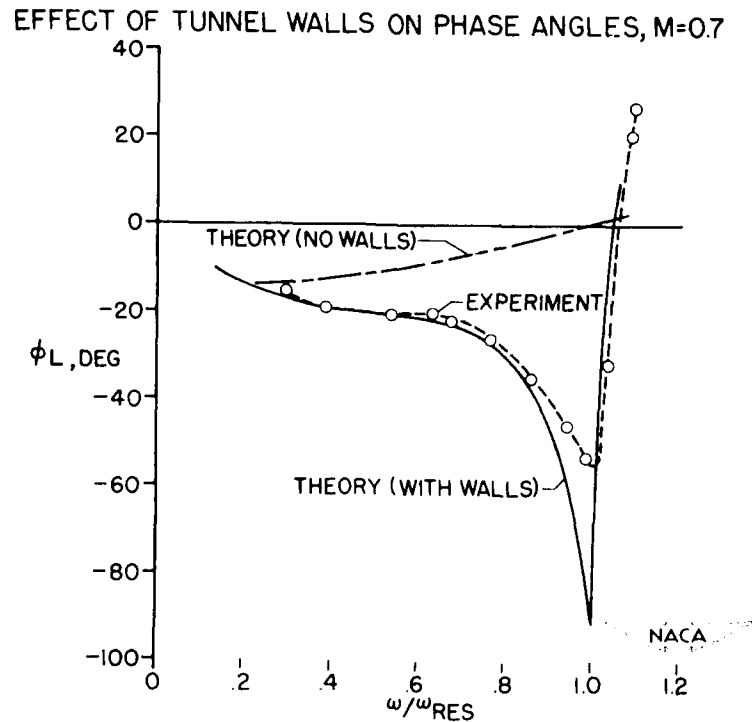


Figure 10.

CONFIDENTIAL

SOME EFFECTS OF WING PROFILE ON THE TWO-DIMENSIONAL  
FLUTTER DERIVATIVES FOR WINGS OSCILLATING IN  
PITCH AT HIGH SUBSONIC SPEEDS

By John A. Wyss

Ames Aeronautical Laboratory

23

An extensive research program has been undertaken at both the Langley and the Ames Aeronautical Laboratory to determine quantitative flutter derivatives for two-dimensional wings oscillating in pitch. In the present paper, emphasis has been placed upon supercritical speeds for which theoretical values are meager or nonexistent. It is well known that present theory, essentially based on potential flow, does not account properly for such factors as flow separation and shock formation; hence the aircraft designer must of necessity look to experimental values for any significant trends at these speeds.

Since the wing profile may be expected to have a significant effect on flow conditions, several models with 2-foot chords were used to determine the effects of wing thickness and thickness distribution. The various wing profiles are illustrated in figure 1.

The NACA 65A008 profile was used as the reference wing. Wing thickness was varied by the use of the 12-, 8-, and 4-percent-thick wings. Wing-thickness distribution was varied by use of wings with maximum thickness located at about 16, 42, and 66 percent of the wing chord.

The short lines along the profile of the reference wing indicate the chordwise locations of the 30 flush-type pressure cells (see refs. 1 and 2) which were used to determine the fluctuating aerodynamic forces. The instrumentation for each of the other models was identical to that of the reference wing.

The electrical outputs from the upper and lower cells at each station were summed electronically to give the instantaneous pressure difference between the upper and lower surfaces of the model. The individual outputs may in turn be calibrated and summed to give the instantaneous change in lift or moment. An electrical transducer indicated the instantaneous angle of attack.

Figure 2 is a front view of a model mounted between two walls installed in the Ames 16-foot high-speed tunnel. These walls form a two-dimensional channel 16 feet high,  $1\frac{1}{2}$  feet wide, and 20 feet long

(ref. 3). The gaps between the ends of the model and the tunnel walls were effectively sealed with sliding felt pads which moved with the model.

The method of oscillating the models in pitch by means of a mechanical oscillator mounted on top of the tunnel is shown in figure 3. The oscillator was mounted directly over one of the walls so that the sector arm and the cable and rod drive system were contained inside the wall. The model was supported by bearings in each wall, with the axis of rotation at the quarter-chord station.

Each model was oscillated at mean angles of attack of  $0^\circ$ ,  $2^\circ$ , and  $4^\circ$  at the same pitch amplitude of  $\pm 1^\circ$  and through the same frequency range from 4 to 40 cycles per second.

As pointed out in a previous paper by Charles E. Watkins, Harry L. Runyan, and Julian H. Berman, the perhaps disconcerting effects of the phenomenon of wind-tunnel resonance must be accounted for either by avoiding conditions at which tunnel-wall effects are significant or by correcting the results for the effects of the tunnel walls (refs. 4 and 5). However, for mixed-flow conditions, such corrections based on potential flow would again not apply; hence, to minimize tunnel-wall effects, all data obtained at frequencies within 10 percent of the tunnel resonant frequency have been omitted. As a matter of interest, the omission of such data had an effect of changing the magnitude of the final summary results by about 4 percent. If data for frequencies within 20 percent of the resonant frequencies were omitted, a further change of less than 1 percent would occur. Although the use of such a procedure does not mean tunnel-wall effects have been completely eliminated over the entire frequency range, it is felt that tunnel-wall effects are not a predominant factor in the trends of the data. The effects of tunnel resonance are perhaps smaller than might be expected. However, in the present investigation, the ratio of tunnel height to wing chord is about twice that used in the investigation described in the previous paper by Charles E. Watkins, Harry L. Runyan, and Julian H. Berman.

Examples of the type of data obtained in the investigation are illustrated in figure 4. Oscillograph traces for 5 of the 15 chord stations are shown for the reference model for subcritical and supercritical Mach numbers. The chordwise locations of the pressure fluctuations are shown along the profile of the wing. The lowest trace on each record indicates the instantaneous angle of attack. The oscillograph traces from the pressure cells represent the variation with time of the difference in pressure between the upper and lower surfaces at each station.

It may be pointed out that, at the lower Mach number, the larger pressure fluctuations occur on the forward portion of the wing. At the

higher Mach number, large pressure fluctuations extend much farther rearward along the chord. In particular, large irregular pressure fluctuations may be noted at the 62.5-percent-chord station which are indicative of the presence of a shock wave.

Figure 5 was prepared to show typical results for several frequencies for the reference model. It may be recalled that the flutter derivative may be expressed as a vectorial quantity. The magnitude of the length of the vector is expressed in terms of the slope of the lift curve per radian in the upper portion of the figure. The phase-angle relationship in degrees between lift and model angle of attack is shown in the lower portion of the figure. Each of these quantities is shown as a function of Mach number.

The lines showing the theoretical values are quite regular and are identified at one end by the frequency in cycles per second to which they pertain. Absolute rather than reduced frequency has been chosen as a parameter since the data appeared more meaningful in this form. The theoretical values up to a Mach number of 0.7 were derived from the work of Dietze (ref. 6). Since it was necessary to extrapolate the theory to the higher Mach numbers, the extension of Dietze's results by Minihinnick to a Mach number of 0.8 (ref. 7) and the values at sonic speed as calculated by Nelson and Berman of the Langley Laboratory (ref. 8) were also used. Such extrapolation may inherently involve some error; nevertheless, a basis for comparing the effects of airfoil shape is established.

To distinguish between the various frequencies, the experimental and theoretical values are each faired with the same type of line. For example, the experimental and theoretical values for a frequency of 8 cycles per second are each shown with a solid line. Examination of the experimental data for a frequency of 8 cycles per second indicates that the trends of both experiment and theory are the same at low Mach numbers. As Mach number increases, a large decrease in the magnitude of the experimental derivative occurs, accompanied by deviations from theory of the phase angle. Although the agreement with theory for the other frequencies is not as precise at the lower Mach numbers, it may be seen that the general trends for all frequencies are nearly the same.

The data from figure 5 is shown in figure 6 in a different form. The experimental magnitude has been divided by the theoretical magnitude, and theoretical phase angle subtracted from experimental phase angle. These quantities are also shown as a function of Mach number. If the experimental and theoretical values exactly agreed, the ratio of the magnitudes of the derivatives would be 1, while the difference in phase angle would be 0.

The faired lines represent the average deviation from theory for the entire frequency range up to 40 cycles per second. It might be noted that the averaging process has the effect of removing frequency as a parameter. However, since each model was oscillated at the same amplitude and through the same range of frequencies, the use of the average deviation from theory allows the over-all effects of airfoil shape and the general trends of the data to be more easily shown.

To provide some indication of the effect of frequency, a companion figure has been prepared. In figure 7, the individual points are plotted from which the average values have been derived. Although these results may at first glance appear to be erratic, it must be noted that the individual points do not indicate an entirely random experimental scatter about the mean line for the various frequencies. For example, examination of the points for 40 cycles per second in the top portion of the figure shows that these points are usually the uppermost value at each Mach number. This figure not only provides some indication of the range of the experimental values, but again illustrates the fact that, although the effect of frequency may be complex, the general trends of the results are represented by the faired average curves.

Figure 8 is a summary figure which shows the effects of the variation of thickness distribution. It may be noted that, in general, the NACA 2-008 wing with maximum thickness toward the leading edge follows theory more closely both in magnitude and in phase angle than those models with maximum thickness located farther rearward. The decrease in the magnitude of the derivative for each model is again apparent at the higher Mach numbers. However, the shift in phase angle is quite small. The most important effect of moving the location of maximum thickness along the chord appears to be in the magnitude of the coefficient rather than a shift in phase angle.

Wing thickness has a much more pronounced effect than wing thickness distribution. This is illustrated in figure 9. The data are for the 12-, 8-, and 4-percent-thick airfoils. As might be expected, the primary effect of reducing wing thickness is to delay any large deviation from theory to a higher Mach number. As wing thickness is decreased, the deviation from theory at the higher Mach numbers is also decreased in both the magnitude of the derivative and its phase angle.

These effects of wing thickness strongly suggest a parallelism with the trends of the lift-curve slope obtained for the steady-state condition at supercritical Mach numbers. Figure 10 has been prepared for the reference airfoil to indicate more clearly that just such a parallelism does exist. This figure is the same as figure 6, with the steady-state curve superimposed on the upper portion. The steady-state data have

been normalized with the Prandtl-Glauert extension of the theoretical lift-curve slope. It may be recalled that the Prandtl-Glauert curve is also obtained as an end condition from flutter theory as the frequency of oscillation approaches zero.

Although the curves do not coincide, the general trends of the magnitudes of the oscillatory coefficients are very similar to the trends for steady-state conditions. Also, the Mach number at which a large departure from theory occurs is nearly the same for the oscillatory and the nonoscillatory case. The primary effect of increasing the angle of attack to  $2^{\circ}$  and  $4^{\circ}$  was to decrease the Mach number at which the divergence from theory occurred.

For the steady-state condition the phase angle is zero; therefore, no corollary for the phase angle with relation to the oscillatory condition is possible. However, except for the 12-percent-thick wing, the phase angle shows only a moderate deviation from theory throughout the speed range of the present investigation.

To summarize, it has been indicated that, at least within the limits of the present investigation, the general trends of the supercritical experimental data for the oscillating wing are such that the magnitude of the coefficients follows the trends of steady-state data, while the phase angle shows only moderate deviations from theory for the thinner wings.

Although a more critical evaluation of these results by an application to a typical flutter analysis must await the reduction of moment data, it would appear that airfoil shape, and in particular wing thickness, becomes an important flutter parameter at supercritical Mach numbers.

It would also appear that the aircraft designer can gain some insight into the effects of mixed flow on the flutter derivatives by a consideration of the more readily available results for steady-state conditions.

## REFERENCES

1. Erickson, Albert L., and Robinson, Hubert C.: Some Preliminary Results in the Determination of Aerodynamic Derivatives of Control Surfaces in the Transonic Speed Range by Means of a Flush-Type Electrical Pressure Cell. NACA RM A8H03, 1948.
2. Wyss, John A., and Sorenson, Robert M.: An Investigation of the Control-Surface Flutter Derivatives of an NACA 65<sub>1</sub>-213 Airfoil in the Ames 16-Foot High-Speed Wind Tunnel. NACA RM A51J10, 1951.
3. Sorenson, Robert M., Wyss, John A., and Kyle, James C.: Preliminary Investigation of the Pressure Fluctuations in the Wakes of Two-Dimensional Wings at Low Angles of Attack. NACA RM A51G10, 1951.
4. Runyan, Harry L., and Watkins, Charles E.: Considerations on the Effect of Wind-Tunnel Walls on Oscillating Air Forces for Two-Dimensional Subsonic Compressible Flow. NACA TN 2552, 1951.
5. Runyan, Harry L., Woolston, Donald S., and Rainey, A. Gerald: A Theoretical and Experimental Study of Wind-Tunnel-Wall Effects on Oscillating Air Forces for Two-Dimensional Subsonic Compressible Flow. NACA RM L52I17a, 1953.
6. Dietze, F.: The Air Forces of the Harmonically Vibrating Wing in Compressible Medium at Subsonic Velocity (Plane Problem). Translation No. F-TS-506-RE, Air Materiel Command, U. S. Army Air Forces, Nov. 1946; Part II: Numerical Tables and Curves. Translation No. F-TS-948-RE, Air Materiel Command, U. S. Air Force, Mar. 1947.
7. Minchinick, I. T.: Subsonic Aerodynamic Flutter Derivatives for Wings and Control Surfaces (Compressible and Incompressible Flow). Rep. No. Structures 87, British R.A.E., July 1950.
8. Nelson, Herbert C., and Berman, Julian H.: Calculations on the Forces and Moments for an Oscillating Wing-Aileron Combination in Two-Dimensional Potential Flow at Sonic Speed. NACA TN 2590, 1952.

## SECTION PROFILES OF MODELS

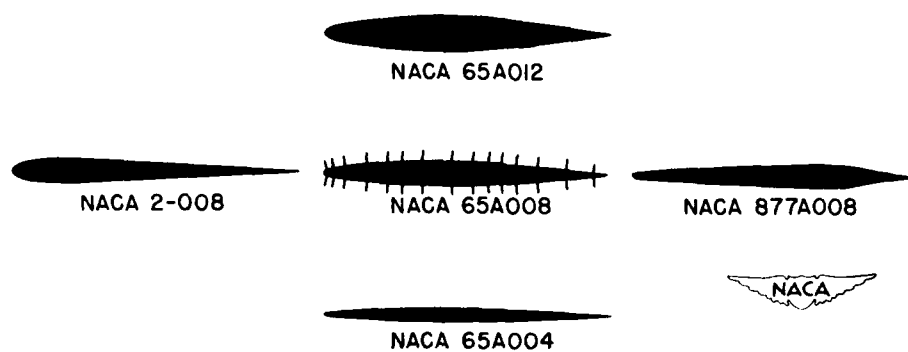


Figure 1.

## MODEL MOUNTED BETWEEN TWO-DIMENSIONAL WALLS



Figure 2.

CONFIDENTIAL

## DIAGRAMMATIC SKETCH OF WING DRIVE SYSTEM

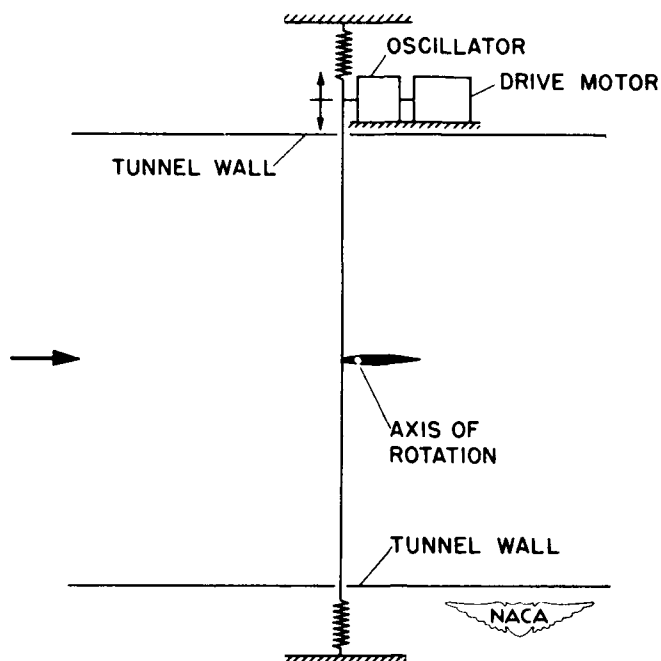


Figure 3.

## TYPICAL OSCILLOGRAPH TRACES

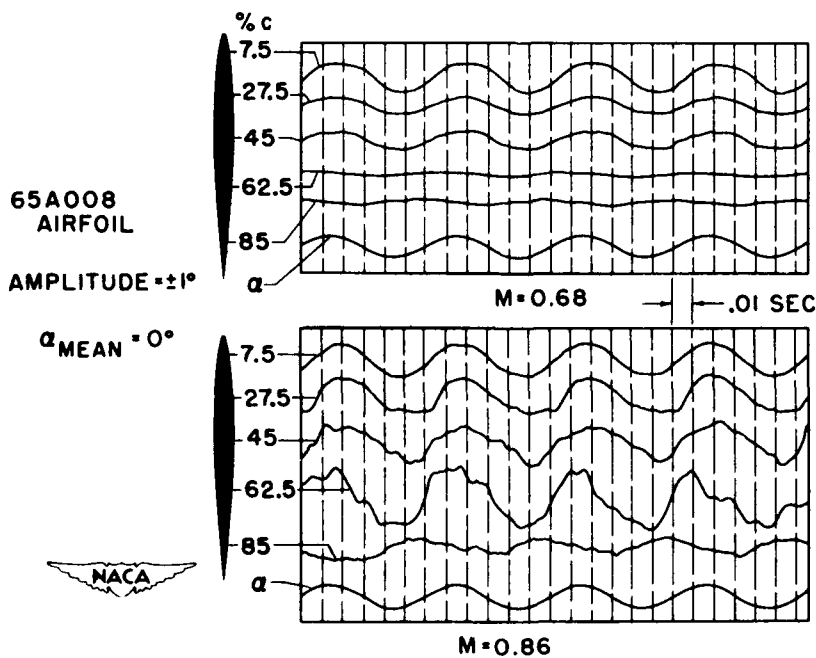


Figure 4.

CONFIDENTIAL

## RESULTS FOR NACA 65A008 AIRFOIL

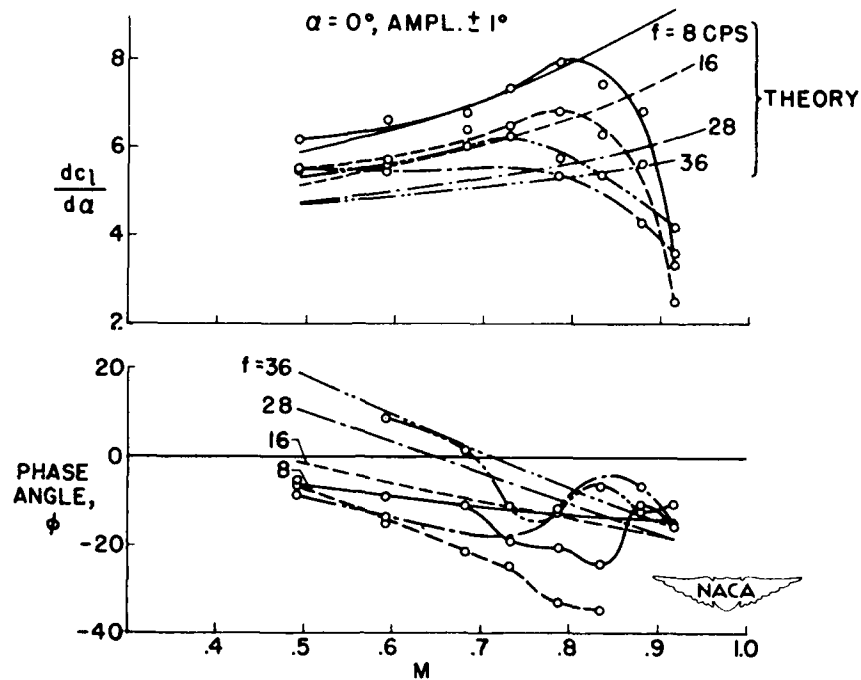


Figure 5.

## DATA NORMALIZED WITH THEORY

NACA 65A008

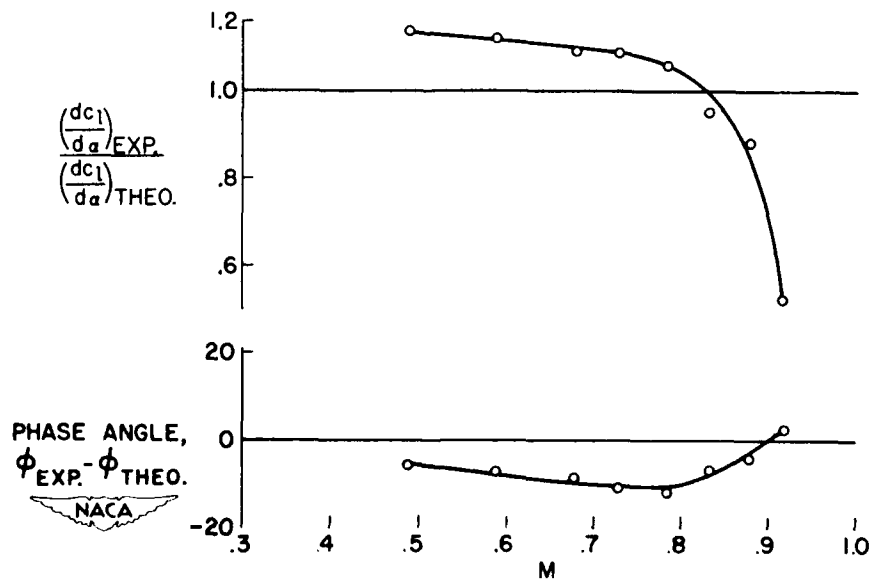


Figure 6.

CONFIDENTIAL

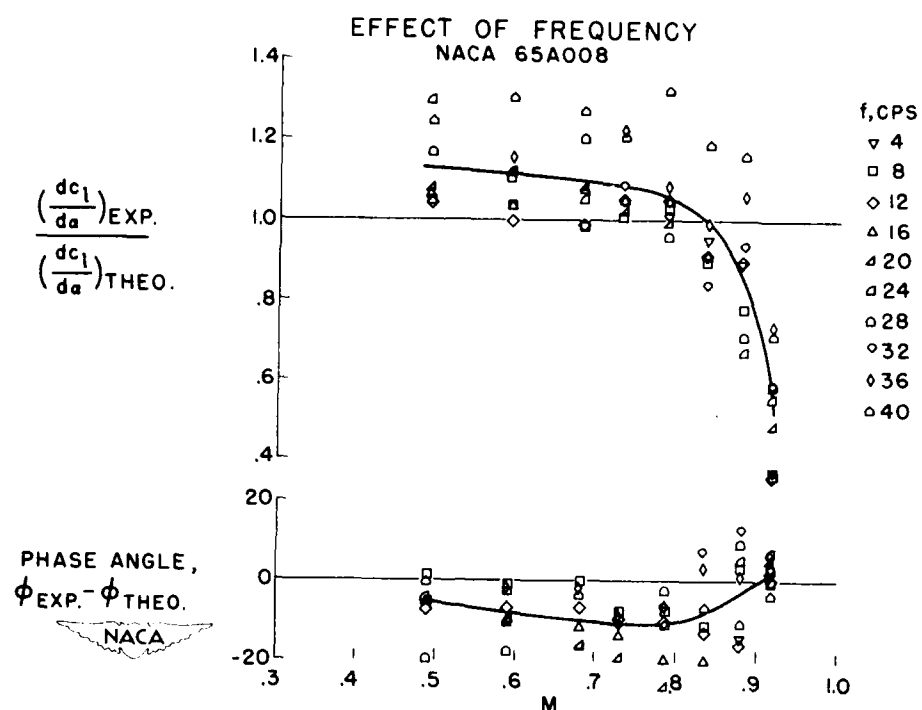


Figure 7.

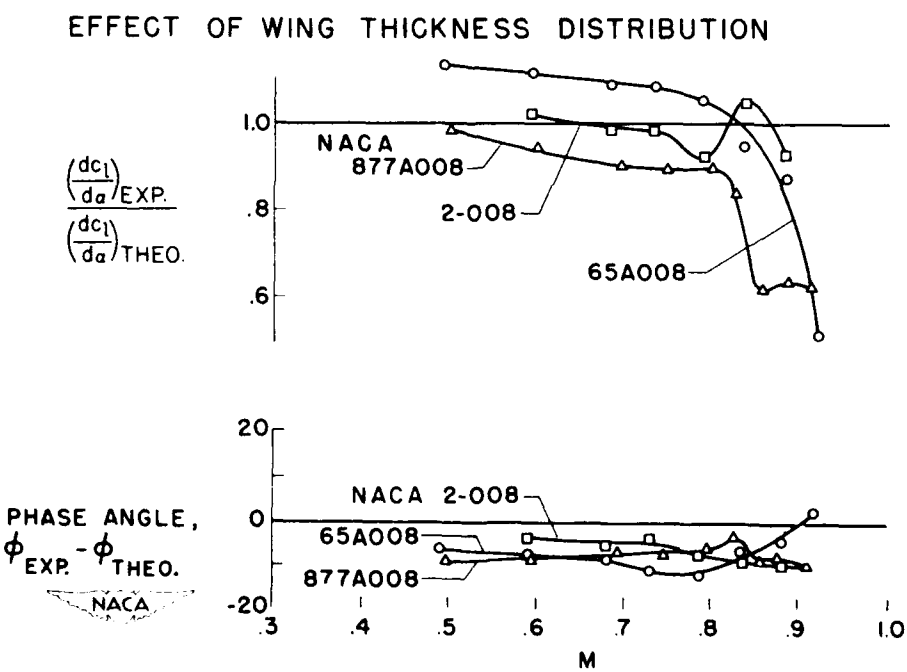


Figure 8.

CONFIDENTIAL

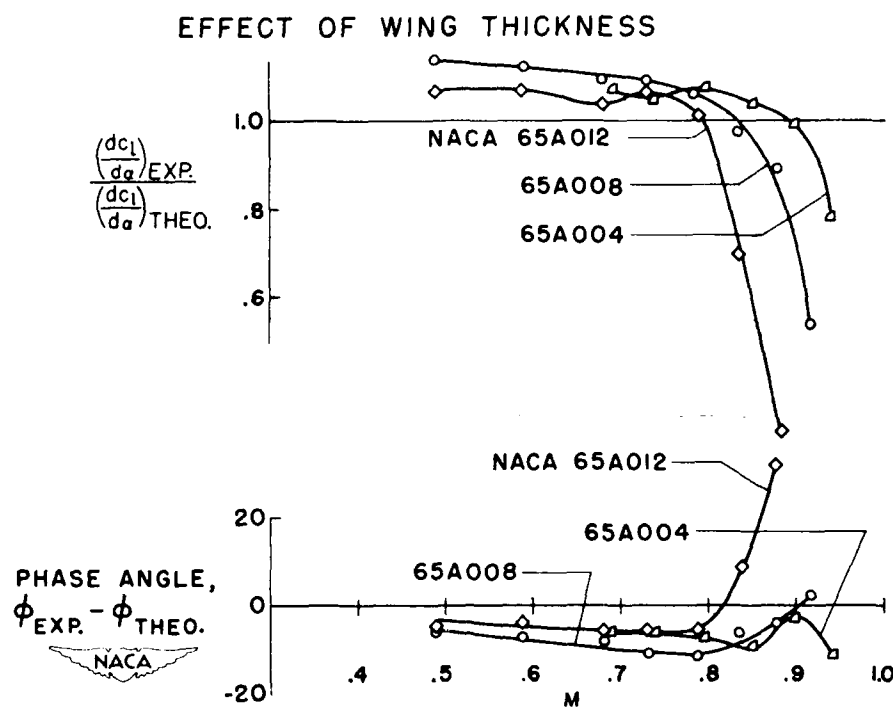


Figure 9.

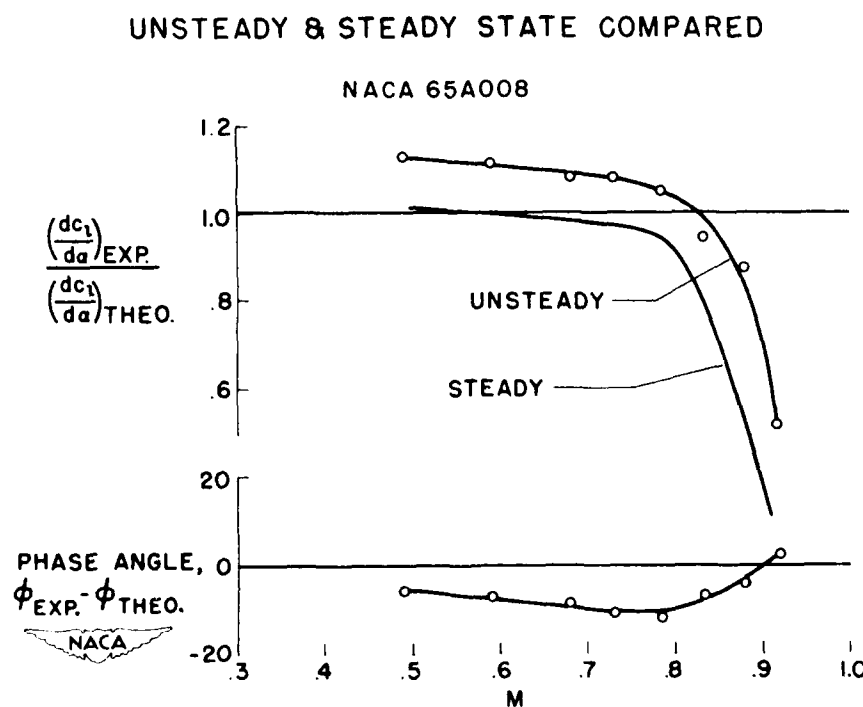


Figure 10.

## DISCUSSION OF THREE-DIMENSIONAL OSCILLATING AIR FORCES

## BASED ON WIND-TUNNEL MEASUREMENTS

By Sherman A. Clevenson and Sumner A. Leadbetter

Langley Aeronautical Laboratory

Experimental determination of the oscillating air forces in the high subsonic speed range for wings of finite aspect ratio is desirable because of a lack of available data, both theoretical and experimental. The purpose of this paper is to present some current results of experiments in the Langley 2- by 4-foot flutter research tunnel and the Langley 16-foot transonic tunnel on wings of finite aspect ratio with and without tip tanks at subsonic and transonic speeds. Inasmuch as the oscillatory aerodynamic coefficients for delta and rectangular wings of small aspect ratio in incompressible flow have recently been tabulated by Lawrence and Gerber (ref. 1), the results of the experimental investigation discussed in this paper will be compared with those of reference 1.

The experimental determination of oscillating air forces is more difficult than that of steady forces; in addition, there is the problem of interpretation of the results as affected by such items as wind-tunnel-wall interference, particularly at high subsonic and transonic speeds. For the two-dimensional case, these effects have been discussed in a previous paper by Charles E. Watkins, Harry L. Runyan, and Julian H. Berman. Before proceeding to the discussion of the current results, a brief illustration of wind-tunnel-wall effects for three-dimensional flow may be in order. Figure 1 shows the amplitude of the lift coefficient and damping-moment coefficient, referred to the mid-chord line, as a function of Mach number. These data were obtained on a rectangular wing of aspect ratio 2 mounted perpendicular to the tunnel wall on a plate that oscillated in the same wall as shown in the figure. The wing was oscillated about its midchord line at a given frequency at various Mach numbers. The predicted critical tunnel resonance region for a two-dimensional wing is shown by the cross-hatched area. The circles represent the experimental results and the solid curves are the results of calculations by the method of Lawrence and Gerber. The reason for the apparent variation of the theoretical incompressible-flow results with Mach number is that, inasmuch as the frequency was held constant in the tests and the airspeed varied, the reduced frequency  $k$ , which is equal to the circular frequency multiplied by the semichord and divided by the airspeed, varied with Mach number. This variation of  $k$  is responsible for the variation of the theoretical results with Mach number. As can be seen, fairly good agreement exists between experiment and theory in the region well away from the critical resonance region, but large variations take place near this range, particularly in the damping moment. However, since in the region

away from critical resonance the data follow a consistent trend, it will be assumed that the effects of tunnel-wall interference in this region are small. Subsequent results in this paper were obtained well away from the critical resonant region, except where stated otherwise, by using either air or Freon-12 as required in any given case.

The first configuration to be discussed is the wing shown in figure 1. For this wing, figure 2 shows the amplitudes of the lift and moment coefficients and the angle by which these coefficients either lead or lag the position of the wing. A moment phase angle shown below the zero line indicates a damped moment. Shown here for comparison are the results of the incompressible-flow analysis of Lawrence and Gerber indicated by the solid curves and the results for two-dimensional incompressible flow (ref. 2) indicated by the dashed curves. The experimental data are shown by the circles. In this figure, these coefficients and phase angles are shown as a function of the reduced-frequency parameter  $k$ , but, as in figure 1, the test results pertain to a constant frequency and varying airspeeds and, hence, varying Mach numbers. The range of Mach number was from 0.30 corresponding to the point at the highest value of  $k$  to 0.78 for the point at the lowest value of  $k$ . Although the calculations are for the incompressible case, they show reasonable agreement for this aspect ratio. The effect of aspect ratio can be observed by comparing experimental data with the results of two-dimensional theory and the theory for aspect ratio 2. The theoretical results for aspect ratio 2 fall close to the experimental data and follow the same trends for the four quantities shown, namely magnitudes of the lift and moment coefficients and phase angles of the lift and moment. Although three-dimensional theory underestimates the magnitudes of the aerodynamic forces, the use of these coefficients in a flutter analysis would tend to result in too high a calculated flutter speed and would thus be nonconservative. On the other hand, the two-dimensional theory overestimates the forces by a considerable amount and would tend to result in too low a calculated flutter speed, hence, overdesign of the aircraft. It is also interesting to note that there is little variation in the magnitudes of the forces and moments at low values of  $k$ , although the phase angles, especially the lift phase angles, do show considerable variation with  $k$ . Other experimental data, not shown, indicate that, even if the Mach number had not been varied as in these tests, these magnitudes would probably still show little variation. It thus appears that steady-state tests may be useful in predicting the magnitude of the oscillatory lift; however, the steady-state tests offer no information as to the phase angles, which may be equally important in a flutter analysis.

Figure 3 serves to show some effects of plan form at a given aspect ratio inasmuch as it contains the results of measurements of the lift and moment on a delta wing of aspect ratio 2, that is, a  $63.4^\circ$  delta

wing oscillating about a line through the midpoint of the root chord and perpendicular to the plane of symmetry. The moments are again referred to the axis of rotation. As in the preceding figure, the results are plotted against  $k$ , and again each point represents a different Mach number. The experimental parameters, lift, moment, and lift and moment phase angles, for this delta wing approximately follow the same trends as previously seen for the rectangular wing of aspect ratio 2. The phase angle again indicates a damped moment. It will be noted that the results of calculations by the method of Lawrence and Gerber for this plan form are in good agreement with the experimental results.

The use of large tanks at the tips of wings raises the question of how they affect oscillating air forces on the wing. The lift forces and phase angles have been obtained on a tank placed over the end of the rectangular wing of aspect ratio 2 as shown in figure 4. The wing extended into the tank approximately to its center line and there was a gap between the wing surface and the tank. The tank was attached to the wing tip through a strain-gage dynamometer, so that the tank forces could be separated from the total forces on the combination. The wing-tank combination was oscillated as a unit about the wing midchord axis. In this figure, lift magnitudes and phase angles are shown as functions of the reduced frequency. For comparison, the results of calculations by the method of Lawrence and Gerber for a rectangular wing of aspect ratio 2 without tip tanks are shown by the solid curves. The coefficients are all based on the same reference area, namely the area of the original wing alone. For reference, the dashed line represents a faired curve through the experimental data presented in figure 2 for the wing alone. From a comparison of this dashed curve with the square test points which represent the wing force in the presence of the tank, it may be seen that the addition of a tank to the wing tip does not increase the lift coefficient on the wing proper by a significant amount. If the comparison of these coefficients were made by taking into account only the exposed area, the lift coefficient on the wing in the presence of the tank would be increased by approximately 25 percent.

The lift on the tank was found to be about one-fourth the total lift on the wing-tank configuration for this low aspect ratio. The phase angles for the wing-tank combination and for the tank in the presence of the wing are about zero at reduced frequencies below 0.2, as are the phase angles for the wing in the presence of the tank. At somewhat higher reduced frequencies, the phase angles of the total lift on the wing-tank combination are consistently smaller than the phase angles on the wing alone and the phase angles on the tank in the presence of a wing are smaller still, being about one-half as large as those for the lift phase angle on the wing alone. From the given lift magnitudes and phase angles, the phase angle of the lift on the wing in the presence of the tank can be deduced and is found to be slightly less than that of the lift phase angle on the wing alone.

CONFIDENTIAL

A region of great importance today is the transonic speed range. Preliminary tests have been made in the Langley 16-foot transonic tunnel with a rectangular wing mounted on the forward portion of a free-fall body as shown in figure 5. The two wing panels oscillated as a unit; whereas the body remained stationary. Tests involving oscillations about the 44-percent-chord station were conducted up to a Mach number of 1.074. The oscillating forces, moments, and moment phase angles obtained are compared with theory in this figure, the moments being referred to the axis of rotation. These coefficients are shown as a function of Mach number and reduced-frequency parameter. The experimental data for the oscillating case (28 cps) are shown by the square test points and for the static case, by the circles. The experimental data for the lift were obtained from strain gages which measured the bending moment at the root of one wing. These data are uncorrected for possible shifts in the spanwise center of pressure and thus show trends rather than exact magnitudes. They were obtained through the critical tunnel resonance range mentioned previously in this paper but no particular resonant effects were noted, probably because of the fact that the Langley 16-foot transonic tunnel has a slotted throat, whereas the resonance data discussed previously by Watkins, Runyan, and Berman are based on the assumption of a two-dimensional closed throat. Another factor that may be of importance is the ratio of tunnel height to wing chord. This model is a three-dimensional model with a ratio of tunnel height to wing chord of 16 as compared to the ratio of 4 for the wing shown in figure 1.

For comparison with the transonic experimental data, the results of two-dimensional compressible-flow theories (refs. 3 to 5) are shown in this figure by the dashed curves and the results of supersonic theory (ref. 6) for a rectangular wing of aspect ratio 3 are shown by the solid curves. The three crosses represent the calculations based on coefficients tabulated by Statler and Easterbrook (ref. 7) for a rectangular wing of aspect ratio 3 at a Mach number of 0.8. All theoretical curves pertain to 28 cps. The experimental lift and moment coefficients may be seen to be much smaller than the theoretical two-dimensional compressible-flow coefficients and also slightly smaller than the results of supersonic theory. It is also interesting to note that the experimental oscillating coefficients are consistently smaller, although only by a small amount, than the experimental static coefficients. The phase angle of the moment remains negative through Mach number 1; this indicates a damped moment. The trend of moment phase angle predicted by two-dimensional theory toward an undamped region as the Mach number increases beyond 1 is thus not realized on wings of low aspect ratio in the Mach number region covered in these tests. Unfortunately no data were obtained at sufficiently high Mach numbers to indicate whether the abrupt change in phase angle predicted by three-dimensional supersonic theory is valid.

CONFIDENTIAL

Briefly summarizing, this paper has dealt with a preliminary, exploratory investigation and has presented a limited amount of data through the subsonic and transonic speed ranges on oscillating air forces. Comparisons of the coefficients tabulated by Lawrence and Gerber for the forces, moments, and their respective phase angles with the experimental data on a rectangular and a delta wing of aspect ratio 2 showed good agreement. The magnitudes of the forces and moments were found to be generally nearly invariant with reduced frequency for small values of  $k$ . The phase angles, however, were found to vary considerably with reduced frequency.

## REFERENCES

1. Lawrence, H. R., and Gerber, E. H.: The Aerodynamic Forces on Low Aspect Ratio Wings Oscillating in an Incompressible Flow. Jour. Aero. Sci., vol. 19, no. 11, Nov. 1952, pp. 769-781.
2. Theodorsen, Theodore: General Theory of Aerodynamic Instability and the Mechanism of Flutter. NACA Rep. 496, 1935.
3. Nelson, Herbert C., and Berman, Julian H.: Calculations on the Forces and Moments for an Oscillating Wing-Aileron Combination in Two-Dimensional Potential Flow at Sonic Speed. NACA TN 2590, 1952.
4. Garrick, I. E., and Rubinow, S. I.: Flutter and Oscillating Air-Force Calculations for an Airfoil in a Two-Dimensional Supersonic Flow. NACA Rep. 846, 1946. (Supersedes NACA TN 1158.)
5. Minchinick, I. T.: Subsonic Aerodynamic Flutter Derivatives for Wings and Control Surfaces (Compressible and Incompressible Flow). Rep. No. Structures 87, British R.A.E., July 1950.
6. Watkins, Charles E.: Effect of Aspect Ratio on the Air Forces and Moments of Harmonically Oscillating Thin Rectangular Wings in Supersonic Potential Flow. NACA Rep. 1028, 1951.
7. Statler, I. C., and Easterbrook, M.: Handbook for Computing Non-Stationary Flow Effects on Subsonic Dynamic Longitudinal Response Characteristics of an Airplane. Rep. No. TB-495-F-12, Cornell Aero. Lab., Inc., Mar. 1, 1950.

CONFIDENTIAL

AERODYNAMIC FORCES INDICATING TUNNEL-WALL  
EFFECTS ON A=2 WING

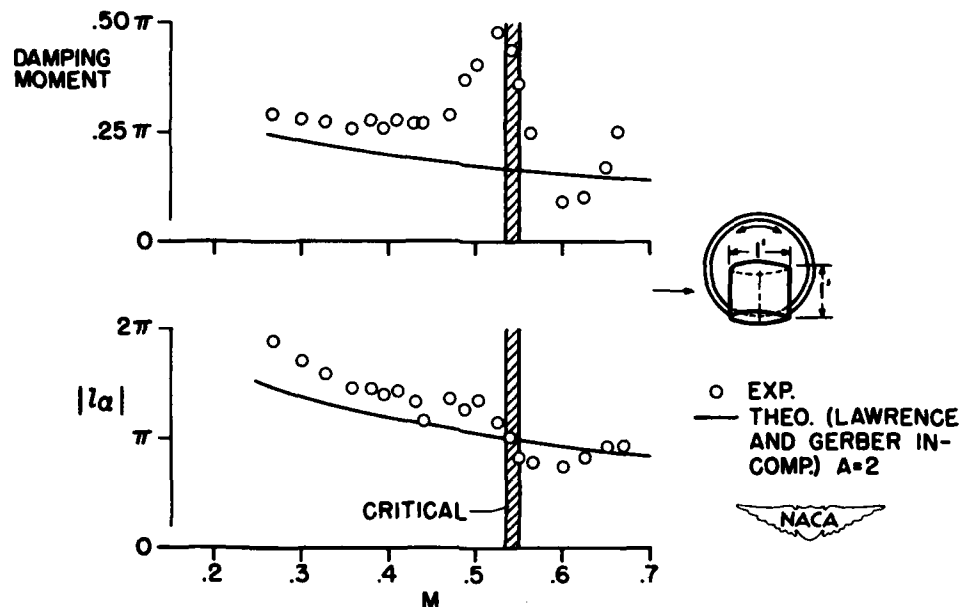


Figure 1.

AERODYNAMIC COEFFICIENTS FOR A=2 RECTANGULAR WING

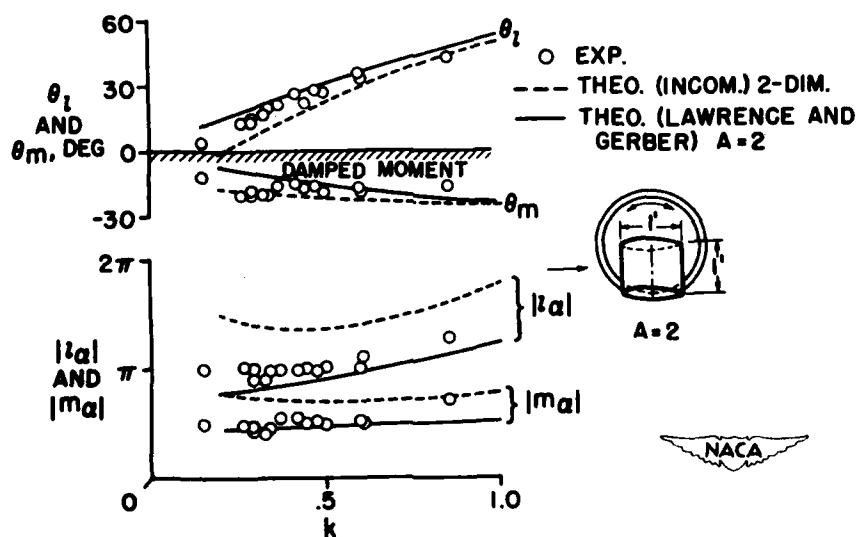


Figure 2.

CONFIDENTIAL

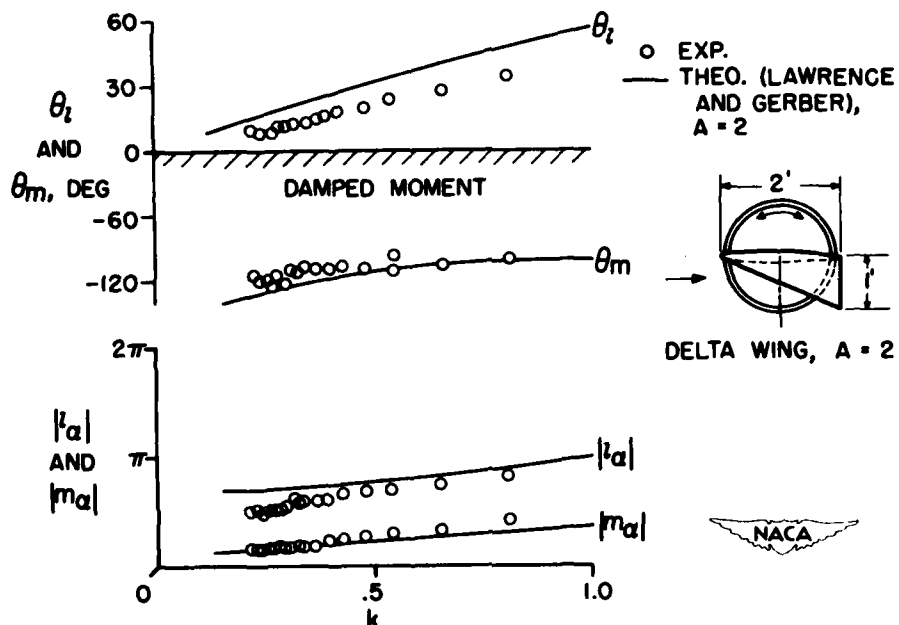
AERODYNAMIC COEFFICIENTS FOR  $A = 2$ ,  $63.4^\circ$  DELTA WING

Figure 3.

## AERODYNAMIC COEFFICIENTS FOR A WING-TANK COMBINATION

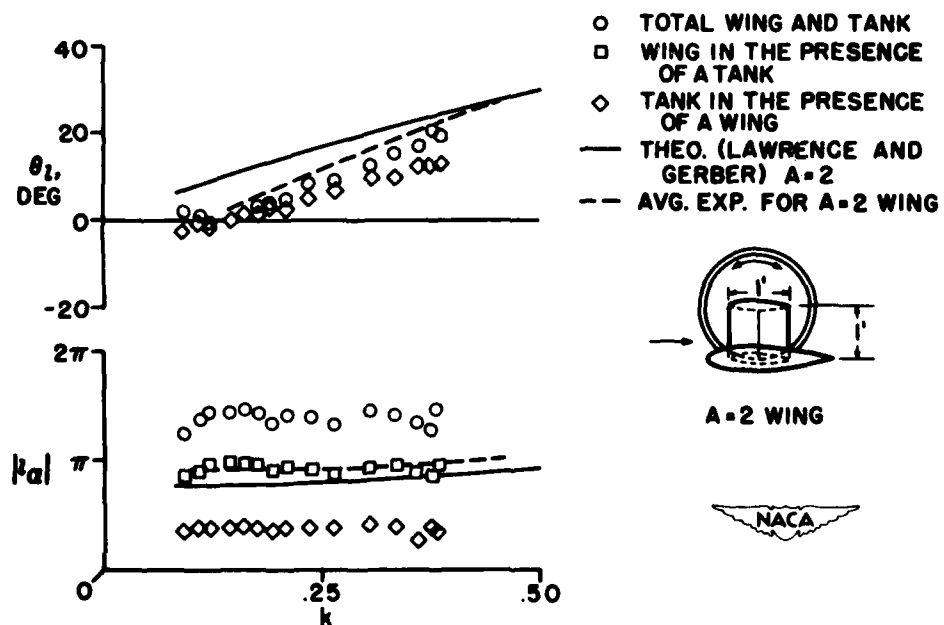


Figure 4.

CONFIDENTIAL

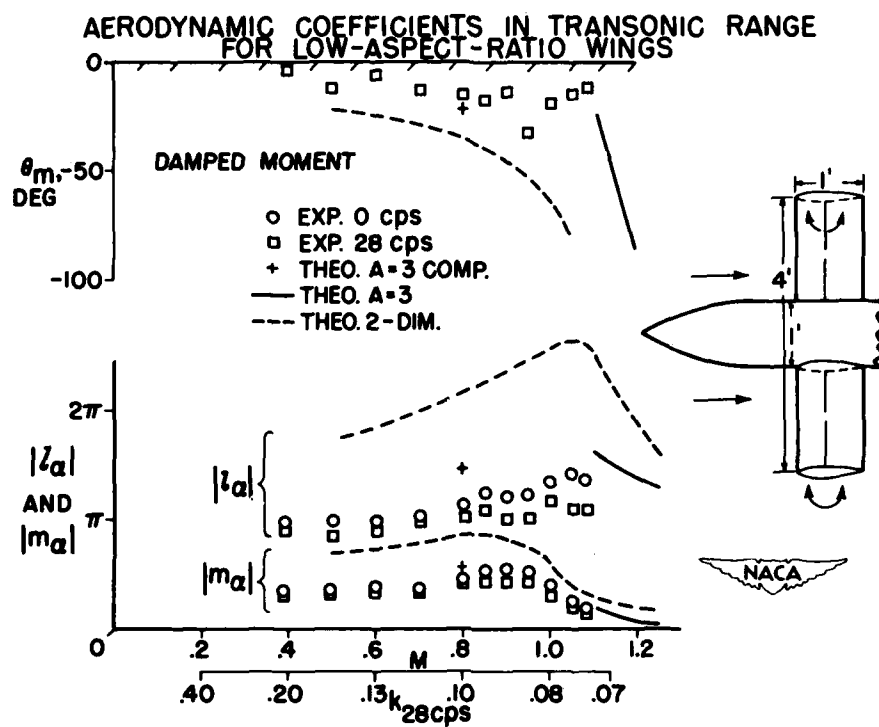


Figure 5.

CONFIDENTIAL

FLUTTER INVESTIGATION OF WING PLAN FORMS AT  
TRANSONIC SPEEDS

By Hugh C. DuBose and Laurence K. Loftin, Jr.

Langley Aeronautical Laboratory

An investigation of the transonic flutter characteristics of a series of systematically varied high-speed wing plan forms is currently in progress in the Langley 26-inch variable-density transonic blowdown tunnel. The purpose of the investigation is to determine the effects of sweepback and aspect ratio on the flutter speed for Mach numbers in the vicinity of 1.0. Those results which have been obtained to date are discussed in this paper.

Inasmuch as no flutter investigations had previously been made in a slotted-throat transonic tunnel, it seemed necessary before embarking on a general investigation to determine whether flutter results obtained in such a tunnel would check those obtained in free air, or in other words, to determine whether the boundaries of the slotted tunnel would influence the results. Accordingly, a short flutter investigation was made in the Langley transonic blowdown tunnel of a wing-body combination which was geometrically and dynamically similar to one for which data were available from tests made by the bomb-drop technique. The results of this investigation, which are taken from reference 1, are summarized in figure 1. The geometry of the wing-body combination is indicated in the upper left part of the figure. The aspect ratio of the wing was 7.38, the panel aspect ratio was 3.01, and the wing thickness tapered from 4 percent at the root to 2 percent at the tip. The results of the investigation are shown in the right part of the figure in terms of the ratio  $V_{EXP}/V_{REF}$  against Mach number, where  $V_{EXP}$  is the experimental flutter speed and  $V_{REF}$  is the reference flutter speed calculated on the basis of two-dimensional incompressible-flow aerodynamic derivatives. The points indicated with circles are from tests made in the transonic blowdown tunnel; those indicated with squares are from the bomb-drop tests. As can be seen, the agreement between the tunnel and flight flutter speeds is excellent.

After these results had been obtained, it seemed reasonable to expect that further transonic flutter tests in the slotted tunnel would produce reliable results. Accordingly, the systematic investigation of the effect of wing plan form on flutter in the transonic-speed range was begun.

The ranges of wing aspect ratio and sweep included in the investigation are indicated in figure 2. For the determination of the effects

of sweep, wings of aspect ratio 4 and sweep angles of  $0^\circ$ ,  $30^\circ$ ,  $45^\circ$ ,  $52.5^\circ$ , and  $60^\circ$  were chosen. For the investigation of the effects of aspect ratio, wings of  $0^\circ$  and  $45^\circ$  sweepback, having aspect ratios of 2, 4, and 6, were chosen. Corresponding panel aspect ratios were 0.91, 1.65, and 2.75, respectively. For all the wings, the taper ratio was 0.6. The streamwise airfoil section was the NACA 65A004 section.

Some of the pertinent structural properties of the wings are shown in the lower right corner of figure 2. The section center of gravity was at approximately 45 percent chord for all the wings. The elastic axis varied from about 40 to 54 percent chord and the radius of gyration about the elastic axis ranged from 24 to 27 percent of the chord. The ratio of the first bending frequency to the uncoupled first torsional frequency varied from approximately 0.10 to 0.36.

In order to obtain flutter at the ranges of air density available in the transonic blowdown tunnel, it was necessary to incorporate various materials and types of construction in the wing models, with those of higher length-to-chord ratio generally requiring stiffer structures. The materials employed consisted of various types of wood, wood impregnated with synthetic resin, and magnesium. In all cases the wings were solid.

The range of Mach number covered in the tests extended from about 0.8 to roughly 1.4. At any particular Mach number, the tunnel pressure was increased until the value of the density-ratio parameter was sufficiently high to produce flutter. For the range of Mach number employed, the density-ratio parameter varied from 9 to 12 for the aspect-ratio-2 wings, from 20 to 70 for the aspect-ratio-4 wings, and from 70 to 130 for the aspect-ratio-6 wings. All the tests were made at an angle of attack of  $0^\circ$ . The models were mounted to a massive fuselage, the nose of which was extended upstream into the entrance cone of the tunnel in order to eliminate the bow shock wave and its reflection on the model from the tunnel wall. In every case, the flutter obtained has been of the classical bending-torsion type. The values of the experimental reduced-frequency parameter have ranged from about 0.2 to 0.3.

The results are presented in conventional form in terms of the ratio of the experimental flutter speed to the reference flutter speed plotted against Mach number. The reference flutter speed here is based on two-dimensional incompressible-flow aerodynamic derivatives and is calculated according to the method developed by Barmby, Cunningham, and Garrick in reference 2. It was assumed in the analysis that the flutter mode could be represented by the uncoupled first torsional and first bending modes. The reduced-frequency parameter and the associated values of the F- and G-functions were weighted along the span in accordance with the variation of the chord. The use of the reference flutter speed as a normalizing factor in the presentation of the results is based on

the assumption that this procedure removes the effects of variations in the structural parameters of the wing and the density of the air so that the ratio of the experimental flutter speed to the reference flutter speed is a function only of Mach number and plan form.

In figure 3 the effect of sweep is shown for aspect-ratio-4 wings having sweepback angles of  $0^\circ$ ,  $45^\circ$ ,  $52.5^\circ$ , and  $60^\circ$ . The ordinate is the ratio  $V_{EXP}/V_{REF}$  and the abscissa is the Mach number. As may be seen, the trends of the variation with Mach number for the wings swept back  $0^\circ$ ,  $52.5^\circ$ , and  $60^\circ$  are rather well defined by numerous test points. Further experimental information is required for the  $60^\circ$  sweptback wing in the Mach number range below 1.0. The curve for this wing has been arbitrarily extended back to a Mach number of 0.8 with a shape which appears to be reasonable. Also, more data are needed for the  $45^\circ$  sweptback wing in the range between Mach numbers of 1.0 and 1.4. Inasmuch as only one test point was obtained at Mach numbers above 1.0, the fairing of the curve for this  $45^\circ$  sweptback wing is rather arbitrary. The curves in figure 3 show that the favorable increase in flutter speed with Mach number in the transonic speed range becomes less pronounced as the sweepback angle is increased; that is, the compressibility effect, although first appearing at about the same Mach number for each of the wings, is consistently less for the more highly swept wings. At Mach numbers of the order of 0.8, the calculated flutter speeds are within 10 percent of the experimental values for the wings of  $0^\circ$ ,  $45^\circ$ , and  $52.5^\circ$  sweepback; whereas, the calculated flutter speed for the  $60^\circ$  sweptback wing is within about 20 percent of the experimental value. The unconservative flutter-speed prediction for some of the wings is rather disturbing; however, more refined calculations might be expected to give better agreement. The flagged square in the upper right part of figure 3 is a flutter point recently obtained by the rocket technique. The wing represented by this point had  $45^\circ$  of sweepback, a taper ratio of 0.2, and a section center-of-gravity position of 37 percent chord. Corresponding values for the wings of the blowdown-tunnel investigation are taper ratio, 0.6, and center-of-gravity position, 45 percent chord. The other pertinent parameters of the rocket wing were rather close to those for the wings employed in the blowdown-tunnel investigation. The difference between the rocket and tunnel data might be attributed to the difference in taper ratio or, perhaps, to inadequacies in the reference-speed calculation.

An interesting practical point is evident in the results shown here. If an airplane is assumed to be flying at a constant altitude, the relationship between its speed and the Mach number is given by a straight line from the origin on this diagram. If the flutter speed of the airplane is approached in the vicinity of Mach number 1.0, this straight line is approximately tangent to the flutter curves for the wings of  $0^\circ$  and  $45^\circ$  sweepback. Consequently, for these angles of wing sweepback, the constant altitude operation of the airplane will be free from flutter

throughout the Mach number range shown if it is flutter-free near Mach number 1.0. On the other hand, it is easily seen that this is not the case for the more highly swept  $52.5^\circ$  and  $60^\circ$  wings, for a straight line passing through the origin cannot have a point of tangency with either of these curves in the Mach number range shown.

The effect of aspect ratio on the wings of  $45^\circ$  sweepback is shown in figure 4 in which the flutter-speed ratio  $V_{EXP}/V_{REF}$  is plotted against Mach number for wings having aspect ratios of 2, 4, and 6. Although, as would be expected, there is some variation with aspect ratio in the flutter-speed ratio at Mach numbers around 0.8, the aspect ratio seems to have little effect on the variation of flutter-speed ratio with Mach number. The excellent agreement between experimental and calculated flutter speeds for the aspect-ratio-2 wings at the lower Mach numbers seems difficult to understand in view of the assumptions of the theory and, perhaps, should be regarded as fortuitous until further information is obtained.

The results presented so far have not dealt with the effect of airfoil thickness ratio. Some indication of the effect of thickness ratio on unswept rectangular wings having aspect ratios of the order of 6 can be obtained from figure 5. Results are presented here for the aspect-ratio-7.38 wing employed in the previously mentioned correlation investigation. This wing had a thickness tapering from 4 percent at the root to 2 percent at the tip. The curve labeled  $t = 0.09c$  was taken from reference 3 and represents data for unswept wings of about 9-percent thickness. The data for this curve were obtained by wind-tunnel, rocket, and bomb-drop methods. As can be seen, reductions in thickness delay the rise in the flutter-speed ratio to a higher Mach number.

With regard to the generality of the results, it might be hoped that the reference-speed calculations have adequately removed from the results the effects of variables such as, for example, the center-of-gravity position and that the curves of  $V_{EXP}/V_{REF}$  against Mach number as given here are a function of plan-form shape only. It is not entirely evident, however, that this is the case and it is thought that further investigation of particular wing plan forms having different values of the various pertinent parameters which go into the reference-speed calculation are required in order to establish the range of applicability of the results obtained.

In summary, the results of a systematic study of the effect of plan-form geometry on flutter in the transonic speed range have indicated a systematic effect of sweepback on flutter in the low supersonic range. The effect is unfavorable in the sense that the increase of flutter speed with Mach number becomes less pronounced as the sweepback angle is increased. The results of the study have also indicated a relatively

small effect of aspect ratio for the aspect ratios and the sweep angle considered. Further investigation is required to establish the generality of the results obtained.

## REFERENCES

1. Bursnall, William J.: Initial Flutter Tests in the Langley Transonic Blowdown Tunnel and Comparison With Free-Flight Flutter Results. NACA RM L52K14, 1953.
2. Barmby, J. G., Cunningham, H. J., and Garrick, I. E.: Study of the Effects of Sweep on the Flutter of Cantilever Wings. NACA Rep. 1014, 1951. (Supersedes NACA TN 2121.)
3. Lauten, William T., Jr., and Barmby, J. G.: Continuation of Wing Flutter Investigation in the Transonic Range and Presentation of a Limited Summary of Flutter Data. NACA RM L9B25b, 1949.

## CORRELATION INVESTIGATION

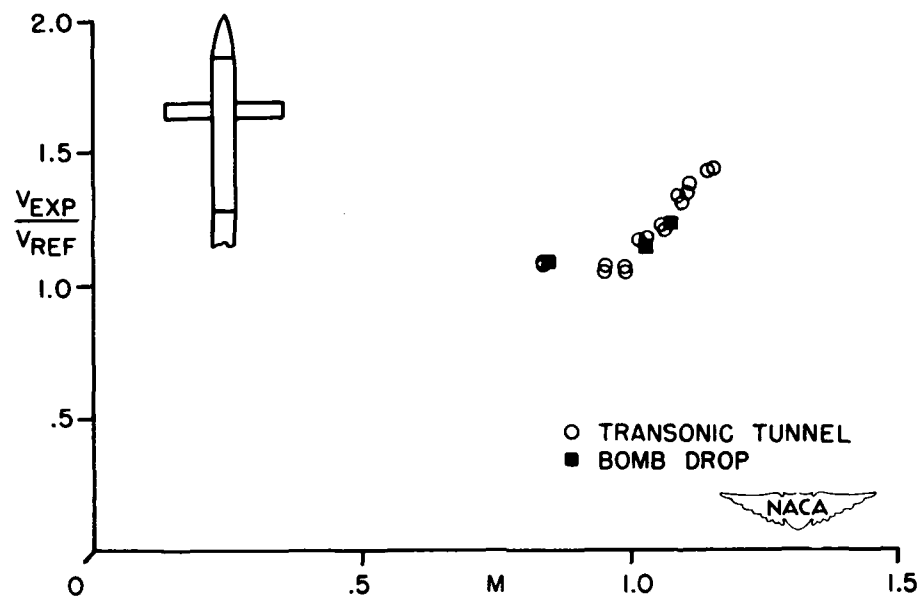


Figure 1.

## PHYSICAL CHARACTERISTICS OF FLUTTER MODELS

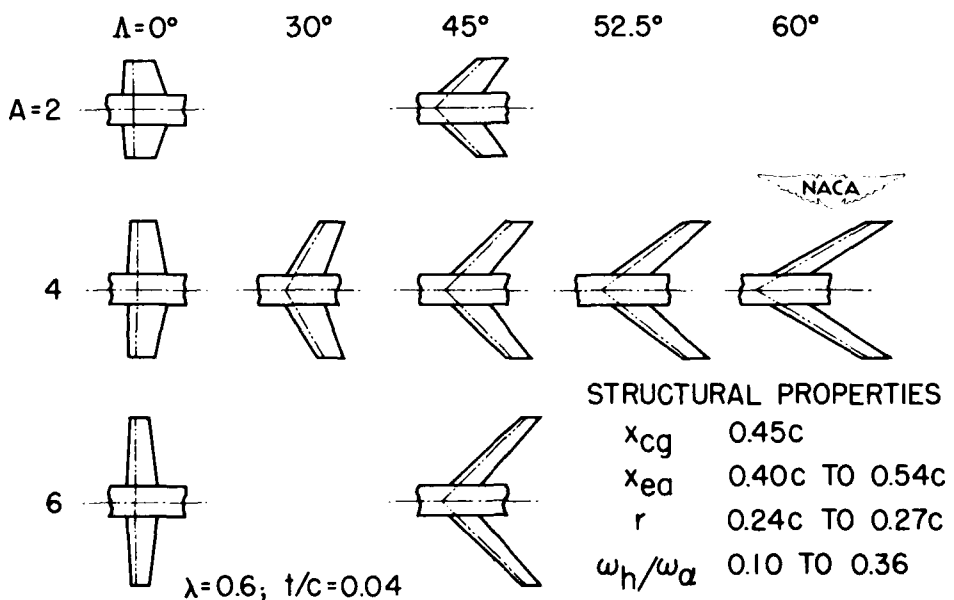


Figure 2.

## SWEEP EFFECT, A=4

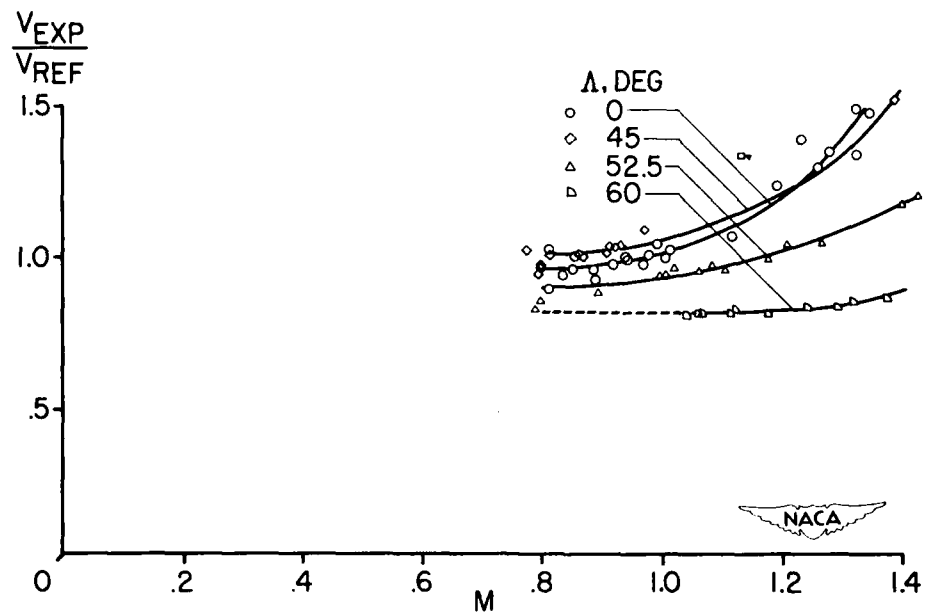


Figure 3.

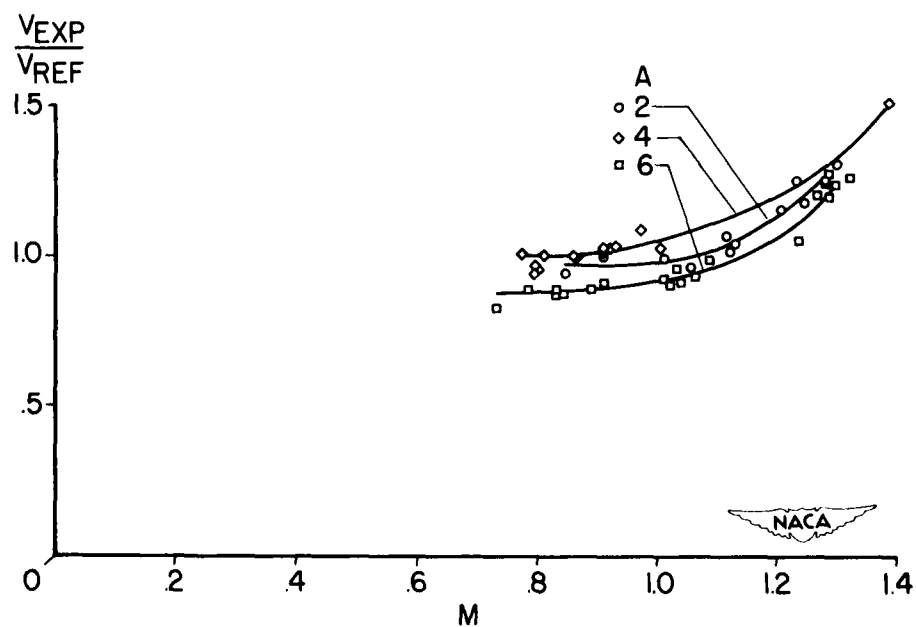
ASPECT-RATIO EFFECT,  $\Lambda = 45^\circ$ 

Figure 4.

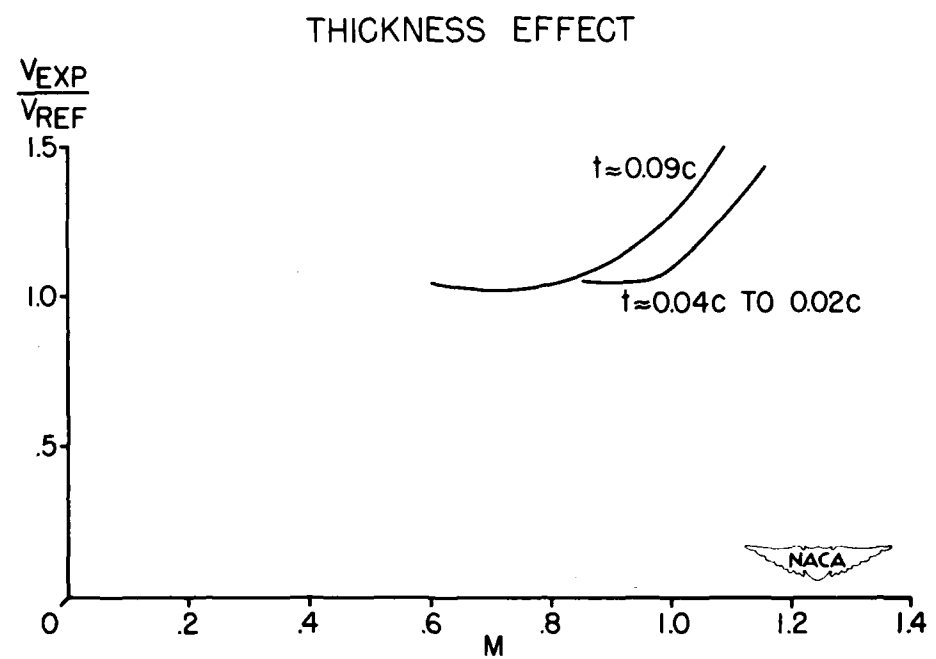


Figure 5.

TUNNEL EXPERIMENTS WITH DYNAMIC FLUTTER MODELS RELATING  
TO THE EFFECTS OF EXTERNAL STORES

By Dennis J. Martin and John L. Sewall

Langley Aeronautical Laboratory

Recently a number of cases of flutter are known to have occurred on fighter and light bomber airplanes that were carrying large external stores. Analytical investigations of these experiences have been very disappointing. Although some correlation has been obtained in a few cases, in others the flutter has occurred at speeds far from that which could be calculated by any commonly used method of analysis.

Considerable interest has therefore developed in flutter problems on wings carrying added masses and external stores. References 1 to 8 include a few of the published investigations on this problem. Industry has asked the NACA to make a general study of this problem with dynamic models. Reference 9 illustrates the use of dynamic models in flutter research. Since most of the airplane accidents have occurred at high speeds it is felt that the effects of compressibility cannot be safely accounted for from results of model tests at low speed. A great deal of valuable experience has been gained with low-speed models; however, the major handicap has been the extrapolation to high Mach numbers. In order to avoid this difficulty the airplane selected for study was dynamically scaled so that the velocity of the model tests would be the same as the velocity of the full-scale airplane; that is, so that this type of scaling would result in a true-speed model. Other parameters important in flutter, such as mass ratio, frequency ratio, and reduced frequency, were selected to be the same on the model as on the full-scale airplane. Figure 1 shows the model, which was 1/6 scale, as it was mounted on the sting in the Langley 16-foot transonic tunnel. The wings were of pod- and spar-type construction and were accurately scaled from the elastic and inertial properties of the full-scale prototype, which is a current fighter-type airplane. The elastic properties of the fuselage were not scaled; although, since the study was intended to include antisymmetric boundary conditions, the rolling moment of inertia of the fuselage was scaled and a rolling degree of freedom could be permitted for the antisymmetric flutter tests. The model was positioned in roll by means of small control surfaces mounted at the aft end of the fuselage and a very soft spring mounted within the fuselage. Plunging motion which may be important in symmetric flutter was not specifically included although the sting flexibility permitted some vertical motion.

The model could be fitted with a set of tanks which were scaled from a tank of 230-gallon capacity. Since flutter problems are often aggravated by the increasing size of the external stores, there was a

second set of tanks that were scaled from a tank of about 3 times this capacity or of about 700-gallon capacity.

One necessary prerequisite of transonic flutter testing is a reliable means of preventing a destructive build-up of amplitude once a flutter condition is attained. The more common methods used at low speeds such as restraining wires or mechanical means within the flow cannot be tolerated at transonic speeds. Several alternative methods have been suggested. The Wright Air Development Center (WADC), for instance, has successfully restrained rudder flutter in flight by quickly changing the mass balance of the control surface. For the tests with this dynamic model the method used was to provide for a quick change in the fore-and-aft location of a small weight within each tip tank. The weight was mounted as a piston in a tube and its position could be controlled by an observer or by an electronic device that monitored the electrical outputs of strain gages on the wings. When the oscillating stress at any station exceeded a pre-determined level the piston would be automatically fired.

During the approach to flutter the response of the model was carefully observed with the piston in the extreme fore-and-aft positions. The piston was always left in the position that appeared closer to flutter, that is, the position that appeared to have less damping as determined by observing the response of the model to random tunnel disturbances. Then, when flutter was encountered, the piston could be quickly fired to a position that appeared to have more damping, and it was hoped that this would result in a condition that was not in a flutter region. The effectiveness of this flutter-arresting gear, as well as the nature of the flutter that was observed, is clearly recorded both in strain-gage oscillograms and motion pictures that were taken throughout the test program.

An example of the results obtained with this dynamic model is shown in figure 2, which is a study of symmetric flutter, that is, the degree of freedom to roll was not permitted in this case. In this figure are the results for the large and small tanks having the same inertial characteristics. The Mach number is shown as a function of the tip-tank center-of-gravity distance fore and aft of the wing elastic axis at the wing-tip station. The fore-and-aft locations of the tank with respect to the wing were not changed; the center of gravity of the tank was changed by moving weights within the tank. The upper curve shows the effect of changing the fore-and-aft location of the center of gravity of the scaled 230-gallon tank while rearranging the weights within each tank so as to hold the moment of inertia about the wing elastic axis constant, thus maintaining a ratio of uncoupled wing bending frequency  $f_h$  to uncoupled torsion frequency  $f_\alpha$  of 0.93. As the center of gravity moves forward and approaches the elastic axis the flutter speed increases rather abruptly, and for center-of-gravity locations in the region just ahead of the elastic axis, it was not possible to obtain flutter in some cases even up to a Mach number of 0.95. The flutter boundary may turn back after reaching the elastic axis which suggests the possibility of a closed flutter region.

The effect of aerodynamic shape of the tank can be seen by a comparison of the lower curve (which pertains to the large tank) with the upper curve (which pertains to the small tank), both tanks having the same total mass and inertia. The reduction in flutter speed, which was about 15 percent in the region covered by the tests, can be attributed to the increased aerodynamic forces resulting from the larger tip tank. All the information given in this figure was obtained with horizontal fins attached to the tanks as shown in figure 2. Removing the fin was found to reduce the flutter speed of the small tank by about 7 percent when the center of gravity was approximately 1 to 2 inches aft, while the removal of the fin from the big tank had only a slight effect tending perhaps to increase the flutter speed by a small amount.

It may be of interest to show how a commonly used analytical method of obtaining a quick estimate of the flutter speed compares with these data. Calculations were made by using incompressible-flow coefficients in which only the primary wing bending and torsion modes were included. The comparisons with experiment are shown in figure 3. Here the calculations are indicated by the dashed curve and the experiment by the solid curve. The lower set of curves are for a wing frequency ratio  $f_h/f_\alpha$  of 0.93 and the effect of rearranging the weights within the tank so as to decrease the frequency ratio to 0.84 is seen to increase the flutter speed, as is indicated by the upper set of curves. As might be expected only the general trends are indicated by these simple calculations, and they are excessively conservative over most of the range. The degree of freedom in roll was not permitted for these tests.

The effect of the rolling degree of freedom is shown in figure 4. These data pertain to the large tank which was ballasted to the 127-gallon condition, and the weight was arranged within the tank to correspond to a ratio of uncoupled symmetric bending frequency to torsion frequency of about 1.04. The solid curve through the circles is for the case where the fuselage was locked, whereas the squares correspond to tests in which the model was free to roll. The addition of the rolling degree of freedom produced little or no effect on the flutter speed in the region where symmetric flutter was encountered. The open points represent conditions reached without flutter. At the same Mach number, points are shown at two values of center-of-gravity locations, corresponding to the piston forward and the piston aft. The tests were discontinued, for example, with the tip tank center of gravity about 4 inches aft (corresponding to the piston-aft condition) because the response of the model appeared to be of nearly equal amplitude to that found with the center of gravity 1.75 inches aft (corresponding to the piston-forward condition). The approach to an unknown flutter boundary had to be made with caution. In the region where the center of gravity was near the elastic axis, firing the piston forward was very effective in arresting the flutter. With

the center of gravity more than 4 inches aft, firing the piston forward once the flutter boundary was reached could result in a condition above the flutter boundary that might cause destruction of the model.

Previous experiences with antisymmetric flutter have indicated that antisymmetric flutter might be critical for forward locations of the tip-tank center of gravity. In that case firing the piston aft would be necessary to move away from the boundary and arrest the flutter. In the tests under discussion, however, antisymmetric flutter was not encountered over the range of weight and frequency ratios covered. Subsequent calculations (using incompressible-flow coefficients and including the rigid-body rolling degree of freedom) have indicated that the boundary for the antisymmetric case was well above the limit of the tests both for forward locations of the tip-tank center of gravity and, as indicated by the upper dashed curves, for rearward locations. The calculations further indicated that reducing the antisymmetric frequency ratio would be necessary to obtain antisymmetric flutter.

The information shown in these figures is representative of the flutter characteristics found from the tests with this dynamic model. A large number of configurations were investigated and the speed range extended up to a Mach number of 0.95; however, the highest Mach number at which flutter was obtained was 0.78, which is close to the force-break Mach number. The general experience with this model has been that, if the tank configuration was such that flutter was not encountered below a Mach number of 0.78, then flutter did not occur up to a Mach number of 0.85 or 0.90 or higher. The damping of the model generally appeared to increase slightly as the speed was increased above 0.80, and the tests were usually discontinued around a Mach number of 0.85.

Now the question naturally arises, how does this model compare with the airplane from which it was scaled? How well can the model behavior be used to predict the behavior of the prototype? Fortunately the prototype has stayed well away from most of the boundaries determined by the model tests; however, it happens that there does exist some flight flutter experience with the full-scale airplane. WADC has completed flutter tests with the tank ballasted with lead at the aft end of the tank in order to obtain flutter. This ballasting corresponds to a fuel condition of 7 percent full in the extreme aft end of the tank. To obtain the 7-percent-full condition in the model test would require the removal of the flutter-restraining piston and tube. Obtaining flutter without the safety device would have resulted in almost certain destruction of the model. Hence, obtaining the test data for the 7-percent-full condition has been postponed until all other required data have been obtained. However, a qualitative comparison can be realized from data obtained at higher fuel conditions. Studies were made of the effects of uncoupled wing bending to torsion frequency ratio and of tip-tank fuel load for the 230-gallon-tank configuration. Plotted in the shaded area shown in figure 5 are

flutter points taken from cross plots for tank fuel conditions from 40 to 121 percent full. For the same frequency ratio the effect on flutter speed of tank fullness is small.

Plotted also is the flight flutter point which is shown as an elongated point because of uncertainties in the amount and distribution of fuel throughout the airplane at the time of flutter. The abscissa is the calculated uncoupled frequency ratio. The results of the flight tests and the wind-tunnel tests thus appear to be in the same range unless a strong effect of fuel load is found between 40-percent fullness (the lowest covered with the model tests) and 7-percent fullness (the condition of the flight flutter point). The addition of more fuselage plunging motion for the model tests might alter these results to a certain extent; however, the results thus far indicate that the flutter characteristics of the model may be close to those of the prototype. Furthermore, there was some motion of the model fuselage due to the sting flexibility and this motion indicates some compliance with the body-freedom boundary condition.

There can be no doubt as to the value of model tests of this type if construction techniques and testing procedures can be developed so that the model behavior can be successfully used to describe the behavior of the full-scale airplane.

The NACA is planning more tests with dynamically scaled models in which vibration equipment may be installed to study prediction techniques with further application to flight flutter testing. In addition free flying models are being designed for which all body degrees of freedom will be permitted in transonic wind-tunnel tests.

## REFERENCES

1. Runyan, Harry L., and Sewall, John L.: Experimental Investigation of the Effects of Concentrated Weights on Flutter Characteristics of a Straight Cantilever Wing. NACA TN 1594, 1948.
2. Pepping, R. A.: Model F2H-2 - Summary Report. Theoretical Investigation of Aero-Elastic Stability of Wings Carrying Full and Partially Full Tip Tanks. Rep. No. 1704 (Contract No. NOa(s)-9768), McDonnell Aircraft Corp., May 26, 1950.
3. Lambourne, N. C., and Weston, D.: An Experimental Investigation of the Effect of Localised Masses on the Flutter and Resonances of a Model Wing. R. & M. 2533, British A.R.C., 1944.
4. Biot, M. A.: Flutter Analysis of a Wing Carrying Large Concentrated Weights. GALCIT Rep. No. 1A (Contract No. 41-2579, Part of Item 1, Materiel Div., Air Corps), Jan. 1942.
5. Minhinnick, I. T., and Yarwood, Jennifer: Interim Note on the Theoretical Effects of an Engine Mass on Wing Flutter. R.A.E. Tech. Note S.M.E. 143, May 1943.
6. Oldaker, M. R., and Leppert, E. L.: Flutter Investigation of the F-94B Airplane With Fletcher 230 Gallon Tip Tanks. Rep. No. 8262, Lockheed Aircraft Corp., Nov. 15, 1951.
7. Gayman, William H.: An Investigation of the Effect of a Varying Tip Weight Distribution on the Flutter Characteristics of a Straight Wing. Jour. Aero. Sci., vol. 19, no. 5, May 1952, pp. 289-301.
8. Bellan, T. M.: Models XF2H-1 and F2H-2 - Flutter Analysis of Wing With Tip Tanks. Rep. No. 1324 (Contracts NOa(s)-6130 and NOa(s)9768), McDonnell Aircraft Corp., Aug. 5, 1949.
9. Kinnaman, E. Berkeley: Flutter Analysis of Complex Airplanes by Experimental Methods. Preprint No. 363, S.M.F. Pub. Fund Preprint, Inst. Aero. Sci., Jan.-Feb. 1952.

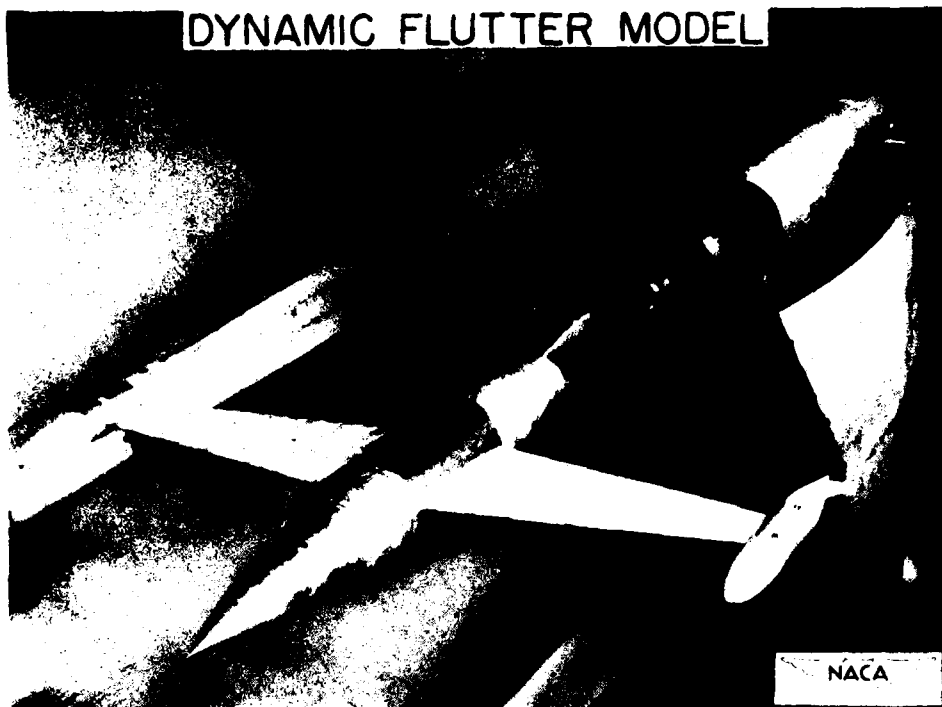


Figure 1.

## FLUTTER STUDIES WITH LARGE AND SMALL TANKS

1.2 - TIP-TANK BALLASTED TO  
155-GAL CONDITION;  
 $f_h/f_a = 0.93$

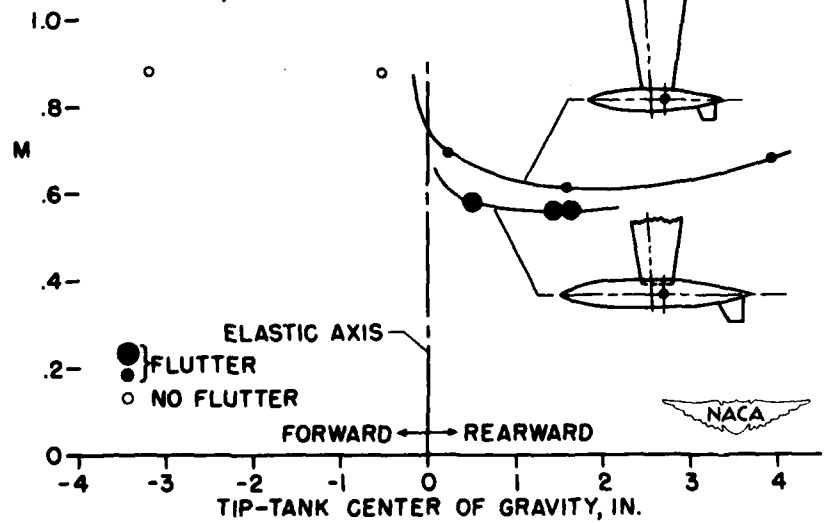


Figure 2.

## COMPARISON OF EXPERIMENT WITH SIMPLE CALCULATIONS

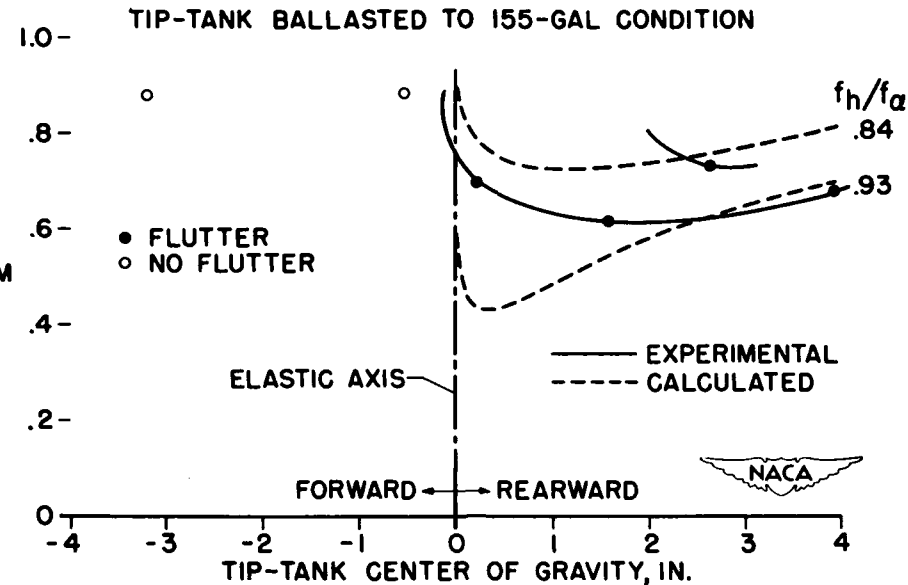


Figure 3.

## EFFECT OF FUSELAGE FREEDOM IN ROLL

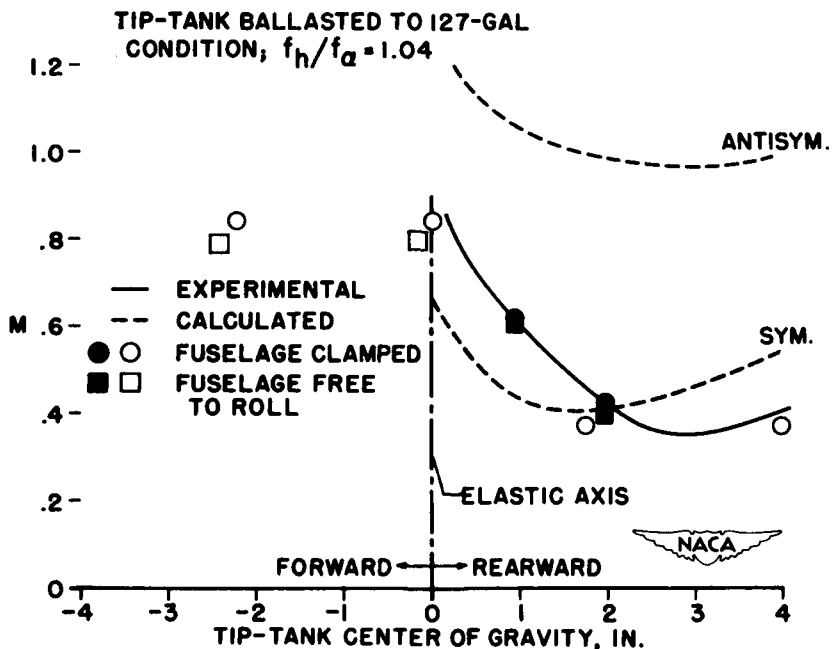


Figure 4.

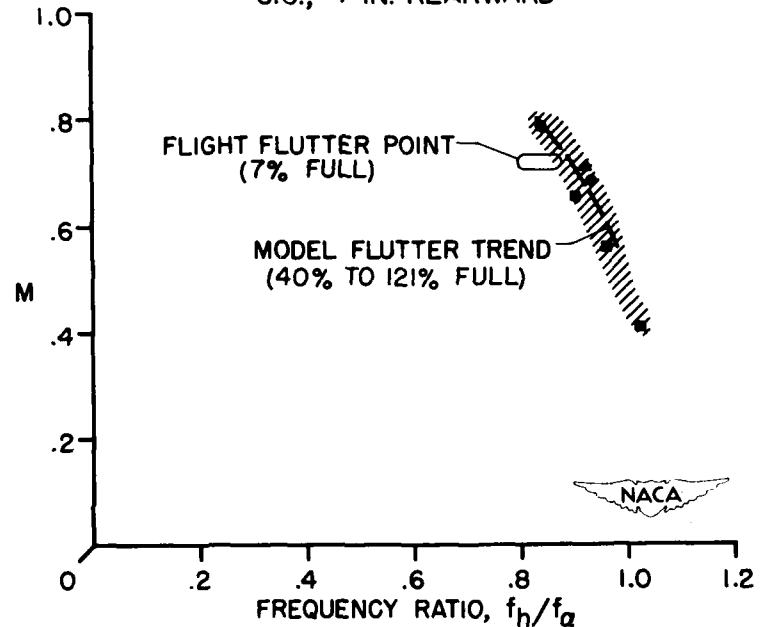
COMPARISON OF FLUTTER DATA FOR PROTOTYPE AND MODEL  
C.G., 4-IN. REARWARD

Figure 5.

## EXPERIMENTS ON PANEL FLUTTER

By John E. Baker and Maurice A. Sylvester

Langley Aeronautical Laboratory

A fairly new flutter problem has arisen which involves the flutter of skin coverings at supersonic speeds. This phenomenon was first suspected in connection with the failure of many early German V-2 rockets, and subsequent analytical work indicated the possibility of such an instability at supersonic speeds. More recently, several built-up wing models, having thin metal skins supported by internal spars, have fluttered during tests at the Langley Aeronautical Laboratory. High-speed motion pictures of these flutter cases indicate that the skin covering was mainly involved, although some flexibility of the primary structure of the wing was also noted.

The motion pictures showing flutter involving the skin coverings of wings were useful in verifying the existence of panel flutter and in demonstrating the nature of this phenomenon. In order to isolate the effects of some of the parameters involved and to eliminate coupling with the flexible spars, further work on simpler models has been carried out, and the rest of the paper is devoted to a discussion of these latter tests. Metal panels were rigidly mounted as a section of the tunnel wall, thus exposing one surface of the panel to the supersonic air-stream. These studies were conducted at Mach numbers of 1.3 and 1.56 on panels which were about 12 inches long and 8 inches wide with clamped edges. The results of the tests at a Mach number of 1.3 have been reported in reference 1.

One series of configurations which were studied at a Mach number of 1.3 consisted of panels clamped at the front and rear edges, the other two edges remaining free. The results of these tests are shown in figure 1. The ordinate is a nondimensional parameter combining panel bending stiffness and dynamic pressure where  $t$  is the thickness,  $c$  is the chord or length of the panel,  $E$  is Young's modulus of elasticity, and  $q$  is the dynamic pressure. For a given panel material, decreasing values of this parameter indicate decreasing thickness, increasing chord, or decreasing altitude. The flutter regions are below the flutter boundaries as indicated. These panels clamped front and rear were tested under conditions of both tension and buckling. It can be noted that, as the panels under tension get thinner or longer, more and more tension is required to eliminate the flutter. On the other hand, introducing very small amounts of buckling into the panels causes the flutter boundary to jump from a value of about 0.045 to a value of about 0.12, which requires much thicker or shorter panels to eliminate the flutter. The amount of buckling did not appear to influence the flutter characteristics and hence the curve is essentially flat

CONFIDENTIAL

in this region. The results at a Mach number of 1.56 follow these trends fairly closely, but the boundaries are below those at a Mach number of 1.3. A lesser tendency for panel flutter is thus indicated at this higher Mach number.

If the results shown in figure 1 are applied to conditions of sea level and a Mach number of 1.3, completely flutter-free aluminum panels, which are 1 foot long and clamped on two edges, would need to be 0.070 inches thick and steel panels would need to be 0.050 inches thick. This type of panel may be representative of the center part of very wide panels, and, therefore, may apply to airplane fuselage panels without longitudinal stringers or wing panels without ribs.

If fuselage stringers and wing ribs are present, these conditions approximate those of panels clamped on all four edges. The information shown in figure 2 for 8- by 12-inch panels clamped on all four edges will give an indication of the extent of the flutter boundaries for this type of configuration. The ordinate is the same as in figure 1, and the left-hand plot is for panels incorporating single buckling, and the right-hand plot is for panels with multiple buckling. A panel with single buckling bows out uniformly into the airstream with the maximum deflection at the center. A panel with multiple buckling, however, is buckled nonuniformly in such a way that by pushing one portion of the panel out of the tunnel, another portion pops into the tunnel. The kind of buckling was controlled in these tests, but there is no indication of the kind that would occur in practice. Since the flutter boundaries in figure 2 are much lower than the boundary for buckled panels shown in figure 1, it is evident that buckled panels clamped on all four edges can be much longer or thinner than buckled panels clamped on two edges and still be flutter free. In comparing the two plots in figure 2 it should be noted that panels having multiple buckling have to be much shorter or thicker to eliminate flutter than panels having single buckling. Here again, the amount of buckling did not affect the flutter boundaries. If the results shown in figure 2 are applied to conditions of sea level and a Mach number of 1.3, 8- by 12-inch steel panels clamped on all four edges would need to be 0.035 inches thick and aluminum panels would need to be 0.045 inches thick in order to be completely flutter free.

There is some indication that the panel failures on the V-2 rocket occurred in a region where the internal and external pressures were nearly in balance. In order to determine if a pressure differential tends to suppress flutter, a study of the effect of a pressure differential across some panels was included in the tests and the results are shown in figure 3. The ordinate is still the same, and the abscissa is the pressure differential across the panels, positive denoting higher pressure behind the panels or, in the case of an aircraft, inside the

CONFIDENTIAL

fuselage. These tests were made at a Mach number of 1.56 on 8- by 12-inch buckled aluminum panels clamped at the front and rear edges. Unequal pressures had a very beneficial effect on panel flutter. In other words, in the presence of even a small positive (or negative) pressure behind the panels, thinner or longer panels can be made flutter free than could otherwise be possible at zero pressure differential. These results substantiate the inferred location of panel failures on the V-2 rockets.

It may be of interest to review briefly the status of theoretical work on panel flutter. Isaacs (ref. 2) and Hayes (ref. 3) have treated the case of a buckled two-dimensional panel in supersonic flow by using steady-state air forces. Essentially, these analyses deal with the airspeed at which the first and second buckling modes coincide, thus leading to a definite static instability and possibly flutter. A criterion based on this type of analysis has indicated possible flutter on panels which are somewhat thicker than some flutter-free panels in the present experiments. In other words, the criterion appeared somewhat conservative or pessimistic.

Miles (ref. 4) has studied the flutter boundaries of both buckled and unbuckled two-dimensional simply supported panels, with the inclusion of first-order frequency effects in the air forces. Results of these analyses show that between Mach numbers of 1 and  $\sqrt{2}$ , all panels, regardless of thickness, are dynamically unstable. Such results are quite unrealistic and Miles states that inclusion of effects of three-dimensional flow is imperative. It is clear that such unpleasant results were not obtained in the present experiments at a Mach number of 1.3, since a finite flutter boundary was obtained.

Some further refinements in the theory were made by Shen (ref. 5) who used exact expressions for the unsteady air forces on a two-dimensional simply supported panel with two degrees of freedom.

Most of the flutter analyses have been based on the first two fundamental vibration modes. The experiments have shown that the panel flutter frequencies generally fall between the second and fifth vibration modes. On the basis of these results, the theoretical work at the Langley Laboratory has been aimed at including higher modes in single-bay panels as well as panels on many supports. The effects of structural damping and panel aspect ratio are also being investigated, and it has been found that the inclusion of a small amount of structural damping brings the flutter boundary from infinity to a finite value.

To summarize, these tests have definitely demonstrated the existence of panel flutter at supersonic speeds, and some means of controlling the flutter tendencies were found. For a given material, thickening or shortening the panels decreases the tendency for flutter. In addition, the presence of a pressure differential is very effective as a means of eliminating flutter.

## REFERENCES

1. Sylvester, Maurice A., and Baker, John E.: Some Experimental Studies of Panel Flutter at Mach Number 1.3. NACA RM L52I16, 1952.
2. Isaacs, R. P.: Transtability Flutter of Supersonic Aircraft Panels. U. S. Air Force Project RAND P-101, The Rand Corp., July 1, 1949.
3. Hayes, W.: A Buckled Plate in a Supersonic Stream. Rep. No. AL-1029, North American Aviation, Inc., May 10, 1950.
4. Miles, John W.: Dynamic Chordwise Stability at Supersonic Speeds. Rep. No. AL-1140, North American Aviation, Inc., Oct. 18, 1950.
5. Shen, S. F.: Flutter of a Two-Dimensional Simply-Supported Uniform Panel in a Supersonic Stream. Contract No. N5ori-07833, Office of Naval Res., Dept. Aero. Eng., M.I.T., Aug. 6, 1952.

## FLUTTER OF PANELS CLAMPED FRONT AND REAR

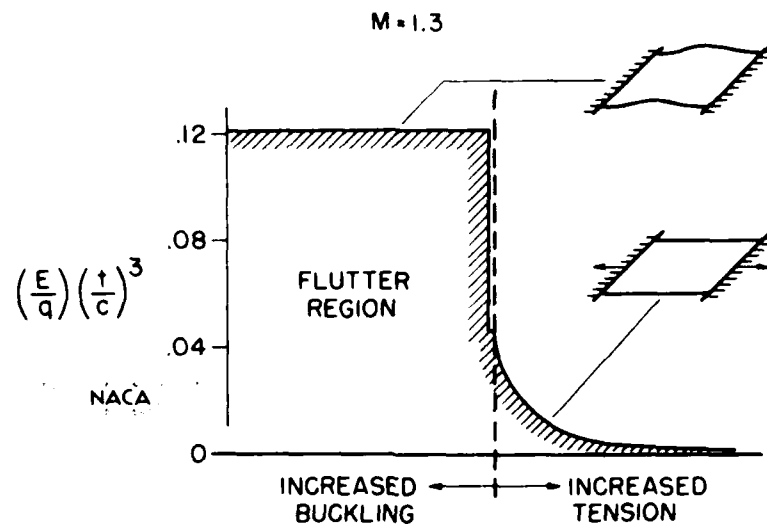


Figure 1.

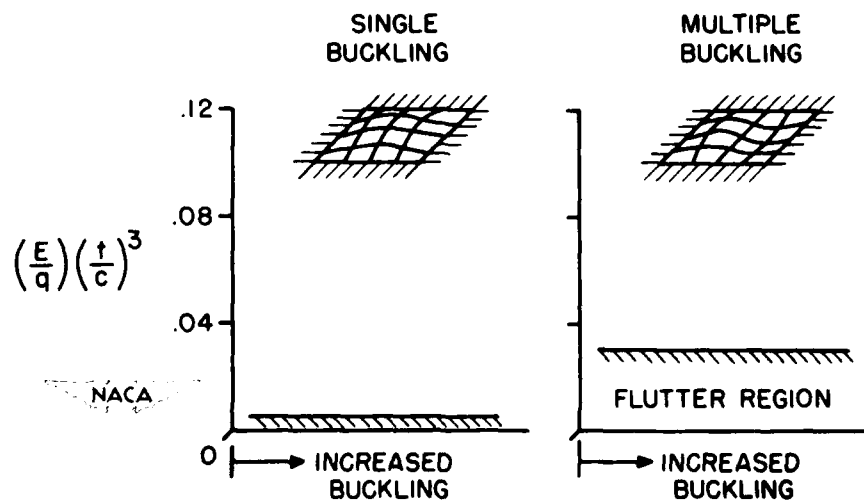
FLUTTER OF PANELS CLAMPED ON FOUR EDGES  
 $M = 1.3$ 

Figure 2.

## EFFECT OF PRESSURE DIFFERENTIAL ON PANEL FLUTTER

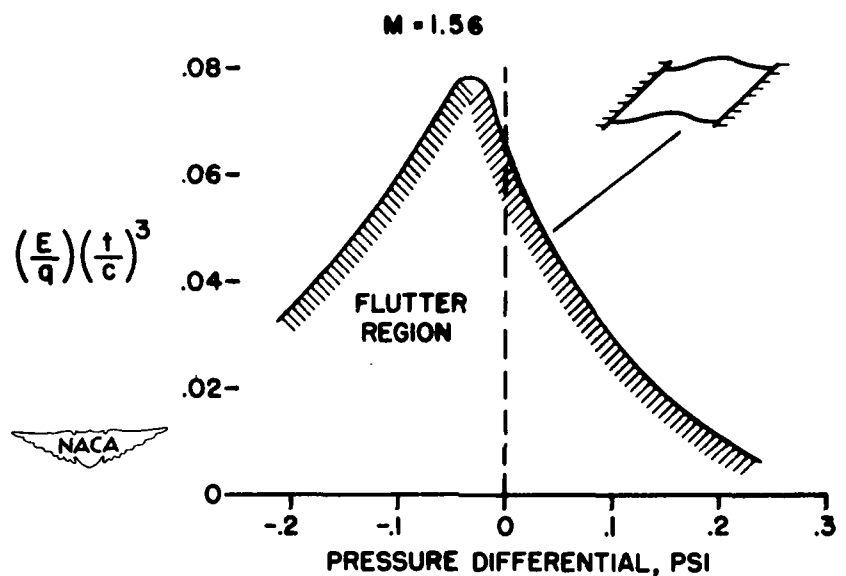


Figure 3.

## FLIGHT FLUTTER EXPERIENCES WITH SPOILERS ON

SWEPT WINGS AND WITH TRIANGULAR WINGS

By David G. Stone and Richard I. Sears

Langley Aeronautical Laboratory

## INTRODUCTION

In the past few months several flutter experiences have been obtained with rocket-powered models intended for other purposes. These models were tested for drag and control effectiveness, but flutter occurred spoiling the aerodynamics of the test. The tests did, however, show a qualitative insight into some interesting, if not dangerous, flutter conditions. This paper is a collection of these experiences to bring to your attention possible conditions of flutter of swept wings having spoilers and of triangular wings of considerable static strength.

## WING FLUTTER INDUCED BY SPOILERS

During an investigation of the aeroelastic effects of swept wings equipped with outboard fixed-spoiler controls, wing failures occurred. Flutter was suspected as the cause of these failures; consequently, additional models were fabricated and equipped with instrumentation so as to record the occurrence of any flutter. Tests with these models showed that flutter did occur and the results are tabulated in figure 1. The tests were made on the  $45^{\circ}$  swept wing as shown at the top of the figure for the spoiler height and location shown. The half-span outboard solid spoiler was installed in a fixed position on a wing having a torsional stiffness of 12 percent of that of a solid duralumin wing.

This stiffness is indicated by the values of  $\frac{(\theta/m)_{SD}}{\theta/m}$ , the ratio of twist per unit moment for a solid duralumin wing to that for the experimental wing.

This wing fluttered to destruction at a Mach number of 0.91 having a flutter frequency of 53.4 cps. A similar case of destructive flutter was encountered when this spoiler was made to have 76-percent solidity by cutting vertical slots. The values of reduced frequency are based on the mean aerodynamic chord. When the wing torsional stiffness was approximately doubled, no flutter was encountered up to the maximum test Mach number of 1.64. A model having a wing of the same stiffness characteristics as those that fluttered with the spoiler, but equipped with fixed 0.3c outboard half-span ailerons, gave no indication of flutter up to the maximum test Mach number of 1.65. This model with ailerons was not

CONFIDENTIAL

equipped with instrumentation to record flutter, but inasmuch as consistent control-effectiveness information was obtained and no wing failure occurred, it can be assumed safely that flutter did not occur. The important point here is that this wing of these stiffness characteristics is flutter-free with fixed ailerons as indicated by the experiment but that flutter is induced by the aerodynamics of placing outboard spoiler controls on the wing. Also, by the empirical boundary of reference 1, this wing is indicated to be flutter-free without controls.

#### FLUTTER OF TRIANGULAR WINGS

A part of the general zero-lift drag program with rocket-powered models, of course, was that of determining the drag of thin triangular wings. These very thin wings, designed and fabricated by methods proved previously to give high over-all static strength, suffered from some sort of flutter vibration during the flight test and, again, the aerodynamic purpose of the program was not realized. Examples of several of these thin triangular wings that fluttered are illustrated in figures 2 and 3. All these models were equipped with telemeters and the telemeter records clearly indicated flutter. Figure 2 shows the geometry of the triangular wings and the type of construction which was wood with the addition of a duralumin plate on the center line and trailing edges and duralumin inlays on the surfaces of the wings. These plates and inlays are shown as the heavy lines on the airfoil-section sketches. Also shown is the ultimate load in bending for which these wings were designed. These values show the wings to be of high static strength. Also, a section effective-stiffness parameter  $EI/c^4$  is shown. This parameter is independent of wing size for wings of the same construction as that shown. The torsional-stiffness parameter  $GJ/c^4$  is approximately  $1\frac{1}{2}$  times these bending values. Figure 3 shows the various vibration mode shapes and frequencies in cycles per second of the wings as determined in the laboratory prior to flight test, the frequencies encountered in flight as the wing fluttered, the corresponding Mach numbers, and the reduced frequencies which are based on the mean aerodynamic chord. The arrows indicate the sequence of the Mach number through the flight test.

Some interesting points are shown in the tabulated data of figure 3. For example, the comparison of the flutter frequencies with the frequencies of the ground-measured modes indicates in most cases that the tip of the wing is bending or flapping and that possibly portions of the trailing edge have a flapping motion which results in higher values of the frequency and reduced frequency.

CONFIDENTIAL

The results for the shoulder wing  $60^\circ$  delta shown at the top of figure 3 are reported in reference 2. This wing had two distinct flutter modes. An attempt to eliminate the flutter by increasing the value of EI of the inner half-span by a factor of 10 with steel inlays was not successful. The model still fluttered; however, the stiffened wing with wing-mounted underslung forward nacelles did not flutter.

Also, a longitudinal-acceleration effect can be noted for the  $60^\circ$  delta and  $52.5^\circ$  delta wings because the record did not indicate flutter during accelerating flight but only during the decelerations connected with coasting flight. For the other cases where flutter did start during accelerating flight (the  $45^\circ$  delta and diamond wings), the flutter did not stop until a lower Mach number was reached during the coasting flight.

Only on the  $60^\circ$  delta wing on the lower-fineness-ratio body (the second model shown in fig. 3 and reported in ref. 3) did wing failure occur for the cases shown. The other models flew correctly at subsonic speeds after the flutter stopped, the flutter in some cases lasting for a duration of 16 seconds.

A word of caution is expressed here about the results inasmuch as these flutter experiences were obtained from models not intended for flutter investigation. The flutter was recorded on accelerometers near the center of gravity. These accelerometers record faithfully the frequency of any vibrations that occur, but the amplitude is considerably attenuated at the flutter frequencies. Consequently, the actual character of the flutter is not exactly known and the severity of the flutter is open to question. These results do show that wings of very high static strength may have poor flutter characteristics.

An empirical flutter boundary based on numerous experiments, primarily for unswept and swept wings having finite tip chords and bending-torsion type of flutter, is presented in reference 1. It is interesting with these recent triangular-wing flutter experiences to place these results in relation to the boundary from reference 1 even though this criterion was not intended to be valid for wings of triangular plan form. Figure 4 shows these wings in relation to the boundary. In this plot the ordinate represents a plan-form, thickness, and altitude parameter and the abscissa is the effective shearing modulus. The boundary line is the line Martin found in 1951 (ref. 1) separating the flutter and no-flutter regions. The solid points indicate flutter; the open ones indicate no flutter. All the triangular wings just discussed, except the one with the inner half-span stiffened by a factor of 10, fall on the flutter side of the boundary. The open points, indicating triangular wings that did not flutter, were either solid duralumin, solid magnesium, or thick wings of wood-metal inlay construction. The flagged solid points in the upper right-hand corner of figure 4 are delta wings taken from the experiments

at  $M = 1.3$  in the Langley supersonic flutter apparatus reported in reference 4. This group of points represents wings of constant thickness and, also, a minimum condition; that is, for a slight decrease in the value of the plan-form and thickness parameter, no flutter occurred. Although they define a slightly higher boundary the points are for  $M = 1.3$  only and may fall nearer the boundary at lower speeds. A wind-tunnel point for a delta wing from reference 5 is shown in the left side of figure 4. This point represents a weak wing which fluttered at a low subsonic speed in a mode similar to the other triangular wings shown.

The rocket-model results and these wind-tunnel results agree fairly well with the empirical boundary that Martin devised. Three  $45^\circ$  delta wings which did not flutter fall in the flutter region of this chart. Also, the wind-tunnel data shown, which were for panel aspect ratios of over 2, indicate the boundary to be conservative. The data presented indicate that the boundary from reference 1 holds fairly well for triangular wings of panel aspect ratio less than 2, but the aspect-ratio factor may be overly conservative for the higher aspect ratios.

#### CONCLUDING REMARKS

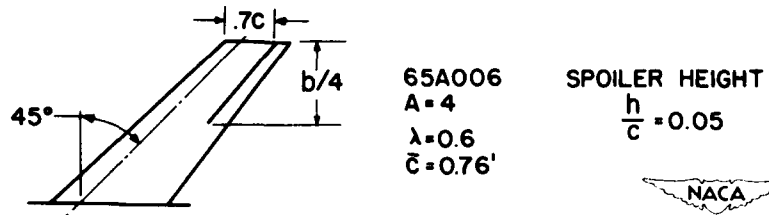
In concluding, then, recent tests of rocket-powered models for control and drag data have yielded information on flutter. These results indicate that flutter may be induced on an otherwise flutter-free swept wing by the addition of spoiler controls and that thin triangular wings of high static strength may possess inadequate flutter characteristics.

## REFERENCES

1. Martin, Dennis J.: Summary of Flutter Experiences As a Guide to the Preliminary Design of Lifting Surfaces on Missiles. NACA RM L51J30, 1951.
2. Judd, Joseph H., and Lauten, William T., Jr.: Flutter of a  $60^{\circ}$  Delta Wing (NACA 65A003 Airfoil) Encountered at Supersonic Speeds During the Flight Test of a Rocket-Propelled Model. NACA RM L52E06a, 1952.
3. Lauten, William T., Jr., and Mitcham, Grady L.: Note on Flutter of a  $60^{\circ}$  Delta Wing Encountered at Low-Supersonic Speeds During the Flight of a Rocket-Propelled Model. NACA RM L51B28, 1951.
4. Tuovila, W. J.: Some Wind-Tunnel Results of an Investigation of the Flutter of Sweptback- and Triangular-Wing Models at Mach Number 1.3. NACA RM L52C13, 1952.
5. Herr, Robert W.: A Preliminary Wind-Tunnel Investigation of Flutter Characteristics of Delta Wings. NACA RM L52B14a, 1952.

CONFIDENTIAL

## WING FLUTTER INDUCED BY SPOILERS



CONTROL	$\frac{(\theta/m)_{SD}}{\theta/m}$	1st BENDING, CPS	1st TORSION, CPS	M	FLUTTER, CPS	$\frac{\omega c}{2V}$
SOLID SPOILER	0.12	29.5	117	0.91	53.4	0.12
76% SOLID SPOILER	.12	28.5	117	.87	56.0	.13
76% SOLID SPOILER	.27	29.5	204	1.64	NO	-
.3C AILERON $\delta = 10^\circ$	.12	29.0	116	1.65	NO	-

Figure 1.

## TRIANGULAR WINGS

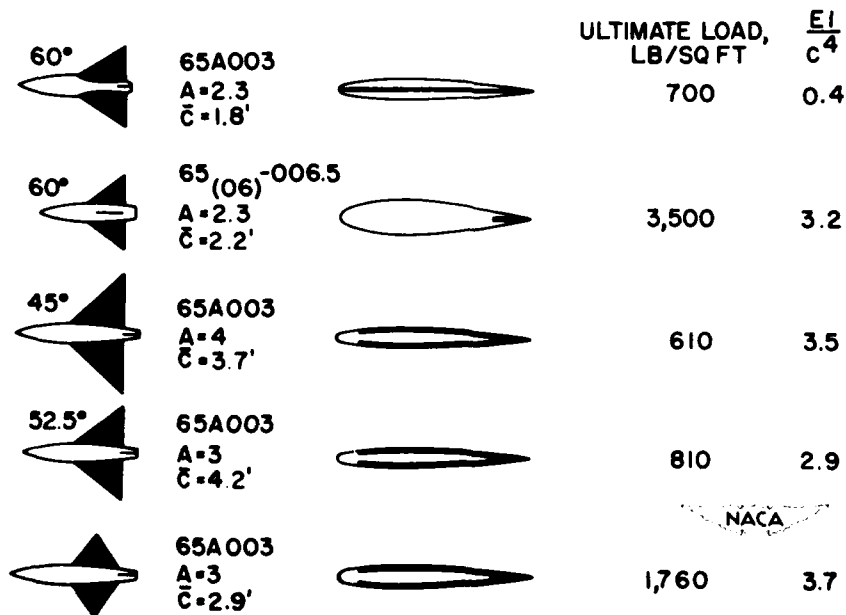


Figure 2.

CONFIDENTIAL

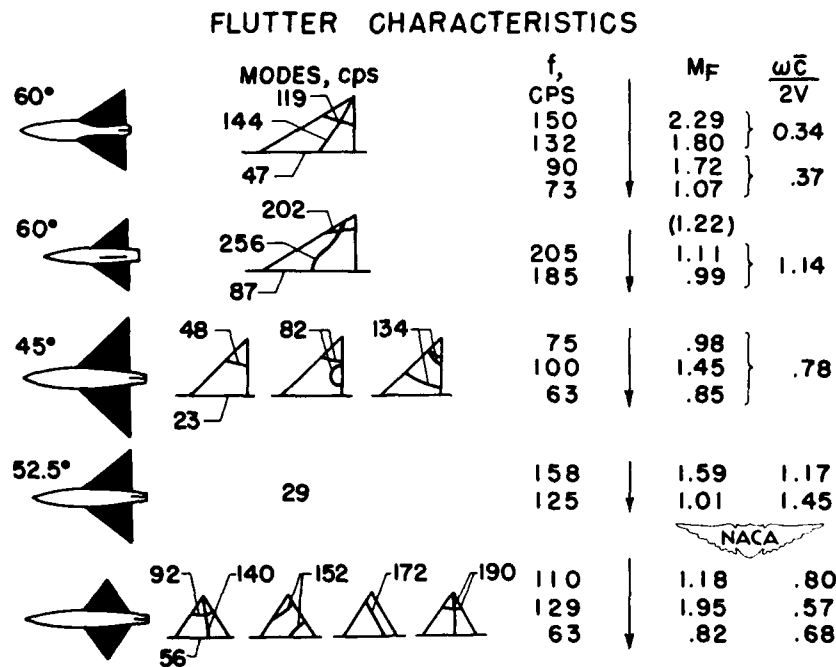


Figure 3.

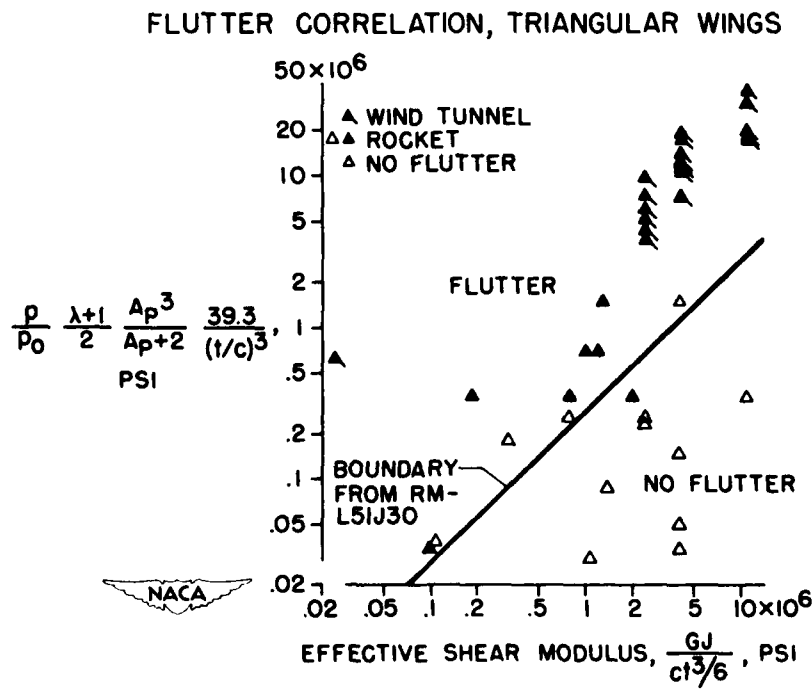


Figure 4.

## SOME OBSERVATIONS ON STALL FLUTTER AND BUFFETING

By A. Gerald Rainey

Langley Aeronautical Laboratory

Manufacturers of propellers and turbines have been concerned with the problem of stall flutter for some time. Airframe manufacturers, on the other hand, have found that the vibrations associated with a related phenomena, buffeting, are of more importance in the design of wings. Recently, however, due to the trend toward thin wing sections and large masses attached to the wings, airframe designers have also become concerned about the problem of stall flutter.

Some of the concern about stall flutter arises because of the fact that stall flutter and buffeting sometimes occur under similar conditions, as pointed out by Hartley A. Soulé and De E. Beeler in a paper presented at the NACA Conference on High-Speed Aerodynamics, Dec. 1951. Both types of vibrations may occur at the same time in a manner which prevents their isolation into two separate phenomena. Usually, however, this is not the case for simple wing models and the two types of vibration can be studied more or less independently. Figure 1 has been prepared to illustrate this less complicated case. This figure shows the boundaries for stall flutter and buffeting for a simple cantilever wing model tested in the Langley 2- by 4-foot flutter research tunnel. The boundaries are shown as functions of angle of attack and Mach number. These boundaries are not necessarily general but, rather, are typical of some boundaries found for this particular wing model.

Since the wing was buffeting at all angles above the buffet boundary shown in figure 1, the question arises as to just how the stall flutter boundary was established. This may be explained by examination of figure 2. This figure shows the time histories of the bending and torsion strains for two typical conditions. The upper set of conditions apply to a case of buffeting below the stall flutter boundary. These traces indicate the type of buffeting which is most commonly encountered, that is, a more or less random bending response in the fundamental bending mode with very little excitation of the torsion. The lower set of time histories at a slightly higher angle of attack shows about the same type of bending trace but the torsion trace indicates a fairly clean sinusoidal variation at about the frequency of the fundamental torsion mode. The stall flutter boundary is defined by the conditions which first produce this steady oscillation.

In the low Mach number region (see fig. 1), where the two phenomena occurred at different angles of attack, no difficulty was experienced in distinguishing between them. In the region near  $M = 0.6$ , however, where the boundaries tend to coincide, it becomes more difficult to define the basic character of the vibrations.

The problem of predicting the stresses associated with these separated flow vibrations has received considerable interest. Recently, for instance, Liepmann (ref. 1) has applied the methods of power spectral analysis to a relatively simple case of buffeting, namely, the response of a tail surface subjected to the wake of a stalled wing. It is hoped that these powerful methods can be extended to the more general case of a wing excited by forces which originate because of the instability of flow on the wing itself. However, there is a need for additional knowledge of the basic nature of the forces acting on stalled wings before the response of even a simple cantilever wing can be successfully calculated; for example, the question arises as to what extent the air forces may be considered linear. Sisto (ref. 2) has concluded that a nonlinear approach is essential in order to predict the response due to stall flutter of turbine blades in cascade. It is possible that the nonlinear aspects of the problem will have to be taken into account in order to predict the loads or stresses involved in wing vibrations due to separated flows.

The problem of predicting the boundaries at which buffeting or stall flutter begins does not appear to be quite as difficult as the prediction of stresses encountered in these phenomena. For instance, the buffet boundaries for moderately thick wings have been successfully calculated empirically (refs. 3 and 4), and new measurements such as those presented in the subsequent paper by Charles F. Coe, Perry P. Polentz, and Milton D. Humphreys should prove useful. It has been found that the buffet boundary depends almost entirely on the aerodynamics of the configuration whereas the stall flutter boundary may be altered by changes of structural parameters such as frequency or damping. This difference in behavior may serve as a general definition of buffeting and stall flutter. For the case of simple straight cantilever wings which encounter torsional stall flutter, it has been found (refs. 5 and 6) that satisfactory information concerning the stall-flutter boundary can be obtained from stability equations provided that measured values of the aerodynamic damping moment are used.

Unfortunately, however, the aerodynamic damping moments for stalled flows depend very much on Reynolds number, Mach number, airfoil shape, mode of vibration, and other parameters so that accumulation of sufficient data to predict the boundaries for arbitrary configurations would be prohibitive. As a result, another approach has been used in order to obtain a rough idea of which configurations may be less susceptible to stall flutter than others. Although these trend studies have not been completed, some of the results of flutter tests of various simple wing models are summarized in figure 3. Most of the wings are thin, highly tapered, and of low aspect ratio in keeping with present design trends.

The column on the left in figure 3 illustrates the basic wing configurations followed by columns listing the aspect ratio, taper ratio,

and airfoil thickness. The fifth column indicates the maximum Mach number of the tests and the last column indicates whether the configuration exhibited a stall-flutter region in the range of conditions over which it was tested. All the wings were tested up to angles of attack well beyond the angle of maximum lift.

The two delta wings - actually there were five structurally different models - exhibited no stall flutter until the stiffness was reduced to the point where they were more or less of academic interest because of their poor load-carrying ability.

The unswept wing had flutter characteristics similar to those reported in reference 6. The two aspect-ratio-4 swept wings did not experience stall flutter. It should be pointed out that all three of the wings of this aspect-ratio-4, taper-ratio-0.2 series were somewhat stronger than conventional design procedures would have required. Wing models of more representative stiffness properties remain to be tested.

The last configuration shown exhibited regions of stall flutter which seemed to be closely associated with the regions of leading-edge vortex flow. Some of the flutter characteristics of this configuration are illustrated in figure 4. In this figure, the stall-flutter boundaries for the  $45^\circ$  swept wing are shown as functions of Mach number and angle of attack. The wings were attached to a fuselage in the Langley high-speed 7- by 10-foot tunnel.

With the wing in the clean condition the large region of flutter shown in figure 4 was found. Analysis of the aerodynamic coefficients for this configuration (ref. 7) indicated that the flutter region coincided very closely with the regions in which leading-edge vortex flow existed. For this reason the wing was equipped with a simple flow control device, the leading-edge notch, and the stall-flutter region was obtained for this condition. With one leading-edge notch on each wing panel at 60 percent of the semispan, the small region of flutter shown in figure 4 was found. When the wing was equipped with an additional notch at about 80 percent of the semispan, no flutter was encountered up to the test limits of Mach number and angle of attack. The notch size is considerably exaggerated in figure 4. The actual notches used in the experiments were about 1 percent of the span in the spanwise direction and about 3 percent of the local chord in the chordwise direction.

There are several effective flow control devices, some of which have previously been discussed in a brief summary paper by Wilbur H. Gray and Jack F. Runckel. It is possible that some of these other devices may have a similar relieving effect on the stall-flutter characteristics in addition to their improvement of stability characteristics.

All the preceding discussion has been concerned with separated flow vibrations which involve essentially one mode - stall flutter in the first torsion mode and buffeting in the first bending mode. These are the most common types encountered on simple wing models; however, it should not be concluded that these are the only important types of separated flow vibrations. When the effect of large external masses is considered the system cannot be regarded as a single-degree-of-freedom system, which excludes coupling effects. The dynamic model discussed in a previous paper by Dennis J. Martin and John L. Sewall was investigated briefly for stall-flutter and buffeting characteristics in the Langley 16-foot transonic tunnel and some of the results are illustrated in figure 5.

Figure 5 shows the variation of bending and torsion stresses with angle of attack at a Mach number of 0.35 for the condition of a lightly loaded tip tank. For this condition the bending and torsion frequencies were well-separated ( $f_h/f_\alpha = 0.5$ ) and there was little coupling between the two modes of vibration. As a result the wing responded, qualitatively, at least, in a manner which might be expected from previous observations of simpler models. That is, the maximum fluctuating peak-to-peak bending stress (referred to as  $\Delta$  bending in the figure) rose gradually as the angle of attack was increased beyond the point where separation began, this point being deduced from the curve of the mean root bending stress. The peak-to-peak torsion stress (referred to as  $\Delta$  torsion in the figure) rose rapidly to a high value over a narrow range of angle of attack. The time histories of the stresses indicated that the wing in the region beyond  $\alpha \approx 10^\circ$  was buffeting in predominantly the first bending mode and that the large amplitudes of first-mode torsion at  $\alpha \approx 9^\circ$  were due to a near approach to torsion stall flutter.

Perhaps the smallness of the range of angle of attack over which the torsion stresses were large can be better interpreted by examination of figure 6. This figure shows the contours of unstable-damping-moment coefficients as functions of angle of attack and reduced velocity. These data apply to a two-dimensional, symmetrical, 10-percent-thick airfoil oscillated in pitch about the midchord line with an amplitude of  $1.2^\circ$  and were obtained by a pressure-cell technique. The solid lines in figure 6 indicate the boundaries for zero aerodynamic damping and the dashed lines above the lower boundary indicate increasing values of unstable-damping-moment coefficients.

Although the conditions applying to these damping measurements are not sufficiently similar to those applying to the flexible model to allow reliable quantitative calculations of the torsion response, certain qualitative features can be obtained by comparison. If the dynamic model had zero structural damping it would have been expected to experience torsion flutter over a wide range of angle of attack and velocity. Inasmuch as

the model had some damping, the stall-flutter boundary might resemble one of the closed contours shown in figure 6. As the angle of attack increased at a substantially constant value of reduced velocity, the flexible wing model to which figure 5 pertains is believed to have passed near or through the left boundary of a contour similar to those shown in figure 6. Over the small angle-of-attack range near  $\alpha = 9^\circ$ , the total damping in the torsion mode must have been very near zero, so that a large torsional response was obtained. Apparently, the damping in the first bending mode remained moderate so that only a moderate amount of bending response was excited by the flow separation.

When the mass in the tank was increased to the equivalent of 66 percent full, the response characteristics were changed appreciably and are illustrated in figure 7. The data on the left side of the figure refer to the condition of the center of gravity of the tip tank at the elastic axis of the wing. This condition has been labeled "neutral c.g. location" and applies to the lightweight condition of figure 5 as well. The data on the right refer to a center-of-gravity position somewhat forward of the elastic axis.

For the neutral c.g. case, the addition of the mass to the tank increased the fluctuating bending stresses while the torsional stresses were reduced. Presumably, this was caused by the changes in effective damping in the two modes associated with the reduction in frequencies. When the center of gravity was shifted forward, causing a large mass unbalance, both the torsion and bending stresses were increased appreciably, and in the range of angle of attack near  $\alpha = 10.5^\circ$ , there were short periods when the bending and torsion time histories indicated a coupled-flutter condition. It may be recalled that normally a forward movement of the center of gravity produces a stabilizing effect. However, it appears that for this case of separated flows this type of coupling created an instability. This possibility is discussed qualitatively by Schallenkamp (ref. 8).

Again, the question arises as to whether these vibrations should be called buffet or stall flutter. In the light of the preceding discussion the following definitions suggest themselves:

When the point is reached where an appreciable amount of separation exists there is a continuous excitation of the structure by the aerodynamic forces caused by separation. The amount the structure responds to this continuous excitation is determined primarily by the damping forces or moments acting on the system. If this damping is very near zero or negative, so that very large and fairly steady responses are obtained, then the vibration may be referred to as stall flutter. If the damping remains positive so that intermittent and somewhat random responses are encountered, then the vibration may be called buffeting.

It would have been desirable to obtain similar information at higher Mach numbers; however, this was not possible because of the stress limitations in the model. Tests were conducted up to a lift coefficient of about 0.2 over a Mach number range from 0.7 to 0.85. The results obtained indicated just the opposite trend from that shown in figures 5 and 7. There was a slight decrease in stresses with increased mass in the tip tank and there was virtually no effect observed when the mass was shifted to the forward position.

In this paper an attempt has been made to describe the phenomenological differences between stall flutter and buffeting. Some experimental results have been presented concerning the boundaries at which these phenomena occur and concerning the stresses involved. These results demonstrate the difficulties that may be encountered in attempting to draw conclusions concerning structural vibrations associated with separated flow on the basis of insufficient information.

## REFERENCES

1. Liepmann, H. W.: On the Application of Statistical Concepts to the Buffeting Problem. Jour. Aero. Sci., vol. 19, no. 12, Dec. 1952, pp. 793-800, 822.
2. Sisto, Fernando: Stall-Flutter in Cascades. Preprint No. 402, S. M. F. Pub. Fund Preprint, Inst. Aero. Sci., Jan. 1953.
3. Gadeberg, Burnett L., and Ziff, Howard L.: Flight-Determined Buffet Boundaries of Ten Airplanes and Comparisons With Five Buffeting Criteria. NACA RM A50I27, 1951.
4. Purser, Paul E., and Wyss, John A.: Review of Some Recent Data on Buffet Boundaries. NACA RM L51E02a, 1951.
5. Victory, Mary: Flutter at High Incidence. R. & M. No. 2048, British A.R.C., 1943.
6. Rainey, A. Gerald: Preliminary Study of Some Factors Which Affect the Stall-Flutter Characteristics of Thin Wings. NACA RM L52D08, 1952.
7. Kuhn, Richard E., and Wiggins, James W.: Wind-Tunnel Investigation of the Aerodynamic Characteristics in Pitch of Wing-Fuselage Combinations at High Subsonic Speeds. Aspect-Ratio Series. NACA RM L52A29, 1952.
8. Schallenkamp, A.: Flutter Calculations for Profiles of Small Chord. R.T.P. Translation No. 1556, British Ministry of Aircraft Production. (From Luftfahrtforschung, vol. 19, no. 1, Jan. 20, 1942, pp. 11-12.)

CONFIDENTIAL

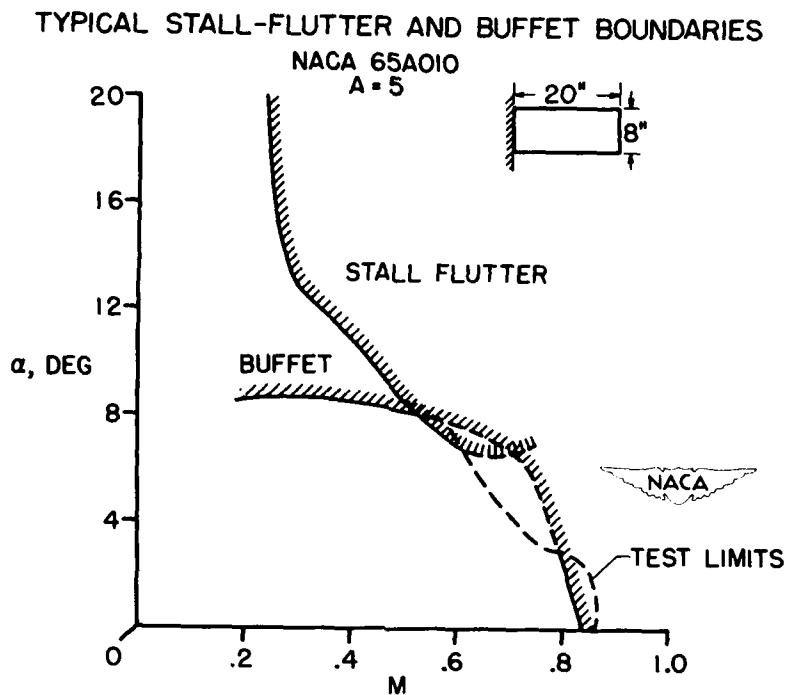


Figure 1.

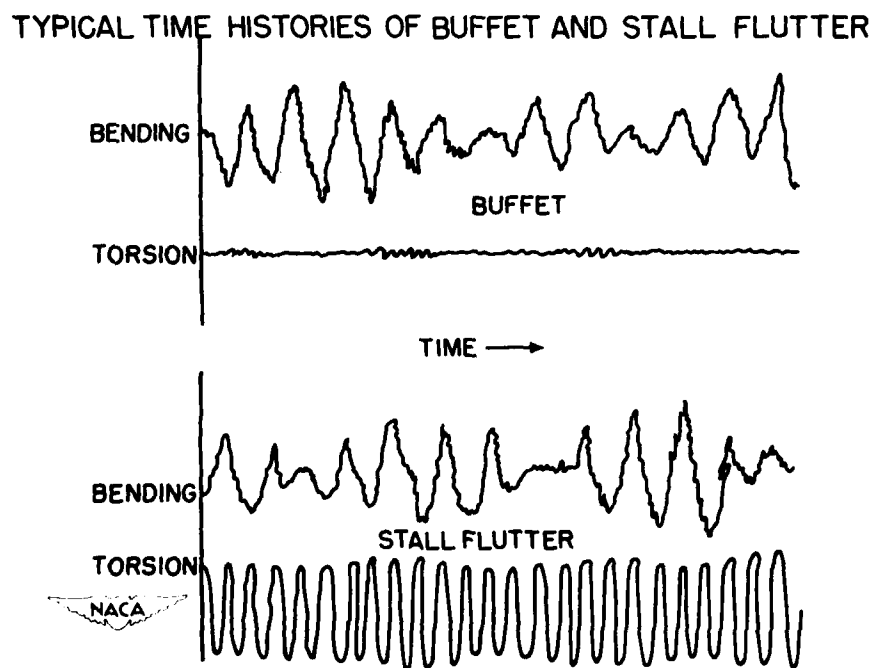


Figure 2.

CONFIDENTIAL

## SUMMARY OF STALL-FLUTTER TREND STUDIES

CONFIGURATION	ASPECT RATIO	TAPER RATIO	THICKNESS RATIO	M MAX	STALL FLUTTER ?
 45° DELTA	4	0	0.04	0.7	NO
 60° DELTA	2.3	0	.04	.7	NO
 Λ = 0°	4	.2	.04	.7	YES
 Λ = 45°	4	.2	.04	.7	NO
 Λ = 60°	4	.2	.04	.7	NO
 Λ = 45°	6	.6	.06	.93	YES



Figure 3.

## STALL-FLUTTER BOUNDARIES FOR 45° SWEPT WING

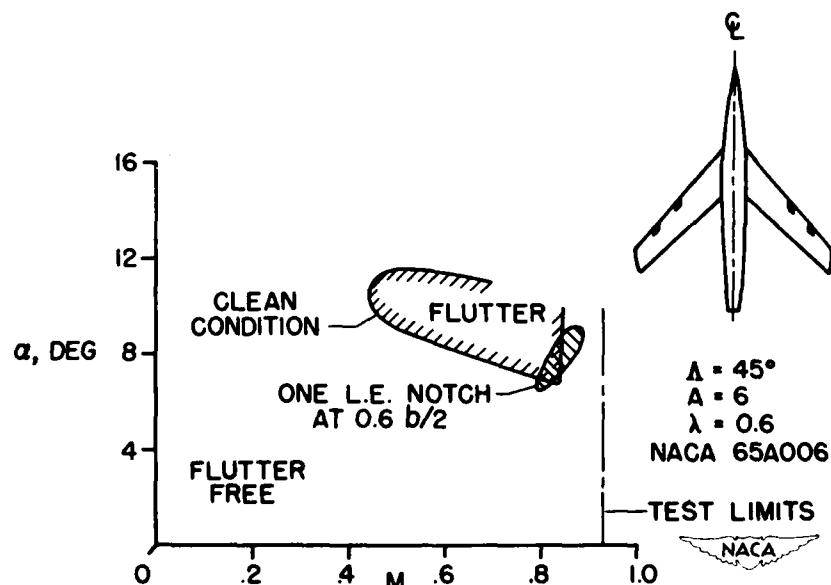


Figure 4.

BENDING AND TORSION STRESSES FOR  
13% FULL TIP TANK

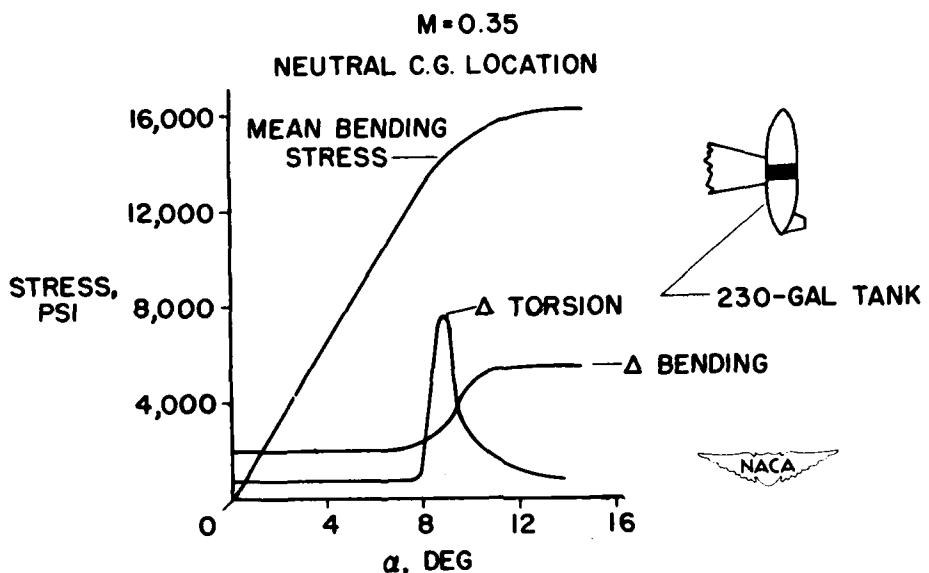


Figure 5.

REGIONS OF UNSTABLE DAMPING IN PITCH

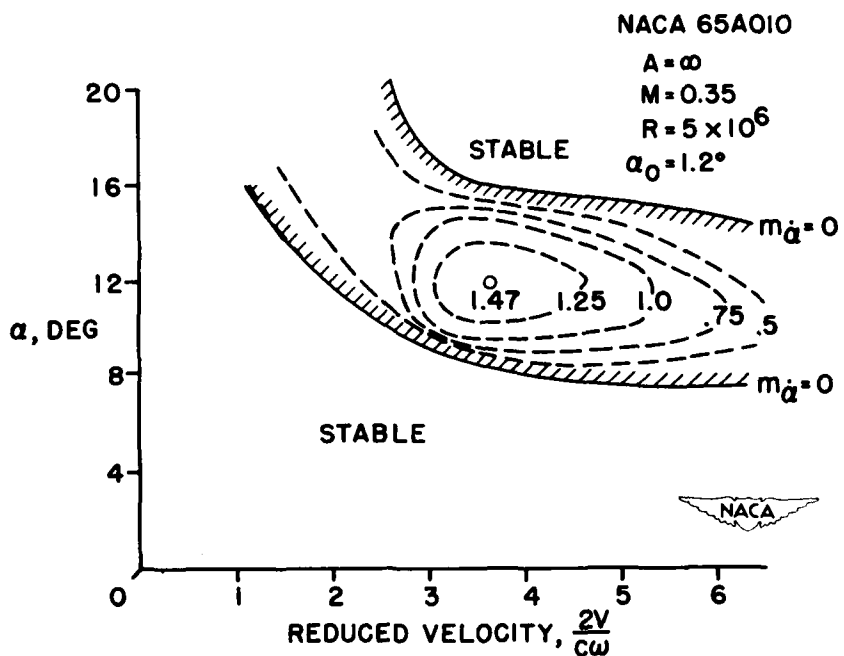


Figure 6.

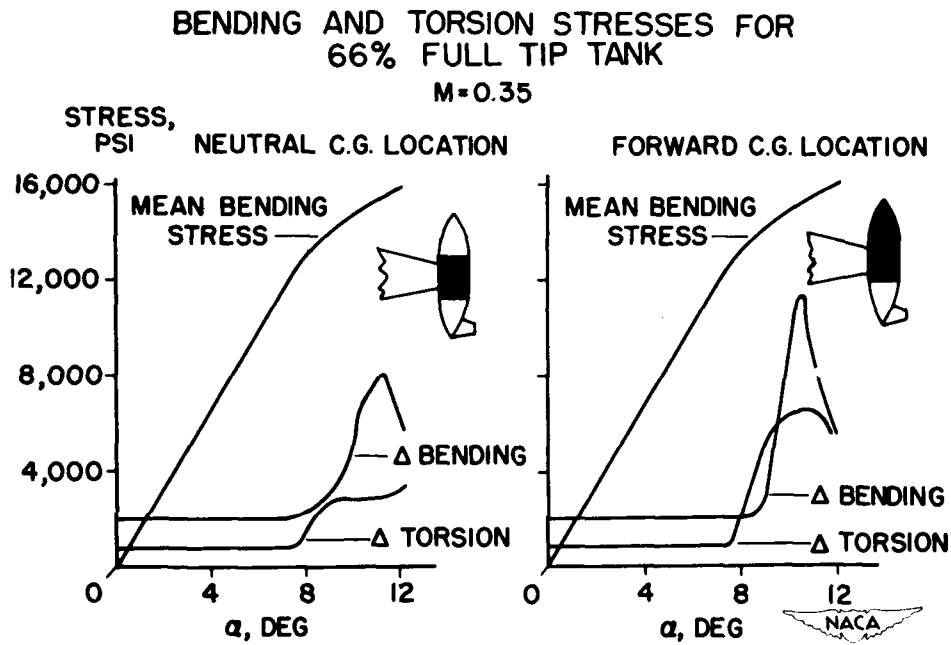


Figure 7.

STUDY OF FLUCTUATING FORCES AND WAKES ON  
TWO-DIMENSIONAL AIRFOILS

By Charles F. Coe, Perry P. Polentz,

Ames Aeronautical Laboratory

and Milton D. Humphreys

Langley Aeronautical Laboratory

INTRODUCTION

Investigations such as references 1 and 2 have established the existence of large pressure pulsations on rigid airfoils. Investigations have now been conducted which show the integrated effects of such pulsations on the fluctuations of lift and pitching moment of airfoils, and which show further details of the local fluctuations of pressure. Figure 1 shows the range of variables used to study the influence of airfoil-section shape on the fluctuations of lift, of pitching moment, and of local panel loads on two-dimensional airfoils. Of the geometric parameters shown, thickness and position of minimum pressure were varied so that fluctuations of the lift on another airfoil mounted in tail locations could be studied.

It is not known at this time the extent to which these results for rigid airfoils in two-dimensional flow apply to elastic, three-dimensional wings and tails. It is believed, however, that the trends shown may reveal important factors affecting the buffeting of aircraft.

The results presented in this paper are derived from two-dimensional tests, conducted primarily in the Ames 16-foot and 1- by  $3\frac{1}{2}$ -foot high-speed tunnels. Reynolds numbers were approximately  $6 \times 10^6$  and  $1.5 \times 10^6$ , respectively. The models were rigid and had chord lengths of 24 inches in the Ames 16-foot tunnel and 6 inches in the Ames 1- by  $3\frac{1}{2}$ -foot tunnel. In both facilities, flush-diaphragm pressure cells were employed to measure fluctuations of pressure and the fluctuations were summed electrically to measure instantaneous lift.

LIFT FLUCTUATIONS

The first results, showing the influence of airfoil-section geometry on the lift pulsations, are based primarily upon data from the

Ames 1- by  $3\frac{1}{2}$  -foot tunnel. In all cases, the trends indicated by results from the Ames 16-foot tunnel are essentially the same.

Figure 2 shows a typical record of the variation of lift with time for the NACA 65-010 airfoil. The Mach number was 0.75, and the angle of attack was  $6^{\circ}$ . All airfoil sections tested thus far suffered unsteady lift similar to that shown in figure 2 at some combinations of lift coefficient and Mach number.

The instrumentation for the Ames 1- by  $3\frac{1}{2}$  -foot tunnel indicated average values of the peak lift fluctuations on a meter. Figure 3 shows values of  $\Delta c_l$  from these readings plotted on the Mach number-lift-coefficient plane. The pulsation intensity in figure 2, representing changes of lift coefficient of 0.14, is shown in figure 3 for an average lift coefficient of 0.8. Plots such as figure 3 were prepared for each airfoil, and from these plots, cross plots were constructed to show the effects on lift fluctuations of each geometric parameter.

Figure 4 illustrates the effect of maximum thickness on the lift fluctuations of a series of airfoils of the symmetrical NACA 65-series, 4, 6, 8, 10, and 12 percent thick. The intensity of the lift fluctuations  $\Delta c_l$  is shown as a function of airfoil thickness for lift coefficients of 0.1, 0.2, 0.4, and 0.6 for various Mach numbers. Examination of the data indicates, first, that reduction of thickness from 12 percent downward initially reduced the lift fluctuations, and second, that, for all lift coefficients above 0.1, a continuing reduction eventually resulted in increased  $\Delta c_l$ . It appears to be true at the lower lift coefficients that reduction of thickness reduces airplane buffeting at high subsonic Mach numbers. At the higher lift coefficients required for maneuvering flight, however, it appears from these data that reducing the thickness below certain values may increase the buffeting. The trend shows an optimum thickness for lift coefficients above 0.1. For those data from the Ames 1- by  $3\frac{1}{2}$  -foot tunnel, the optimums fall from 10 percent downward depending on Mach number. The higher the Mach number, the smaller was the optimum thickness. Data from the Ames 16-foot tunnel for some symmetrical 65A-series airfoils show similar trends. As thickness increased from the optimum, the rise is believed to be due to the shock wave. As thickness is reduced from the optimum, the rise is believed to be due to separated flow near the leading edge.

Figure 5 summarizes the effect of camber on the unsteady lift of a group of 65-series, 4-percent-thick airfoils cambered for ideal lift coefficients of 0, 0.2, and 0.4. At the lower lift coefficients, the

airfoil cambered for an ideal lift coefficient of 0.4 had the larger lift fluctuations. At the higher lift coefficients shown, with one exception at a Mach number of 0.9, the cambered airfoils had smaller lift fluctuations than did the symmetrical airfoil. A possible explanation for the exception is that separation may occur on the lower surface at the leading edge for high cambers. The limited trends shown by these results do not differ greatly from those shown by results of an investigation previously conducted on 6-percent-thick airfoils (ref. 2). In this previous investigation, it was indicated that the use of camber reduced large local pulsations of pressure associated with flow separation near the leading edge.

These trends differ somewhat from those obtained in the Ames 1- by  $3\frac{1}{2}$ -foot tunnel for 12-percent-thick airfoils of the same series. For the thicker airfoils, moderate camber caused larger lift fluctuations.

Figure 6, which shows data from reference 2, shows another means of alleviating the large flow fluctuations resulting from separation at the leading edge. A 15-percent-chord leading-edge flap was installed on the 6-percent-thick airfoil as a means of incorporating variable camber. At high lift coefficients, the flap reduced  $\Delta p/q$  along the chord not only at a Mach number of 0.6 but also at 0.8 and to a lesser extent at 0.9.

At a  $c_n$  of about 0.6, the separated flow on the basic airfoil was relatively mild and, as would be expected, the deflection of flap had no advantage. The flap deflections shown are near optimum for the normal-force coefficient shown. The optimum flap deflection increased linearly with angle of attack.

The effect of the chordwise location of minimum pressure, the last of the geometric parameters investigated, appears in figure 7 for a family of symmetrical, 10-percent-thick, 6-series airfoils with minimum pressures at 30, 40, 50, and 60 percent chord. Although comparison of the results for minimum pressures at 40, 50, and 60 percent chord discloses only small differences, the lift of sections with minimum pressures at 40 and 50 percent chord appears to be slightly steadier.

#### PITCHING-MOMENT FLUCTUATIONS

From some of the tests in the Ames 16-foot tunnel, an indication of the fluctuations of pitching-moment coefficient about the 25-percent-chord point was obtained. Figure 8 shows these results. Peak-to-peak fluctuations of pitching-moment coefficient  $\Delta c_m$  are shown as functions of thickness for 65A-series airfoils and as a function of the position of minimum pressure for 8-percent-thick airfoils.

In general, on the basis of these results, it appears that the effects of these geometric parameters on pitching-moment fluctuations differ slightly from their effects on the lift fluctuations. Except for the very thin wings at low Mach numbers and lift coefficient of 0.6, pitching-moment fluctuations probably will have little influence on the selection of an airfoil.

#### LOCAL FLUCTUATIONS

In order to obtain a better understanding of the effects of thickness and of minimum-pressure location on the lift and pitching-moment fluctuations, pressure fluctuations have been recorded at various stations along the chord of six airfoils. Oscillograph records which show the pressure fluctuations and the phase relationships between fluctuations at the various stations along the chord have been taken.

Figure 9 shows a typical oscillograph record for the NACA 65A004 airfoil at a Mach number of 0.6 and angle of attack of  $6^{\circ}$ . At this angle the principal pressure fluctuations were near the leading edge; therefore, only the traces for the first six stations are shown. The positions of all the measuring stations are marked on the sketch of the airfoil at the left to give an indication of the coverage. Each trace represents the fluctuation with time of the difference between the pressures on the upper and lower surfaces at the station indicated. The trace at the bottom marked "sum" is the summation of the outputs of all the pairs of cells at the 15 stations.

This record shows a phase shift of approximately  $180^{\circ}$  between the region near the leading edge where the flow was supercritical (the region including the first three traces) and the region which was subcritical (shown by the remaining traces). Other records for higher airspeeds show the same tendency for a phase reversal. The fact that these phase differences may occur anywhere from the leading edge to the trailing edge indicates that local fluctuations may not give a true indication of the unsteady lift of an airfoil and also that the buffeting intensities encountered by an airplane may not provide a reliable measure of the local panel load to be expected.

Figure 10 shows the local pressure fluctuations for six airfoils at a Mach number of 0.8. The curves show the peak-to-peak fluctuations of pressure coefficient  $\Delta p/q$  without regard to phasing as a function of the chordwise station  $x/c$ . Local fluctuations are shown on a separate plot for each of the airfoils sketched on the plots. The plots are arranged so that a variation of thickness ratio is in the vertical direction and a variation of the position of minimum pressure is in the horizontal direction.

At this Mach number, the maximum fluctuations occurred in the region of the pressure rise through the shock wave. Generally the magnitudes of these maximum fluctuations in this region approximated the magnitude of the measured rise in static pressure on the airfoil surface.

#### NORMAL-FORCE FLUCTUATIONS ON AN AIRFOIL IN TAIL LOCATIONS

In order to study the effects of thickness and of minimum-pressure position on the fluctuations of normal force on an airfoil in tail locations, a two-dimensional NACA 65A004 airfoil was mounted, as shown in the sketch on figure 11, with its leading edge 1 wing-chord length behind the trailing edge of the airfoils shown in figure 10 and, in addition, behind a 2-percent-thick airfoil of the 65A-series. The chord of the tail airfoil was one-half that of the wings. Its vertical position was varied and its angle of attack was adjusted so that it operated at low enough normal-force coefficients to avoid its own direct buffet conditions. The normal force on the tail was also summed from the outputs of pressure cells.

Figure 11 shows the intensity of normal-force-coefficient fluctuations of the tail  $\Delta c_{n_t}$  in positions above and below the extended chord plane of three 65A-series wings with thicknesses of 2, 4, and 8 percent. These results are presented for a Mach number of 0.6 and wing angles of attack of  $4^\circ$  and  $6^\circ$ . As can be seen, the thinner the airfoil, the greater were the fluctuations of normal force on the tail. Angles of attack less than  $4^\circ$  are not shown since, for these angles, the fluctuation intensities were generally almost negligible. From these data as well as from those for the other four airfoils, there is the indication that a tail may be buffeted even though it is a considerable distance above and below the wing. There does not appear to be a sharp rise in intensity in the immediate region where a large defect of total pressure might be expected in the wake. If this is true, the location of a tail in the wake of a wing may not significantly alter the buffeting of the tail by the flow disturbances originating at the wing. It should also be pointed out that small changes of the angle of attack of the tail appeared to have almost negligible effects on the fluctuations of normal force on the tail. Since the buffeting of the tail due to fluctuations of dynamic pressure would vary with angle of attack, it appears then that the buffeting measured was due primarily to fluctuations of stream angle rather than to fluctuations of dynamic pressure.

Figure 12 shows the maximum values of normal-force fluctuation on the simulated tail plane plotted on the vertical scale as a function of wing thickness and position of minimum pressure of the wing. The curves

show results for Mach numbers of 0.6 and 0.8 and for a wing angle of attack of  $6^{\circ}$ . An angle of attack of  $6^{\circ}$  is shown since the buffeting of the tail was generally small for wing angles of  $4^{\circ}$  or less.

Figure 12 shows that an optimum thickness and an optimum position of minimum pressure may exist for the airfoils investigated. In this case of 8-percent-thick airfoils, an optimum minimum-pressure location appears to be near 50 percent; whereas, for the 65A-series airfoils, an optimum thickness might be about 7 percent. For the 4-percent-thick airfoils, there is the indication that a position of minimum pressure closer to the leading edge than for the 8-percent airfoils may be desirable at a Mach number of 0.6. This difference seems logical since a leading-edge separation which causes poor flow for the thinner airfoils may be alleviated somewhat by a forward movement of the minimum-pressure position.

In general, with regard to the maximum intensities of the fluctuations resulting from each of the airfoils investigated, the tail buffeting was most severe when the local fluctuations on the wings showed evidence of leading-edge separation or when pressure fluctuations occurred over a large percentage of the wing chord. Intense local fluctuations of pressure due to the shock wave at transonic speeds, as on the NACA 65A008 and 65A004 airfoils, did not cause severe tail buffeting.

From these data, it appears that the characteristics of the lift fluctuations on the tail tended to follow those of the lift fluctuations on the wing.

#### CONCLUSIONS

The principal conclusions which may be drawn from this investigation are the following:

1. The effects of thickness and of the position of minimum pressure are nearly the same on lift fluctuations of the wings and on the normal-force fluctuations on another airfoil in tail locations. It appears that the effects of these geometric parameters on the pitching-moment fluctuations of the wings may differ slightly from their effects on the lift fluctuations.
2. Within the limits of the lift data presented, an optimum wing thickness might be near 6 percent, the optimum position of minimum pressure being slightly ahead of the 50-percent chord point.
3. For thin airfoils, moderate camber may reduce lift fluctuations at the higher lift coefficients without significantly affecting the fluctuations at low lift coefficients.

As mentioned before, these results are for rigid airfoils in two-dimensional flow. It is not known at this time whether they apply directly to three-dimensional elastic airplanes, but it is believed that the trends shown may indicate important factors which affect buffeting.

## REFERENCES

1. Humphreys, Milton D.: Pressure Pulsations on Rigid Airfoils at Transonic Speeds. NACA RM L51I12, 1951.
2. Humphreys, Milton D., and Kent, John D.: The Effects of Camber and Leading-Edge-Flap Deflection on the Pressure Pulsations on Thin Rigid Airfoils at Transonic Speeds. NACA RM L52G22, 1952.

## RANGE OF VARIABLES

THICKNESS	0.02c TO 0.12c
CAMBER	0 TO $0.6c_l$
NOSE FLAP, 0.15c	$\delta = 0^\circ$ TO $\delta = -10^\circ$
MINIMUM PRESSURE POSITION	0.07c TO 0.7c
MACH NUMBER	UP TO 0.9
ANGLE OF ATTACK	$0^\circ$ TO $6^\circ$

NACA

Figure 1.

## TYPICAL UNSTEADY LIFT RECORD

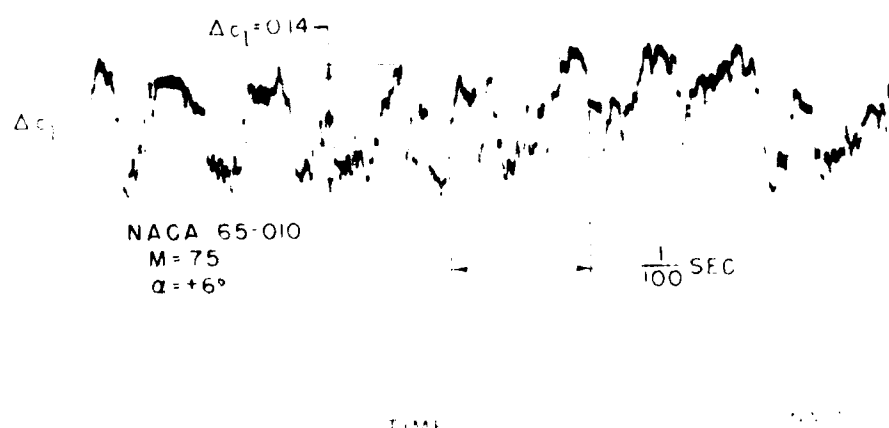


Figure 2.

## UNSTEADY LIFT CHARACTERISTICS FOR NACA 65-010

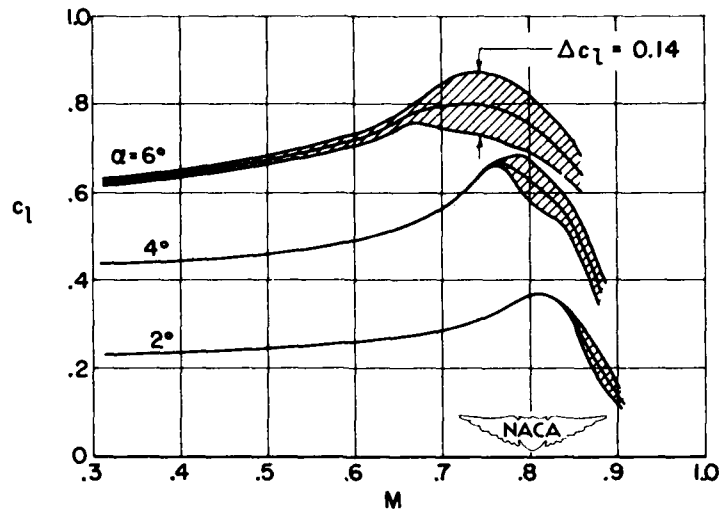


Figure 3.

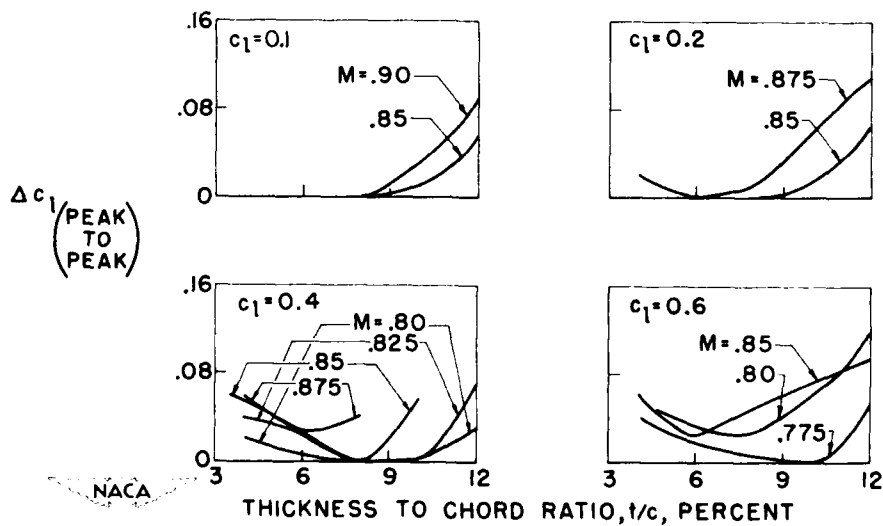
EFFECT OF THICKNESS ON UNSTEADY LIFT  
NACA 65-0XX SECTIONS

Figure 4.

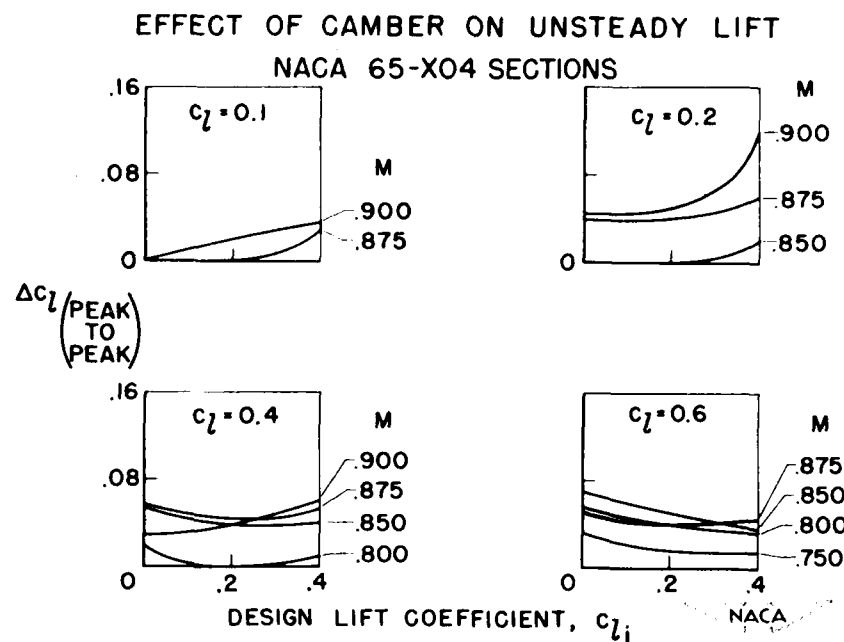


Figure 5.

## FLAP EFFECTS ON PRESSURE PULSATIONS

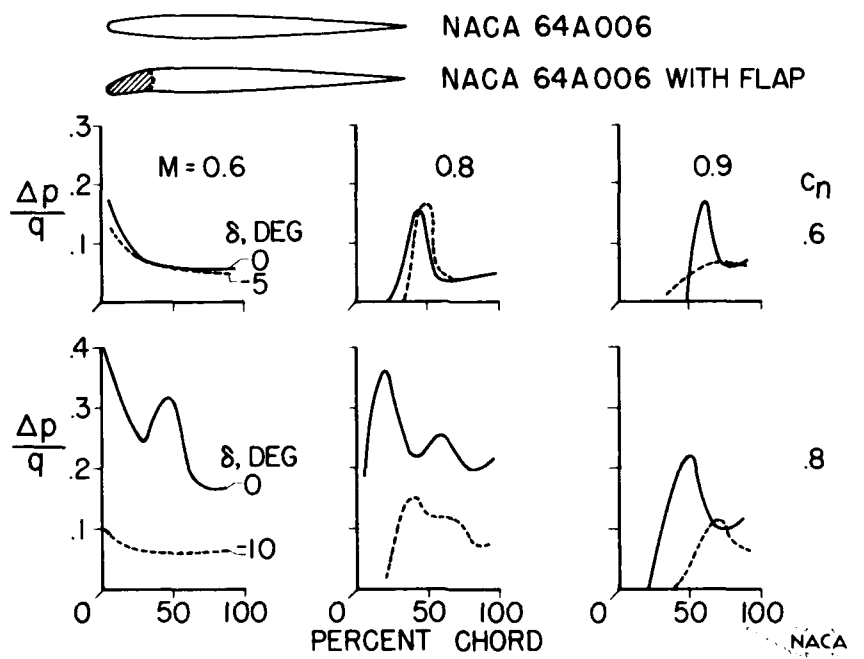


Figure 6.

EFFECT OF POSITION OF MINIMUM PRESSURE  
ON UNSTEADY LIFT, NACA 6X-010 SECTIONS

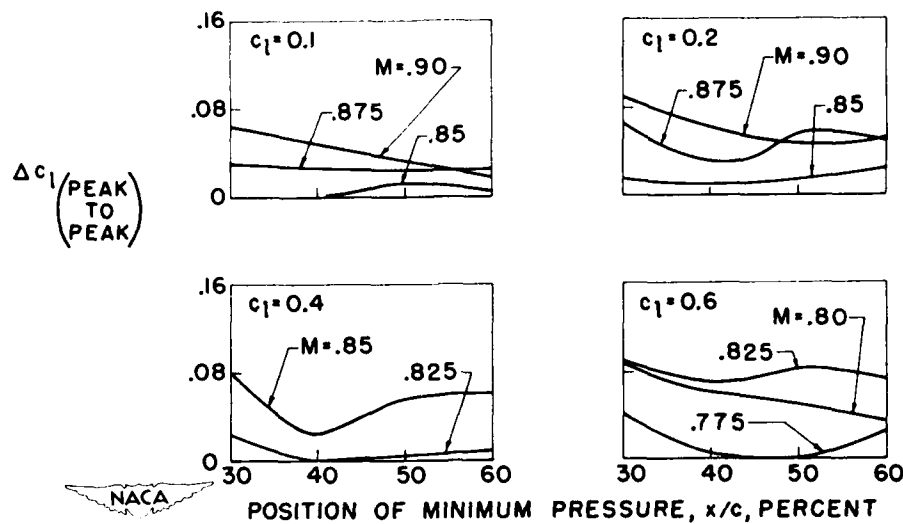


Figure 7.

$\Delta c_m$  AS A FUNCTION OF THICKNESS  
AND POSITION OF MINIMUM PRESSURE

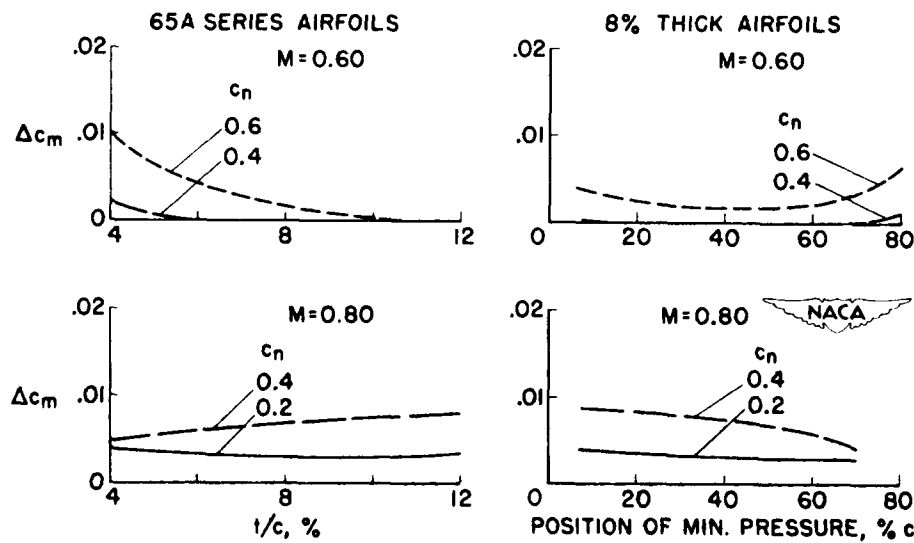


Figure 8.

TYPICAL LOCAL PRESSURE FLUCTUATIONS  
65A004,  $M=0.60$ ,  $\alpha = 6^\circ$

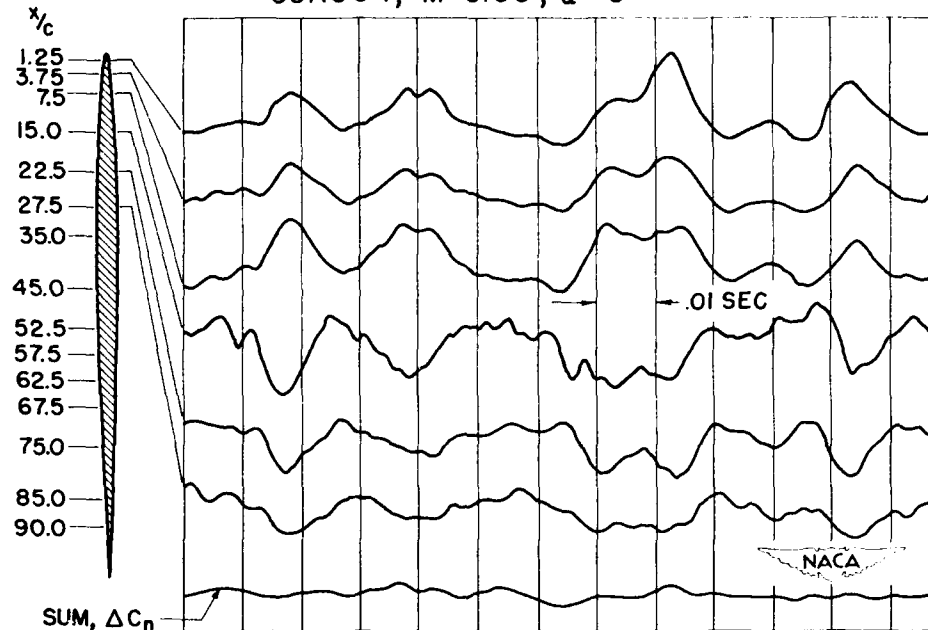


Figure 9.

## LOCAL PRESSURE FLUCTUATIONS ON 6 AIRFOILS

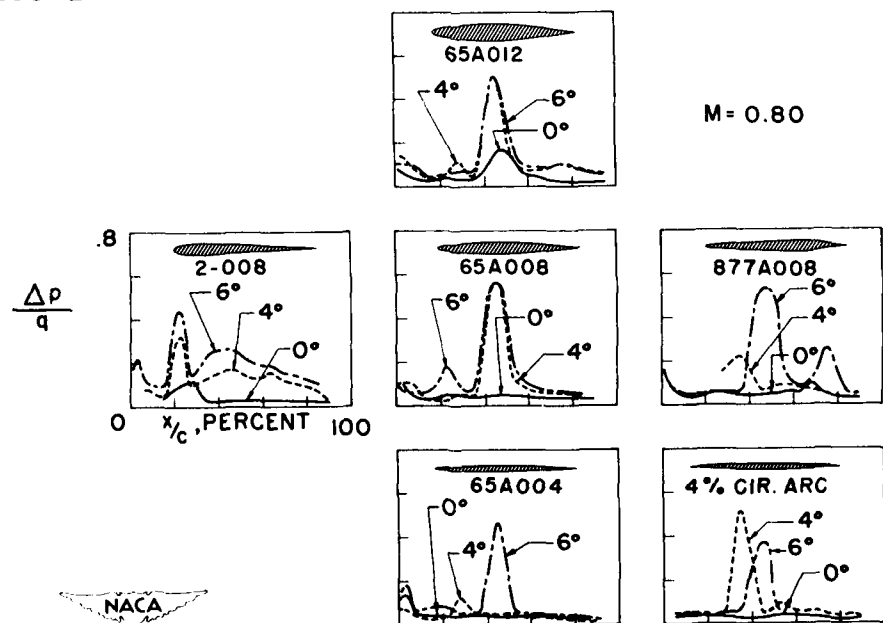


Figure 10.

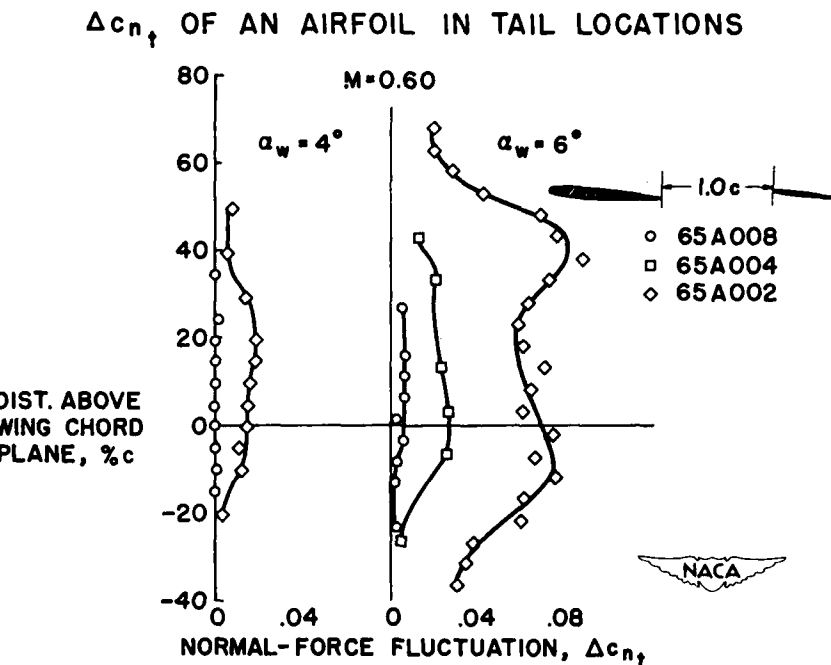


Figure 11.

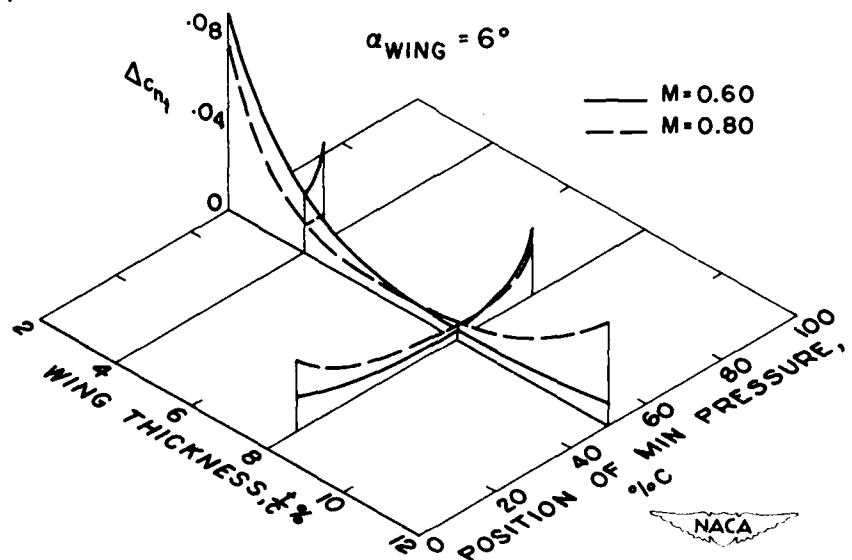
 $\Delta c_{n_t}$  ON A 65A004 AIRFOIL PLACED BEHIND A WING

Figure 12.

CONFIDENTIAL

353

## PRESSURE FLUCTUATIONS DUE TO JETS

By Leslie W. Lassiter and Harvey H. Hubbard

Langley Aeronautical Laboratory

## INTRODUCTION

A turbojet exhaust is a generator of intense pressure fluctuations. At large distances from the engine these are recognized as high-level noise, and in the immediate vicinity of the exhaust stream the magnitudes of these fluctuations may be great enough to impose serious loads on the structural components. Such loads are not, in the usual sense, buffeting loads since they are entirely of acoustic origin but, as will be shown, they have some characteristics similar to those of a buffeting load.

Structurally, these pressure fluctuations may lead to severe vibration and accelerated fatigue. To date, the actual failures from this cause have been confined to the secondary structure - the panels and stiffeners. The regions where failures have occurred and the types of engine installation with which they are associated are illustrated schematically in figure 1. Where the engines have been mounted on struts underneath and slightly forward of the wing, with small clearance between the jet stream and the wing trailing edge, there have been fatigue failures of the secondary wing structure in the region shown by the shading. Some airplanes having the engines alongside the fuselage have also experienced fatigue failures, in this case, of the secondary fuselage structure adjacent to the jet stream. Another region expected to become critical in the future, as engine thrusts increase, is the tail assembly. There the primary structure as well as the panels may be affected, as is pointed out subsequently.

Past experience has shown that the pressure fluctuations observed at a given point near a jet are affected by three general groupings of parameters: (1) the geometry of the point, that is, its location with reference to the jet exit; (2) flow conditions in the jet stream; and (3) the internal history of the flow. The present discussion will deal only with the effects of variations of the point of observation and the flow conditions in the jet stream.

Some preliminary measurements are available from an engine operating at rated thrust in the static condition. However, these full-scale data are for the unchoked operating condition only. Since there is also considerable interest in the effects of overpressuring a jet, some model data will be presented to illustrate the phenomena encountered in the choked, or overpressured, range.

CONFIDENTIAL

## GEOMETRIC EFFECTS

For subsonic jet flow, the spectrum of jet pressure fluctuations is continuous; that is, it contains all frequencies within a given band. A typical spectrum obtained at a point 2 diameters from the jet boundary at an axial distance of 15 diameters from the nozzle of a J-33 turbojet engine of 3,300 pounds thrust and  $18\frac{3}{8}$ -inch exit diameter is shown in figure 2.

figure 2. This is a logarithmic plot of amplitude as a function of frequency. It illustrates the continuous nature of the frequency content and, by the vertical spread of traces, the randomness of amplitude also. The figure shows also that a frequency predominance, or peaking of the spectrum, occurs. In figure 2 the components from 100 to 300 cps are the largest. The predominant frequencies vary with position along the jet boundary; near the nozzle the more important frequencies are of the order of 600 to 1000 cps whereas at points farther downstream the predominant frequencies are much lower and the spectrums are of the type shown in figure 2.

There is also a considerable variation of pressure magnitude with distance along the jet. Spatial distributions of the magnitude of pressure fluctuations as obtained from measurements along a line parallel to the  $15^{\circ}$  theoretical jet boundary and 2 nozzle diameters away from it are given for a high and a low frequency band in figure 3. The broken-line curve indicates the distribution of components between 150 cps and 15,000 cps; the solid-line curve represents the distribution of components between 15 cps and 150 cps. The specified frequency bands were selected only as a matter of convenience. The lower band, however, may be of special interest since many of the secondary structural resonances may lie between 15 and 150 cps. In the higher frequency distribution a maximum is indicated at a point 1 nozzle diameter downstream; however, the spectrum pictures indicate that this peaking is largely due to a high-pitched component thought to be compressor or turbine whine. The significant feature of this curve is that it clearly shows that pressures in this frequency range are greatest near the nozzle. In contrast, the curve for the lower frequency components shows an increase with distance until a maximum of about 5.5 lb/sq ft occurs at a point 15 nozzle diameters downstream of the exit. The curve is comparatively flat so that appreciable low-frequency components appear over a distance range from approximately 5 to 20 diameters. A comparison of the two curves shows that at distances greater than about 5 diameters the pressure is predominately of frequencies less than 150 cps. This fact accounts for the belief that primary members in the tail assembly may be affected eventually.

Figure 3 has described the variation of pressure magnitudes near the jet boundary as a function of axial distance. It is of interest also to observe what changes are produced by increasing radial distance. The effects observed in a plane normal to the jet axis and located at a distance of 15 diameters downstream (the maximum of the low-frequency curve) are shown in figure 4. This is a plot of over-all pressure magnitude as a function of distance in diameters from the theoretical jet boundary. The turbojet curve indicates a rather gradual decrease of pressure with radial distance in the range from 2 to 11 diameters. Since it was not feasible with the available equipment to make measurements close to the hot jet stream, some data for a model cold air jet are included to indicate the probable trend at distances of less than 2 diameters. The model air-jet data indicate a rapid change of pressure magnitude with changing distance and, since model and turbojet data exhibit the same trend in the overlap range, the turbojet curve may also become steep at distances less than 2 diameters.

#### EFFECT OF NOZZLE PRESSURE RATIO

Up to this point the discussion has dealt only with geometric effects and all the trends illustrated relate to a given set of unchoked flow conditions. The remainder of the discussion illustrates the effects on pressure fluctuations at a given location as the flow conditions are varied and points out the differences between subsonic (unchoked) and overpressured (choked) operation. Overpressuring normally occurs in a turbojet engine during thrust augmentation at take-off or in high-altitude operation. Since full-scale data are not available for such conditions, data from small-diameter unheated air jets will be used to illustrate some of the phenomena encountered.

The variation of over-all pressure-fluctuation magnitude with nozzle pressure ratio is shown in figure 5. This is a plot of pressure magnitude in pounds per square foot as a function of nozzle pressure ratio, observed at a point 3 diameters downstream and 1 diameter from the theoretical boundary of a 1-inch model jet. Nozzle pressure ratios ranging from low subsonic to the highly overpressured conditions were studied. The dashed line represents the boundary between the subsonic and overpressured ranges. The magnitude of pressure fluctuations is seen to increase rapidly throughout the subsonic range and up to a nozzle ratio of about 3.5 in the overpressured range. At this point the magnitude is of the order of 20 times the value observed just before choking occurs. Further increase of nozzle pressure ratio results in a sudden decrease of pressure magnitude, followed eventually by another, more gradual increase at high pressure ratios.

The large hump in this curve is associated with a rather sudden change in the frequency spectrum of the fluctuations as illustrated in figure 6. The lower spectrum in this figure is similar to the continuous spectrum of figure 2 except that the predominant frequency components occur higher in the spectrum because of the smaller diameter of the model jet. This is the type of spectrum generated when the nozzle pressure ratio is subcritical and the flow is entirely subsonic. Shortly after the critical ratio is reached, however, a discrete frequency component of very high intensity appears in the spectrum. The upper part of figure 6 illustrates that type of spectrum. It should be noted that the ordinate scales here differ by a factor of 100. Although the effect is not readily apparent because of the different ordinate scales, the discrete component occurs in addition to the continuous fluctuations. Without this discrete component the magnitude curve would presumably be much flatter and of considerably lower level in the range of nozzle pressure ratios from approximately 2 to 4.5. This discrete component has been observed in various nozzle configurations and in nozzles of various diameters and therefore does not appear to be a characteristic peculiar to the test setup. Other experimenters (refs. 1 and 2) have also observed this phenomenon.

Thus in traversing the given range of nozzle pressure ratios a jet generates two entirely different types of pressure fluctuations - a continuous-spectrum type and a discrete-frequency type. The continuous type has been found to be associated with turbulence in the jet stream. On the other hand, at the present time, a complete explanation of the discrete component, or screech, is lacking. Tests have shown, however, that an oscillatory motion of the first shock formation in the flow is definitely associated with the screech condition. Whether this phenomenon is the cause or merely an effect of the screech condition remains to be determined. It is interesting to note that the screech can be eliminated by introducing a small auxiliary jet of air into the main stream and normal to it. The British have also succeeded in reducing pressure fluctuations of this type by the insertion of small, tooth-like prongs into the periphery of the flow at the nozzle (ref. 2). Reduction by this latter means is obtained only with some thrust loss, however.

#### RÉSUMÉ

The physical characteristics of the fluctuating pressure field about a jet have been discussed with the use of experimental data from an unchoked turbojet engine and from model jets. Full-scale measurements indicate that the greatest pressure magnitudes occur at about 15 nozzle diameters downstream of the jet exit. The spectrum of these fluctuations was shown to be continuous and to contain large components in the range below 150 cps. Model jet experiments indicate the presence of a very intense discrete frequency component in the choked range of operation.

## REFERENCES

1. Powell, Alan: A "Schlieren" Study of Small Scale Air Jets and Some Noise Measurements on Two-Inch Diameter Air Jets. Rep. No. NC 136, Univ. College, Southampton (British), Dec. 1951.
2. Westley, R., and Lilley, G. M.: An Investigation of the Noise Field From a Small Jet and Methods for Its Reduction. Rep. No. 53, College of Aero., Cranfield (British), Jan. 1952.

## AREA OF FAILURES

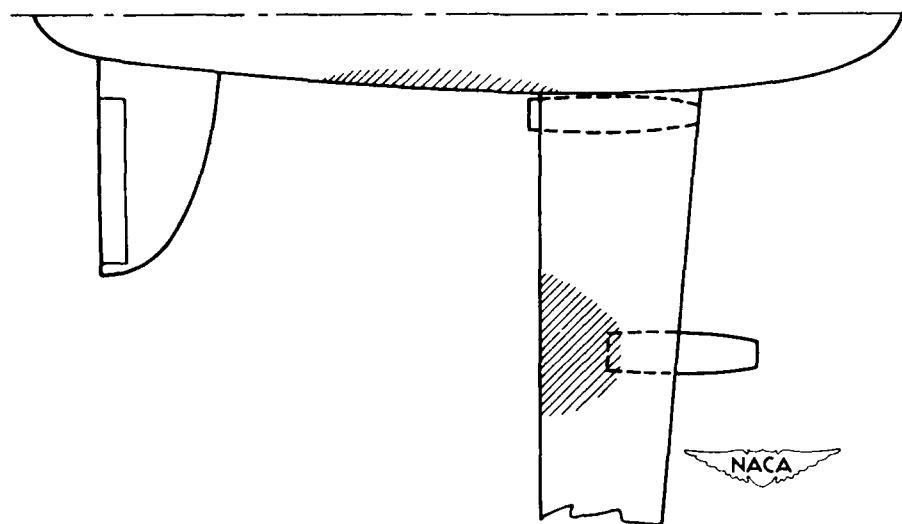


Figure 1.

## TYPICAL TURBOJET SPECTRUM

MAGNITUDE OF  
PRESSURE  
FLUCTUATIONS

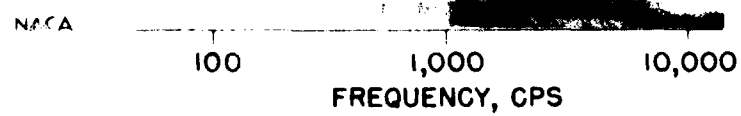


Figure 2.

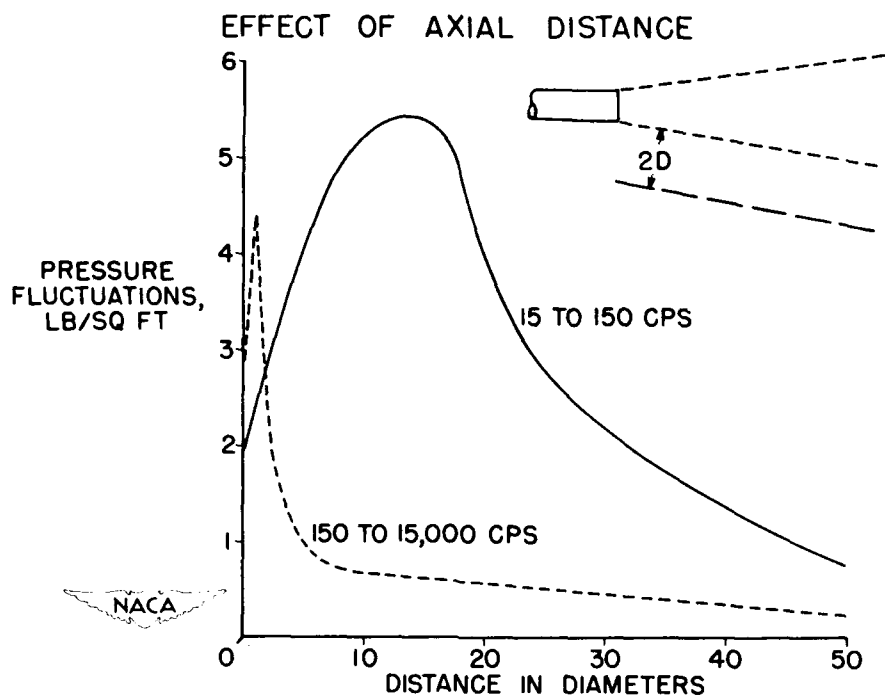


Figure 3.

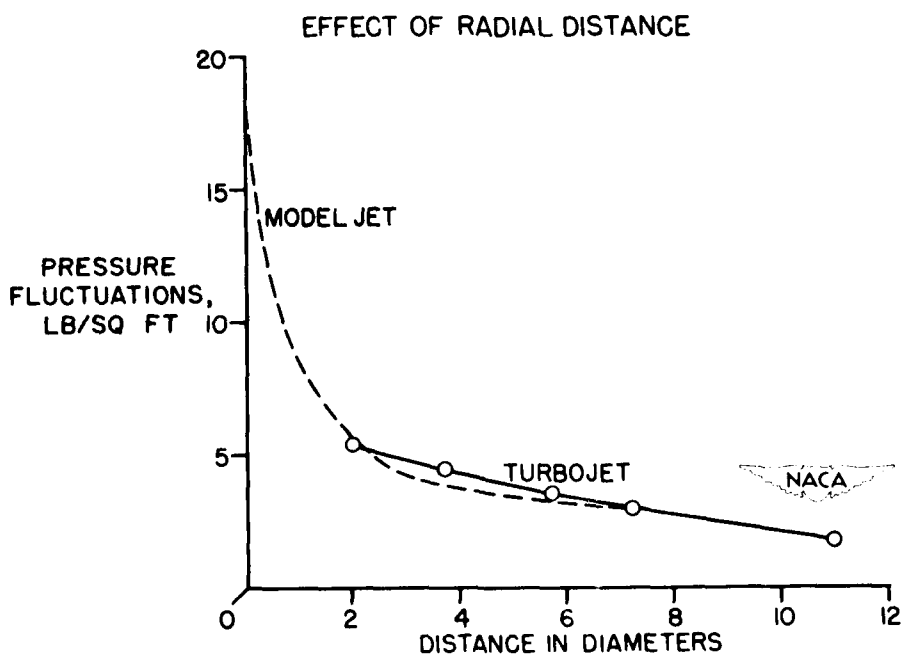


Figure 4.

CONFIDENTIAL

## EFFECT OF NOZZLE PRESSURE RATIO

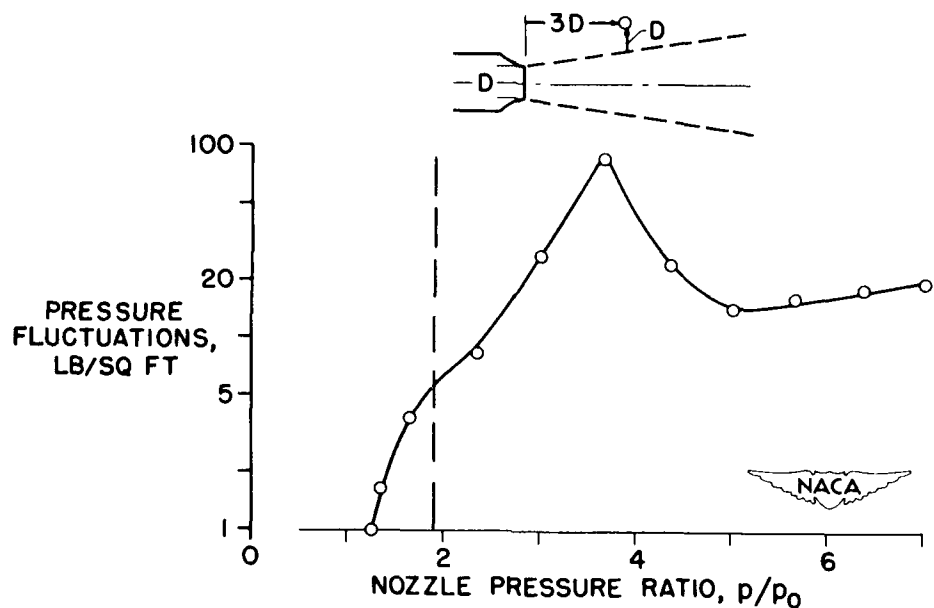


Figure 5.

## FREQUENCY SPECTRUMS OF PRESSURE FLUCTUATIONS

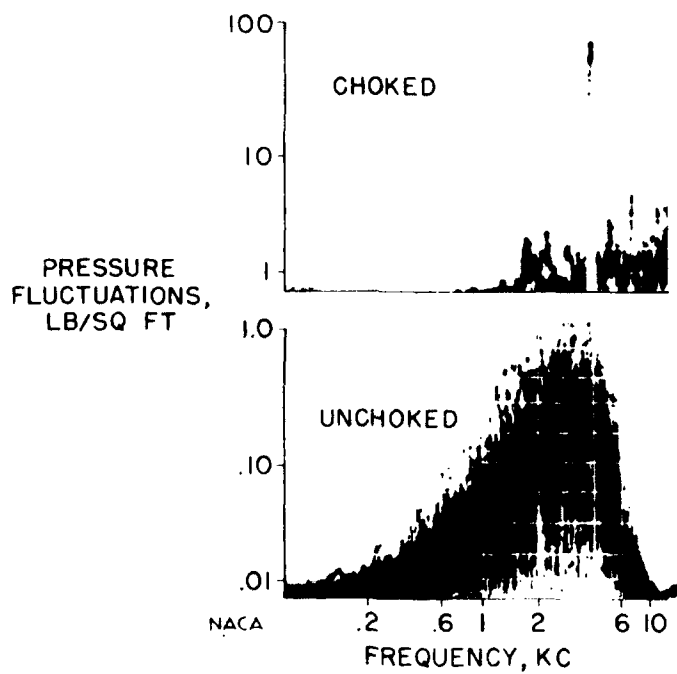


Figure 6.

CONFIDENTIAL

CONFIDENTIAL

361

## LANDING LOADS

CONFIDENTIAL

## AN EXPERIMENTAL INVESTIGATION OF WHEEL SPIN-UP DRAG LOADS

By Benjamin Milwitzky and Dean C. Lindquist

32

Langley Aeronautical Laboratory

## INTRODUCTION

In recent years the problems associated with landing-gear drag loads have assumed increased importance in the design of airplanes. Although drag loads may lead to critical design conditions for such items as landing-gear-drag bracing, parts of the wing, engine mounts and nacelles, tail booms, the afterfuselage, and even tail surfaces, comprehensive reliable information on drag loads is meager and existing data are often in conflict.

The drag-loads problem may be logically resolved into two major aspects, namely, (a) the external applied loads, which are the forces developed between the tire and the runway during the wheel spin-up process in landing, and (b) the dynamic loads induced in the landing gear and various other parts of the airplane structure by the applied loads. The applied ground loads serve as the forcing function which, in conjunction with the mass and flexibility characteristics of the airplane, governs the dynamic response of the structure and, thus, the loads and stresses developed in the airframe.

At the present time a number of dynamic-analysis methods exist which, while not perfect and often laborious, permit reasonable accuracy in the calculation of the dynamic response if the forcing function is known. One of the main problems seems to be: What is the forcing function? This paper is therefore concerned primarily with the applied ground loads and the physical phenomena involved in the wheel spin-up process, in particular, with the variation of the actual coefficients of friction developed between the tire and the runway. The results to be presented cover four distinct types of impact conditions; namely, impacts with forward speed, impacts with forward speed and reverse wheel rotation, stationary spin-up drop tests, and forward-speed impacts with wheel prerotation.

In the past, attempts to investigate systematically the applied ground loads and the coefficient of friction by correlation of flight-test results have generally been impeded by difficulties introduced by the large amount of scatter normally found in flight-test data as a result of the large number of uncontrolled and generally unmeasured variables involved and, probably most important, by the fact that such data are usually obtained with strain gages mounted somewhere in the landing-gear structure, which give a measure of the local strain or response

rather than of the applied ground loads. The results of spin-up drop tests have also been subject to question because of the artificial conditions imposed.

As a result, it was felt that one of the best contributions that the NACA could make in the field of ground loads at this time would be to study the applied drag loads and the wheel spin-up phenomenon under controlled conditions and with instrumentation specifically designed to measure the applied ground loads. The Langley impact basin was chosen for the initial phases of this program and a removable concrete landing strip was installed for the tests. The impact-basin equipment permits a fairly large amount of control in presetting and measuring the impact parameters involved and also permits the use of specialized instrumentation which would be difficult to incorporate in an airplane.

#### EQUIPMENT AND INSTRUMENTATION

The impact-basin equipment consists primarily of a carriage which is catapulted down a track and which incorporates a dropping mechanism for producing an impact of the landing gear with the runway. Thus, the equipment may be likened to a drop-test tower on wheels. A schematic view of the impact-basin carriage equipped for landing-gear testing is shown in figure 1. The maximum forward speed of the carriage is 60 miles per hour and the maximum dropping weight is 2500 pounds. Wing lift forces are simulated mechanically. The landing gear used in the present investigation is a main-landing-gear unit designed for a T-6 or SNJ trainer airplane having a gross weight of about 5000 pounds. The gear is fitted with a 27-inch smooth-contour (type I) tire having a non-skid tread. The tire inflation pressure is 32 pounds per square inch. In the present tests the gear was inclined forward at  $15^{\circ}$  with respect to the vertical. All tests are on a concrete surface.

A sketch of the landing-gear installation is shown in figure 2. Of the various types of specialized instrumentation used in the tests, probably the most important is the two-component axle dynamometer which was specially developed for this investigation. This axle dynamometer, which is of the electrical strain-gage type, measures the vertical and drag forces transmitted from the axle to the fork of the landing gear. Although the axle-dynamometer measurements do not differ greatly from the applied ground loads, there is a difference, equal to the inertia reaction of the mass between the dynamometer and the ground. The actual applied ground loads are therefore obtained by adding these inertia forces, which are determined from accelerometer measurements, to the axle-dynamometer measurements. Measurements of the ground loads obtained in this manner check very closely with data obtained simultaneously with a ground dynamometer or reaction platform in stationary spin-up drop tests.

Also included in these tests was instrumentation to measure the instantaneous skidding velocity of the surface of the tire with respect to the runway. The skidding velocity was obtained from measurements of the axle translational velocity, the wheel angular velocity, and the effective skidding radius of the tire.

A special effort was made to employ high-frequency instrumentation and recording equipment in order to minimize instrument-response errors.

## RESULTS AND DISCUSSION

### Fundamentals of Wheel Spin-Up Process

Forward-speed tests. - Figure 3 shows several typical time histories of the applied ground loads as measured in impacts with forward speed and illustrates some of the fundamentals of the wheel spin-up process. Data are presented for impacts at a given vertical velocity  $V_{V_0}$ , 9.6 feet per second in this case, and at horizontal velocities of 12, 30, and 57 miles per hour. In the upper graph, the top curves show time histories of the applied vertical load and the bottom curves show the drag load. The lower graph shows the variation of the coefficient of friction during the spin-up process. The coefficient of friction is simply the instantaneous ratio of the applied drag load to the applied vertical load. It should be noted that the friction-coefficient scale does not extend down to zero.

A number of basic effects can be seen from this figure. As the forward speed is increased the time to reach the maximum drag load and the time required for wheel spin-up is increased. During this period the tire is skidding relative to the runway as the wheel is being accelerated from zero initial rotational velocity up to ground-rolling speed by the drag load. The area under the drag-load-time curve represents an impulse which, acting through the radius of the skidding tire, produces an angular impulse that must equal the change in angular momentum of the wheel during the spin-up process. The higher the initial horizontal velocity, the greater is the required impulse for spin-up, the more the skidding is prolonged, the greater is the vertical load when the wheel comes up to speed, and the greater is the maximum drag load.

As can be seen, the increased drag loads are accompanied by a substantial increase in the vertical load. This increase in the vertical load arises from two sources; namely, (a) increased friction in the shock strut which results from the larger bending moments produced by the inclination of the resultant of the vertical and drag forces with respect to the axis of the shock strut and (b) the component of the drag force along the axis of the shock strut which tends to increase the rate

of closure of the strut, with consequent increase in the shock-strut axial force.

The lower graph (fig. 3) shows that the coefficient of skidding friction increases with time during the spin-up process. Since the skidding velocity is greatest at the instant of initial contact and drops to zero at the instant of spin-up, it is evident that the coefficient of friction increases as the skidding velocity decreases. This effect can also be seen by examining the three lower curves at given instant of time before spin-up. The curve for 57 miles per hour represents the highest skidding velocity and indicates the lowest coefficient of friction. The maximum values of the coefficient of friction, which correspond to very small values of the instantaneous skidding velocity just prior to spin up, also decrease with increasing forward speed, probably because of the greater temperature of the surface of the tread rubber which results from the greater work done by the skidding friction force. A more detailed discussion of the characteristics of the skidding friction will be presented in a subsequent section.

Forward-speed tests with reverse wheel rotation.- In an attempt to extend the range of the investigation beyond the 60 miles per hour maximum speed of the carriage, forward-speed tests were made with reverse wheel rotation. The carriage was propelled at its maximum speed and the landing wheel was rotated backward to simulate horizontal velocities at initial contact up to 186 miles per hour.

Figure 4 shows results of two typical tests near the extremes of the horizontal-velocity range obtained in this phase of the investigation. The solid curves are for an initial relative horizontal velocity  $V_{REL}$  of 76 miles per hour, whereas the dashed curves are for 186 miles per hour. The vertical velocity in these tests was 7.5 feet per second.

The results for 76 miles per hour are similar in character to those previously discussed. The high-speed results, however, are markedly different. First of all, the time to spin-up is greatly increased, as might be expected, and the wheel does not come up to speed until very much after the maximum vertical load is reached. The drag load throughout the time history, as well as the maximum drag load, is considerably reduced. Similarly the maximum vertical load is much less, because of the reduced friction in the shock strut, which results from the fact that the resultant ground force is more nearly aligned with the axis of the shock strut.

The cause of the smaller loads at high speed is the much lower coefficient of friction throughout most of the time history, which results from the higher skidding velocity and the increased heating of

the tire surface. In the later stages of the spin-up process, however, the coefficient of friction increases as the skidding velocity decreases, just as in the previous cases. Since the vertical load is fairly small at the instant of spin-up, the maximum drag load is likewise low.

An interesting phenomenon in the case of the high-speed impact is the sudden reduction in the slope of the drag-load-time curve shortly after contact and the marked drop off in the coefficient of friction. Apparently, at this point the critical temperature of the tread rubber is exceeded, because of the very high skidding velocity, and the area of the tire in contact with the runway becomes molten. This situation appears to be only temporary and ceases to exist as the skidding velocity decreases.

#### Comparison of Maximum Loads in Various Types of Tests

Forward-speed tests and forward-speed tests with reverse wheel rotation.-- Figure 5 shows the maximum vertical and the maximum drag loads obtained in the ordinary forward-speed tests and in the forward-speed tests with reverse wheel rotation plotted against the relative horizontal velocity at initial contact. All tests are for a vertical velocity at contact of 7.5 feet per second. The solid circles and the solid-line curves are data from the forward-speed tests below 60 miles per hour; the open squares and the long-dash curves are data from the forward-speed tests at the maximum carriage velocity with reverse wheel rotation.

In order to check on the validity of the reverse-rotation technique, the carriage was also propelled at low speeds and the landing wheel was spun up backward to simulate the original forward-speed tests between 30 and 60 miles per hour. These overlapping tests are shown by the open diamonds and triangles for carriage velocities of 33 and 14 miles per hour, respectively. There appear to be some secondary effects of carriage speed, but in this low-speed region such effects would be expected to be small. Tests are now in progress to extend the overlapping range to higher relative velocities in order to obtain a better evaluation of this effect. Present indications are that reduced carriage speeds result in smaller loads for a given relative horizontal velocity. This result arises from the fact that reverse-rotation tests do not duplicate the ratio of the skidding velocity to the forward speed of the carriage, called the slip ratio. The effects of slip ratio will be discussed in more detail later. Because of the difference in slip ratio, the actual loads in a true forward-speed test should be somewhat larger than are indicated by the data from the forward-speed tests with reverse rotation. The exact amount of this difference cannot be determined at the present time since there is no way of obtaining actual forward-speed data above 60 miles per hour in the impact basin.

As can be seen from figure 5, the maximum drag load reached a maximum at about 80 miles per hour. At this horizontal velocity the instant of spin-up coincides in time with the occurrence of the maximum vertical load, as can be seen from figure 4. Above this speed, because of the reduced coefficient of friction, the maximum drag load decreased with increasing forward speed, as previously indicated by the time histories. The vertical load increased markedly with increasing drag load, because of shock-strut friction, then dropped as the drag load decreased at the higher horizontal velocities, also as previously noted. The dip in the curve of maximum vertical load at a horizontal velocity of about 20 miles per hour corresponds to the condition of minimum friction in the shock strut. At speeds below 20 miles per hour the resultant force tends to deflect the gear forward; at speeds above 20 miles per hour the resultant force tends to deflect the gear rearward. At about 20 miles per hour the bending moment, and thus the strut friction, reaches a minimum, with consequent reduction in the vertical load.

Spin-up drop tests.- In figure 6 the maximum vertical and maximum drag loads obtained in spin-up drop tests are compared with the results of the forward-speed tests previously discussed. In these drop tests the carriage was stationary and the landing wheel was spun up backward before the impact to simulate the effect of forward speed. The vertical velocity at contact in these tests was also 7.5 feet per second. The open circles and short-dash curves show the drop-test data; the solid-line and long-dash curves represent the forward-speed results and are the same as the curves of figure 5.

As can be seen, the spin-up drop tests were in fairly good agreement with the forward-speed tests at the low relative horizontal velocities, the drop tests yielding slightly higher drag loads. At speeds above about 40 miles per hour, however, the drop tests yielded considerably smaller drag loads and smaller vertical loads than did the forward-speed tests, the latter result again indicating the effects of strut friction. These reductions in load are due primarily to the much smaller coefficients of friction in the spin-up drop tests than in the forward-speed tests throughout most of the horizontal-velocity range, which result from the rubbing of the tire in one spot on the concrete in the case of the drop tests. A better understanding of the nature of the coefficient of friction can be obtained from the following discussion.

#### Variation of Coefficient of Friction

Figure 7 shows the variation of the coefficient of skidding friction during impact for the three types of tests previously discussed, namely, the impacts with forward speed below 60 miles per hour, the impacts with forward speed and reverse wheel rotation, and the spin-up drop tests. In this figure the coefficient of friction is plotted

against the instantaneous skidding velocity of the tire with respect to the runway. Each curve shows the variation of the coefficient of friction during a particular test run. For the sake of clarity, results are shown from only three runs for each type of test. The highest skidding velocity shown for any particular curve is somewhat less than the relative horizontal velocity at initial contact, which is indicated by the numbers next to each curve. At the instant of initial contact the skidding velocity is, of course, exactly equal to the relative horizontal velocity. Immediately after contact, however, the drag and vertical loads are so small that the instrument error becomes significant; consequently, the friction coefficients during a very short interval after contact are not shown. The right-hand extremities of each curve presented therefore start out at relative horizontal velocities slightly below the initial velocity. When the skidding velocity reaches zero the spin-up process is finally completed. Thus the course of the impact appears in this figure from right to left. The actual data points for any given run exhibited very little scatter and relatively smooth curves could therefore be drawn through the points with almost no fairing. It should be again noted that the friction-coefficient scale does not extend down to zero.

Let us first examine the results of the forward-speed tests. The main point to be made here is that the coefficient of friction decreases with increasing skidding velocity, from almost 0.9 at 5 miles per hour to about 0.7 at 50 miles per hour.

In the case of the forward-speed tests with reverse wheel rotation, at the low skidding velocities there is general agreement with the true forward-speed data. There is also the general trend of a decreasing coefficient of friction with increasing skidding velocity. This decreasing trend is evident throughout the entire skidding-velocity range and indicates coefficients of friction as low as 0.3 at skidding velocities of 150 miles per hour. It should be noted, however, that, even in the case of impacts at high initial relative velocities, the coefficient of friction reaches fairly high values as the skidding velocity is reduced in the later stages of the spin-up process.

It can be seen that in the early stages of each impact the curves depart from the general trend and the initial values of the coefficient of friction are fairly high. For example, the data from the test at an initial horizontal velocity of 118 miles per hour start out at a coefficient of friction of about 0.6 and rapidly drop to the general trend. This short duration effect is believed to represent a transitional stage from an initially cold rubber surface to a more-or-less equilibrium condition represented by the general trend. In other words, for the cold tire the variation of the coefficient of friction with skidding velocity appears to follow a limiting curve through the upper initial points; whereas, for the operating-equilibrium condition the variation is

represented by the lower trend, as is diagrammatically illustrated in figure 8. Both trends indicate a decrease in coefficient of friction with increasing skidding velocity, the rate of decrease being more pronounced for the "hot" curve.

In the case of the extremely high initial relative velocity of 186 miles per hour (fig. 7), the apparent temporary liquification of the tread rubber shortly after initial contact, because of the very high skidding velocity in this region, is manifested by the local drop in the friction coefficient. This effect was previously discussed in connection with the time histories shown in figure 4.

The equilibrium trend for the forward-speed tests with reverse rotation shows a more rapid decrease in the coefficient of friction with skidding velocity than is indicated by the forward-speed tests below 60 miles per hour. This result is apparently due to the effects of slip ratio, which was previously defined as the ratio of the skidding velocity to the forward speed of the wheel. Reverse-rotation tests have higher slip ratios than true forward-speed tests. As a result there is less fresh runway brought into contact with the tire per unit time than in a true forward-speed test, and therefore less cooling effect and a greater tendency for contamination of the runway in the tire contact area by abraded or molten rubber, with a consequent reduction in the coefficient of friction.

The effect of slip ratio is even more marked in the spin-up drop tests. For low initial relative horizontal velocities, the coefficients of friction are generally of the same order as in the forward-speed tests. At these low skidding velocities heating and runway contamination are negligible, even though the tire is always rubbing in one spot on the concrete. At the higher initial relative velocities, however, the tire surface rapidly becomes soft and even molten, and the concrete becomes loaded with gummy rubber which acts as a lubricant. As a result, the transition from a cold tire surface to a hot tire surface is very rapid, and the coefficient of friction becomes very small throughout practically the entire spin-up process. It can be seen that the higher the initial relative velocity, the smaller is the coefficient of friction. For example, at an initial relative horizontal velocity of 155 miles per hour, the average coefficient of friction is less than 0.4. These unrealistically low coefficients of friction in spin-up drop tests indicate why some manufacturers have had to resort to special artificial reaction-platform surfaces in order to realize coefficients of friction more compatible with experience and with design requirements.

It is hoped to be able to establish some of the effects previously discussed more quantitatively in the final report on this investigation.

## Effects of Prerotation

The last subject to be considered deals with the effects of wheel prerotation in reducing drag loads. It appears that one of the main reasons that prerotation has not come into wider use stems from a general belief that the reductions in drag load would be very small unless the prerotation speed is matched almost exactly with the ground-rolling speed, a requirement which may be rather difficult to achieve in practice.

Figure 9 shows how prerotation affects the drag load. The upper curves are time histories of the vertical load; the lower curves are drag-load time histories. Results are shown for three prerotation speeds ranging from no prerotation to 93 percent or almost complete prerotation. These tests were made at a vertical velocity of 9.6 feet per second and a horizontal carriage velocity of 57 miles per hour. These results show that wheel prerotation permits a major reduction in drag load as well as an accompanying reduction in vertical load.

In order to show more clearly the effect of prerotation on the maximum drag load, Figure 10 presents a graph of the ratio of the maximum drag load with prerotation to the maximum drag load without prerotation, as a function of the percent prerotation. These results are also for a carriage horizontal velocity of 57 miles per hour and a range of vertical velocities. The data for the high vertical velocities representative of design sinking speeds indicate substantial reductions in maximum drag load, even for partial prerotation. For example, 50 percent prerotation reduces the drag load by almost 40 percent in these tests. At the lowest vertical velocity, however, partial prerotation, while still beneficial, does not permit as marked a reduction in drag load.

The foregoing results correspond very closely with what would be predicted from curves of maximum drag load against initial relative horizontal velocity, such as previously shown in figure 5.

In evaluating these prerotation results, a word of caution is necessary. In the prerotation tests discussed here the carriage horizontal velocity was 57 miles per hour. As can be seen from figure 5 this velocity is below the forward speed at which the hump in the maximum drag-load curve occurs. At speeds below the hump, reducing the relative velocity by prerotation, even partial prerotation, always serves to reduce the drag load. For horizontal velocities above the hump, however, partial prerotation could very well produce an increase in drag load if the relative velocity were reduced to values in the vicinity of the hump. This possibility should always be considered in the design of prerotation devices and care taken to insure that the relative velocity produced by prerotation is well below the hump velocity. This

restriction still provides a great deal of latitude in matching the forward speed and does not violate the previous conclusion that appreciable reductions in drag load can be obtained even with incomplete prerotation. It would also appear that prerotation should be advantageous from the standpoint of fatigue, due to reduction of the fore-and-aft oscillatory loading (so-called spin-up and spring-back loads) dynamically induced by the drag load.

#### SUMMARY OF RESULTS

This paper has presented some recently obtained information on landing-gear applied drag loads and on the nature of the wheel spin-up phenomenon in landing. These results are based on a program of tests under controlled conditions, which is still in progress in the Langley impact basin. In particular, a study has been made of the nature and variation of the coefficient of friction between the tire and the runway and the relationships between forward-speed impacts, forward-speed impacts with reverse wheel rotation, spin-up drop tests, and forward-speed impacts with wheel prerotation. A summary of the major findings follows:

1. The maximum applied drag load increases with increasing initial horizontal velocity, reaches a maximum value at the horizontal velocity at which wheel spin-up coincides in time with the occurrence of the maximum vertical load, then decreases as the horizontal velocity is further increased, primarily because of a reduction in the coefficient of friction with increasing skidding velocity.
2. The vertical load increases substantially with increasing drag load, because of increased friction in the shock strut which results from the bending moments produced by the inclination of the resultant ground force with respect to the axis of the shock strut.
3. Because of differences in slip ratio, forward-speed impacts with reverse wheel rotation give somewhat smaller loads at the higher relative horizontal velocities than true forward-speed impacts; the higher the forward-speed in the reverse rotation impacts, of course, the smaller is the difference in load.
4. At horizontal velocities representative of actual airplanes, stationary spin-up drop tests give considerably smaller drag and vertical loads than impacts with forward speed.
5. The coefficient of friction between the tire and runway decreases appreciably with increasing skidding velocity. During an impact there is a transition from an initially cold tire surface to a more-frictional

equilibrium condition; consequently the coefficient of friction starts out at fairly high values representative of the cold tire and rapidly drops to values corresponding to the equilibrium condition. Both trends indicate a decrease in coefficient of friction with increasing skidding velocity. It should be noted, however, that even in the case of impacts at high initial relative velocities, the coefficient of friction reaches fairly high values as the skidding velocity is reduced in the later stages of the spin-up process.

6. The variation of the coefficient of friction with skidding velocity is also dependent on the slip ratio. The importance of slip ratio is particularly marked in the case of spin-up drop tests. For low relative velocities the coefficients of friction in drop tests are approximately the same as in forward-speed tests. At higher relative velocities, however, the coefficient of friction drops to very small values as a result of the effects of heating and lubrication of the contact area by abraded or molten rubber.

7. Wheel prerotation, even partial prerotation, appears to be very effective in reducing drag loads. Care should be taken, however, to insure that the relative velocity produced by prerotation is well below the velocity at which the drag-load hump occurs, otherwise the drag load may be increased rather than reduced. This restriction still permits considerable latitude in matching the forward speed and does not violate the conclusion that prerotation can greatly reduce the maximum drag load.

#### CONCLUDING REMARKS

As has been previously mentioned, the results of the present investigation were obtained with a small landing gear equipped with a relatively low-pressure tire. Just how general these results are is as yet unknown. In particular, similar data are needed to determine the effects of wheel size, tire pressure, vertical load, rate of change of vertical load, slip ratio, heating produced by the skidding energy absorbed by the tire, different runway surfaces and materials, and other factors which may influence the coefficient of friction.

It is expected that data on some of the gross effects of size will be obtained in flight tests of a specially instrumented B-29 airplane now being started. A systematic study of the effects of many of the other important parameters, however, will probably have to wait on the availability of the landing-loads track now under construction.

## IMPACT BASIN CARRIAGE AND LANDING GEAR

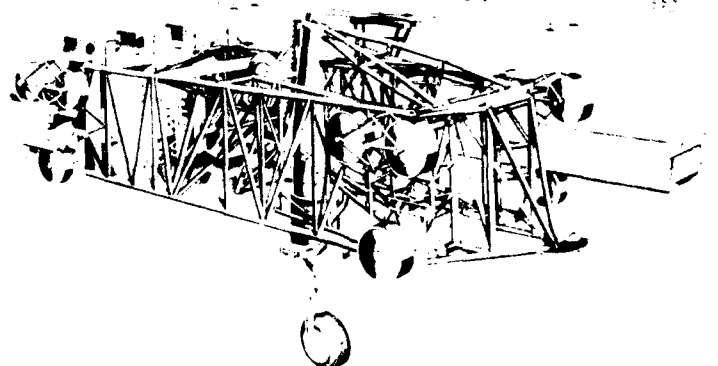


Figure 1.

## LANDING GEAR AND INSTRUMENTATION

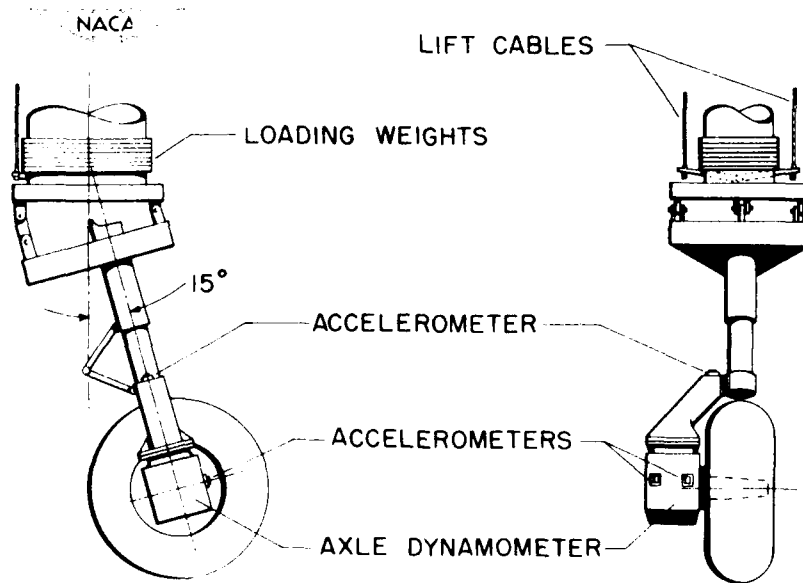


Figure 2.

## SPIN-UP TIME HISTORIES - FORWARD SPEED TESTS

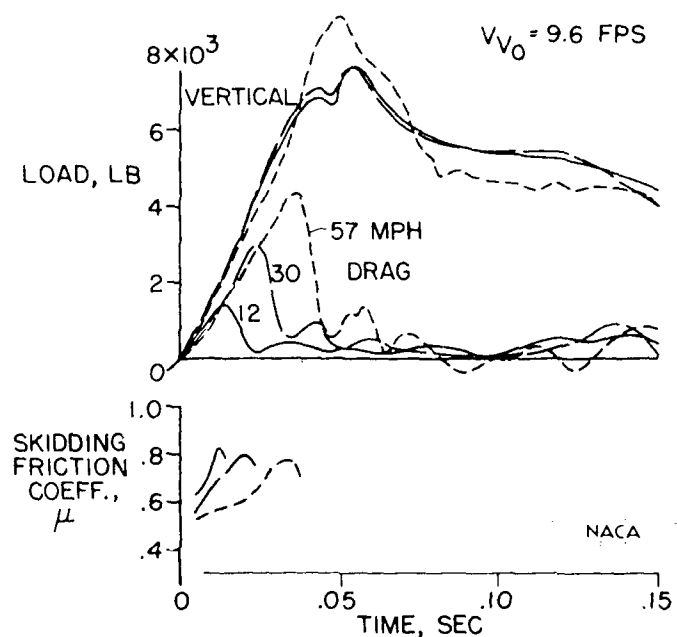


Figure 3.

## FORWARD-SPEED - REVERSE-ROTATION TESTS

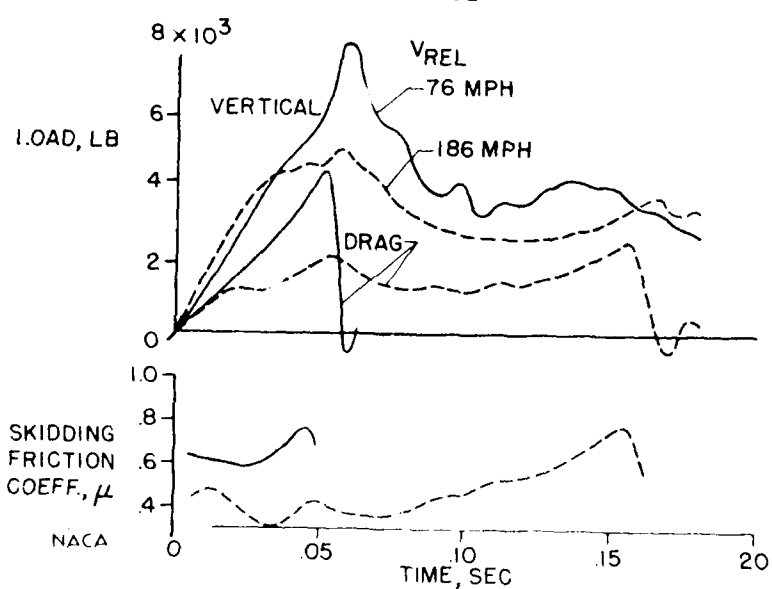
 $V_{V_0} = 7.5 \text{ FPS}$ ;  $V_{\text{CARRIAGE}} = 57 \text{ MPH}$ 

Figure 4.

CONFIDENTIAL

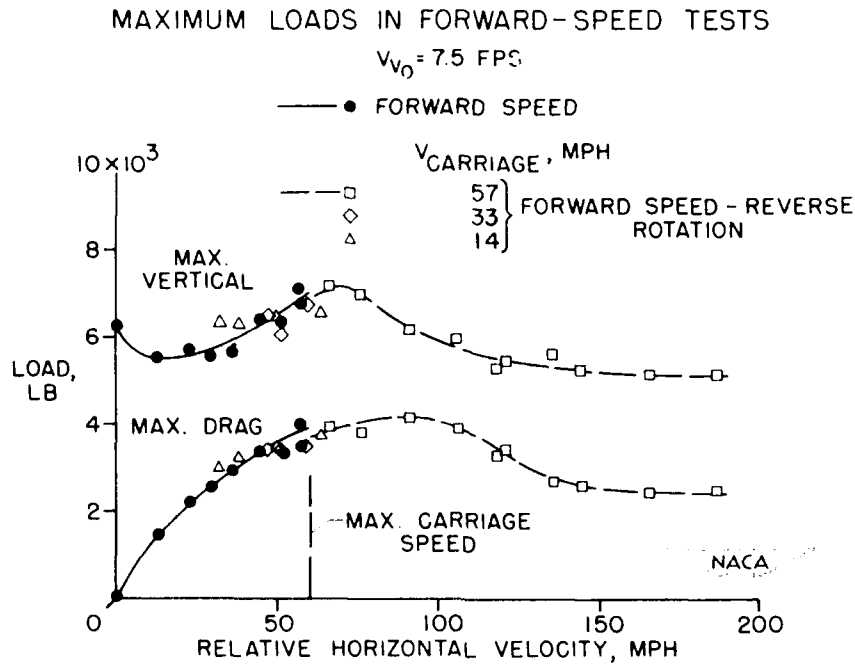


Figure 5.

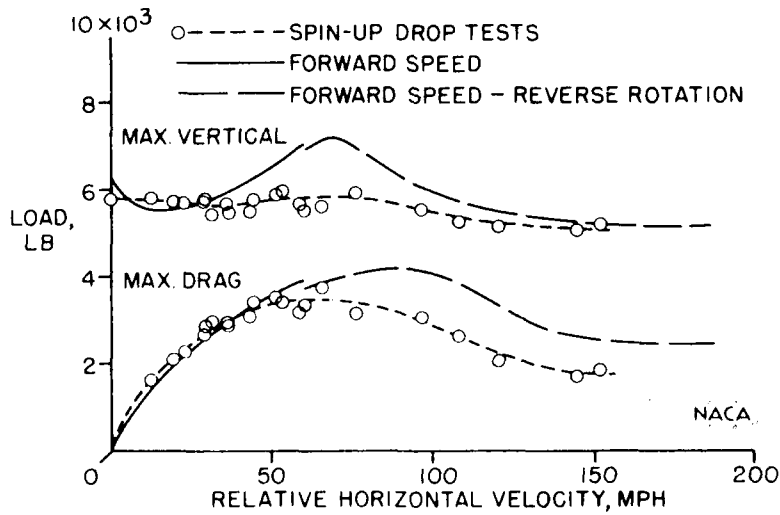
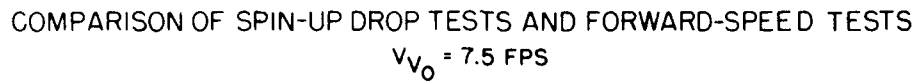


Figure 6.

CONFIDENTIAL

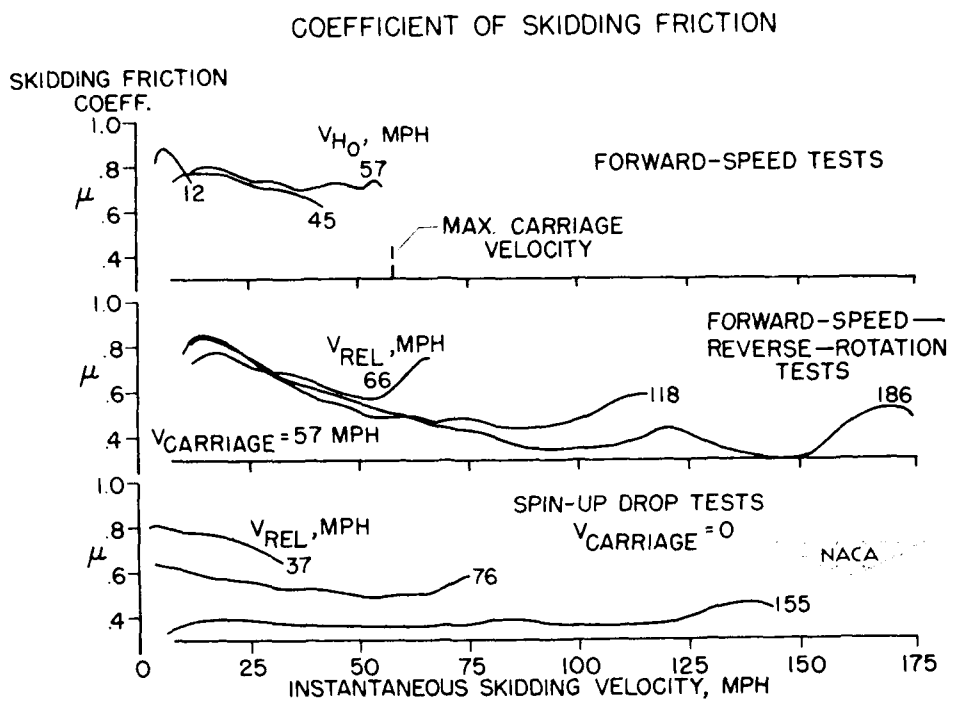


Figure 7.

## FRICTION COEFFICIENT - DIAGRAMMATIC

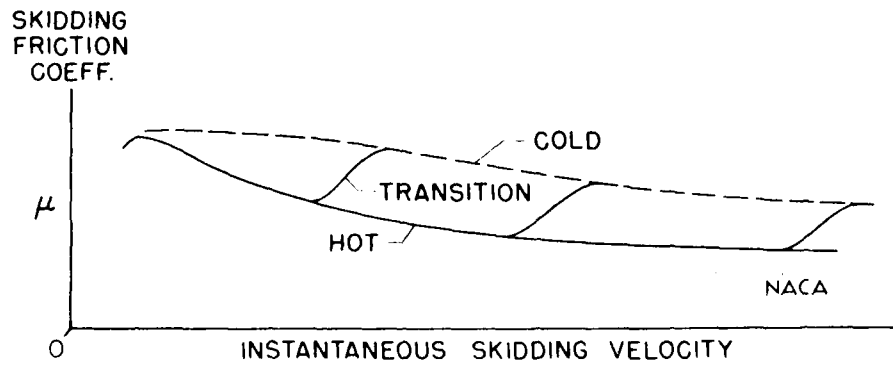


Figure 8.

## EFFECT OF PREROTATION ON LOAD TIME HISTORIES

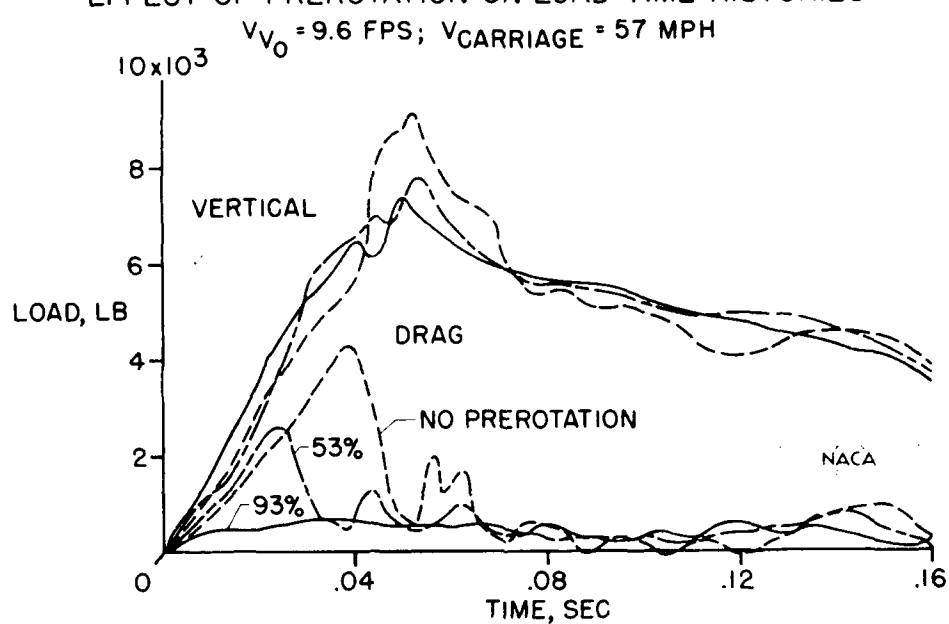


Figure 9.

## EFFECT OF PREROTATION ON MAXIMUM DRAG LOAD

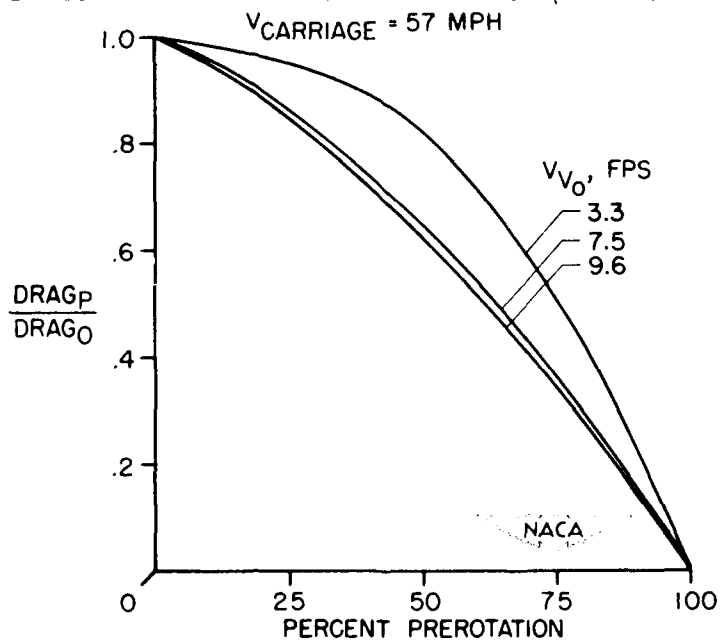


Figure 10

SOME MEASUREMENTS OF STATIC DEFLECTIONS AND YAWED  
ROLLING CHARACTERISTICS OF LARGE TIRES

By Upshur T. Joyner and Walter B. Horne

Langley Aeronautical Laboratory

33

INTRODUCTION

In order to supply information that is needed for the determination of the loads which can be imposed by a tire on a landing gear under conditions of yawed rolling and ground maneuvering and to supply tire constants for use in the study of shimmy, the NACA has undertaken a program which consists of static-deflection tests and yawed-rolling tests of large tires. Although the rolling tests were not made at the high speed of actual operation, the results of both static deflection and rolling tests may, nevertheless, be of interest because most of these data have not previously been available on such large and heavily loaded tires. Comparison is made between theory and experiment for several cases.

STATIC TIRE TESTS

The test setup for the static-deflection tests is shown in figure 1. This figure shows parts of the six-component combined-load testing machine at the Langley Laboratory, in which the static deflection tests were made. Loads and moments in various required combinations were applied to the tire by means of a hydraulically operated loading head appearing at the top of the photograph, to which the tire mounting bracket is attached. The tire rests on a concrete surface which is mounted on the weighing head of the machine and the forces exerted on the concrete surface by the tire are measured on a six-component balance built into this head. The vertical load applied to a single tire by the machine was as much as 90,000 pounds in the case of the largest tire, and other forces and moments were correspondingly large. Deflections were measured by means of the array of scales, dial gages, and protractors shown, and tire pressure was measured by the pressure gage.

Five different tire sizes were used in the static-deflection tests. These are shown in figure 2. These tires are, from the left, as follows:

- (1) A 27-inch, type I (smooth-contour), 10-ply-rating tire
- (2) A 45-inch (15.0-20), type III (low-pressure), 14-ply-rating tire

(3) A 44-inch, type I (smooth-contour), 10-ply-rating tire

(4) A 56-inch ( $56 \times 16$ ), type VII (extra-high-pressure), 24-ply-rating tire

(5) A 56-inch ( $56 \times 16$ ), type VII (extra-high-pressure), 32-ply-rating tire.

All tires were tested over a range of vertical load up to twice the rated static loading and over a range of inflation pressure from well below the rated value to well above this value. For these conditions, the following kinds of information have been obtained:

(1) Vertical tire deflection as a function of vertical load

(2) Change in tire pressure with change in vertical load

(3) Footprint area as a function of vertical tire deflection

(4) Side load and lateral shift of the center of pressure as a function of side tire deflection

(5) Lateral spring constant for different amounts of vertical tire deflection

(6) The variation of torsion moment with angle of yaw about a vertical axis through the center of the wheel.

The complete results of these tests are contained in a paper just now being published by the NACA (reference 1).

Figures 3 and 4 are based on the experimental data given in reference 1 and are shown as examples of the range and consistency of the data presented. Figure 3 shows the variation of side force with side tire deflection for the  $56 \times 16$ , 24-ply rating tire under two vertical loads. Other vertical loads were also used but are omitted here in the interests of figure clarity. Side load was generally carried up to incipient slipping. In the case of the curve for the 60,000-pound load shown, loading was stopped when a severe wrinkle developed in the tire. The arrow points on the curve for the 40,000-pound load indicate the loading and unloading sequence used. An appreciable amount of hysteresis or slippage is apparent and this is true of all tests made. The theoretical curve was calculated for a vertical loading of 50,000 pounds by means of a theory developed by Thorson at Boeing (reference 2). The agreement between theory and experiment in this case is excellent, and this comparison will give added confidence in the theory, which needed confirmation for tires in this range of size and load. In addition to this side-load information, load-deflection measurements were made in

the vertical direction on all tires, and also in the fore-and-aft direction for the 56-inch, 32-ply-rating tire.

Figure 4 shows the variation of moment about the wheel vertical center line as a function of twist angle. Hysteresis is even more pronounced than in figure 3, with a residual angular shift of as much as 6° following loading and unloading. These curves give a measure of the steering moment which would be required to turn the wheel on a standing airplane if this tire were used on a steerable gear.

#### ROLLING TESTS

In the absence of equipment which would be required to make full-scale, full-speed dynamic tests, a towing rig has been improvised (fig. 5). This rig can be loaded to a total weight of 100,000 pounds, and this weight is equally divided between two test tires. These two test tires are yawed in opposite directions to cancel side forces and eliminate the necessity for a restraining track. Side forces and moments are measured by means of strain-gage connections to the truss between the wheels, whereas the drag forces are measured by strain gages in the towing cables.

A closer view is given of one tire under yawed rolling conditions in figure 6. The elevation drawing in the lower part of this figure shows the approximate deflection of the tread center line. The plan view (upper part of figure) shows the rearward offset of the side force or pneumatic caster, under conditions of yawed rolling. The product of the value of this pneumatic caster and the value of the side force gives the value of the moment which tends to align the rolling tire with its direction of motion.

The research program on rolling tires is restricted to one tire size, namely, the 56 × 16, 24-ply-rating tire. At present, tests have been completed with vertical loads of 17,000 and 24,000 pounds, and a few sample results are shown for side force, pneumatic caster, and moment, which were referred to previously. All runs are being made on dry concrete. It is planned to extend the investigation to loadings up to the full rated static load of 50,000 pounds. A range of yaw angles is being investigated, and the vertical deflection is set at the rated value of 32 percent of full tire deflection under each vertical load, as well as at two smaller deflections.

The variation of side or cornering force in yawed rolling as a function of yaw angle is shown in figure 7 for two different vertical loads. The corresponding theoretical curves were calculated from the same theoretical study previously mentioned, and the agreement here is

also good. It remains to be seen how good the agreement will be at the higher loads to be used later.

Figure 8 shows the values of pneumatic caster and their variation with angle of yaw. The data so far obtained do not show any effect of weight on pneumatic caster. However, it should be emphasized that the yawed rolling data presented in these slides are for a small range of vertical load and any general conclusions drawn now would be premature.

The variation of self alining moment with angle of yaw is shown in figure 9. This moment may be considered as the product of the side force and pneumatic caster. However, as mentioned in the description of the tow test rig, the side force and the moment were actually measured and the pneumatic caster was calculated. References in the literature (see digest contained in reference 3) state that this self alining moment should become negative at some large value of yaw angle, but the Langley Laboratory has not measured any negative moments.

#### CONCLUDING REMARK

In summary, the planned static-deflection tests have been completed and a paper is soon to be released on the results by the NACA. The yawed-rolling test program on the 56 x 16, 24-ply-rating tire is continuing and is at present about one third finished. Comparison of the experimental results available at present with theoretical calculations shows good agreement.

#### REFERENCES

1. Horne, Walter B.: Static Force-Deflection Characteristics of Six Aircraft Tires Under Combined Loading. (Prospective NACA paper)
2. Thorson, K. R.: A Rational Method for Predicting Tire Cornering Forces and Lateral Stiffness. Boeing Doc. No. D-11719, Boeing Airplane Co., Mar. 28, 1951.
3. Hadekel, R.: The Mechanical Characteristics of Pneumatic Tyres. S. & T. Memo. No. 5/50, British Ministry of Supply, TPA3/TIB, Mar. 1950.

CONFIDENTIAL

383

TEST SETUP FOR STATIC TIRE TESTS

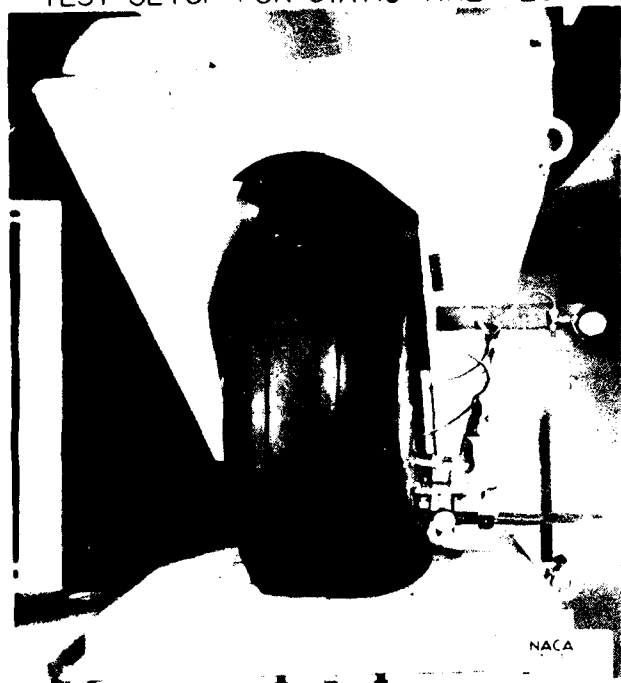


Figure 1.

TIRES USED IN STATIC TESTS



Figure 2.

CONFIDENTIAL

SIDE FORCE FROM STATIC TESTS FOR 56 x 16 TIRE  
TIRE PRESSURE = 160 PSI

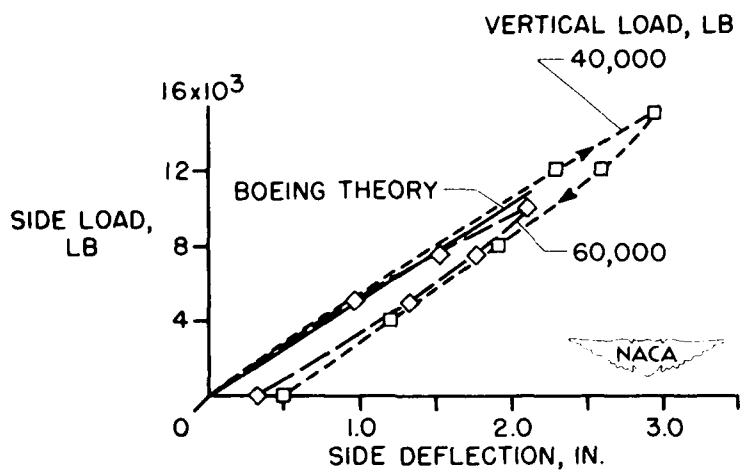


Figure 3.

TORSIONAL STIFFNESS FROM STATIC TESTS  
TIRE PRESSURE = 200 PSI

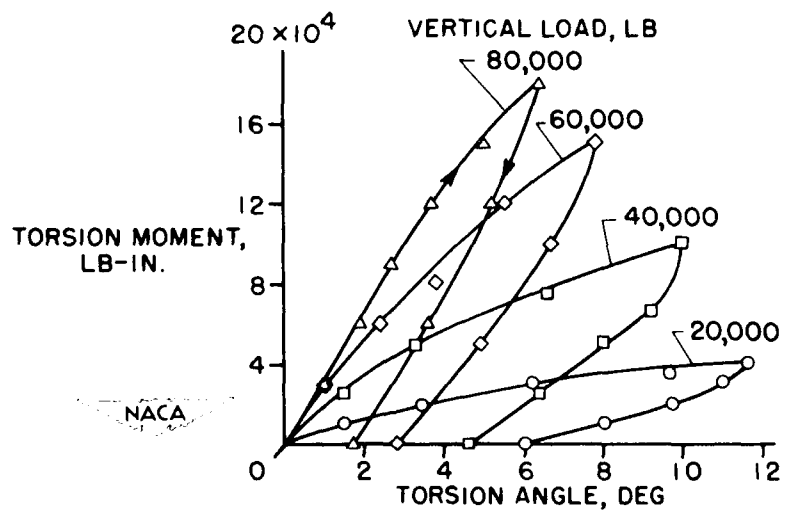


Figure 4.

## SCHEMATIC OF ROLLING-TIRE TEST EQUIPMENT

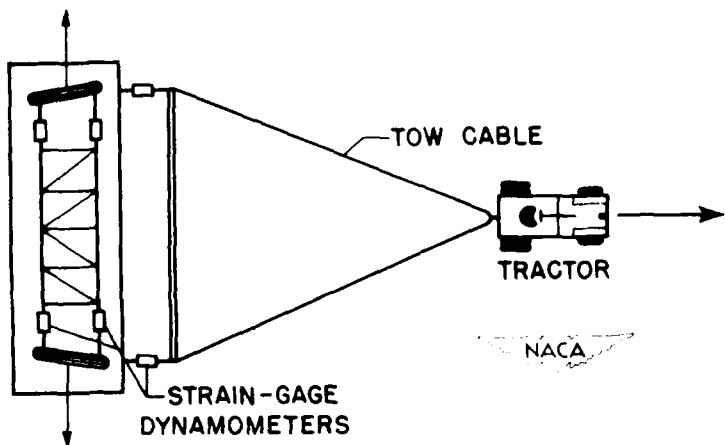


Figure 5.

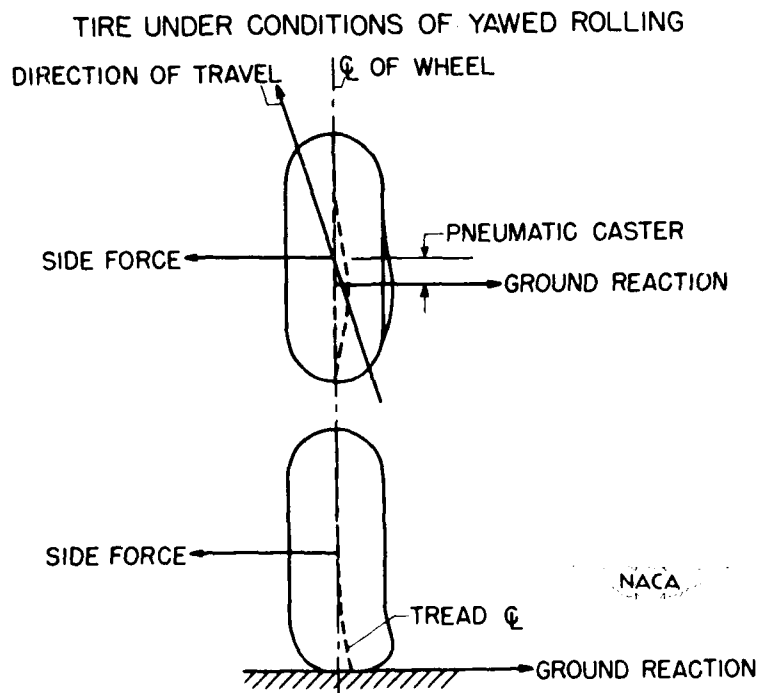


Figure 6.

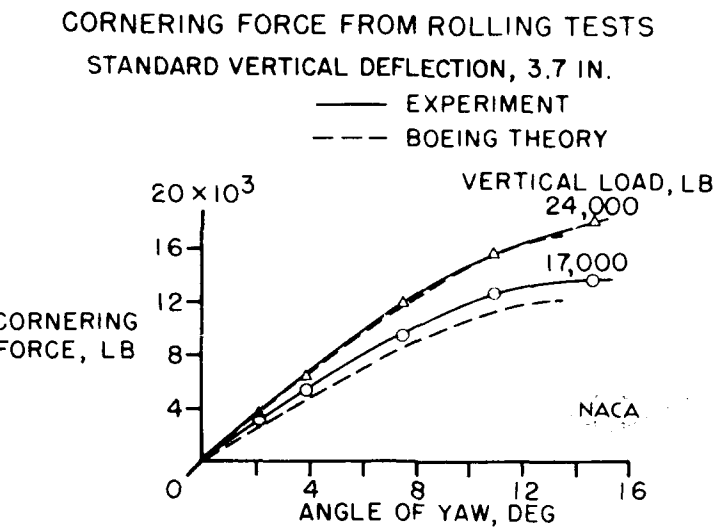


Figure 7.

PNEUMATIC CASTER FROM ROLLING TESTS  
STANDARD VERTICAL DEFLECTION, 3.7 IN.

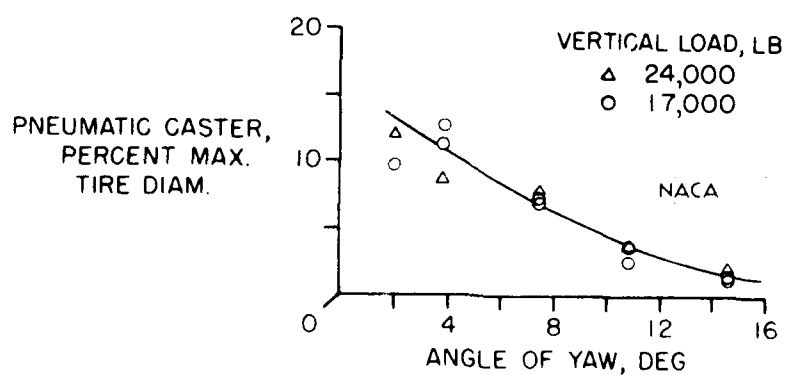


Figure 8.

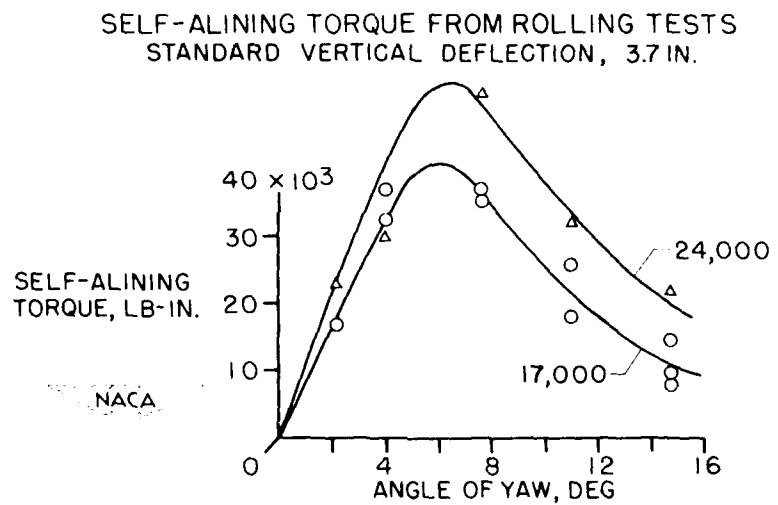


Figure 9.

SOME MEASUREMENTS OF LANDING CONTACT CONDITIONS OF  
TRANSPORT AIRCRAFT IN ROUTINE OPERATIONS

By Norman S. Silsby and Emanuel Rind

Langley Aeronautical Laboratory

One aspect of the problem of rationalizing the requirements and procedures of design for landing loads is that of determining the severity of the landing approach conditions likely to be encountered by an airplane, that is, the magnitudes of sinking speeds, horizontal speeds, attitude angles, angular velocities, lift-weight ratio, and so forth, which may exist at the instant of touchdown and the degree of correlation between these quantities. For the case of aircraft-carrier operations, a substantial amount of statistical information on landing approach conditions has been obtained by the Navy and is being continually augmented. For land-based operations, on the other hand, very little suitable information is available, particularly for modern transport operations.

34

The National Advisory Committee for Aeronautics has recently undertaken the project of measuring landing approach conditions of current transport airplanes during routine operations. A photograph of the equipment used for obtaining this information is shown as figure 1. This equipment consists essentially of a constant-speed motion-picture camera fitted with a telescopic lens of 40-inch focal length, supported on a vertical shaft which provides for tracking only in azimuth. The trailer in which the equipment is mounted can be raised on jacks to permit accurate leveling of the camera and provide a rigid support.

A sample frame from a typical landing sequence is shown in figure 2. The camera is set up at 800 to 1,000 feet from the runway. The actual distance of the airplane from the camera can be determined within 3 or 4 percent from the photographs by measuring the image wheel-rim diameter. The arrangement is such that evaluation of sinking speed, roll attitude, and rolling velocity at touchdown is relatively simple and rapid. Horizontal velocity can also be determined. As shown in this figure, the instant of contact can usually be determined readily by the appearance of smoke from the tire. The spot of light appearing in the center of the frame is produced by instrumentation in the camera to denote azimuth angle and is not due to any installation on the airplane. Pilots are unaware that the landings are being monitored. The relative position of the wheels indicates a large roll angle for this landing, which is discussed subsequently.

The equipment was set up about the middle of January at the Washington National Airport with the permission and cooperation of the

ND-B184 362

NACA CONFERENCE ON AIRCRAFT LOADS FLUTTER AND  
STRUCTURES: A COMPILATION OF PAPERS PRESENTED (U)

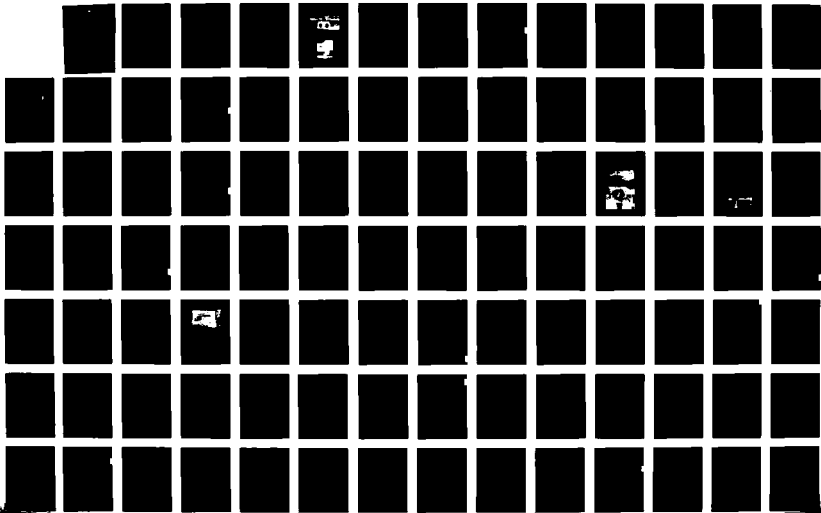
5/6

NATIONAL AERONAUTICS AND SPACE ADMINISTRATION

UNCLASSIFIED

WASHINGTON DC 4 MAR 53 XG-XD

DTIC



airport authorities. Since that time, it has been in operation about 20 hours during which 194 landings were photographed. Of these, 126 were suitable for evaluation. These included measurements for 10 airplanes representing most of the major types in current service: Douglas DC-6, DC-4, and DC-3, Convair 240 and 340, Martin 202 and 404, and Lockheed Lodestar, Constellation, and Super Constellation.

From these measurements, sinking speeds, roll attitude angle, and rolling velocity have been evaluated and a brief statistical analysis of the results has been made. The accuracy in terms of probable error in the quantities determined is the following: for sinking speed,  $\pm 0.1$  to  $\pm 0.2$  ft/sec; for rolling velocity, approximately  $\pm 1/4$  deg/sec; and for roll attitude angle, less than  $\pm 0.1^\circ$ . The number of observations obtained to date is too small to permit isolation of various possible influences such as airplane type, airline policy, wind speed and direction, and so forth. The results should be considered as applying to the general class of transport operations under clear-air, daytime conditions. Wind velocities ranged from calm up to about 20 mph.

Figure 3 gives histograms of the percentage of the landings occurring in various ranges of sinking speeds. The graph on the left shows the sinking speed of the center of gravity for 126 landings, and that on the right, the sinking speed of the wheel touching down first for 108 landings. The histograms for the two cases are generally similar. The mean value of sinking speed of the center of gravity for the landings observed was 1.3 ft/sec and no landing exceeded a sinking speed of 3.2 ft/sec. The mean and maximum values of sinking speeds for the first wheel to touch (1.4 and 3.6 ft/sec, respectively) were slightly higher than for the center of gravity.

Figure 4 shows the same results in terms of the probability of exceeding given values of sinking speed. The left-hand plot again refers to the center of gravity, and the right-hand plot, to the first wheel to touch down. The test points define the cumulative frequency distribution, that is, the percentage of landings in which given values of sinking speed were exceeded. Pearson type III curves shown by the solid lines were fitted to the data to provide an indication of the sinking speed likely to be encountered in greater numbers of landings than were actually observed. The dashed curves indicate the region in which the true probability curve can be expected to occur, regardless of the number of observations, with a confidence of 95 percent. The results for the sinking speed of the center of gravity indicate, for example, that 1 percent of the landings, under the conditions of the observations, will equal or exceed 3.0 ft/sec. A sinking speed of 4.0 ft/sec will probably be equaled or exceeded only once in about 4,000 landings. There appears to be no significant difference between the probability to exceed a given sinking speed of the center of gravity and of the wheel to touch first.

Figure 5 presents histograms of the percentage of landings occurring in various ranges of roll attitude angles shown on the left for 100 landings and in various ranges of rolling velocities shown on the right for 101 landings. The mean value of roll attitude angle was  $1.1^\circ$ , and 87 percent of the landings evaluated for roll angle did not exceed  $2^\circ$ . For 99 percent of the landings the roll angle was less than  $4^\circ$ . One landing of the 100 observed was made at a roll angle of  $5\frac{1}{2}^\circ$  at touchdown.

Figure 1 was from this landing. The positive and negative values of rolling velocity refer to rolling in the direction of the wheel touching first and rolling away from the wheel touching first, respectively. As can be seen from the figure, there were almost twice as many occurrences of rolling in the direction of the wheel touching first as there were of rolling away from the wheel to touch first. The mean value of rolling velocities was 0.5 deg/sec and no rolling velocity exceeded 3 deg/sec. The low rolling velocities obtained account for the small differences between sinking speeds of the center of gravity and of the wheel to touch first.

Figure 6 shows the results of roll attitude angle and rolling velocity in terms of the probability of exceeding given values of the roll attitude angle shown on the left and rolling velocity shown on the right. The plotted points again define the cumulative frequency distribution, the solid lines are Pearson type III curves, and the dashed lines indicate the 95-percent confidence band. The graph on the left indicates that one roll angle in 100 landings would probably equal or exceed  $4.3^\circ$ , and out of 1,000 landings one would probably equal or exceed about  $6.2^\circ$ . The analysis indicated that there was no correlation between roll attitude and sinking speed, nor between rolling velocity and sinking speed. The limitation of roll angle imposed by some part of the airplane other than the landing gear contacting the ground first is from  $8^\circ$  to  $16^\circ$  for four-engine transport airplanes and from  $17^\circ$  to  $21^\circ$  for twin-engine transport airplanes. The results for the rolling velocity indicate that 1 percent of the landings would be expected to equal or exceed 3.3 deg/sec when rolling toward the wheel touching first and about 2.3 deg/sec when rolling away from the wheel touching first. One in 1,000 landings would probably equal or exceed about 4.2 deg/sec or 3.3 deg/sec when rolling toward or away from the wheel touching first, respectively.

In conclusion, the analysis of the results obtained to date on the landing contact conditions of routine transport operation indicate that sinking speeds of about  $3\frac{1}{3}$  and 4 ft/sec will occur once in 1,000 landings.

This applies for the center of gravity of the airplane or the first wheel to touch. For the same number of landings, rolling velocities of as much as 4 to  $4\frac{1}{2}$  deg/sec and roll attitude angles of as much as  $6^\circ$  to  $6\frac{1}{2}^\circ$  may be expected.

**CONFIDENTIAL**

The equipment and technique employed for these measurements have been found to be accurate and practical, at least for daytime operations. Continued operation of the project, in which horizontal velocities will also be determined, is expected to yield information on the influence of various factors such as airplane characteristics, landing technique, and weather conditions.

**CONFIDENTIAL**

## EQUIPMENT FOR MEASURING LANDING APPROACH CONDITIONS

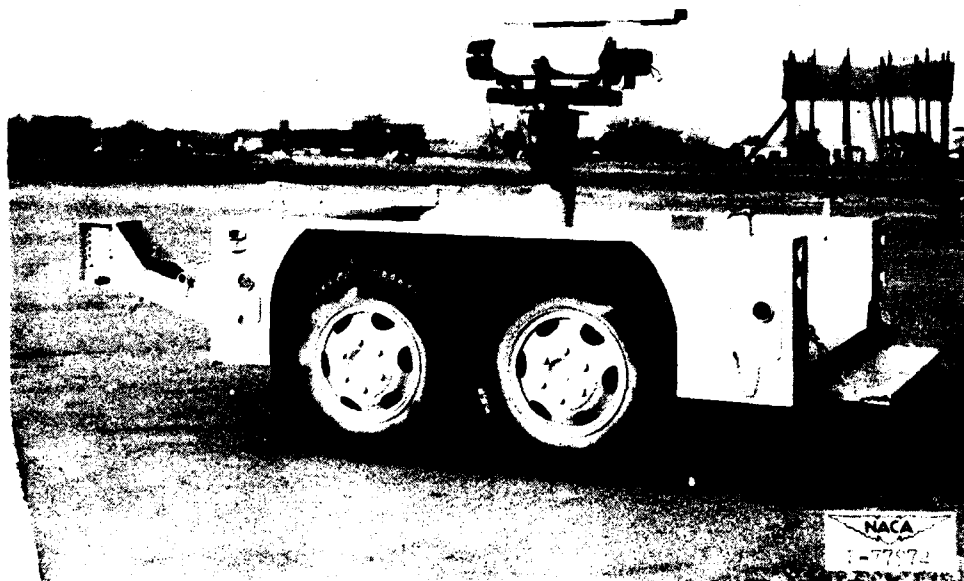


Figure 1.

SAMPLE FRAME FROM A LANDING SEQUENCE SHOWING SMOKE PUFF AT TIRE CONTACT



Figure 2.

CONFIDENTIAL

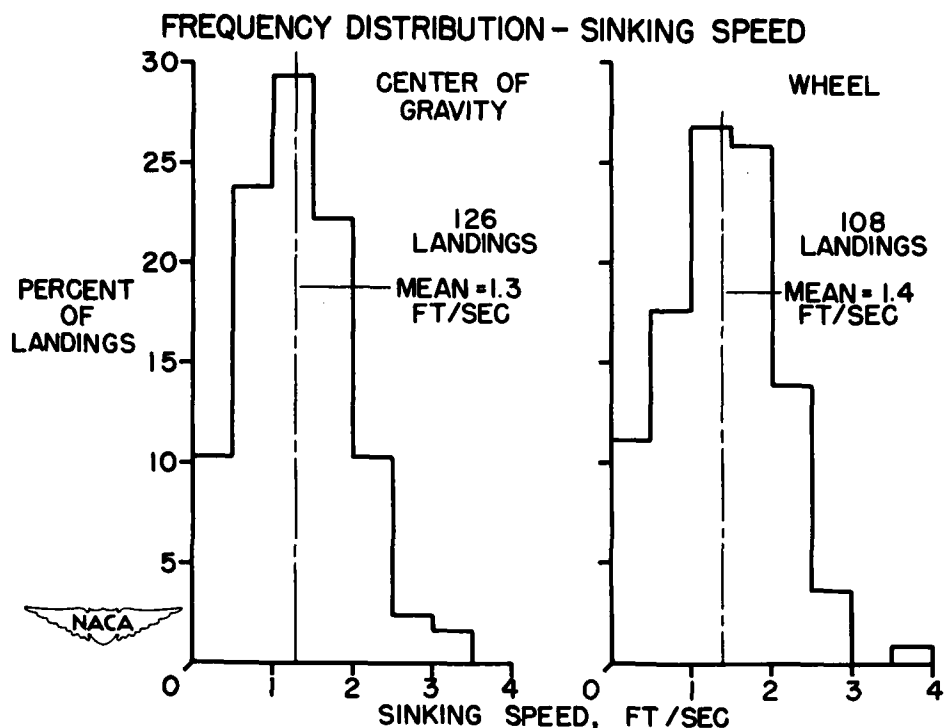


Figure 3.

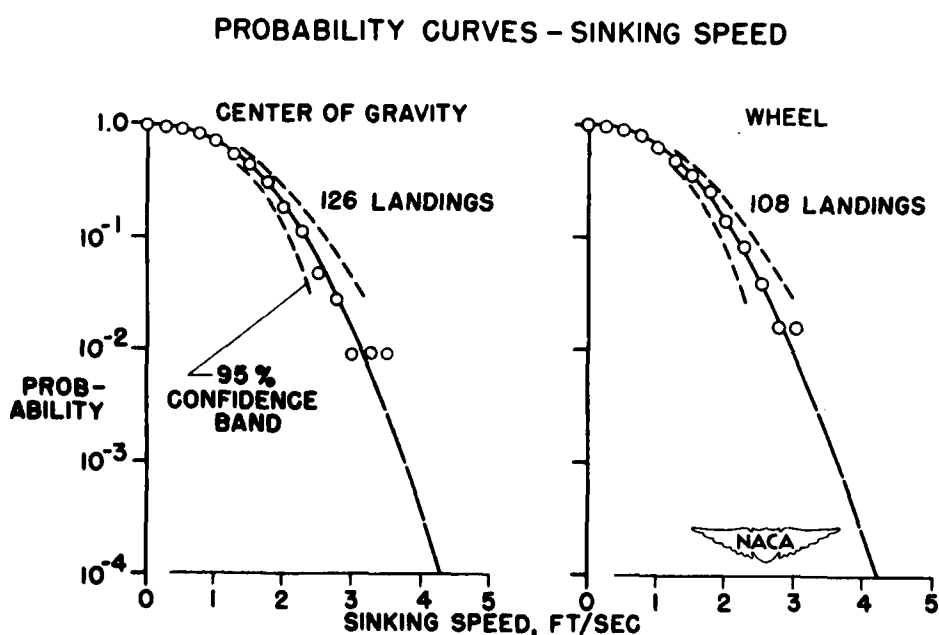


Figure 4.

CONFIDENTIAL

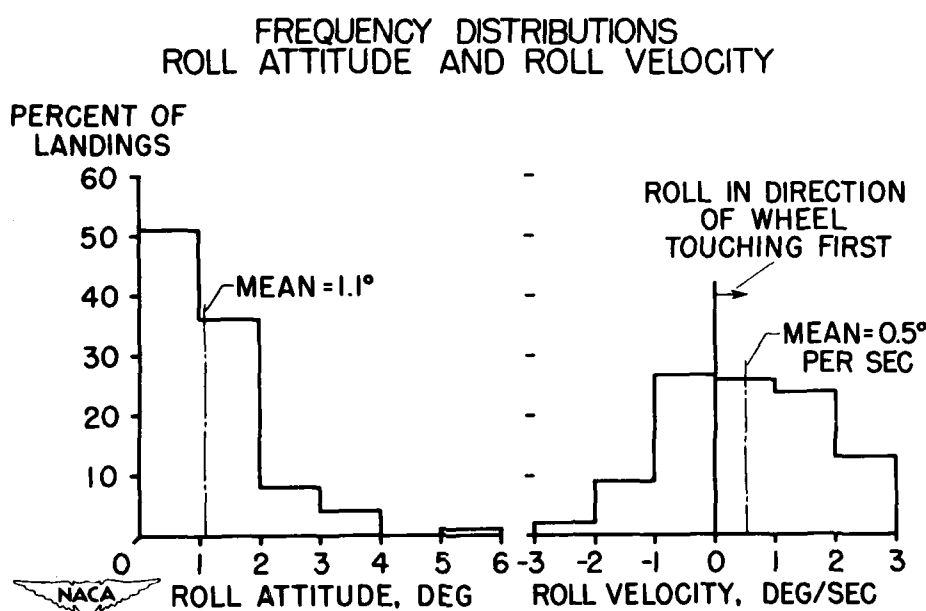


Figure 5.

## PROBABILITIES—ROLL ATTITUDE AND ROLL VELOCITY

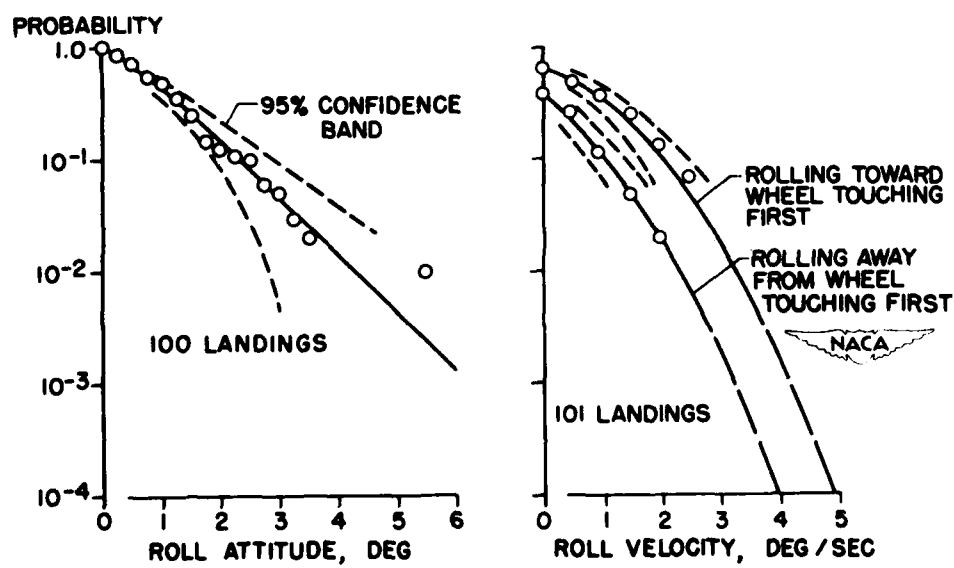


Figure 6.

A STUDY OF THE EFFECTS OF INTERACTION BETWEEN A NONLINEAR  
LANDING GEAR AND A FLEXIBLE AIRFRAME DURING LANDING IMPACT

By Francis E. Cook and Benjamin Milwitzky

Langley Aeronautical Laboratory

INTRODUCTION

In the design of airplanes for landing it is usually assumed that the flexibility of the airframe has little or no effect on the behavior of the landing gear. Thus, landing-gear characteristics are often developed by means of drop tests in a jig with a concentrated dropping mass. Also, landing-gear load time histories obtained on a rigid-body basis are frequently used as the forcing function in making a dynamic analysis to determine the loads and stresses in flexible airplane structures. Such procedures are conservative since the interaction between the deformations of the airplane structure and the landing gear should produce some alleviation in the applied landing-gear force. This paper presents an analysis of this interaction effect for the case of a conventional nonlinear oleo-pneumatic landing gear coupled with a flexible structure.

Whereas the conventional oleo-pneumatic landing gear involves air-compression springing in the tire and in the shock strut and turbulent or velocity-square damping, previous studies of this interaction problem (refs. 1 to 5) limited their consideration to idealized linear-spring landing gears with either no damping at all or viscous damping. It was felt that the velocity-square damping, in particular, might lead to larger reductions in the applied landing-gear load than was indicated by the previous studies because of the fact that the decreased shock-strut telescoping velocities permitted by the deflections of the flexible structure result in smaller shock-strut hydraulic resistance in the case of velocity-square damping. The present brief study was therefore undertaken to investigate the effect of interaction of landing gear and flexible structure with more realistic representation of the landing gear.

35

ANALYSIS

An analysis of the conventional oleo-pneumatic landing gear attached to a rigid mass is given in reference 6. The system considered is shown by the blocked-in area in figure 1. This treatment, which considers the velocity-square damping of the metering orifice, air compression springing

in the shock strut, and the nonlinear force-deflection characteristics of the tire, was shown to give good agreement with experimental results. In the present investigation the dynamical system has been augmented by an additional degree of freedom, representing a fundamental deflection mode of the wing. The more complex distributed system of the actual airplane in its fundamental mode, as shown on the left of figure 1, can be represented by the equivalent lumped system shown on the right.

The total motions of the main masses are made up of a rigid-body translation and an oscillation in the fundamental mode relative to the nodal point. The mass  $m_1$  represents the effective mass which acts directly on the landing gear;  $m_2$  is the unsprung mass below the shock strut. The remainder of the airplane mass is represented by  $m_3$ , which can be considered to be spring connected to  $m_1$ . The spring constant  $k$  is determined to give the same natural frequency as in the fundamental mode considered.

The sum of the three masses equals half the total airplane mass. The relative proportions of the main masses, as expressed by the mass ratio  $m_3/m_1$ , are determined by the airplane mass distribution, stiffness distribution, and landing-gear location. The equation for the mass ratio is

$$\frac{m_3}{m_1} = \frac{m_1 + m_3}{\sum M_j \phi_j^2} \phi_{LG}^2 \quad (1)$$

where

$M_j$  mass at any station  $j$

$\phi_j$  deflection of station  $j$  in the mode, relative to the nodal point

$\phi_{LG}$  deflection of landing-gear station

The spring constant  $k$  is given by

$$k = \frac{m_1 m_3}{m_1 + m_3} \omega_n^2 \quad (2)$$

where

$\omega_n$  circular frequency in fundamental mode

It can be seen from equation (1) that, for any given mass and stiffness distribution, the mass ratio depends on the deflection of the landing-gear station relative to the nodal point. If the landing gear is located at the nodal point,  $\phi_{LG} = 0$ . Thus, the mass ratio is zero and the airplane is a rigid body as far as the fundamental mode is concerned. For any given airplane the farther away the landing gear is from the nodal point, the larger is  $\phi_{LG}$  and the greater is the mass ratio. Everything else being equal, airplanes with landing gears in the fuselage should have higher mass ratios than similar airplanes with landing gears in the more conventional location in the inboard nacelles.

An examination of a number of existing airplanes shows that the mass ratio can vary between almost 0 and about 0.4 to 0.5. If the trend toward moving large masses outboard and moving the landing gear inboard continues, airplanes of the future might be expected to have considerably higher mass ratios than exist at present.

#### RESULTS AND DISCUSSION

In order to illustrate the effects of interaction, several typical case-history studies will be presented for a range of mass ratios and two airplane natural frequencies. All calculations to be presented are for an initial vertical impact velocity of 10 feet per second.

In the first of the two cases to be discussed the mass and flexibility characteristics considered are the same as those of a World War II four-engine bomber having a normal gross weight of about 65,000 pounds. This airplane will be referred to as airplane I. The natural frequency of the fundamental bending-torsion mode of airplane I is 3.4 cycles per second. The characteristics of the actual airplane landing gear were used in the calculations. Figure 2 shows time histories of the applied landing-gear force for mass ratios of 0, 0.23, and 0.5. The mass ratio of 0 applies to the case of the airplane considered as a rigid body. The actual airplane had a mass ratio nearly equal to 0 since the landing-gear location, which was in the inboard nacelle, coincided very closely with the nodal point of the first bending-torsion mode. The mass ratio 0.23 would be obtained if the landing gear had been located in the fuselage. The mass ratio 0.5 would apply if the landing gear had been located in an outboard position between the inboard and outboard nacelles.

As can be seen from figure 2, the greatest landing-gear force is obtained for  $m_3/m_1 = 0$ , that is, for the airplane considered as a rigid body. As a result of the interaction between the flexible structure and

the landing gear, the mass ratio of 0.23 gives a 5-percent reduction in the maximum landing-gear load. For the mass ratio 0.5, the maximum landing-gear load is reduced by 11 percent.

Similar calculations have been made for a configuration representative of a modern multijet bomber equipped with a bicycle landing gear and having a gross weight of 125,000 pounds and a natural frequency of 1.4 cycles per second in the fundamental bending torsion mode. This airplane will be referred to as airplane II. With the landing gear in its normal location in the fuselage, the mass ratio of airplane II is 0.21. In figure 3 the load time history for this mass ratio is compared with that which would be obtained if the airplane were a rigid body, that is, a mass ratio of 0. As can be seen, the interaction of the structural flexibility with the landing gear reduces the maximum applied load by about 9 percent. In order to study the effect of increased mass ratio, the landing gear was assumed to be located about halfway out on the wing, giving a mass ratio of 0.79. For this case interaction reduces the applied load by about 25 percent.

Figure 4 summarizes the alleviating effects of interaction on the maximum applied landing-gear load. The ordinate is the ratio of the maximum landing-gear load with interaction to the maximum load for the airplane considered as a rigid body. The abscissa is the mass ratio. The calculations have been extended to include mass ratios considerably higher than those known to be applicable to present airplanes in order to show how interaction might affect the applied loads for unconventional configurations or possible future airplanes. The reduction in applied load due to interaction is particularly evident at the higher mass ratios and at the lower natural frequency typical of the more flexible modern airplanes.

Next, consider how the results of a dynamic analysis might be affected by neglecting the alleviation in the applied landing-gear load produced by interaction. The calculated bending moments in the wing root of airplane I will be used as an example. In figures 5 and 6 root bending moments which were calculated for the coupled system, that is, with interaction between flexible structure and landing gear, are compared with the root bending moments determined by computing the dynamic response of the structure to the rigid-body forcing function under the assumption of no interaction. The small sketch on the right of figure 5 shows the system for the response calculation. The solid-line curves are the interaction calculations, the dashed-line curves are the calculated response to the rigid-body forcing function. The curves start out at the steady-flight bending-moment value which exists at the instant of initial contact. The differences in these curves are due to differences in the maximum applied load as well as differences in the shape of the applied-load time history.

The results shown in figure 5 are for a mass ratio of 0.23 which, in the case of this airplane, applies when the landing gear is at the fuselage. It can be seen that the maximum negative bending moment from the response calculations is about 7.5 percent larger than the value computed for the coupled system. Figure 6 shows a similar comparison for the higher mass ratio of 0.5. For the airplane considered this mass ratio would be obtained with the landing gear in an outboard position between the nacelles. In this case, the moments determined by calculating the response to the rigid-body forcing function are about 5 percent too large.

#### SUMMARY OF RESULTS

In summary, several case histories which have been investigated indicate that interaction between the landing gear and the flexible structure has a relieving effect on the applied landing-gear load and confirm earlier studies of this problem with regard to order of magnitude. It is also shown that the use of the rigid-body forcing function to calculate the response of the structure in a dynamic analysis under the assumption of no interaction gives conservative results. For the mass ratios typical of most present-day airplanes, neglect of interaction leads to relatively small errors. However, it appears that if configurations having higher mass ratios and low natural frequencies are developed, consideration of interaction may become important in order to avoid overconservatism.

## REFERENCES

1. Fairthorne, R. A.: The Effects of Landing Shock on Wing and Under-carriage Deflexion. R. & M. No. 1877, British A.R.C., 1939.
2. Stowell, Elbridge Z., Houbolt, John C., and Batdorf, S. B.: An Evaluation of Some Approximate Methods of Computing Landing Stresses in Aircraft. NACA TN 1584, 1948.
3. McPherson, Albert E., Evans, J., Jr., and Levy, Samuel: Influence of Wing Flexibility on Force-Time Relation in Shock Strut Following Vertical Landing Impact. NACA TN 1995, 1949.
4. Pian, T. H. H., and Flomenhoft, H. I.: Analysis and Experimental Studies on Dynamic Loads in Airplane Structures During Landing. Jour. Aero. Sci., vol. 17, no. 12, Dec. 1950, pp. 765-774, 786.
5. O'Brien, T. F., and Pian, T. H. H.: Effect of Structural Flexibility on Aircraft Loading. Part 1. Ground-Loads. AF Tech. Rep. No. 6358, pt. 1, WADC, U. S. Air Force, M.I.T., July 1951.
6. Milwitzky, Benjamin, and Cook, Francis E.: Analysis of Landing-Gear Behavior. NACA TN 2755, 1952.

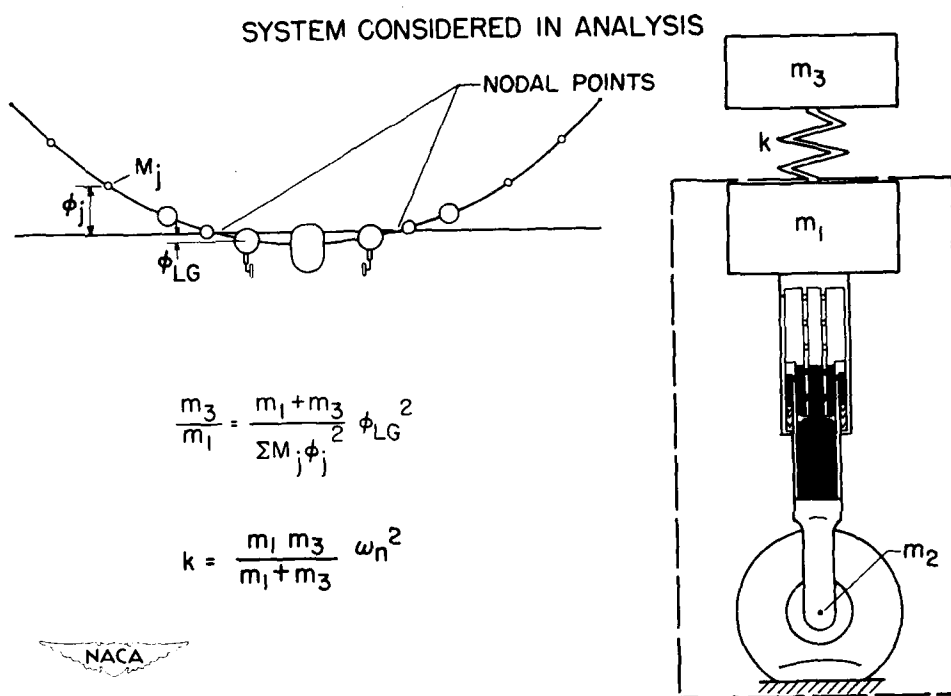


Figure 1.

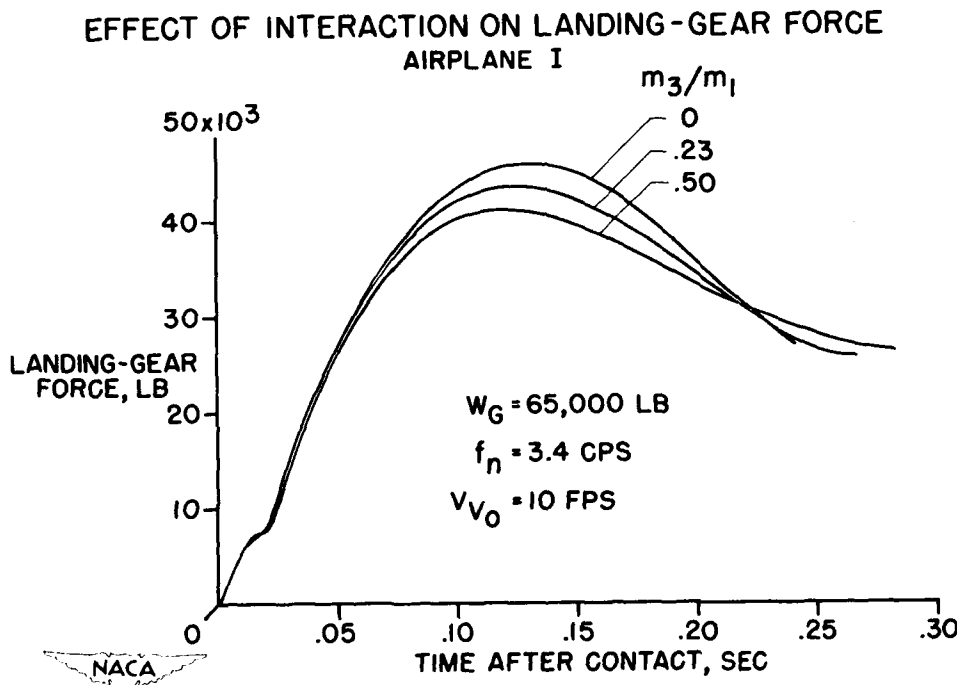


Figure 2.

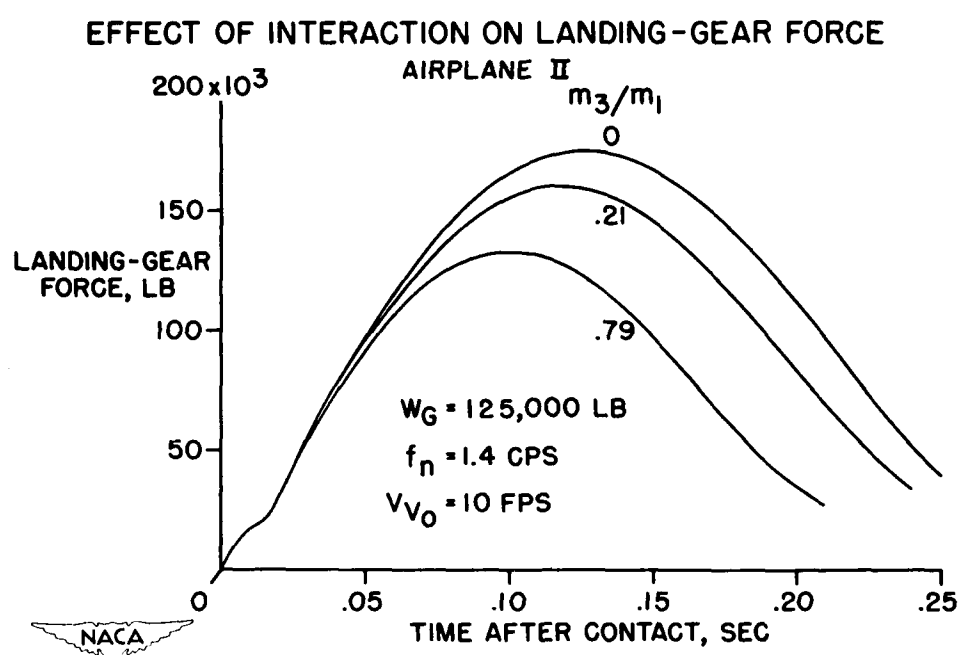


Figure 3.

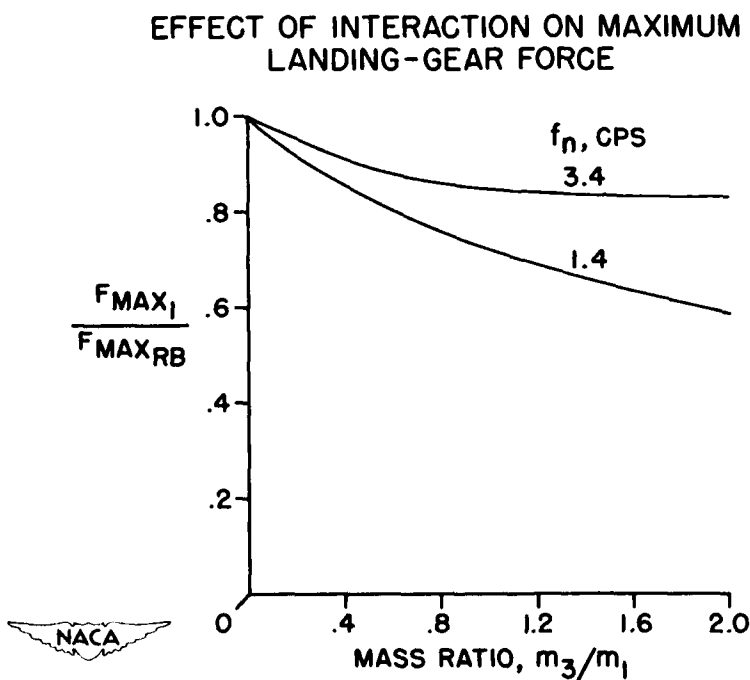


Figure 4.

## COMPARISON OF BENDING-MOMENT CALCULATIONS

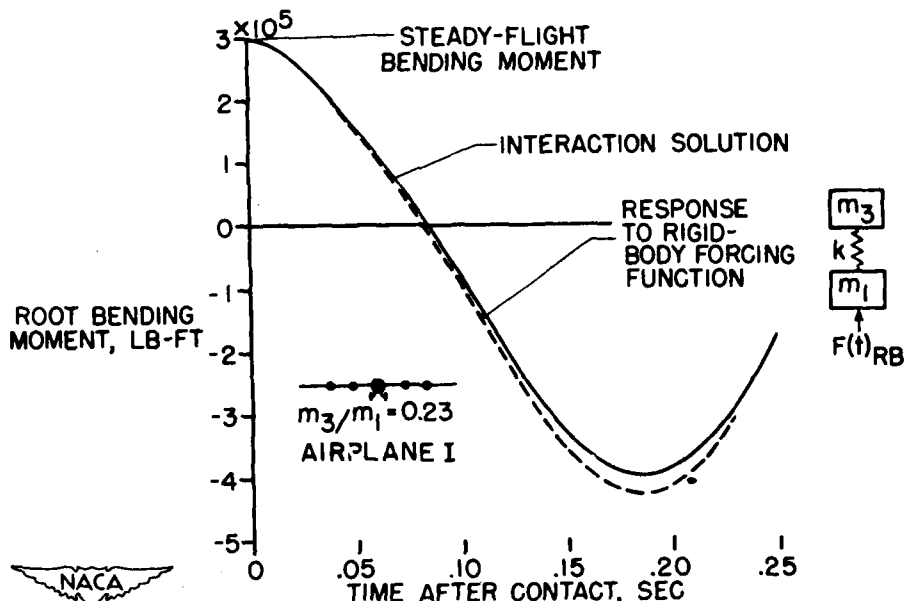


Figure 5.

## COMPARISON OF BENDING-MOMENT CALCULATIONS

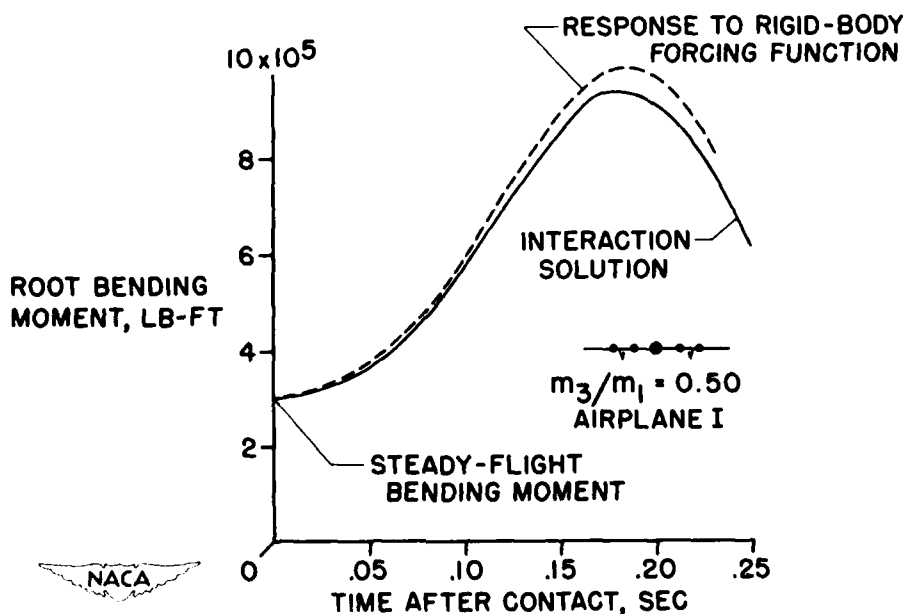


Figure 6.

## ESTIMATION OF WATER LANDING LOADS ON HYDRO-SKI EQUIPPED AIRCRAFT

By Emanuel Schnitzer

Langley Aeronautical Laboratory

Load investigations on hydro-skis have been going on for some time at the Langley Aeronautical Laboratory and it is the purpose of this paper to present the status of this research. Although hydro-ski equipped aircraft may be operated from snow, ice, or sod in addition to water, this discussion will be restricted to water operations and, more specifically, to the loads encountered in these operations. The problem of hydrodynamic behavior pertinent to water operations is treated in references 1 to 9 and will not be considered here.

The problem considered in this paper may be stated as follows: For specified ranges of initial landing velocity, attitude, and ski geometry, what are the loads and their distributions during impact? The results of the work on this problem will be presented in the following order. First, theoretical methods for computing hydro-ski landing loads will be touched on and their results compared with experimental data. Then the effect of chine immersion in reducing hydro-ski impact loads will be reviewed. Next, the use of shock-strut mountings for further reduction of hydro-ski loads will be discussed, and, finally, hydro-ski pressure distributions calculated by a recently developed method will be compared with experimentally obtained pressures on flat and V-bottom rectangular skis.

Some of the nomenclature and the pertinent parameters used in the following discussion of the basic load theory are shown in figures 1 and 2. Figure 1 pictures a hydro-ski equipped aircraft in the landing condition, while figure 2 illustrates some of the many shapes which actual ski configurations may assume. The plan forms shown in figure 2 include the rectangular, V-step, and triangular shapes. The cross sections shown, some of which have been enlarged for clarity, include flat and V-bottom skis of several dead-rise angles and having flared and vertical chines, and also curved bottom shapes.

In order to begin the discussion of the basic load theory, consider the aircraft of figure 1, which is landing with the resultant velocity  $V_R$ . The component of this velocity normal to the ski bottom is designated  $V_N$ . Since viscous forces along the ski are usually very small during impact, the resultant hydrodynamic force is directed normal to the ski bottom and is designated  $F_N$ . For practical impacts of such narrow, heavily loaded bodies, it can be shown that, for a given ski, this normal force at any instant is a function principally of the wetted length  $l_w$ , the

trim  $\tau$ , and the normal velocity  $V_N$ . Consequently, the force on the impacting ski shown in figure 1 is the same as the force on this same ski in the planing condition, for identical values of wetted length, trim, and normal velocity. The problem is thus simplified in that it now becomes similar to that of a wing in steady flight for which the force at any instant is determined by the downwash momentum. Substitution of the relation between this force and the wetted length into the classical equation of motion results in a differential equation which can be integrated to yield impact load time histories.

Two methods have been developed at the National Advisory Committee for Aeronautics for estimating the downwash momentum for hydro-skis having negligible longitudinal bottom curvature. One, which is termed the deflected-mass theory, involves the computation of this downwash momentum, while the other, which is termed the planing-data theory, involves the determination of this momentum from planing data obtained with the ski model in question. The deflected-mass theory (ref. 10), which is simple to apply, is at present restricted to skis of rectangular plan form, whereas the planing-data theory (ref. 11), although involving additional work, is more general and may be extended to skis of varied plan form and cross section.

The deflected-mass theory has been substantiated in comparisons with experimental data from references 12 to 14 covering wide ranges of trim, dead-rise angle, flight-path angle, and ski loading. Examples of the agreement between this theory and experimental data are shown in figures 3 and 4. The variation of impact load factor with time after contact during a typical landing of a rectangular flat-plate hydro-ski is given in figure 3, while figure 4 gives the load-factor variation for a typical landing of a rectangular V-bottom hydro-ski. The loads on the two figures should not be compared since the landing speed is greater for figure 4 than for figure 3. The agreement shown between theory and experiment, however, indicates that the deflected-mass theory may be used with reasonable accuracy to predict loads on relatively straight-sided, rectangular hydro-skis and to determine trends with ski geometry and fuselage weight over the practical range of hydro-ski landing conditions. Although the loads predicted by the planing-data theory have been checked with only limited data, the results of the checks, in addition to theoretical considerations, indicate that this theory should be equally valid over this range.

In order to test the applicability of the more general planing-data theory for plan forms other than rectangular, comparisons were made of load time histories calculated by this theory with impact data for a flat-bottom, V-step hydro-ski (ref. 15). A typical impact is illustrated in figure 5, in which the solid line is the theory for the V-step ski and the circles are the corresponding experimental data. The quality of the

agreement shown indicates that the planing-data theory can also be used with reasonable accuracy to predict loads on skis of nonrectangular plan form. The dashed line is included as a matter of interest to show the difference between the theoretical force curves for a rectangular and a V-step ski, for identical landing conditions.

Since the planing-data theory shows promise for calculation of loads on hydro-skis of varied plan form, extensive high-speed experimental planing data collected in towing tanks have been made available in references 16 to 23 for use in practical hydro-ski landing calculations. The planing data were collected with the series of hydro-ski models shown in figure 2 for wide ranges of wetted length and trim. The effects of plan form and bottom cross-sectional shapes on impact characteristics may be determined by substituting these data into the planing-data theory for the desired cases.

At this point, it might be of interest to discuss the load-reducing quality of the hydro-ski with the aid of figure 6. This figure shows the variation of maximum load with flight-path angle at water contact for V-bottom models having angles of dead rise of  $30^{\circ}$ . The circles represent data collected in high-trim experimental landings of a heavily loaded hydro-ski (ref. 13). The upper dashed line represents the wide-float seaplane theory of references 24 and 25, which are based on Wagner's expanding-plate solution (refs. 26 and 27) and assume no immersion of the float side or chines. The error which would be introduced through the use of this theory for computing loads on narrow hydro-skis is illustrated by the separation between the dashed line and the data points. The solid line, which was computed from the deflected-mass theory, follows the wide-float theory until the flight-path angle is reached above which chine immersion occurs (roughly  $2^{\circ}$  for this case). At this point the wetted width ceases to expand, which results in a slower build-up of downwash momentum, allowing deeper penetrations with consequent reduction of load. This line agrees fairly well with the experimental data. The beneficial effect of chine immersion on loads for narrow, heavily loaded hydro-skis is thus indicated for single impacts. This effect was also demonstrated in actual multiple-impact landing tests made at the towing tanks with free-flying models. In these tests, which are described in references 5 and 7, the load reduction appeared to result from two separate causes. First, the narrow skis penetrated the water to considerable drafts, allowing a large vertical travel for absorption of sinking-speed energy and for knifing through waves, and, second, the hydro-ski equipped aircraft exhibited improved hydrodynamic behavior inasmuch as vertical and pitching oscillations in rough water were reduced, with a consequent reduction in the amplitude and severity of successive bounces in a landing run.

A further means for reduction of water landing loads which has been considered is that of mounting hydro-skis on shock struts. The essential

principle of operation of the shock-mounted hydro-ski is that the shock strut permits a greater vertical travel of the aircraft than the rigidly mounted ski does. This greater travel over which the vertical momentum can be dissipated results in a smaller hydrodynamic force. The shock strut has the additional desirable feature of reducing rebound velocity, thereby minimizing the tendency of the initial conditions of subsequent impacts to be more severe than the conditions of the first impact in a landing run.

There are three basic methods for mounting hydro-skis on shock struts, examples of which are illustrated in figure 7. One method, shown at the upper left, consists of mounting the hydro-ski so that its trim relative to the aircraft is constant, with the shock strut acting as in a conventional landing-gear arrangement. A second method, shown at the upper right, consists of mounting the hydro-ski so that it may trim relative to the aircraft, with the shock strut resisting the trimming motion. The latter type of shock-mounted hydro-ski has been employed in a current design. A third method, shown at the bottom, consists of using variable-dead-rise skis with hinged sides and employing shock struts that resist upward flapping of these sides.

The method developed for computing loads and motions during hydro-ski impacts has been adapted to impact calculations for the fixed-trim type of shock-mounted hydro-ski. The result of a sample computation is illustrated in figure 8, which provides an estimate of the amount of load reduction that might be provided by the fixed-trim type of shock mounting. This example represents a typical high-speed landing of a 16,000-pound aircraft equipped with twin flat-bottomed rectangular hydro-skis, 2 feet wide. The upper line in the plot represents the rigid case and the lower line represents the shock-mounted case, both for the same ski. The load reduction achieved by the shock strut for this case was 35 percent, while the vertical rebound velocity, not shown here, was reduced by 50 percent. Some experimental checks of this analytical approach are contemplated upon completion of landing tests now being conducted at the towing tanks with free-flying scale models.

The decrease in landing loads achieved by means of shock struts can also be realized through the use of narrower skis. Such skis would, however, exhibit increased drag during the take-off run. The designer may therefore sacrifice part of the inherent landing-load-reducing quality of the narrower ski for an increase of take-off lift-drag ratio by using a wider ski mounted on a shock strut.

The water-pressure distribution on an impacting hydro-ski, which is of interest for ski design and for obtaining the variation of pitching moment on an aircraft during landing, will now be considered. A method

has been advanced for estimating the instantaneous pressure distribution on straight-sided rectangular hydro-skis during water impact (ref. 28). This method is based on the observation that the pressure distribution along the longitudinal center line of a rectangular flat-bottomed ski depends only on the normal-force coefficient. On this basis, the longitudinal-center-line pressure distribution for an immersing ski at a given trim may be obtained from the classical two-dimensional pressure distribution (ref. 29) for an infinitely wide planing plate at the trim for which the normal-force coefficient is the same as that of the ski.

To illustrate the accuracy of this procedure, figure 9 presents comparisons of the pressure estimation procedure with experimental data for flat and V-bottom rectangular hydro-skis (refs. 12 and 30), respectively. The relative pressures on the two skis should not be compared, since the landing velocity of the V-bottom ski was greater than for the flat-plate ski. The computed longitudinal-center-line distributions were obtained by the method mentioned, while the computed transverse distributions were obtained from modifications of classical two-dimensional wide- and narrow-body theories (refs. 31 and 32). These comparisons demonstrate that the pressure-estimation procedure may be used with reasonable accuracy to evaluate the effects of aspect ratio on hydro-ski pressure distributions during impact. The effect of a wheel well and a pulled-up bow on hydro-ski pressure distribution are shown in reference 33.

In summarizing, two approaches have been developed to the problem of calculating hydro-ski landing loads. Both are based on evaluation of downwash momentum; one makes use of a computed downwash momentum and applies to flat and V-bottom skis of rectangular plan form, while the other makes use of planing data and applies to skis of varied cross section and plan form. An adaptation of this approach has been used for investigating the effect of shock-strut mounting on hydro-ski landing loads, and results indicate that substantial load reductions may be achieved by means of such mountings. A procedure for estimating hydro-ski pressure distributions has been devised which is applicable, over a wide range of wetted aspect ratio, to flat and V-bottom skis of rectangular plan form. All of this material, with the exception of the calculations for the shock-mounted ski, is covered in the references.

Some of the problems remaining to be solved include determination of the effects of trimming shock mounts on ski loads, the effects of longitudinal ski twist and of extreme longitudinal curvature, ski upwash loads on fuselages, and impact loads on skis following submergence of the leading edge below the water surface.

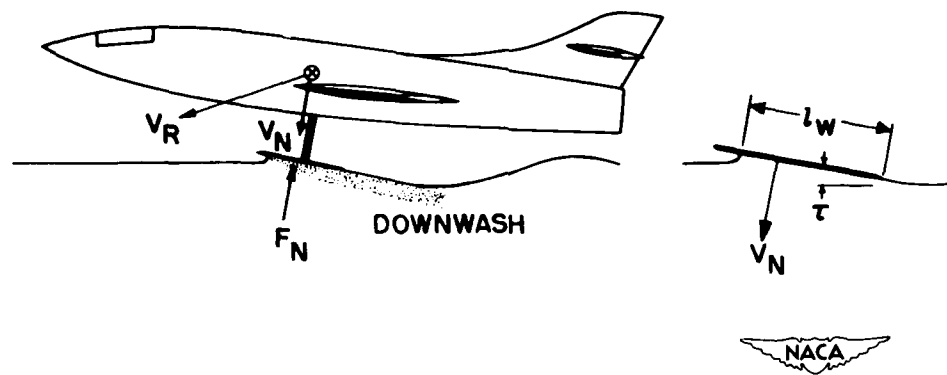
## REFERENCES

1. Dawson, John R., and Wadlin, Kenneth L.: Preliminary Tank Tests of NACA Hydro-Skis for High-Speed Airplanes. NACA RM L7I04, 1947.
2. Wadlin, Kenneth L., and Ramsen, John A.: Tank Spray Tests of a Jet-Powered Model Fitted With NACA Hydro-Skis. NACA RM L8B18, 1948.
3. Ramsen, John A.: The Effect of Rear Chine Strips on the Take-Off Characteristics of a High-Speed Airplane Fitted With NACA Hydro-Skis. NACA RM L9B10a, 1949.
4. Fisher, Lloyd J.: Model Ditching Investigations of Three Airplanes Equipped With Hydro-Skis. NACA RM L9K23, 1950.
5. Wadlin, Kenneth L., and Ramsen, John A.: Tank Investigation of the Grumman JRF-5 Airplane Fitted With Hydro-Skis Suitable for Operation on Water, Snow, and Ice. NACA RM L9K29, 1950.
6. Ramsen, John A., and Gray, George R.: Tank Investigation of the Grumman JRF-5 Airplane With a Single Hydro-Ski and an Extended Afterbody. NACA RM L51E21, 1951.
7. McKann, Robert E., Coffee, Claude W., and Arabian, Donald D.: Hydrodynamic Investigation of a  $\frac{1}{13}$ -Scale Model of the Consolidated Vultee Skate 7 Seaplane Equipped With Twin Hydro-Skis - TED No. NACA DE 342. NACA RM SL51F07a, Bur. Aero., 1951.
8. Ramsen, John A., Wadlin, Kenneth L., and Gray, George R.: Tank Investigation of the Edo Model 142 Hydro-Ski Research Airplane. NACA RM SL51I24, U.S. Air Force, 1951.
9. Ramsen, John A., and Gray, George R.: Tank Investigation of the Grumman JRF-5 Airplane Equipped With Twin Hydro-Skis - TED No. NACA DE 357. NACA RM SL52D17, Bur. Aero., 1952.
10. Schnitzer, Emanuel: Theory and Procedure for Determining Loads and Motions in Chine-Immersed Hydrodynamic Impacts of Prismatic Bodies. NACA TN 2813, 1952.
11. Smiley, Robert F.: The Application of Planing Characteristics to the Calculation of the Water-Landing Loads and Motions of Seaplanes of Arbitrary Constant Cross Section. NACA TN 2814, 1952.

12. Smiley, Robert F.: An Experimental Study of Water-Pressure Distributions During Landings and Planing of a Heavily Loaded Rectangular Flat-Plate Model. NACA TN 2453, 1951.
13. Batterson, Sidney A., and McArver, A. Ethelda: Water Landing Investigation of a Model Having a Heavy Beam Loading and a 30° Angle of Dead Rise. NACA TN 2015, 1950.
14. McArver, A. Ethelda: Water-Landing Investigation of a Model Having Heavy Beam Loadings and 0° Angle of Dead Rise. NACA TN 2330, 1951.
15. Miller, Robert W.: Water-Landing Investigation of a Flat-Bottom V-Step Model and Comparison With a Theory Incorporating Planing Data. (Prospective NACA paper)
16. Wadlin, Kenneth L., and McGehee, John R.: Planing Characteristics of Three Surfaces Representative of Hydro-Ski Forms. NACA RM L9C03, 1949.
17. Wadlin, Kenneth L., and McGehee, John R.: Planing Characteristics of Six Surfaces Representative of Hydro-Ski Forms. NACA RM L9L20, 1950.
18. Land, Norman L., and Fontana, Rudolph E.: Preliminary Tank Tests of Some Hydro-Ski—Wheel Combinations in the Planing Condition. NACA RM L52H15, 1952.
19. Land, Norman S., and Pelz, Charles A.: Force Characteristics in the Submerged and Planing Condition of a  $\frac{1}{5.78}$ -Scale Model of a Hydro-Ski-Wheel Combination for the Grumman JRF-5 Airplane. NACA RM L52B28, 1952.
20. Kapryan, Walter J., and Weinstein, Irving: The Planing Characteristics of a Surface Having a Basic Angle of Dead Rise of 20° and Horizontal Chine Flare. NACA TN 2804, 1952.
21. Blanchard, Ulysse J.: The Planing Characteristics of a Surface Having a Basic Angle of Dead Rise of 40° and Horizontal Chine Flare. NACA TN 2842, 1952.
22. Chambliss, Derrill B., and Boyd, George M., Jr.: The Planing Characteristics of Two V-Shaped Prismatic Surfaces Having Angles of Dead Rise of 20° and 40°. NACA TN 2876, 1953.
23. Weinstein, Irving, and Kapryan, Walter J.: High-Speed Planing Characteristics of a Rectangular Flat Plate Over a Wide Range of Trim and Wetted Length. (Prospective NACA paper)

24. Mayo, Wilbur L.: Analysis and Modification of Theory for Impact of Seaplanes on Water. NACA Rep. 810, 1945. (Supersedes NACA TN 1008.)
25. Milwitzky, Benjamin: A Generalized Theoretical and Experimental Investigation of the Motions and Hydrodynamic Loads Experienced by V-Bottom Seaplanes During Step-Landing Impacts. NACA TN 1516, 1948.
26. Wagner, Herbert: Über Stoss- und Gleitvorgänge an der Oberfläche von Flüssigkeiten. Z.a.M.M., Bd. 12, Heft 4, Aug. 1932, pp. 193-215.
27. Wagner, Herbert: Landing of Seaplanes. NACA TM 622, 1931.
28. Smiley, Robert F.: A Semiempirical Procedure for Computing the Water-Pressure Distribution on Flat and V-Bottom Prismatic Surfaces During Impact or Planing. NACA TN 2583, 1951.
29. Pierson, John D., and Leshnover, Samuel: An Analysis of the Fluid Flow in the Spray Root and Wake Regions of Flat Planing Surfaces. Preprint No. 166, S.M.F. Fund Paper, Inst. Aero. Sci. (Rep. No. 335, Project No. NR 062-012, Office of Naval Res., Exp. Towing Tank, Stevens Inst. Tech.), Oct. 1948.
30. Smiley, Robert F.: A Study of Water Pressure Distributions During Landings With Special Reference to a Prismatic Model Having a Heavy Beam Loading and a  $30^{\circ}$  Angle of Dead Rise. NACA TN 2111, 1950.
31. Pierson, John D., and Leshnover, Samuel: A Study of the Flow, Pressures, and Loads Pertaining to Prismatic Vee-Planing Surfaces. S.M.F. Fund Paper No. FF-2, Inst. Aero. Sci. (Rep. No. 382, Project No. NR 062-012, Office of Naval Res., Exp. Towing Tank, Stevens Inst. Tech.), May 1950.
32. Korvin-Kroukovsky, B. V., and Chabrow, Faye R.: The Discontinuous Fluid Flow Past an Immersed Wedge. Preprint No. 169, S.M.F. Fund Paper, Inst. Aero. Sci. (Rep. No. 334, Project No. NR 062-012, Office of Naval Res., Exp. Towing Tank, Stevens Inst. Tech.), Oct. 1948.
33. Batterson, Sidney A.: Water Landing Investigation of a Hydro-Ski Model at Beam Loadings of 18.9 and 4.4. NACA RM L51F27, 1951.

**HYDRO-SKI-EQUIPPED AIRCRAFT IN  
THE LANDING CONDITION**



NACA

Figure 1.

**HYDRO-SKI CONFIGURATIONS**

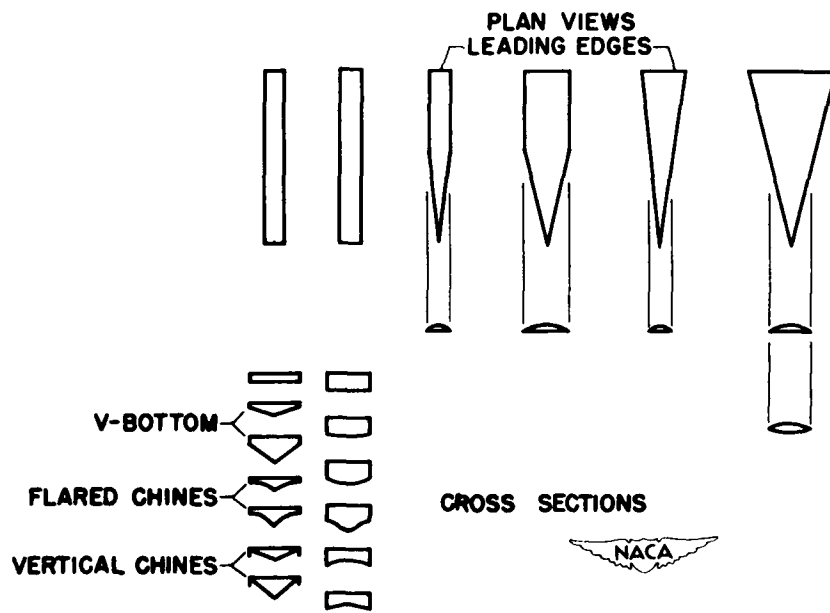


Figure 2.

## IMPACT LOAD ON A FLAT RECTANGULAR HYDRO-SKI

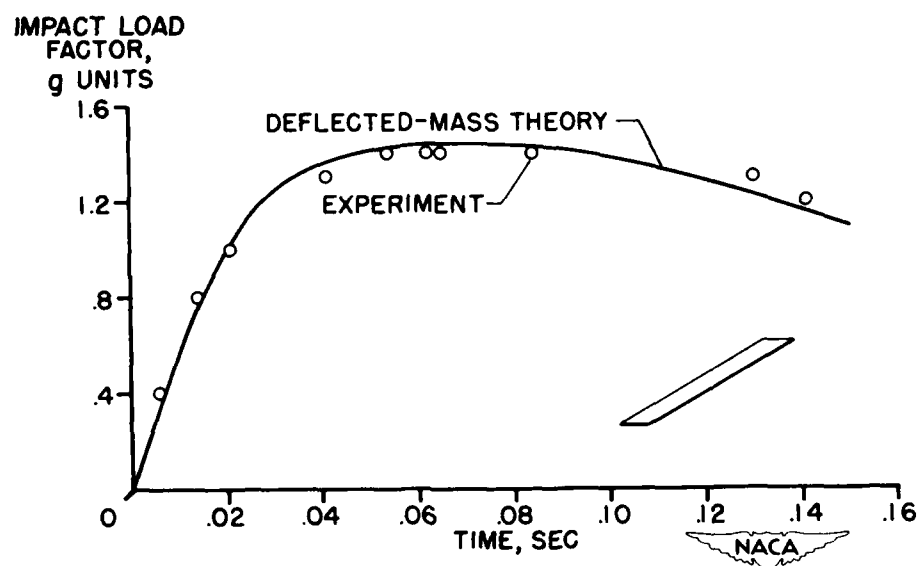


Figure 3.

## IMPACT LOAD ON A V-BOTTOM RECTANGULAR HYDRO-SKI

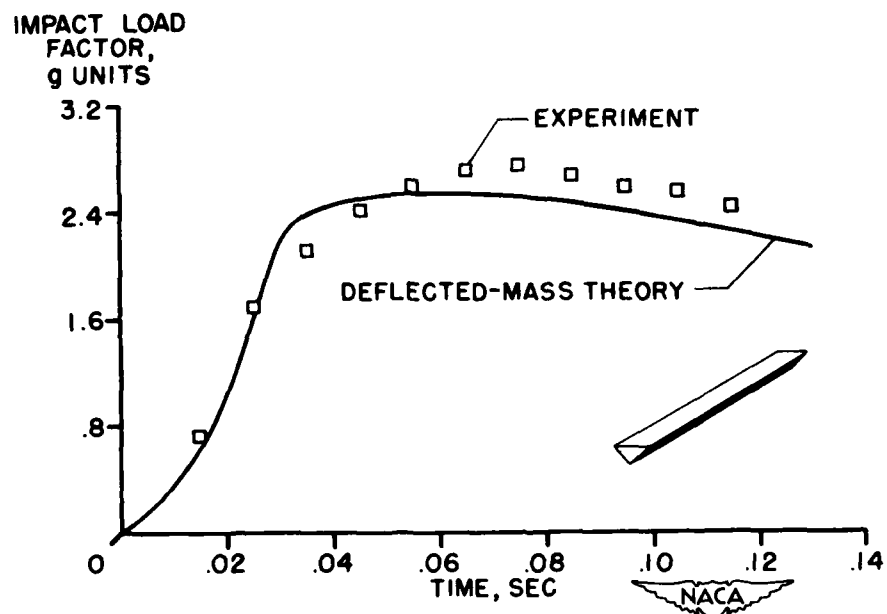


Figure 4.

## COMPARISON OF RECTANGULAR AND V-STEP HYDRO-SKI IMPACTS

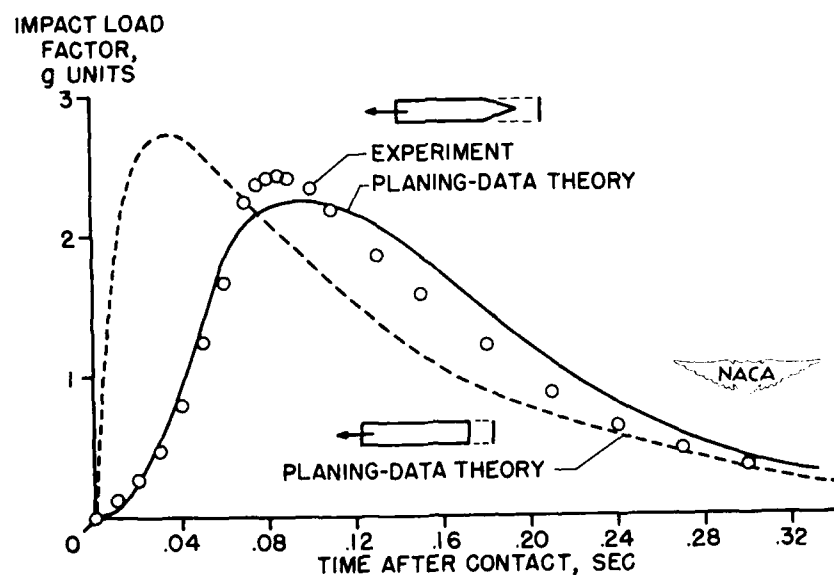


Figure 5.

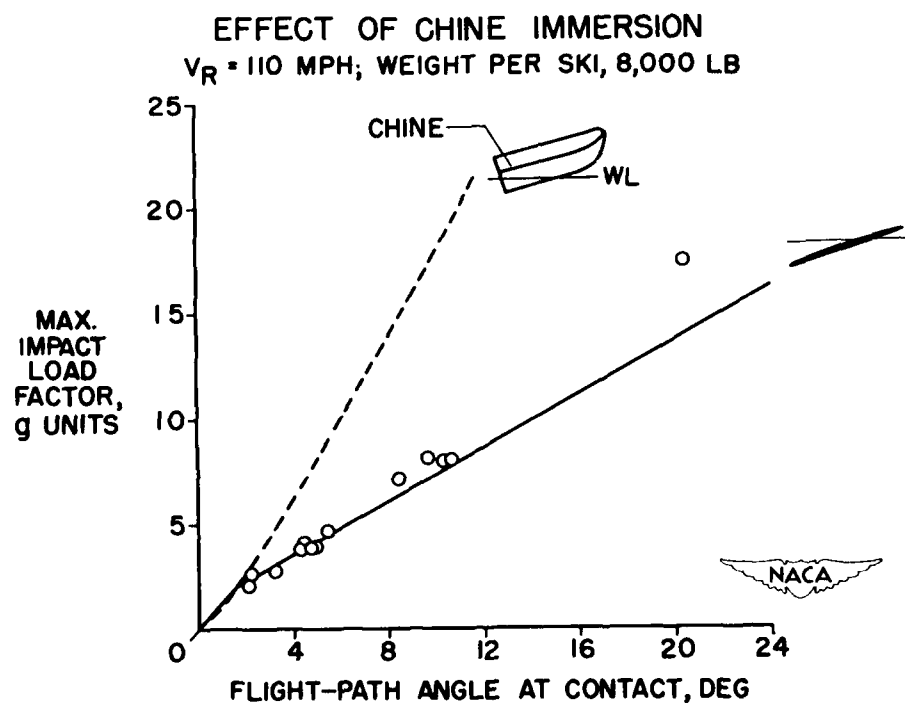


Figure 6.

## METHODS OF SHOCK-MOUNTING HYDRO-SKIS

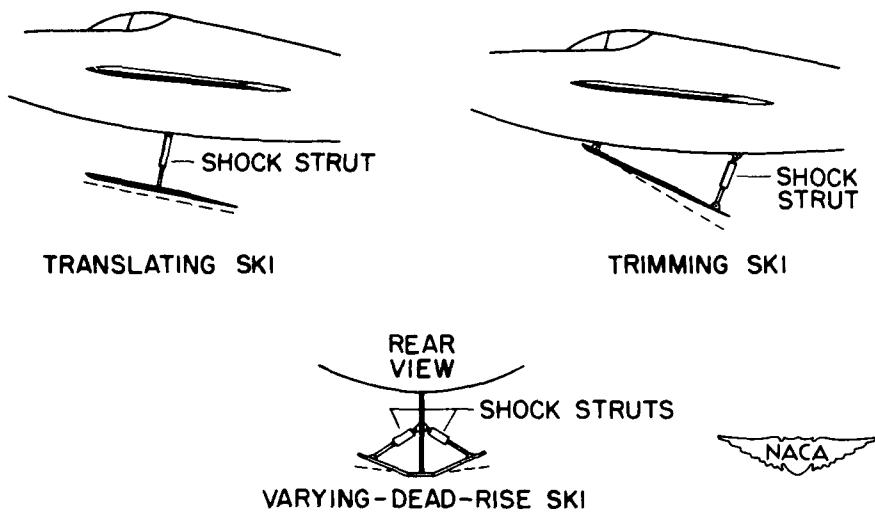


Figure 7.

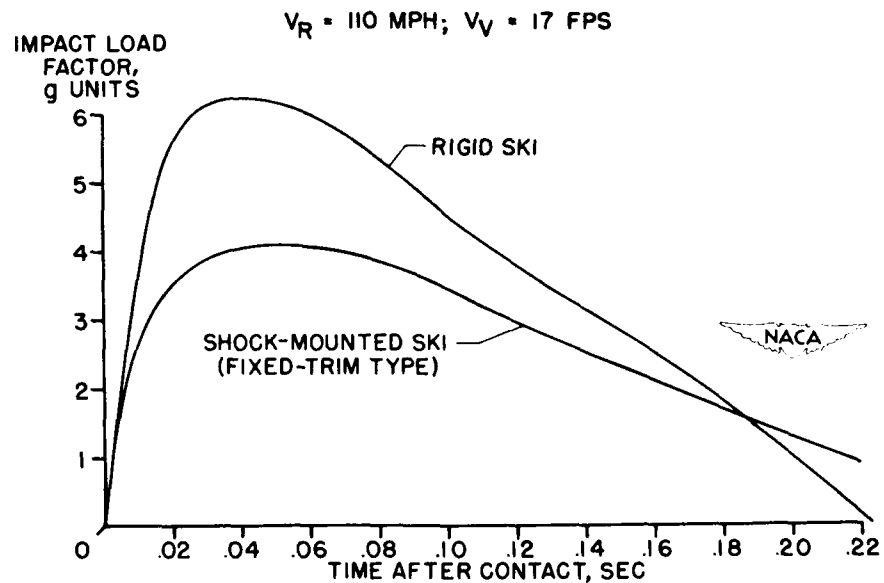
COMPARISON OF HYDRO-SKI LANDINGS WITH AND  
WITHOUT SHOCK STRUTS

Figure 8.

### CALCULATED AND EXPERIMENTAL PRESSURE DISTRIBUTIONS

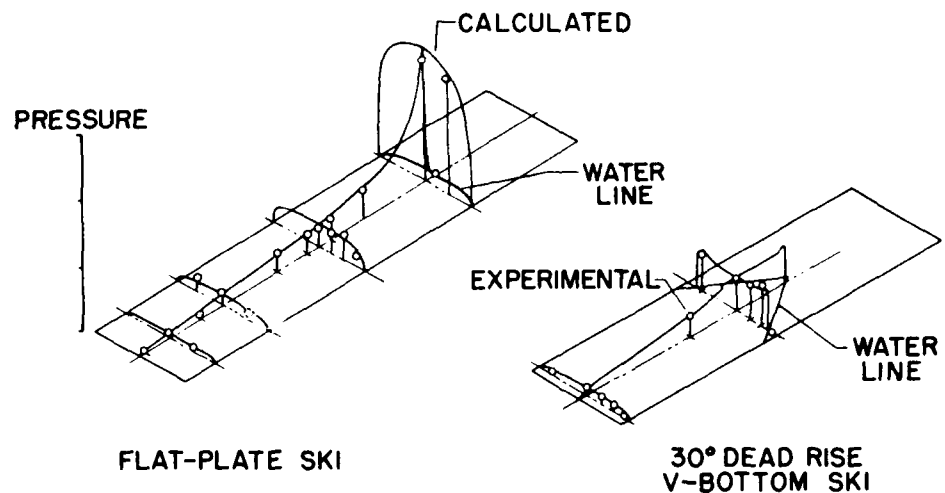


Figure 9.

~~SH~~ CONFIDENTIAL

421

## LOADS IN CRASH LANDINGS

CONFIDENTIAL

ACCELERATIONS AND HARNESS FORCES MEASURED  
IN FULL-SCALE CRASH STUDIES

By Jacob C. Moser

Lewis Flight Propulsion Laboratory

Recent experimental evidence has indicated that human beings can withstand accelerations in excess of those imposed in airplane crashes involving extensive damage to the airplane structure. In view of this the Lewis Flight Propulsion Laboratory is engaged in a study of the loads transmitted to airplane personnel compartments in a crash. The data obtained are intended as a contribution to the general background of engineering information required for the design of improved seats and personnel safety harness. This work is part of a general program on crash survival, in which instrumented aircraft are crashed under circumstances simulating a take-off or landing accident. In this study data were obtained with small, two-passenger, J-3 airplanes and large C-82 cargo-type airplanes.

Survival of the crash impact is a function of two primary factors:

- (1) Transmission of crash accelerations through the airplane structure
- (2) The response of the passenger and his restraint to these accelerations

The stall-spin landing accident was selected for study of light-plane-crash survival on the basis of Cornell Crash Injury Research Foundation records. These records showed that the stall-spin is a common light-plane accident and that passengers in the rear seat often survive when properly restrained. However, collapse of the fore portion of the cabin is usually fatal to the front passenger, and for this reason information on acceleration and harness tensions is of little interest in the front part of the airplane.

37

In order to simulate loads obtained in a stall-spin crash, airplanes manned by two dummies were run along the ground into an earthen barrier whose front slope was arranged to cause simultaneous impact of the nose, the left wing, and the left wheel as happens in most stall-spin crashes of this airplane. Figure 1 shows the airplane in a position simulating the moment of impact. Airplane impact speeds ranged from 42 to 60 miles per hour.

Figure 2 shows the two dummies in place. The rear dummy on which instrumentation was concentrated was designed by the Wright-Patterson

Aeromedical Group to simulate a 200-pound human in structure, weight distribution, and joint movement. Accelerometers were mounted on the chest and in the head, and tensiometers were connected to both ends of the seat belt and to one end of the shoulder harness. These restraints were attached directly to primary members of the structure. Accelerometers were also installed on the structure just under the rear seat to measure acceleration of the seat attachments.

In interpreting data, use was made of conclusions (see ref. 1) from physiological studies of the effect of acceleration on human beings. Stapp discovered that severity of physiological damage depends on the magnitude, rate of increase, and duration of acceleration.

Figure 3 presents decelerations transmitted to the floor structure at the location of the rear-seat attachments. These decelerations represent the driving force, in the problem, which acts to shake the passenger restrained by seat belt and shoulder harness. This figure compares the magnitude of decelerations obtained in three crashes where the impact speeds were 42, 47, and 60 miles per hour. Decelerations in g units are plotted against time following initial airplane impact with the barrier. This figure shows all significant data, values beyond 0.25 second being less than 1 g.

Observe first that the peak decelerations experienced in each crash lie between 26 to 34 g's in spite of the fact that the kinetic energy of an airplane crashed at 60 miles per hour is over twice that for one crashed at 42 miles per hour. Structural failure limits the deceleration transmitted to the seat to about 30 g's. The duration of the significant acceleration increases with impact speed as one would expect.

The moderating effect of the crumpling airplane structure on the acceleration loads transmitted to the seat can be appreciated from the fact that the engine deceleration in the 60-mile-per-hour crash was about 62 g's as compared with 33 g's for the seat shown here.

Figure 4 indicates the response of the passenger to movement of his seat attachments. This figure compares deceleration of the rear passenger's chest with the seat attachments under him in the 42-mile-per-hour crash. Note how his inertia combined with normal seat-belt slack and compliance cause his response to lag about 0.02 of a second in the onset of seat deceleration and to reduce the rate of increase of deceleration. Comparative rates are 2,400 g's per second for the seat and 950 g's per second for the chest. This reduction in rate indicates that harness compliance offers protection to the passenger and that physiological damage is measured by acceleration of his chest, not his seat attachments. These chest decelerations obtain a peak value of about 32 g's compared with the 26 g's of structural members. This increase

is due to the velocity acquired by the dummy with respect to the seat as the seat belt and shoulder harness stretched and became taut following the onset of seat deceleration.

The harness tensions recorded in the 42-mile-per-hour test are presented in figure 5 in which tensions in pounds are plotted against time. The shoulder harness attains a peak tension of approximately 1,200 pounds and is sustained above 1,050 pounds for 0.05 of a second. Both ends of the seat belt have nearly the same peak tensions, about 1,150 pounds. The dip in the seat-belt tension is believed to be due to momentary forces transmitted to the dummy's hips by his legs, which become wedged between the front seat and fuselage members. Shoulder-harness and seat-belt forces summed vectorially and compared with the recorded accelerations indicate that the passenger had an apparent weight much less than his true weight. All of the dummy's mass is not applied to the shoulder harness and seat belt. Some of it is supported through the dummy's legs by the airplane structure and some is transmitted to the seat by friction with the dummy's buttocks.

The information obtained with the airplane that was crashed at 42 miles per hour is typical of that obtained at higher impact speeds. As the impact speed increased, the maximum decelerations recorded on the passenger's chest increased from 32 to 50 g's; the rate of onset of deceleration, from 950 to 2,200 g's per second; and the duration of significant decelerations, from 0.024 to 0.1 of a second. The maximum total harness restraining force increases from 3,500 to 5,800 pounds.

Studies of crash loads made with twin-engine cargo planes were similar to those conducted with the light airplanes. It was possible to relate the decelerations transmitted to personnel compartments to airplane damage experienced in the crash.

The damage imposed on C-82 cargo airplanes was provided by obstructions arranged as shown in figure 6. The airplane arrives at this crash barrier at approximately 95 miles per hour. The propellers strike the abutments at full engine power, the main landing gear is broken by the same abutments, and the four spike-studded poles rip through the wings. The airplane then hits the ground on the slope beyond the barrier and slides to rest. (See ref. 2 for more details of this barrier.)

In the two crashes for which data will be presented, the crash experience differed only in the angle of contact of the airplane with the slope beyond the barrier. In one crash this angle of contact was about  $30^\circ$  and only moderate deformation to the fuselage structure resulted. In the second crash the contact angle was  $16^\circ$  and complete collapse of the fore structure of the fuselage was obtained. In both crashes the airplanes carried about 15,000 pounds of cargo, including

CONFIDENTIAL

6,300 pounds of fuel in their outboard wing tanks for a gross weight of approximately 44,000 pounds.

In the milder crash test (impact angle of  $3^{\circ}$ ), damage to the fuselage structure was slight, except that the floor was buckled by the impact of the fuselage belly with the ground and by the nose wheel being driven through the floor.

Accelerometers installed in the C-82 airplanes had a linear response, within  $\pm 5$  percent, to acceleration frequencies up to 100 cycles per second. However, analysis of the significance of deceleration data must consider the time duration for which the deceleration exists as well as the peak values encountered. Structural forces in elastic systems do not develop until relative displacements of the system components occur. It is necessary, therefore, to compare the frequency response of the system to the frequency of the impressed decelerations producing these displacements. Since our primary concern in this discussion is with the passenger and his restraints which constitute a mass-spring system having low-frequency response, the acceleration data, recorded during the crash on magnetic tape, were filtered electronically to attenuate frequencies above 20 cycles per second. It is recognized that consideration of the passenger plus his restraints as a simple elastic system represents an oversimplification and that further work in this field will require some change from the cutoff frequency of 20 cycles per second employed here for the passenger-restraint problem.

The acceleration history of the forward-cargo-compartment floor under the passenger dummy obtained in the  $3^{\circ}$  crash is shown in figure 7. Vertical and longitudinal acceleration components in g units are plotted against time, upward and forward components being indicated as positive.

In the zone marked A the propellers struck the barrier, the main landing gear was broken from the airplane, and the propeller and its reduction gearing were torn away. These events imposed only moderate accelerations, peak values of -4 g's vertical and +5 g's longitudinal being sustained for 0.02 of a second.

In the time interval marked by zone B the first poles at the barrier passed through the wing, the airplane nose gear collapsed and was driven through the fuselage floor, and the fuselage itself struck the ground. During this time the airplane experiences its highest accelerations, reaching peak values of  $\pm 10$  g's vertical and -7 g's longitudinal; an average longitudinal acceleration of -2 g's persisted for 0.2 of a second.

In time interval C the second pole passed through the wing and the airplane slowed to rest by friction and by plowing in the ground. There is a marked decline in the accelerations during this period, vertical

CONFIDENTIAL

accelerations being produced by bouncing and vibration of the airplane structure. The magnitude of the longitudinal acceleration declined to an average value of -1.5 g's.

The accelerations measured on the floor of the pilot's compartment located at about wing level are shown in figure 8. The peak vertical accelerations in the pilot's compartment of +8 and about -5 g's correspond to  $\pm 10$  g's measured on the cabin floor. The longitudinal accelerations are attenuated in transmission to the pilot's compartment from the fuselage belly, where the accelerating forces are applied. Peaks of about -4 g's in the pilot's compartment are only half those measured on the cabin floor. The average longitudinal accelerations are about -2 g's for the two locations. Since there is no relative longitudinal displacement between the cockpit and cargo compartment floor, these average accelerations must be the same over the same gross time intervals.

When acceleration records are superimposed there is no question that the pilot and cargo compartments act as a unit, except during the B interval when the greatest damage is being inflicted on the fuselage belly. These damaging forces are attenuated in their transmission to the cockpit by collapsing structure.

Included in figure 8 are the shoulder-harness and seat-belt loads. Peak values of these loads correlate with peak downward accelerations. When the accelerations are downward, the dummy's buttocks are separated from the seat and only the shoulder harness and seat belt restrain him. When the vertical accelerations of the seat are upward, the dummy is forced into his seat and the friction between buttocks and seat contributed in large measure to the restraining force.

A comparison of the seat-belt and shoulder-harness loads for the pilot and passenger shown in figure 9 reflect the attenuation of the accelerations transmitted to the pilot's compartment, the peak harness and seat-belt tensions being higher for the passenger than for the pilot. The belt tensions for pilot and passenger are in phase. The seat-belt loads reach a peak at about 750 pounds for the passenger and at 300 pounds for the pilot. Shoulder-harness tensions remain below 300 pounds for both the pilot and passenger.

In computing the total force applied to the dummy, the friction between buttocks and seat and the upward forces transmitted through the seat must be added vectorially to the shoulder-harness and seat-belt tensions shown here.

Now consider the crash in which the airplane strikes the ground at an impact angle of  $16^\circ$ . When the airplane arrives at the  $16^\circ$  slope, the nose fairing peals off and rolls under the belly and the entire fuselage

CONFIDENTIAL

in the region of the cockpit crushes down to about the original cockpit height alone. This fuselage failure is followed by impact of the engines and front wing surfaces with the ground and the airplane rocks about the wings. Obviously, in the crushed portion of the fuselage, survival is impossible. The accelerations measured in the rear portion of the fuselage that did not collapse are of interest, however. Accelerometers located in this zone were mounted on the midship floor, on the floor near the rear cargo doors, and on the fuselage walls at the midship station. Figure 10 compares the longitudinal accelerations measured. The customary acceleration-time coordinates are employed. Of particular interest in this figure are the accelerations that followed fuselage contact with the ground at the beginning of collapse. In the time interval between 0.6 and 0.8 of a second, in which the fuselage collapse occurred, the midship floor experienced an average deceleration of 5 g's whereas the rear floor suffered an average deceleration of 2.5 g's. However, peak decelerations as high as 11 g's were recorded at both locations. Just as the accelerations associated with the collapse of the fuselage subside, the engines and wings strike the ground to impose the decelerations observed between 0.8 and 1.0 second. Of particular interest now is the fact that the decelerating force acting on the nacelle and wings is transmitted through the intact upper fuselage structure to give the sustained decelerations of 7 g's measured on the right wall. When these loads are transmitted through the intact wall structure, the rear floor experiences higher decelerations than the midship floor where the adjacent walls have failed. Peak decelerations of 10 g's appear at the rear floor as compared with 8 g's at the midship floor.

The data from this crash also provide an opportunity to evaluate the longitudinal deceleration imposed on the airplane by the passage of the poles through the wing and its fuel tanks. During the passage of the second pole through the wing, no other force was acting to slow the airplane. A deceleration of about  $\frac{1}{2}$  g's was measured on the fuselage floor during the passage of this pole.

For purposes of comparison it is interesting to note that in the 30 to 100 cycles per second frequency range deceleration peaks of 55 g's appear on the fuselage wall. These peak accelerations are attenuated in their transmission to the cargo compartment floor to 20 g's at the rear and 30 g's at midship.

#### CONCLUDING REMARKS

Decelerations transmitted through collapsing airplane structure indicated in this report are generally lower than those which would

CONFIDENTIAL

appear in transport or fighter aircraft which have much more rigid structure than cargo-type aircraft on which this report was based. Similar data on these more rigid airplane types will be obtained in future work.

#### REFERENCES

1. Stapp, John Paul: Human Exposures to Linear Deceleration. Part 2. The Forward-Facing Position and the Development of a Crash Harness. AF Tech. Rep. No. 5915, Part 2, U.S.A.F., Wright-Patterson Air Force Base (Dayton), Dec. 1951.
2. Black, Dugald O.: Facilities and Methods Used in Full-Scale Airplane Crash-Fire Investigation. NACA RM E51L06, 1952.

430

CONFIDENTIAL

AIRPLANE AGAINST BARRIER

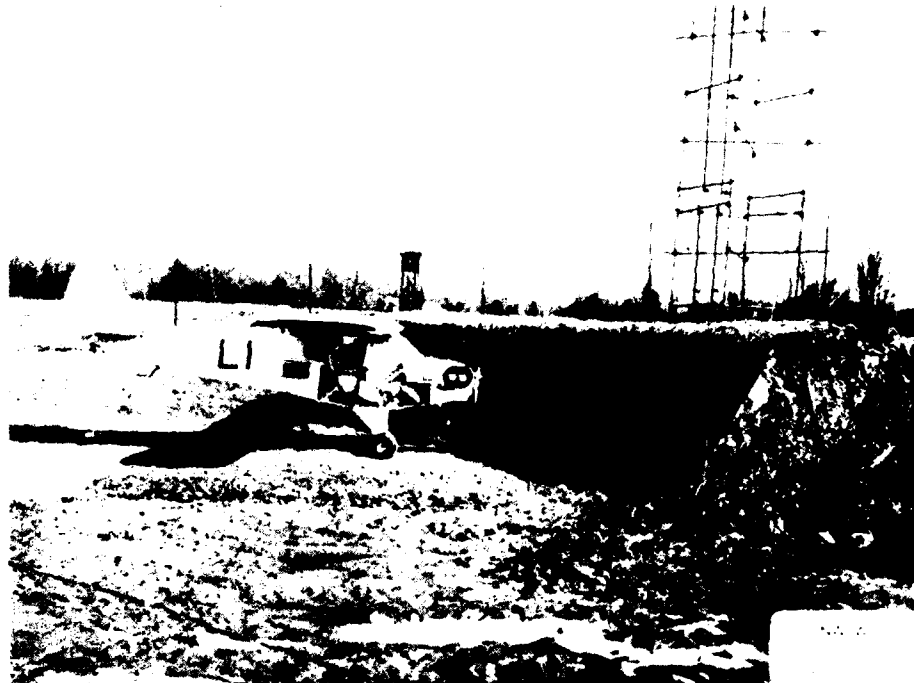


Figure 1.

DUMMIES IN AIRPLANE

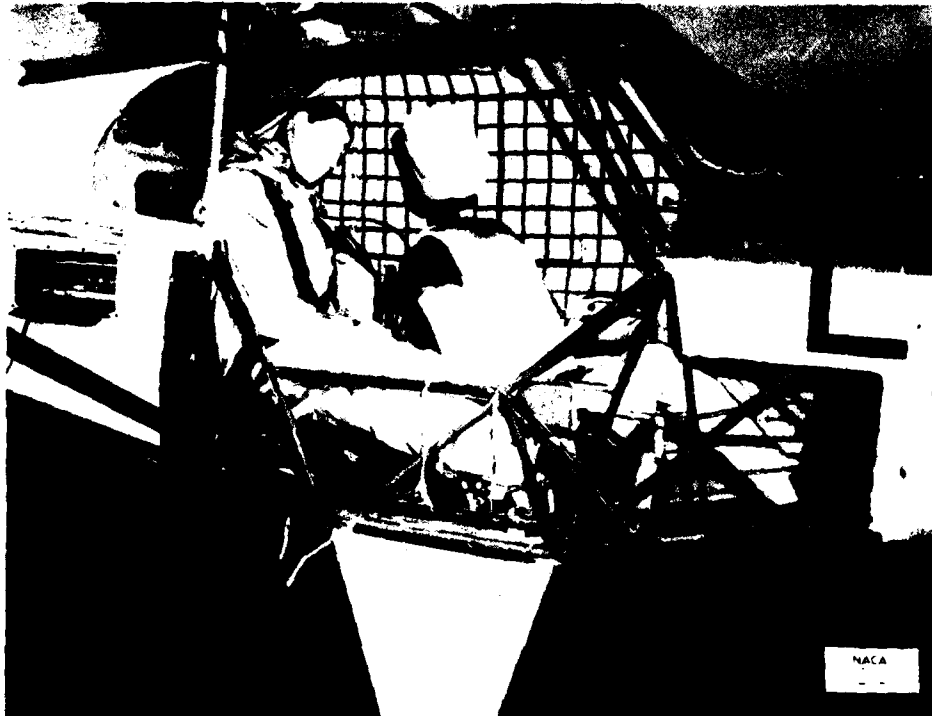


Figure 2.

CONFIDENTIAL

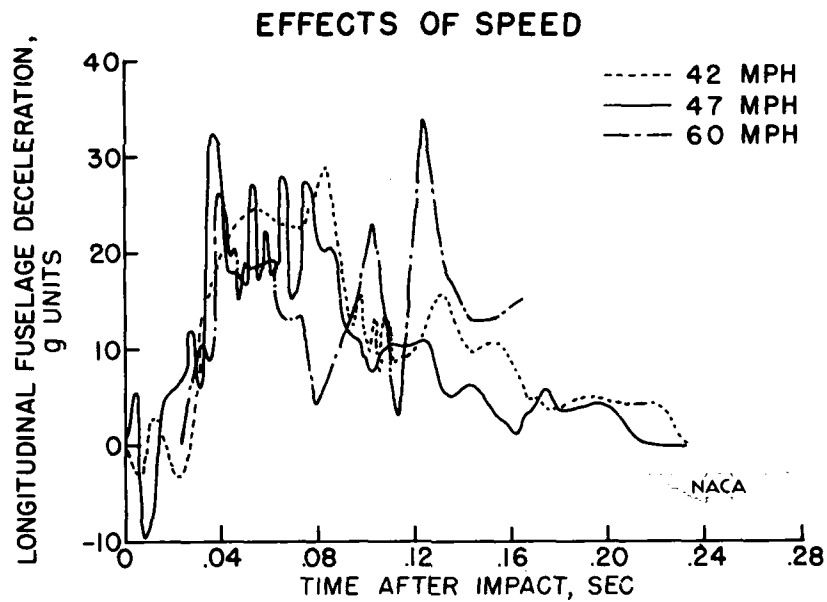


Figure 3.

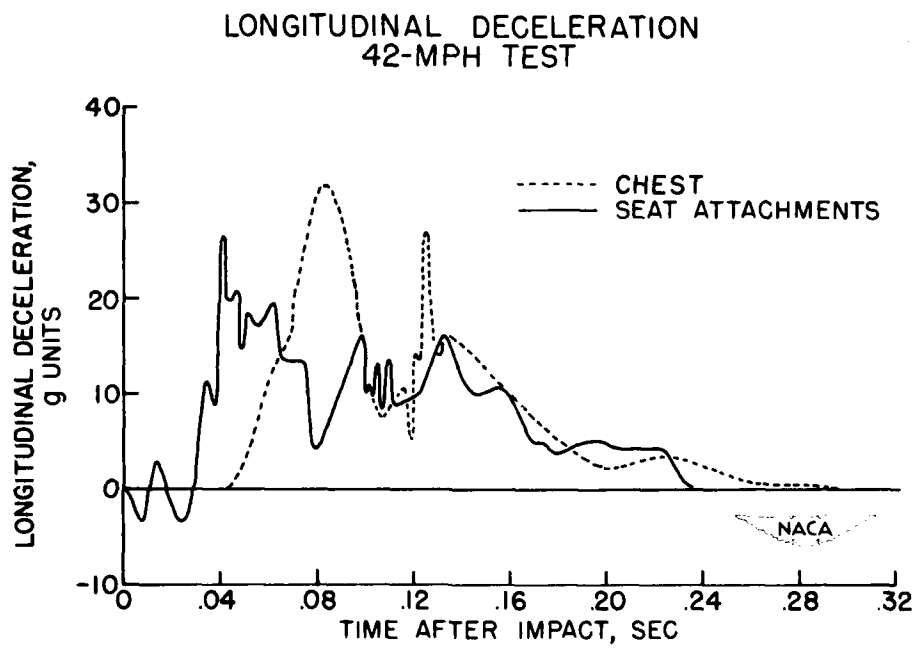


Figure 4.

CONFIDENTIAL

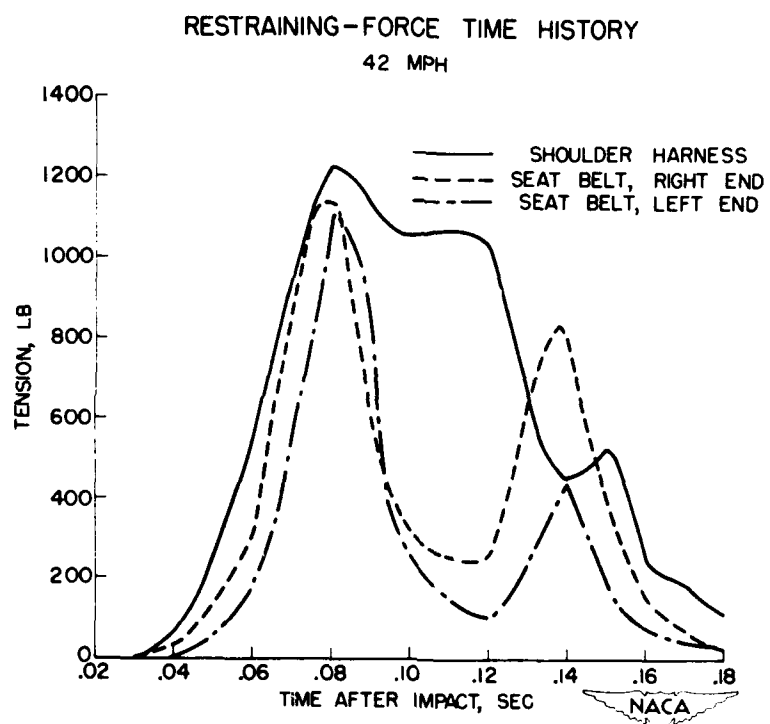


Figure 5.

## C-82 AIRPLANE CRASH BARRIER

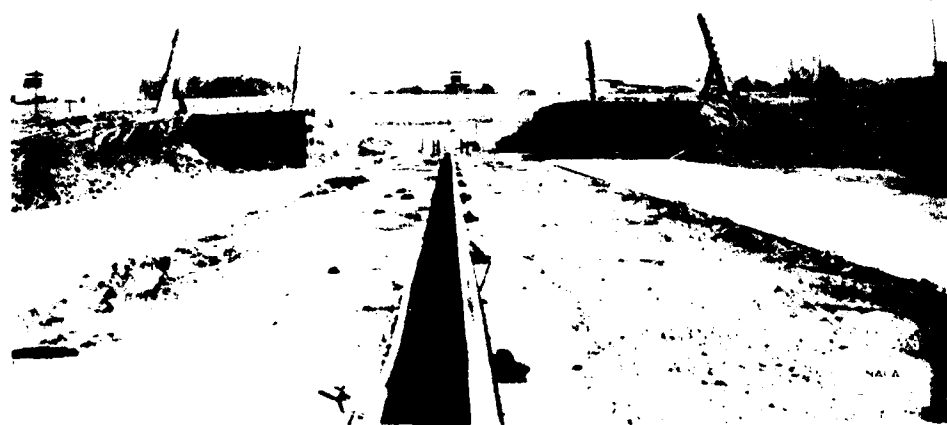


Figure 6.

CONFIDENTIAL

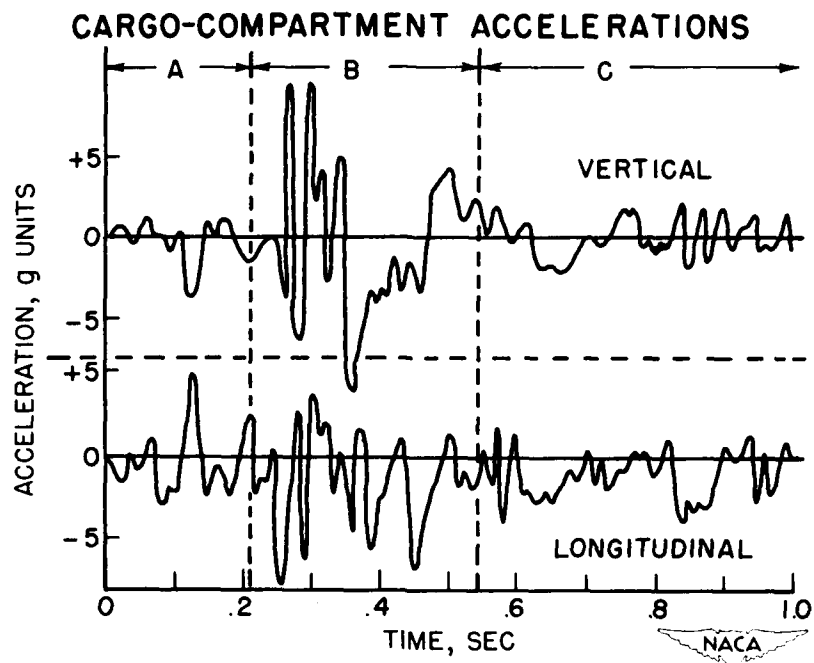


Figure 7.

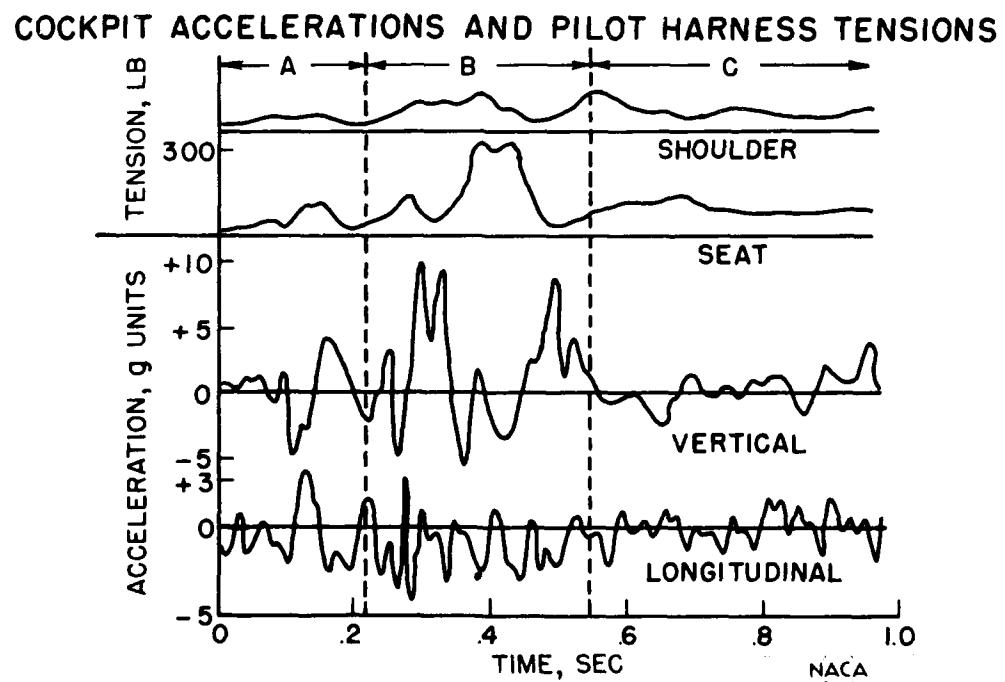


Figure 8.

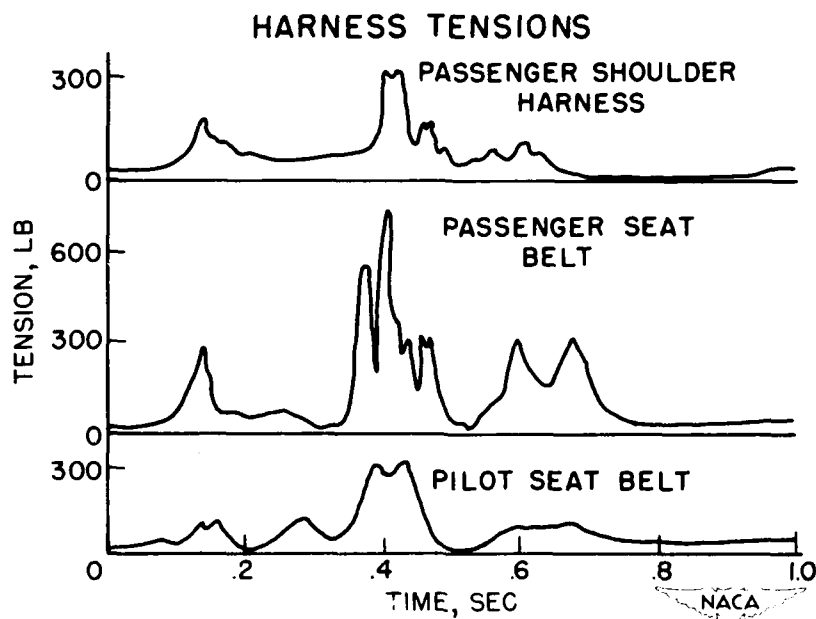


Figure 9.

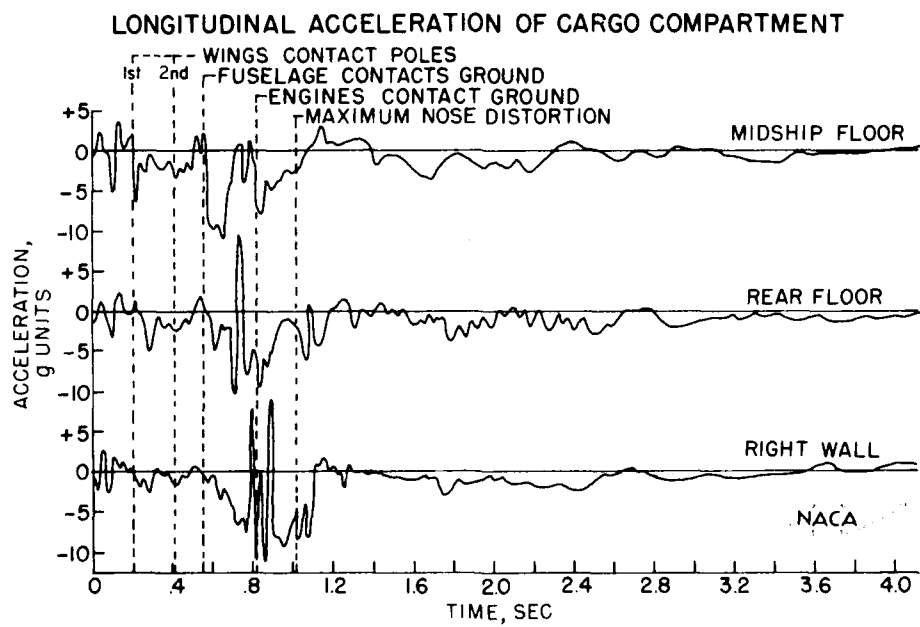


Figure 10.

CONFIDENTIAL

435

**FATIGUE**

CONFIDENTIAL

SOME RECENT RESEARCH IN FATIGUE OF  
AIRCRAFT MATERIALS

By Herbert F. Hardrath and Walter Illg

Langley Aeronautical Laboratory

Fatigue research has, in the past, consisted mainly of large numbers of tests most of which have been performed to prove the adequacy of a specific material or design. Many other tests have been performed, usually on rotating-beam specimens, in order to compare the fatigue properties of one material with those of another or to investigate the effects of certain parameters such as notches, welds, surface finishes, and the like. In spite of the tremendous volume of data available, practically no usable quantitative correlations have been developed.

In an effort to correlate some of the results and thus reduce the amount of testing required in the future, a systematic study of certain phases of the fatigue problem was undertaken. The first parameter chosen in this study was the effect of notches on fatigue strength. This parameter was chosen because of its fundamental importance in design against fatigue failure. It also proved to be particularly well suited for analysis because of the large quantity of data available. Two phases of this research are described: first, the prediction of the notch-size effect in fatigue and second, some preliminary observations regarding the effect of plasticity on the fatigue behavior of notched parts.

Reference 1 presents the method of prediction for steels. Several hundred sets of fatigue tests of notched and unnotched steel specimens were analyzed to determine the stress concentration factor effective in fatigue. For brevity, this factor will be referred to as the fatigue factor. It was found that the Neuber technical factor (ref. 2) provided the skeleton for a method which could predict the fatigue factor for the endurance limits of steel specimens. The Neuber formula appears in figure 1. It is seen that the predicted factor  $K_N$  is dependent upon the elastic stress concentration factor  $K_T$  which may be determined theoretically or experimentally, the absolute radius at the base of the notch  $R$ , the included angle in the notch  $\omega$ , and a constant  $R'$  which is described by Neuber as being the radius of a minimum block of material across which it is assumed that no stress gradient exists. Figure 2 presents a relationship between the value of the constant  $R'$  and the ultimate strengths of a wide range of steels. It was found that the Neuber formula together with this curve for  $R'$  gave reasonably accurate predictions of the fatigue factor at the endurance limit for steel specimens tested under completely reversed stress.

This analysis has now been extended to the aluminum alloys of current interest. Since the available data were much more limited in scope than they had been for steels, several series of tests were undertaken. Tests at the Langley Aeronautical Laboratory included axially loaded 24S-T3 sheet specimens with single central holes and rotating-beam specimens with circumferential grooves. The widths and ratio of hole diameter to width in the sheet specimens were systematically varied. Ten combinations have been tested to date. Battelle Memorial Institute, under NACA contract, performed a large number of tests on axially loaded sheet specimens containing holes, notches, and fillets (refs. 3 to 6). Nine configurations, four theoretical stress concentration factors, four mean stresses, and three materials - 24S-T3 and 75S-T6 aluminum alloy and 4130 steel - were included in the latter study. In order to facilitate cross checks between the Langley and Battelle results, all the sheet specimens in the two investigations were made from the same lot of material and all were electropolished at Battelle.

Although considerable attention was given to maintaining consistent techniques at the two laboratories and to careful monitoring of the testing equipment, considerable scatter was found in the data, particularly for unnotched 75S-T6 specimens tested at a stress ratio of -1 (ref. 7). The best curves through total scatter bands for a given configuration were used to evaluate the geometric size effect in fatigue for 24S-T3 and 75S-T6 materials. In both cases the value 0.02 inch for the material constant in the Neuber formula gives the best over-all prediction. The accuracy of this prediction is illustrated in figure 3. In this figure is plotted the ratio of the Neuber factor to the fatigue factor for various values of the radius of curvature at the bases of notches. The various configurations included in this study are represented by these sketches and the data for each shape are indicated by the corresponding symbols. The open symbols are for 24S-T data and the solid symbols are for 75S-T. It is seen that most of the points lie within a 10-percent band on each side of the ideal value of 1 for the ratio of the factors. All but one of the remaining predictions by the Neuber formula are conservative. This may be considered as being a reasonable agreement between the predicted factor and experimental results.

A similar comparison is given in figure 4 for a series of tests on unpolished sheet specimens tested at the National Bureau of Standards (NBS). (See refs. 8 to 10.) The stress raisers were single central holes and the specimens were tested under completely reversed axial load. The S-N curves for unnotched specimens were, in most cases, somewhat lower than the curves obtained in the NACA - Battelle series on polished specimens. These differences are presumably due to scratches in the unpolished surfaces. The S-N curves for specimens with holes, on the other hand, are about the same for polished and unpolished materials.

The resulting fatigue factors are consequently lower for the unpolished series than those experienced in tests of polished specimens, and the Neuber prediction correspondingly tends to be conservative. When the data for the NBS notched specimens are compared with the data for unnotched specimens tested by Battelle and NACA, the fatigue factors and Neuber factors agree within  $\pm 10$  percent for about 70 percent of the cases.

Most other data on the effect of notches in fatigue of aluminum alloys are limited to tests of rotating-beam specimens with very sharp grooves. The fatigue factors obtained from these data scatter rather widely and probably cannot, at present, be correlated by any simple relation. When these data are compared on the basis of the average of scatter bands including all the data for both materials, however, the Neuber prediction is again found to be excellent. Additional experiments which will extend the range of the existing data are currently being performed at Battelle Memorial Institute.

In general, it may be stated that it appears that the notch size effect in fatigue of 24S-T and 75S-T aluminum alloys can be predicted with reasonable accuracy by the Neuber formula and a material constant of 0.02 inch for the low-stress end of the S-N curve for completely reversed axial load.

The second part of the paper deals with the prediction of fatigue factors at somewhat higher stresses. As the stress level in a fatigue test is increased it is obvious that the stress concentration factor must decrease until a value approximately equal to unity is reached at the ultimate strength. A large number of test results were analyzed to find a trend in this decrease in stress concentration factor for steel specimens. Figure 5 shows a curve which is representative of the change in fatigue factor as a function of maximum nominal stress. The highest point on this curve corresponds to the fatigue factor at the endurance limit and is predicted by the Neuber factor as shown by the tick labeled  $K_N$ . The theoretical factor  $K_T$  is also indicated for purposes of comparison.

It appeared reasonable to expect that this curve was related to the curve for plastic stress concentration factors for static loading which was previously developed at the Langley Laboratory (ref. 11). Figure 6 presents a comparison between the two curves. The top curve in this slide is the curve for the plastic factor and is stated mathematically by the formula  $K = 1 + (K_T - 1) \frac{E_S}{E}$ . The curve for the fatigue factor is shown as a dashed line as before and the values of Neuber factor and theoretical factor are indicated by the horizontal lines. It turns out that the curve for the fatigue factor can be approximated by a

relation similar to the one for the plastic factor except that a factor  $1/2$  is required in the second term. The reason for this factor  $1/2$  is not known, but the correlation with fatigue-test results has been very good in approximately 100 cases where steel specimens were tested under completely reversed axial load or as rotating beams. In certain other cases the fatigue factor is greater than  $K_p$ . In these cases, however, the endurance limit for unnotched specimens exceeds or approaches the yield stress of the material. It appears that the stress-strain curve for such material must be drastically changed before failure can occur by fatigue, and a simple relation between fatigue notch factors and plastic considerations based on the original properties may not be possible.

An extension of this type of analysis to aluminum alloys has unfortunately met with less success. The results of tests of the aluminum alloys appear to be subject to considerably more scatter than is present in results of tests in steel. An analysis of  $K_F$  as a function of stress in aluminum alloys, consequently, presents an extremely confusing picture. In an attempt to improve this situation, the data for the Battelle tests were refaired slightly in some cases and new comparisons were made. To date, the most successful correlation has been obtained in 24S-T. Figure 7 illustrates that the curves for the fatigue factors frequently lie somewhat higher than the curve for the plastic factor.

Auxiliary experimental work has been initiated with the objective of determining the changes in stress which occur at the base of a notch in a specimen subjected to repeated completely reversed loading. One test has been completed to date. In this case the specimen contained symmetrical-edge notches with  $K_T = 2$  and the maximum nominal stress was 40 ksi. The strains at the bases of the notches were measured during 56 cycles of completely reversed load. The observed strain history was then duplicated in a simple unnotched specimen and the required loads were measured to obtain the corresponding stresses. Figure 8 illustrates the results in the form of curves of the maximum local strain and local stress against the number of cycles of load applied. Note that the zeros in the ordinate have been suppressed on both sides. The strains oscillated between these two curves during succeeding cycles and the stresses oscillated in a similar manner. It is seen that the range of strain decreased rapidly during the first few cycles and appears to approach an asymptote during subsequent cycles. The corresponding stress range, on the other hand, increased rapidly at first and more slowly later; this increase indicates that the material was being strain hardened. The stress concentration factor had changed from an initial value of 1.4 to a final value of 1.65. An extrapolation of the results of fatigue tests at Battelle (ref. 4) on a geometrically similar specimen yielded a fatigue factor of approximately 1.60 and

failure should have occurred in approximately 1000 cycles. This check in the factors is better than anticipated in view of the fact that only 5 percent of the total cycles to failure had been applied in this test. Further tests of this type are planned and it is expected that the results will aid in interpreting the action of stress raisers in fatigue and perhaps give some information regarding the basic fatigue mechanism.

In summary, it has been found that the geometrical size effect on the long-life fatigue strength of notched parts made of 24S-T and 75S-T aluminum alloys can be predicted by the previously proposed Neuber technical factor together with a material constant of 0.02 inch for most of the data presently available; the variation in fatigue stress concentration factor with increasing stress can be predicted for steels reasonably well by an empirical modification of plastic stress considerations; and special experiments in which the stresses at the bases of notches are studied during repeated load cycles indicate that the stresses at the notches increase with succeeding cycles.

CONFIDENTIAL

## REFERENCES

1. Kuhn, Paul. and Hardrath, Herbert F.: An Engineering Method for Estimating Notch-Size Effect in Fatigue Tests on Steel. NACA TN 2805, 1952.
2. Neuber, H.: Theory of Notch Stresses: Principles for Exact Stress Calculation. J. W. Edwards (Ann Arbor, Mich.), 1946.
3. Grover, H. J., Bishop, S. M., and Jackson, L. R.: Fatigue Strengths of Aircraft Materials. Axial-Load Fatigue Tests on Unnotched Sheet Specimens of 24S-T3 and 75S-T6 Aluminum Alloys and of SAE 4130 Steel. NACA TN 2324, 1951.
4. Grover, H. J., Bishop, S. M., and Jackson, L. R.: Fatigue Strengths of Aircraft Materials. Axial-Load Fatigue Tests on Notched Sheet Specimens of 24S-T3 and 75S-T6 Aluminum Alloys and of SAE 4130 Steel With Stress-Concentration Factors of 2.0 and 4.0. NACA TN 2389, 1951.
5. Grover, H. J., Bishop, S. M., and Jackson, L. R.: Fatigue Strengths of Aircraft Materials. Axial-Load Fatigue Tests on Notched Sheet Specimens of 24S-T3 and 75S-T6 Aluminum Alloys and of SAE 4130 Steel With Stress-Concentration Factor of 5.0. NACA TN 2390, 1951.
6. Grover, H. J., Hyler, W. S., and Jackson, L. R.: Fatigue Strength of Aircraft Materials. Axial-Load Fatigue Tests on Notched Sheet Specimens of 24S-T3 and 75S-T6 Aluminum Alloys and of SAE 4130 Steel With Stress-Concentration Factor of 1.5. NACA TN 2639, 1952.
7. Grover, H. J., Hyler, W. S., Kuhn, Paul, Landers, Charles B.. and Howell, F. M.: Axial-Load Fatigue Properties of 24S-T and 75S-T Aluminum Alloy As Determined in Several Laboratories. (Prospective NACA Paper)
8. Brueggeman, W. C., Mayer, M., Jr., and Smith, W. H.: Axial Fatigue Tests at Zero Mean Stress of 24S-T Aluminum-Alloy Sheet With and Without a Circular Hole. NACA TN 955, 1944.
9. Smith, Frank C., Brueggeman, William C., and Harwell, Richard H.: Comparison of Fatigue Strengths of Bare and Alclad 24S-T3 Aluminum-Alloy Sheet Specimens Tested at 12 and 1000 Cycles Per Minute. NACA TN 2231, 1950.

CONFIDENTIAL

**CONFIDENTIAL**

**443**

10. Brueggeman, W. C., and Mayer, M., Jr.: Axial Fatigue Tests at Zero Mean Stress of 24S-T and 75S-T Aluminum Alloy Strips With a Central Circular Hole. NACA TN 1611, 1948.
11. Hardrath, Herbert F., and Ohman, Lachlan: A Study of Elastic and Plastic Stress Concentration Factors Due to Notches and Fillets in Flat Plates. NACA TN 2566, 1951.

**CONFIDENTIAL**

## NEUBER FACTOR

$$K_N = 1 + \frac{K_T - 1}{1 + \frac{\pi}{\pi - \omega} \sqrt{R'/R}}$$

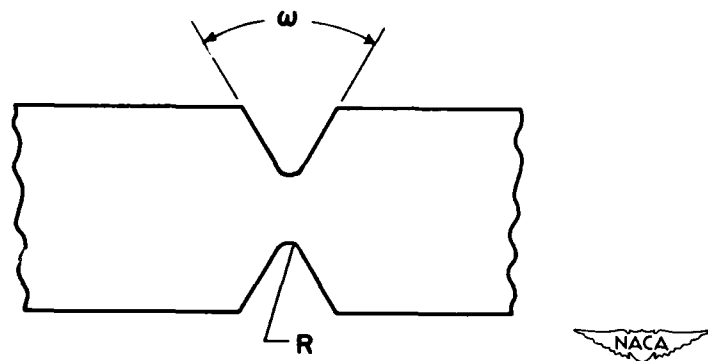


Figure 1.

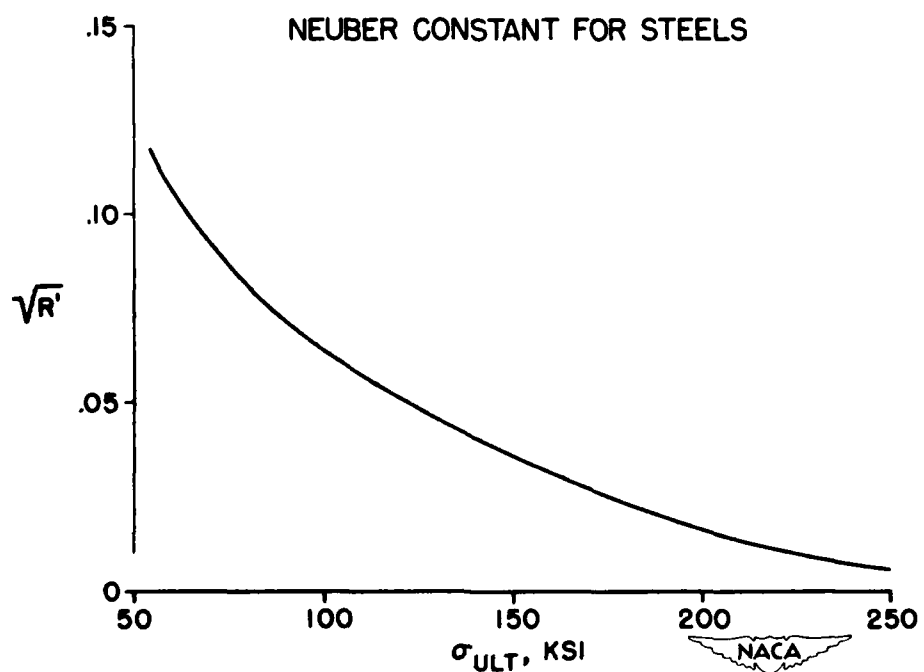


Figure 2.

NOTCH SIZE EFFECT FOR 24S-T3  
AND 75S-T6 (NACA & BATTELLE)

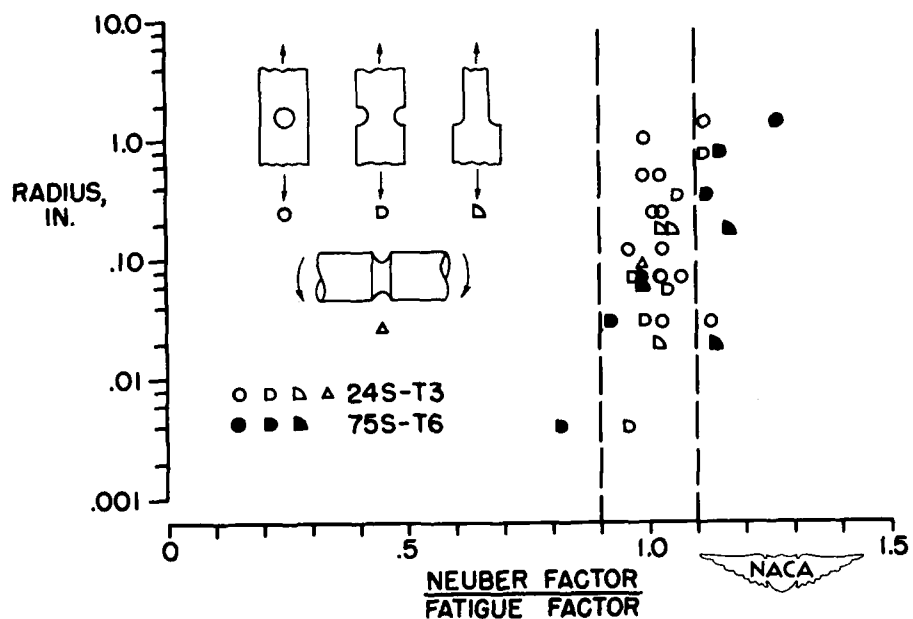


Figure 3.

NOTCH SIZE EFFECT FOR 24S-T3 AND 75S-T6 (NBS)

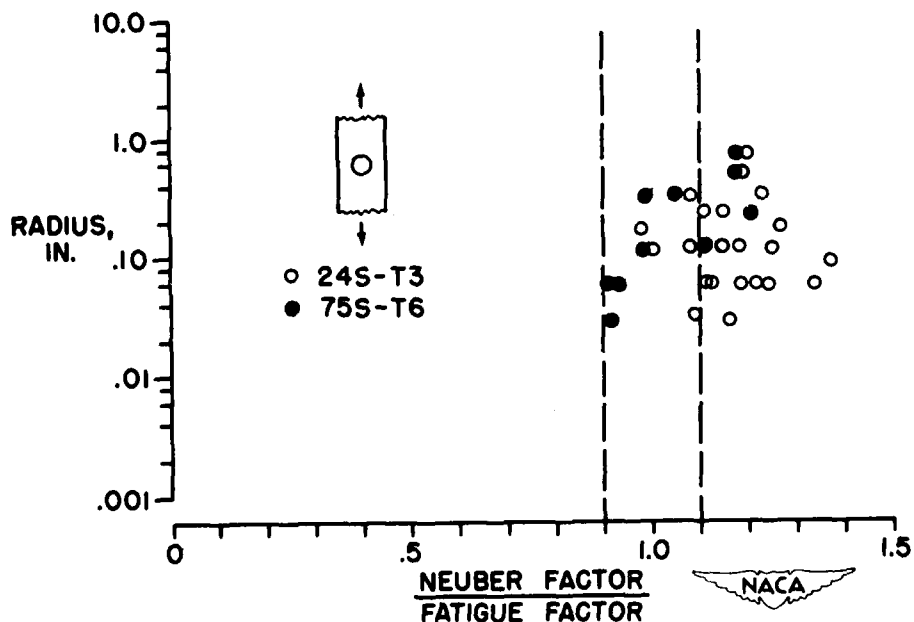


Figure 4.

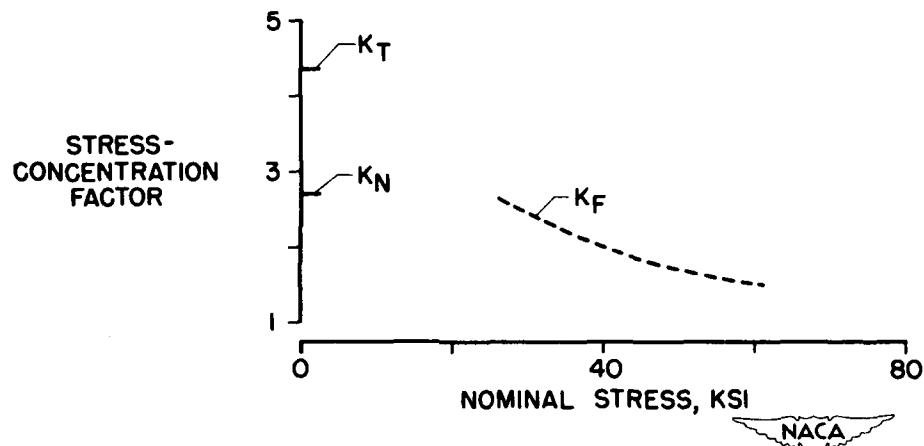
EFFECT OF PLASTICITY ON  $K_F$  (STEEL)

Figure 5.

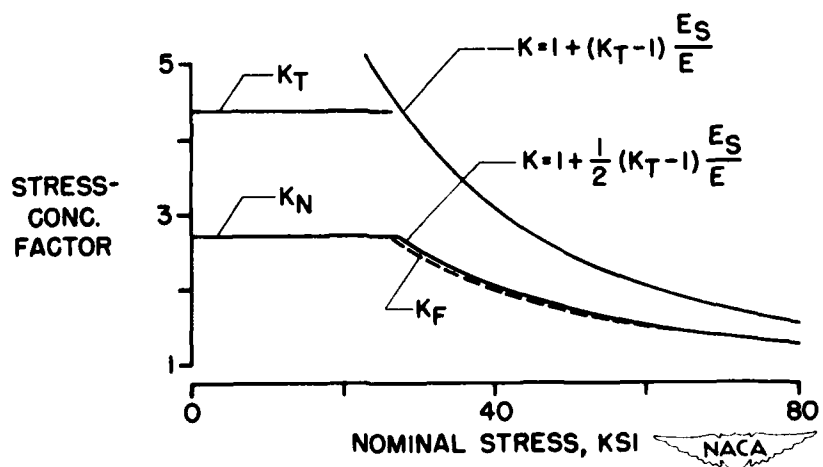
EFFECT OF PLASTICITY ON  $K_F$  (STEEL)

Figure 6.

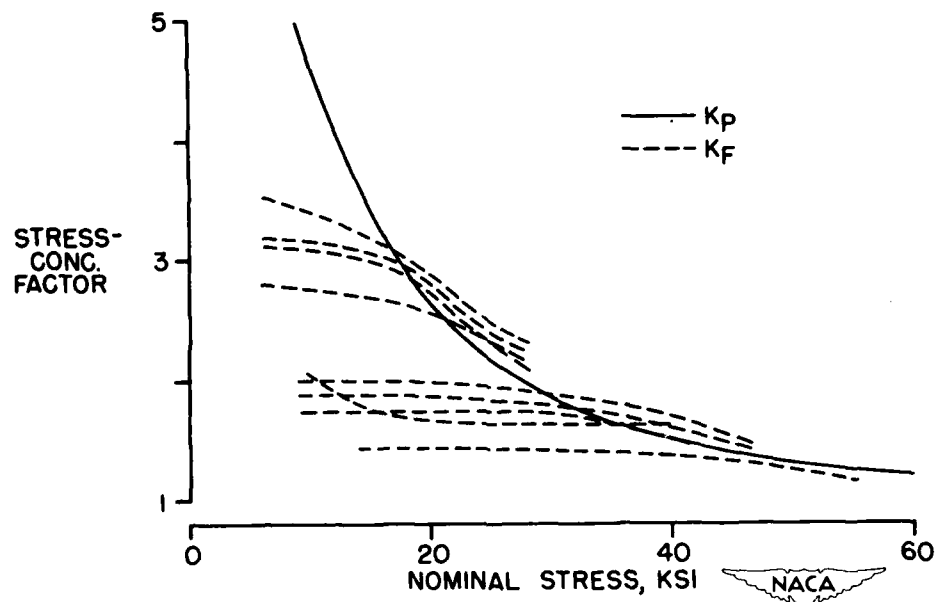
EFFECT OF PLASTICITY ON  $K_F$  (24S-T3)

Figure 7.

## PLASTIC ACTION DURING CYCLIC LOADING (24S-T3)

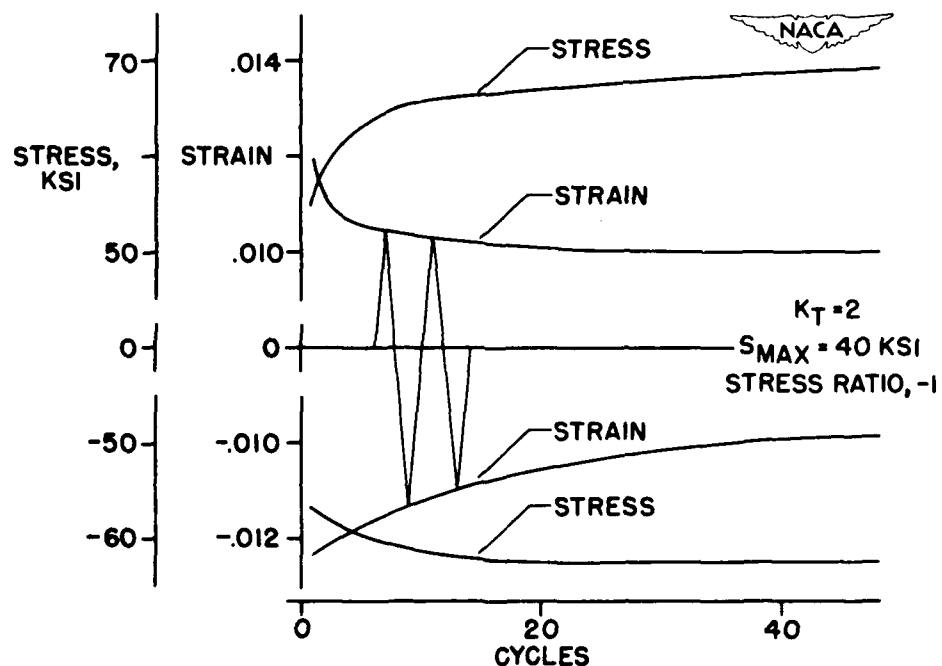


Figure 8.

RESULTS OF CONSTANT-LEVEL FATIGUE TESTS OF  
C-46 WING STRUCTURES

By M. James McGuigan, Jr.

Langley Aeronautical Laboratory

At the present time a fatigue investigation is being conducted on full-scale airplane-wing structures by the National Advisory Committee for Aeronautics. The wings used are obtained from C-46 "Commando" transport airplanes. The method of testing being used in this investigation is the resonant-frequency method utilizing concentrated masses to reproduce the flight stresses over a portion of the wing. Half of the test setup is shown in figure 1. The wing and a portion of the fuselage mounted in an inverted position between two vertical steel backstops can be seen. The control table is in the foreground. The concentrated masses are attached to the wing at the tip at the left of the figure.

These concentrated masses were proportioned and located so as to reproduce the design bending moment, shear, and torque at a specific wing station (station 214) for the level-flight, low-angle-of-attack condition. The design bending moment was rather closely reproduced, not only at the selected station, but also, within a few percent, over a considerable portion of the span.

Thus far in the program eight complete wings have been tested. Two were tested at a high load level with an alternating load of 1 g, three wings at an intermediate level with an alternating load of 0.625g, and two at a lower level with an alternating load of 0.425g. One specimen has been tested at an alternating load of 0.35g. All these constant-level tests are run with a 1 g or level-flight mean load given by the concentrated masses. The lifetimes for these tests varied from about 30,000 to 1,200,000 cycles. These lifetimes correspond to the number of cycles to the inception of a fatigue failure; for the purposes of this investigation, a failure is defined as a break in the material of the wing that is approximately 1/4 inch long and as deep as the material in which it originated.

Thus far in the investigation about 60 separate and distinct fatigue failures have occurred and have been divided into four main types. Figure 2, which is a plan view of the tension surface of the wing, shows the location of these four types. Failures of type 1 originated at the corners of inspection cutouts. Failures of type 2 occurred in a riveted tension joint running chordwise near the center line of the aircraft. Failures of type 3 occurred in a riveted shear joint, indicated by the number 3, where the shear web of the front spar was riveted to the tension flange of that spar. Failures of type 4 included all the remaining

failures which originated at several miscellaneous discontinuities in section or shape, such as the edge of a reinforcing doubler plate. Failures of this type are scattered considerably over the test specimen.

The wings are constructed almost entirely of 24S-T alclad and the over-all spread in number of cycles to failure for all the failures that occurred is comparable to the spread obtained in tests on small specimens of this material. The largest spread thus far occurred at the intermediate level and was 4.4 to 1.0 for all failures. However, when the spread for each of the aforementioned types of failure is examined individually a lower value is obtained for most types. As can be seen in figure 3, for the ten type 1 failures at the intermediate level the spread is only 1.5 to 1.0, and for four of these failures which originated at the same location in the structure the spread is only 1.2 to 1.0. For the six type 2 failures the spread is only 2.2 to 1.0 and for the six type 3 failures, 1.8 to 1.0. The twelve type 4 failures had a spread of 4.4 to 1.0 which accounts for the larger over-all figure.

In general the spread in lifetime for all failures is comparable to that expected of tests run on simple specimens by the commonly used procedures. The spread for similar failures repeatedly occurring in the same localities was, however, small by such standards. It should be realized, however, that the number of failures in each case is rather small for a true spread determination.

In order to obtain information on the stresses in the material where fatigue failures originated, subsequent specimens were instrumented with wire resistance strain gages. Since the measurement of the true maximum stress caused by a stress raiser was not practical, these strain gages were located so as to exclude the effects of stress concentrations and measure only the nominal stress in the vicinity of the stress raiser. An effective stress-concentration factor or fatigue-strength reduction factor was then deduced from the data. This factor was found by first determining an effective maximum stress from unnotched specimen data for the same material at the same load ratio and lifetime as that noted in the C-46 tests. The effective stress so found was then divided by the measured maximum nominal stress to find the effective stress-concentration factor.

Figure 4 shows the range of concentration factors calculated for the various types of failures which occurred during the intermediate-level tests. Also shown is the average factor for each type of failure. At inspection cutouts the concentration factor varied only from 3.7 to 4.6 and averaged about 4.1, riveted tension joints varied only from 2.2 to 2.6 and averaged 2.3, and the riveted shear joints ranged from 2.9 to 3.7 and averaged 3.1. As might be expected the fourth type varied considerably more than all the others, namely, from 2.6 to 5.0. The information given in figures 3 and 4 is presented in reference 1.

Only one type of failure lends itself to a theoretical treatment. This is the type 1 failure which occurred at inspection cutouts. A theoretical stress-concentration factor has been derived by Greenspan for a "square" cutout with a corner radius proportional to its width. By utilizing this factor and making a correction for the actual corner radius of the cutouts in question, theoretical concentration factors were calculated for all the cutouts where fatigue failures occurred. These theoretical factors varied from 3.0 to 4.8 for the various cutouts and compared well with the experimental factors of 3.7 to 4.6.

The tests at the higher and lower levels indicate about the same relative magnitude of concentration factor as those shown at the intermediate level. However, for failures occurring at the same identical locations in the structure there is a decreasing trend in concentration factor with increasing load level. In figure 5 this trend is shown graphically. In this figure the stress-concentration factor is plotted as a function of the maximum nominal stress during a loading cycle as measured with strain gages. The lower curve is the experimental data from about 50 failures of all types that occurred during the tests. All the points fall within the scatter bands shown by the dotted lines. The upper curve is the concentration factor in the plastic range obtained from the theory described in the paper by Herbert F. Hardrath and Walter Illg. It may be seen that the experimental curve has the same shape as that predicted by the theory even though it is displaced slightly. The fact that there is qualitative agreement between existing theory and results of tests on a full-scale airplane is somewhat encouraging.

Another phase of this investigation was that concerned with fatigue-crack propagation. Several of the fatigue cracks in the wing outer panels were allowed to grow until a considerable amount of the tension surface had failed. The rate at which the cracks grew is shown in figure 6, in which the percentage of cross-sectional material failed in the tension surface is plotted as a function of the number of cycles of load applied. It may be seen from this figure that the propagation of the cracks was relatively slow until somewhere between 2 and 10 percent of the tension material had failed. At this point the slopes of the curves abruptly become very steep and thereby indicate a rapid propagation of the crack thereafter. The similarity in the shape of the curves for all four levels can be noted, and also the fact that the percentage of material failed at the time crack growth becomes rapid is less at the higher load levels than at the lower levels.

The bottom right-hand curve shows the growth of the failure which occurred during the test conducted with an alternating load of 7.5 percent of the ultimate design load. This level was one suggested by the British as a fatigue proof test for new airplanes. From this curve it can be noted that the failure initiated at about 1,200,000 cycles, but

the complete failure of the wing was not eminent for this loading until almost 2,000,000 cycles had been applied. The lifetime aimed for by the British at this level was 2,000,000 cycles.

This investigation also indicated that the natural frequency of the test wings was not affected by fatigue damage until after a fatigue failure had originated. Even after a failure had occurred the change in natural frequency was very small, amounting to only about 2.0 percent with as much as 55 percent of the tension material failed.

Since these tests were run at the resonant frequency of the specimens any change in the damping of the structure should result in a change in the amplitude of vibration of the wings, and no such change in amplitude was noted during the course of the test. In addition damping measurements were taken periodically from the die-away function of the wing. These measurements also indicated no significant changes in damping.

It therefore appears that measurements of the natural frequency or structural damping characteristics of an airplane wing would be of no practical value as an indication of incipient fatigue failure.

In summary, fatigue tests simulating rather closely the design stress conditions have been conducted at four different stress levels on C-46 wings. These tests indicate a spread in lifetime, for all types of failures, comparable to the spread properties of the material itself. Failures repeatedly occurring at the same locations in the structure exhibited quite small spreads in lifetime. Experimental stress-concentration factors were calculated to give some idea of the magnitude of concentration factors that might be expected from various stress raisers when incorporated in an actual aircraft structure. Fatigue-crack propagation was investigated and it was found that all failures grew slowly until a certain amount of the wing section had failed and grew rapidly after this point was reached. It was also found that changes in the natural frequency or structural damping characteristics appeared impractical as an indication of incipient fatigue failure.

#### REFERENCE

1. McGuigan, M. James, Jr.: Interim Report on a Fatigue Investigation of a Full-Scale Transport Aircraft Wing Structure. NACA TN 2920, 1953.

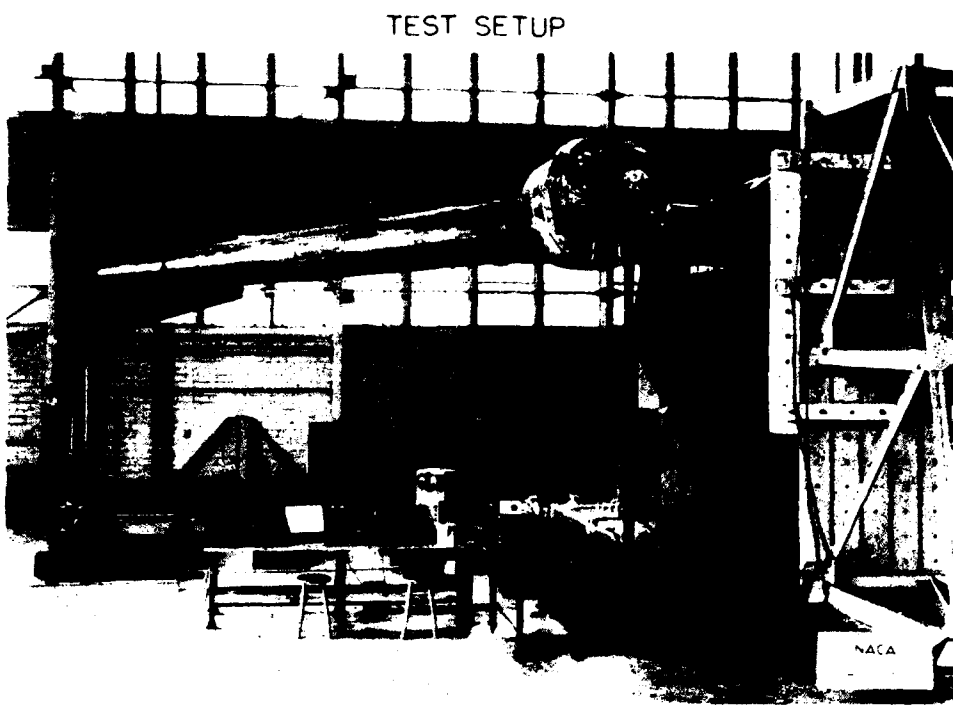


Figure 1.

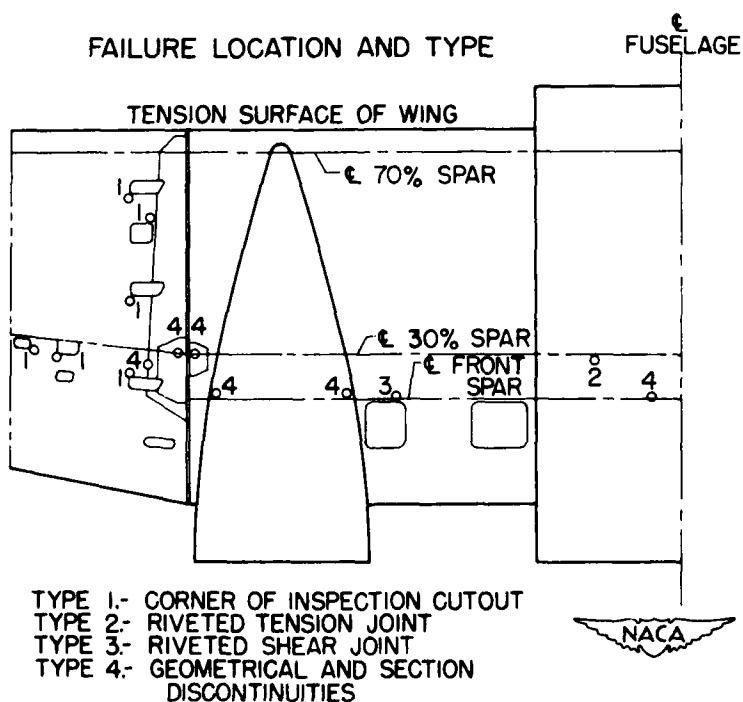


Figure 2.

## SPREAD IN LIFETIME

TYPE OF FAILURE	DESCRIPTION OF TYPE	NUMBER OF FAILURES	SPREAD IN FATIGUE LIFE
1	INSPECTION CUTOUT	10	1.5 TO 1.0
2	RIVETED TENSION JOINT	6	2.2 TO 1.0
3	RIVETED SHEAR JOINT	6	1.8 TO 1.0
4	GEOMETRICAL AND SECTION DISCONTINUITIES	12	4.4 TO 1.0



Figure 3.

## STRESS-CONCENTRATION FACTORS

TYPE OF FAILURE	DESCRIPTION OF TYPE	RANGE OF STRESS-CONCENTRATION FACTORS	AVERAGE FACTORS	THEORETICAL CONCENTRATION FACTORS
1	INSPECTION CUTOUT	3.7 TO 4.6	4.1	3.0 TO 4.8
2	RIVETED TENSION JOINT	2.2 TO 2.6	2.3	
3	RIVETED SHEAR JOINT	2.9 TO 3.7	3.1	
4	GEOMETRICAL AND SECTION DISCONTINUITIES	2.6 TO 5.0	4.0	



Figure 4.

## VARIATION OF K WITH NOMINAL STRESS

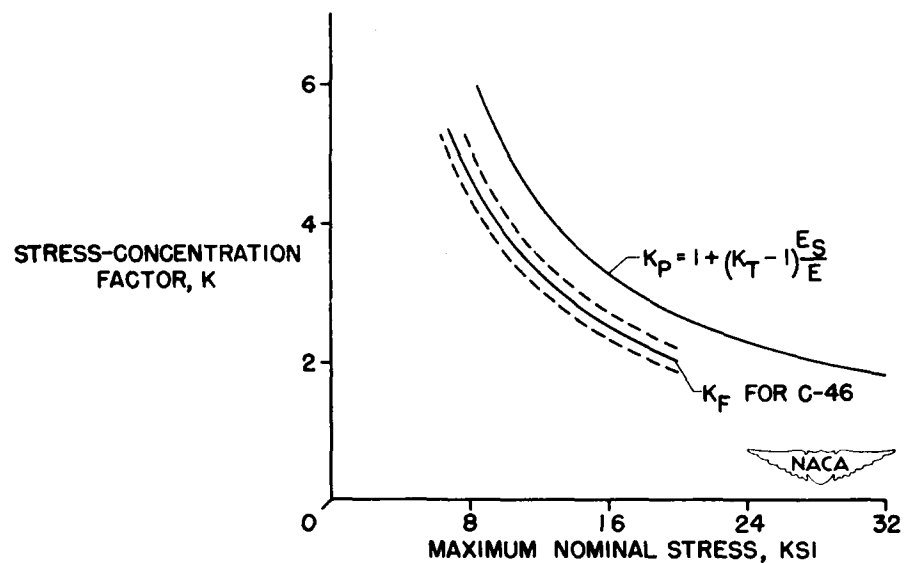


Figure 5.

## PROPAGATION OF FATIGUE CRACKS

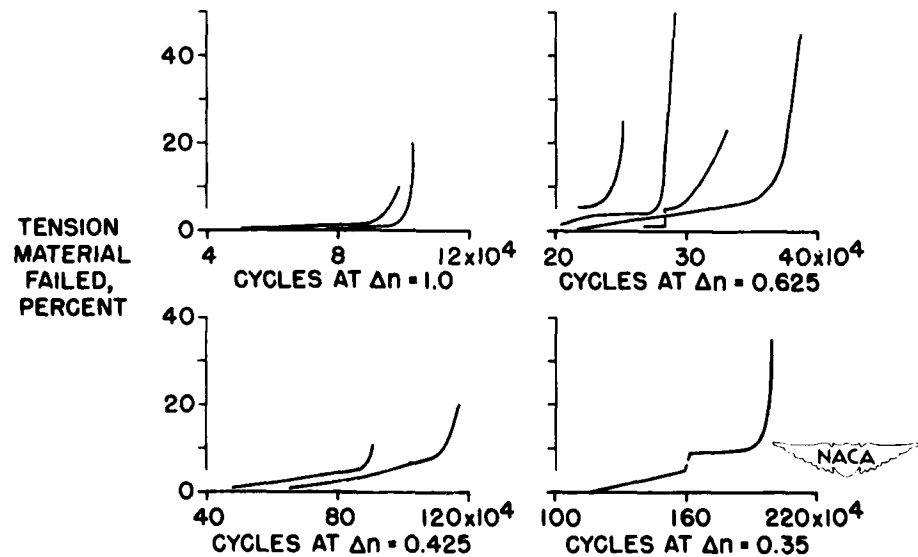


Figure 6.

**CONFIDENTIAL**

457

## **STRUCTURAL HEATING**

**CONFIDENTIAL**

## RECENT RESEARCH ON AERODYNAMIC HEATING AT SUPERSONIC SPEEDS

By Leo T. Chauvin and Joseph P. Maloney

Langley Aeronautical Laboratory

The purpose of the present paper is to report data on aerodynamic heating for hemispherical noses and fuselages that have recently been obtained.

For an airplane or guided missile with seeker devices or radar installation in the nose of the fuselage, a round nose may be more desirable than a pointed nose. Since the effect of aerodynamic heating may be very important, some tests were conducted in the preflight jet at the Pilotless Aircraft Research Station at Wallops Island, Va. The test Mach numbers ranged from 1.62 to 2.54 for a Reynolds number of approximately  $4.5 \times 10^6$  based on a nose diameter of 4 inches. This Reynolds number corresponds in free flight to a 4-inch-diameter nose at sea-level or a 2-foot-diameter nose at 50,000 feet altitude.

The measured equilibrium skin temperatures on the hemispherical nose are shown in figure 1. The equilibrium skin temperature expressed as a ratio to stagnation temperature is plotted on a radial scale, which indicates the location at which the measurements were made. The three temperature curves are for Mach numbers 1.62, 2.05, and 2.54. The tests show a temperature ratio of 1, corresponding to stagnation temperature, occurring at the front of the nose.

The equilibrium skin temperature reduces gradually along the surface. At the 90° station the skin temperature is about 95 percent of the stagnation temperature. Only a very small Mach number effect on the equilibrium temperature was evident for these tests.

The heat-transfer coefficients measured during the transient aerodynamic heating of the hemispherical nose are shown in figure 2. The method of correlation used in this figure is the basic method used for subsonic heat-transfer data and has been used satisfactorily up to a Mach number of 2.5 on several research missiles. The local heat-transfer coefficient  $h$  is contained in the term  $hl/k$  which is the Nusselt number. The ordinate is the Nusselt number times the Prandtl number to the  $-1/3$  power. The abscissa is the Reynolds number based on the length along the surface measured from the stagnation point. The air properties are based upon conditions just outside the boundary layer. Heat-transfer data are shown for a smooth, highly polished nose at Mach numbers from 1.62 to 2.54 and also for a nose at  $M = 1.99$ , having a rougher surface, corresponding to a very fine sand blast. The

nose tested at  $M = 1.99$ , in both the smooth and rough conditions, is 6 inches in diameter.

Below a Reynolds number of  $2 \times 10^6$ , the data points for the rougher nose fall above the data points for the smooth nose. Transition from a laminar to a turbulent boundary layer occurred for the smooth nose between the  $45^\circ$  and  $60^\circ$  stations, corresponding to a Reynolds number of about  $1 \times 10^6$  where the heat-transfer parameter increased rapidly and reached a maximum at a Reynolds number of about  $2.5 \times 10^6$ . Above this Reynolds number the data for the smooth and rough nose group together. For comparison, the heat transfer on a flat plate for a turbulent boundary layer calculated by the equation  $\text{Nu Pr}^{-1/3} = 0.0296 R^{0.8}$  is shown by the top curve. The heat transfer for a laminar boundary layer for a flat plate calculated by the equation  $\text{Nu Pr}^{-1/3} = 0.33 R^{0.5}$  is shown by the bottom curve. The heat-transfer data obtained ahead of the  $45^\circ$  station indicate laminar heat transfer, and fall considerably above the flat-plate line. It has been shown theoretically for a conical nose that the laminar heat transfer exceeds that for a flat plate by the factor  $\sqrt{3}$ . The heat transfer on a cone for a laminar boundary layer is shown by the middle line and calculated by the equation  $\text{Nu Pr}^{-1/3} = 0.571 R^{0.5}$ . By analogy, it is to be expected that the laminar heat transfer of a hemispherical nose would exceed that of a flat plate, which is what is experimentally observed. The heating condition for these tests expressed as the ratio of skin temperature to adiabatic wall temperature is approximately 0.7 (adiabatic wall hotter than the skin). For the Reynolds number and heating condition of the test, no Mach number effect on the heat transfer was evident. The results for the smooth nose at different Mach numbers are quite consistent.

Attention is now turned to the aerodynamic heating of slender bodies of revolution at zero angle of attack. For Mach numbers above 2.5, the basic method of correlation which was used in figure 2 is inadequate because of the greater effects of Mach number and heating conditions. A method including these parameters is therefore necessary. In figure 3 is shown a correlation that takes these into account. The abscissa is the Reynolds number based on the length  $\delta$ , the boundary-layer thickness. The ordinate is the heat-transfer coefficient  $h$  expressed as the Nusselt number  $h\delta/k$  multiplied by a factor  $F$ . The factor  $F$  is a theoretical function combining the effects of Mach number, Prandtl number, and heating potential. This theory has been reported in reference 1. Shown on this figure are recent heat-transfer measurements at Mach numbers from about 1.6 to 3.7 obtained in flight on the RM-10 research missile illustrated. The parameters are based on conditions just outside the boundary layer.

The experimental points are divided into two groups according to the manner of obtaining boundary-layer thickness. For the points labeled "measured  $\delta$ ," the thickness was obtained directly by a boundary-layer rake. For the calculated points, the thickness was obtained by interpolating with the aid of theory between the nose and a point where the boundary layer was measured with a rake. The heating potential, taken as the adiabatic wall temperature minus the skin temperature, covered a very wide range varying from  $-729^{\circ}$  to  $67^{\circ}$  F. The experimental measurements fall fairly close to the theoretical curve and show no tendency for increased scatter at the higher Mach numbers and heating potentials as was experienced with earlier types of correlations.

In summary, equilibrium temperatures and heat-transfer coefficients for a hemispherical nose have been measured up to a Mach number of 2.54 at Reynolds numbers corresponding to a 4-inch-diameter nose at sea level or a 2-foot-diameter nose at 50,000 feet. The heat-transfer coefficient has been measured on the RM-10 parabolic body of revolution in flight up to a Mach number of 3.7 and correlation with compressible theory accomplished.

#### REFERENCE

1. Donaldson, Coleman duP.: Heat Transfer and Skin Friction for Turbulent Boundary Layers on Heated or Cooled Surfaces at High Speeds. NACA RM L52H04, 1952.

CONFIDENTIAL

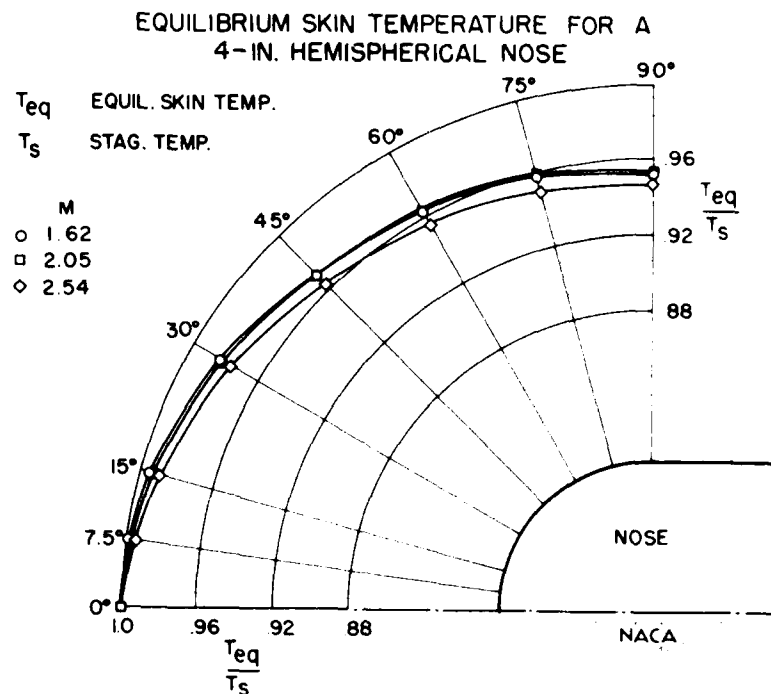


Figure 1.

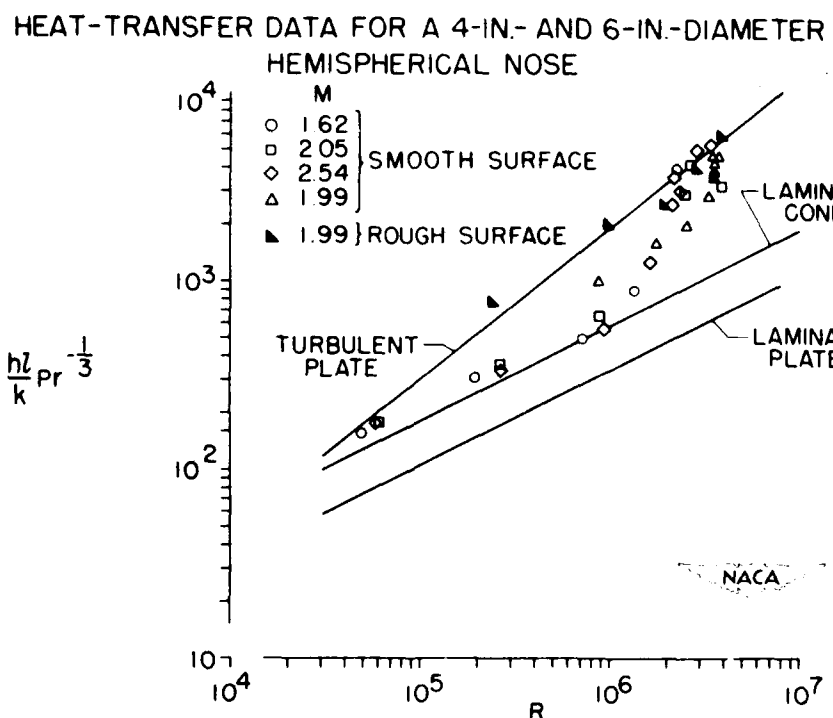


Figure 2.

CONFIDENTIAL

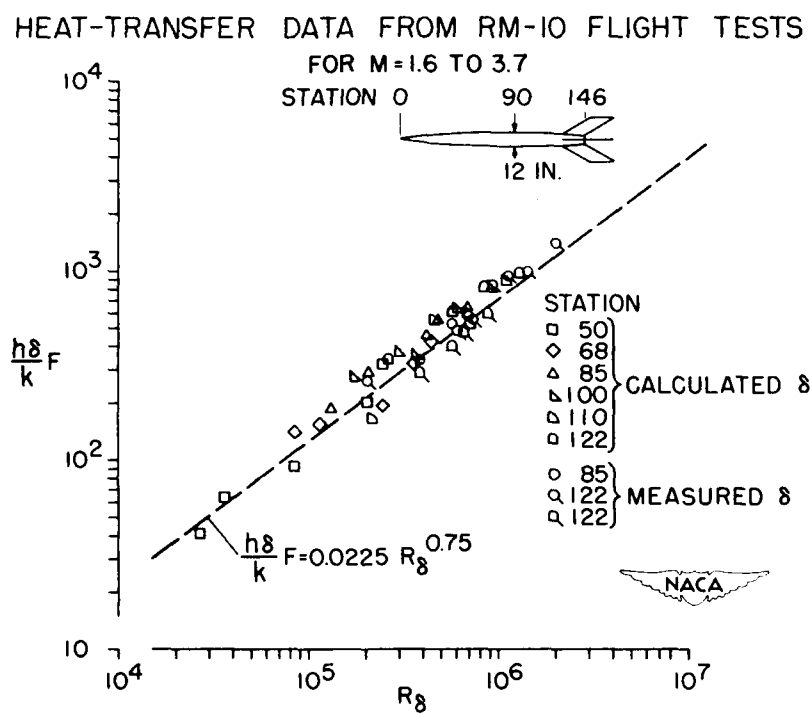


Figure 3.

CONFIDENTIAL

465

## SUPersonic JET TESTS OF SIMPLIFIED WING STRUCTURES

By Richard R. Heldenfels and Richard J. Rosecrans

Langley Aeronautical Laboratory

As part of an investigation of the effects of aerodynamic heating on aircraft structures, the Langley Structures Research Division is testing multiweb wing structures under aerodynamic conditions similar to those obtained in supersonic flight. The first such test was made to obtain data on the temperature distribution in a small multiweb wing structure; however, the aerodynamic loads played an important and unanticipated role in that the model experienced a dynamic failure near the end of the test. Additional tests have been made to gather information on the nature and causes of failure and to investigate some design changes that might prevent failure. In this paper the tests conducted to date are described and the results are presented with the aid of diagrams and observations based on motion-picture studies and the probable causes of the failures obtained will be indicated.

An NACA facility at the Pilotless Aircraft Research Station at Wallops Island, Va. was used for these tests. This facility is a blow-down jet that incorporates a heat accumulator for stagnation-temperature control. The model structures are placed in the free jet at the exit of a Mach number 2. 27 × 27 inch nozzle. During a typical test, the stream static pressure is maintained at about one atmosphere and the free-stream temperature at about 75° F. The corresponding stagnation temperature of 500° F provides a temperature potential of 425° that is available to heat the model. These conditions can be maintained in the jet for about 9 seconds following a 2-second starting period. An additional 3 seconds are required to shut down the jet, so that the total elapsed time is 14 seconds per test.

If the model is assumed to be a full-scale structure, the test then accurately reproduces both the aerodynamic heating and loading that would be experienced during a brief flight at Mach number 2 at sea level on a warm day, a rather severe condition. If, however, the model is assumed to be only a quarter-scale structure, the test then reproduces the heating experienced by a full-scale airplane flying at Mach 2 at 40,000 feet for about  $2\frac{1}{2}$  minutes. The local air pressures, however, do not follow the same similarity laws as the heating and would be exaggerated by a factor of four on the quarter-scale model.

The model chosen for the first test was a somewhat idealized section of an untapered, thin skin, multiweb wing as shown in figure 1. The airfoil section was a 5-percent-thick symmetrical circular arc and the model was constructed of 24S-T3 aluminum alloy except for the bulkheads and

CONFIDENTIAL

mounting fixtures which were of steel. The model was mounted vertically in the jet at an angle of attack of  $0^{\circ}$  with its leading edge just downstream of the nozzle exit plane. The model extended completely through the jet with about  $2/3$  of the span in the airstream.

After the jet started, the model remained stationary for approximately  $\frac{1}{2}$  seconds; then, a vibratory motion started and the model was soon destroyed. About  $1\frac{1}{2}$  seconds elapsed between the first sign of trouble and the first failure, an additional second being required for the progressive destruction of the model.

Motion pictures of the test showed that the first sign of trouble was skin buckling near the leading edge. The buckles appeared and disappeared rapidly, moving toward the trailing edge. The cable guys shook loose and a buckle settled in the most rearward skin panel. This panel tore out along rivet lines, the trailing edge piece blew away and progressive disintegration followed until destruction was completed.

A study of this failure indicates that the rapid heating of the model must have been the primary cause of failure or the model would have shown some sign of distress earlier in the test. When the test started, the model was at  $50^{\circ}$  F, but eight seconds later the skin near the leading edge had reached  $332^{\circ}$  while parts of the internal structure had risen to only  $80^{\circ}$ . The temperature distribution in the model will be discussed in more detail in the next paper by George E. Griffith. For the present purpose, it is sufficient to know that the model temperatures increased at a rapid rate and varied greatly throughout the model.

The principal structural effect of this rapid, nonuniform heating was that substantial thermal stresses were induced in the model, including compressive stresses in the chordwise direction sufficient to buckle the skin. These particular stresses result from the restraint provided by the bulkheads located outside the jet. The buckled model skin apparently created an unstable aeroelastic condition that resulted in some form of localized flutter. Initially, it was thought that panel flutter may have caused the failure, but the available data on panel flutter and subsequent tests of similar models indicate that the phenomenon observed in this test was not the form of panel flutter discussed in a previous paper by John E. Baker and Maurice A. Sylvester, but a more complex type of flutter.

The first test yielded very little data on the failure and in itself was not conclusive because of certain peculiarities of the model and its supports. Additional tests were conducted with smaller models like that shown in figures 2 and 3. These models represented small

wings of 20-inch chord and span that extended into the jet from a support somewhat representative of the side of a fuselage. The models extended into the jet through a plate parallel to and just inside the lower jet boundary. They were seven inches short of spanning the jet. All models had 5-percent-thick, symmetrical circular-arc airfoil sections.

The table presented as figure 4 lists some significant dimensions of the various models tested. The model numbers are listed in the first column. The other columns give the material, the skin thickness  $t_S$ , the thickness of the internal webs  $t_W$ , the thickness of internal ribs  $t_R$ , if any, and finally the thickness of the tip bulkhead  $t_B$ , all dimensions being in inches. Thus, the second model was constructed of 24S-T3 aluminum alloy and it had a skin thickness of 0.064 inch. The internal webs were 0.025 inch thick, and no internal ribs were used, but a 0.25-inch bulkhead was placed at the tip. This second model was essentially a half-size version of the first model, although some of the construction details were changed.

This model was tested in the same manner as model 1, and although its thinner skin heated faster, it survived longer than the first one. The first evidence of trouble was buckling of the most rearward skin panel about 10 seconds after the test started. The tip of the trailing edge separated about  $1\frac{1}{2}$  seconds later and successive pieces were peeling off when the air supply was exhausted 14 seconds after the test started. If the jet had continued to run, the model probably would have been completely destroyed.

In the motion pictures of the test, the skin buckle, near the tip and just forward of the trailing-edge member, seemed stationary, but close study revealed a definite suggestion of vibration. The same sequence of events was observed in both side views of the model, that is, skin buckling, vibration, and successive disintegration. The top view, however, showed that the model was fluttering prior to failure and that the initial fracture included a part of the tip bulkhead. The flutter continued as the model broke up. The vibrations were particularly severe while the jet was shutting down, but this latter action is a characteristic of the jet and is not associated with the heating or failure of the model.

The failure of this second model was fundamentally the same as that of the first in that skin buckling induced the model to flutter and then fail. Certain differences were evidenced in the shape of the buckle and the longer time required to induce failure. These differences can be explained in part by the change in detail design, particularly in the tip region, and the resulting changes in the thermal stress distribution.

CONFIDENTIAL

The skin of this model was heated very rapidly, a point near the leading edge rising from 74° F to 400° F in 10 seconds, at which time the skin temperature was beginning to stabilize although some of the webs had risen to only 240° F. This temperature distribution induced thermal stresses in the model, particularly compressive stresses in the hot skin. Differential expansion between the skin and webs caused compression in the spanwise direction while the restraint offered by the tip and root ribs created compression in the chordwise direction. Approximate calculations and the recorded strains indicated that these two types of stresses were of about the same order of magnitude, around 6,000 psi. The chordwise stresses were the more important, however, because the stresses in this direction were of the same order of magnitude as the critical chordwise compressive stress. This critical stress was only 1/4 of the critical stress in the spanwise direction because of the long narrow skin panels. The concentration of the buckling near the tip indicates that the tip rib was a major factor, an observation further supported by the fact that the initial fracture was apparently a tension failure of the tip rib at a section weakened by several rivet holes.

The strain-gage data collected during this test provided some approximate values of the static thermal stresses, as mentioned before, but these data are not very reliable because of large temperature effects on the strain gages. These data shed additional light on the failure, however, in that they give the frequency and phasing of vibrations of some parts of the model. At the time of failure, the model was fluttering at about 230 cycles per second. The model did not experience flutter of the individual panels, but a chordwise mode in which the airfoil section vibrated with about  $1\frac{1}{2}$  waves along the chord and with the maximum amplitude in the vicinity of the trailing edge. Thus, the motion pictures of the test show this flutter as a "tail-wagging" action.

The results of this test, then, indicate that the immediate cause of failure, chordwise flutter, was induced by thermal buckling of the model skin. If this analysis is correct, then, both flutter and the resulting failure should not occur if buckling is prevented. Structural changes that may prevent buckling are an increase in skin thickness, a reduction in the stiffness of the tip rib, or the addition of transverse ribs. Each of these changes has been incorporated in a test model. Changes in the root connection have not yet been investigated because the test of model 2 indicated that the buckling occurred in the tip region.

Model 3 was nearly identical to model 2, as shown in figures 2 and 4 except for the skin thickness which was increased from 0.064 to 0.081 inch. This change not only increased the critical stress of the

CONFIDENTIAL

skin but also decreased the thermal stresses induced during the test. This model showed no signs of distress when tested at zero angle of attack. The 27 percent increase in skin thickness was thus sufficient to prevent buckling and failure. This model was also tested at angles of attack of  $1.5^{\circ}$  and  $3^{\circ}$  and it survived both without difficulty. In the final test at an angle of attack of  $5^{\circ}$ , however, the model failed statically. This failure was expected since the calculated aerodynamic loads were about 1000 pounds per square foot, enough to cause compressive buckling of the skin near the root.

The motion pictures of the final test of model 3 showed that the model vibrated during the starting period, stabilized as soon as supersonic flow was established, and then flopped over when the dynamic pressure reached the required level.

Model 4 was similar to model 2 except for a change in the tip bulkhead, a light bulkhead 0.025 inch thick being used instead of the 0.25-inch bulkhead on model 2. This change was expected to reduce the thermal stresses in the tip region and prevent skin buckling. This model showed no particular evidence of buckling during the test, but it went into a chordwise flutter mode about 5 seconds after the jet started. The vibrations increased in amplitude very rapidly and the model was torn off at the root less than  $1/2$  second after the flutter began.

The movies of this test showed the usual initial model vibrations associated with jet starting. The model then remained stationary until a hint of trouble occurred, after which it was suddenly torn off at the root. High-speed motion pictures taken at 650 frames per second, however, clearly show the chordwise flutter mode of about  $1\frac{1}{2}$  waves along the chord. The flutter increased in severity until the airfoil section became greatly distorted. The model then began to flop over and a fracture started at the leading edge near the root. This fracture quickly proceeded to the trailing edge, severing the model from the supporting structure.

The analysis of this test has not yet been completed, but the preliminary results show that model 4 was fluttering at 240 cycles per second, about the same frequency as model 2. The amplitudes were larger on model 4, however, because the light tip bulkhead offered very little resistance to chordwise distortion. The large reduction in the stiffness of the tip bulkhead was thus completely ineffective in preventing failure; it had the opposite effect since the failure occurred sooner and more violently.

Models 5 and 6 incorporated chordwise ribs as shown in figures 3 and 4. These ribs were the same distance apart as the webs, forming

square skin panels, so that the critical stress in the chordwise direction was raised to a safe value. Model 5 was similar to model 2 except for the ribs, whereas model 6 had a thinner skin, with a thickness of 0.050 inch instead of 0.064 inch. The thinner skin should lead to higher thermal stresses and lower critical values; however, the stresses should still not exceed the critical. Each model was tested at an angle of attack of 0° and survived the test in good condition.

In addition to preventing thermal buckling of the skin, the use of internal ribs further discourages chordwise flutter because of the extra stiffness provided. Some of the natural modes of vibration of models 4 to 7 were determined experimentally and those without internal ribs experienced modes involving cross-sectional distortion at much lower frequencies than those with ribs. The second bending frequency of the ribbed models was easily determined, but it was not found for the ribless ones because of the more predominant chordwise modes.

The last model (model 7) to be discussed was similar to model 2 but the material was changed, mild steel being used instead of aluminum alloy. The change in material was accompanied by a reduction in skin and web thicknesses such that the critical compressive stress of model 7 was about the same as that of model 2. The thicknesses of steel used were 0.043 inch for the skin and 0.018 inch for the webs. Thus, model 7 weighed over twice as much as model 2 but had only slightly more static strength. The changes should have resulted in high thermal stresses in model 7, so that the skin was expected to buckle and initiate chordwise flutter of the model. Model 7 did not react as expected, however, in that it survived the test in good condition. Nevertheless, there was some slight evidence of surface distortion at the end of the test. Analysis of this test is as yet incomplete and the preliminary results have failed to reveal the conditions that prevented thermal buckling; however, the change of materials was, without doubt, an important factor.

In conclusion, seven small multiweb wing structures have been tested under simulated supersonic flight conditions. The significant dimensions of these wings are listed in figure 4. Models 1, 2, and 4 failed dynamically as a result of chordwise flutter. This flutter was incited apparently by thermal buckling of the skin that was, in turn, induced by aerodynamic heating. These three models were basically alike but incorporated different tip bulkheads. The characteristics of the failure were affected by the changes in chordwise stiffness, with model 4 (the one with the lightest tip bulkhead) experiencing the most violent flutter. The other models were similar to model 2 but incorporated structural modifications that prevented flutter. Thus the thicker skin of model 3, the internal ribs of model 5, and the steel material used in model 7 were each effective. The internal ribs were not only effective in preventing flutter of model 5, which had the same skin thickness

as model 2, but they also prevented flutter of model 6 which had even thinner skin. From the weight standpoint, the use of internal ribs was the most efficient method of preventing flutter of the particular configuration investigated. On the other hand, the conversion to steel resulted in a two-fold increase in the weight of that part of the structure exposed to the jet. The use of internal ribs, however, may not be the most efficient method of preventing chordwise flutter of other multiweb wing designs. It is also well to point out that all these tests were of very brief duration and that the models were still experiencing transient heating when the air supply was exhausted; thus, they may not have survived a longer test.

Research on the structural problems associated with transient aerodynamic heating is still in its early stages, but the implications of the tests described here are clear. The effects of aerodynamic heating and loading on aircraft structures must be considered as a single, combined problem, or factors which vitally affect the structural integrity of an aircraft may be overlooked.

CONFIDENTIAL

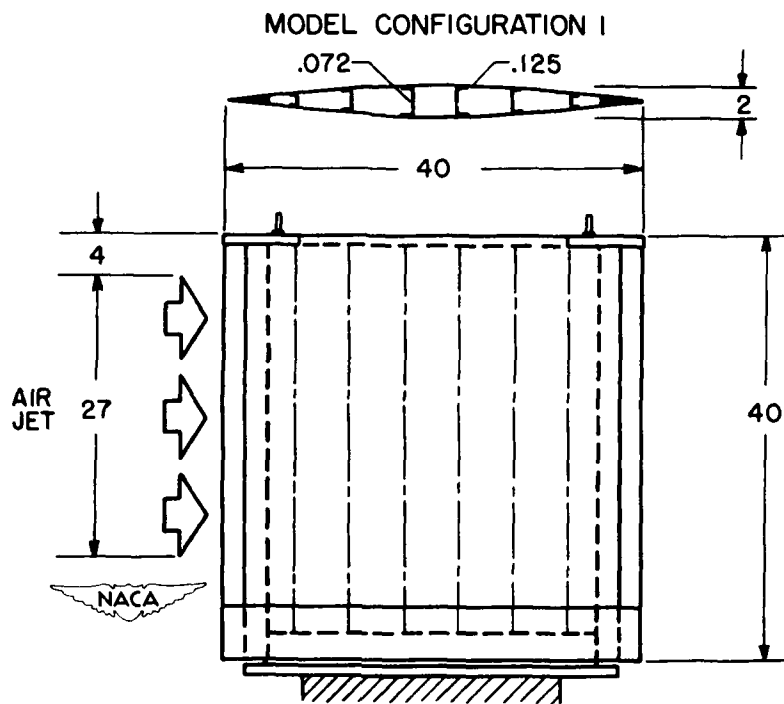


Figure 1.

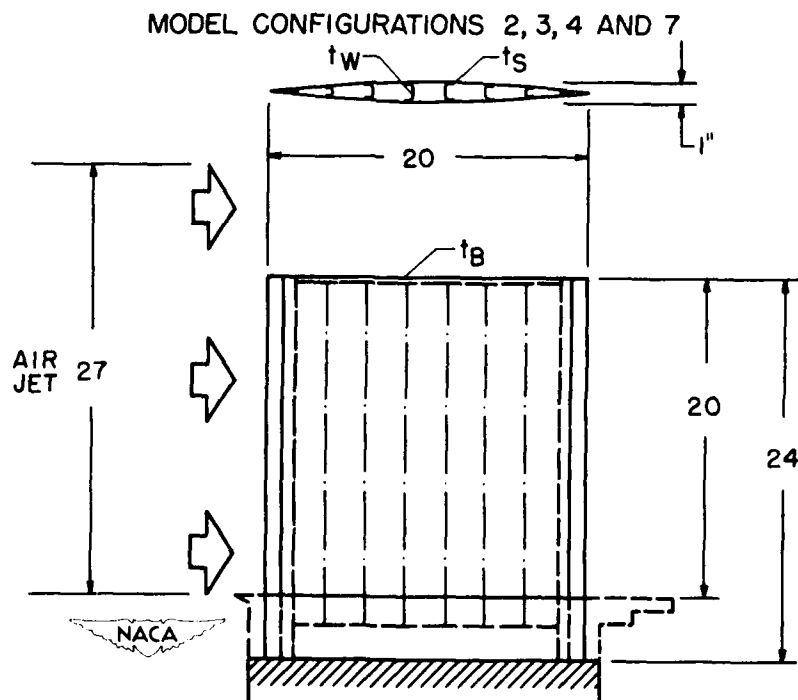


Figure 2.

CONFIDENTIAL

## MODEL CONFIGURATIONS 5 AND 6

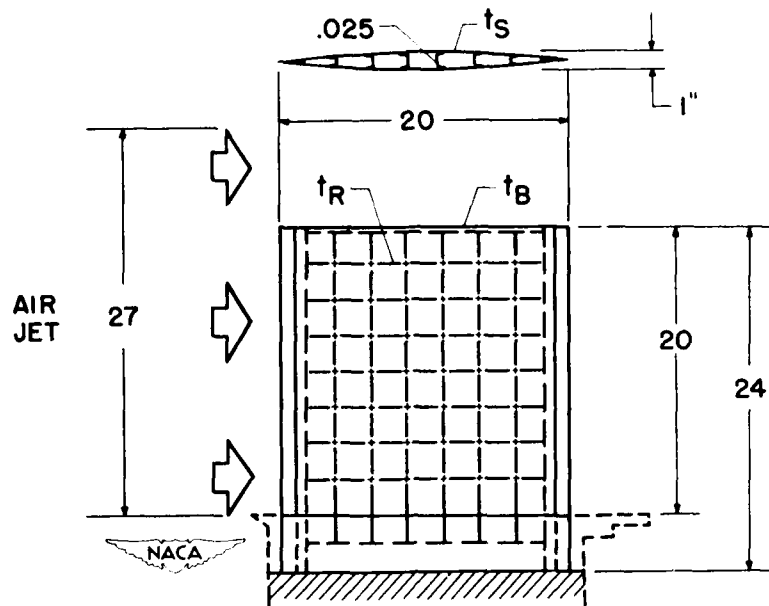


Figure 3.

## MODEL DIMENSIONS

MODEL	MAT.	$t_s$	$t_w$	$t_r$	$t_b$
1	24S-T3	0.125	0.072	—	1*
2		.064	.025	—	.25
3		.081		—	.25
4		.064		—	.025
5		.064		0.025	.25
6		.050		.025	.25
7	STEEL	.043	.018	—	.25

\* STEEL BULKHEAD

Figure 4.

TRANSIENT TEMPERATURE DISTRIBUTION IN AN  
AERODYNAMICALLY HEATED MULTIWEB WING

By George E. Griffith

Langley Aeronautical Laboratory

In order to determine the structural effects of transient aerodynamic heating, the first requisite is a knowledge of the temperature distribution throughout the structure. Methods exist for predicting the temperatures, but there is a lack of test data to check their reliability, particularly in or near internal stiffening where heat conduction effects are important. The purpose of this paper is to present some experimental data obtained on a model with such stiffening, to describe procedures for calculating the temperatures, and to show the correlation existing between the experimental and calculated results.

The experimental values were obtained from the first model described in the previous paper by Richard R. Heldenfels and Richard J. Rosecrans. But before looking at the test results, let us first consider means of predicting the temperatures. In aerodynamically heated structures, heat from the boundary layer is either absorbed by the skin or else conducted to other parts of the structure, radiated to the atmosphere, or transferred to the contents by conduction, convection, or radiation. For the problem under consideration only absorption and conduction are of any significance, since at the low temperatures involved, radiation from the model to the atmosphere is negligible, and very little heat is lost to the air contained within the model.

Figure 1 shows a few of the possible methods of calculating the temperatures. As a means of approximating the skin temperature away from any heat sink, consider an element of skin as shown for method I in the figure. Heat conduction along the skin is assumed to be negligible; hence all the heat from the boundary layer is used in raising the temperature of the skin element. The simple heat balance at this point is described by an ordinary differential equation. (See, for example, ref. 1.)

To find the temperatures through a thin slice of a uniformly heated solid section or through a very thick skin, consider the slab geometry, method II. This geometry is similar to the first except that the thickness has increased considerably. Again the horizontal flow of heat is considered negligible, but now some of the heat entering from the boundary layer is conducted vertically along the material. Addition of the single space dimension leads to a partial-differential equation, but the heat-conduction problem is still a simple one (which can be solved as indicated in ref. 2, p. 801).

Consider, as shown in figure 1 for method III, a piece of skin with a web or stiffener attached. Heat enters from the boundary layer but near the stiffener a considerable amount of the heat is conducted along the skin, then down into the stiffener. Because of the change in geometry, this heat-conduction problem is considerably more difficult than the previous ones; again a partial-differential equation applies.

For a portion of any solid section, method IV, heat from the boundary layer can be conducted both vertically and horizontally. This two-dimensional flow of heat represents a difficult problem and leads to a more complicated partial-differential equation.

Methods I and II denote approximations to the actual conditions, whereas methods III and IV can be considered as representing the true conditions; likewise, although methods I and II are simple to solve, methods III and IV are complex. It is desirable to use the least complicated method whenever the results agree satisfactorily with experiment. Solutions to the partial-differential equations, especially of the forms used for methods III and IV, are difficult and tedious to obtain, but other methods - only slightly less exact - yield essentially the same results. As indicated in the key, the same procedure was used for both methods III and IV - in this case, a numerical procedure. (See ref. 2, pp. 806, 807, and 816.)

As a first step in calculating the temperature distribution throughout the multiweb wing, the wing cross section was subdivided into the two regions shown in figure 2, one for the leading or trailing edge, the other for any skin and web combination. This simplification in geometry assumes that the rate of change of the temperature across the boundaries - at the skin extremities and along the center line - is zero, or that no heat enters or leaves at these points. The results indicate that this is a valid assumption for this type of structure. Complete temperature distributions, using methods III and IV, were found for each of the two geometries shown. In addition, skin temperatures and temperatures in the webs and at some points in the interior of the solid nose section were approximated, as indicated in figure 1, using methods I and II.

The heat-transfer coefficients used in the calculations were obtained using turbulent flow, flat-plate theory based on local flow conditions just outside the boundary layer of the circular-arc airfoil. (See ref. 3.) The adiabatic wall temperature was obtained by extrapolating the experimental skin temperature histories.

Shown in figure 3 are typical temperature histories of two points, one on the skin removed from the heat sink afforded by the web, and one at the web center line. Experimental and calculated temperatures are plotted against the time. The skin temperature - represented by the

circles - rises rapidly to a final value of about  $305^{\circ}$  F in 8 seconds, considerably less than the adiabatic wall temperature of  $446^{\circ}$  F. On the other hand, the web temperature is lower and lags considerably behind the skin temperature; this condition illustrates that some time elapses before heat can be conducted down into the web and that, since the web temperature at the end of the test is still much lower than the skin temperature, an appreciable additional time would be needed to reach the steady-state condition.

Results predicted by both methods I and III agree well with the measured skin temperature, but method III overestimates the true web temperature, possibly because the riveted joint between skin and web offers some resistance to the flow of heat not taken into account in the analysis. Method II underestimates the web temperature because it does not account for the horizontal flow of heat along the skin and into the web.

Figure 4 shows temperature distributions at both 4 and 8 seconds for a skin and web combination. Skin temperatures are plotted vertically above the skin and the web temperatures horizontally to the right. Experimental skin temperatures are shown as circles, experimental web temperatures as squares. Method III, which gives the complete temperature distribution, agrees well with the skin temperatures because of the conduction of some of the heat into the web. These temperatures are somewhat lower where the web flange joins the skin. Method I, using the combined thickness of skin and web flange where they are in contact, gives almost as good agreement but is not so reliable for the skin alone close to the web. As illustrated in figure 3, method III predicts temperatures in the web generally higher than the experimental values. The temperatures at both 4 and 8 seconds are shown to illustrate that even at the lower temperatures appreciable differences exist between the skin and interior temperatures. Perhaps it is well to recall that the magnitudes of any induced thermal stresses depend upon such differences.

Similar temperature distributions for both 4 and 8 seconds are shown in figure 5 for the leading-edge section. Center-line temperatures for the solid section and skin temperatures are plotted above the surface. Because of the difficulty in thermocouple installation, only two thermocouples (located as shown in the fig.) give a basis for comparison with the calculations. Method III is in fairly good agreement with the experimental values for both the solid section and the skin. Method I agrees well with the experimental skin temperature but overestimates the skin temperature near the solid section. Method II shows good agreement with the experimental temperature in the solid section. This agreement indicates that in this section heat from the boundary layer is conducted generally downward into the interior with little heat conducted sidewise

CONFIDENTIAL

which is also substantiated in that the variation through the thickness (not shown) is quite small - a maximum of approximately  $15^{\circ}$ . The temperatures at different times have been shown in order to give an indication of how the temperature distribution changes with time.

Shown in figure 6 is the temperature distribution for the entire model, including center-line temperatures for the solid leading and trailing edges, skin temperatures, and temperatures at the center line of the webs. Calculated temperatures were obtained using method III. Experimental skin temperatures appear as circles and interior center-line temperatures as squares. Generally good agreement exists between the calculated and measured temperatures. Note the sink effects of the webs and solid sections. Although the temperatures shown are not very high, differences in excess of  $200^{\circ}$  F occur between the surface and interior sufficient to produce substantial thermal stresses.

This discussion has been limited to only the first of the several models tested, and described in the previous paper by Richard R. Heldenfels and Richard J. Rosecrans. The data shown are fairly representative of the results obtained for the other models, although the agreement in some cases was not as good as for the model illustrated. No pronounced effects were observed with small changes in angle of attack; as the angle of attack increased the lower surface became hotter slightly faster than the upper surface, as predicted by the local heat-transfer coefficients.

In conclusion, comparisons of measured and calculated temperatures in a multiweb wing show good agreement when the significant type of heat flow is taken into consideration. Approximate methods, when used with care, may also give satisfactory results, as, for example, in using method I to predict the skin temperature some distance from a web or stiffener, or in using method II (a slab method) for the interior of solid sections. Approximate methods are less satisfactory in the vicinity of a web or stiffener because the web can drain a large amount of heat from the skin. Since the magnitude of heat drained by such a heat sink is a function of the geometry and materials, substantially smaller or larger discrepancies might be obtained for different structures. Approximate methods, then, are advisable in some cases, but judgement - based upon a physical understanding of the possible heat flow - should be exercised in using them.

CONFIDENTIAL

## REFERENCES

1. Lo, Hsu: Determination of Transient Skin Temperature of Conical Bodies During Short-Time, High-Speed Flight. NACA TN 1725, 1948.
2. Kaye, Joseph: The Transient Temperature Distribution in a Wing Flying at Supersonic Speeds. Jour. Aero. Sci., vol. 17, no. 12, Dec. 1950, pp. 787-807, 816.
3. Chauvin, Leo T., and deMoraes, Carlos A.: Correlation of Supersonic Convective Heat-Transfer Coefficients From Measurements of the Skin Temperature of a Parabolic Body of Revolution (NACA RM-10). NACA RM L51A18, 1951.

## HEAT-FLOW CALCULATIONS

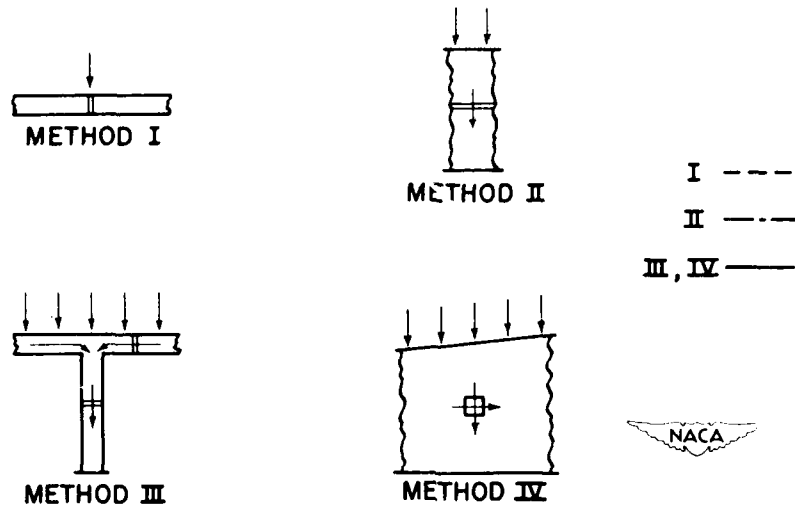


Figure 1.

## SUBDIVISION OF WING CROSS SECTION

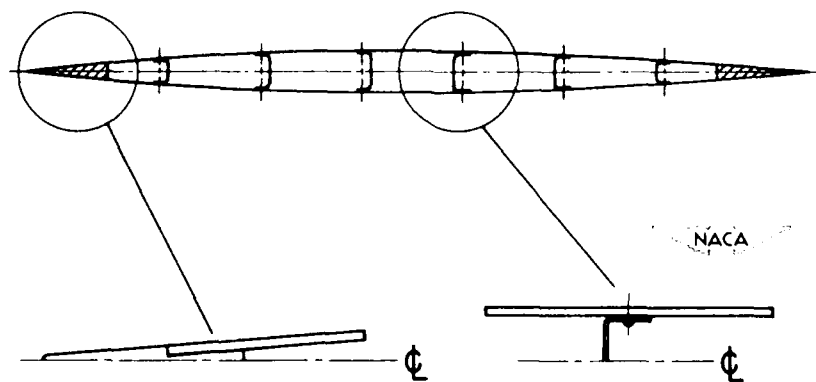


Figure 2.

## TEMPERATURE HISTORIES

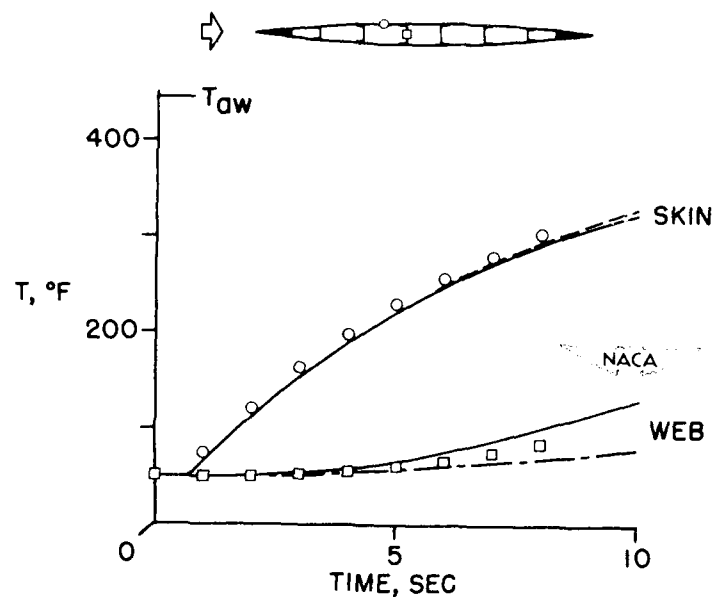


Figure 3.

## SKIN AND WEB TEMPERATURE DISTRIBUTION

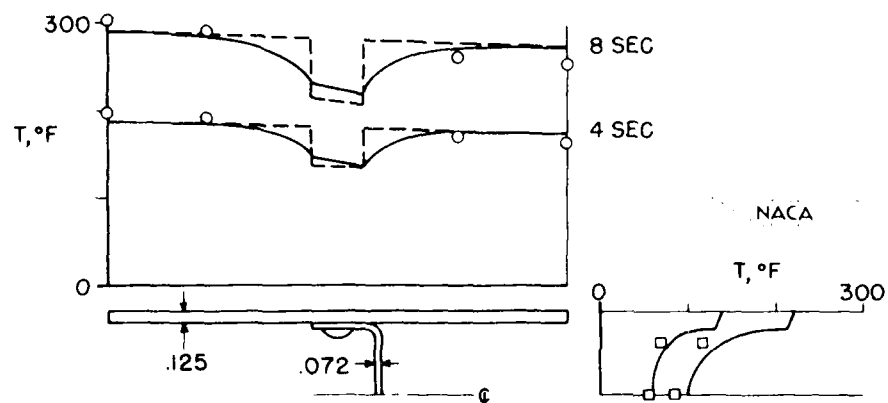


Figure 4.

## NOSE-SECTION TEMPERATURE DISTRIBUTION

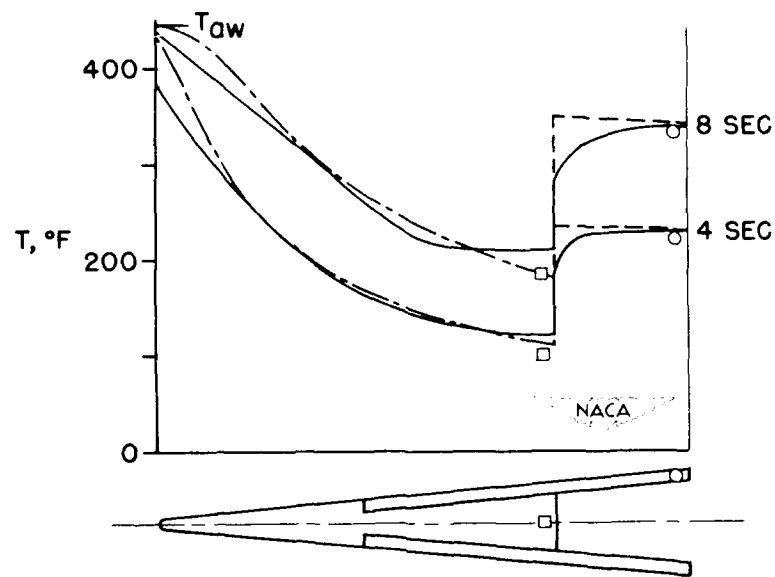


Figure 5.

## TEMPERATURE DISTRIBUTION AT 8 SECONDS

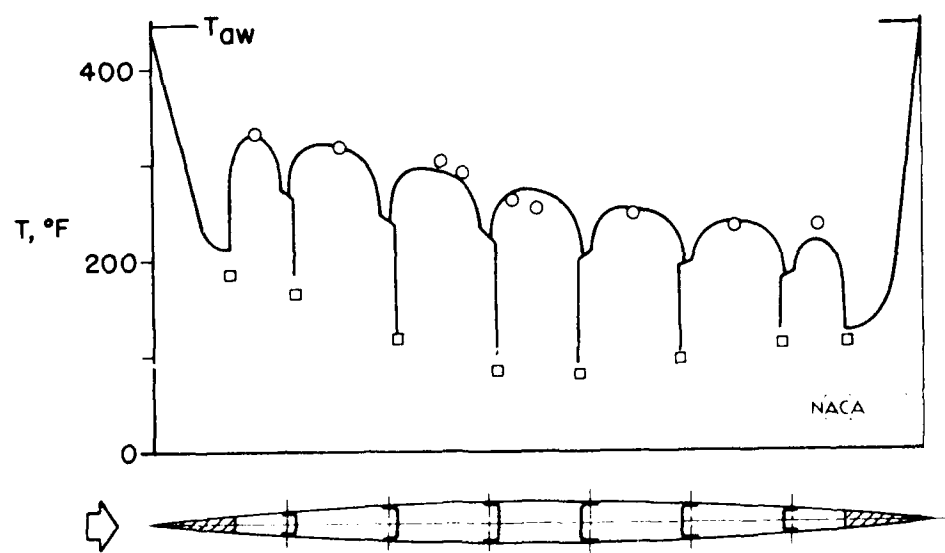


Figure 6.

STRUCTURAL EFFICIENCIES OF VARIOUS ALUMINUM, TITANIUM,  
AND STEEL ALLOYS AT ELEVATED TEMPERATURES

By George J. Heimerl and Philip J. Hughes

Langley Aeronautical Laboratory

43

The effect of steady rather than transient heating conditions on the properties of materials are considered in this paper. An attempt will be made to give a general picture of the efficient temperature ranges for a few high-strength aluminum, titanium, and steel alloys for some short-time compression-loading applications in which creep is not a factor. Both the properties and the weights of the materials are considered in the analysis. Some of the materials, such as the titanium alloys RC-130A and RC-130B, the aluminum alloy XA78S-T6, and the steel Stainless W, are relatively new. The materials cover a wide range of strengths and densities. In order to provide data for making the comparisons, compressive stress-strain tests were made at normal and elevated temperatures. The materials were kept at the test temperature approximately 1/2 hour before the load was slowly applied.

Figure 1 shows the variation of Young's modulus of elasticity with temperature obtained for two high-strength aluminum alloys (extruded 75S-T6 (ref. 1) and XA78S-T6 sheet), two titanium alloys (RC-130A sheet and RC-130B forging), and three heat-treated sheet steels (SAE 4340, Stainless W, and Inconel X). At normal temperatures the moduli vary from about  $10 \times 10^6$  psi for the aluminum alloys to  $17 \times 10^6$  psi for the titanium alloys and about  $30 \times 10^6$  psi for the steels. The moduli for all the materials reduce with temperature, the effect becoming more pronounced as the temperature increases.

Figure 2 shows the variation of the compressive yield stress (0.2-percent offset) with temperature found for these materials. The strengths range from about 30 ksi for the aluminum alloys to about 220 ksi for the steels at normal temperatures. With the exception of Inconel X, a marked decrease in strength with increase in temperature is evident in all instances. The aluminum and titanium alloys and two of the steels have lost about half their normal strength at approximately 400° F, 800° F, and 850° F, respectively. Inconel X, a good high-temperature material, shows almost a negligible effect of temperature over the range covered.

From the results given in the two figures, together with the use of the stress-strain curves, various structural-efficiency comparisons can be made. First the materials are compared on a strength-efficiency basis with the compressive yield stress as the criterion for strength and the density taken into account. The steels are approximately three times as

heavy and the titanium alloys one and two-thirds times as heavy as the aluminum alloys. Figure 3 shows the strength-efficiency comparisons. The stress-density ratio, the ordinate, measures the efficiency of the material - the higher this ratio, the more efficient the material on a strength-weight basis. With the exception of Inconel X, all the materials are about equally efficient at normal temperatures. The steels and titanium alloys retain this efficiency much better than the aluminum alloys as the temperature increases. The steels appear to be somewhat more efficient than the titanium alloys from about 300° F to 800° F. Inconel X is the most efficient material above about 950° F.

The materials are now compared on an elastic stiffness-efficiency basis in figure 4. Here the modulus-density ratio is the measure of the efficiency. At normal temperatures, the materials all have roughly the same efficiency. The efficiency for the aluminum alloys, however, decreases rapidly with increase in temperature. At the higher temperatures, the steels are the most efficient of the materials on this basis and the titanium alloys are next in order.

For column buckling and the buckling of long plates in compression or in shear, the structural efficiency for a material at a given temperature is found by a somewhat more complicated method by plotting the calculated buckling stress-density ratio against an appropriate structural index (see ref. 2). Rather than show all these curves for each material and temperature, comparisons are made over the temperature range only for a small and a large value of the index for each application. The comparisons of the materials for column buckling are shown in figures 5 and 6. Figure 5 is for a small value of the index, corresponding to a small load or long column. In the index,  $P_{cr}$  is the buckling load,  $c$  is the end fixity,  $f$  is the shape factor, and  $L$  is the column length. The efficiency is measured by the stress-density ratio, the stress being the buckling stress associated with the buckling load  $P_{cr}$ . The aluminum alloys are the most efficient up to about 300° F; from about 300° F to 900° F, the titanium alloy RC-130B is the most efficient; at still higher temperatures, Inconel X is the best. Figure 6, for a large value of the index corresponding to a large load or short column, indicates quite a different comparison. In this case, with the exception of Inconel X, all the materials now have about the same efficiency up to about 300° F. From there up to about 800° F, the titanium alloys and two of the steels have about the same efficiency; above about 950° F, Inconel X is the most efficient.

The efficiencies of the materials are compared in figures 7 and 8 in a similar manner for the buckling of long plates in compression for small and large values of the plate index. In figure 7, comparisons are made for a small value of the index, corresponding to a small load or wide plate. In this index,  $P_{cr}$  is the buckling load,  $k$  is the plate

buckling coefficient, and  $b$  is the plate width. The efficiency is measured by the stress-density ratio, the stress being the buckling stress. For plate buckling, the advantages of the light-weight materials are evident, the aluminum alloys being the most efficient up to about  $450^{\circ}$  F and the titanium alloys from  $450^{\circ}$  F up to about  $1,000^{\circ}$  F. Above  $1,000^{\circ}$  F, Inconel X is the most efficient. Figure 8, for a large value of the index corresponding to a large load or narrow plate, shows that the same order of efficiency still holds, although the efficient temperature range for the aluminum alloys is reduced to about  $300^{\circ}$  F. Inasmuch as both the efficiency and the index for shear loading are proportional to those for compression loading, the comparisons for plates loaded in compression also apply to plates loaded in shear (ref. 2).

Figure 9, which summarizes the comparisons, indicates in a general way the efficient temperature ranges and the order of efficiency for the various comparisons - compressive strength, elastic stiffness, column buckling, and plate buckling. Parts (A) and (B) for columns and plates signify small and large loads, respectively. In this summary, the most efficient material of each of the class of alloys is taken as the basis for comparison. For each comparison, three bar graphs are shown, the first for the aluminum alloys, the second for the titanium alloys, and the third for the steels. The order of efficiency for each material is indicated by the degree of cross-hatching, with the highest efficiency corresponding to the heaviest cross-hatching as indicated. An example will illustrate the use of the figure. If elastic stiffness at  $300^{\circ}$  F is under consideration, the third bar in the group shows that a steel will be more efficient than a titanium alloy (the second one) which in turn is more efficient than the aluminum alloys. Without going into detail in the comparisons, it can be seen that the high-strength aluminum alloys are either equally or more efficient than the titanium or steel alloys for all applications except stiffness up to about  $300^{\circ}$  F. From about  $300^{\circ}$  F to  $950^{\circ}$  F, the titanium alloys appear to be superior for plate buckling and equally or more efficient for column buckling; these alloys also compare well with steels for compressive strength up to about  $900^{\circ}$  F. The steels are the most efficient for elastic stiffness and equally or more efficient for compressive strength over the entire temperature range. At temperatures above about  $1,000^{\circ}$  F, a heat-resistant steel is the most efficient for column and plate buckling.

In conclusion, it should be recalled that these comparisons apply only to short-time compression loading in which creep is not a factor and that the results for the individual materials are subject to change depending upon the condition and treatment of the material. The final selection of a material for a particular application will also ordinarily depend upon many additional considerations.

## REFERENCES

1. Roberts, William M., and Heimerl, George J.: Elevated-Temperature Compressive Stress-Strain Data for 24S-T3 Aluminum-Alloy Sheet and Comparisons With Extruded 75S-T6 Aluminum Alloy. NACA TN 1937, 1949.
2. Heimerl, George J., and Barrett, Paul F.: A Structural-Efficiency Evaluation of Titanium at Normal and Elevated Temperatures. NACA TN 2269, 1951.

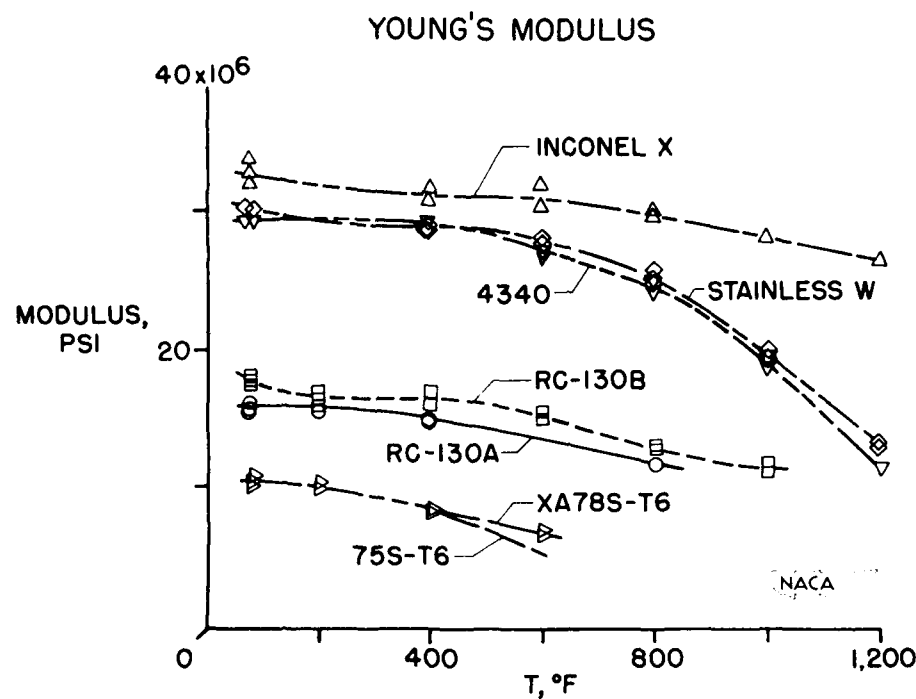


Figure 1.

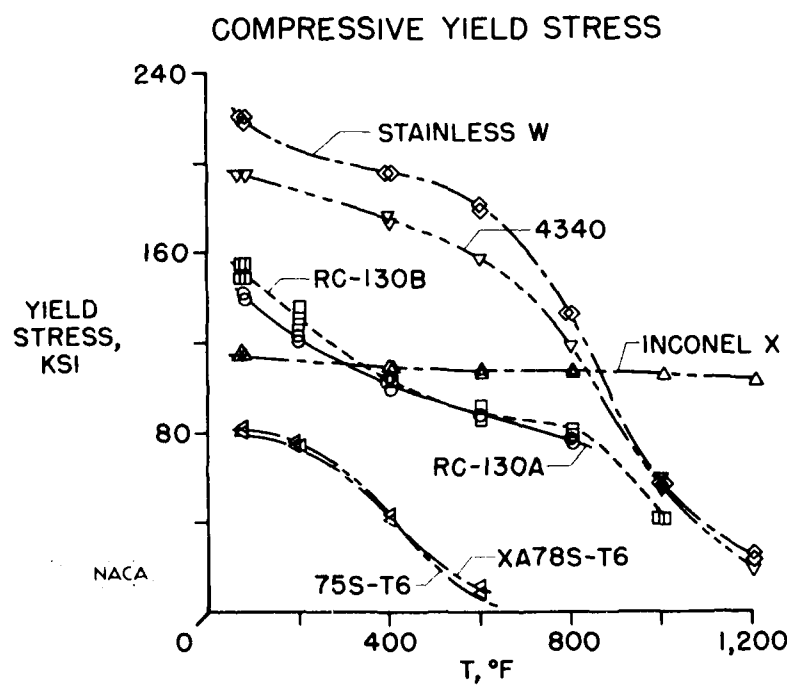


Figure 2.

CONFIDENTIAL

## STRENGTH EFFICIENCY

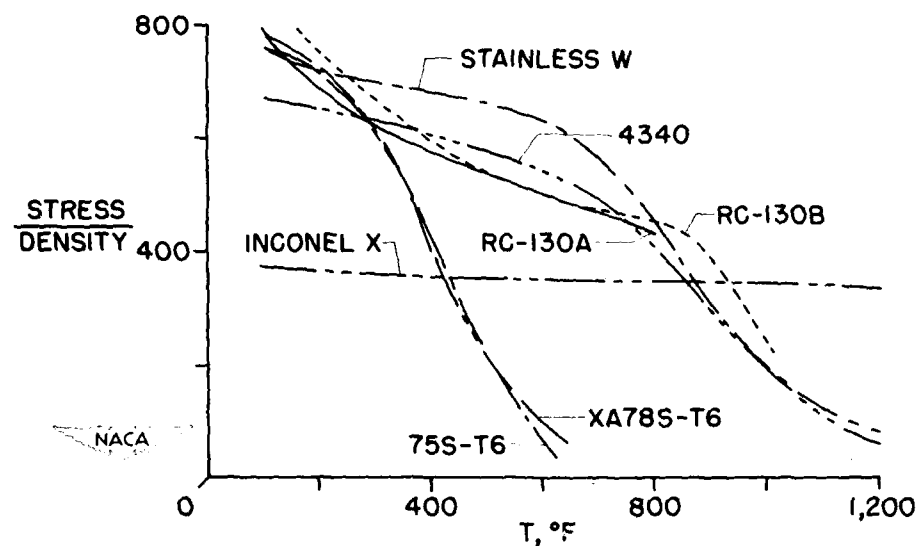


Figure 3.

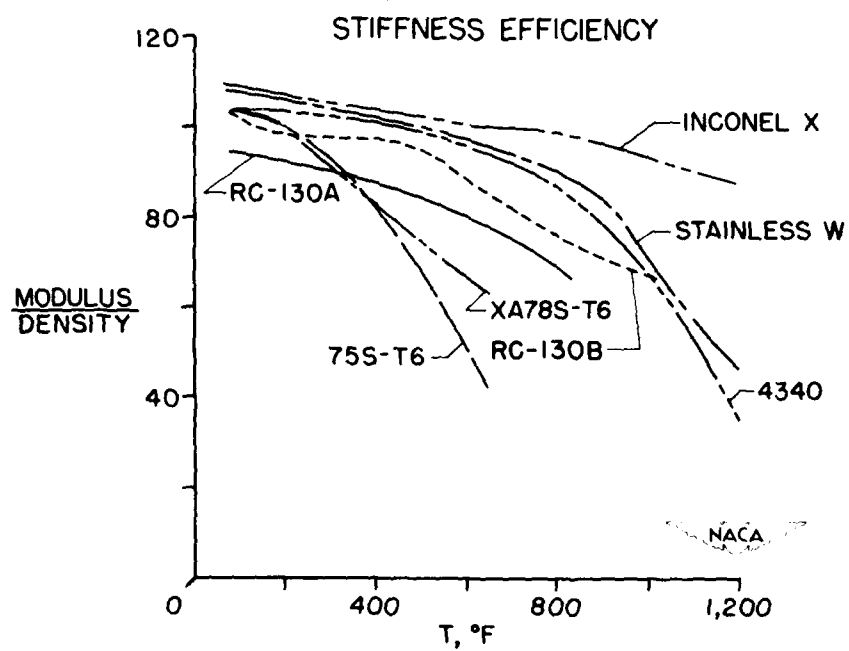


Figure 4.

CONFIDENTIAL

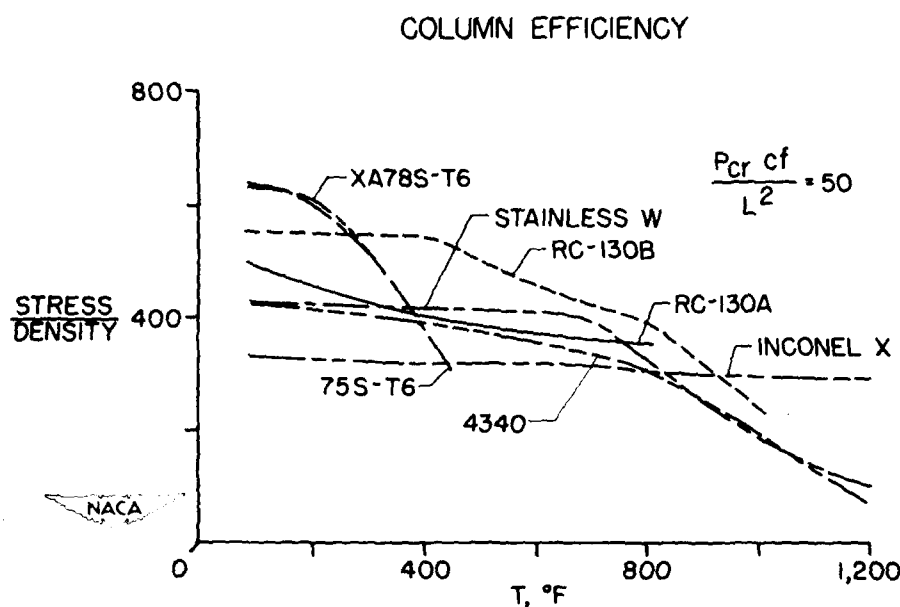


Figure 5.

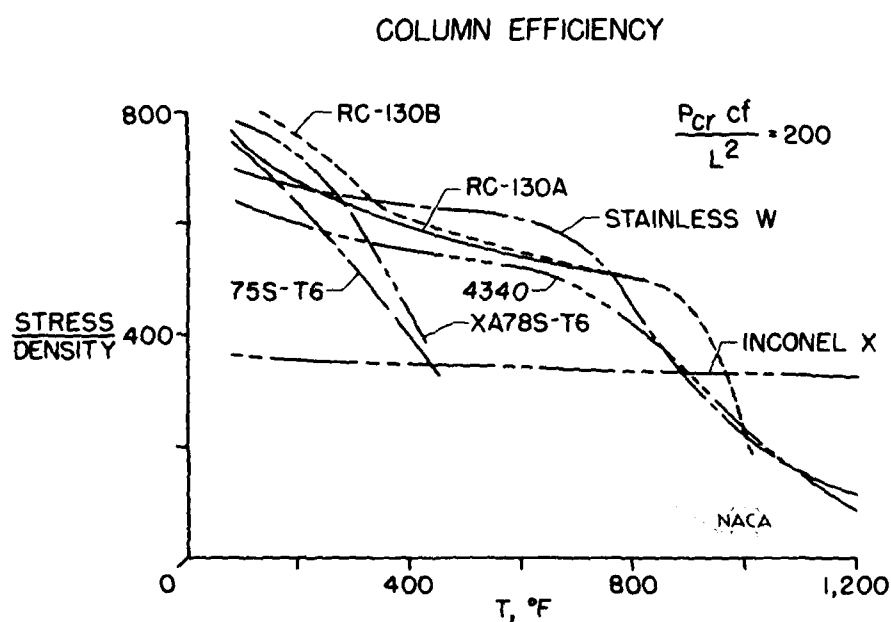


Figure 6.

## PLATE EFFICIENCY

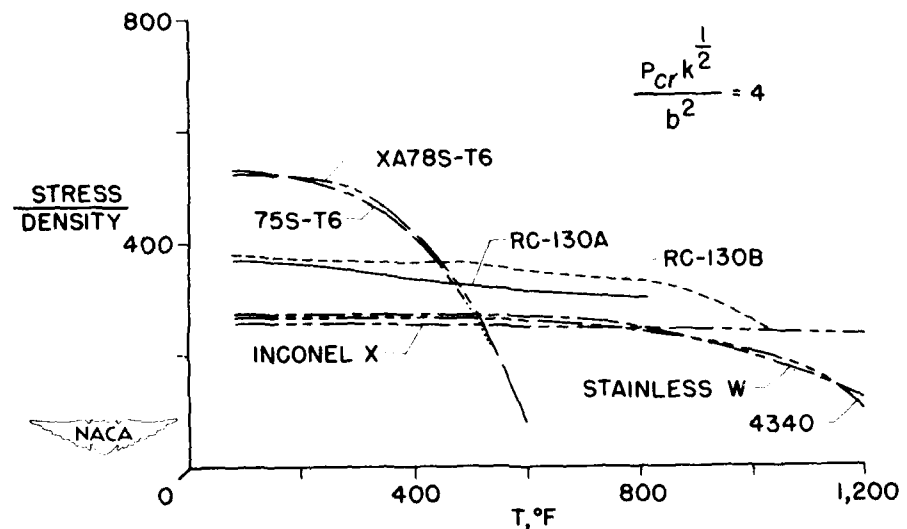


Figure 7.

## PLATE EFFICIENCY

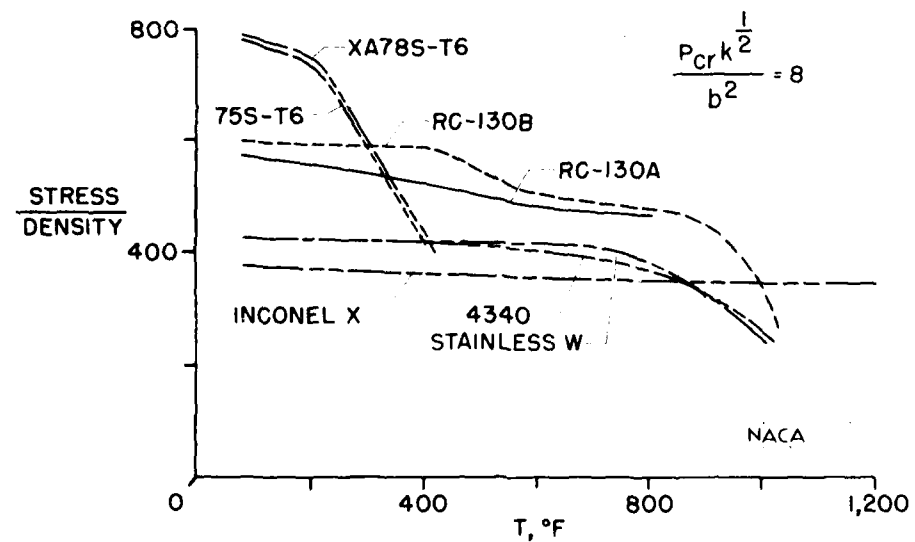


Figure 8.

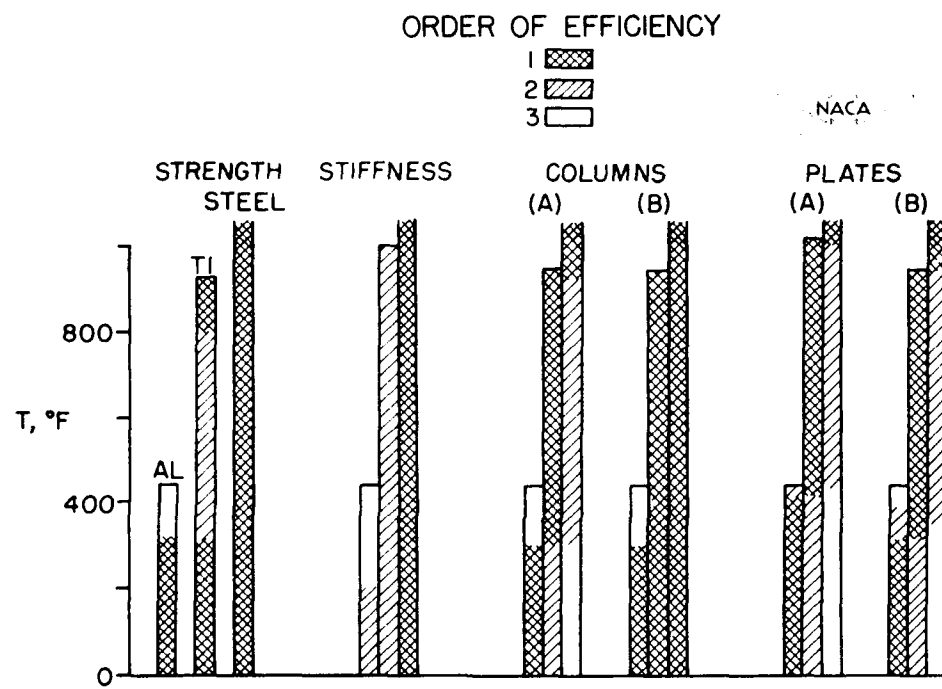


Figure 9.

AN INVESTIGATION OF STRENGTH CHARACTERISTICS OF STRUCTURAL  
ELEMENTS AT ELEVATED TEMPERATURES

By Eldon E. Mathauser and Charles Libove

Langley Aeronautical Laboratory

The determination of the strength of structural elements at elevated temperatures has become increasingly more important because of the aerodynamic heating experienced by aircraft flying at supersonic speeds. As the temperature of the aircraft structure increases, the ability of the structure to support a given load decreases. This decrease in strength is a result of changes in the material properties accompanying temperature increase - notably a lowering of the yield strength and a decrease in the stiffness or modulus of elasticity as well as a decrease in the creep resistance of the material.

As indicated in figure 1 the problem of determining structural strength is actually twofold, namely, the determination of the strength of a member under short-time loading where creep effects do not have to be considered and the determination of the strength under long-time loading where creep within the member must be considered. Some of the methods that are available for determining these strengths for structural elements subject to uniform temperature and which indicate recent theoretical and experimental investigations of the National Advisory Committee for Aeronautics in regard to this problem are reviewed briefly. Three general types of structural elements - columns, plates, and stiffened panels - are discussed.

Insofar as the short-time strengths of columns and plates are concerned, past work on plastic buckling has led to a practical solution of the problem (ref. 1). Briefly, this work indicates that the stress-strain curve is the key to the calculation of buckling and maximum strength. The short-time strength of columns and plates at elevated temperatures can therefore be calculated by making appropriate use of the stress-strain curve which corresponds to the temperature of the structural element. Figure 2, for example, shows the result of such calculations for columns. This figure shows a plot of buckling stress against slenderness ratio for columns made of 75S-T6 aluminum alloy. The solid lines represent the critical or tangent-modulus buckling stresses for the columns at six different temperatures ranging from room temperature to 600° F. The dashed curves show the buckling stresses for the columns as determined by the Euler column formula. The stress-strain curve for the material at each temperature shown was used to obtain the values of tangent modulus necessary in computing the column curves. The maximum loads that can be supported by columns, determined from actual tests, are, in general, in good agreement with these

calculated results. Note that the effectiveness of this material for supporting column loads decreases very rapidly for temperatures above 300° F.

A slightly different approach has been found to be successful for determining the short-time strength of stiffened panels. In the case of columns and plates, the stress-strain curve for the material at the appropriate temperature was used to determine the maximum load for the member. For stiffened panels, an "effective" stress-strain curve is useful. This effective stress-strain curve is obtained by an actual compression test of a short stiffened panel. The results of such a test are shown in figure 3. The solid line is the result of a test at 400° F on a stiffened panel made of 24S-T3 aluminum alloy and shows stress plotted against unit shortening. The dashed line represents the material stress-strain curve at the same temperature. The difference between these two curves shows the effect of local buckling. The panel tested was a short panel with a slenderness ratio  $L/\rho$  of 20. The slopes of this effective stress-strain curve are used in preference to the slopes of the material stress-strain curve for determining values of the tangent-modulus. With this information the maximum loads for panels of identical cross section but of longer lengths can be determined from the generalized Euler column formula. Figure 4 shows a comparison between calculated maximum stresses for stiffened panels and experimentally determined maximum stresses. The solid-line curves were obtained by making use of the effective stress-strain curve for the panel at the appropriate temperature. The test points shown are the maximum stresses determined from laboratory tests on stiffened panels made of 24S-T3 aluminum alloy. The figure shows that satisfactory agreement exists in general between the calculated maximum stresses and the experimentally determined maximum stresses for the panels at both of the temperatures indicated.

In the study of long-time or creep strength of structural components, the most work, both theoretical and experimental, has so far been done on columns. A theoretical analysis was made at the NACA of the creep behavior of an idealized H-section column under constant temperature and constant load (ref. 2). This work has recently been extended to the solid-section column (ref. 3).

In the analysis of the creep strength of a solid column, a material creep law was selected in the form presented in figure 5 where  $\epsilon$  is the total strain,  $\sigma$  is the applied stress for the creep test, and  $t$  is the time after application of the stress. The symbols  $A$ ,  $B$ , and  $K$  designate material constants whose values depend on the temperature and  $E$  is Young's modulus which is also a function of the temperature. The total strain is composed of two parts - an elastic part which results immediately upon application of the stress and a time-dependent part. This type of creep equation was suggested by Battelle Memorial Institute

for 75S-T6 aluminum alloy at 600° F and since has been found to hold approximately for this material at other temperatures and for at least one other material - a low alloy steel at 800° F and 1100° F. The type of creep curves which this creep relation implies are shown for several values of stress. The exponent K whose numerical value is less than 1 causes the creep curves to be concave downward. If the value of K were 1, the creep curves would be straight lines. The curves shown approximate those for 75S-T6 aluminum alloy at 600° F for which  $K \approx 2/3$ .

Shanley's creep hypotheses were used as a basis of generalizing the creep law to cover stress varying with time. The usual assumptions which permit the use of elementary beam theory were made regarding the column. In addition, it was assumed that the column was pin-ended, that the initial curvature was in the form of a half sine wave, that the deflected shape always remained sinusoidal but the amplitude increased with time, and that the load was applied rapidly enough so that negligible creep occurred during the loading period but not so rapidly that dynamic effects had to be considered. The equations resulting from the analysis of the solid column are quite difficult to solve, but useful parameters have been obtained from these equations. These parameters will be shown later in connection with experimental test results.

The experimental study of the creep strength of columns at the NACA was confined to short-time creep tests which lasted a few hours rather than hundreds of hours. The purpose of the experimental study was two-fold - to obtain design data as well as to correlate the data with the parameters of the previously mentioned theory. The columns were made of 75S-T6 aluminum alloy which was selected because the creep law previously shown was found to apply to this material. The columns were tested in a pin-ended condition at temperatures ranging from 300° F to 600° F. The midheight deflection was recorded autographically against time during the creep test. A typical set of this deflection data is shown in figure 6. This figure shows midheight deflection as a fraction of the column thickness plotted against time for two different columns tested at 300° F. The initial out-of-straightness at the midheight, the applied stress, and the slenderness ratio are all indicated. The highest point of each curve corresponds to collapse of the column. It is interesting to note that the lateral deflection immediately prior to collapse of the column is still a small percentage of the column thickness and that collapse is rather sudden. This fact is useful because it indicates that a small deflection analysis should be valid, insofar as deflections are concerned, over practically the entire lifetime.

The most significant information from this type of plot is the column lifetime. The information on column lifetime has been abstracted from forty curves of this type. A portion of these results (that portion which is for a temperature of 600° F) is illustrated in figure 7. The parameters used in this plot were revealed by the theoretical analysis

previously mentioned. The lifetime parameter is a combination of three quantities; namely, the actual lifetime of the column expressed in hours  $t_{cr}$ , the material creep constants B and K previously mentioned, and the average stress  $\bar{\sigma}$  in pounds per square inch applied on the column. The crookedness parameter is composed of two quantities which are the measured initial out-of-straightness of the column at the midheight  $d_0$  expressed as a fraction of the column thickness b and the average stress  $\bar{\sigma}$  applied on the column. The theory predicts that for a given ratio of the average applied stress to the Euler buckling stress a single curve should be obtained of lifetime parameter plotted against crookedness parameter. Each of the dashed curves which have been drawn on the basis of test data represents a different value of this stress ratio ranging from 0.1 to 0.9 as shown. The dashed curves indicate that, when the ratio of the applied stress to the Euler buckling stress decreases, the lifetime of the column increases. Also, when the column out-of-straightness increases, the lifetime decreases. Plots similar to this one were obtained from the creep tests on columns at other temperatures. This type of plot can be used directly for determining the actual lifetime of columns for any out-of-straightness and applied stress. For example, if values are fixed for out-of-straightness and desired lifetime and a value of applied stress is selected, the stress ratio  $\bar{\sigma}/\sigma_E$  is determined. This stress ratio can then be solved for the slenderness ratio  $L/\rho$ . Figure 8 shows the result of such calculations. This figure shows the lifetime of 75S-T6 aluminum-alloy columns at 600° F. The out-of-straightness  $d_0/b$  for the columns is 0.01, where  $d_0$  is the measured initial out-of-straightness at the mid-height and b is the column thickness. The zero time curve, which represents the tangent-modulus stress for the columns, was obtained from the material stress-strain curve. The remaining curves showing lifetime were obtained by cross-plotting the information shown in figure 7. Test data show good agreement with these curves. Similar plots for any other ratio of  $d_0/b$  can be prepared from figure 7, which showed the column lifetime parameter plotted against the column crookedness parameter.

It is believed that no theoretical work has been published on the creep behavior of plates. Test data also are lacking on this subject. However, some qualitative remarks can be offered on what might be expected of a plate supported along its four edges when subjected to edge compression sufficient to cause creep. As was found to be the case for columns, initial imperfections should play an important part in determining the lifetime of a creeping plate provided the plate is not seriously buckled by the applied load. When the plate is loaded initially with a load greater than the buckling load, the size of the buckles will probably mask the effect of the relatively small initial imperfections. This latter conjecture is supported to some extent by creep tests performed by the NACA on plates as stiff as stiffened panels.

These tests were performed on stiffened panels made of 24S-T3 aluminum alloy. The tests for all panels were designed to be short-time creep tests. The load applied in every case was sufficiently high to cause some visible buckling of the panel skin. Some of the data obtained from these tests are presented in figures 9 and 10. Figure 9 shows creep-test data for three panels of the same length and cross section. The results are shown in terms of unit shortening plotted against time. The average stress applied on each panel is shown absolutely and also as a percentage of the maximum short-time strength obtained by rapid loading of an identical panel. Collapse of two of the panels occurred when the unit shortening reached approximately 0.9 percent. The short dashed lines indicate the point at which accelerated shortening began. This point is usually labeled as the beginning of third-stage creep in the usual tensile creep test. Note that for the two panels tested to failure, the accelerated shortening began at the same value of unit shortening, in this case, 0.006. The results of two of these creep tests are shown in figure 10 in conjunction with the rapid loading strength test of an identical panel. The result of a rapid loading test is given by the solid curve which show stress plotted against unit shortening. The results of the creep tests from figure 9 are shown on horizontal lines in figure 10 which represent the stress level at which the panels were tested. The vertical tick marks show the amount of unit shortening which occurred every thirty minutes during the creep test. The circles represent the point at which the creep rate or rate of unit shortening began to increase. Note that the amount of unit shortening corresponding to the start of accelerated creep is equal to the unit shortening corresponding to the maximum stress obtained in the rapid loading test. This observation was made for all panels tested. Also, note that the panels subject to creep failed or collapsed at a unit shortening which was somewhat less than the unit shortening corresponding to the same stress level obtained in the unloading portion of the rapid loading test.

Few conclusions can be made as yet from this preliminary investigation of creep strength of panels. However, if additional test data substantiate the trends shown, an approximate solution may be developed which will be helpful for predicting the long-time or creep strength of panels.

In summary, it can be said that the short-time maximum strength of members such as columns, plates, and stiffened panels can be predicted with satisfactory accuracy at any temperature. The stress-strain curve for the material at the appropriate temperature is needed for the column or the plate. For the stiffened panel, the effective stress-strain curve is needed. In the field of long-time strength, the situation is not so satisfactory. Insofar as columns are concerned, the theory mentioned previously offers considerable promise for predicting long-time strength. For plates and stiffened panels, however, no theory has as yet been developed for predicting creep strength of these members. Both

theoretical and experimental work in this direction will be necessary before a practical solution is found.

## REFERENCES

1. Heimerl, George J., and Roberts, William M.: Determination of Plate Compressive Strengths at Elevated Temperatures. NACA Rep. 960, 1950. (Supersedes NACA TN 1806.)
2. Libove, Charles: Creep Buckling of Columns. Jour. Aero. Sci., vol. 19, no. 7, July 1952, pp. 459-467.
3. Libove, Charles: Creep-Buckling Analysis of Rectangular-Section Columns. (Prospective NACA paper.)

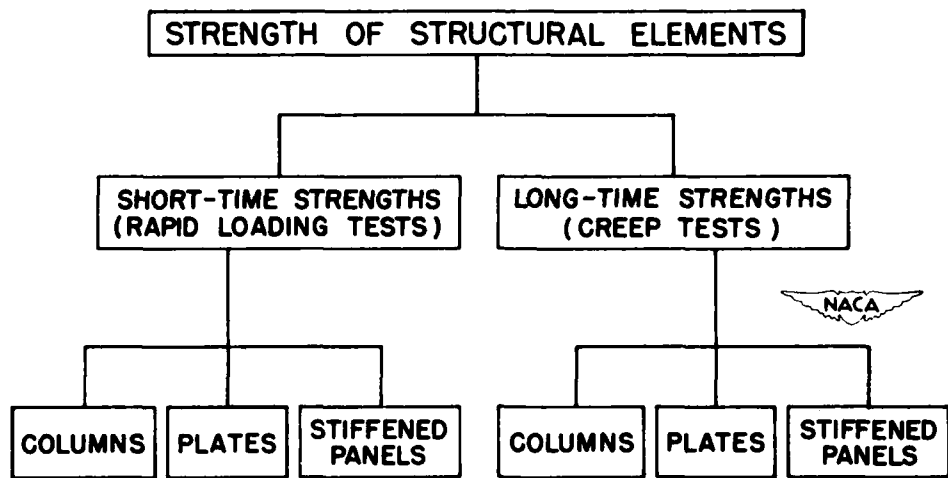


Figure 1.

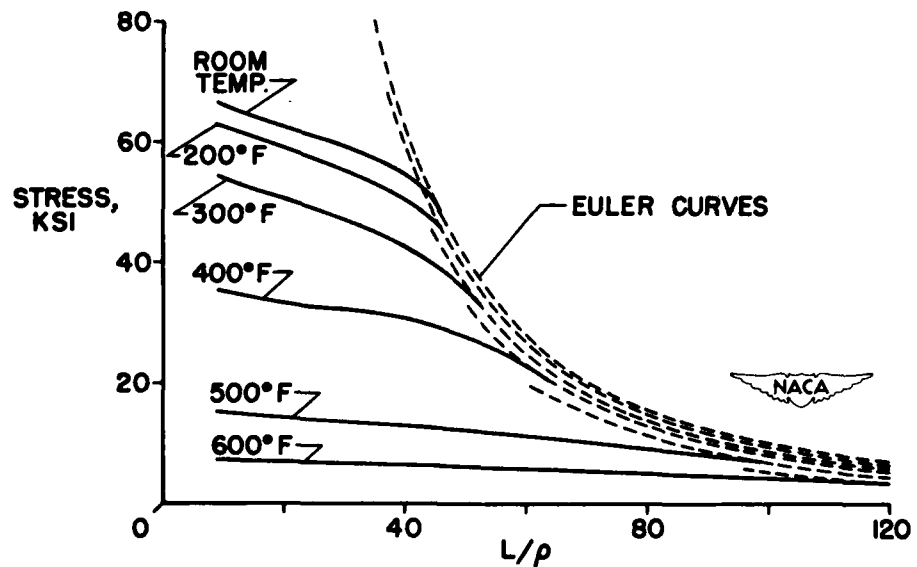


Figure 2.

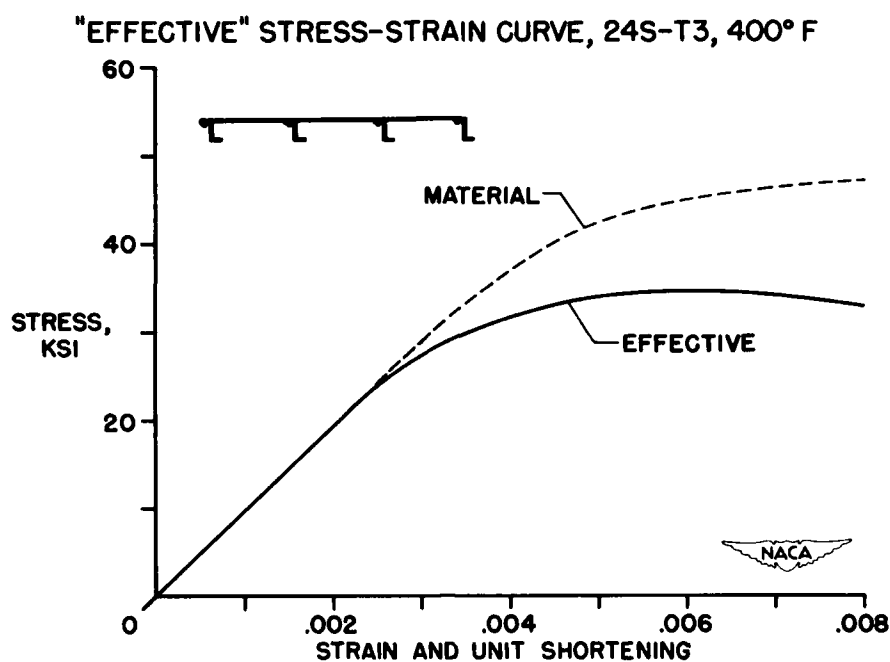


Figure 3.

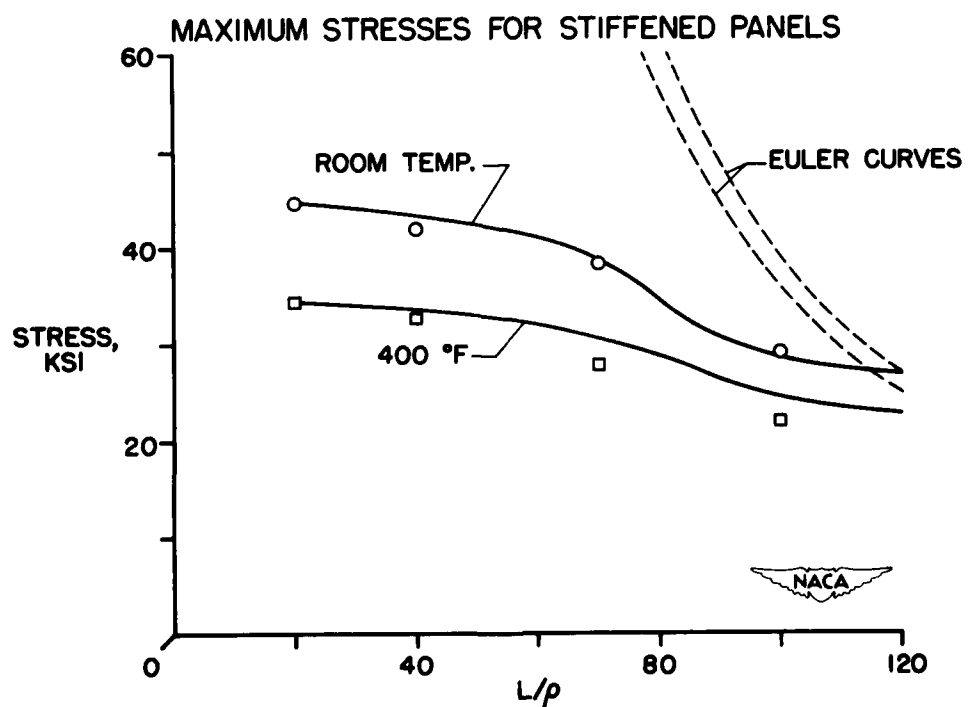


Figure 4.

CONFIDENTIAL

501

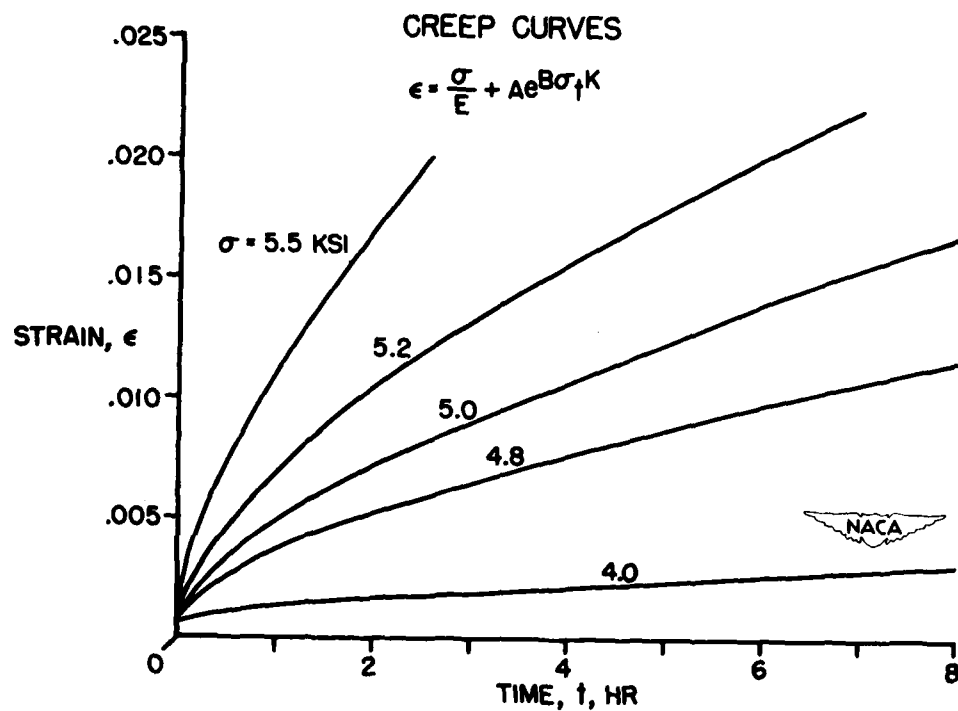


Figure 5.

## COLUMN CREEP DEFLECTION RESULTS, 75S-T6, 300° F

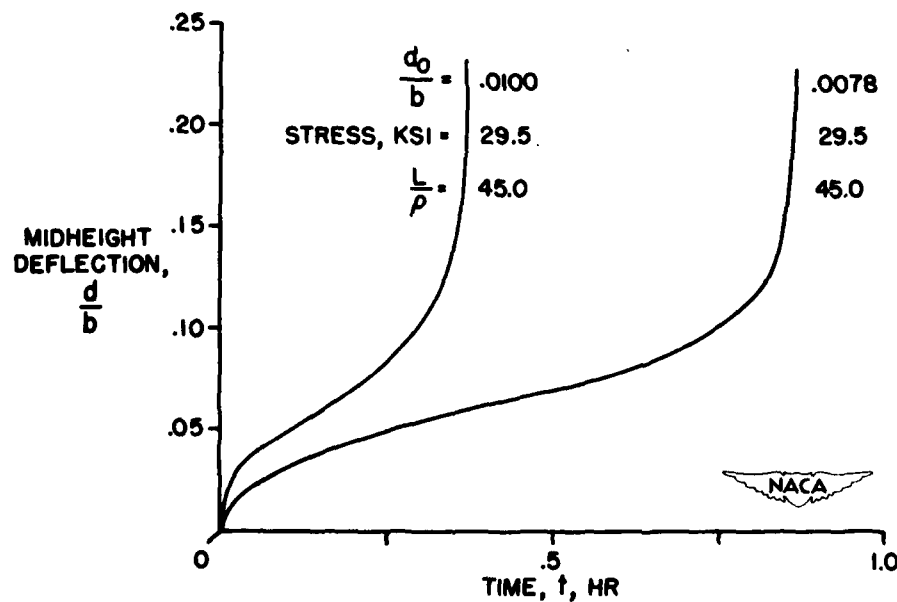


Figure 6.

CONFIDENTIAL

CONFIDENTIAL

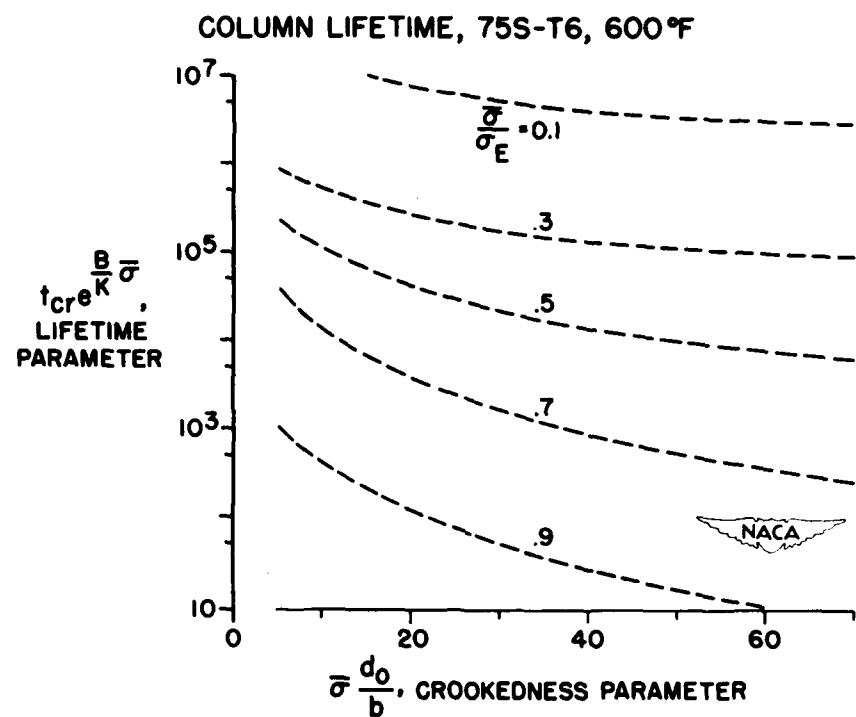


Figure 7.

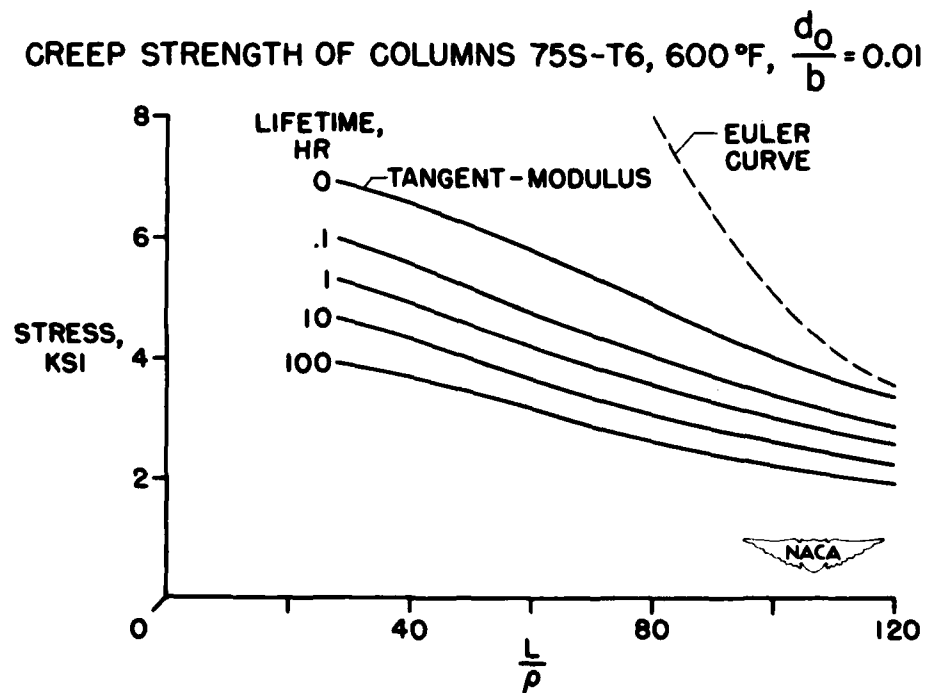


Figure 8.

CONFIDENTIAL

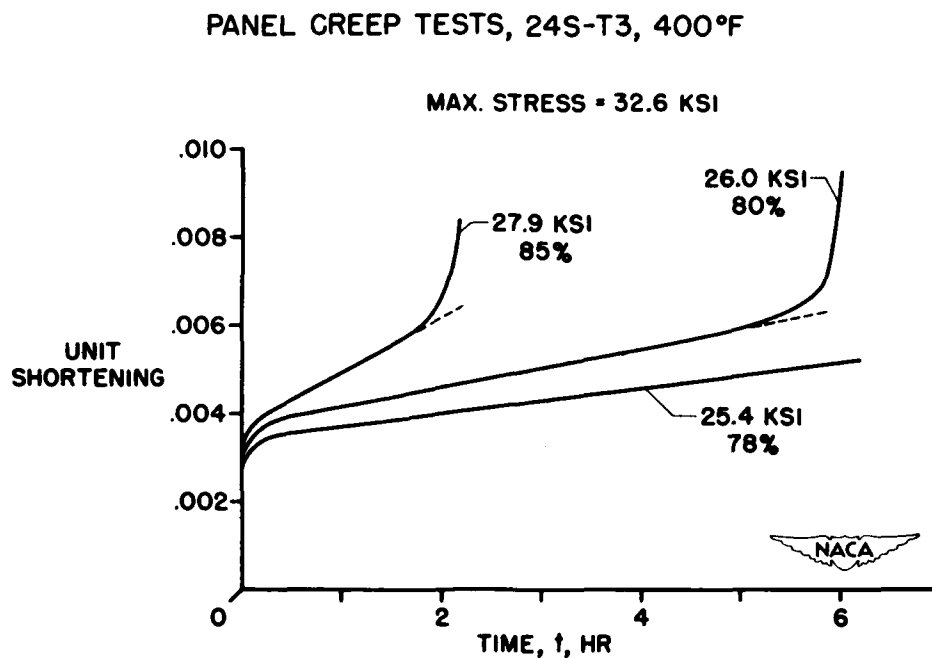


Figure 9.

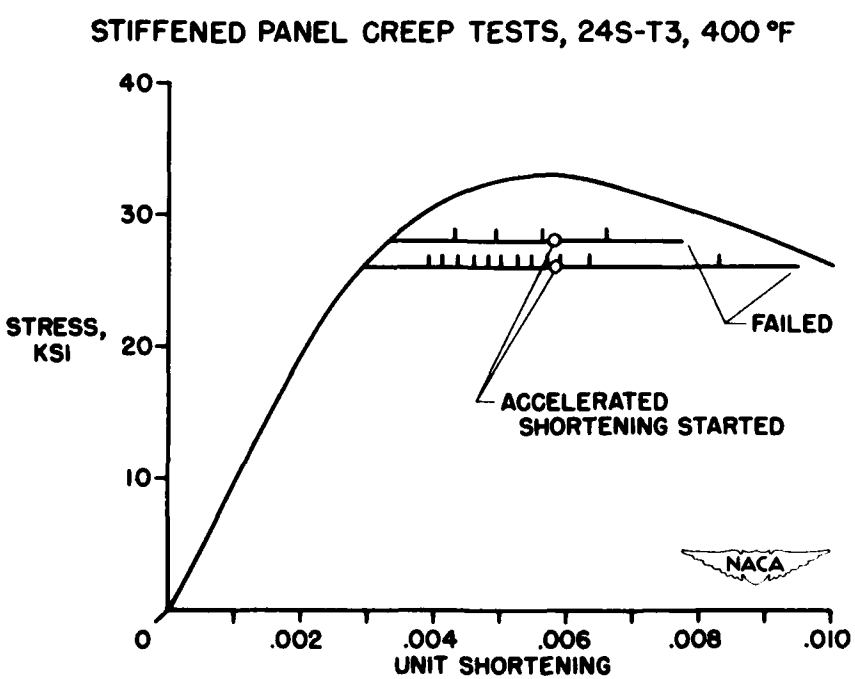


Figure 10.

**CONFIDENTIAL**

**505**

## **STRESSES AND DEFLECTION**

**CONFIDENTIAL**

REMARKS ON STRESS ANALYSIS OF CIRCULAR SEMIMONOCOQUE  
CYLINDERS WITH RECTANGULAR CUTOUTS

By Harvey G. McComb, Jr., and Floyd R. Schlechte

Langley Aeronautical Laboratory

The problem to be discussed is that of finding the stresses about a cutout in a circular cylinder of semimonocoque construction. The structure consists of a thin-walled cylinder that is stiffened longitudinally by stringers and circumferentially by rings. Some possible loading conditions on the shell are seen in figure 1.

An investigation of the stresses about such cutouts is important in order to provide a means for the rational design of fuselages in the neighborhood of large doors, windows, or other openings and in order to facilitate the determination of the most efficient type of reinforcement.

The stress analysis of structures of this type has long been based on the conventional assumptions that the stringers carry only direct stress and the sheet carries only shear stress which is constant within each bay. On the basis of these assumptions, a straight-forward stress analysis of cutouts in stiffened shells can conceivably be made. However, such an analysis would involve setting up approximately as many simultaneous equations as there are intersections of stringers and rings, and since the number of equations needed can easily run into the hundreds, such laborious solutions are not practical.

A method for handling the cutout problem has been developed which is based on the same conventional assumptions but which involves the solution of only a few simultaneous equations instead of several hundred. The procedures developed are based on Cicala's idea (ref. 1) of working with perturbations due to the cutout on the stress field which would occur in the shell without a cutout. The method is versatile enough to handle any type of end loading as well as the effects of reinforcement about the cutout.

The assumptions made in this analysis are stated briefly. The stringers are supposed to be uniform and equally spaced around the shell, and the sheet is of constant thickness. The stringers carry only direct stress, and the sheet takes only shear stress which is constant within each bay. The rings have a finite bending stiffness in their own planes, but they do not restrain longitudinal displacements of the stringers. And, lastly, it is assumed that the difference between the radius of the neutral axis of the ring and the radius of the middle surface of the sheet is negligible.

The method of solution is analogous to a method for analyzing flat sheet stringer panels which was presented at the annual meeting of the Institute of the Aeronautical Sciences in New York City in January 1953 and is currently available, reference 2. A brief synopsis of this method of analysis will now be given. The fundamental idea is that the stress distribution in the shell with cutout is a superposition of the stress distribution which would exist in the structure if it did not have a cutout and certain stress perturbations which arise because of the cutout. The continuous structure without cutout will be called the "basic" structure. The stress distribution which would exist in this structure will be called the "basic" stress distribution. The first step in the analysis is to find the basic stress distribution. The second step is to superpose certain perturbation stress distributions on the basic stresses in the basic structure in such a manner as to eliminate the effects of that portion of the shell which lies within the cutout.

Solutions to three unit problems are the tools for this method of analysis. These unit problems consist of finding the stress distributions caused by three types of unit loadings imposed on a basic shell infinite in length as shown in figure 2. The solutions will be called the "unit perturbation solutions." The first unit perturbation solution required is the stress distribution due to a unit concentrated force applied to a stringer of the basic shell at a station and acting in the direction of the stringer. Another unit perturbation solution required is the stress distribution due to unit loads uniformly distributed along the stringers and rings bounding one shear panel of the shell in such a manner as to cause shear in that panel. Finally, the stress distribution caused by a unit load uniformly distributed along only one stringer of the shell between two rings is needed. These loads will be called the concentrated perturbation load, the shear perturbation load, and the distributed perturbation load. (See fig. 2.)

These three unit-load problems have been solved. For a particular perturbation load the solution depends on three parameters: the number of stringers in the shell and the two parameters  $B$  and  $C$  shown in figure 2 which are given as

$$B = \frac{EA}{GLt} \frac{b}{L} \quad C = \frac{1}{2\pi} \frac{mAR^5}{IL^3}$$

where  $E$  is Young's modulus;  $G$ , the shear modulus;  $A$ , the area of a stringer;  $b$ , the arc distance between stringers;  $t$ , the thickness of the sheet;  $L$ , the distance between rings;  $R$ , the radius of the shell;  $I$ , the moment of inertia of the cross section of the ring; and  $m$ , the total number of stringers in the shell. Thus,  $B$  is a sheet-stringer

parameter, being the ratio of the extensional stiffness of the stringers to the shear stiffness of the sheet times the shear panel aspect ratio, and  $C$  is a parameter which includes ring bending flexibility. In the limiting case, when the rings are rigid in bending in their own planes,  $C$  becomes zero. Formulas have been developed for these three perturbation loadings giving the stringer loads at every station in the structure and shear flows in every shear panel (fig. 2). By using these formulas, tables of influence coefficients can be computed for each of the three perturbation loadings giving stringer loads and shear flows in the neighborhood of the load due to a unit magnitude of that load. To date tables of influence coefficients have been computed for a 36-stringer shell and for various values of the parameter  $B$ , but only for the limiting case of  $C = 0$  which corresponds to rigid rings.

A discussion is now given of how the perturbation loads with their tabular unit solutions can be used to solve actual cutout problems in circular semimonocoque shells. Consider a shell loaded at the ends in some known manner. Suppose this shell has a cutout on one side which, for simplicity, interrupts only two stringers and removes three shear panels. First, assume that the cutout does not exist and think of the shell as being continuous. By using elementary beam theory, the basic stress distribution is determined. Then, in addition to the known external loads, place on the basic structure the perturbation loads shown in figure 3. The magnitudes of these perturbation loads are adjusted so that the boundary conditions at the cutout are satisfied. Then, the structure can be cut at the boundary of the cutout, and the portion of the structure within the cutout can be removed along with the perturbation loads without disturbing the rest of the structure. The stresses outside the cutout in the basic structure under the external loading and the perturbation loads are precisely the same as the stresses in the actual structure with cutout under the external loading alone. This method involves setting up and solving a system of simultaneous linear algebraic equations. In this case, taking advantage of conditions of symmetry which usually exist, the solution involves three equations and three unknowns. The data for these equations are obtained from tables of influence coefficients which can be calculated from the formulas that have been developed.

The method of analysis can be extended to handle problems of reinforced coaming stringers. For instance, the structure shown in figure 3 may have stringer reinforcement of constant area extending one bay on either side of the cutout as shown in figure 4. The perturbation loading system for this problem is shown in figure 5. In addition to the loads imposed for the unreinforced structure, perturbation loads are applied to the basic portions of the reinforced stringers (fig. 5), and their reactions are placed on the excess reinforcing portions. The magnitudes of the perturbation loads are adjusted to satisfy the boundary conditions at the cutout and continuity conditions along the coaming stringers.

The solution of this problem involves five equations and five unknowns, or maybe seven equations and seven unknowns, depending upon the symmetry in the problem.

Shear reinforcement about the cutout can be handled also by this type of analysis. For example, instead of the reinforced coaming stringers, suppose the shear panels indicated by hatching in figure 6 are reinforced by some additional thickness of sheet. The perturbation loads to be imposed are shown in figure 7. The procedure is analogous to the case of coaming stringer reinforcement. The perturbation loads are adjusted in magnitude to satisfy the boundary conditions at the cutout and continuity at the reinforced shear panels. This problem involves the solution of five simultaneous equations.

To summarize, the salient features of the method are as follows: By using tables of influence coefficients, a system of a few simultaneous equations is set up and solved in order to get the magnitudes of a system of perturbation loads on the basic structure which will force the boundary conditions and continuity conditions to be satisfied about the cutout; then, stresses are obtained by superposition. This procedure is in marked contrast to that of setting up the many equations which would be needed by a straight-forward approach based on the same conventional assumptions of the theory of stiffened shells. So far, only some tables of influence coefficients for the limiting case of rigid rings are available; but further tables can be computed for flexible rings, and this work is in progress.

A test program is being conducted along with the theoretical investigation. Figure 8 illustrates a test specimen cantilevered from the backstop. Extensive testing has been done on this specimen under many loading conditions and with various sizes of cutouts.

Since the tables of influence coefficients which are ready at the present time do not account for ring flexibility, a direct comparison with experiment is not possible. Nevertheless, it may be of interest to make a few comparisons of the rigid-ring theory with test results. Such a comparison may not be too unreasonable since the cylinder which has been tested had fairly heavy rings.

In figure 9 is presented a comparison of the experimental shear stresses with those calculated by the rigid-ring theory in the net section around the shell for a shell under pure torsion. The left-hand plot is for a  $30^\circ$  wide cutout. The right-hand plot is for a  $70^\circ$  wide cutout. The continuous stepwise line is the result of present rigid-ring calculations, and the circles are test points. For comparison, the theoretical solution for no cutout is shown by the dashed line. Even with the assumption of rigid rings, the calculations show correctly

the trends in the stresses. However, sufficient concentration of shear stresses is not obtained near the cutout. A plausible explanation for the discrepancy is that the mathematically rigid rings in the theoretical calculations may tend to carry the effects of the cutout too far around the shell and move the points of maximum shear stress away from the edge of the cutout.

In figure 10 are shown the stringer stresses around the shell under torsion at a ring bordering the cutout. Again, the rigid-ring computations predict correctly the trends in the stresses and are in very good agreement with the stresses obtained for the 30° cutout. However, the calculated stress concentration is too low for the 70° cutout.

When tables of influence coefficients incorporating ring flexibility have been computed, direct comparisons between theory and experiment will be possible. However, the fact that even rigid-ring calculations show the trends in the stresses is encouraging. An investigation of the importance of the fineness of the grid of stringers and rings may be of interest. The stress gradients obtained in tests are very steep, suggesting that more accurate calculated stresses may result if a finer grid is formed by inserting fictitious rings and stringers somewhere between the actual ones.

#### REFERENCES

1. Cicala, P.: Effects of Cutouts in Semimonocoque Structures. Jour. Aero. Sci., vol. 15, no. 3, Mar. 1948, pp. 171-179.
2. McComb, Harvey G., Jr.: Stress Analysis of Sheet Stringer Panels With Cutouts. Preprint No. 394, S.M.F. Fund Paper, Inst. Aero. Sci., Jan. 1953.

## CYLINDRICAL SHELL WITH CUTOUT

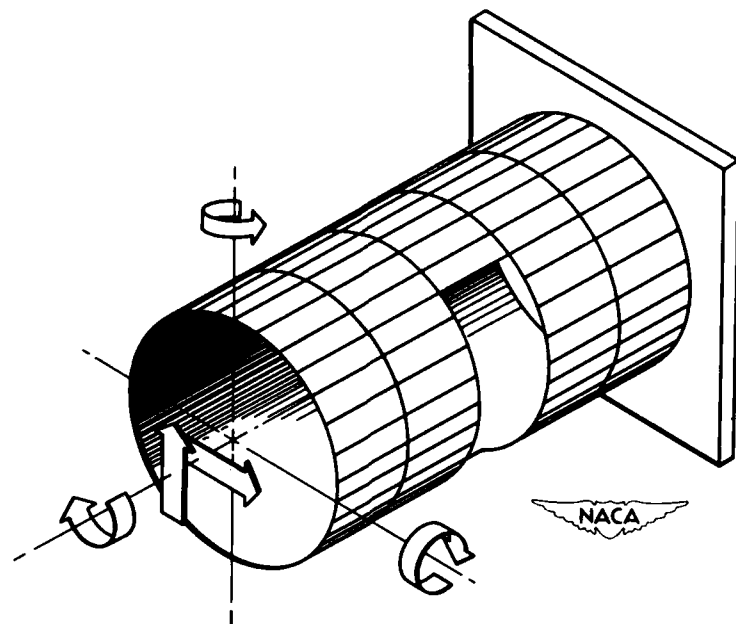


Figure 1.

## PERTURBATION LOADS

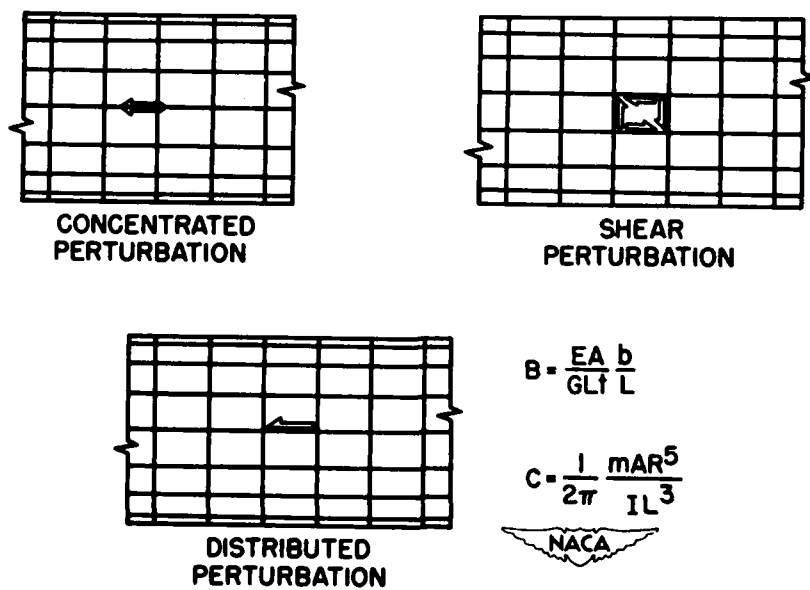


Figure 2.

## APPLICATION OF PERTURBATION LOADS

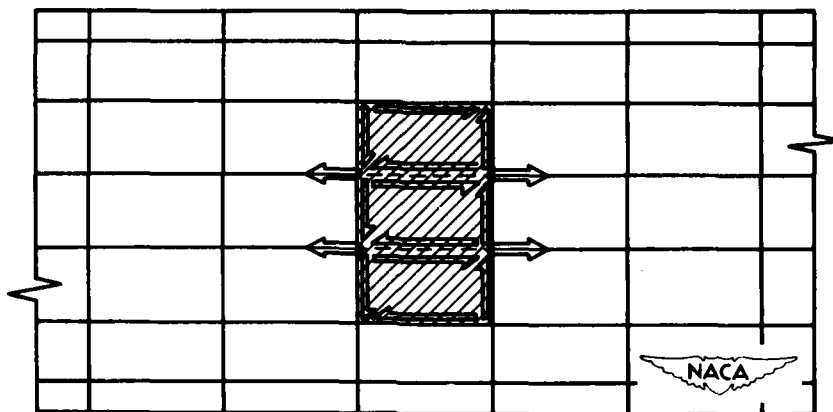


Figure 3.

## REINFORCED COAMING STRINGERS

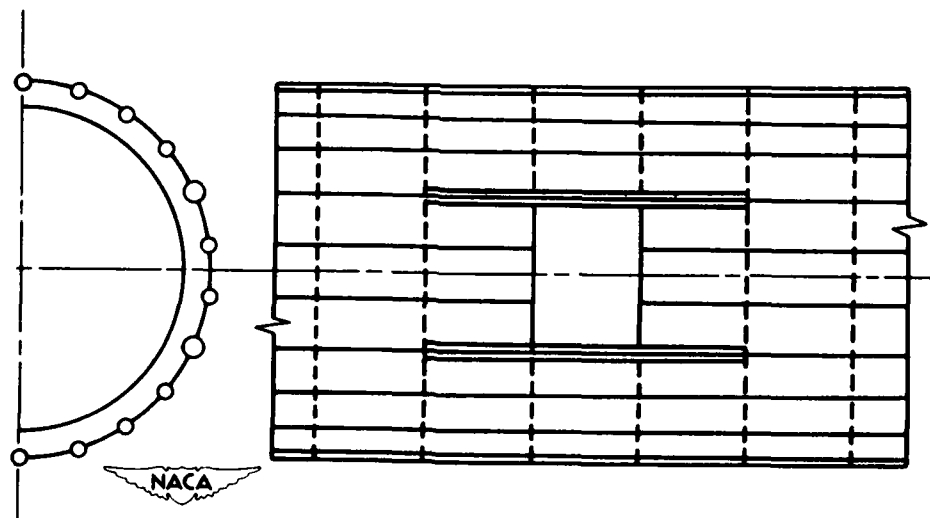


Figure 4.

## PERTURBATION LOADS FOR STRINGER REINFORCEMENT

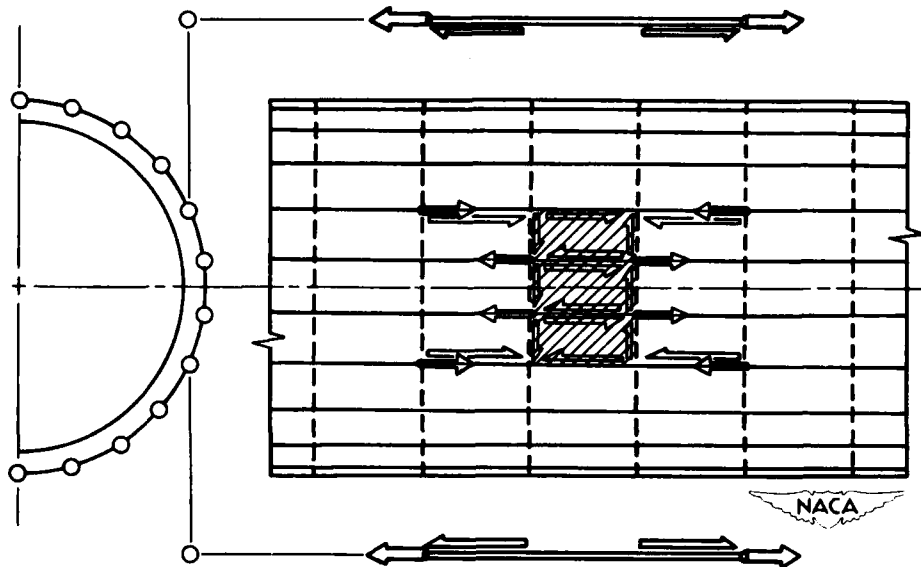


Figure 5.

## CUTOUT WITH SHEAR REINFORCEMENT

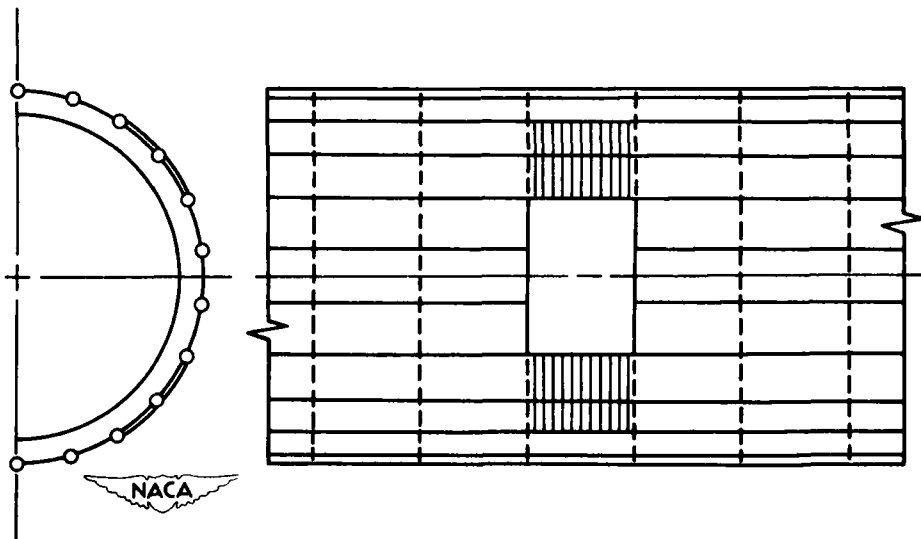


Figure 6.

## PERTURBATION LOADS FOR SHEAR REINFORCEMENT

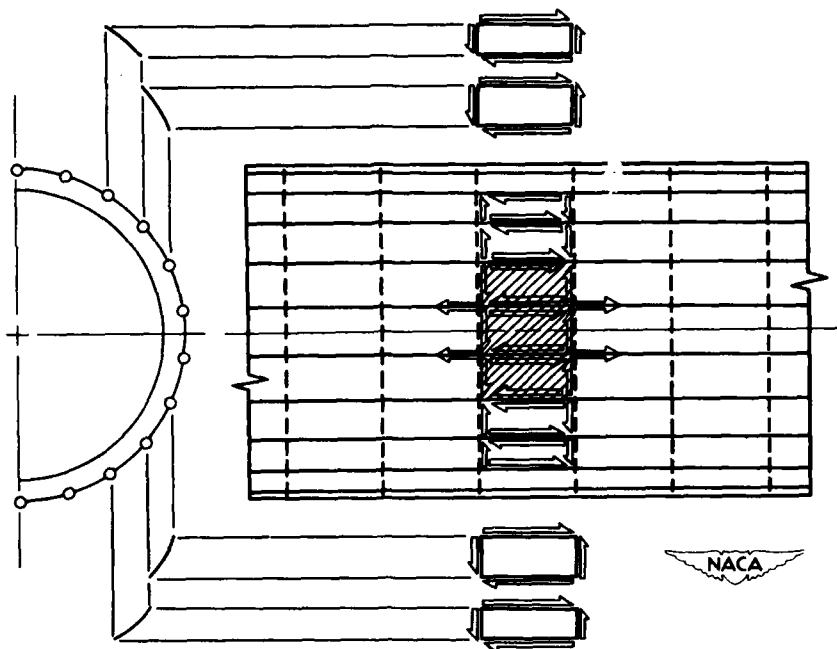


Figure 7.

## CYLINDER CUTOUT TEST

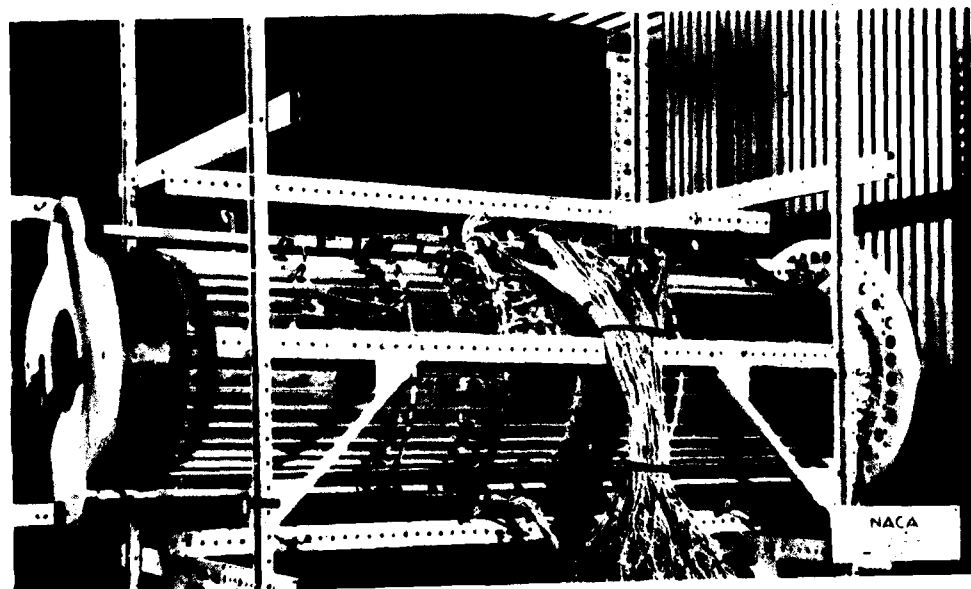


Figure 8.

## SHEAR STRESSES IN NET SECTION TORQUE LOAD

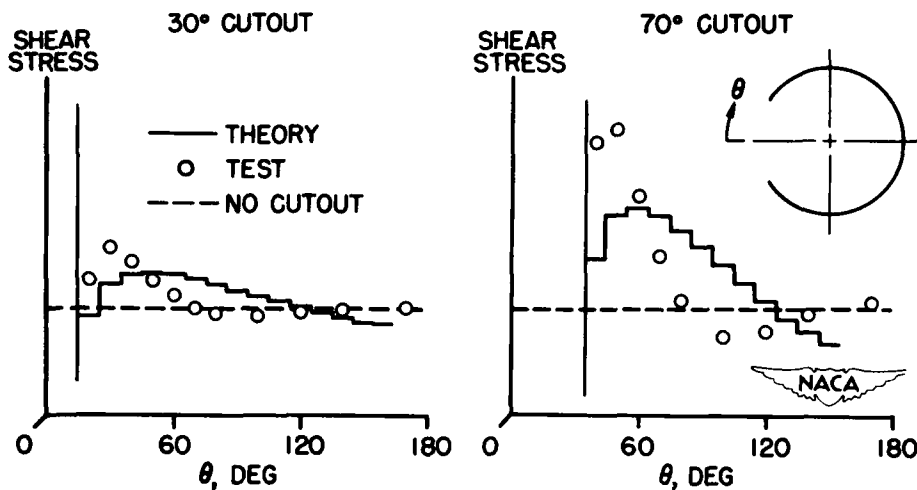


Figure 9.

## STRINGER STRESSES AT RING BORDERING CUTOUT TORQUE LOAD

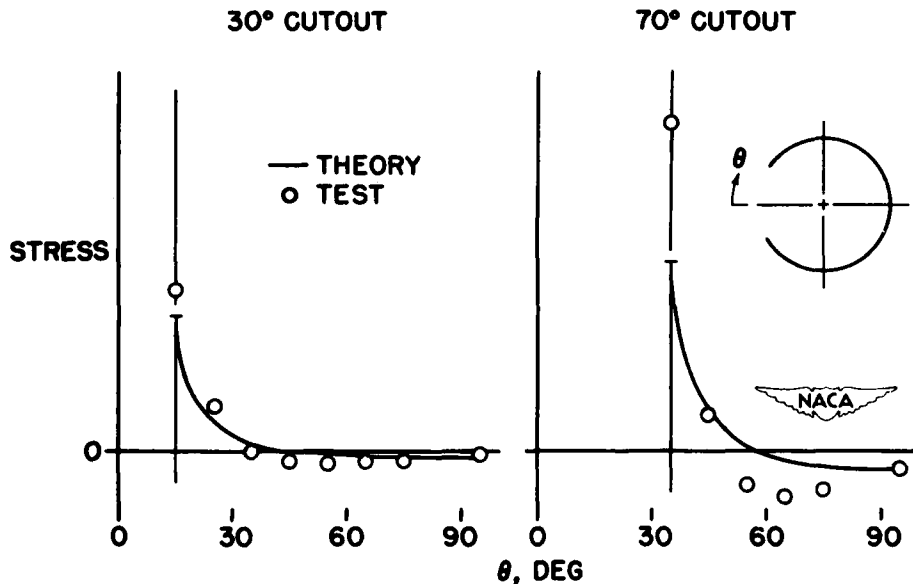


Figure 10.

## A SIMPLE METHOD OF ANALYSIS OF SWEPT-WING DEFLECTIONS

By William A. Brooks, Jr., and George W. Zender

Langley Aeronautical Laboratory

In order to obtain simple relationships between loads, deflections, and angles of attack, the complex problem of analyzing the deformations of swept wings must be treated by employing simplifying assumptions. By way of simplification, the swept wing is commonly idealized into a straight beam with the intent of applying elementary beam theory. An effective root of the idealized beam is determined empirically by obtaining good comparisons with experiment and usually turns out to be located somewhere within the triangular root section.

One important disadvantage of the effective-root concept is its lack of uniqueness. With a given loading, the best root location for calculating deflections is not the same as the best location for calculating angles of attack. A similar variation with the type of loading (bending or torsion) also occurs. Thus the effective root concept may involve the experimental determination of many root locations.

With the objective of eliminating these uniqueness difficulties and the empirical approach associated with the effective root, a study (ref. 1) was made of solid wing models of various plan forms to determine the possibility of deriving a simple method of analysis, involving elementary beam theory, which would apply regardless of the type of loading and the particular deformation being sought. The various plan forms considered are shown in figure 1.

The models were made of 24S-T4 aluminum alloy and had uniform thickness and a constant chord. The swept and M or W plan form models had 30°, 45°, and 60° sweep angles. The Λ and swept-tip models had only a 45° sweep angle. All models were full-span models with a center section which was clamped between two flat bearing blocks. Loads symmetrical to the longitudinal center line were applied to the models.

The tests verified that for solid swept wings of fairly large aspect ratios the portion of the wing outboard of the root triangle (fig. 2) behaves like an ordinary cantilever beam and that the coupling of bending and torsion inherent to a swept wing seems to occur primarily within the root triangle. These observations suggest another approximate method of calculating the deformations of the swept wing; namely, the deformations of the outboard section are computed by elementary beam theory and to these deformations are then added the rigid-body displacements resulting from deformation of the triangular root section. Thus the problem is reduced to finding the deformation of the root triangle.

The model tests previously referred to indicated that the angle of attack  $\alpha$  of the root triangle, or the rotation of the root triangle in a plane parallel to the clamped root, was negligible (fig. 3). This observation enables a simple approximate energy solution for the deflections of the root triangle to be made. Figure 2 shows a deflection  $\bar{w}$  and a slope  $\bar{\beta}$  (rotation in a plane perpendicular to the clamped root) which are found from the deflections of the root triangle and which may be used to compute the rigid-body displacements of the outboard section of the wing.

In the treatment of a swept wing, the effects of the deformations  $\bar{w}$  and  $\bar{\beta}$  of the triangular root section are added to the elementary deflections of the outer part to obtain the total deflection  $w$  (fig. 2). The distortions  $\bar{w}$  and  $\bar{\beta}$  have a marked effect on the outboard deflections for most types of loading. However, the angle of attack of the outboard section is not affected by these deformations, and, therefore, only the elementary beam theory is necessary to evaluate the angles of attack of swept wings, and M or W, A, and swept-tip wings as well.

Figure 4 shows a comparison between theory and experiment for a concentrated lift load applied at the tip of the  $45^\circ$  swept model. In this figure, as well as in the figures which follow, the deformations are plotted against the ratio  $\xi/l$ , where  $\xi$  is the distance from the clamped root and  $l$  is the semispan of the wing. On the left the center-line deflections of the wing are shown and on the right the angles of attack are shown. Angles of attack are considered positive if the leading edge of the model deflects upward with respect to the trailing edge. The curves represent the calculated values, and the symbols represent test data. The experimental data indicate that the angles of attack are negligibly small within the root triangle. Although a comparison is shown only for the  $45^\circ$  swept model, the agreement is typical of the  $30^\circ$  and  $60^\circ$  swept models.

Figure 5 shows a comparison between theory and experiment for the  $45^\circ$  swept model when loaded with a streamwise torque - torque in a plane parallel to the clamped root. For this loading which produces coupled bending and torsion there is exceptionally good agreement between theory and test for all the swept models tested. The solution indicates that for this case there is no deformation of the triangular root section - an occurrence which is substantiated by the test data presented here. Therefore, for the case of streamwise torque the curves for both deflection and angle of attack are obtained from elementary beam theory alone.

In order to demonstrate the general applicability of the method, M or W wing models were investigated. For calculating the deflections and angles of attack, the M or W wing is separated as shown in figure 6. The outer quarter-span is treated the same as the inner quarter-span; that

is, the M or W wing is considered to be two distinct swept wings. After the deformations of each part are found, they are all summed in the proper manner to produce the total deformation.

The deformations of the  $45^\circ$  M or W model loaded with a tip lift load are shown in figure 7. Similar agreement was obtained for the  $30^\circ$  and  $60^\circ$  M or W models. An examination of the complete set of data revealed that the difference between theory and experiment decreases as the sweep angle becomes smaller.

When the  $45^\circ$  M or W model is loaded with streamwise torque, the deformations are as shown in figure 8. Both the inner and outer portions of the model are under combined bending and torsion which produce deflections and angles of attack. The short horizontal part of the angle-of-attack curve results from assuming that the triangle at the junction of the outer and inner wing portions is treated in the same manner as the root triangle; namely, the angle-of-attack changes within the triangular section are negligible.

In the treatment of the  $\Delta$  model, the wing is separated into parts as shown in figure 9. The inner quarter-span of the  $\Delta$  wing is treated like a swept wing whereas the outer portion is treated as an unswept cantilever beam. The calculated deflection and angle of attack of the  $\Delta$  wing have been found to be in good agreement with the test data.

By investigating a swept-tip wing, a model having only the outer quarter-span swept, the effect of sweeping the outer quarter-span may be isolated. The outer portion may be analyzed in the same manner that the outboard quarter-span of the M or W wing is treated. Proper summation of the individual deflections and rotations again produces the total deflection and rotation.

Figure 10 shows the swept-tip model subjected to streamwise torque at the tip. Under this type of loading the inner part of the model is subjected to torsion only and, therefore, experiences no deflection. The outer quarter-span is subjected to combined bending and torsion which result in both deflections and angles of attack.

Although to this point attention has been restricted to solid wings of uniform thickness, the procedure of treating the outboard portion of the wing as an ordinary cantilever beam on which the distortions of the root triangle are superposed is undoubtedly valid for solid wings with nonuniform thickness and for built-up wings also. Of course, the solution to the deflections of the root triangle of a built-up wing will be more complicated than the solution for solid wings because cross-sectional distortion due to warping and shear lag will probably have to be considered. There is, however, reason to believe that the statement made concerning calculation of the angles of attack of a solid wing of

uniform thickness will apply to the built-up wings: namely, that elementary theory applied to the outboard section of the wing will produce satisfactory results.

With these thoughts in mind, the solid-wing theory which was just presented was compared to the test results obtained from the built-up  $45^\circ$  swept box beam (ref. 2) shown in figure 11. The box beam was constructed to represent the main structural component of a full-span, two-spar,  $45^\circ$  swept wing with a rectangular carry-through bay. The box was supported by steel rollers at the corners of the carry-through bay which was free to distort.

The deflection and angle of attack of the box beam loaded with symmetrical tip lift loads are shown in figure 12. On the left are shown the deflections of the front and rear spars. The solid curves result from the application of elementary beam theory including shear deformation to the outboard portion of the wing and the carry-through bay, and the application of plate theory to the root triangle. Secondary effects such as shear lag and cross-sectional distortion were disregarded in the calculation of the solid curves. However, realizing that these secondary effects may be of importance when dealing with built-up structures, the deflections due to warping were determined by an approximate method and were added to the previously calculated deflections, resulting in the dashed curves.

On the right the angles of attack are presented. The solid curves were obtained by applying elementary theory plus shear deformation only to that portion of the wing which is outboard of the root triangle. The change in angle of attack due to warping was added to the angles of attack obtained from elementary theory and shear deformation, producing the dashed curve. The experimental data again indicate that the angle of attack of the root triangle is negligibly small. Thus, it appears that the simplifying assumption used in the solution to the deflections of the solid root triangle may also be used in the solution to the deflections of the built-up root triangle.

Figure 13 shows the deflections and angles of attack of the same box beam symmetrically loaded with tip torque in a plane perpendicular to the leading edge. On the left are shown the deflections of the front and rear spars. The solid curve was obtained in the same manner discussed for the preceding figure. The dashed curve is obtained by adding an approximation of the effect of cross-sectional warping to the results given by the solid curve. On the right, the solid line is the angles of attack calculated from elementary theory plus shear deformation, and the dashed line is the sum of the effects of warping and the elementary theory. Although the magnitude of the secondary effects is shown to affect the deflections appreciably, the angles of attack are not seriously influenced by secondary effects, and elementary theory

alone suffices. The same approach was used for the box beam with antisymmetric loads (ref. 3), and the agreement shown here between test and theory is typical of the results for the antisymmetric loads.

In summary, an approximate method of calculating the deformations of solid wings of uniform thickness having swept, M or W,  $\Lambda$ , and swept-tip plan forms has been presented. The method employs an addition to the elementary beam theory to account for the effect of the triangular root portion of a swept wing on the deformation of the outboard section of the wing. Although the addition is necessary for calculating deflections, for calculating angles of attack elementary beam theory alone suffices. Application of the elementary theory to built-up wings produces a good approximation to angles of attack since the secondary effect of cross-sectional warping has only a minor influence on angles of attack. In general, the secondary effects have an appreciable influence on the deflections of built-up structures; therefore, the treatment presented here gives only an approximation to the deflections of built-up structures.

## REFERENCES

1. Zender, George W., and Brooks, William A., Jr.: An Approximate Method of Calculating the Deformations of Solid Wings Having Swept, M or W,  $\Lambda$ , and Swept-Tip Plan Forms. NACA RM L53A23. (Prospective NACA paper.)
2. Zender, George, and Libove, Charles: Stress and Distortion Measurements in a  $45^\circ$  Swept Box Beam Subjected to Bending and to Torsion. NACA TN 1525, 1948.
3. Zender, George W., and Heldenfels, Richard R.: Stress and Distortion Measurements in a  $45^\circ$  Swept Box Beam Subjected to Antisymmetrical Bending and Torsion. NACA TN 2054, 1950.

## DETAILS OF SOLID MODELS

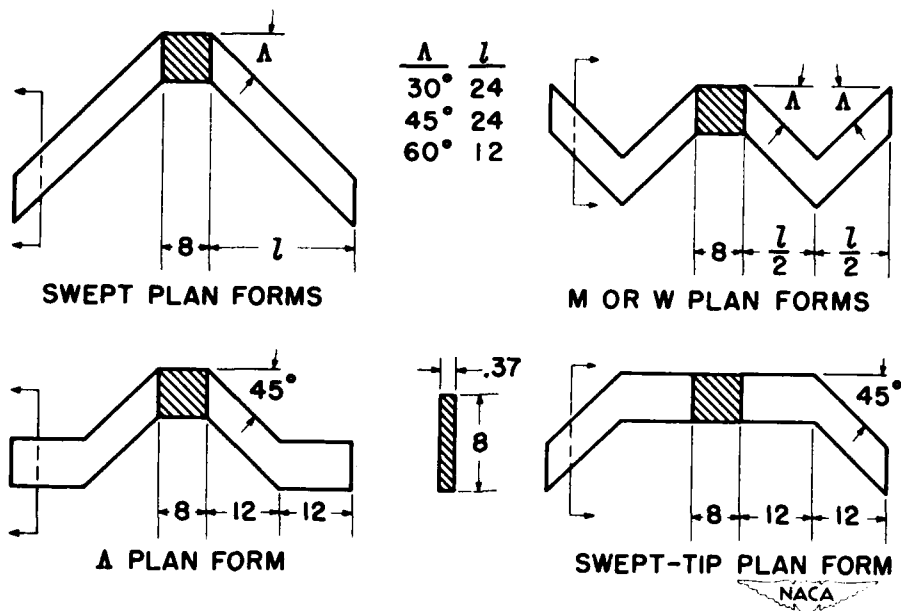


Figure 1.

## SWEPT MODEL CONSIDERED BY PARTS

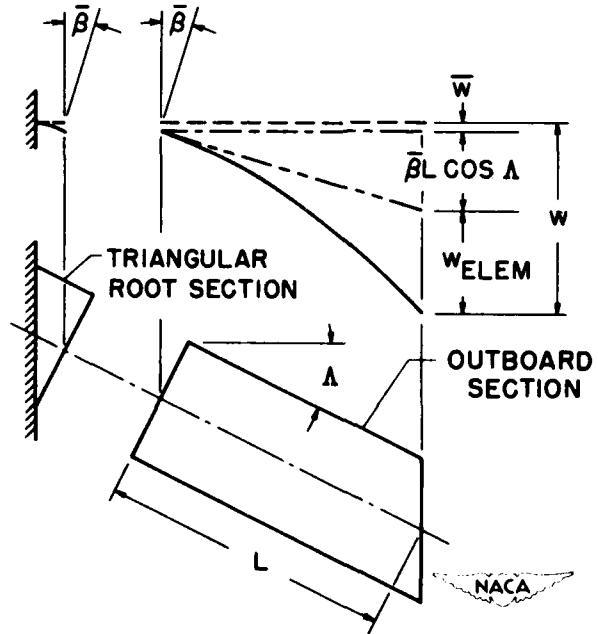


Figure 2.

## ROOT TRIANGLE

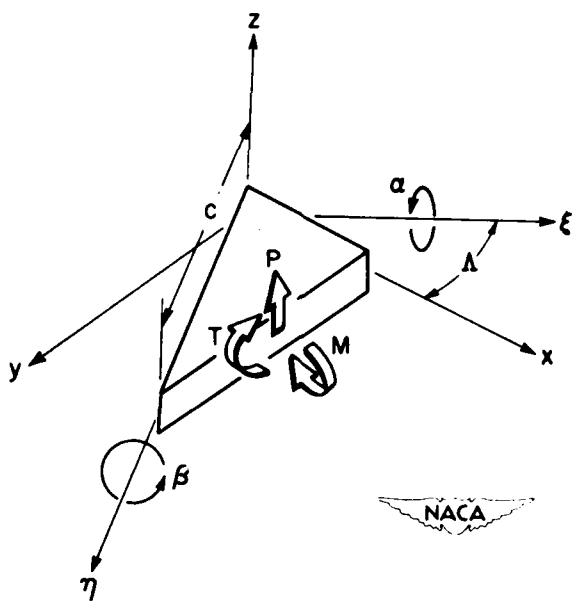


Figure 3.

## DEFORMATION OF 45° SWEPT MODEL WITH LIFT LOAD

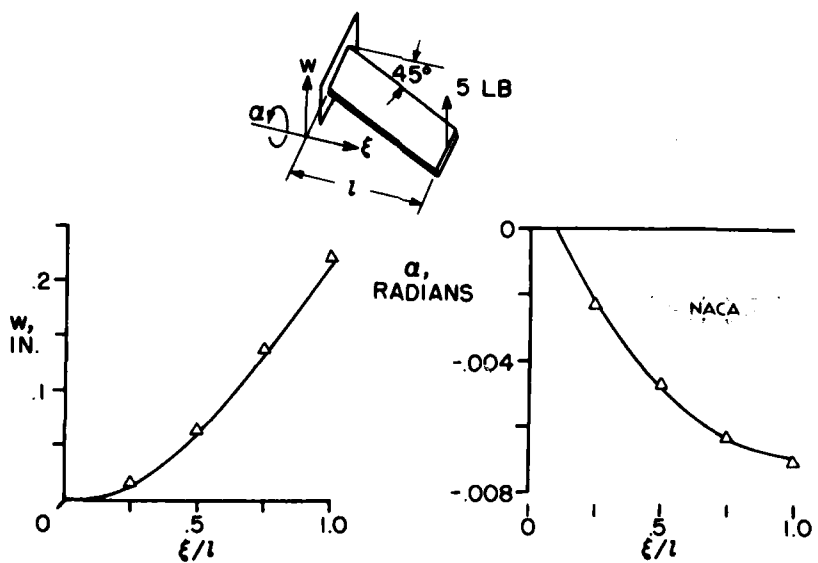


Figure 4.

## 45° SWEPT MODEL LOADED WITH STREAMWISE TORQUE

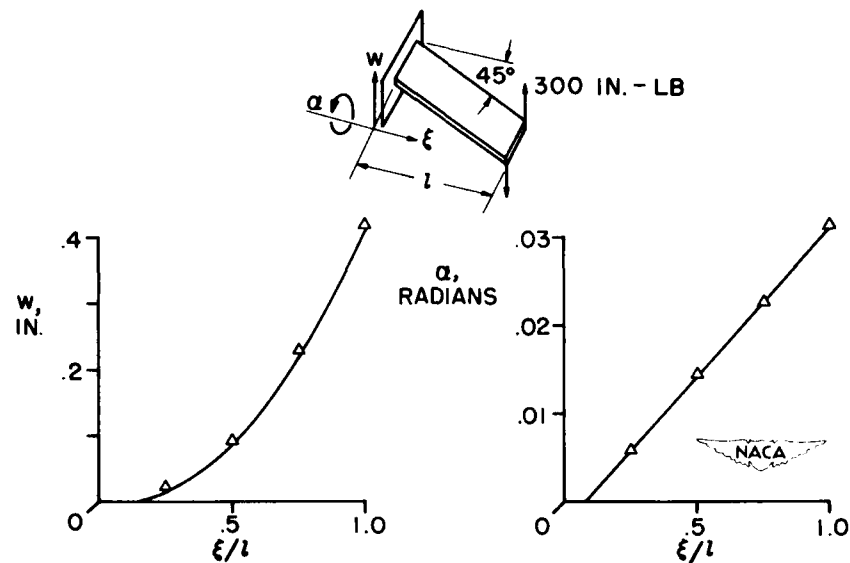


Figure 5.

## IDEALIZATION OF M OR W MODELS

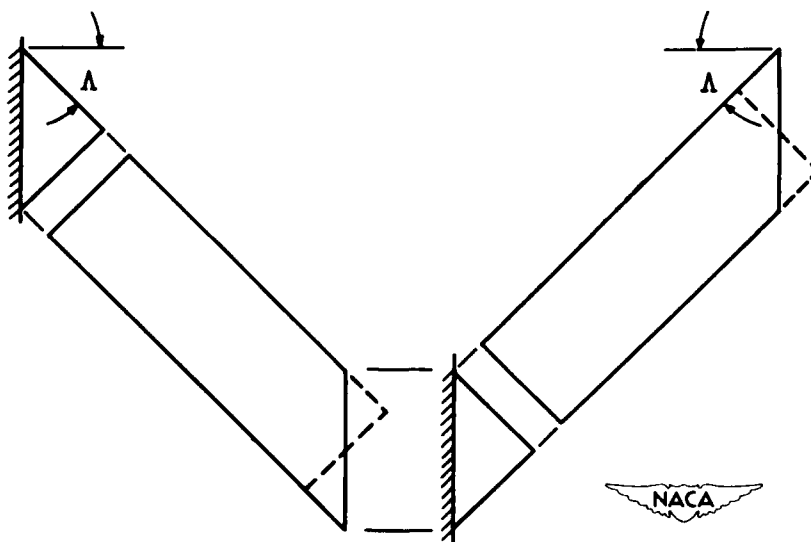


Figure 6.

## 45° M OR W MODEL WITH TIP LIFT LOAD

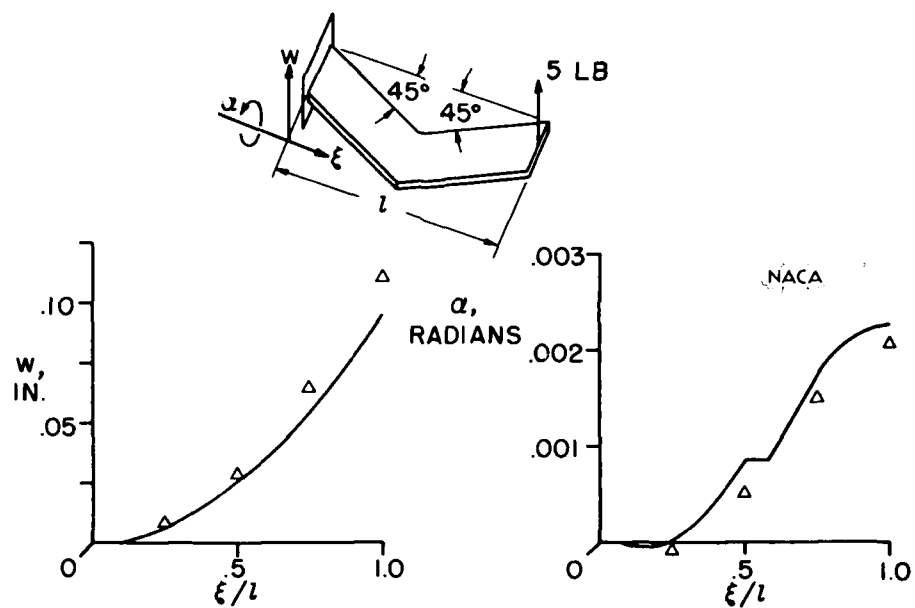


Figure 7.

## 45° M OR W MODEL LOADED WITH STREAMWISE TORQUE

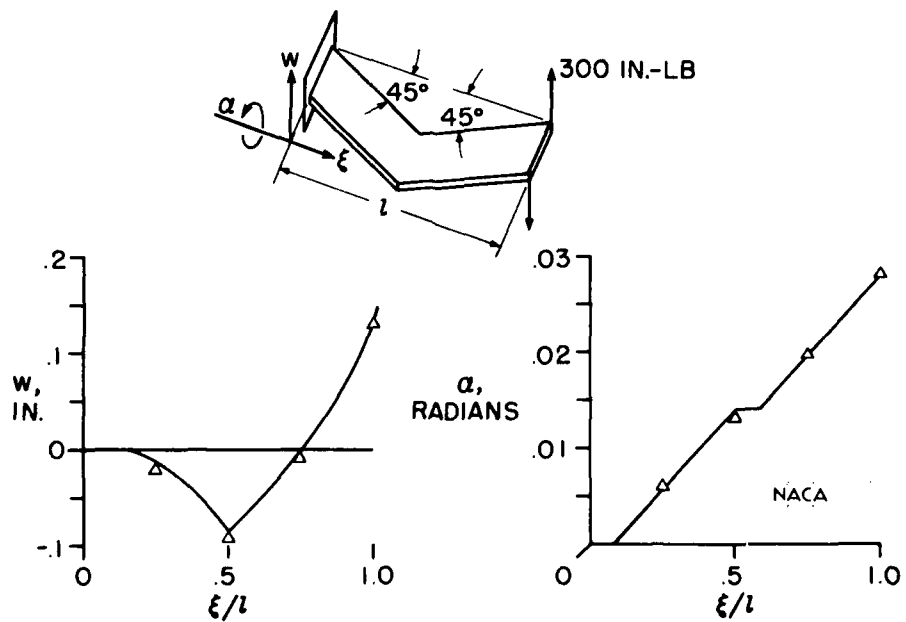


Figure 8.

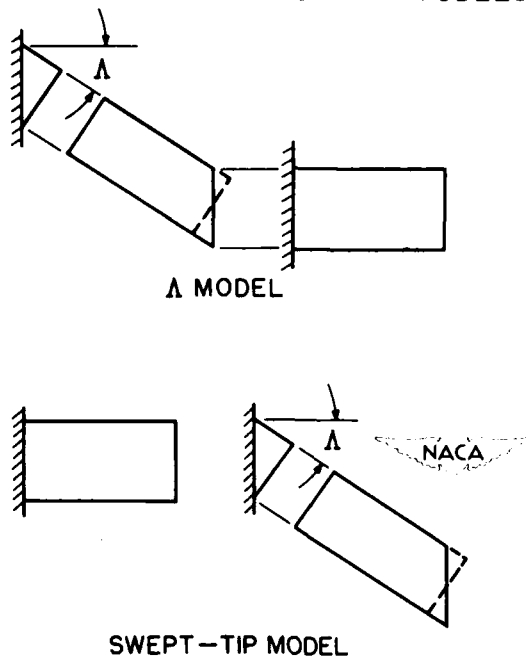
IDEALIZATION OF  $\Delta$  AND SWEPT-TIP MODELS

Figure 9.

## SWEPT-TIP MODEL LOADED WITH STREAMWISE TORQUE

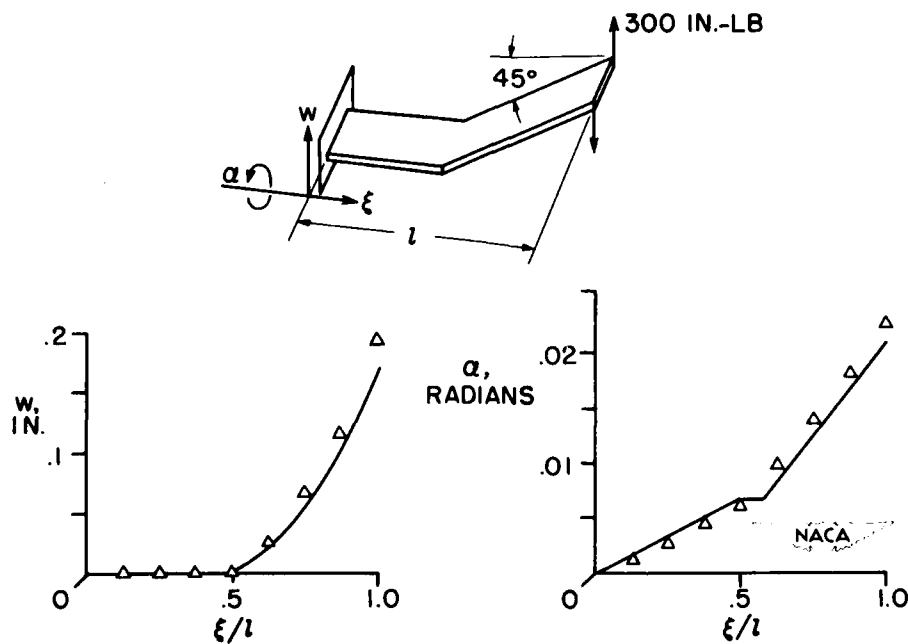


Figure 10.

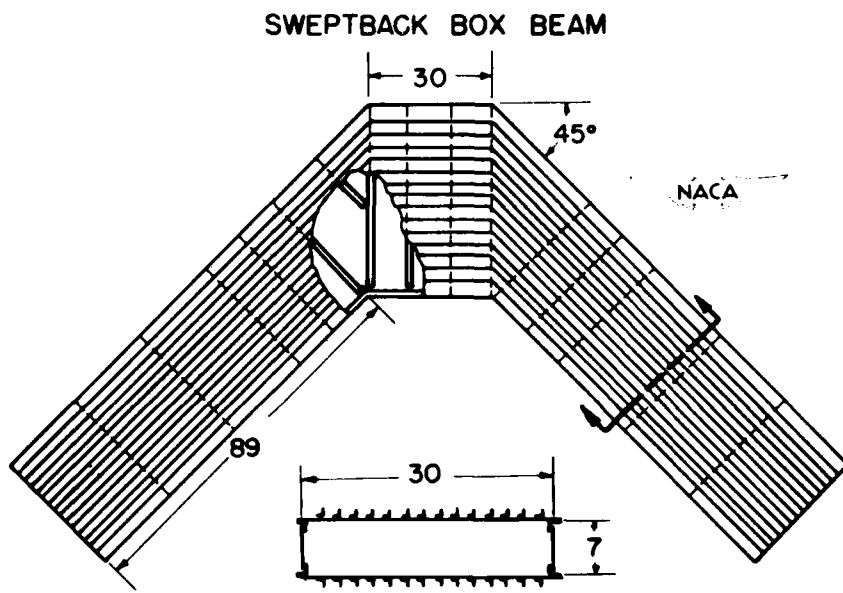


Figure 11.

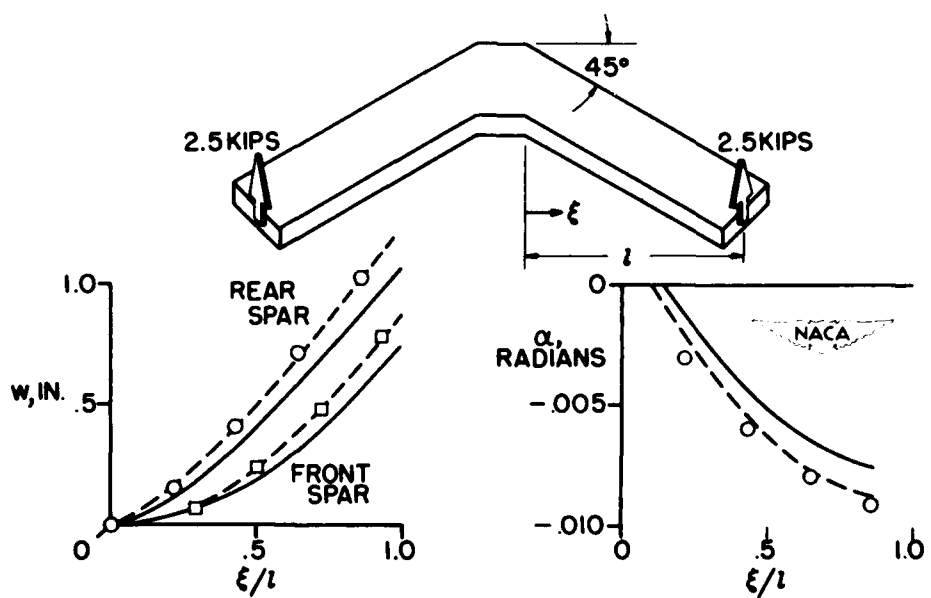
**DEFORMATION OF 45° SWEPT BOX WITH LIFT LOAD**

Figure 12.

## DEFORMATION OF 45° SWEPT BOX WITH TORQUE LOAD

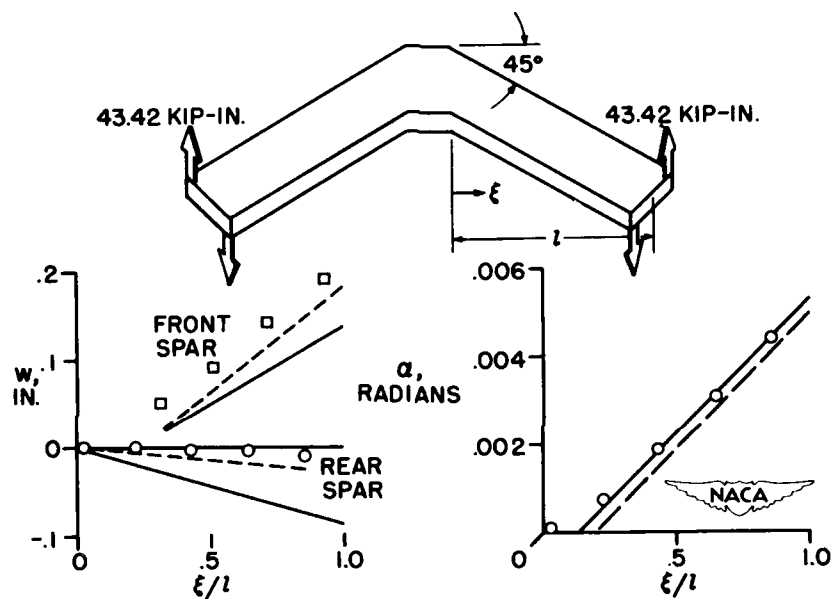


Figure 13.

**CONFIDENTIAL**

**529**

**STRENGTH**

**CONFIDENTIAL**

SOME RECENT DATA ON THE STRENGTH CHARACTERISTICS  
OF WINGS WITH THICK SKINS

By Roger A. Anderson, Richard A. Pride,  
and Aldie E. Johnson, Jr.

Langley Aeronautical Laboratory

Requirements of strength, stiffness, and aerodynamic smoothness often dictate the use of a thick skin for thin, high-speed airfoils. The structural design problem for such an airfoil resolves into providing a system of internal supports which will enable the thick skin to carry the required flight loads. In order to stabilize a thick skin the internal supporting structure must be stiff, and this stiffness must be achieved without undue complexity and at the least possible weight. This paper will deal primarily with the strength of thick-skin construction as influenced by two types of internal support systems.

Figure 1 shows the types of wing structure to be discussed. The first cross section illustrated is a circular-arc airfoil without internal stiffening. The strength characteristics of such an airfoil serve as a convenient lower limit with which the strength of internally stiffened thick-skin airfoils may be compared. The second cross section shown is the familiar multiweb wing structure. The role played by the full-depth webs in controlling the stability and strength of the cover skins will be discussed in the light of recent tests and theory. A variation of the multiweb wing is the multipost stiffened wing. It will be shown that, under certain conditions, a line of posts and stiffeners may be used to replace a solid web for production reasons or for weight economy.

When dealing with thick-skin construction it is desirable to express certain structural dimensions in terms of the skin thickness; thus the thickness of the beam  $H$  will be given as the ratio of beam thickness to skin thickness  $H/t_S$ .

The strength of a long aluminum-alloy circular-arc airfoil in pure bending is shown in figure 2. Here the bending stress at the midchord of the beam at failure is plotted as a function of the ratio  $H/t_S$  for various values of  $H/c$ , the thickness ratio for the cross section. The curves for a 4-, an 8-, and a 10-percent-thick airfoil are derived from an ultimate-strength theory (ref. 1) based upon the progressive flattening of the cross section as the beam bends, the so-called "Brazier effect." The circles are experimental results which appear to confirm this theory. It is seen that, because of the flattening that occurs during bending of a hollow beam, the stress level at failure is generally low. Flattening can be prevented by a stiff internal structure,

with a resulting increase in the failure stress. One practical type of internal structure consists of full-depth spanwise webs.

The results of bending tests on multiweb beams in which the spacing and depth of the spanwise webs have been varied are shown in figure 3. Here the average compressive stress in the beam covers at failure has been plotted against the  $H/t_S$  ratio. The covers have been divided up into widths  $b_S$  such that values of 25, 30, 40, and 60 have been produced for  $b_S/t_S$ . For each  $b_S/t_S$  value the depth of the webs was varied to cover a range of ratios of beam thickness to skin thickness. Curves have been faired through the test data obtained. As would be expected, the stress level at failure increases as the ratio of web spacing to skin thickness decreases. However, for any value of  $b_S/t_S$  the actual stress level reached at failure is strongly dependent upon the stiffness characteristics of the webs, and therefore the results must be qualified by the other information supplied in the figure. The test data apply to beams with channel-type webs formed from sheet metal with a 4t bend radius between the web and the attachment flange. The ratio of web thickness to skin thickness is 0.41. The importance of these two specifications will be brought out in succeeding figures. A comparison of the test data of figure 3 with the curves of figure 2 shows that high average stresses in the beam covers at failure can be obtained with a multiweb beam for a wide range of  $H/t_S$  values. As  $H/t_S$  increases, the stress level at failure slowly decreases because of the loss of stiffness in the webs due to web buckling; web buckling can be forestalled, of course, by a change in web thickness.

For  $b_S/t_S$  equal to 30, the effect of changes in web thickness is shown in figure 4. Again these test data apply to formed channels with a 4t bend radius. The effect of increasing web thickness, given as the ratio  $t_W/t_S$ , is to produce increases in the stress level at failure. Under a given set of design conditions, however, the web thickness which leads to the highest beam efficiency is determined by the strength-weight ratio, and the weight of the webs is also increased as  $t_W/t_S$  is increased.

A way of increasing the strength of a multiweb beam which does not involve a weight increase is to improve the stiffness of the joints between the webs and the covers. Four beams were built, identical in all dimensions except the details of the joint design (fig. 5). All the joints are strongly riveted but they vary widely in stiffness because of the variation in the bend radius. In each case the line of rivets was kept as close as possible to the plane of the web to minimize the eccentricity. The first joint has essentially a zero bend radius, which can be obtained

with an extrusion, and the eccentricity is a minimum. The other three joints cover a range of bend radii encountered in production practice. The results of bending tests on these beams are shown in the bar graph. The height of the bar indicates the average stress in the cover at failure and the height of the shaded portion indicates the stress at which buckling of the cover occurred. The variation in the stress at failure is seen to be very substantial. The beam with webs of zero bend radius carries a bending moment 40 percent greater than the beam with webs of 4t bend radius; the latter beam is representative of best production practice with 75S-T6 aluminum alloy. It is estimated that a further increase of a few percent in beam strength would be obtained if the joint eccentricity were reduced to zero by achieving symmetry such as is given by a T-connection between webs and covers. Thus we see that differences in design and production procedures can cause large variations in allowable design stresses. A buckling theory has been developed which takes into account the support stiffness of the webs as influenced by the attachment-flange eccentricity and the web thickness (ref. 2). The theory may therefore be used to predict the effectiveness of stiffeners and channel-type webs when used to stiffen thick sheet. The correlation of this theory with the results of a series of multiweb-beam tests is shown in figure 6.

Here the buckling stress has been plotted against the  $H/t_S$  ratio for the beam. The solid curve gives the buckling-stress prediction for the test beams built with a 4t bend radius in the webs. The curve and the test points are for beams with a ratio of web spacing to skin thickness of 30 and a ratio of web thickness to skin thickness of 0.41. Calculations based on an earlier NACA theory (ref. 3) for the buckling of multiweb beams are shown by the dashed curve. The earlier theory is based upon the assumption of an integral joint between the webs and covers. This theory is known to agree with beam tests in which the joint stiffness is adequate to prevent deflections of the cover along the web attachment lines. With flexible joints, a reduction in buckling stress can be expected, as predicted by the new theory and confirmed by the test results. This reduction in buckling stress is also a measure of the reduction in the failure stress, since failure follows buckling very closely at low values of  $b_S/t_S$ .

In order to determine the over-all reduction in failing stress of multiweb beams with formed-channel webs, an investigation is also being made of the strength of beams with extruded channels which have essentially a zero bend radius. The strength of such beams is being determined from an analysis of the failing stresses of short compression panels stiffened by extruded Z-stiffeners. Such data are available from previous NACA investigations of stiffened panels (refs. 4 and 5). Through a rational procedure, the proportions of multiweb beams are obtained which should

have a failing stress in bending equal to the failing stress in compression of short stiffened panels of certain proportions. The results of this analysis have been compared with the data from the few tests of multiweb beams with extruded channels that are available, and in these instances the analysis gave a correlation.

Figure 7 shows the failure stresses predicted for extruded-channel web beams by this analysis. They may be compared directly with the stresses shown in figure 3 for beams with formed channels. This comparison indicates that an increase in strength ranging from 25 to 35 percent is attained by changing from formed sheet-metal channels to extruded channels. This strength increase is achieved without an increase in beam weight and is attributed to the improvement in the stiffness of the joints between the webs and covers. Strength increases of this order of magnitude could be converted into rather substantial savings in the beam weight required to carry a given loading.

So far this discussion has been limited to the strength of multiweb beams in bending alone. A few tests in combined bending and torsion and in pure torsion have also been made to see if a simple parabolic interaction curve could be used to describe the failing strengths of these beams under combined-stress conditions. In order to verify such an assumption, a reasonable value for the ultimate strength in torsion must be calculated or obtained in a test. Diagonal-tension theory (ref. 6) has been used to make a strength prediction for a three-cell beam tested in pure torsion and the prediction was found to be about 15 percent conservative for this beam. The beam had closing webs that were as thick as the covers in order to carry the shear flow around the box, and the failure was confined to a forced crippling of the lighter interior webs. Other pure-torsion tests have been planned in which the number of cells will be increased to determine the correlation with the theory for plane diagonal tension under conditions in which there is a considerable variation in the shear flow in the different cells. At the present time, however, it appears that for multiweb beams with heavy closing webs and lighter interior webs, diagonal-tension theory may be used to estimate the strength under a torsion moment, and a parabolic interaction with bending moment may be assumed. The results of a few combined-load tests indicate that this procedure leads to a conservative strength prediction.

This survey will be concluded with a discussion of current research on the multipost stiffened beam. A comprehensive summary of the available theory and design data for this type of construction was presented at the annual meeting of the Institute of the Aeronautical Sciences in January 1953 (ref. 7). More recent results are presented in the following paragraphs.

Figure 8 gives a detailed view of the structure. A pair of small stiffeners and spaced vertical posts or uprights have been used to replace

a full-depth web. Such a replacement might be desirable from the stand-point of improving the interior accessibility of the structure and also to avoid the buckling that occurs in thin solid webs. It was pointed out previously that, as  $H/t_g$  increases, a loss in strength of a multi-web beam occurs because of the buckling of the thin webs. Also, as  $H/t_g$  increases, the solid webs become an increasingly large proportion of the beam weight. Theoretical studies have indicated that a combination of posts and stiffeners of small moment of inertia can perform the functions of a solid web of equal or greater weight under certain loading conditions. In bending, the post-stiffener combination can constrain the compression cover to buckle in a desirable manner; that is, it can force a longitudinal node to form along the line of stiffeners and posts. The combinations of stiffener stiffness, post stiffness, post spacing, and so forth required to form a node have been established theoretically (ref. 8) and the behavior has been confirmed by a number of tests.

The beams tested in this series (fig. 9) were tubes of 14S-T6 aluminum alloy with rectangular cross sections. In the first test the plain tube was failed in bending, with buckling occurring at a stress of about 6,000 psi and failure occurring at about 30,000 psi. In the succeeding tests a solid channel web and three different post-stiffener combinations were placed down the center line of the tube. The weight of each of these center-line supports was the same. The post spacing was varied to give ratios of post spacing to cover width of 2, 1, and 1/2. As shown by the shaded portions of the bar graphs, each of the post-stiffener combinations and the solid web raised the buckling stress for the compression cover to about 23,000 psi. This buckling occurred with a longitudinal node down the center line of the cover, and in the loading range beyond buckling the buckles in the compression cover were not transmitted by the posts to the tension cover. Just prior to failure, however, the buckle pattern shifted to a form with transverse nodes across the cover which caused large axial forces in the posts. Failure resulted when the connections between the posts and the stiffeners and between the stiffeners and the covers failed. On the basis of these few tests, it appears that small, rather than large, post spacings are slightly more effective in resisting final failure and that for equal weight a combination of stiffeners and posts can be just as effective as a solid web in stabilizing the compression cover in a pure-bending test.

When torsion is combined with bending, the role played by the posts in stabilizing the beam depends upon a number of factors in addition to their axial stiffness and spacing. The most important of these factors are the ratio of shear stress to bending stress present in the beam covers and the end fixity and bending stiffness of the posts. The importance of these factors is best illustrated with interaction curves established by theory and tests.

The curves of figure 10 give the interaction of shear stress arising from torsion and compression stress arising from bending for the cover of a long rectangular tube stabilized by different types of center-line supports. The dotted curve is the computed buckling interaction curve obtained for the cover with a small longitudinal stiffener but no posts when the assumption is made that the side walls of the tube do not restrain the mode of buckling. With the addition of closely spaced, infinitely stiff posts, pin-connected to the stiffeners, theory indicates that buckling should occur at the combinations of compression and shear stress given by the dashed curve. It is noticed that in pure shear the post-stiffener combination is theoretically no more effective than the stiffeners alone but as the ratio of bending to shear stress increases the posts provide a stabilizing effect on the cover.

A pure-torsion test was made on this tube with pin-connected posts at a post-spacing ratio equal to unity, and the buckling stress is denoted by the square on the shear axis (fig. 10). The spread between this test point and the dashed curve is attributed to the edge restraints offered by the side walls during buckling, which are not accounted for in the theoretical prediction. These edge restraints can become large during the formation of a continuous skewed buckle around the unequal-width walls of a tube buckling in shear. At the other loading extreme, pure bending, these continuity restraints are not as large and the result of a test with pin-connected posts, as denoted by the square on the compression axis, is in better agreement with theory.

The solid interaction curves in figure 10 were established by tests on the same tube and post-stiffener combination with the exception that the posts were connected to the stiffeners in a manner which introduced a fair amount of end fixity in the posts. Thus the stiffeners and posts were capable of developing some Vierendeel truss action to resist cover buckling. The inner solid curve is faired through the test points which define the combinations of shear and compression stress that cause buckling of the beam. The spread between the inner solid curve and the dashed curve may now be attributed to the continuity restraints caused by the side walls of the beam and to the Vierendeel truss action in the post-stiffener combination. The shape of the resulting interaction is very favorable in that a high percentage of the buckling loads in pure torsion and pure bending alone must be applied in combination to cause buckling. When the ratio of bending stress to shear stress present in the beam is high, the post-stiffener combination is able to provide about the same stability to the compression cover as would be expected for a solid web.

The outer curve is faired through the stress combinations causing failure of the tube. For the beam proportions tested here, the margin between buckling and failure is seen to be small when the loading is predominantly torsion and to increase substantially when the loading is predominantly bending.

To summarize the data that have been presented: A completely hollow wing with thick skin has definite limitations as regards bending strength. The strength of thick-skin wings is greatly increased, however, by the addition of thin spanwise webs as stiffening elements. The stiffening effect of these webs has been shown to be highly influenced by the way the webs are joined to the skins, but this characteristic is predictable and can be controlled by good detail design. A variation of the multiweb design, the multipost stiffened structure, shows promise as a means of replacing some of the webs in a multiweb wing. Such a replacement will improve interior accessibility and may reduce the weight of the internal structure.

## REFERENCES

1. Fralich, Robert W., Mayers, J., and Reissner, Eric: Behavior in Pure Bending of a Long Monocoque Beam of Circular-Arc Cross Section. NACA TN 2875, 1953.
2. Anderson, Roger A., and Semonian, Joseph W.: Charts Relating Critical Compressive Stress of Longitudinally Supported Plates to the Effective Deflectional and Rotational Stiffness of the Supports. (Prospective NACA paper)
3. Schuette, Evan H., and McCulloch, James C.: Charts for the Minimum-Weight Design of Multiweb Wings in Bending. NACA TN 1323, 1947.
4. Hickman, William A., and Dow, Norris F.: Data on the Compressive Strength of 75S-T6 Aluminum-Alloy Flat Panels With Longitudinal Extruded Z-Section Stiffeners. NACA TN 1829, 1949.
5. Hickman, William A., and Dow, Norris F.: Data on the Compressive Strength of 75S-T6 Aluminum-Alloy Flat Panels Having Small, Thin, Widely Spaced, Longitudinal Extruded Z-Section Stiffeners. NACA TN 1978, 1949.
6. Kuhn, Paul, Peterson, James P., and Levin, L. Ross: A Summary of Diagonal Tension. Part I - Methods of Analysis. NACA TN 2661, 1952.
7. Badger, D. M.: Notes on the Analysis and Design of Multi-Post Stiffened Wings. Preprint No. 393, S.M.F. Fund Preprint, Inst. Aero. Sci., Jan. 1953.
8. Anderson, Roger A., Wilder, Thomas W., III, and Johnson, Aldie E., Jr.: Preliminary Results of Stability Calculations for the Bending of Box Beams With Longitudinally Stiffened Covers Connected by Posts. NACA RM L52K10a, 1952.

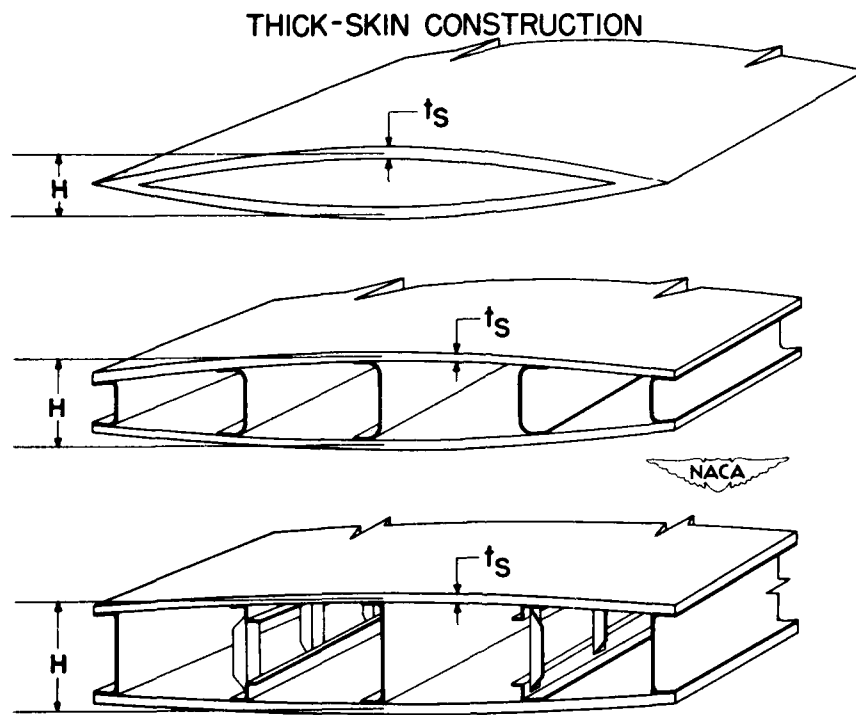


Figure 1.

## BENDING STRENGTH OF CIRCULAR-ARC AIRFOILS

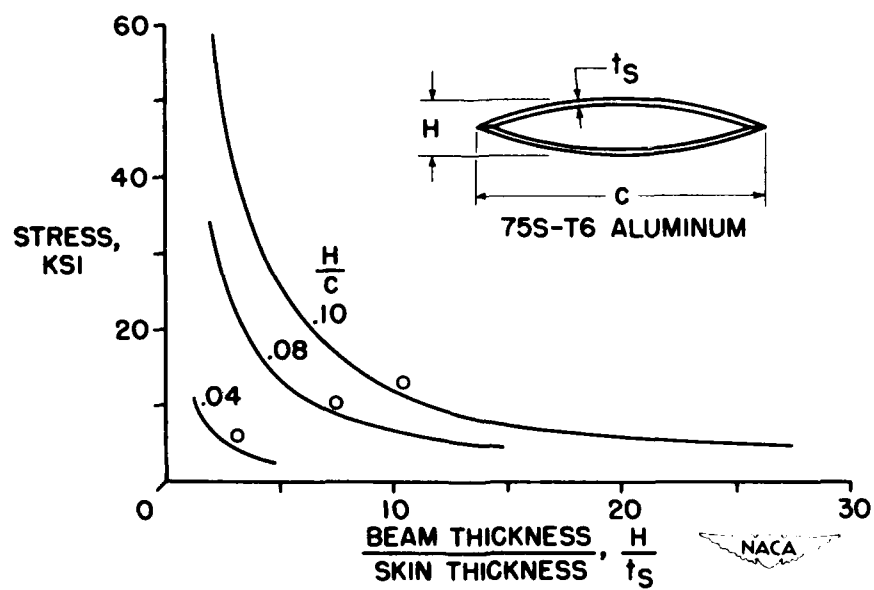


Figure 2.

## EFFECT OF WEB SPACING ON STRENGTH

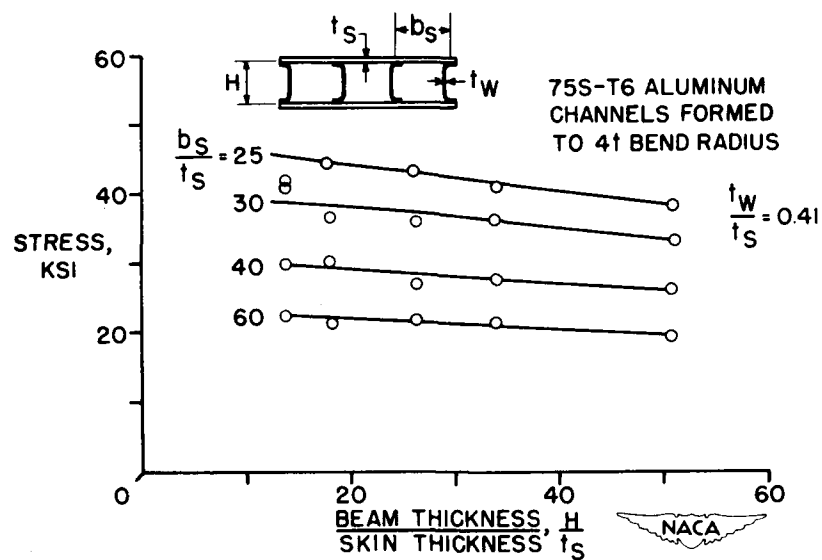


Figure 3.

## EFFECT OF WEB THICKNESS ON STRENGTH

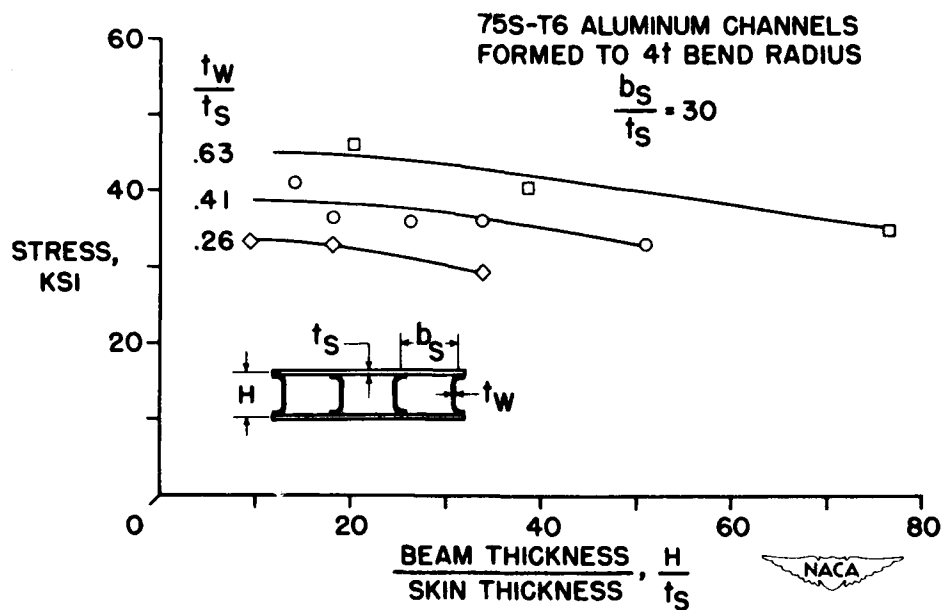


Figure 4.

## EFFECT OF JOINT DETAIL ON STRENGTH

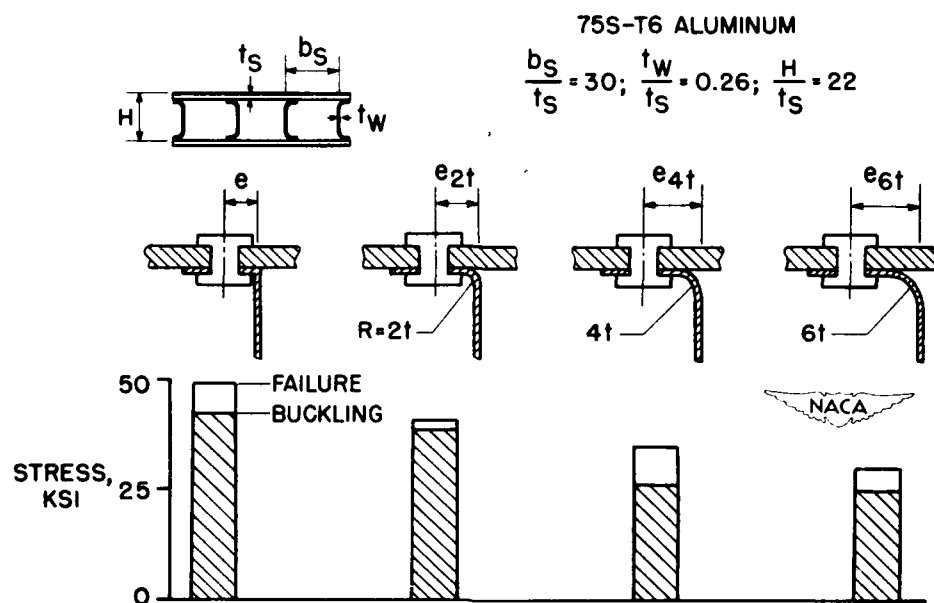


Figure 5.

## COMPARISON OF THEORETICAL AND EXPERIMENTAL BUCKLING

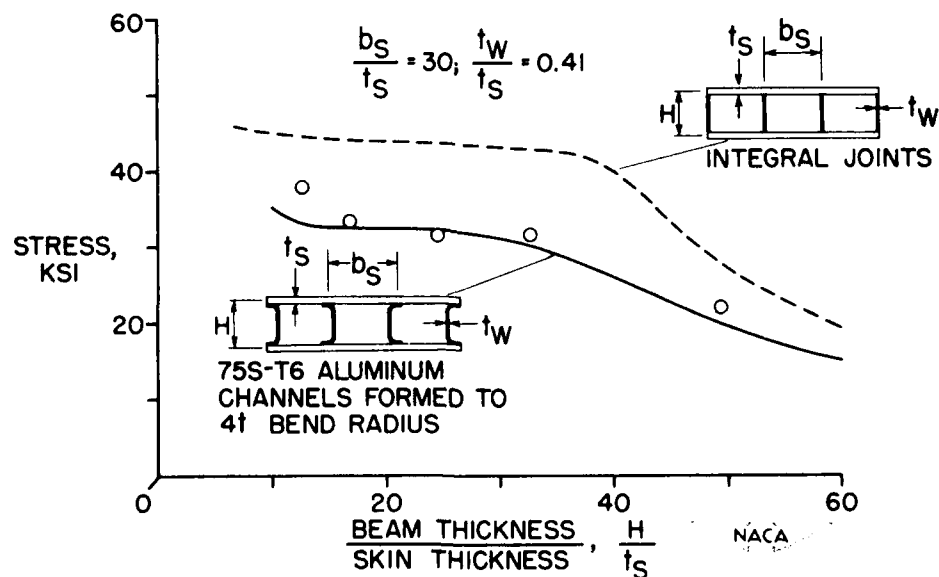


Figure 6.

## EFFECT OF WEB SPACING ON STRENGTH

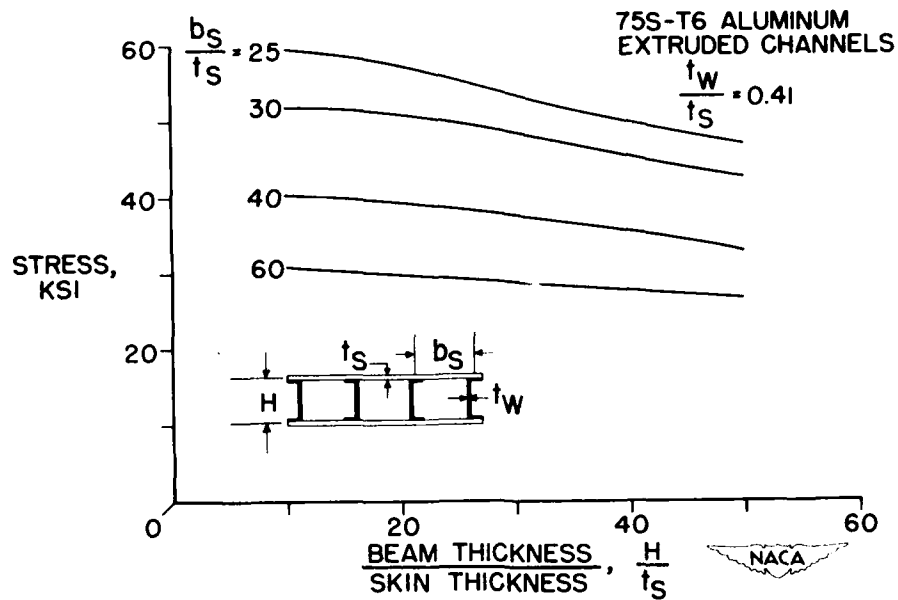


Figure 7.

## MULTIPOST STIFFENED BEAM

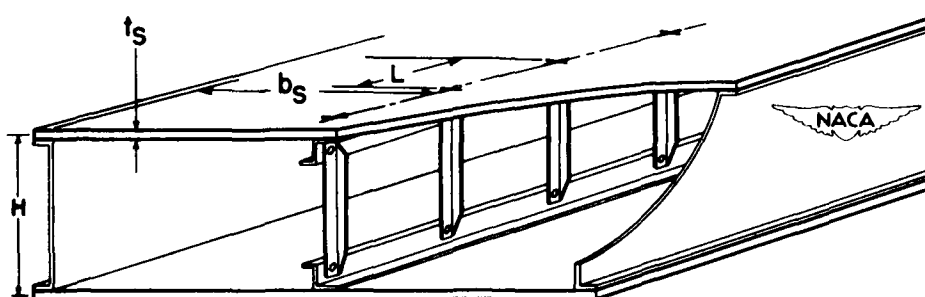


Figure 8.

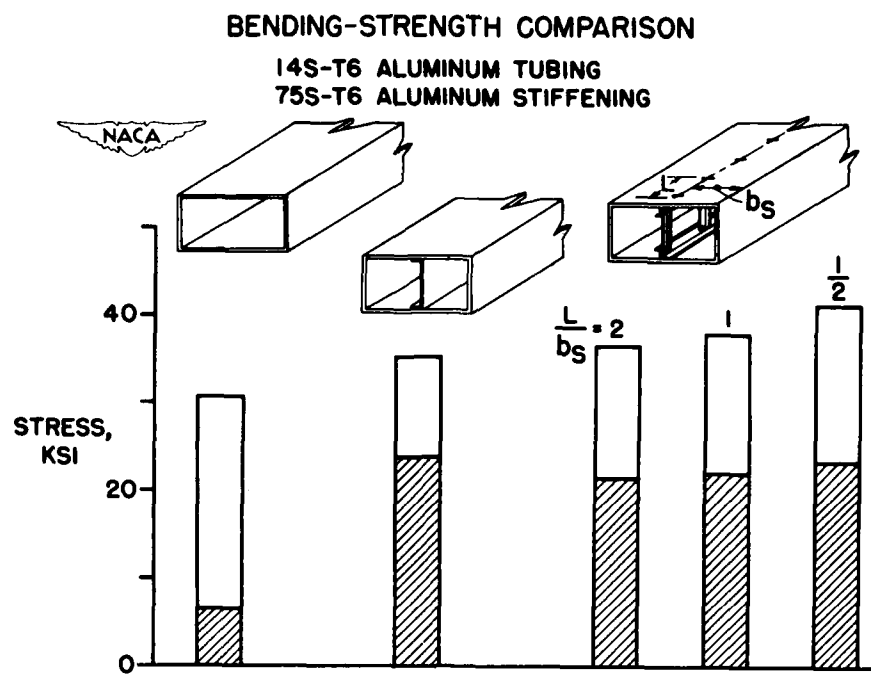


Figure 9.

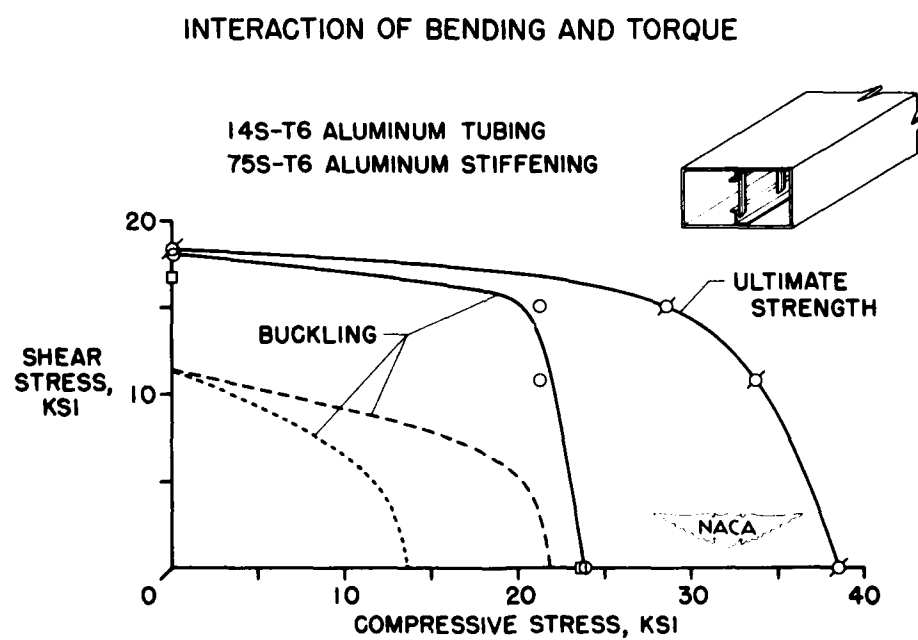


Figure 10.

## A STUDY OF INTEGRALLY STIFFENED PLATES

By Norris F. Dow, Charles Libove, and L. Ross Levin

Langley Aeronautical Laboratory

## INTRODUCTION

The idea of integral stiffening has stimulated much interest as is evidenced by the heavy forging press program (ref. 1) and the number of recent papers describing the merits of such construction (see, for example, ref. 2). Because the majority of these papers are concerned with possible gains in production efficiency, little information is yet available on the structural characteristics of integrally stiffened construction.

This paper presents a summary of progress on studies of the structural characteristics, together with examples of design applications for several components of the airframe.

## TYPES OF INTEGRAL STIFFENING CONSIDERED

The types of integral stiffening considered are cross sections suitable for press-forging or machining, namely, simple rectangular ribs integral with the skin and fairing into it with circular fillets (see fig. 1). The configurations under consideration vary from simple longitudinal or transverse ribbing to two-way longitudinal and transverse ribbing, or ribbing skewed at equal values of  $\theta$  to the longitudinal axis. Of the variety of proportions considered, this paper is concerned with those shown in figure 2 where can be seen a specific cross section for testing and comparisons with theory, and a series of proportions for studies of structural efficiency. The latter sections have rib spacings of 20 times the skin thickness and various rib heights, but the same equivalent thicknesses, and, therefore, the same weights.

48

## ELASTIC CONSTANTS

The first step in the study of integrally stiffened plates such as these is the determination of their elastic constants - that is, for example, the stretching and shearing stiffnesses and the bending and twisting stiffnesses. Unfortunately, difficulties arise in the calculation of the elastic constants because of uncertainties regarding the transverse effectiveness of the ribbing. For example, in a thick, low, well-filletted rib a large part of the material is effective in resisting

transverse stretching, whereas in a thin, tall rib only a small part of the material is effective.

Difficulties also arise with the stiffening on only one side of the skin. One-sidedness introduces "coupling" between distortions, such that, for example, if tension is applied in one direction, bending is produced transverse to that direction.

A theory has been developed for the elastic constants (ref. 3) which takes into account these various difficulties. As for corrugated-core sandwich-type plates (ref. 4), 15 elastic constants are needed to describe completely the force-distortion relationships of the integrally stiffened plates, including the coupling actions previously mentioned. The adequacy of the theory is indicated by the typical comparisons of calculation and experiment shown in figure 3. The longitudinal bending stiffness and twisting stiffness of a plate with skewed ribbing are plotted in figure 3 in terms of  $\theta$ , the angles of skew of the ribs. The calculated curves are compared with experimental points measured on cast plates of the proportions shown in figure 2. The agreement for both stiffnesses is within the relatively large scatter occasioned by the inherently poor dimensional tolerances of sand castings. Similar agreement has been found for other elastic constants.

#### APPLICATIONS

With the elastic constants determined, the basis is laid for the design of integrally stiffened plates for a variety of applications. Designs of flat plates for the compression surface of the wing and for shear webs of beams and of curved plates for fuselage construction will be discussed.

##### Compression Members

First, consider flat plates for compression. The standard theory of elastic buckling of long, orthotropic flat plates is well-known (see ref. 5). This theory is adequate for integrally stiffened plates, as is shown in figure 4 where the measured (ref. 6) and calculated critical loads of skew-stiffened plates are compared for varying angles of skew of the ribbing.

This comparison is solely for long plates in the elastic range. For short plates which act like columns and for plastic buckling, the peak buckling strength occurs for a value of  $\theta$  less than  $45^\circ$  because, with the ribs more in line with the load, the column bending stiffness is raised (see fig. 3) and the onset of plasticity delayed.

For plastic buckling no rigorous theory is available and a rule of thumb, corresponding to the secant modulus method for ordinary plates (ref. 7), is proposed - namely, that plastic buckling occurs at the same strain as if the plate remained elastic. (See fig. 5.) In order to determine the plastic buckling load corresponding to the buckling strain, the load-strain curve of the plate for compression with buckling prevented is needed. The initial slope of this curve can be obtained from elastic theory, and the remainder experimentally or approximately by assuming that vertically the curve is affinely related to the material stress-strain curve. This assumption has been found to be reasonably correct for strains up to about 1 percent.

The proposed rule of thumb for plastic buckling is supported by the data shown in figure 6 where two experimental buckling loads are compared with the curve of buckling load against calculated elastic buckling strain.

Although further substantiation is needed, for want of a more rigorous analysis this method of predicting plastic buckling was used to derive efficiency curves for integrally stiffened plates. Typical results shown in figure 7 are for plates with square-pattern ribbing skewed at  $45^{\circ}$ . The design conditions - namely, the plate width and the compressive load - are combined in the structural index (ref. 8) used as abscissa. The ordinate, which incorporates the equivalent thickness of the plate, gives essentially the reciprocal of the weight required to meet the design conditions. Accordingly, the weight saving of the integrally stiffened plates over unstiffened plates is indicated by the height of the curves for the various ratios of rib depth to skin thickness relative to the curve for no ribs at all.

As an example of the weight saving possible, consider the box beam, cited in a previous paper by Roger A. Anderson, Richard A. Pride, and Aldie E. Johnson, Jr., which had the best combination of stiffeners and posts down its center. The cover of this beam had a structural index value of 1.02 ksi and achieved an ultimate stress of 41 ksi. At the same value of the structural index, an integrally stiffened plate of approximately the indicated proportions can develop an equivalent stress of 52 ksi without buckling, and hence permit a weight saving of approximately 20 percent. At an index value of 0.51 ksi, representative of the beam without any center supports, the integrally stiffened plate of the indicated proportions can achieve a slightly higher buckling stress than that achieved by the unstiffened plate with its center supports at maximum load. In this case, integrally stiffened plate spans twice the width of the unstiffened plate with a slight weight saving in addition to the weight saved by the elimination of the center supports.

Curves like these may be calculated for other configurations and proportions and be used for design charts for compression loadings.

### Shear Webs

For shear loadings, again elastic buckling is discussed in the literature (ref. 9), and plastic buckling may be handled in a manner similar to the way it was for compression. The agreement between theory and one experiment for the elastic case is shown in figure 8 for the proportions used for test specimens with varying angles of skew of the ribbing.

For shear in the elastic range, the peak buckling strength occurs at  $60^\circ$ . For plastic buckling and for ultimate shear strength, a value of  $\theta$  approaching  $45^\circ$ , which permits the ribbing to carry shear load directly by diagonal tension and compression, would be more effective.

If the shear buckling strength characteristics (fig. 9) are considered from the structural-index point of view (ref. 10), integrally stiffened shear webs are seen to permit weight saving over conventional construction for a wide range of values of the structural index, the percent saving depending upon the proportions. These curves were calculated, by using diagonal-tension theory, similarly to the way the curve for the conventional beam was calculated (ref. 11). Curves like these may be derived for other proportions and configurations.

### Combined Compression and Shear

For combined compression and shear, there are some experimental results which indicate that, in the elastic range (that is, for large values of plate width to rib height), a parabolic interaction curve is a reasonable approximation for both of these configurations. (See fig. 10.) Since the pure compression and pure shear cases can be calculated, the establishment of the interaction curve permits the calculation of the elastic buckling stresses under various combinations of longitudinal compression and shear. These particular curves, which are for plates of equal weight, also show the advantage of the  $45^\circ$  skew-stiffened configuration over longitudinal and transverse stiffening for the whole range or combined loadings in the elastic range.

No data are yet available in the plastic range. However, on the assumption that a parabolic interaction curve also holds in the plastic range, figure 11 was prepared to bring out the limited region in which the  $45^\circ$  stiffening configuration is less effective. For small values of plate width to rib height (that is, well up in the plastic range) and for practically pure compression, some configuration, such as the longitudinally and transversely stiffened, which puts more material in the longitudinal direction may be more efficient.

### Curved Plates

The foregoing discussion of flat plates applies in a similar way to curved plates. For elastic buckling, the theories intended for orthotropic sandwich-type plates (ref. 12) may be adapted to predict the buckling of curved, integrally stiffened plates.

Structural indexes for curved plates, suitable for fuselage construction, however, are not as well established as for flat plates. Hence, a valid demonstration of the suitability of integrally stiffened construction for this application is difficult. Although a comparison may be made of a conventionally stiffened cylinder for which data are available (ref. 13) and an integrally stiffened cylinder designed to have the same weight (fig. 12), this comparison may be unfair because this particular stiffened cylinder may be inefficiently proportioned. Moreover, any comparison on the basis of the same weight does not indicate the possible amounts of weight saving. Despite these reservations, the fact that calculations show that an integrally stiffened cylinder could carry twice the compressive load and nearly three times the shear load carried by the conventional construction suggests that integral stiffening is fully as applicable to curved-plate construction as to the flat-plate constructions previously cited.

### CONCLUDING REMARKS

The examples presented in this paper have shown that theories are available for the design of integrally stiffened plates for a variety of applications, and have indicated possibilities for weight saving in the use of integral stiffening for the compression surface of the wing, for shear webs, and for fuselage construction. The magnitude of the weight saving varies with both the proportions and the configuration of stiffening. One configuration stands out, however, as offering greater possibilities for weight saving for any given proportions than the others considered, over the widest range of design conditions; namely, a square pattern of ribbing, possibly oriented longitudinally and transversely for pure compression in the plastic range, but skewed at  $45^\circ$  for all other loading conditions.

## REFERENCES

1. Stone, Irving: Where AF Heavy Press Program Stands. Aviation Week, vol. 58, no. 19, Mar. 2, 1953, pp. 98-104.
2. Anon.: The Big Squeeze. SAE Jour., vol. 61, no. 1, Jan. 1953, pp. 29-32.
3. Dow, Norris F., Libove, Charles, and Hubka, Ralph E.: Formulas for the Elastic Constants of Plates With Integral Waffle-Like Stiffening. (Prospective NACA paper)
4. Libove, Charles, and Hubka, Ralph E.: Elastic Constants for Corrugated-Core Sandwich Plates. NACA TN 2289, 1951.
5. Timoshenko, S.: Theory of Elastic Stability. McGraw-Hill Book Co., Inc., 1936, pp. 380-382.
6. Dow, Norris F., and Hickman, William A.: Preliminary Experiments on the Elastic Compressive Buckling of Plates With Integral Waffle-Like Stiffening. NACA RM L52E05, 1952.
7. Stowell, Elbridge Z.: A Unified Theory of Plastic Buckling of Columns and Plates. NACA Rep. 898, 1948. (Supersedes NACA TN 1556.)
8. Heimerl, George J., and Barrett, Paul F.: A Structural-Efficiency Evaluation of Titanium at Normal and Elevated Temperatures. NACA TN 2269, 1951.
9. Thielemann, Wilhelm: Contribution to the Problem of Buckling of Orthotropic Plates, With Special Reference to Plywood. NACA TM 1263, 1950.
10. Shanley, F. R.: Weight-Strength Analysis of Aircraft Structures. McGraw-Hill Book Co., Inc., 1952.
11. Kuhn, Paul, Peterson, James P., and Levin, L. Ross: A Summary of Diagonal Tension. Part I - Methods of Analysis. NACA TN 2661, 1952.
12. Stein, Manuel, and Mayers, J.: Compressive Buckling of Simply Supported Curved Plates and Cylinders of Sandwich Construction. NACA TN 2601, 1952.
13. Kuhn, Paul, Peterson, James P., and Levin, L. Ross: A Summary of Diagonal Tension. Part II - Experimental Evidence. NACA TN 2662, 1952.

## CONFIGURATIONS OF INTEGRAL STIFFENING

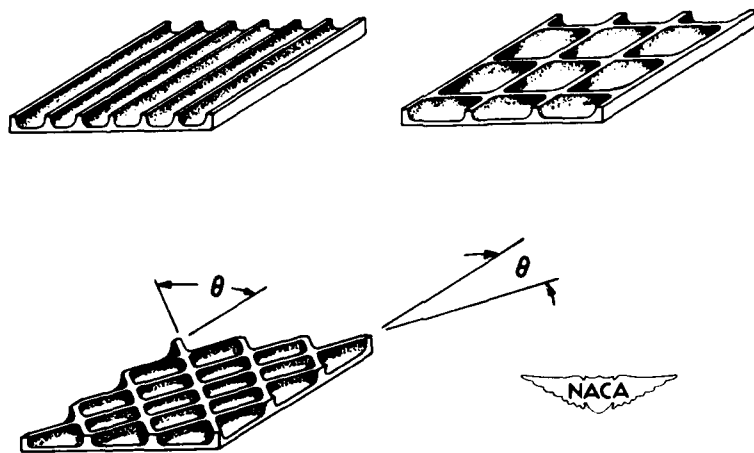


Figure 1.

## PROPORTIONS OF CROSS SECTIONS

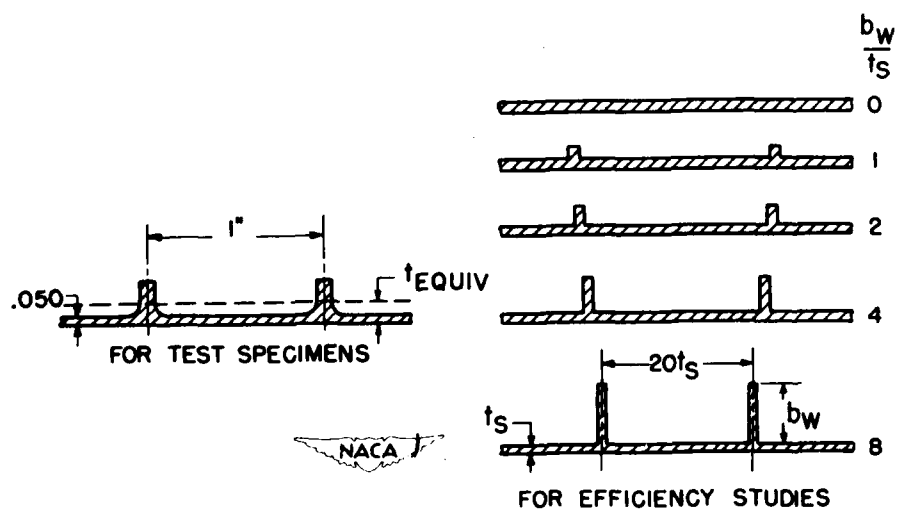


Figure 2.

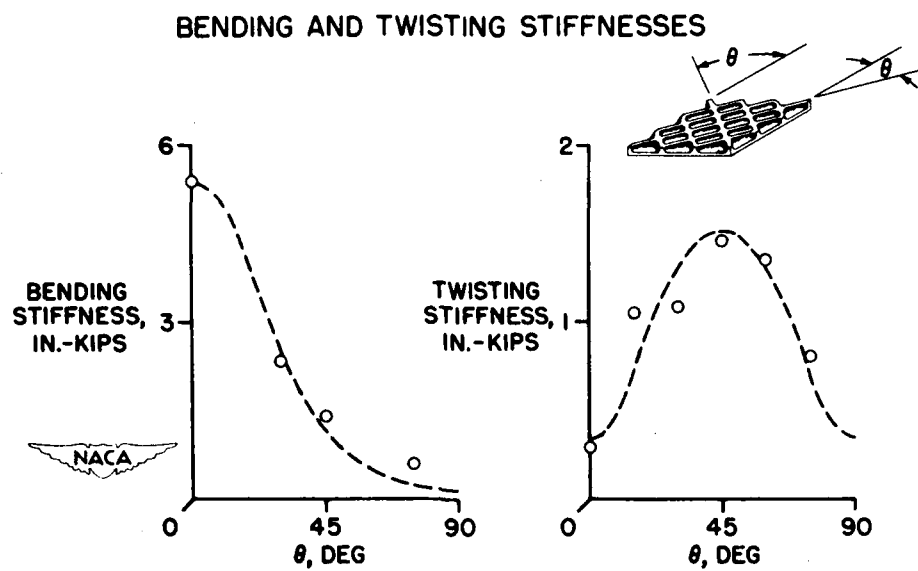


Figure 3.

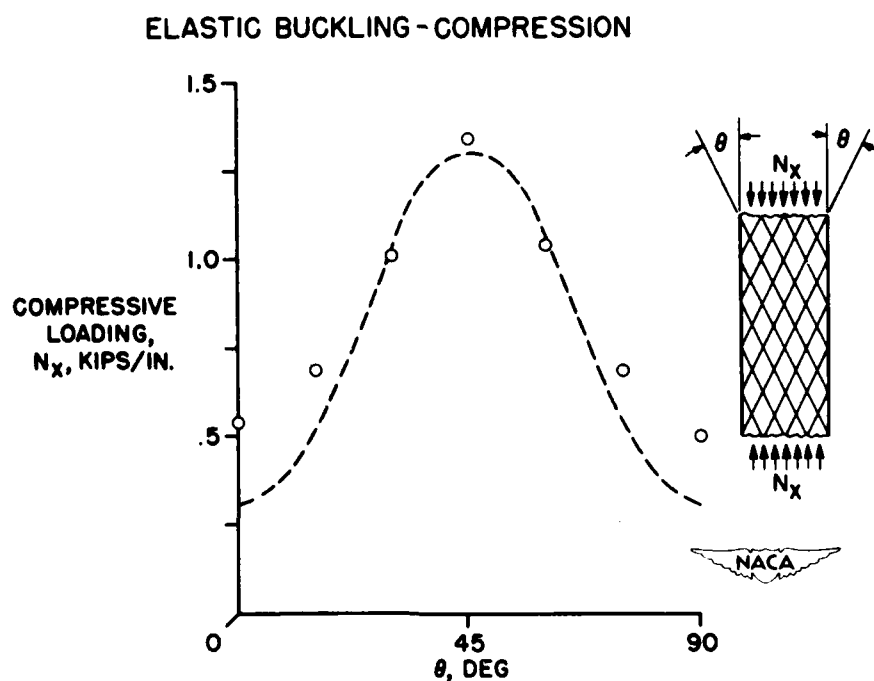


Figure 4.

## PLASTIC BUCKLING ASSUMPTION

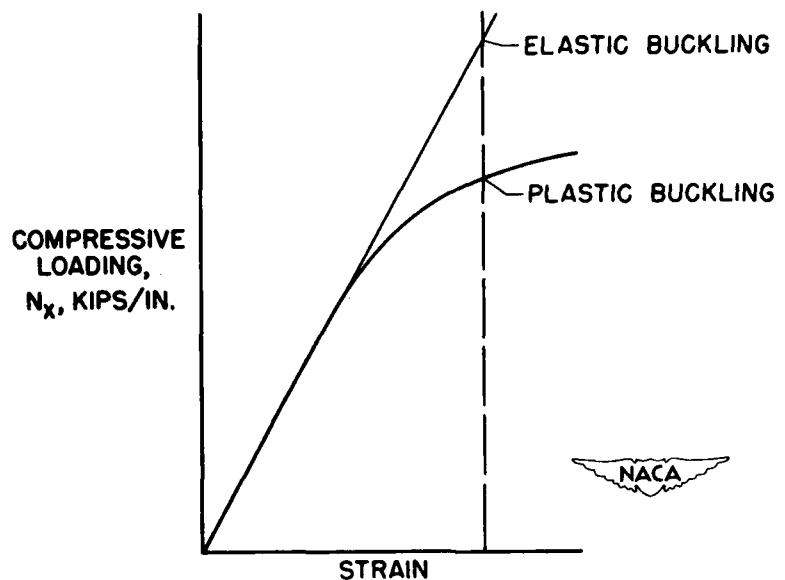


Figure 5.

## PLASTIC BUCKLING - COMPRESSION

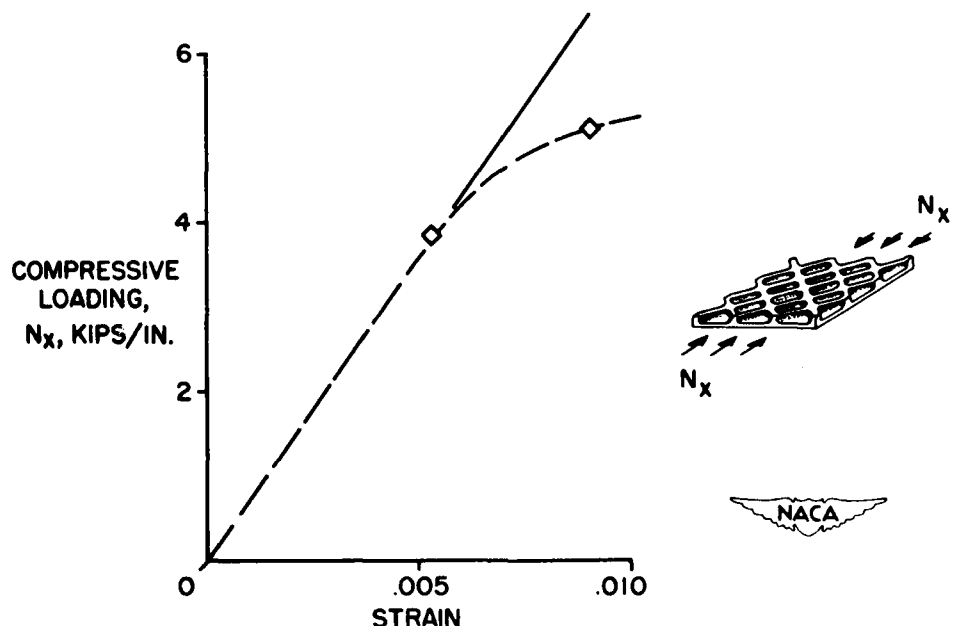


Figure 6.

## STRUCTURAL EFFICIENCY—COMPRESSION, 75S-T6

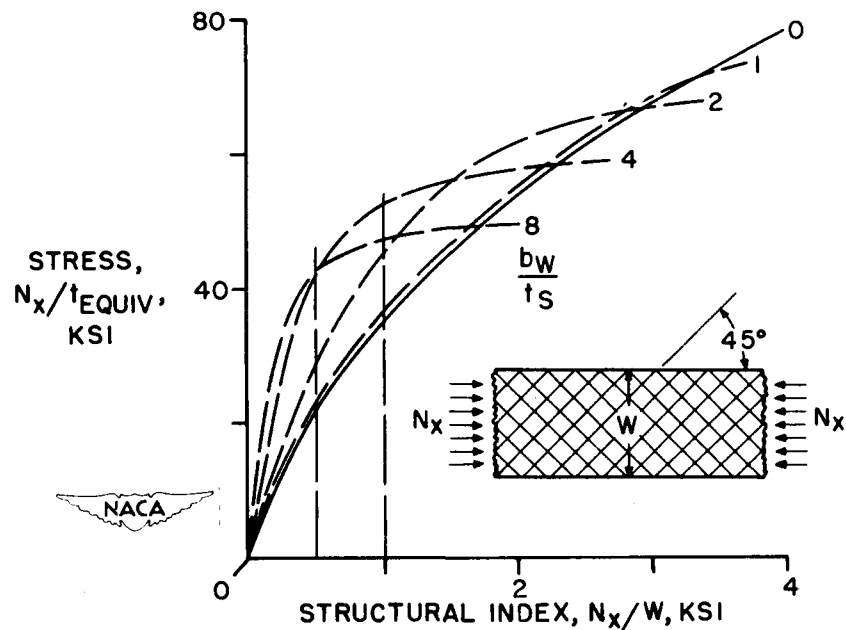


Figure 7.

## ELASTIC BUCKLING - SHEAR

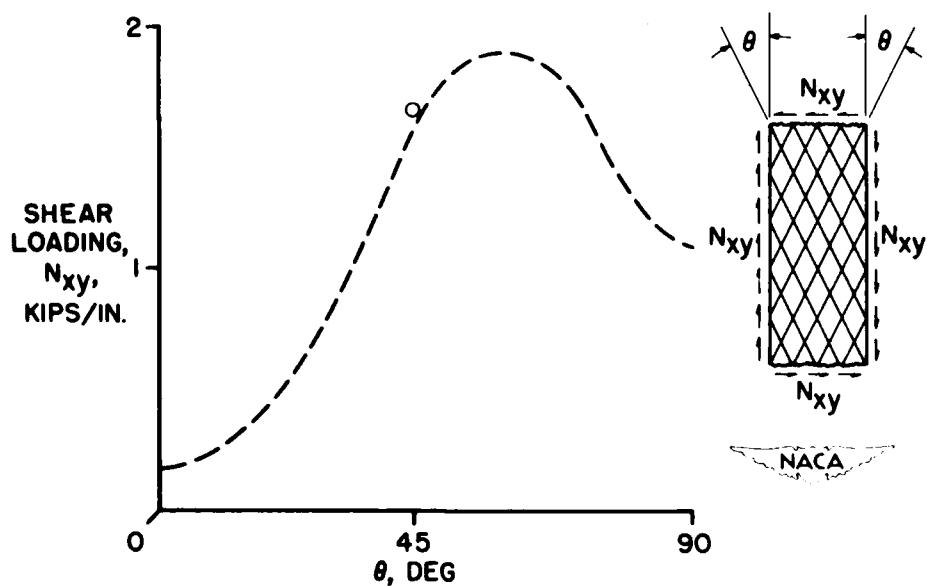


Figure 8.

## STRUCTURAL EFFICIENCY - SHEAR, 75S-T6

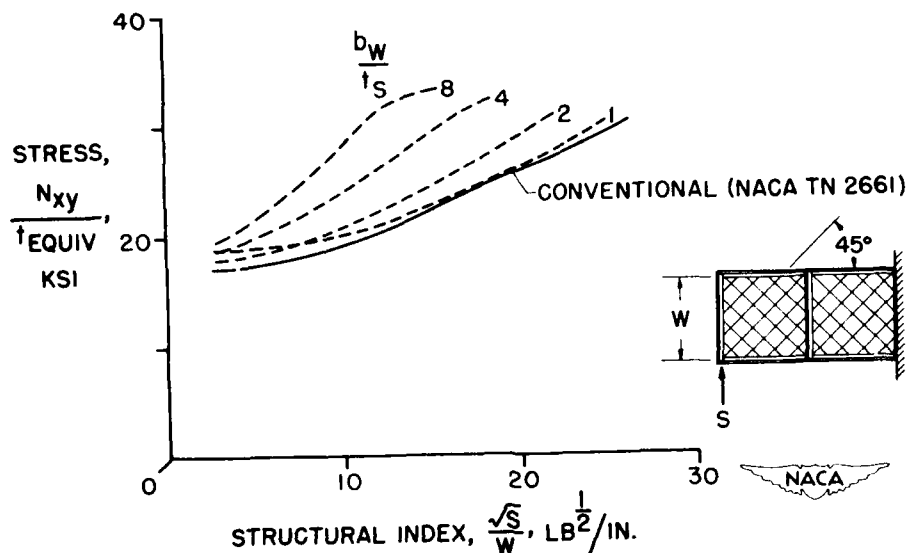


Figure 9.

## ELASTIC BUCKLING - COMBINED STRESSES

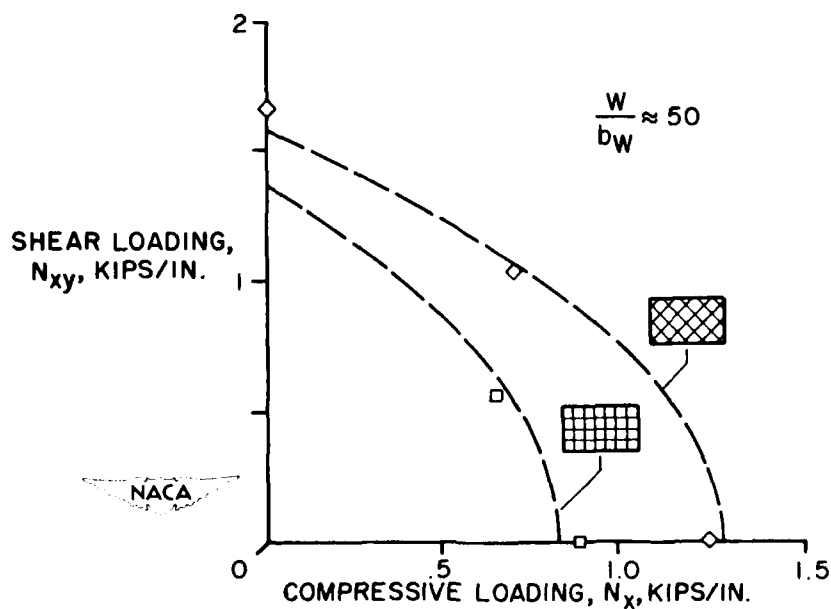


Figure 10.

## PLASTIC BUCKLING - COMBINED STRESSES

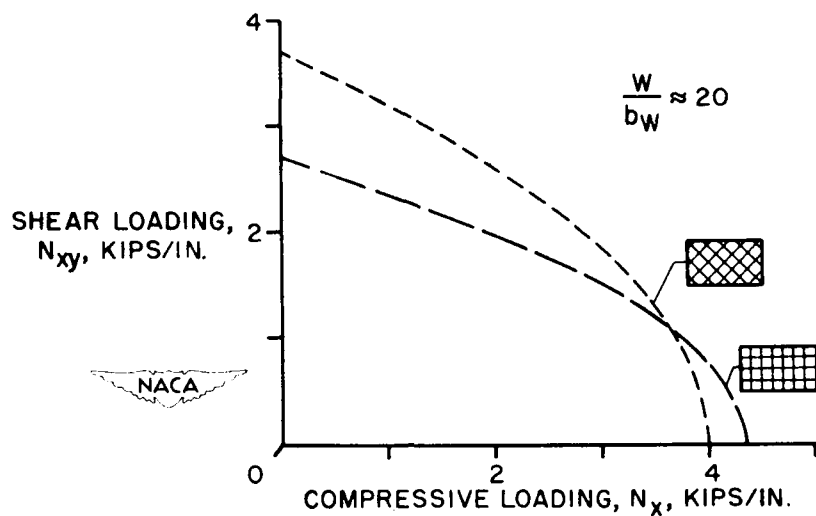


Figure 11.

## STRENGTH OF CYLINDERS - COMBINED STRESSES

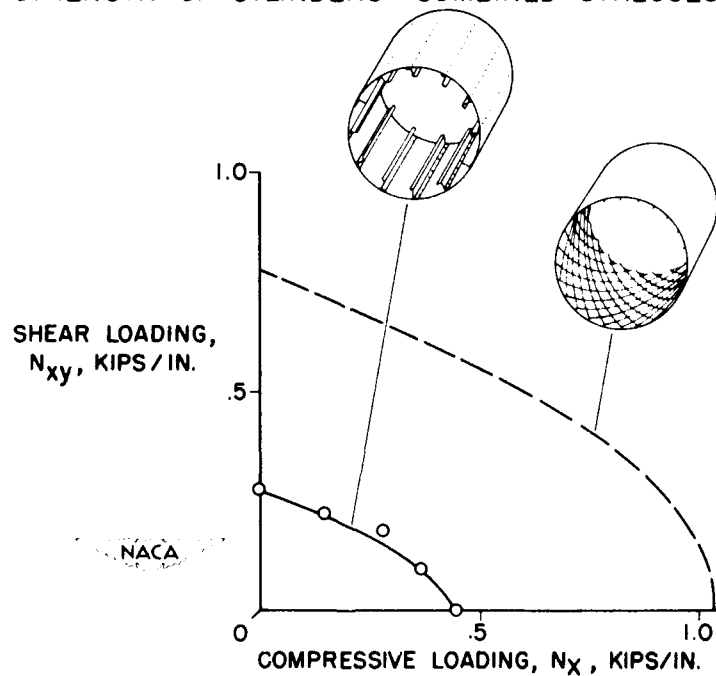


Figure 12.

## CALCULATIONS ON PLASTICALLY ORTHOTROPIC SHEET

By Elbridge Z. Stowell and Richard A. Pride

Langley Aeronautical Laboratory

Most of the aluminum-alloy sheet used in aircraft construction has nearly the same properties in the transverse direction as in the longitudinal (or rolling) direction. Such sheet may safely be considered as isotropic for most stress computations. However, for sheet made of stainless steel or titanium, this assumption is no longer valid. The properties of sheet from these materials may vary widely in the two principal directions and such sheet may not be considered as isotropic. There is a problem of how to allow for this difference of properties in computations. One such problem is shown in figure 1.

Here are presented buckling test data obtained in the Structures Research Laboratory on 301 stainless steel. Note that instead of a single line of points, such as would be obtained for an isotropic material, there are two lines of points, one for the plate loaded in the longitudinal direction and the other in the transverse direction. The curves labeled L and T (longitudinal and transverse) were computed from the empirical formula shown, taken from a book for designers published in 1950. It seems clear that there is room for improvement here, since the curves miss the points by a wide margin, and none of the details concerning this formula will therefore be presented. Instead this paper will discuss some of the things one needs to know for calculations in the plastic range; calculations, for example, which would yield curves actually going through the two lines of test points in this figure.

The behavior of such materials, which are called orthotropic, is best illustrated in figure 2, where a comparison is made of isotropic and orthotropic materials. On the left are shown the properties exhibited by an isotropic material. On the upper left is a stress-strain curve, which follows the usual trend when the stress enters the plastic range. On the bottom left is the corresponding curve for Poisson's ratio, starting at the value  $\nu$  in the elastic range and approaching  $1/2$  as the plastic strain becomes larger and larger.

On the right are shown the corresponding curves for a plastically orthotropic material. The straight-line portion of the stress-strain curve is the same as on the figure at the left, but in the plastic range the curve splits into 3 branches, one for each of the principal directions  $x$ ,  $y$ , and  $z$ . On the bottom right is shown the corresponding behavior of Poisson's ratio. It starts at the elastic value of  $\nu$  as with the curve on the left, but in the plastic range it splits into six branches. In the general case, three branches lie above the value  $1/2$  and the remaining three lie below. Deviations from the isotropic value may thus be quite large.

There are some materials for which on the upper right figure the  $y$  and  $z$  curves might be the same. In that case the Poisson's ratio curve on the lower right would show only three branches instead of the full six.

In order to make computations, a knowledge of the stress-strain relations for a material of this kind is necessary. The following relations suggest themselves as plausible extensions of the relations for an isotropic material:

$$\epsilon_x = \frac{\sigma_x}{E_x} - \mu_{yx} \frac{\sigma_y}{E_y} - \mu_{zx} \frac{\sigma_z}{E_z}$$

$$\epsilon_y = -\mu_{xy} \frac{\sigma_x}{E_x} + \frac{\sigma_y}{E_y} - \mu_{zy} \frac{\sigma_z}{E_z}$$

$$\epsilon_z = -\mu_{xz} \frac{\sigma_x}{E_x} - \mu_{yz} \frac{\sigma_y}{E_y} + \frac{\sigma_z}{E_z}$$

The strains  $\epsilon_x$ ,  $\epsilon_y$ , and  $\epsilon_z$  are given in terms of the applied stresses  $\sigma_x$ ,  $\sigma_y$ , and  $\sigma_z$ . The remaining quantities in the formulas are all characteristics of the material.  $E_x$ ,  $E_y$ , and  $E_z$  are the secant moduli on their respective stress-strain curves at the applied stresses. The six Poisson's ratios are those appropriate to the three moduli.

These relations indicate that if all three stress-strain curves and all six Poisson's ratios are known, the strains resulting from any combination of direct stresses can be computed. It would appear that nine quantities altogether would be needed: three moduli and six Poisson's ratios. However, the situation is not nearly so bad as it appears. The Poisson's ratio curve on the lower left of figure 2 is derivable from the stress-strain curve at the upper left. It seems reasonable to suppose that the six Poisson's ratio curves on the lower right are also derivable from the three stress-strain curves at the upper right.

In order to discover these relations, accurate values of Poisson's ratio for all three loading directions are necessary. Tests were accordingly made to provide the necessary data. Two sets of block specimens were prepared from 24S-T4 aluminum-alloy bar stock. Measurements of all Poisson's ratios were made by two methods which showed substantial agreement.

The test results are shown in figures 3 and 4. The left-hand side of the figure shows the stress-strain curves for the bar stock. The curves for loading in the y- and z-directions were the same, indicating that the blocks were isotropic in the y-z plane. For loading in the x-direction, the Poisson's ratios  $\mu_{xy}$  and  $\mu_{xz}$  should then be the same. The right-hand figure shows the test points for both  $\mu_{xy}$  and  $\mu_{xz}$ . The theoretical curve which one would get from an isotropic material fits the test points well, as it should.

On the other hand, for loading in the y- or z-directions, the Poisson's ratios  $\mu_{yz}$  and  $\mu_{yx}$  should be different. Figure 5 shows the same stress-strain curves as before, on the left, and the two different Poisson's ratios on the right. One of them becomes larger than 0.5, while the other stays less than 0.5. For the individual values, empirical relations have been found, and the curves through the points have been computed from these relations. Note that if transverse strains were computed for a plate like this, loaded in the y-direction, errors of from 50 to 100 percent would result if the plate were considered as remaining isotropic in the plastic range.

The expressions which relate Poisson's ratio with the stress-strain curves are as follows:

For isotropic material:

$$\mu_{x,y,z} = \frac{1}{2} - \left( \frac{1}{2} - v \right) \frac{E_{x,y,z}}{E}$$

For orthotropic material:

$$\left. \begin{array}{l} \mu_{yz} \\ \mu_{yx} \end{array} \right\} = \mu_y \left( 1 \pm 0.83 \mu_y \sqrt{\frac{E_y}{E_z'} - \frac{E_y}{E_x'}} \right)$$

where  $E_y$  is taken at strain  $\epsilon_y$ ,  $E_z'$  at strain  $\mu_{yz}\epsilon_y$ , and  $E_x'$  at strain  $\mu_{yx}\epsilon_x$ . The expression for an isotropic material stressed in either the x, y, or z-directions is a theoretical formula based on plasticity theory. From this formula, when the elastic value  $v$  is known, Poisson's ratio at any stress can be determined by finding the secant modulus at that stress and putting it in the formula. For an orthotropic material which has three different stress-strain curves, two of the six Poisson's ratios are given by the above formula. This formula involves one of the isotropic values previously given, with an

empirical plus and minus correction term to be added or subtracted. Use of the upper sign gives  $\mu_{yz}$  and the lower sign,  $\mu_{yx}$ . The three secant moduli are taken at the strains indicated. These formulas were used to compute the curves in figure 4. The other four Poisson's ratios would be given by similar formulas.

Thus if all three stress-strain curves are known, the six Poisson's ratios may be computed from them and need not be measured individually in the laboratory.

One other quantity needs to be defined before computations can be made in the plastic region. That is the stress intensity, which is a certain combination of stresses acting together to determine the amount of plasticity present in any specific case. For an orthotropic material the stress intensity must be independent of choice of axes, and must include the isotropic value as a special case. A calculation in two dimensions, in which only direct stresses are used, shows that the stress-strain-intensity curve lies between the individual stress-strain curves in the x- and y-directions.

With the stress intensity properly defined, the buckling stress of an orthotropic plate may be computed in much the same manner as that of an isotropic plate. In figure 5 are shown the buckling curves for a simply supported plate made of material whose stress-strain curves are shown on the left, labeled x and y. The curve labeled i is the stress-strain intensity curve. The curves on the right, labeled x and y, give the theoretical buckling stresses when the plate is loaded in the x- and y-directions, respectively.

In order to check the theoretical buckling curves, buckling tests were made on orthotropic stainless-steel sheet, with some specimens loaded in the longitudinal direction and some in the transverse direction. These buckling tests gave the two sets of points which were shown in figure 1 and which are now shown repeated on the right-hand side of figure 5.

The agreement indicates that the buckling theory for plastically orthotropic material is adequate for practical calculations on material such as stainless steel or titanium sheet when stressed into the plastic range.

## BUCKLING DATA ON STAINLESS-STEEL PLATE

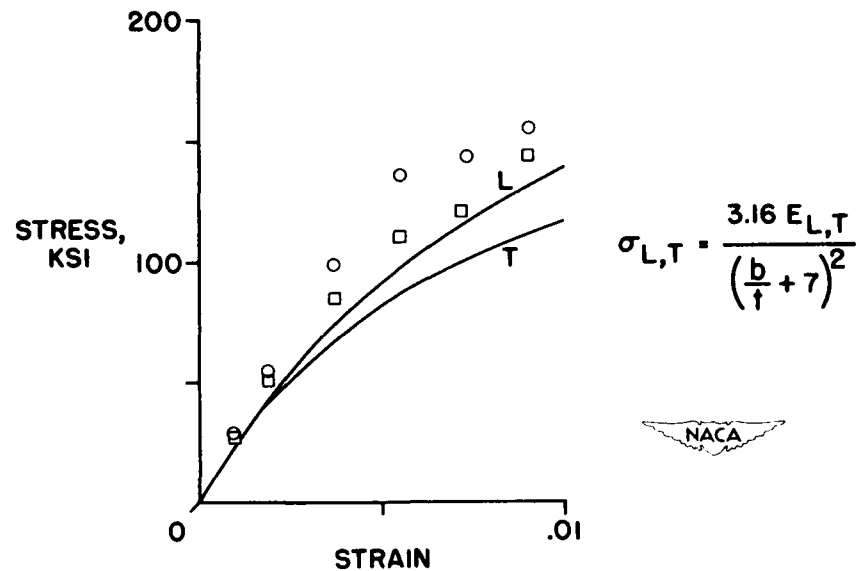


Figure 1.

## TYPES OF MATERIAL

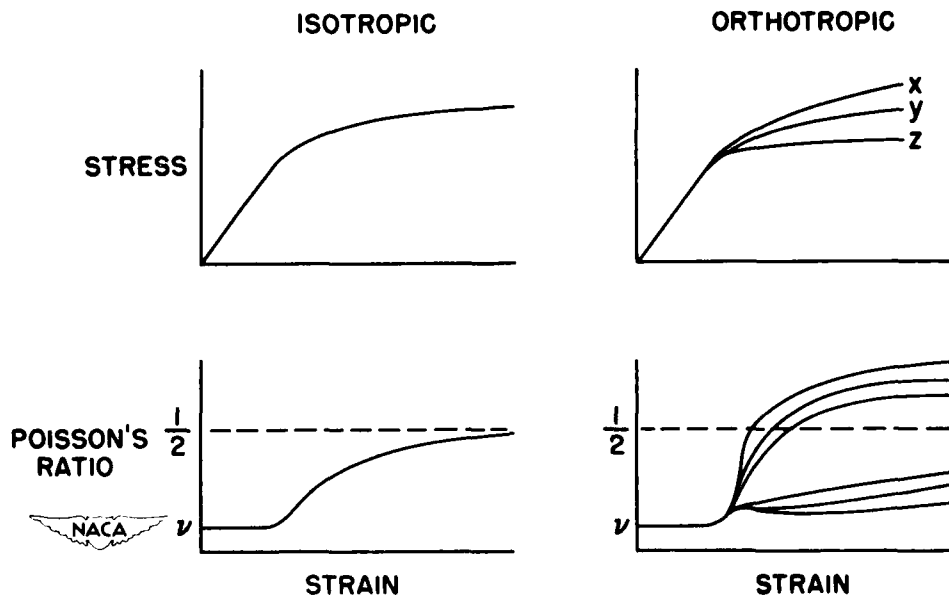


Figure 2.

## POISSON'S RATIO DATA (24S-T4)

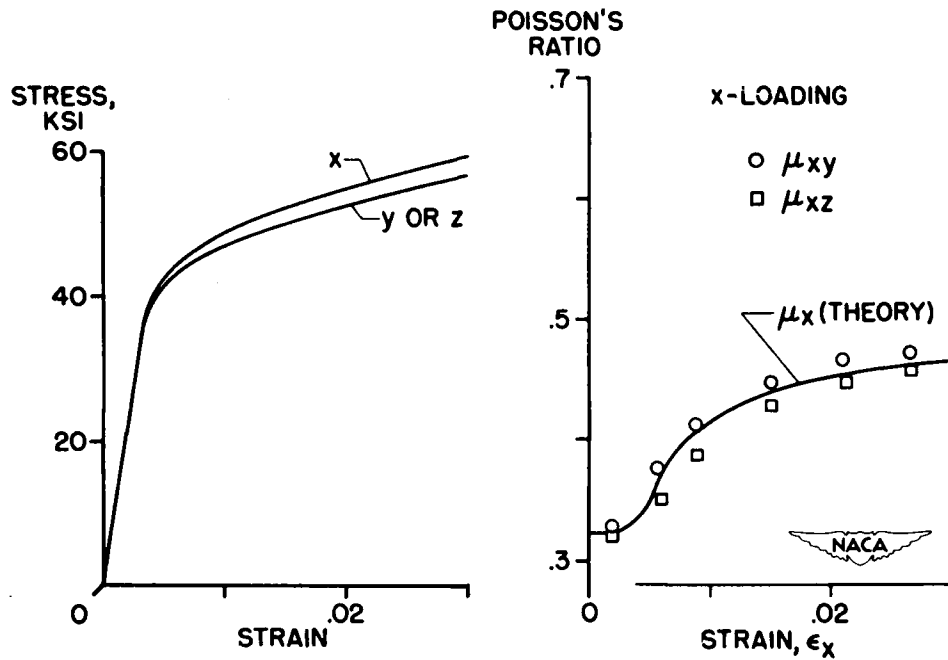


Figure 3.

## POISSON'S RATIO DATA (24S-T4)

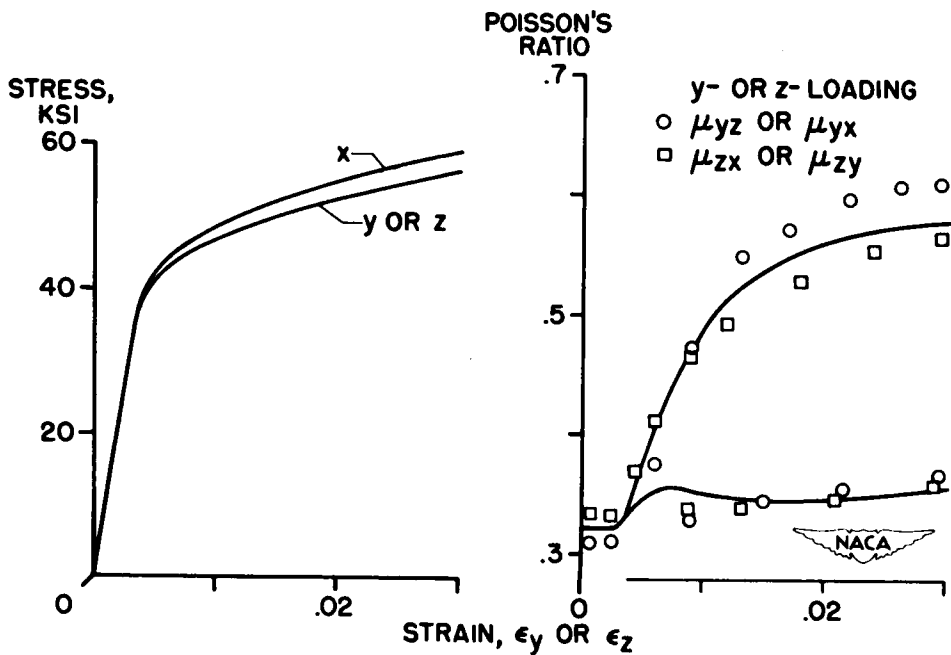


Figure 4.

## ORTHOTROPIC PLATE BUCKLING (TYPE 301 STAINLESS STEEL)

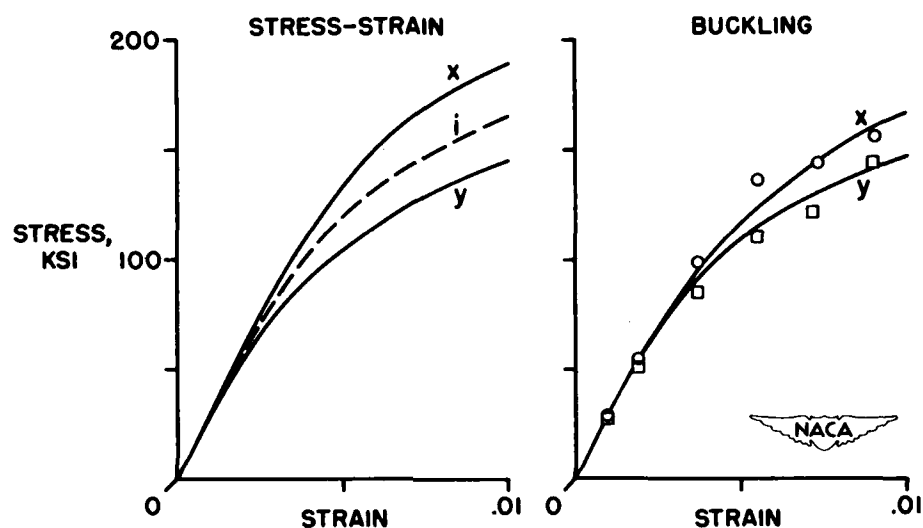


Figure 5.

**CONFIDENTIAL**

**563**

**DYNAMICS**

**CONFIDENTIAL**

MOMENT OF INERTIA AND DAMPING OF FLUID IN TANKS  
UNDERGOING PITCHING OSCILLATIONS

By Edward Widmayer, Jr., and James R. Reese

Langley Aeronautical Laboratory

For some airplanes the quantity of fuel carried in wing-mounted tanks comprises a large percentage of the total mass of the wing. It has become evident that the sloshing of these large masses of fuel may cause important dynamic effects. In a recent paper (ref. 1) the case of model tanks mounted on a wing undergoing translation following instantaneous release has been treated. It was shown that a fairly complicated physical process takes place and that the effective mass and damping depend sharply on the number of cycles after the start of the motion. The present study deals with the moment of inertia and damping of large tanks undergoing pitching oscillations with amplitudes of a few degrees. The dynamic effects of the fuel for this case are of significance, for example, in the flutter phenomenon and are particularly important in those cases where the susceptibility of a wing to flutter is critically dependent on the wing bending-torsion frequency ratio.

Some of the tank shapes and the dynamic system used are shown in figure 1. The shapes were as follows: tank A, an actual 185-gallon tip tank with baffles; tank B, a 58-gallon circular cylinder; and tank C, a 230-gallon tank with a square profile. These tanks were oscillated about a transverse axis as shown in figure 1. In addition, a 1/3-scale model of tank B was oscillated as shown here and also about the cylindrical axis in which configuration it will be referred to as tank D. With the exception of the round profile, the tanks were mounted in a simple spring-inertia dynamic system shown here. This system could be caused to oscillate by a step release from an initial angular displacement or could be oscillated at a constant amplitude by supplying energy through a weak spring. The decaying oscillations resulting from a step release were investigated at various degrees of tank fullness for all tank shapes. Further studies were made on the 185-gallon tank oscillating at a constant amplitude. The effective inertia of the fluid was obtained from a knowledge of the stiffness and measured natural frequency of the system. A measure of the energy dissipation was obtained from a study of the rate of decay of the oscillation for the case of the step release and from the work required to maintain a constant amplitude of oscillation, as obtained from a moment-displacement diagram.

A convenient place to begin the study of the inertia of fluids as a function of tank fullness is the tank-full condition. Theoretical solutions for the fluid inertia for the tank-full condition have been given

in reference 2 for the two-dimensional elliptic tank and are given by

$$\frac{I_{eff}}{I_{solid}} = \left( \frac{\left(\frac{a}{b}\right)^2 - 1}{\left(\frac{a}{b}\right)^2 + 1} \right)^2 \quad (1)$$

where  $a/b$  is the ratio of the major axis to the minor axis,  $I_{eff}$  is the fluid inertia about the fluid centroid, and  $I_{solid}$  is the solid inertia about the fluid centroid. This relation is represented in figure 2 as the lower solid curve, and notably enough the same curve also holds for the ellipsoid of revolution. This work has been extended in reference 3 to the case of arbitrary two-dimensional tank shapes. In reference 3, it has been shown that there is a direct analogy between the torsional modulus for solid sections and the fluid inertia of full tanks which is given by

$$\frac{I_{eff}}{I_{solid}} = 1 - \frac{\rho J_p}{I_{solid}} \quad (2)$$

where the  $I$ 's are as defined in equation (1),  $J_p$  is the torsional modulus for the solid section, and  $\rho$  is the mass density of the fluid. The case of a full tank of rectangular section is shown by the upper solid curve of figure 2. The following observations may be made from these curves: For low fineness ratios, such as for a round or square tank (which has a fineness ratio of 1), there is little or no transmitted moment of inertia and the fluid moment of inertia is low as compared with the solid inertia; however, as the fineness ratio becomes large, the inertia ratio tends toward unity and, moreover, the differences due to tank shape become small as shown by the convergence of the curves. Several experimental points corresponding to the shapes investigated are shown in figure 2. Note the excellent agreement with theory for the square shape C and for the round shape D. The experimentally determined moment-of-inertia ratios for shapes A and B have been plotted at their fineness ratios which are defined as the maximum length to the maximum thickness. It may be seen that for these shapes the results fall near the theoretical curves although the theoretical curves are for rectangular and elliptic shapes. This agreement between the experimental and theoretical fluid inertias even when there is some deviation in tank shape suggests that the theoretical solutions offer a good basis for estimating the fluid inertia of new tank configuration and, as will be noted, help in the estimation of the inertia results for the partially full tank.

Some experimental results for the partially full tank are presented in figure 3. The ratio of the effective fluid inertia to the solid inertia for the same amount of fluid is shown as a function of tank fullness. The full-tank condition for the various shapes shown here is the same as that shown in figure 2. As before, the effect of tank shape on the inertia ratio may be seen; as the fineness ratio is increased, the inertia ratio for a given tank fullness is increased. Note that, for a wide variation in tank fullness of from 10 to 100 percent, the inertia ratio varies but little. In order to illustrate the effect of frequency on the data, tank A, the 185-gallon tank, was tested over a range of frequencies from 2 to 8 cycles per second. The resulting variation is shown in the top curve of figure 3 by the shaded area. In order to indicate the effect of size, the 1/3-scale model of tank B was tested over a considerable frequency range. The results which are independent of frequency over the range tested are given by the dashed line (fig. 3) and indicate the effect of size on the moment of inertia may not be important. In light of the small variation of the curves with tank fullness, the results shown for the full-tank condition take on added significance because it appears that the inertia ratio for any tank fullness may be estimated for engineering purposes if the ratio of the fluid inertia to the solid inertia can be determined either experimentally or analytically.

In the study of damping, it was found, as in reference 1, that a complicated physical process takes place which leads to wide changes in the damping with time history, that is, with the number of cycles. Fairly complicated wave motions exist in the tank, even for small oscillations, and give rise to the possibility of a conservative transfer of energy from the tank to the fuel and subsequently back to the tank; thus, the ordinary inference of damping drawn from the ratio of successive peak amplitudes of decaying oscillations of the tank must be modified. In order to illustrate this phenomenon, a "standard-type" semilogarithmic plot of amplitude against number of cycles for the partially full 185-gallon tank as obtained from a step release is given in figure 4. During the first few cycles after release, before sloshing has developed, the rate of decay is small and indicates that there is little apparent damping. As sloshing develops, the curve becomes increasingly steep as energy is being both dissipated and transferred to the fuel. After considerable decrease in the amplitude, the curve reverses its slope and indicates that energy is being fed back into the tank. It was worthy of note that this second peak was not known to become nearly as large as the initial amplitude. In view of the nonlinear nature of the effective damping it would appear that, when it is necessary to treat the damping analytically, some averaged value for the desired conditions must be used.

In figure 5 is shown the variation of the damping factor with tank fullness. The data in the upper two curves are for forced oscillations at a constant tip amplitude of 0.8 inch. The lower curve is obtained

CONFIDENTIAL

from the first few cycles after release from an initial tip amplitude of 0.8 inch before the full sloshing has developed, that is, from the solid line shown in figure 4. For the upper curves in the case of steady oscillations, where it is assumed that the violent sloshing action has become statistically independent of time, a marked difference in the size of the damping factor from that pertaining to the step release (the lower curve) may be noted. The two upper curves shown for the forced-oscillation case differ in the range of frequencies covered and thus indicate an effect of frequency. For a given percent-full condition the frequency of the upper points is approximately 1.6; the frequency of the lower points and the damping factor at the higher frequency is consistently larger than at the lower frequency. It is seen that the damping factor becomes small at the extremes of tank fullness and that the maximum values tend to occur at the middle of the curve. It was also noted in the course of this work that the damping factor exhibited a tendency to increase as the amplitude of oscillation was increased.

Before concluding, it may be appropriate to consider briefly the effects of viscosity. With respect to the fluid inertia, viscosity would enter primarily in the thickness of the boundary layer formed on the container walls and would tend to make the fluid in the boundary layer fully effective in contributing to the system inertia. In reference 2, it is shown that for periodic motion the thickness of the boundary layer is given by

$$\lambda = \left( \frac{2v}{\omega} \right)^{1/2} \quad (3)$$

where  $\lambda$  is the boundary-layer thickness,  $v$  is the kinematic coefficient of viscosity, and  $\omega$  is the circular frequency. With water as the fluid and the frequencies of these experiments, the boundary-layer thickness was shown not to exceed 0.028 inch and, consequently, may be considered negligible. With respect to the influence on the damping characteristics, it may be remarked that the studies of reference 1 have indicated that, within the viscosity range of current-type fuels, no influence of viscosity could be detected for the case of a tank undergoing translation. Although no data are available for the pitching case, it is felt that, in the range of turbulent damping, the damping is relatively unaffected by viscosity.

In conclusion, it may be said that these studies indicated that some hope exists for engineering approximations of the effective-mass moment of inertia of fluids in wing-supported tanks by using as a convenient basis the tank-full condition. For the range investigated, the tank size, frequency, and amplitude of oscillation were found to have

CONFIDENTIAL

little influence on the effective inertia. With regard to the damping action of the fluid, it was found that the step-release type of motion contributes little to the damping of the system during the initial stages of the oscillation and that, after the establishment of sloshing, the apparent damping becomes nonlinear. For a forced oscillation, it was noted that considerable damping was present over a range of tank fullnesses and that the damping action appeared to be a function of the frequency and amplitude.

## REFERENCES

1. Merten, Kenneth F., and Stephenson, Bertrand H.: Some Dynamic Effects of Fuel Motion in Simplified Model Tip Tanks on Suddenly Excited Bending Oscillations. NACA TN 2789, 1952.
2. Lamb, Horace: Hydrodynamics, Sixth ed., Cambridge Univ. Press, 1932.
3. Miles, John W.: An Analogy Among Torsional Rigidity, Rotating Fluid Inertia, and Self-Inductance for an Infinite Cylinder. Jour. Aero. Sci., vol. 13, no. 7, July 1946, pp. 377-380.

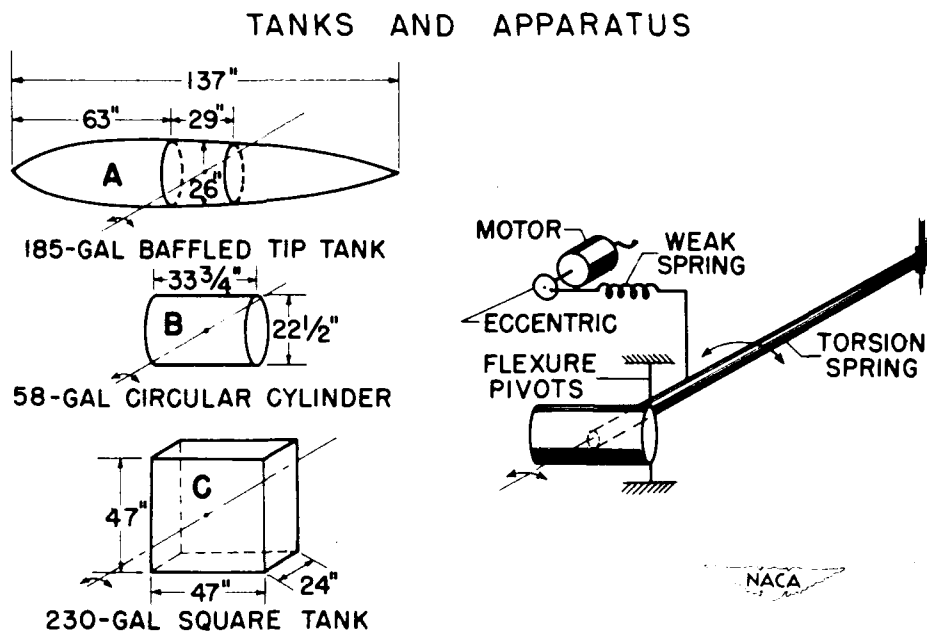


Figure 1.

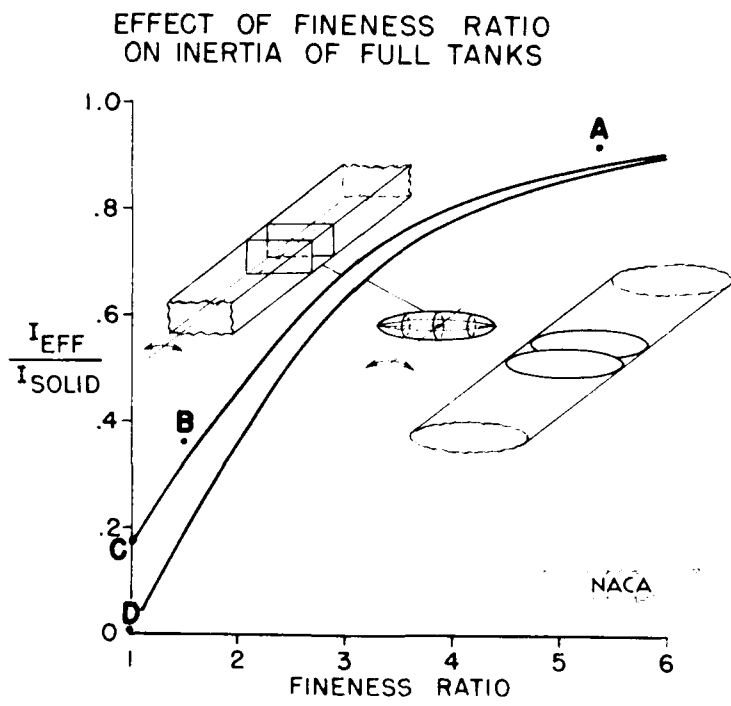


Figure 2.

## EFFECT OF TANK FULLNESS ON INERTIA

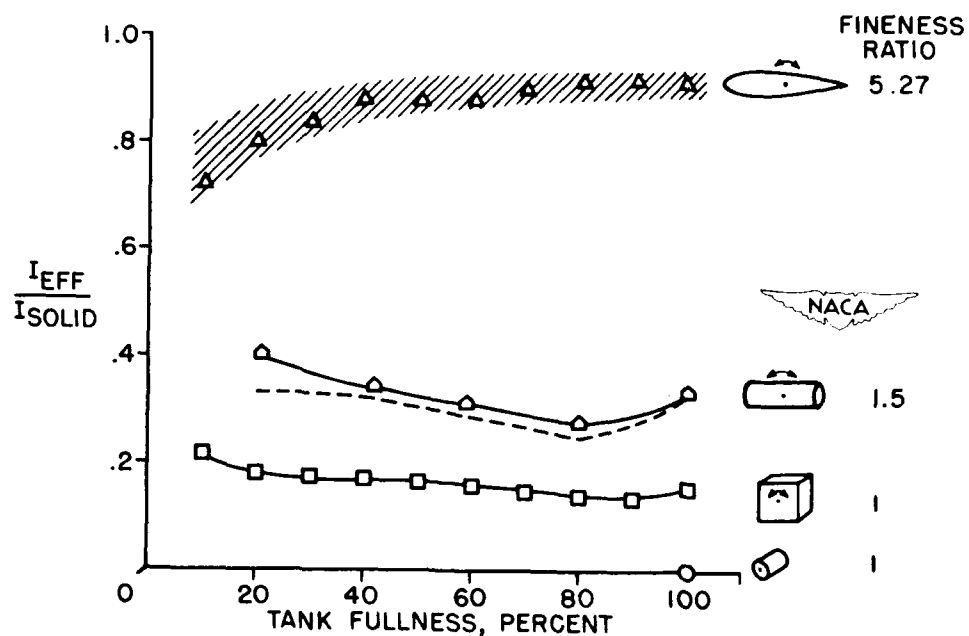


Figure 3.

## AMPLITUDE DECREMENT FOR STEP RELEASE

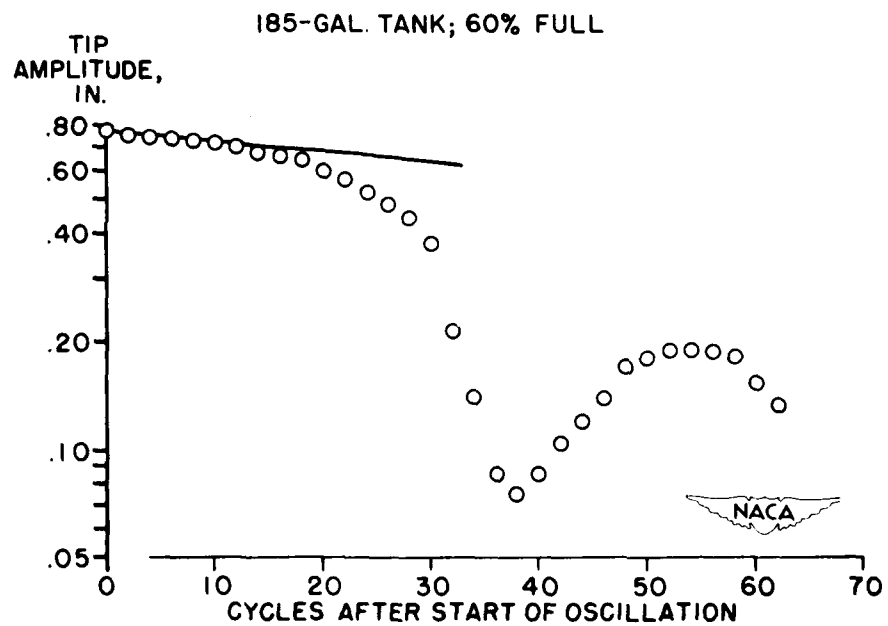


Figure 4.

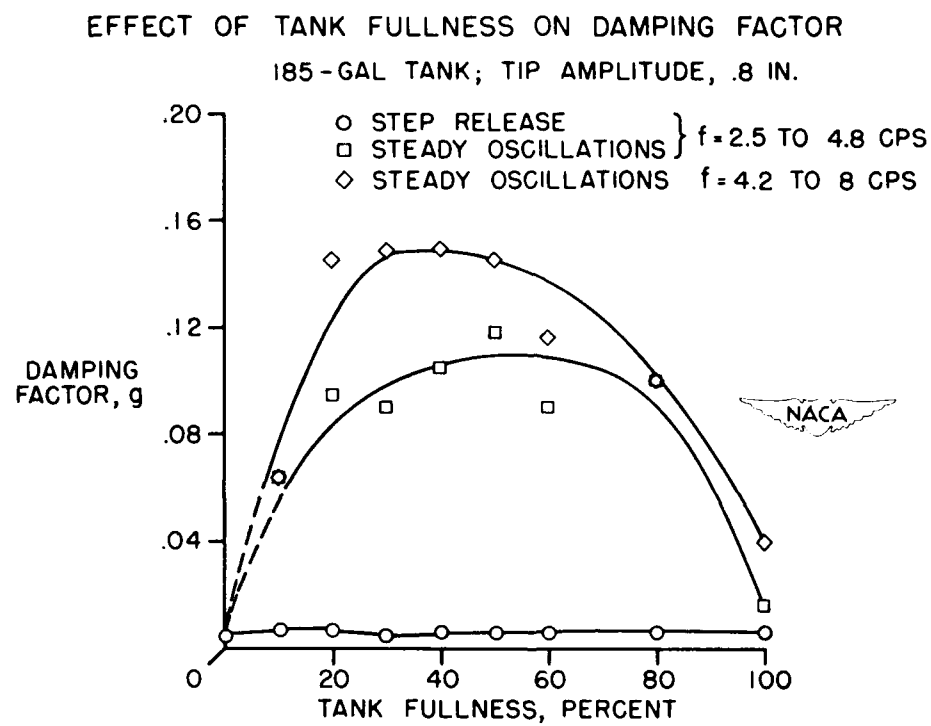


Figure 5.

CORRELATION OF CALCULATION AND FLIGHT-TEST STUDIES  
OF THE EFFECT OF WING FLEXIBILITY ON  
STRUCTURAL RESPONSE DUE TO GUSTS

By John C. Houbolt

Langley Aeronautical Laboratory

This paper presents some additional information on the behavior of flexible aircraft in gusts. It deals with both calculations and flight studies which examine the manner in which gust loads are magnified or otherwise affected by structural flexibility, and it assesses the extent to which these flexibility effects may presently be analyzed in some cases.

The material to be presented is divided into two phases. The first phase deals with studies made on the basis of single- or discrete-gust encounter, and the second phase deals with some studies made for the more realistic condition of continuous-turbulence encounter. The discrete-gust studies will be considered first. Figure 1 is used to define some of the terms which will be used. Here, an airplane is being swept upward by a gust. Because of wing flexibility, particularly bending flexibility, the accelerations will be different at each spanwise station. One convenient measure of flexibility effects may be obtained by comparing the peak incremental acceleration developed at the fuselage, designated as  $\Delta n_f$ , with the incremental acceleration at the nodal points of the fundamental mode,  $\Delta n_n$ . These accelerations are of interest because they both have been considered in the deduction of gust intensities from measured accelerations. Another measure of flexibility effects may be obtained by comparing the actual incremental wing stresses to what these incremental stresses would be if the airplane were rigid. Both measures are used herein.

In order to establish what the numerical values of these flexibility measures are in practical cases, flight tests were made in clear rough air with three different aircraft, the DC-3, the M-202, and the B-29. References 1 to 4 report some of these flight tests. These aircraft were chosen because they were available and because they were judged to a fairly representative of rather stiff, moderately flexible, and rather flexible aircraft, respectively, when judged on the basis of higher speed, lower natural frequencies, and greater mass distribution in the outboard wing sections. Typical acceleration results obtained from these flights are shown in figure 2. The ordinate is the incremental acceleration of the fuselage and the abscissa is the incremental acceleration at the nodal points. Only positive accelerations are shown, but a similar picture was obtained for negative acceleration values. The

solid line is the line indicating a 1 to 1 correspondence; whereas the dashed line is a mean line through the flight points. The slope of this line is the amplification which results from flexibility; thus, the fuselage accelerations are five percent greater on the average than the nodal accelerations for the DC-3, 20 percent for the M-202, and 28 percent for the B-29. It should be mentioned that the picture is not changed much if given in terms of strains; that is, if the incremental root strains for the flexible case are plotted against the strains that would be obtained if the airplane were rigid, similar amplification factors are found.

In an attempt to see whether these amplification factors could be predicted, some calculation studies were made by considering the airplanes to fly through single sine gust of various lengths. The results are shown in figure 3. The ordinate is the ratio of the incremental root strain for the flexible aircraft to incremental root strain that is obtained for the aircraft considered rigid. The abscissa is the gust-gradient distance in chords, as shown in the sketch. The curves shown were obtained from an analysis which included two degrees of freedom, vertical motion of the airplane, and fundamental wing bending. (See refs. 5 and 6.) These curves show a significant increase in the amplification or response ratio in going from the DC-3 to the M-202 to the B-29. It is, perhaps, of interest to remark that the amount of amplification is, in fact, related to the aerodynamic damping associated with vertical-wing oscillations. This damping depends in a large way on the mass distribution of the airplane and is lower for higher outboard mass loadings. The curves thus reflect the successively higher outboard mass loadings of the M-202 and B-29.

The important point to note about figure 3 is that the general level of each curve is in good qualitative agreement with the amplification values found in flight. Thus, the 1.05 value for the DC-3 roughly represents the average of the lower curve, the 1.20 value for the M-202 the average of the middle curve, and the 1.28 value for the B-29 the average of the upper curve. A more direct quantitative comparison would be available if a weighted average of the calculated curves could be derived by taking into account the manner in which the gust-gradient distances are distributed in the atmosphere. No sound method is available for doing this, however, and this over-all qualitative comparison will therefore have to suffice.

Figure 4 shows what is obtained when calculation and flight results are correlated in more detail. In this figure, the strain ratio is plotted against the interval of time for nodal acceleration to go from the 1 g level to a peak value. This interval is thus like but not the same as the gust-gradient distance. A word, perhaps, should be mentioned here on the procedure used for determining the rigid-body reference strain in the flight condition. Actually, the values used were

equivalent values and are equal to the strains that would develop in pull-ups having accelerations equal to the accelerations that were measured at the nodal points. The agreement seen between the calculated results and the flight results is actually quite fair when the complexity of the problem and the fact that the calculations are for a highly simplified version of the actual situation are considered. In contrast to the well-behaved single gusts assumed in the calculations, the gusts encountered in flight are repeated in nature and are highly irregular in shape. These factors may well account for the higher amplifications found in flight, especially in the range of higher time-to-peak values; in this range not only are the amplification effects associated with the predominant gust shapes present but, because of the irregular shapes of the gusts, so are some of the amplification effects associated with shorter gust lengths.

The results thus far presented give a reasonably fair picture; the discrete-gust approach permits a reasonably good evaluation of the general nature of flexibility effects. The degree of resolution permitted by this approach, however, is limited.

In order to further the resolution it seems natural to turn to an approach which considers the continuous-turbulence nature of the atmosphere. One method that suggests itself for treating the case of continuous turbulence and which is presently receiving much attention is the adaptation of the methods of generalized harmonic analysis, often called power-spectral methods. Figure 5 has been prepared to illustrate the application of this approach to the gust-response problem. (See ref. 7 for the application of the approach to an airplane having the degrees of freedom of vertical motion and pitch.) The top sketch denotes a representative input function which characterizes the atmosphere;  $\Phi_1$  may be interpreted as a measure of the power contained in the harmonic component of the turbulence which has a frequency  $\Omega$ , this frequency being inversely related to the wave length  $L$  of the component as shown. The second sketch represents a transfer function which characterizes the airplane;  $T$  represents the amplitude of the response variable, such as stress, bending moment, or acceleration, which develops for a continuous sinusoidal-gust encounter. This function provides a convenient means for taking into account the various degrees of freedom of the airplane like the free-body mode, the fundamental wing bending and torsion modes illustrated, and higher modes as well. The next two sketches represent output functions which are derived directly from the first two by the multiplications indicated. The area  $A$  can be used to determine the amount of time that will be spent in flight above a given load level; by considering, in addition, the area  $A_1$ , it is possible to estimate the number of peak loads that are expected at various load levels, a quantity which should be significant in fatigue studies.

Figure 6 shows the transfer functions for stress that were obtained for the three aircraft by considering the degrees of freedom of vertical motion and fundamental wing bending. The fuselage, fuel loads considered, and the spanwise station for which the functions apply are given in figure 6. The velocities used were 185 mph for the DC-3 and 250 mph for both the M-202 and B-29; the curves apply to a sinusoidal gust having an amplitude of 1 fps. The solid curve is for the flexible aircraft; the dashed curve, for the aircraft considered rigid. These curves show clearly the different bias that each airplane has to various frequency components of the atmosphere. The first hump is associated with vertical translation of the aircraft; the second hump, with wing bending. The percentage by which the flexible curves overshoot the rigid curves, of course, is a measure of flexibility effects. This overshoot reflects the characteristics of the transient-response curves shown earlier; it is noted that, as before, there is a significant growth in the percentage overshoot in going from the DC-3 to the M-202 to the B-29. As was mentioned in the discrete-gust studies, this overshoot is related to the aerodynamic damping associated with wing-bending oscillations; thus, the curves denote a successive decrease in this damping going from the DC-3 to the B-29 airplane.

Because the curves for each airplane are different in shape, and especially because there is a marked difference in their height, it should be quite clear that the output functions are considerably different. A further discussion of these output functions is considered beyond the scope of this paper, but, in general, it may be stated that the higher the transfer function, the higher will be the average stress level in flight, and the greater will be the number of peak stresses per unit time. Before passing from figure 6 it is perhaps worthy to note that the transfer functions are often more easily calculated than are the dynamic-response curves of the discrete-gust approach.

Figure 7 shows a correlation of some of the results obtained by the harmonic-analysis approach with flight results. The plot introduces again the previously used strain ratio, that is, the ratio of the peak incremental root bending strain for the flexible airplane to the peak incremental root strain for the aircraft considered rigid. The ordinate applies to the experimental flight values; the abscissa, to the harmonic-analysis theory. The three circled points are the results for the three airplanes. As a matter of added interest, a single acceleration point, the only one computed and which applied to the M-202, has been inserted on the plot as though the coordinates involved the ratio of fuselage to nodal acceleration. The very good correlation shown by this plot is, to say the least, very gratifying; it shows that good correlation may be obtained between calculation and flight results and, moreover, that the harmonic-analysis approach appears to be a suitable method to use.

The pertinent points of this paper may be summed up as follows: Calculation and flight studies have been made on several aircraft to determine the manner in which gust loads are magnified by wing flexibility. This study indicates that an approach based upon single-gust encounter can be used to evaluate how one airplane compares relative to another in respect to the general level of these flexibility effects. This discrete-gust approach also shows over-all qualitative correlation with flight results; it, however, does not permit detailed resolution of the flexibility effects. A more appropriate approach appears to be one which considers the continuous-turbulence nature of the atmosphere and which is based on generalized harmonic analysis. Not only does it permit airplanes to be compared relative to one another in more detail but it does provide good quantitative correlation with flight results. It also offers many useful ramifications, such as application to fatigue studies, which are not permitted by the discrete-gust approach.

## REFERENCES

1. Shufflebarger, C. C., and Mickleboro, Harry C.: Flight Investigation of the Effect of Transient Wing Response on Measured Accelerations of a Modern Transport Airplane in Rough Air. NACA TN 2150, 1950.
2. Mickleboro, Harry C., and Shufflebarger, C. C.: Flight Investigation of the Effect of Transient Wing Response on Wing Strains of a Twin-Engine Transport Airplane in Rough Air. NACA TN 2424, 1951.
3. Mickleboro, Harry C., Fahrer, Richard B., and Shufflebarger, C. C.: Flight Investigation of Transient Wing Response on a Four-Engine Bomber Airplane in Rough Air With Respect to Center-of-Gravity Accelerations. NACA TN 2780, 1952.
4. Murrow, Harold N., and Payne, Chester B.: Flight Investigation of the Effect of Transient Wing Response on Wing Strains of a Four-Engine Bomber Airplane in Clear Rough Air. (Prospective NACA paper)
5. Houbolt, John C., and Kordes, Eldon E.: Gust-Response Analysis of an Airplane Including Wing Bending Flexibility. NACA TN 2763, 1952.
6. Kordes, Eldon E., and Houbolt, John C.: Evaluation of Gust Response Characteristics of Some Existing Aircraft With Wing Bending Flexibility Included. NACA TN 2897, 1953.
7. Press, Harry, and Mazelsky, Bernard: A Study of the Application of Power-Spectral Methods of Generalized Harmonic Analysis to Gust Loads on Airplanes. NACA TN 2853, 1953.

## FUSELAGE AND NODAL ACCELERATIONS

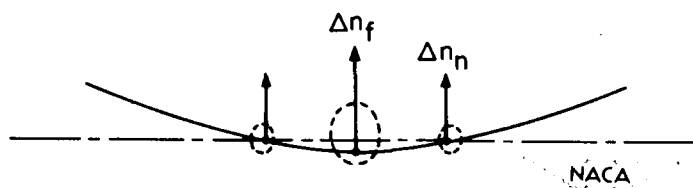


Figure 1.

## ACCELERATION MEASURED IN CLEAR ROUGH AIR

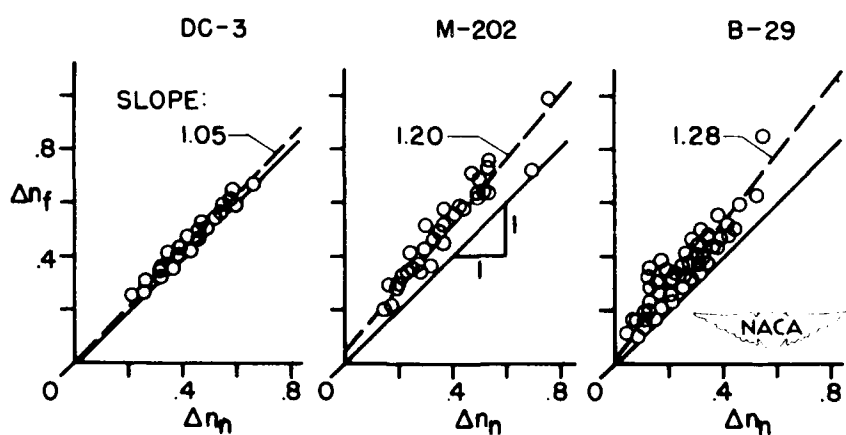


Figure 2.

## STRAIN AMPLIFICATION FOR SINGLE GUST ENCOUNTER

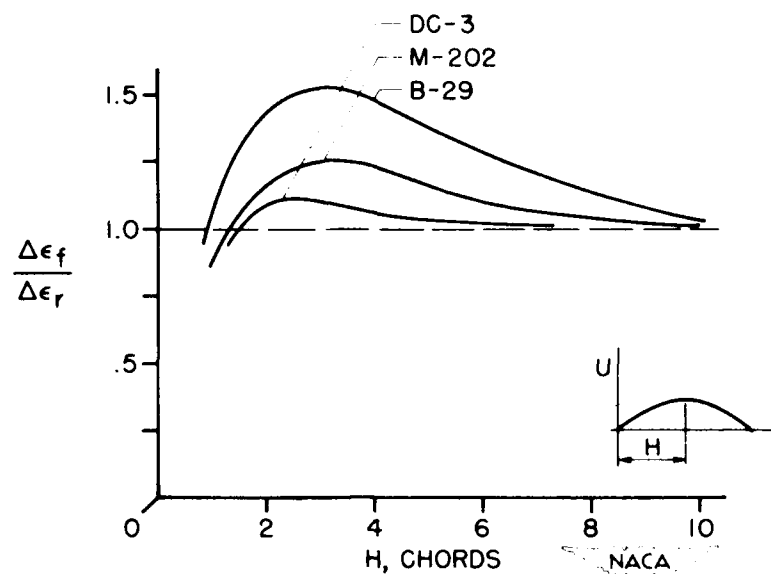


Figure 3.

## B-29 ROUGH-AIR STRAIN AMPLIFICATION

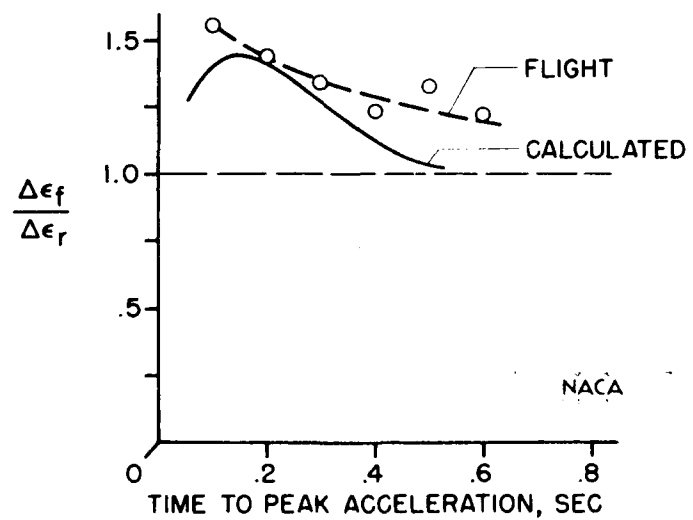


Figure 4.

## NATURE OF GENERALIZED HARMONIC ANALYSIS APPROACH

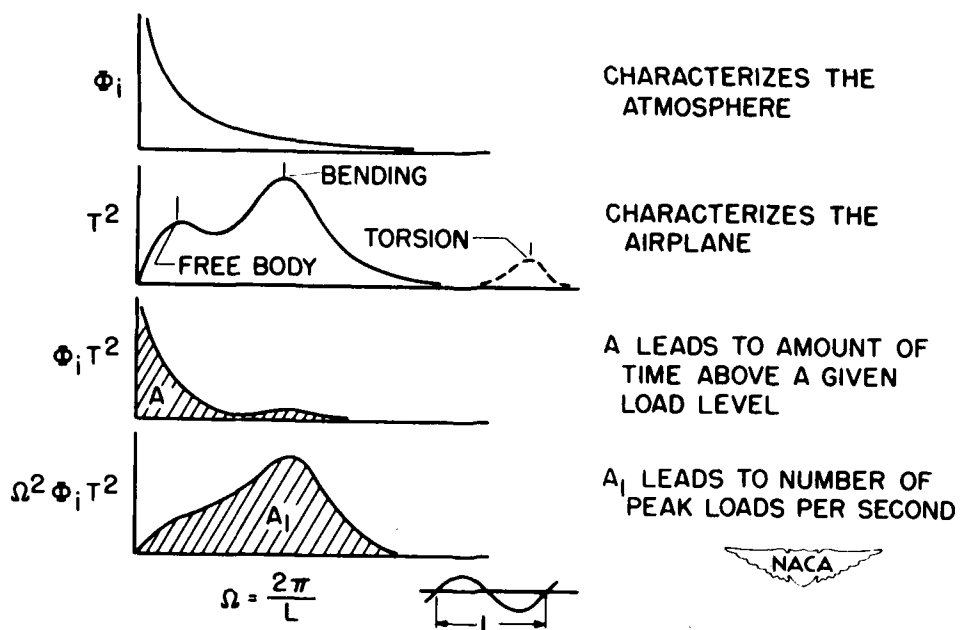


Figure 5.

## TRANSFER FUNCTIONS

FUSELAGE LOAD FUEL LOAD STATION, IN.	DC-3 CREW ONLY 1/2 FULL 50	M-202 1/2 FULL 1/2 FULL 56	B-29 CREW ONLY FULL 60
--	-------------------------------------	-------------------------------------	---------------------------------

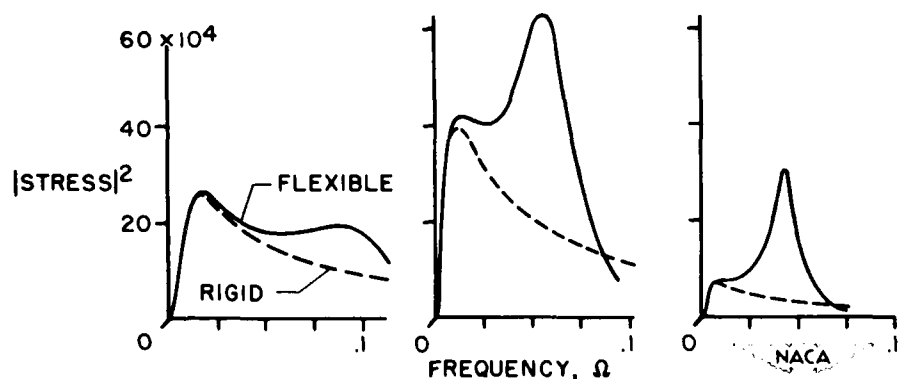


Figure 6.

## STRAIN AMPLIFICATION FOR CONTINUOUS TURBULENCE

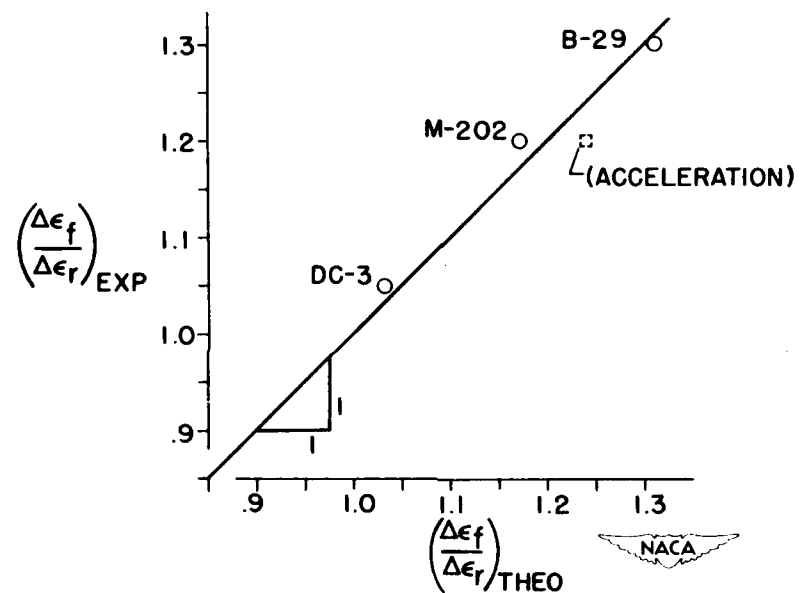


Figure 7.

## ON TRAVELING WAVES IN BEAMS

By Robert W. Leonard and Bernard Budiansky

Langley Aeronautical Laboratory

In addition to static loads, aircraft structures must often sustain rapidly applied loads such as those that might result from hard landings, the release of heavy bomb loads, or the jettisoning of external fuel tanks. In the analysis of the transient stresses produced by such loads, most of the methods in use today involve the superposition of natural modes of vibration of the structure calculated with elementary engineering beam theory. For very rapidly applied loadings, however, this approach is known to have certain shortcomings. For sharp impacts of short duration, many modes are often required for a satisfactory degree of convergence; perhaps even more serious is the fact that the use of elementary theory in the calculation of the necessary higher modes is inaccurate because of the neglect of such effects as transverse shear deformation and rotary inertia which become increasingly important for higher and higher modes.

A classically recognized alternative to the modal method of calculating transient stresses in elastic bodies is the traveling-wave approach, which seeks to trace directly the propagation of stresses through the body. Investigations of the possible application of this method to bending problems have only recently been begun in earnest. Among other things, it has been found that elementary beam theory is totally inadequate for the formulation of a traveling-wave method, but that a modified theory suggested by Timoshenko (ref. 1), which includes the effects of transverse shear deformation and rotary inertia, may be used.

In Timoshenko's theory, the motion of a vibrating beam may be described by four linear partial-differential equations. The quantities governed by the equations are the moment  $M$ , shear  $V$ , deflection  $y$ , and cross-sectional rotation  $\psi$  which are illustrated on the sketch of a beam element in figure 1. The variables on which these quantities depend are the coordinate along the beam  $x$  and the time  $t$ .

These beam differential equations, incorporating transverse shear deformation and rotary inertia, belong to the class known as hyperbolic differential equations. They have associated with them the two characteristic velocities  $c_1$  and  $c_2$  defined in figure 1. The velocity  $c_1$ , which is the propagation velocity of a sharp variation in bending moment, depends on the ratio of bending stiffness  $EI$  to the mass moment of inertia per unit length  $I_m$ ; the velocity  $c_2$ , which is the propagation velocity of a sharp variation in vertical shear, depends on the ratio of shear stiffness  $A_SG$  to the mass per unit length  $m$ . Further, the Timoshenko beam equations are associated with two networks of characteristic lines in the space-time plane as illustrated in figure 1 for

a uniform beam. The slopes of these lines at any point in the space-time plane are determined by the magnitudes of the velocities  $c_1$  and  $c_2$  at that point.

In accordance with the usual "method of characteristics" (ref. 2), Timoshenko's partial differential equations of motion may be replaced by an equivalent system, each equation of which is valid in a different one of the directions taken by the characteristic lines. The advantage obtained in this transformation lies in the fact that the new "characteristic" form contains only total differentials instead of the partial derivatives contained in the original system and is, thus, apparently well suited to solution by numerical methods.

In effecting a numerical solution, the total differentials in the new system are replaced by finite differences forming a system of characteristic difference equations valid along the characteristic lines. In addition, a basic grid of the characteristic lines having the smaller slope, shown in figure 1 as solid lines, is utilized.

A typical space-time plot showing such a grid for a uniform beam is presented in figure 2. The unknown quantities in the equations are to be determined at the intersections of the basic grid. The steeper characteristic lines are included by drawing them, for each mesh of the basic grid, through the point 1 as indicated in figure 2 on the large-scale sketch of a typical mesh. This arrangement was suggested by Pfeiffer in a paper published in Germany in 1947 (ref. 3). When the characteristic difference equations are written along the lines of such a mesh, a formula may be derived giving the unknown quantities at the point 1 in terms of their values at the points 2, 3, and 4. Thus, beginning from boundaries where the necessary conditions are known, the solution may be stepped off mesh-by-mesh over the space-time plane.

In testing this numerical procedure the very special case of a uniform beam with the two characteristic velocities  $c_1$  and  $c_2$  equal has been considered at some length, since, for this case, the two sets of characteristic lines coincide; this restriction not only permits the use of simpler numerical formulas, but, in some cases, the derivation of exact closed-form solutions as well.

The first such case considered was that of a uniform cantilever beam given a step velocity at the root. The time history of the root moment is presented in figure 3. To give some idea of the time range involved, the point corresponding to half the period of the first mode of vibration is marked on the time scale. The solid line is the numerical solution, obtained with a grid which divided the beam into 20 segments. The dotted curve was obtained by a modal solution of Timoshenko's equations which used the first eight modes. It should be emphasized that

these modes are the true modes of Timoshenko's theory, incorporating the effects of transverse shear deformation and rotary inertia. The two solutions for moment are seen to agree quite well.

In figure 4 is shown the time history of the shear at the root of the same cantilever beam. Note the discontinuities, which occur in the numerical solution each time the discontinuous wave front returns to the root after being reflected at the tip, and the violent oscillations immediately following each boost by the wave front. While the two solutions agree elsewhere, they are, as might be expected, in disagreement in the regions of violent oscillation. These oscillations were thought by some to result from some sort of instability in the numerical process. In order to determine whether this supposition was true, a uniform simply supported beam subjected to a step moment at one end was considered. For this problem, an exact closed-form solution could be obtained.

The time history of shear at one end of the simply supported beam is shown in figure 5. In this plot, the full period of the first mode is indicated on the time scale. Again, the solid curve is a 20-segment numerical solution, b.. in this case, the dotted curve is the exact closed-form solution. Note that the violent oscillations are also predicted by this solution and, thus, are in accord with the theory. However, as might be expected, the numerical solution does not agree with the exact solution in these regions.

It may be of interest that the scale of vertical shear gives directly the dynamic overshoot factor. Thus, values as high as fifteen times the static response are predicted by Timoshenko's theory when the moment is applied suddenly.

In order to check the accuracy of the numerical solution in a more practical case where the applied load is continuous, the simply supported beam was again considered, but with an applied ramp-platform type of moment as shown in figure 6. The time to reach the peak value of the applied moment was approximately one-seventh of the period of the first mode. The plot in figure 6 shows the shear at the end of this beam. The curves are the same type as those obtained for the last problem; namely, a 20-segment numerical solution and an exact closed-form solution. The agreement is seen to be excellent. Again the shear scale is in terms of dynamic overshoot factor. Thus, the shear reaches a value approximately three and one-half times the static response.

In all the examples that have thus far been discussed the characteristic velocities  $c_1$  and  $c_2$  were taken to be equal. These results have recently been published in more detail in reference 4.

Since the publication of reference 4, computed results have been obtained in still another problem involving a simply supported beam

subjected to a ramp-platform type of moment. In this case, however, unequal characteristic velocities have been assumed. The shear at the end of this beam is shown in figure 7, where a 20-segment numerical solution has been compared with an essentially converged modal solution up to a time equal to the period of the first mode of vibration. In this case, the modal solution can be considered to be the desired result. The numerical solution is seen to disagree with the modal result in the neighborhood of the second extremity of the curve. A 30-segment solution carried past the point of disagreement showed some improvement, but it appears that a still finer grid must be utilized to produce very good agreement with the modal solution.

The results of the examples carried out with the traveling-wave numerical procedure encourage the viewpoint that such analyses may eventually be of practical usefulness. The chief difficulty, the need for a very fine grid in the general case of unequal characteristic velocities, may yet be overcome by modifications of the numerical process which are under consideration. If the difficulty cannot be overcome in this way, it may very well be offset by the use of modern high-speed computing machines. Indeed, the greatest asset of the numerical process is its simple routine nature and the ease with which it may be set up, which adapts it to the use of such machines. This quality contrasts with the relative complexity of the mathematical analysis required in using such methods as the modal method. The numerical procedure remains to be set up and tested for nonuniform beams, but no serious difficulties are foreseen in accomplishing this objective.

## REFERENCES

1. Timoshenko, S.: Vibration Problems in Engineering. Second ed., D. Van Nostrand Co., Inc., 1937, pp. 337-338.
2. Courant, R., and Friedrichs, K. O.: Supersonic Flow and Shock Waves. Pure & Appl. Math., vol. I, Interscience Publishers, Inc. (New York), 1948, pp. 38-59.
3. Pfeiffer, F.: Über die Differentialgleichung der transversalen Stabschwingungen. Z.a.M.M., Bd. 25/27, Nr. 3, June 1947, pp. 83-91.
4. Leonard, Robert W., and Budiansky, Bernard: On Traveling Waves in Beams. NACA TN 2874, 1953.

## BASIC ELEMENTS OF TIMOSHENKO BEAM THEORY

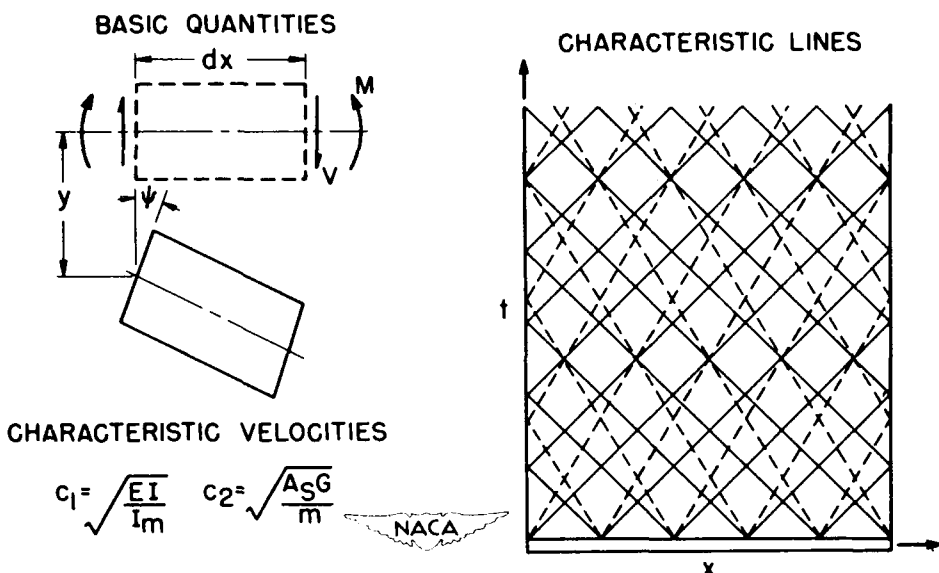
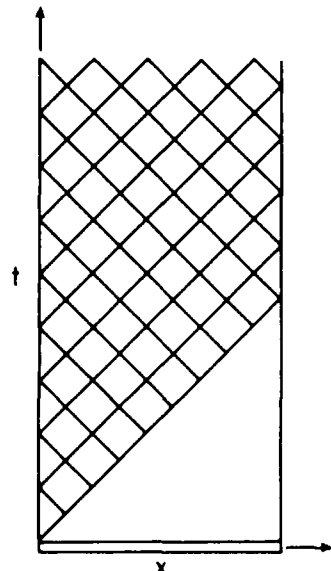


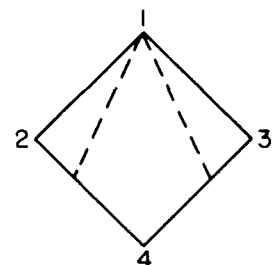
Figure 1.

## BASIC GRID FOR NUMERICAL SOLUTION

## SPACE-TIME PLANE



## TYPICAL MESH



NACA

Figure 2.

## TIME HISTORY OF ROOT MOMENT - CANTILEVER BEAM

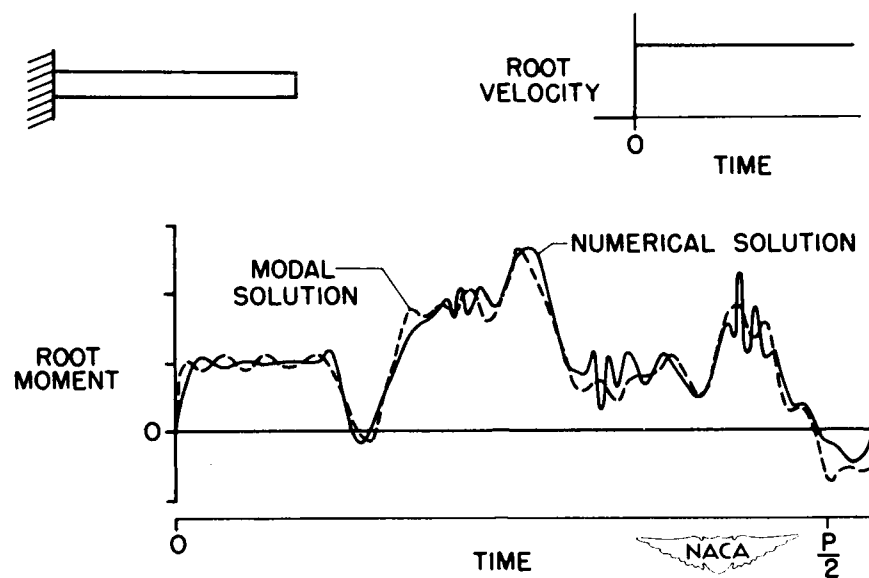


Figure 3.

## TIME HISTORY OF ROOT SHEAR - CANTILEVER BEAM

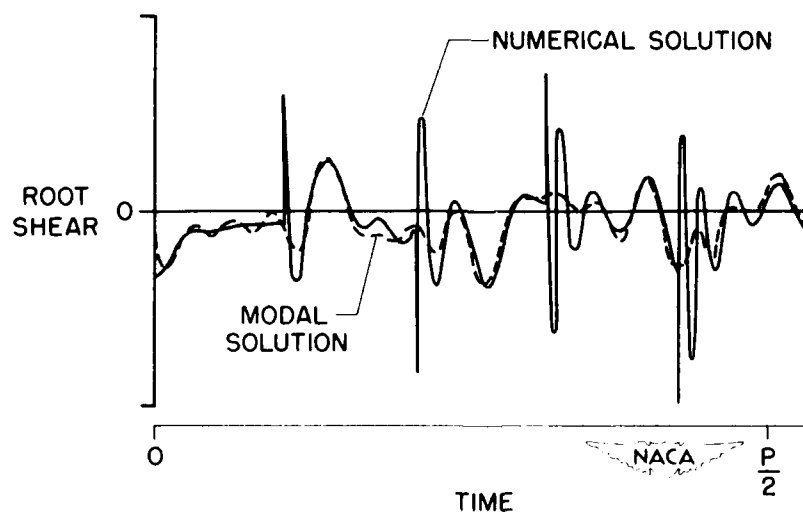


Figure 4.

## TIME HISTORY OF END SHEAR - SIMPLY SUPPORTED BEAM

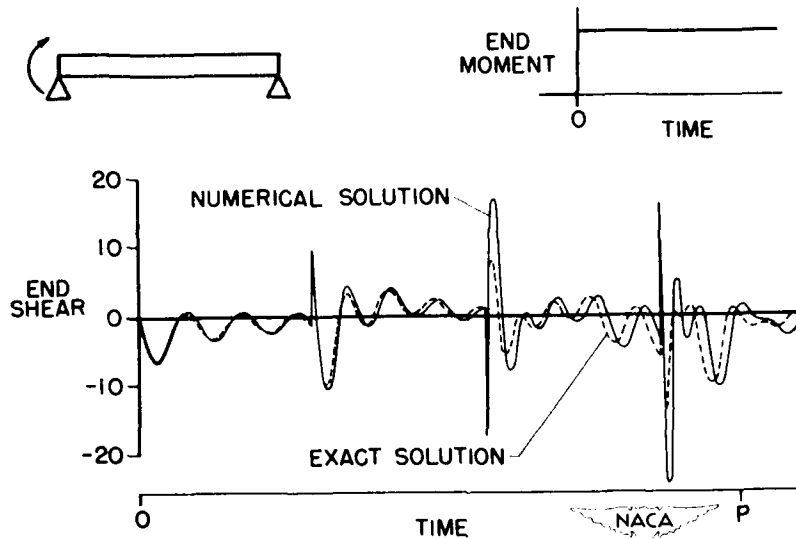


Figure 5.

## TIME HISTORY OF END SHEAR - SIMPLY SUPPORTED BEAM

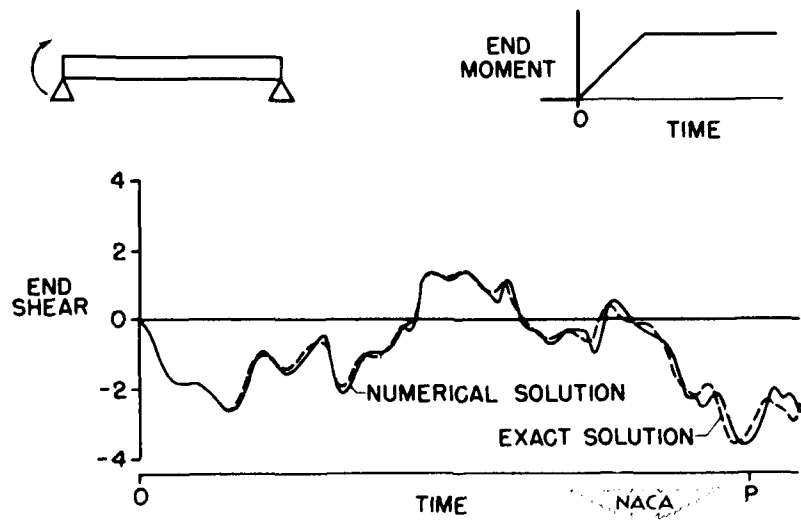


Figure 6.

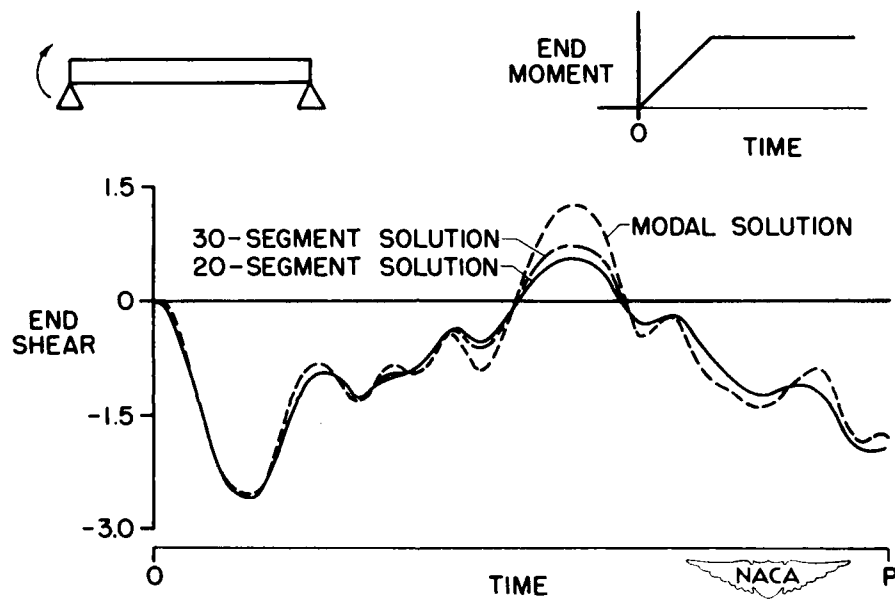
TIME HISTORY OF END SHEAR - SIMPLY SUPPORTED BEAM -  $C_1 \neq C_2$ 

Figure 7.

SHEAR-LAG EFFECTS IN BEAM VIBRATIONS AND THE  
SUBSTITUTE-STRINGER APPROACH

By William W. Davenport and Edwin T. Kruszewski

Langley Aeronautical Laboratory

53

In the dynamic analyses of aircraft, the natural frequencies of shell-type beams are of basic importance. Investigations show that the effect of shear lag on the natural frequencies of shell structures may be of considerable importance. An indication of the magnitude of shear-lag effects is shown in figure 1 which is taken from the results of reference 1. In this reference exact vibration analyses were made of hollow thin-walled box beams of uniform wall thickness such as the one shown in figure 1. It was found, for such a box beam of cross-sectional aspect ratio  $c/H = 3.6$  and plan-form aspect ratio  $L/c = 6.0$ , that the inclusion of shear lag reduces the frequency of the first symmetrical mode by 3 percent, the second symmetrical mode by 12 percent, and the third symmetrical mode by 15 percent as illustrated in the figure. Furthermore, it was also found that the reduction is even greater for shallower beams, that is, beams with larger cross-sectional aspect ratios.

Although these results show that shear lag is important, the question of how to include the shear-lag effect in the vibration analysis of actual structures remains to be answered.

The cross section of a beam typical in general form of a structure found in aircraft is shown in the upper left-hand corner of figure 2. Such a structure is not readily idealized to a box beam of uniform thickness. A method for including shear lag in an actual structure of this type is the one based on the well-known substitute-stringer approach. The idealization associated with this approach is shown in figure 2. This idealization consists of 4 flanges concentrated at the corners of the box and four stringers in the covers. These flanges and stringers are assumed to carry all the normal or bending stress. The flanges and stringers are connected by sheets which carry only shearing stresses. Most of the geometrical properties of the idealized structure may be obtained from the geometry of the actual structure as follows. The area of the flange  $A_F$  is such that the moment of inertia about the neutral axis of the flanges in the idealized structure is the same as the moment of inertia of the spars in the actual structure. The area of the substitute stringer  $A_L$  is such that the inertia of the substitute stringers is the same as the inertia of the cover sheets and stringers in the actual structure about the principal bending axis. The thickness  $t_W$  is taken equal to the actual spar web thickness and  $t_S$  is taken equal to the

actual cover-sheet thickness. The location of the substitute stringer, however, is left undetermined. It is this location, defined by  $b$ , which determines the amount of shear lag permitted in the idealized structure.

In connection with static stress problems, Kuhn and Peterson in reference 2 made extensive studies of the effect of varying the location of the substitute stringers and arrive at recommended values of  $b$  that would give good results for maximum stresses. These recommended values for  $b$ , however, will not necessarily yield satisfactory results for vibration frequencies. In another investigation, in which the effect of shear lag on vibration frequencies was studied, Anderson and Houbolt in reference 3 arbitrarily assumed the location of the substitute stringer at the centroid of area of the half-cover, but the error involved in the arbitrary location of the substitute stringer was not investigated. It is desirable to study the effect on vibration frequency of varying  $b$  with the hope that a value giving good results for higher as well as lower modes might be discovered.

This study was carried out in the present investigation by applying the substitute-stringer idealization to the uniform thin-walled rectangular beam shown in figure 3. On the left side of this figure is shown the cross section of the rectangular tube. It has a depth of  $H$  and a width of  $c$ . The wall thickness is  $t$  and is assumed to be constant over the entire circumference. The idealized or substitute stringer structure has both the spar thickness  $t_w$  and the cover thickness  $t_s$  equal to  $t$ , the thickness of the rectangular tube. The area of the flange  $A_F$  accounts for only the bending stiffness of the side wall and is equal to  $\frac{1}{6} H t$ . The area of the substitute stringer  $A_L$  includes the area of the half-cover and is equal to  $\frac{1}{2} ct$ . The distance of the stringer area from the flange, that is, the dimension  $b$ , is varied in the substitute-stringer solution.

On the basis of the simplifying assumptions, that is, the stringers and flanges carry only normal stresses and sheets carry only shear, it was possible to get exact solutions of the frequency for the idealized structure, which include both shear lag and transverse shear. In figure 4 the results obtained for various values of  $b$  for the first three symmetrical free-free modes are shown for a typical cross-sectional aspect ratio of 3.6 and a plan-form aspect ratio of 6.0.

The effect of varying  $b$  is shown by this family of curves. The abscissa is the ratio of  $b$  to  $b_c$  where  $b_c$  is the distance from the flange to the centroid of area of the half-cover. A value of  $b/b_c$  of unity means that the substitute stringer is located at the centroid of area of the half-cover, as shown in the corresponding small sketch. In this case, this means that the stringer is located halfway to the middle of the cover. A value of  $b/b_c$  of 2 for this case means that the

substitute stringer is located at the middle of the cover. A value  $b/b_c = 0$  means that the substitute stringer area is combined with the flange area. This idealization corresponds to a solution where shear lag is neglected.

The ordinate is the ratio of  $\omega$  to  $\omega_e$  where  $\omega$  is the frequency obtained from the substitute-stringer solution and  $\omega_e$  is the exact frequency obtained from the solution in reference 1, when both shear lag and transverse shear are included. A value of  $\omega/\omega_e$  of unity therefore means that the results obtained from the substitute-stringer approach are the same as the results from the exact solution.

There exists a value of  $b$  for each mode that makes the frequency of the substitute-stringer idealization equal to the frequency of the exact solution. Also it can be seen that these curves cross the horizontal line  $\omega/\omega_e$  of unity within a narrow region.

Figure 5 shows the results from similar calculations and comparisons for rectangular tubes of cross-sectional aspect ratio of 1.0 and  $\infty$ . The case of  $\infty$  is the limiting case of a very shallow beam. For a cross-sectional aspect ratio of 1 (which resembles structures similar to fuselages) the location of the substitute stringer does not seem to be too important. There is quite a range of values for  $b/b_c$  where there is good agreement with the exact theory. This insensitivity of the solution to the position of the substitute-stringer location is brought about by the fact that there is very little shear lag in a box beam of small cross-sectional aspect ratio. As the cross-sectional aspect ratio gets larger the sensitivity becomes greater as shown here by the steepness of the slopes in this family of curves for  $c/H$  of infinity. In this case the effects of transverse shear vanish completely and only shear-lag effects remain. For all these cross-sectional aspect ratios, including the extreme case of  $\infty$ , a value of  $b/b_c$  in the vicinity of 0.54 seems to give good agreement for the modes considered. (See figs. 4 and 5.) This ratio is slightly less than that found in reference 2 for statical problems which is 0.65.

A hollow rectangular beam is now considered that is assumed to have at each point of its cross section a thickness  $t$  that carries shear and also a different thickness  $t'$  that carries normal stress; this assumption approximates the situation in an actual structure in which stringers and flanges carry normal stress but do not carry shear. The example considered is shown in figure 6. The value of  $c/H$  is 3.6 and  $L/c$  is 6; in addition,  $t'/t$ , the ratio of effective thickness for normal stress to effective thickness for shear, is 2. The calculations are again made for the first three symmetrical modes of a free-free beam. From these curves it is seen that a value of  $b/b_c$  of approximately 0.54 still yields an accurate representation for the rectangular tube.

As a result of the fact that a single value of  $b$  may be found that gives good agreement for at least the first three symmetrical modes, it is believed that the substitute-stringer idealization may be used with considerable success to take into account shear-lag effects in the dynamic analysis of an actual shell-type structure.

## REFERENCES

1. Budiansky, Bernard, and Kruszewski, Edwin T.: Transverse Vibrations of Hollow Thin-Walled Cylindrical Beams. NACA TN 2682, 1952.
2. Kuhn, Paul, and Peterson, James P.: Shear Lag in Axially Loaded Panels. NACA TN 1728, 1948.
3. Anderson, Roger A., and Houbolt, John C.: Effect of Shear Lag on Bending Vibration of Box Beams. NACA TN 1583, 1948.

## FREQUENCY REDUCTION DUE TO SHEAR LAG

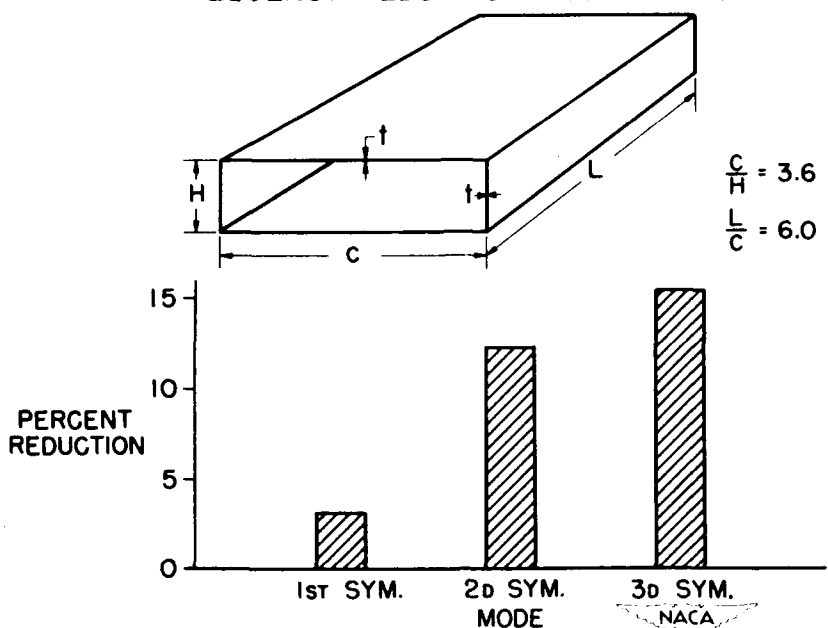


Figure 1.

## SUBSTITUTE-STRINGER IDEALIZATION

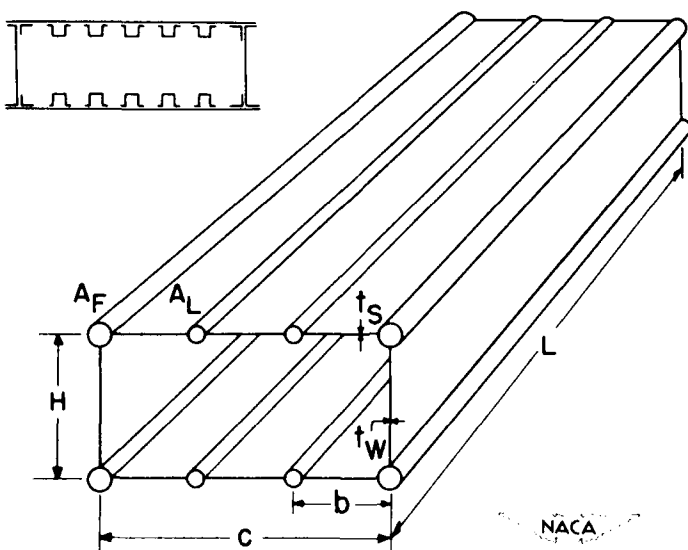


Figure 2.

CONFIDENTIAL  
UNCLASSIFIED

## IDEALIZATION FOR RECTANGULAR TUBE

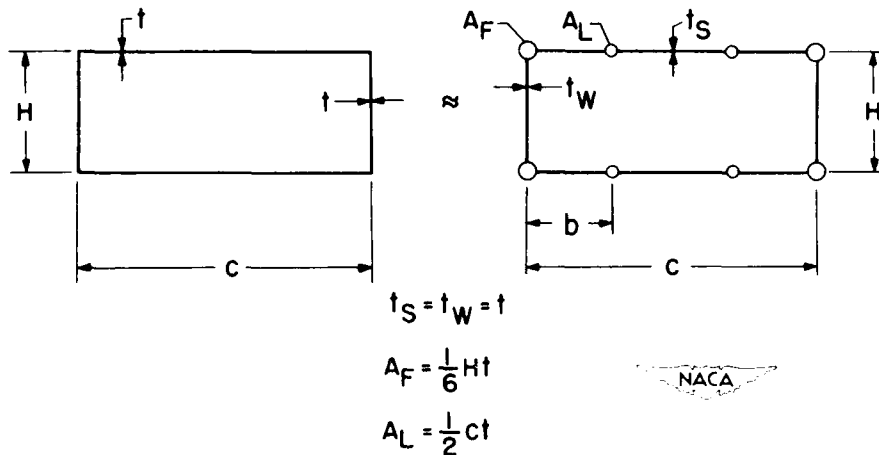


Figure 3.

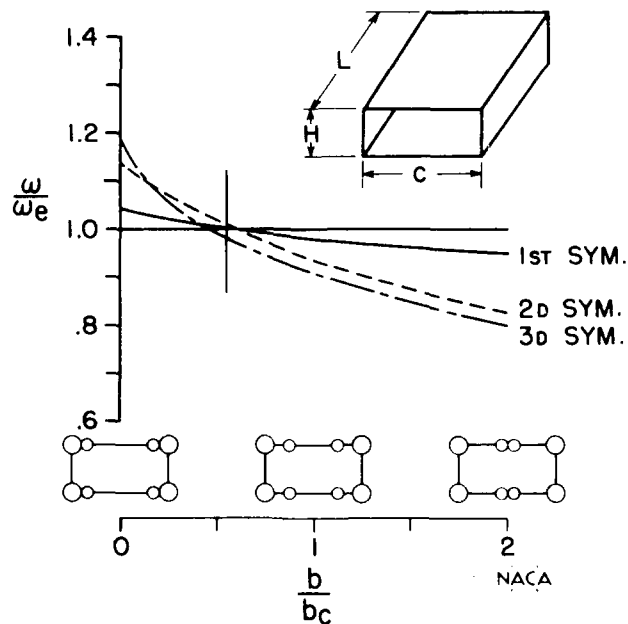
EFFECT OF STRINGER LOCATION ( $\frac{c}{H} = 3.6$ ,  $\frac{L}{c} = 6.0$ )

Figure 4.

CONFIDENTIAL  
UNCLASSIFIED

CONFIDENTIAL

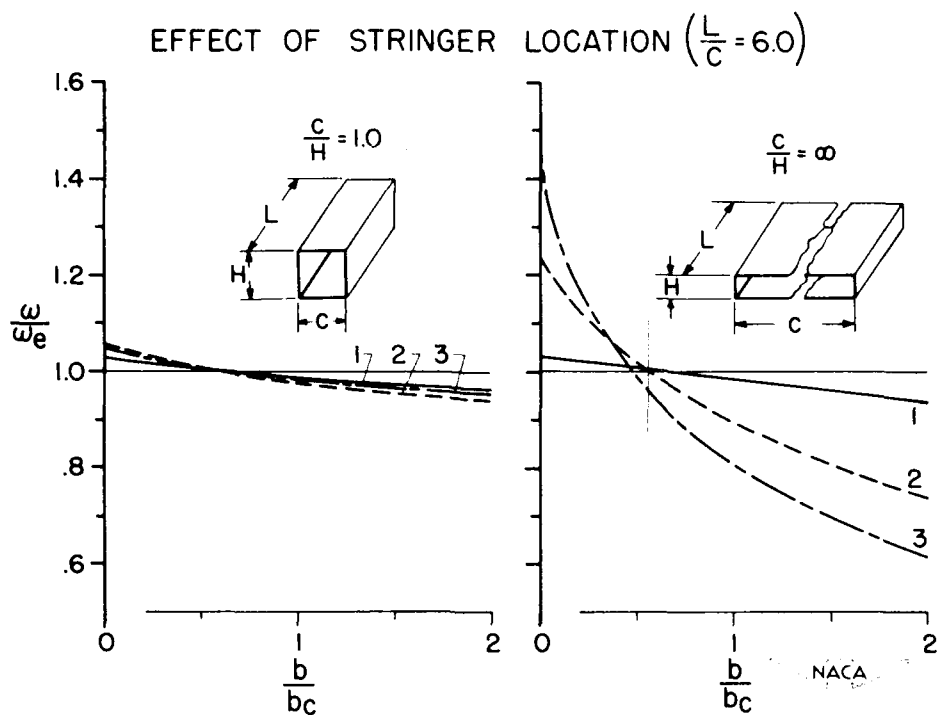


Figure 5.

## UNEQUAL EFFECTIVE SKIN THICKNESSES

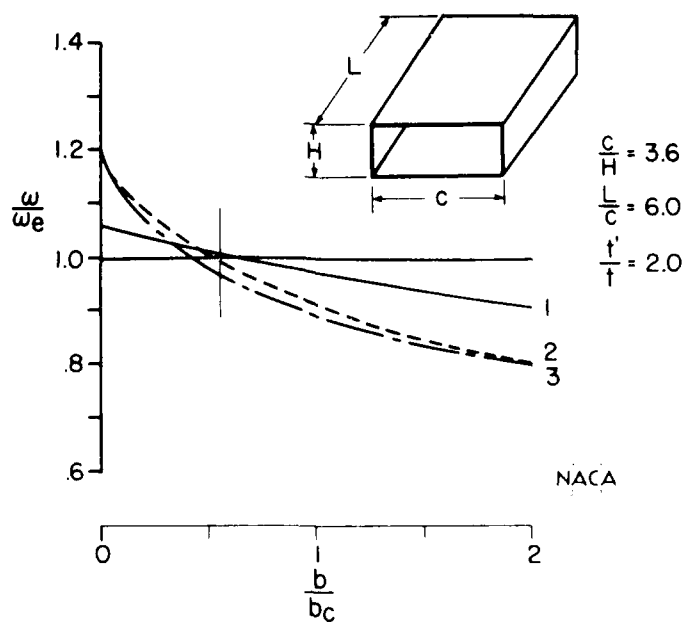


Figure 6.